

The XENON1T Spin-Independent WIMP Dark Matter Search Results and a Model  
to Characterize the Reduction of Electronegative Impurities in its 3.2 Tonne Liquid  
Xenon Detector

Zachary Schuyler Greene

Submitted in partial fulfillment of the  
requirements for the degree of  
Doctor of Philosophy  
in the Graduate School of Arts and Sciences

COLUMBIA UNIVERSITY

2018

© 2018  
Zachary Schuyler Greene  
All rights reserved

## ABSTRACT

The XENON1T Spin-Independent WIMP Dark Matter Search Results and a Model to Characterize the Reduction of Electronegative Impurities in its 3.2 Tonne Liquid Xenon Detector

Zachary Schuyler Greene

Over much of the last century evidence has been building for a new component of our universe that interacts primarily through gravitation. Known as cold dark matter, this non-luminous source is predicted to constitute 83% of matter and 26% of mass-energy in the universe. Experiments are currently searching for dark matter via its possible creation in particle colliders, annihilation in high-density regions of the universe, and interactions with Standard Model particles. So far dark matter has eluded direct detection so its composition and properties remain a mystery.

Weakly interacting massive particles (WIMPs) are hypothetical elementary particles that interact on the scale of the weak nuclear force. They naturally satisfy predictions from extensions of the Standard Model and are one of the most favored dark matter candidates. A number of direct detection experiments dedicated to observing their predicted interactions with atomic nuclei have been constructed over the last 25 years.

Liquid xenon dual phase time projection chambers (TPCs) have led the field for spin-independent WIMP searches at WIMP masses of  $> 10 \text{ GeV}/c^2$  for most of the last decade. XENON1T is the first tonne-scale TPC and with 278.8 days of dark matter data has the strictest limits on WIMP-nucleon interaction cross sections above WIMP masses of  $6 \text{ GeV}/c^2$ , with a minimum of  $4.1 \times 10^{-47} \text{ cm}^2$  at  $30 \text{ GeV}/c^2$ . XENON1T and the analysis of its result are discussed, with an emphasis on discriminating between background and WIMP-like events.

Interactions in liquid xenon produce light and charge that are observed in a TPC. These signals are attenuated by electronegative impurities such as  $\text{O}_2$  and  $\text{H}_2\text{O}$ , which adds uncertainty to our analysis and can decrease our sensitivity. Methods on measuring the charge loss are presented, followed by a physics model that describes the

behavior of the electronegative impurities over the lifetime of XENON1T.

# Contents

<b>Contents</b>	<b>i</b>
<b>List of Figures</b>	<b>vii</b>
<b>Acknowledgements</b>	<b>xxxvii</b>
<b>1 Dark Matter</b>	<b>1</b>
1.1 $\Lambda$ CDM Model . . . . .	2
1.2 Evidence for Dark Matter . . . . .	4
1.2.1 Dynamical Constraints . . . . .	4
1.2.2 Gravitational Lensing . . . . .	5
1.2.3 Cosmic Microwave Background . . . . .	8
1.3 Dark Matter Candidates . . . . .	10
1.3.1 Axions . . . . .	11
1.3.2 WIMPs . . . . .	12
1.3.3 Cold, Warm, or Hot . . . . .	13
1.3.4 Modified Gravity . . . . .	14
1.4 WIMP Detection Methods . . . . .	15
1.4.1 Colliders . . . . .	16
1.4.2 Indirect Detection . . . . .	17
1.4.3 Direct Detection . . . . .	18
1.5 Direct Detection Experiments . . . . .	20
1.5.1 Superheated Liquid Detectors . . . . .	22

1.5.2	Scintillation Crystals . . . . .	22
1.5.3	Germanium Detectors . . . . .	25
1.5.4	Cryogenic Bolometers . . . . .	25
1.5.5	Noble Gas Detectors . . . . .	26
<b>2</b>	<b>Liquid Xenon and Time Projection Chambers</b>	<b>29</b>
2.1	General Properties . . . . .	30
2.2	Signal Production . . . . .	32
2.2.1	Primary Scintillation . . . . .	33
2.2.2	Secondary Scintillation . . . . .	34
2.2.3	Stopping Power . . . . .	35
2.2.4	Recombination . . . . .	38
2.3	Interactions . . . . .	43
2.3.1	Photons . . . . .	45
2.3.2	$\beta$ -Decays . . . . .	46
2.3.3	Neutrinos . . . . .	47
2.3.4	Neutrons . . . . .	48
2.4	Electronic Recoils . . . . .	51
2.5	Nuclear Recoils . . . . .	52
2.6	Time Projection Chambers . . . . .	54
2.6.1	Working Principle . . . . .	54
2.6.2	Photomultiplier Tubes . . . . .	57
2.6.3	Signals . . . . .	60
2.6.3.1	Position Reconstruction . . . . .	60
2.6.3.2	Discrimination . . . . .	61
2.6.3.3	Energy Reconstruction . . . . .	64
<b>3</b>	<b>The XENON1T Experiment and Dark Matter Search</b>	<b>67</b>
3.1	The XENON1T Detector . . . . .	67
3.1.1	PMTs . . . . .	67
3.1.2	TPC . . . . .	75

3.1.3	Cryogenic System . . . . .	78
3.1.4	Purification . . . . .	82
3.1.5	ReStoX . . . . .	85
3.1.6	Krypton Distillation . . . . .	87
3.1.7	Water Shield . . . . .	89
3.1.8	Calibrations . . . . .	89
3.1.8.1	Internal . . . . .	91
3.1.8.2	External . . . . .	94
3.1.9	Data Acquisition . . . . .	94
3.1.10	Slow Control System . . . . .	99
3.2	Detector Characterization . . . . .	100
3.2.1	PMT Gain . . . . .	100
3.2.2	Light Collection Efficiency . . . . .	103
3.2.3	Position Reconstruction . . . . .	105
3.2.4	S2 <i>x-y</i> Correction . . . . .	106
3.2.5	Electron Lifetime . . . . .	107
3.2.6	Secondary Scintillation Gain . . . . .	111
3.2.7	Average Photon Detection and Charge Extraction Efficiencies	113
3.2.8	Combined Energy Spectrum . . . . .	114
3.2.9	Light and Charge Yield . . . . .	117
3.2.10	Bias and Smearing . . . . .	118
3.3	Backgrounds . . . . .	119
3.3.1	Electronic Recoils . . . . .	119
3.3.1.1	$^{85}\text{Kr}$ . . . . .	119
3.3.1.2	$^{222}\text{Rn}$ . . . . .	120
3.3.1.3	$^{136}\text{Xe}$ . . . . .	122
3.3.1.4	Solar Neutrinos . . . . .	123
3.3.2	Nuclear Recoils . . . . .	123
3.3.2.1	Radiogenic Neutrons . . . . .	123
3.3.2.2	Muon Induced Neutrons . . . . .	124

3.3.2.3	Neutrinos . . . . .	125
3.3.3	Surface Background . . . . .	125
3.3.4	Accidental Coincidence . . . . .	131
3.4	Dark Matter Results . . . . .	133
3.4.1	Electronic and Nuclear Recoil Calibrations . . . . .	133
3.4.2	Acceptances . . . . .	134
3.4.3	Findings . . . . .	135
<b>4</b>	<b>Electronic and Nuclear Recoil Calibrations</b>	<b>141</b>
4.1	Purpose of Calibrations . . . . .	142
4.2	Liquid Xenon TPC Modeling . . . . .	143
4.2.1	Electronic Recoils . . . . .	145
4.2.2	Nuclear Recoils . . . . .	147
4.2.3	Detector Effects . . . . .	152
4.2.4	Selection Criteria . . . . .	158
4.2.5	Backgrounds . . . . .	159
4.2.6	Statistical Inference . . . . .	159
4.2.7	Markov Chain Monte Carlo . . . . .	161
4.3	Results . . . . .	166
4.3.1	Detector Physics Model and Backgrounds . . . . .	166
4.3.2	Acceptances . . . . .	172
4.3.3	Light and Charge Yields . . . . .	174
<b>5</b>	<b>Purity and the Electron Lifetime</b>	<b>185</b>
5.1	Effects of Electronegative Impurities . . . . .	185
5.1.1	Photon Attenuation . . . . .	186
5.1.2	Charge Depletion . . . . .	187
5.2	Measuring the Electron Lifetime . . . . .	192
5.2.1	S2/S1 . . . . .	192
5.2.2	$\alpha$ -decays . . . . .	193
5.2.3	$^{83m}\text{Kr}$ . . . . .	196

5.2.4	$\gamma$ -rays . . . . .	198
5.2.5	$^{222}\text{Rn}$ vs. $^{83\text{m}}\text{Kr}$ . . . . .	202
5.3	Electron Lifetime Model . . . . .	204
5.3.1	Columbia Demonstrator . . . . .	205
5.3.2	Impurity Removal . . . . .	206
5.3.3	Vaporization and Condensation . . . . .	210
5.3.4	GXe Purification . . . . .	212
5.3.5	Outgassing and Leak . . . . .	215
5.3.5.1	Outgassing Sources . . . . .	216
5.3.5.2	Outgassing Model . . . . .	220
5.3.5.3	Time-Invariant Impurity Sources . . . . .	222
5.3.5.4	Leak Model . . . . .	224
5.3.6	Getter Defficiencies . . . . .	225
5.3.7	Impurity Spikes . . . . .	227
5.3.8	Hardware Upgrades . . . . .	231
5.3.9	Field Dependence . . . . .	233
5.4	Electron Lifetime Fit . . . . .	235
5.4.1	Statistical Inference . . . . .	235
5.4.2	Markov Chain Monte Carlo . . . . .	236
5.4.3	Results . . . . .	239
5.4.4	$^{83\text{m}}\text{Kr}$ Evolution . . . . .	243
	<b>Bibliography</b>	<b>247</b>



# List of Figures

1.1 Rotational velocity vs. radius (left) and image (right) of galaxy NGC 6503. In the left panel visible components are represented by the dashed line, gas by the dotted, and dark halo by the dashed-dotted. Image credit: (left) [3], (right) [5]. . . . .	5
1.2 Coma Cluster as seen by Sloan Digital Sky Survey and Spitzer Space Telescope. Image credit: [6]. . . . .	5
1.3 (left) A red galaxy distorts the light from a more distant blue galaxy to produce an Einstein “horseshoe” ring. (right) A diagram of strong lensing. The red source is bent by the blue lens, with the solid orange lines that connect to it representing the light’s true trajectory. The observer incorrectly views the source’s position as indicated by the dashed orange lines, and the image behind them. Image credit: (left) [7], (right) [8]. . .	6
1.4 X-ray emission from hot gas (pink) and mass centroids (blue) from gravitational lensing after collision of cluster 1E 0657-558. The white bar in the right panel represents 200 kpc at cluster. The separation between the colors provides evidence for Dark Matter. Image credit: (left) [10], [11], NASA/CXC/CfA/STScIMagellan/U.Arizona/; Lensing Map: NASA/STScI; ESO WFI; Magellan/U.Arizona/D.Clowe et al. (right) [11].	7
1.5 CMB as observed by Planck. Temperature deviations $\delta T/T \sim 10^{-5}$ . Image credit: [18]. . . . .	9

1.6	Angular power spectrum for CMB from Planck using the $\Lambda$ CDM model. Residuals are shown in the bottom panel. The model matches the data well at $l < 15$ and $l > 30$ . The horizontal axis changes from linear to logarithmic at $l = 29$ and is marked by the vertical dashed grey line. Image credit: [20]. . . . .	10
1.7	Axion-double photon coupling with respect to axion mass. The shaded regions have been excluded by different experiments. Invisible axion models KSVZ and DFSZ are drawn along the yellow band. Image credit: [27]. . .	12
1.8	Dark matter detection methods. High energy particle collisions may create dark matter that would result in missing transverse energy (bottom). Indirect detection looks for signatures (e.g. neutrinos, photons) of possible dark matter annihilation in the universe (top). Direct detection experiments search for signs of dark matter scattering off Standard Model particles (right). Image credit: [53]. . . . .	16
1.9	Diagram of a collision at the LHC. Image credit: [56]. . . . .	17
1.10	Energy channels. Image credit: [65]. . . . .	21
1.11	Orientation of the Earth’s rotation around the Sun. The change in alignment of the Earth’s and Sun’s velocities causes the amount of dark matter passing through the Earth to change, appearing as a “WIMP wind” with a 1-year period. The annual modulation should be present for any DM velocity distribution as long as it does not align with that of the Sun. Image credit: [72]. . . . .	21
1.12	Spin-dependent WIMP-proton cross-section 90% C.L. limits for PICO-60 $\text{C}_3\text{F}_8$ (thick blue, [73]), PICO-60 $\text{CF}_3\text{I}$ (thick red, [80]), PICO-2L (thick purple, [81]), PICASSO (green, [76]), SIMPLE (orange, [82]), and PandaX-II (cyan, [83]). Indirect limits from IceCube (dashed and dotted pink, [84]) and SuperK (dashed and dotted black, [85], [86]) for $b$ quark (dotted) and $\tau$ lepton (dashed) annihilation are shown. The shaded purple region is constrained parameter space for the minimal supersymmetric model from [87]. Image credit: [73]. . . . .	23

1.13 Residual event rate between 2-6 keV <sub>ee</sub> as measured by DAMA/NaI and DAMA/LIBRA. A fit of $A \cos[\omega(t - t_0)]$ where $t_0$ = June 2nd and $A$ is the best-fit amplitude is overlaid, with vertical dashed lines corresponding to expected maxima. For 14 years they have observed an annual modulation with $9.3\sigma$ . Claiming this modulation is due to dark matter is controversial, as they are unable to discriminate between different interaction types and a number of experiments have surpassed their sensitivity with no significant findings. Image credit: [90]. . . . .	24
1.14 Expected integral spectra for Xe (green), Ge (blue), Ar (red), and Ne (black) for spin-independent elastic scattering of 100 GeV/c <sup>2</sup> WIMPs with cross section $\sigma = 10^{-45}$ cm <sup>2</sup> per nucleon. The rates assume perfect energy resolution and are calculated using the Standard Halo Model. The dots correspond to average thresholds for each element. Image credit: [115]. .	26
1.15 Status of spin-independent WIMP cross section from 0.5-1000 GeV/c <sup>2</sup> before XENON1T run-combined analysis (Chap. 3). Regions of possible signals from DAMA/LIBRA (shaded green, [124]) and the silicon detector of CDMS II (shaded blue, [125]) are shown. Exclusion limits from PICO-60 (solid yellow line, [73]), DEAP-3600 (dashed purple $> 20$ GeV/c <sup>2</sup> , [126]), SuperCDMS (dashed blue, [127]), NEWS-G (dashed purple $< 20$ GeV/c <sup>2</sup> , [128]), CRESST (solid red, [129]), CDMSLite2 (solid blue, [130]), LUX (solid orange, [120]), PandaX-II (solid dark blue 2016 [83], dashed dark blue, 2017 [121]), XENON100 (solid green, [131]), and XENON1T First Results (dashed green, [132]) are plotted. Four typical super-symmetric (SUSY) models (CMSSM, NUHM1, NUHM2, and pMSSM10) with constraints from ATLAS Run 1 are shown (shaded yellow) for reference [133]. The cross section of neutrino coherent scattering is marked by the orange dashed line and shaded region. Image credit: [27]. . . . .	28
2.1 Phase diagram of xenon. Image credit: [134]. . . . .	30

2.2	Signal generation pathways for electronic and nuclear recoils. Describe paths of electrons. Image credit: [140]. . . . .	35
2.3	Field-dependent drift velocity for solid ( $-116^{\circ}\text{C}$ ) and liquid ( $-110^{\circ}\text{C}$ ) xenon. Image credit: [141]. . . . .	36
2.4	Mass stopping power for alphas (blue), $e^-$ (green), and protons (pink). Electronic (long dashed), nuclear (short dashed), and total (solid) stopping powers for each are shown. The electronic stopping power is more significant except for $e^-$ at $\gtrsim 15$ MeV. Data from [142]. . . . .	37
2.5	Electronic (top, $\gamma$ ) and nuclear (bottom, neutron) recoil tracks for 20 keV scatters. Excitons (red circles), ions (blue), and heat (grey) are marked along the track. The electronic recoil produces $\sim 20\times$ as many ions as excitons while for nuclear recoil they are roughly equal. Heat is only relevant in NRs and leads to signal quenching. The electronic recoil has a path of $\sim 1 \mu\text{m}$ while the much denser 10 nm of the NR compels higher recombination. Image credit: [140]. . . . .	39
2.6	Measurements of charge collected ( $q \propto 1 - r$ ) for LAr and LXe with respect to $E_d$ . Squares correspond to LXe and were measured with $\varsigma N_0 E = 0.15 \text{ kV cm}^{-1}$ . Triangles and circles are LAr and were measured at $\varsigma N_0 E = 0.84 \text{ kV cm}^{-1}$ . Curves are fits to data using the Thomas-Imdel box model [148]. . . . .	42
2.7	Scintillation yield as a function of LET in LXe. Open circles represent electrons, alpha particles, and fission fragments. Solid circles represent relativistic heavy particles. Open squares mark gamma-rays. Solid lines trace various fits to $\beta$ - $\gamma$ data from [147]. Image credit: [147]. . . . .	44

- 2.8 Mass attenuation coefficient and attenuation length for 1 keV to 100 MeV photons. Photoelectric absorption (red dashed), Compton scattering (green), coherent (Rayleigh and Thomson) scattering (purple), and pair production (blue) are shown in addition to the total (solid black). The discontinuity at  $\sim 5$  keV occurs just above the binding energy of the L-shell electrons and is due to an increase in photoelectric absorption. A similar process occurs for the K-shell at roughly 40 keV. Data from [160]. . . . . 46
- 2.9 Predicted integral spectra for xenon (green), germanium (blue), argon (red), and neon (black) for WIMP elastic scattering (left) and coherent neutrino-nucleus elastic scattering (right). The expected WIMP spectra are for  $m_\chi = 100$  GeV/c<sup>2</sup> with a cross section of  $10^{-45}$  cm<sup>2</sup> per nucleon, computed using [67] and assuming the standard halo model (Sec. 1.4.3). The circles mark characteristic thresholds. The expected CNNS integral rates are shown for 10 m from a 3 GW<sub>th</sub> nuclear reactor and the ISIS neutron spallation source [163] (fluxes of  $4 \times 10^{13}$  and  $10^7 \nu$  cm<sup>-2</sup> s<sup>-1</sup>, respectively). The majority of CNNS events occur below the thresholds of each material. Both plots assume perfect energy resolution. Image credit: [144]. . . . . 48
- 2.10 Spin-dependent recoil spectra for <sup>129</sup>Xe and <sup>131</sup>Xe for elastic and inelastic scatters. WIMP masses of 100 GeV/c<sup>2</sup> with cross section  $\sigma_n^0 = 10^{-40}$  cm<sup>2</sup> and 1000 GeV/c<sup>2</sup> with cross section  $\sigma_n^0 = 10^{-39}$  cm<sup>2</sup> are assumed. Elastic scattering is preferred across all recoil energies, though at larger  $E_R$  and  $m_\chi$  inelastic has a greater relative impact. Inelastic scattering drops to 0 at  $E_R = 0$  keV because conservation of momentum mandates that the nucleus cannot be excited while the atom remains at rest after an interaction. Image credit: [164]. . . . . 50
- 2.11 Fraction of nuclear recoil energy that produces excitons and ions  $L(E)$  in xenon using Lindhard's theory (green) [171]. . . . . 53

- 2.12 Spin-independent cross-section evolution for WIMPs with  $m_\chi \sim$  30-70 GeV/c<sup>2</sup>. Solid markers represent realized values while empty squares denote projected. Purple markers refer to germanium (Sec. 1.5.3) as well as CsI and NaI detectors (Sec. 1.5.2), orange represent cryogenic bolometers (Sec. 1.5.4), turquoise denotes single-phase noble liquid chambers, and green symbolizes dual-phase. For approximately the last decade LXe detectors have led the search and are projected to continue to do so. Image credit: [135]. . . . . 55
- 2.13 Attaching rate constant  $k_S$  for O<sub>2</sub>, N<sub>2</sub>O, and SF<sub>6</sub> with respect to electric field. At larger  $E_d$   $k_S$  increases for N<sub>2</sub>O and decreases for O<sub>2</sub> and SF<sub>6</sub>. Image credit: [175]. . . . . 57
- 2.14 Diagram of a PMT. An incident photon hits the photocathode and ejects an photoelectron. With each dynode the more  $e^-$  are freed, creating an amplified signal. Image credit: [177]. . . . . 58
- 2.15 Quantum efficiency with respect to wavelength for the Hamamatsu R11410 PMT, used in XENON1T. The peak efficiency occurs near the xenon scintillation wavelength 178 nm at  $\sim 35\%$ . Image credit: [179]. . . . . 59
- 2.16 Diagram of an interaction in a LXe TPC. The S1 is immediately observed by the PMTs. The  $e^-$  drift towards the top of the detector, where they are extracted across GXe, creating the S2. A typical waveform is shown at the bottom. The S2 is significantly larger than the S1 due to the amplification of electroluminescence. The relative intensity of light in the PMTs, or PMT hit pattern, can be used to determine the  $x$ - and  $y$ -coordinates of the interaction. Image credit: Lutz Althüser. . . . . 61
- 2.17 Position reconstruction for events in the second science run of XENON1T. Top PMT hit patterns are used to determine  $x$  and  $y$  while  $z = v_d t_d$ . The number of events drops dramatically at lower radii due to the self-shielding of LXe. . . . . 62

- 2.18 S2 (proportional) vs. S1 (prompt) for XENON1T calibration data. Electronic recoils are from the  $^{220}\text{Rn}$  decay chain as progeny  $^{212}\text{Pb}$  undergoes  $\beta$ -decay with an end-point energy of 569.9 keV (red). Nuclear recoils are from americium beryllium ( $^{241}\text{AmBe}$ ) (blue). S2/S1 is larger for electronic recoils, which enables discrimination between possible WIMPs and the ER background. . . . . 63
- 2.19 Field dependence of light ( $S(E)/S_0$ , red) and charge ( $Q(E)/Q_0$ , blue) yields.  $S_0$  is the light yield at zero field and  $Q_0$  is the charge yield at infinite field. Electronic recoils are shown as solid diamonds and are measured from  $^{57}\text{Co}$  122 keV  $\gamma$ -rays. 56.5 keV elastic neutron scatters from  $^{241}\text{AmBe}$  and  $^{252}\text{Cf}$  are marked by hollow squares. Nuclear recoils are marked by hollow squares and are from elastic 56.5 keV neutron scatters from  $^{241}\text{AmBe}$  and  $^{252}\text{Cf}$ . Solid circles represent  $^{210}\text{Po}$  5.3 MeV  $\alpha$ -decays. Sparser ionization densities precipitate stronger field-dependence for electronic scatters than for nuclear and alpha, signifying  $E_d$  can be tuned for improved ER-NR discrimination. Image credit: [183]. . . . . 65
- 3.1 Quantum efficiency of top (left) and bottom (right) PMT arrays. PMTs with the highest QE are placed in the center of the bottom array to maximize light collection while those with the lowest are placed in the outermost region of the top array. Image credit: [184]. . . . . 69
- 3.2 Top (left) and bottom (right) PMT arrays. Top PMTs are installed inside the diving bell above the anode and screening mesh in a radial distribution to minimize uncertainty in radial position reconstruction. Bottom PMTs are packed tightly below the cathode and a second screening mesh to maximize light collection. The screening meshes reduce interference between the anode (cathode) and top (bottom) PMT electric fields. Image credit: [184]. . . . . 69
- 3.3 Schematic of the Hamamatsu R11410-21 PMT. Image credit: [186]. . . . . 70

3.4 Afterpulses for a PMT from XENON1T. He <sup>+</sup> , CH <sub>4</sub> <sup>+</sup> , N <sub>2</sub> <sup>+</sup> , Ar <sup>+</sup> , and single- and double-ionized xenon are present and marked by red lines. The large fraction of Xe suggests a leak may be present, but to confirm Xe <sup>+</sup> and Xe <sup>++</sup> should be monitored. If a leak exists afterpulsing may eventually hit a critical value at which point the PMT can no longer operate reliably. The second, less-understood afterpulsing mechanism discussed in the text is visible as the roughly uniform distribution at $\sim$ 0.5 PE. . . . .	73
3.5 Schematic of the TPC. Image credit: [184]. . . . .	76
3.6 Finite element (COMSOL Multiphysics) simulation for the electric field field inside and around the TPC. Field and equipotential lines are shown. The voltages for the cathode, gate, and anode are -12, 0, and 4 kV, respectively, and are the settings for Science Run 0. The field is mostly uniform throughout the detector, which is important for limiting biases that come from recombination, impurity attachment, etc. Image credit: [184]. . . . .	77
3.7 Diagram of the cryostat. Image credit: [190]. . . . .	79
3.8 Layout of the cryogenic system. Three cooling towers - two with PTRs and one backup LN <sub>2</sub> - liquify GXe that returns to the TPC. LXe is carried from the bottom of the cryostat to the purification system (Sec. 3.1.4) through a heat exchanger system, while returning xenon flows into the bottom of the TPC with excess gas diffusing into the GXe. A portion of purified GXe is extracted before the heat exchanger and used to maintain pressure inside the diving bell. Connections with ReStoX (Sec. 3.1.5) are also shown. Image credit: [184]. . . . .	80
3.9 The various systems that handle xenon in the experiment: cryostat, cryogenic system, purification system, cryogenic distillation column, ReStoX, bottle racks, and gas analytics station. The water shield flange marks the boundary between the service building and the water Cherenkov detector. Image credit: [184]. . . . .	82

3.10 Layout of the purification system. The standard flow path during normal operations is highlighted in blue. Image credit: [184]. . . . .	84
3.11 ReStoX with major components labeled. Image credit: [184]. . . . .	86
3.12 Krypton distillation column. Inlet gas is cooled by a heat exchanger and input condensor as it passes to the package tube. Xenon gas that reaches the top of the column is liquified by the cryo-cooler and falls to the bottom, where it is heated by the reboiler. Krypton cannot condense due to its lower boiling point. The off-gas removes this high-krypton xenon, and high-purity xenon at the bottom of the column is returned to the other systems via the gas outlet. Image credit: [184]. . . . .	88
3.13 Arrival time of light to muon veto PMTs helps reconstruct the muon trajectory (black line). Image credit: [184]. . . . .	90
3.14 Photo from inside the water tank during commissioning. The muon veto PMTs can be seen around the perimeter covered in black bags to shield them from the light. The neck of the cryogenics system extends through the hole in the back from the service building to the cryostat, with the inner vessel wrapped in mylar visible beneath. . . . .	91
3.15 The XENON1T experiment with the water tank (left) and service building (right). A depiction of inside the water tank hangs on the outside. ReStoX (first floor), DAQ (second), and the cryogenic system (third) are visible in the service building. . . . .	92
3.16 Layout of the calibration source box in the purification system. Locations of $^{220}\text{Rn}$ , $^{83\text{m}}\text{Kr}$ , and $\text{CH}_3\text{T}$ are marked by dotted rectangles. Filters are installed to catch debris. Connections to and from the cryostat (turquoise) and pumps and getters (red) are shown. The vacuum pump (yellow) is used to evacuate the chamber before use. . . . .	93

- 3.17 Interior of the water tank. The belts highlighted in blue, maroon, and red, and the portion of the U-belt that extends underneath the cryostat is visible. Six wires - three extending from the roof to the cross and three from the cross to the cryostat - adjust the liquid level and are marked in dark yellow. The connection from the service building to the cathode is shown in bright yellow. The chain fixes the cryostat to the floor of the water tank to counter buoyancy forces. The large metal structure is the skeleton from the below-ground clean room used while installing the TPC. PMTs for the muon veto are attached to the water tank. Image credit: [184]. . . . . 95
- 3.18 Calibration belts around the cryostat. The I-belt and U-belt are shown in blue and red and have collimators present. The green cylinder is the neutron generator. Image credit: [184]. . . . . 96
- 3.19 Example of a waveform from XENON1T. The bottom panel shows hits (red circles) for each PMT channel with larger areas representing greater intensity. An S1 (76.2 PE) is visible at  $\sim 380 \mu\text{s}$ , marked by the blue circle in the middle panel. The shape of the S1 (left) and the light seen by the bottom PMT array (center right) are shown in the top panel. At  $\sim 1000 \mu\text{s}$  an S2 (2120.1 PE) occurs. Its shape (center left) and light distribution in the top PMT array (right) are shown in the top panel. The red cross marks the  $x$ - $y$  coordinates from the position reconstruction algorithm (Sec. 3.2.3). PMTs near the cross that are white are turned off. S2s are marked by green circles in the middle panel. Two smaller ( $< 40$  PE) S2s follow the primary S2 by  $\sim 150 \mu\text{s}$ . Image credit: XENON1T processor. . . . . 97
- 3.20 Schematic of the data acquisition. Image credit: [184]. . . . . 98
- 3.21  $^{83\text{m}}\text{Kr}$  32.2 and 9.4 keV events. Uncorrected and corrected S1s for both decays are shown in the top left and top right panels. The bottom left panel shows S1 and  $\text{S2}_b$  for the 32.2 keV, and bottom right shows cS1 and c $\text{S2}_b$ . . . . . 101

3.22 Single photoelectron spectrum of a Hamamatsu R11410 PMT. Image credit: [185] . . . . .	102
3.23 Gains for five PMTs monitored for SR0 and SR1. Means and $\pm 3\%$ are shown. All appear to be stable. . . . .	103
3.24 Light yield in slices of $z$ and $\phi$ from $^{83m}\text{Kr}$ 32.2 keV decay. . . . .	104
3.25 $x$ - $y$ position reconstruction resolution $\pm 1\sigma$ for SR1 as a function of number of electrons and $S2_b$ . At lower $n_e$ the resolution becomes worse due to the limited S2 scintillation. At $n_e \lesssim 100 e^-$ ( $S2_b \lesssim 1000$ PE) the position resolution becomes extremely poor. . . . .	106
3.26 Positions of background events for SR1. The 1 tonne fiducial mass used in the SR0-only analysis is defined by $-92.9 < z < -9$ cm, $r < 36.94$ cm and shown in green. The 1.3 tonne fiducial mass for this analysis has a more complicated shape, having $z_{\min} = -94$ cm, $z_{\max} = -8$ cm, and $r_{\max} = 42.84$ cm. It is outlined in blue ( $r_{\max}$ is shown in left panel). The active volume is marked in black. Events that appear outside the active volume are wall events that were not properly reconstructed. Those that appear below the cathode result extended drift times due to field inhomogeneities, which is why they become more exaggerated near the bottom corner of the TPC. . . . .	107
3.27 Relative S2 light yield for the top (left) and bottom (right) PMT arrays. Light from $e^-$ extracted across the GXe is concentrated in the small number of PMTs directly above in the top array. Large fluctuations in the top array are due primarily to dead PMTs while smaller are from variation in gains. A larger solid angle results in a more uniform distribution across $\phi$ in the bottom array. . . . .	108
3.28 Electron lifetime measurement using $^{83m}\text{Kr}$ . The red line represents the best-fit value of $671.18 \pm 4.14 \mu\text{s}$ and extends over the region the fit was computed. Details on the method of the fit are in Sec. 5.2.3. . . . .	109

3.29 Electron lifetime over SR0 and SR1. Markers represent measurements using the 32.2 keV decay of $^{83\text{m}}\text{Kr}$ . The green line and shaded region represent the median and credible region using the posterior of the fit. A hotspot in June forced a gate washing, where the gate was briefly lifted out of the LXe. It is suspected the LXe came in contact with parts of the TPC previously only in gas, injecting impurities into the liquid. The model is derived using $\alpha$ -decays from $^{222}\text{Rn}$ , $^{220}\text{Rn}$ , and $^{218}\text{Po}$ and is discussed in Sec. 5.3. . . . .	110
3.30 Single electron spectrum. Peaks correspond to integer numbers of $e^-$ and are visible and the spectrum is fit with Eq. 3.8 (blue). Individual peaks for for $1e^-$ (magenta), $2e^-$ (green), $3e^-$ (red), $4e^-$ (light purple), $5e^-$ (brown), and $6e^-$ (dark blue), along with the processor efficiency (red) are drawn. Best-fit values are listed in Tab. 3.3. . . . .	112
3.31 (left) Example of fitting cS1 and cS2 <sub>b</sub> from mono-energetic signals to find $g_1$ and $g_{2\text{b}}$ . (right) Evolution of $g_1$ and $g_{2\text{b}}$ over the first eight months of SR1. They are stable to within 0.4% and 1.4% ( $\pm 1\sigma$ credible intervals) respectively. . . . .	113
3.32 Combined energy spectrum for XENON1T. Regions between $55 < E < 140$ and $2350 < E < 2550$ keV are blinded for $^{124}\text{Xe}$ double-electron capture and the theorized $^{136}\text{Xe}$ neutrinoless double $\beta$ -decay. . . . .	116
3.33 Energy resolution $\sigma_E/E$ using for the monoenergetic interactions in Fig. 3.33. Data is from EXO Phase II (turquoise stars, [202]), PandaX (green squares, [203]), XENON100 (orange circles, [189]), and LUX (blue triangles, [204]). . . . .	116

3.34 Light and charge yield from mono-energetic signals. Note that unlike the light and charge yield discussed in Sec. 4.3.3 the units are PE keV <sup>-1</sup> (instead of ph keV <sup>-1</sup> and e <sup>-</sup> keV <sup>-1</sup> , respectively) and are calculated by dividing the cS1 (cS2 <sub>b</sub> ) by the energy of the interaction. Dashed lines correspond to the median yields. We can see the charge yield increasing slightly, which is possibly due to the growing rate of single e <sup>-</sup> from the gate climbing. Charge yield is not shown for <sup>222</sup> Rn because it is significantly lower than its electronic recoil counterparts at $6.47 \pm 0.10$ PE keV <sup>-1</sup> due to the fact it decays via $\alpha$ -emission. . . . .	117
3.35 S1 (left) and S2 (right) fractional bias and smearing. The S1 fractional bias (blue) at low values is negative but moves towards 0. The S2 fractional bias converges to roughly 0.05 at large values. The S1 and S2 fractional smearing (red) have a range of $\sim$ 0.2 at low values and tighten to within a few percent at large S1 and S2. . . . .	119
3.36 <sup>nat</sup> Kr/Xe concentration during Science Run 1. An average value of $0.66 \pm 0.11$ is found over the combined run analysis. SR0 is not shown as online krypton distillation (Sec. 3.1.6) decreased the concentration by more than a factor of 100. An increase of $0.693^{+0.114}_{-0.132}$ ppt y <sup>-1</sup> is observed for SR1. . .	120
3.37 <sup>222</sup> Rn (red), <sup>218</sup> Po (blue), and <sup>214</sup> BiPo (green) event rates before and after radon distillation. A decrease of $\sim$ 20% is observed. <sup>222</sup> Rn has a higher rate because its progenies may be left in a charged state and pulled outside the FV. . . . .	121
3.38 Predicted electronic recoil energy background spectrum in a 1 t fiducial volume from Monte Carlo. The left panel gives the ER expectation from 0 to $> 2614.5$ keV ( <sup>208</sup> Tl). The right panel examines the 0-250 keV range. Predictions can be compared to combined energy spectrum in Fig. 3.32. Image credit: [162]. . . . .	122

- 3.39 PTFE (left) and copper (right) differential yields for radiogenic neutrons per decay of parent nucleus. Dashed lines show the contributions of spontaneous fission only while solid show SF and ( $\alpha$ , n) reactions. Decays are shown for  $^{238}\text{U} \rightarrow ^{230}\text{Th}$  (black),  $^{235}\text{U} \rightarrow ^{207}\text{Pb}$  (red),  $^{226}\text{Ra} \rightarrow ^{206}\text{Pb}$  (green),  $^{232}\text{Th} \rightarrow ^{228}\text{Ac}$  (blue), and  $^{228}\text{Th} \rightarrow ^{208}\text{Pb}$  (pink). Image credit: [162]. . . . . 124
- 3.40 Neutron flux for WIPP, Soudan, Kamioka, Boulby, Gran Sasso, and Sudbury labs. Image credit: [207]. . . . . 124
- 3.41 Energy spectrum of the nuclear recoil background in the 1 t FV broken down by component. Image credit: [162]. . . . . 125
- 3.42 Decay chains for  $^{232}\text{Th}$  (left) and  $^{238}\text{U}$  (right). Image credit: [208], [209]. 127
- 3.43 Science Run 1 background events. Evens are plotted in  $r$ - $z$  ( $r^2$ - $z$ ) in the left panel. By selecting events inside the 1.3 t fiducial volume (blue) the background rate decreases by more than a factor of 200. Wall events are reconstructed symmetrically about the TPC boundary due to imperfect position reconstruction resolution (Sec. 3.2.3), with the exception of  $z \gtrsim 10$  cm where events from PMTs and other materials occur at smaller  $r$ .  $x$ - $y$  position are shown on the right with the colors corresponding to  $\log_{10}(\text{cS2}_b/\text{cS1})$ . Events in the center are the electronic recoil background. Events along the walls lose charge as they drift, resulting in an undercorrected  $\text{S2}_b$  and can leak into the nuclear recoil band ( $\log_{10}(\text{cS2}_b/\text{cS1}) \approx 1.25$ -2). The 1 t (green) and TPC boundary (black) are marked. The color bar is for the right panel only. . . . . 128
- 3.44 Expected surface background distribution in cS1-cS2<sub>b</sub>. Electrons from wall events attach to the PTFE as they drift, decreasing the S2 and potentially moving it into the NR band. Projections are shown for cS1 (top) and cS2<sub>b</sub> (right) for all events in blue, and between the NR median (red dashed line) and  $-2\sigma$  (solid black) in orange. The surface background's largest contribution in our ROI is predicted to be at  $\text{cS2}_b \lesssim 400$  PE,  $\text{cS1} \lesssim 20$  PE. 129

- 3.45  $^{222}\text{Rn}$  and  $^{218}\text{Po}$  decay rates ( $R_{222\text{Rn}}$ ,  $R_{218\text{Po}}$ ) from February-September 2017 for radial cuts of 29, 32, 36.94, and 39 cm. For all cuts  $R_{222\text{Rn}} > R_{218\text{Po}}$  and  $dR_{222\text{Rn}}/dt > dR_{218\text{Po}}/dt$ , though the latter converge at larger radii. The increase is caused by  $e^-$  buildup on the teflon that pushes events in the  $-\hat{r}$  direction. Residuals (in same units) show no bias from fits. . . . . 130
- 3.46 Decay rate increase (Fig. 3.45) dependence on  $r^2$ . Larger radii produce a greater rate increase due to their proximity to the wall. This helps estimate the scale of  $dR/dt$  when selecting the FV. . . . . 130
- 3.47 Expected accidental coincidence distribution in cS1-cS2<sub>b</sub> space for the 1.3 t FV. Isolated S1s and S2s are randomly coupled to imitate real events in the TPC. S1 and S2 corrections are applied and events that pass the cuts are plotted. Projections are shown for cS1 (top) and cS2<sub>b</sub> (right) for all events in blue, and between the NR median (red dashed line) and  $-2\sigma$  (solid black) in orange. The majority of events in the reference region are in cS1  $\lesssim 10$  PE, cS2<sub>b</sub>  $\lesssim 500$  PE. . . . . 132
- 3.48 Dark matter detection livetime. The green line displays the total run time for all dark matter data before livetime losses to DAQ insensitivity to events (7.8% SR0, 1.2% SR1), times when the muon veto was either deactivated or triggered coincidentally with the TPC (1.2%), and photo-ionization and delayed electron extraction due to high energy events in the TPC (4.4%). The blue line is the final exposure used in this analysis totaling 278.8 days. Shaded regions represent  $^{220}\text{Rn}$  (pink),  $^{83\text{m}}\text{Kr}$  (red),  $^{241}\text{AmBe}$  (aqua), NG (blue), and LED (grey) calibrations. The dashed black line marks the earthquake on January 18, 2017. . . . . 133

- 3.49 Nuclear recoil acceptances for WIMPs from this analysis. Processor efficiency is shown in green, processor efficiency with S1 and S2 cuts in blue, total acceptance across all  $cS2_b$  in black, and total acceptance inside the reference region in pink. Dashed and solid acceptance lines correspond to SR0 and SR1 acceptances, respectively. The shaded regions are the 68% credible interval for SR1. Spectra are shown for 10 (dashed), 50 (dotted), and 200 (dash-dotted)  $\text{GeV}/c^2$  WIMPs. The 10  $\text{GeV}/c^2$  WIMP has significantly less of its distribution overlap with the acceptance (true also with proper rates) than the 50 and 200  $\text{GeV}/c^2$  WIMPs, which will lead to a worse limit. . . . . [135](#)
- 3.50 Best-fit background and 200  $\text{GeV}/c^2$  WIMP predictions for combined run analysis assuming  $\sigma_{SI} = 4.7 \times 10^{-47} \text{ cm}^2$ . Dashed (solid) lines and hollow (filled) markers represent 1.3 t and 0.9 t volumes, respectively. The horizontal axis is the projection along  $cS2_b$  normalized by subtracting the electronic recoil mean  $\mu_{ER}$  and dividing by the  $1\sigma_{ER}$  quantile. Most backgrounds do not change significantly between the two volumes, with the exception of the surface. The best-fit WIMP signal is shown in purple. Shaded regions represent the 68% Poisson probability region for the expectation of total background. Image credit: [\[123\]](#). . . . . [137](#)
- 3.51 Dark matter search data spatial distributions. 1.3, 0.9, and 0.65 t masses are marked by solid pink, short-dashed blue, and long-dashed green, respectively, with the solid black line tracing the TPC boundary. Events inside the 1.3 fiducial mass are drawn as pie charts representing the relative probabilities of background and signal components using the best-fit  $\sigma_{SI} = 4.7 \times 10^{-47} \text{ cm}^2$  for a 200  $\text{GeV}/c^2$  WIMP. Grey dots represent events outside of the FV. Dark and light yellow regions illustrate the  $1\sigma$  and  $2\sigma$  radiogenic neutron background for SR1. Image credit: [\[123\]](#). . . . . [138](#)

- 3.52 Dark matter search data in cS1-cS2<sub>b</sub> (left) and  $r_{\text{rec}}^2$ -cS2<sub>b</sub> (right) parameter space for 1.3 t fiducial mass. Events are drawn as pie charts following Fig. 3.51. Dark (light) shaded regions correspond to  $1\sigma$  ( $2\sigma$ ) percentiles of ER (grey) and surface (blue) backgrounds. Purple dashed and solid lines correspond to  $1\sigma$  and  $2\sigma$  regions for a 200 GeV/c<sup>2</sup> WIMP. The red dotted lines (left) represent the signal region and the vertical lines (right) mark the 0.9 t (dashed blue) and 1.3 t (solid magenta) fiducial masses. The vertical shaded regions are outside the region of interest. The grey lines (left) display iso-energy contours in keV<sub>nr</sub>. Image credit: [123]. . . . . 139
- 3.53 90% confidence level upper limit on spin-independent WIMP cross section from this analysis (black line) with  $1\sigma$  (green) and  $2\sigma$  (yellow) sensitivity bands. Previous LUX [120] and PandaX-II [121] results are plotted in red and blue for comparison. The inset shows these limits and  $\pm 1\sigma$  bands normalized to the median sensitivity of this analysis as well as the normalized median of the PandaX-II sensitivity band (dotted blue line). Image credit: [123]. . . . . 140
- 4.1 Total background model from First Results with 50, 90, and 99% contours for 6 (left), 50 (center), and 1000 (right) GeV/c<sup>2</sup> WIMPs. The bright yellow region is the electronic recoil band, which was fit using a similar method to this section. Accidental coincidence is visible as the horizontal strip around cS2<sub>b</sub> = 150 PE. The expected signal region changes with WIMP mass. . . . . 143

- 4.2 Steps for fitting electronic and nuclear recoil bands. The signal (NR) model, background (ER) model, and additional inputs (e.g. detector model, S2 threshold, AC) (red) make up the parameters (yellow) in the fit. Each parameter is constrained by its prior distribution (yellow). Parameters convert truth MC (grey) to cS1 and cS2<sub>b</sub> in the fast MC (yellow), which is then binned. Data (pink) from calibrations is binned and the likelihood (aqua) is computed using the histograms and prior distributions. A Markov Chain Monte Carlo (MCMC) (aqua) calculates the values of the parameters for the next iteration. The posterior is shown in green. Blue arrows represent steps that are only done once. . . . . 145
- 4.3 Simulated neutron energy spectra in fusion region of the NG (red dashed line) and at the pulse shape discriminator during calibration before installation at LNGS (blue shaded region). Deconvolution of data from calibration (black solid line) is also shown. Spectra are normalized by the 2.2-2.7 MeV range. Image credit: [182]. . . . . 148
- 4.4 Positions of events from SR1  $^{241}\text{AmBe}$  calibration. Events are clustered in the region of the detector closest to the  $^{241}\text{AmBe}$  source. The black line marks the 1 t fiducial volume. Aside from the higher ER background, the SR0 distribution looks similar since the source was placed in the same location inside the water tank. . . . . 149
- 4.5 Positions of events from SR1 neutron generator calibration. Events are densely distributed in the region of the TPC closest to the NG source. The black line shows the 1 t fiducial volume. . . . . 149

4.6 S1- and S2 <sub>b</sub> -dependent detector parameter 68% credible intervals for SR0 (left) and SR1 (right). Processor efficiency (red) is plotted with respect to the S1 axis but in units of hits. Filter boxes were installed on the DAQ between the SR0 <sup>241</sup> AmBe calibration and dark matter data taking so separate processor efficiencies and S1 and S2 biases and smearings are used (shown as transparent in same color). The filter boxes led to improvement, particularly for the processor efficiency and S1 bias and smearing. The uncertainty on the processor efficiency also decreased. . . . .	155
4.7 Proposed stretch move update step for walker $\boldsymbol{\theta}_i$ (blue) with the Affine-Invariant Ensemble Sampler MCMC in two dimensions. The proposed state $\boldsymbol{\theta}_p$ (red) uses the difference between $\boldsymbol{\theta}_i$ and a randomly selected walker $\boldsymbol{\theta}_j^{(1)}$ (green) from $S^{(1)}$ and a scale factor $z$ . Additional walkers from $S^{(0)}$ (light blue) and $S^{(1)}$ (light green) are shown. . . . .	163
4.8 Gelman-Rubin test statistic for the electronic and nuclear recoil band fitting. . . . .	166
4.9 cS1 for SR0 <sup>220</sup> Rn calibration. The median and 68% credible region from the posterior are shown as the solid lines and shaded regions, respectively, and matches the data well. Aside from <sup>220</sup> Rn, the only contributor to data is accidental coincidence, which has a small contribution and is visible in pink at the bottom. The sum of AC and <sup>220</sup> Rn is shown in blue. . . . .	167
4.10 cS1 for SR1 <sup>220</sup> Rn calibration. The median and 68% credible region match the data well. AC is shown in pink at the bottom of the plot. The sum of <sup>220</sup> Rn and AC are shown in blue. . . . .	167
4.11 cS2 <sub>b</sub> for SR0 <sup>220</sup> Rn data with median and 68% credible interval in slices of cS1. The model matches the data well, with the possible exception of the $50 < \text{cS1} < 70$ PE slice where the model may predict slightly lower cS2 <sub>b</sub> , but limited statistics make it difficult to tell. . . . .	168

4.12 cS2 <sub>b</sub> for SR1 <sup>220</sup> Rn calibration in slices of cS1. The results from the band fitting match the data well, though in the $0 < \text{cS1} < 10$ PE slice the data may follow a slightly narrower distribution, and the $50 < \text{cS1} < 70$ PE slice, which similar to the SR0 results (Fig. 4.11) suggests the model predicts lower cS2 <sub>b</sub> . . . . .	170
4.13 cS1- $\log_{10}(\text{cS2}_b/\text{cS1})$ distribution for the SR0 <sup>220</sup> Rn calibration. Electronic (red) and nuclear (blue) recoil (calculated using SR0 <sup>241</sup> AmBe fit) medians and $\pm 2\sigma$ are marked in solid and dashed lines. Accidental coincidence is shown in the bottom panel. . . . .	171
4.14 cS1- $\log_{10}(\text{cS2}_b/\text{cS1})$ distribution for the SR1 <sup>220</sup> Rn calibration. Electronic recoil median and $\pm 2\sigma$ are shown as red solid and dashed lines. Nuclear recoil are computed using the SR1 <sup>241</sup> AmBe calibration fit and shown in blue. . . . .	172
4.15 cS1 for SR0 <sup>241</sup> AmBe calibration. The total number of events (blue) agrees reasonably well with the data. Single- (red) and multiple-scatter (green) neutrons are shown. Multiple-scatters make up a larger fraction of events at low cS1. Electronic recoils (gold) make up a decent fraction of the total events, especially at $\text{cS1} \gtrsim 50$ PE where they are $> 30\%$ . Accidental coincidence is barely visible along the bottom and is expected to be responsible for $\sim 2$ events. . . . .	173
4.16 cS1 for SR1 <sup>241</sup> AmBe calibration. The total number of events from the band fitting (blue) is compared with data. Single- (red) and multiple-scatter (green) nuclear recoils are shown. The fraction of multiple-scatter events increases at low cS1. The low-ER background (gold) and AC (pink) contribute $\sim 60$ and $\lesssim 2$ events, respectively. . . . .	174
4.17 cS2 <sub>b</sub> in slices of cS1 for SR0 <sup>241</sup> AmBe data. The band fitting results (blue) match the data nicely. The ratio of multi- (green) to single-scatter (red) neutrons is higher at low cS2 <sub>b</sub> . The electronic recoil band (gold) is easily visible. AC (pink) is too low to observe. . . . .	175

- 4.18 cS2<sub>b</sub> for SR1  $^{241}\text{AmBe}$  calibration data in slices of cS1. The median and 68% credible interval of the fit (blue) is compared to the data. Single-scatter (red) and multiple-scatter (green) nuclear recoils, ER (gold), and AC (pink) are shown. The ER background contributes only  $\sim 3\%$  of all events. AC is too small to be visible. . . . . 176
- 4.19 cS1- $\log_{10}(cS2_b/cS1)$  distribution for the SR0  $^{241}\text{AmBe}$  calibration. The top panel shows the total while the rest show the contributions from different components normalized with respect to the total. Medians and  $\pm 2\sigma$  from electronic (red) and nuclear (blue) recoil bands are shown as solid and dashed lines. The ER lines are taken from SR0 ER band fit. . . . . 177
- 4.20 cS1- $\log_{10}(cS2_b/cS1)$  distribution for the SR1  $^{241}\text{AmBe}$  calibration. The total is shown in the top panel with the separate contributors displayed below. The electronic recoil band median and  $\pm 2\sigma$  are derived from the SR1 ER band from the fit. Nuclear recoil lines are blue. . . . . 178
- 4.21 cS1 for NG calibration. The fit agrees with the data. Single-scatter (red) and multiple-scatter (green) neutrons are shown. ER background (gold) is responsible for  $\lesssim 25$  events. Accidental coincidence (pink) is too small to be observed but makes up 7-10 events. . . . . 179
- 4.22 cS2<sub>b</sub> for SR1 NG calibration in slices of cS1. The fit (blue) matches the data nicely, though in the  $10 < cS1 < 20$  PE slice the model predicts a lower cS2<sub>b</sub>. Similar to  $^{241}\text{AmBe}$  the ratio of multi- (green) to single-scatter neutrons (red) is larger at low cS2<sub>b</sub>. ER background (gold) and AC (pink) have too few events to be visible. . . . . 180
- 4.23 cS1- $\log_{10}(cS2_b/cS1)$  distribution for the SR1 neutron generator calibration band fitting. Medians and  $\pm 2\sigma$  for the electronic (red) and nuclear (blue) recoil bands are shown as solid and dashed lines, respectively. Electronic recoil lines are taken from the SR1 ER model from the fit. . . . . 181

- 4.24 Fraction of nuclear recoil events in SR1  $^{241}\text{AmBe}$  calibration that result from multiple scatters. In the main panel red and blue lines mark the median and  $\pm 2\sigma$  for single and multiple scatters, respectively (at  $cS1 > 60$  PE the number of multiple scatter events is too low for calculation). Multiple scatters will be pushed to smaller  $\log_{10}(cS2_b/cS1)$ . The effect becomes more dramatic at lower  $\log_{10}(cS2_b/cS1)$  due to a couple effects. The first is a larger number of scatters will lead to a smaller  $cS2_b/cS1$ . Additionally the S1s are corrected by the LCE map according the position of the largest scatter, so S1s in a higher-LCE region would be over-corrected. This also leads to the magnitude of the dip between SS and MS percentiles extending to higher  $cS1$  at lower  $\log_{10}(cS2_b/cS1)$ . At sufficiently high  $cS1$  ( $\gtrsim 40$  PE) the  $cS2_b$  must be large enough that S1s from other scatters do not have much effect, since a secondary scatter with a large S1 should also contain a large  $S2_b$  and fail the multiple scatter cut. The top and right panels are integrated over the main panel and show the multiple scatter fraction with respect to  $cS1$  (top) and  $\log_{10}(cS2_b/cS1)$  (right). . . . . 182
- 4.25 Nuclear recoil energy-dependent efficiencies calculated using 400 samples randomly drawn from the posterior of the band fit. Best-fit values are shown for S1 (pink) and S2 (light blue) selection, S2 threshold (green), processor (red), and  $cS1$  threshold (dark blue) efficiencies. Dashed lines represent medians from SR0 while solid lines and shaded regions show SR1 medians and 68% credible regions. . . . . 183
- 4.26 Nuclear recoil energy-dependent efficiencies for WIMPs from this analysis. Processor (green), processor with S1 and S2 selection (blue), total ignoring the reference region (black), and total in the reference region (pink) efficiencies are shown. Dashed and solid acceptance lines correspond to SR0 and SR1 acceptances, respectively. The shaded regions are the 68% credible interval for SR1. Spectra are shown for 10 (dashed), 50 (dotted), and 200 (dash-dotted)  $\text{GeV}/c^2$  WIMPs in purple. . . . . 183

- 4.27 Photon and charge yields electronic recoils. This result is shown in blue at  $82 \text{ V cm}^{-1}$  (SR1) and its extrapolation to  $200 \text{ V cm}^{-1}$  is shown in green. The purple band represents XENON100 tritium calibration [198], red triangles and orange squares represent LUX  $^{127}\text{Xe}$  [221] and tritium [197], respectively, and grey triangles represent PIXeY  $^{37}\text{Ar}$  [222]. The black line shows the NEST v2.0 beta at  $82 \text{ V cm}^{-1}$  prediction. This analysis has  $> 10\%$  acceptance for events with energies higher than the dashed blue line (Sec. 4.3.2). . . . . 184
- 4.28 Photon and charge yields for nuclear recoils. This result at  $82 \text{ V cm}^{-1}$  is shown in blue. It is not an independent measurement since the model is constrained by previous work.  $L_y$  measurements are represented by purple triangles [223], grey triangles [224], light green triangles [225], and magenta triangles [226].  $Q_y$  are represented by purple diamonds [183], red band [227], black squares [228] and light blue triangles [226].  $L_y$  and  $Q_y$  from the same measurement are shown by orange squares [229]. The NEST v1.0 model was used to constrain our fit and is shown as the green band [173]. This analysis has  $> 10\%$  acceptance for events with energies higher than indicated by the dashed blue line (Sec. 4.3.2). . . . . 184
- 5.1 Absorption coefficient for photons at 1 ppm  $\text{H}_2\text{O}$  vapor (solid red) and  $\text{O}_2$  (dashed green). The Xe scintillation spectrum is overlaid for comparison (dashed blue).  $\text{H}_2\text{O}$  impacts Xe scintillation considerably more than  $\text{O}_2$  when at the same concentration. Image credit: [233],  $\text{H}_2\text{O}$  data from [234]. 187
- 5.2 Fraction of initial intensity of xenon scintillation with distance for various concentrations of  $\text{H}_2\text{O}$  (left) and  $\text{O}_2$  (right). Image credit: [233]. . . . . 188
- 5.3 Drift velocity (here defined as  $W$ ) dependence on reduced electric field  $E_d/N$  where  $N$  is the number of molecules per volume. Points are from experimental data [236]–[239] and curves are from calculations.  $1 \text{ Td} = 10^{-17} \text{ V cm}^2$ . LXe has a higher drift velocity than GXe at  $E_d/N \lesssim 1 \text{ Td}$  ( $1 \text{ Td} = 10^{-17} \text{ V cm}^2$ ). Image credit: [240]. . . . . 189

- 5.4 Temperature-dependent drift mobility for holes in LXe. Data is shown as empty triangles. A fit using Eq. 5.6 is shown as the solid line. Image credit: [246] (redrawn from [241]). . . . . 191
- 5.5 cS1 (left) and  $\alpha$ -corrected cS1 (right) dependence on  $z$ . The large  $\alpha$ -decay S1s deep in the TPC saturate the bottom PMTs, causing an under-corrected cS1, which results in the distortion seen in the left panel. Near the top ( $z \gtrsim -5$  cm) a similar effect is observed from top PMT saturation. The distortion is corrected in the right panel where the effect is much less significant. The red and blue boxes highlight the events selected to calculate  $\tau_e$ . The colors of data markers correspond to S2<sub>b</sub>. . . . . 195
- 5.6 Electron lifetime measurements using <sup>222</sup>Rn (left) and <sup>218</sup>Po (right) from October 29-31, 2017. The red and blue lines correspond to <sup>222</sup>Rn and <sup>218</sup>Po, respectively, and are drawn in the drift time region that was used for the fit (see text for event selection). They are each drawn in both panels to show the S2<sub>b</sub> overlap, highlighting the need for the  $\alpha$ -corrected cS1 cut. The pink dashed lines mark the boundaries derived from the preliminary fit outside of which events were not considered for the final fit. The electron lifetime measurements agree within uncertainty. . . . . 196
- 5.7 cS1s for <sup>83m</sup>Kr during final Science Run 1 calibration (left). The S1 delay time cut is remarkably efficient at selecting <sup>83m</sup>Kr and rejecting background. S1 delay time cut dependence of events from 500-2000 ns (right). A fit with an exponential gives a half-life of  $158 \pm 12.6$  ns, which is in agreement with the accepted value of 154.4 ns. . . . . 197
- 5.8 Electron lifetime measurement using <sup>83m</sup>Kr from January 23-25, 2018. . . 198
- 5.9 cS1 vs. cS2<sub>b</sub> for  $r_{\text{rec}} < 36.94$  cm,  $-6 < z < -85$  cm for dark matter search data from April 1-7, 2017 following the SR1 <sup>241</sup>AmBe calibration. <sup>129m</sup>Xe and <sup>131m</sup>Xe photopeaks are fit with a 2-dimensional gaussian to reject other background. The red contours mark the  $4\sigma$  lines. . . . . 199

- 5.10  $^{129\text{m}}\text{Xe}$  and  $^{131\text{m}}\text{Xe}$  events following the SR0  $^{241}\text{AmBe}$  calibration. Data is omitted during  $^{83\text{m}}\text{Kr}$  and  $^{220}\text{Rn}$  calibrations. Fits using  $R(t) = R_0 \exp(-t/t_{1/2}) + C$  give half-lives of  $8.66 \pm 0.26$  and  $11.51 \pm 0.43$  days, respectively, which match the known values of 8.88 and 11.93 days. . . . . 200
- 5.11 Electron lifetimes for  $^{131\text{m}}\text{Xe}$  (left) and  $^{129\text{m}}\text{Xe}$  (right) for April 1-7, 2017 (same as in Fig. 5.9). The red lines mark the region of the fit -  $70 < t_d < 710 \mu\text{s}$  and  $100 < t_d < 710 \mu\text{s}$  for  $^{131\text{m}}\text{Xe}$  and  $^{129\text{m}}\text{Xe}$ , respectively. The change in fit boundary is to remove higher energy events from detector materials that reach deeper inside the LXe, visible at  $t_d \lesssim 50 \mu\text{s}$  in the right panel. The electron lifetimes agree with one another. . . . . 200
- 5.12 Electron lifetime measurements from S2/S1 (blue circles), combined  $^{222}\text{Rn}$ - $^{218}\text{Po}$  (green triangles),  $^{222}\text{Rn}$  (yellow triangles),  $^{220}\text{Rn}$  (red triangles),  $^{218}\text{Po}$  (turquoise triangles), and  $^{83\text{m}}\text{Kr}$  (black circles).  $^{83\text{m}}\text{Kr}$  (orange shaded),  $^{220}\text{Rn}$  (red),  $^{241}\text{AmBe}$  (green), and NG (blue) calibrations are shown as highlighted regions. Events that disrupt the electron lifetime evolution are marked by numbers at the top of each panel. . . . . 201
- 5.13 Relative electron yield with respect to  $[-90 \leq z \leq -85 \text{ cm}, r < 36.94 \text{ cm}]$  for  $^{129\text{m}}\text{Xe}$  (left) and  $^{222}\text{Rn}$  (right) for  $V_c = 8 \text{ kV}$  ( $\sim 80 \text{ V cm}^{-1}$ ) inside the 1T FV (black line). A decline in yield in the  $-z$  direction leads to the incorrect observation that the electron lifetime is lower than its true value. The imbalance between the top and bottom of the TPC is  $\gtrsim 2\times$  larger for  $^{222}\text{Rn}$ , causing its  $\tau_e$  to appear lower than its  $\gamma$  counterparts. . . . . 203



- 5.18 Heater power  $\dot{Q}_H$  (red) and purification flow (blue) from May 2-8, 2016. On May 4th circulation is stopped, decreasing the heat load in the GXe.  $\dot{Q}_H$  rises to  $\sim 120$  W, so to satisfy Eq. 5.16  $\dot{Q}_{\text{GXe}} \sim 140$  W. When purification resumes on May 6th there is a sharp drop in  $\dot{Q}_H$  while the heat exchanger and other materials equilibrate before returning to a stable value. . . . .  
[211](#)
- 5.19  $\dot{Q}_H$  over the lifetime of XENON1T. Sudden spikes and sporadic behavior result from compensating for rapid increases or decreases in heat from the GXe. Long-term downward trend is caused by the PTR cooling power decreasing over time. The corrected trend used in the fit is shown. . . . .  
[213](#)
- 5.20 Electron lifetime using LXe with (white region) and without (blue) GXe circulation for the Demonstrator. The electron lifetime more than doubles in the first iteration over a roughly 10-day span. A period follows with only LXe purification, but is too short to observe much decrease. Upon re-initiating GXe flow the lifetime drops a bit - possibly due to trapped impurities in the GXe tubing - but then begins to climb again. The final block reveals the electron lifetime does decrease with LXe-only circulation. Longer periods with and without GXe purification are needed for better assessment. Image credit: [255]. . . . .  
[214](#)
- 5.21 Purification of only xenon gas from August 22 - September 2, 2016, marked by green dashed lines. Electron lifetime measurements are from  $^{222}\text{Rn}$ - $^{218}\text{Po}$  combined data. The purpose of the operation was to study the exchange of impurities between the gas and liquid, which depends on vaporization/condensation and outgassing. . . . .  
[215](#)

- 5.22 Outgassing rate  $q$  as a function of time for outdiffusion. A sample at temperature  $T_1$  is heated to  $T_2$  at point  $A$ . Because the gas concentration in the sample remains unchanged during this process (assume quickly heated) the outgassing at  $C$  is equivalent to  $B$  (diagonal dashed lines represent constant concentration). From  $C$   $q$  quickly joins the  $T_2$  curve, which begins its exponential descent (Eq. 5.22) earlier. At  $D$  the sample is restored to  $T_1$  where it returns to its original curve at  $E$  but at an earlier time  $F$ . Image credit: [256]. . . . . 218
- 5.23 Relative temperature variations for sensors on the  $\text{LN}_2$  coldfinger (blue), in the unpowered cooling tower (black), and just below the LXe surface (pink). The variation is defined as the  $(T - T_{\text{med}})/T_{\text{med}}$  where  $T_{\text{med}}$  is the median temperature across all data. The  $\text{LN}_2$  coldfinger shows the most volatility. The GXe changes by  $\sim 2\%$  in the first several months of operation but is since stable within 1%. The LXe decreases by roughly 1% in the first couple months as adjustments to the detector were made. Since then its variation is  $\ll 1\%$ . . . . . 222
- 5.24 Periods of getter defficiencies for November 26 - December 5, 2016 (left) and October 25-30, 2017 (right).  $^{222}\text{Rn}$ - $^{218}\text{Po}$  combined (green),  $^{222}\text{Rn}$ , (yellow triangles),  $^{218}\text{Po}$  (turquoise), and  $^{212}\text{Bi}$  (red) electron lifetimes are shown.  $^{83\text{m}}\text{Kr}$  (shaded orange),  $^{220}\text{Rn}$  (purple), and  $^{241}\text{AmBe}$  (green) calibrations are highlighted. The cause of the first defficiency in 2016 is not understood, as detector parameters are stable during this period. The getter defficiency in October 2017 is likely caused by an excess of impurities that were released from the  $^{220}\text{Rn}$  calibration. Each resulted in a total drop of  $\lesssim 10 \mu\text{s}$ . The power glitch on November 21, 2016 causes a sudden purity decrease (Sec. 5.3.7). . . . . 226
- 5.25 Installation of the third QDrive in the purification system from September 29 - October 5, 2016. Lifetimes are measured with  $^{222}\text{Rn}$ - $^{218}\text{Po}$  combined data (green).  $^{220}\text{Rn}$  and  $^{241}\text{AmBe}$  calibrations are shaded purple and turquoise, respectively. . . . . 232

5.26 Electron lifetime measurements following the end of SR1. Initial drops in purity are due to a power disruption, blackout, and gate washings. Subsequent changes are caused by upgrades to the purification system. . .	232
5.27 $^{222}\text{Rn}$ concentration before and after the magnetic pump upgrade. A drop from $12.5 \pm 0.2$ to $6.8 \pm 0.2 \mu\text{Bq kg}^{-1}$ is observed. Preliminary plot. . . .	233
5.28 Field-dependent attachment rates for $\text{O}_2$ , $\text{N}_2\text{O}$ , and $\text{SF}_6$ . Because is analysis uses $\text{O}_2$ to model all impurities the attachment rate will decrease with electric field. Image credit: [175]. . . . .	234
5.29 Examples of $\boldsymbol{\theta}_p$ using DEMC (left) and DEMC snooker update (right) in two dimensions. Example of normal DEMC proposal (item 3a). The difference between two randomly selected walkers $\boldsymbol{\theta}_{r_1}, \boldsymbol{\theta}_{r_2}$ is used to propose an update to the $i^{\text{th}}$ walker using Eq. 5.36 in two dimensions. $\boldsymbol{\theta}_p$ and $\boldsymbol{\theta}_{r_1} - \boldsymbol{\theta}_{r_2}$ are at a slight tilt with respect one another due to $\mathbf{z}$ . Example of DEMC snooker update proposal (item 3b). An update is proposed using difference of projections of $\boldsymbol{\theta}_{r_1}, \boldsymbol{\theta}_{r_2}$ along $\boldsymbol{\theta}_{r_3} - \boldsymbol{\theta}_i$ where $\boldsymbol{\theta}_{r_3}$ is a third randomly drawn walker using Eq. 5.40. . . . .	239
5.30 Electron lifetime model and data over the lifetime of XENON1T. Electron lifetimes calculated via the S2/S1 method (blue circle), $^{222}\text{Rn}$ - $^{218}\text{Po}$ (green triangle), $^{212}\text{Bi}$ (red triangle), $^{218}\text{Po}$ (turquoise triangle), $^{222}\text{Rn}$ (yellow triangle), and $^{83\text{m}}\text{Kr}$ (black circle) are shown. The best-fit trend (red line) and 68% credible region (shaded blue) are overlaid for comparison. Dashed lines correspond to events that affected the evolution of the electron lifetime.	244
5.31 Combined energy spectrum over $z$ for 0-1500 keV using the $\alpha$ -decay (top) and $^{83\text{m}}\text{Kr}$ (bottom) S2 <sub>b</sub> corrections. For the $\alpha$ -corrected spectrum the mono-energetic peaks curve towards higher $E$ deeper in the detector, indicating they are overcorrected. This occurs to an extent with the $^{83\text{m}}\text{Kr}$ -corrected spectrum at higher energy, but can be explained by the effects of an inhomogeneous electric field. Events near the top of the detector may saturate PMTs in the top array. . . . .	245



# Acknowledgements

First and foremost, I would like to thank my advisor, Elena Aprile, who welcomed me into her research group in 2014. I owe this dissertation and my remarkable research experience over the past four years to your guidance and encouragement. You exemplify scientific excellence and innovation, and are a role model for young academics.

I would like to give a special thanks to Qing Lin, Patrick de Perio, and Fei Gao. You committed your time and energy to helping me grow as a graduate student. So much of what I have learned over the years is thanks to you. I feel fortunate to have had you as mentors.

I would also like to thank postdoctoral fellows and research scientists Guillaume Plante, Marc Weber, Luke Goetzke, Marcello Messina, and Alfio Rizzo. Your patience and encouragement over the years, especially at the beginning, shaped my four years in the group.

I have had a lot of fun working alongside graduate students Matt Anthony, Yun Zhang, Joey Howlett, and Tianyu Zhu. The experiments, analyses, and trips I've shared with you were among the most memorable of my time at Columbia. I am also happy to have had the opportunity to get to know Damon Daw, who worked in our group for a couple of years.

I am grateful to Marcela Stern. You are one of the kindest and most diligent people I know. You made my life easier on so many occasions. It has been such a pleasure knowing you.

I feel extremely fortunate to have gotten to know Jeremy Dodd these last six years. You are both a mentor and friend, and were there for me in times of uncertainty. You

had a remarkable impact on my time at Columbia, and I am forever grateful.

I am especially thankful to my friends and fellow PhD students Felix Clark, Matt Anthony, Laura Havener, Ryne Carbone, Geoff Iwata, and Russell Smith. I feel privileged to have made such long-lasting friends during this experience. Your support during difficult times, both personally and professionally, has been indispensable. I especially want to thank Felix Clark, who was my roommate, along with Rex Brown.

I am eternally grateful to my family, who has supported and believed in me my entire life. My parents, Pam and Brock, give me the confidence and love that motivates me. My brother, Spencer, is the bravest and most inspiring person I know. I also want to thank my aunt, Diana, uncle, Mark, and cousins, Marissa and Tyler for their encouragement. I consider myself very lucky to have such strong relationships with you.

My family has been through some difficult times. Your love and support gave me the courage and confidence to face these challenges. You continue to teach me the importance of kindness, hard work, and *joie de vivre*, and most important of all, family. You have made me who I am. I love you.

To my parents, Pam and Brock, and brother, Spencer



# Chapter 1

## Dark Matter

For much of the last century evidence has been building for two non-luminous components of our universe that cannot be explained with our current model of physics. The first is the acceleration of the expansion of the universe, which is hypothesized to result from an unknown kind of energy known as dark energy. Measurements estimate dark energy composes  $\sim 70\%$  of matter in the current observable universe. The second is the presence of a gravitational field that is many times too large to be caused by ordinary - or baryonic - matter, but whose source cannot be seen. Dark matter (DM) is a hypothetical form of matter that does not interact electromagnetically and provides the additional massive component that would solve this discrepancy. Observations predict that dark matter constitutes  $\sim 26\%$  of the universe. In dark energy and dark matter the term “dark” is a relic from their early histories and today both are understood to be invisible.

This chapter presents an overview of dark matter and the different methods of detection. It begins with a summary of the  $\Lambda$ CDM model (Sec. 1.1) followed by a discussion on evidence of dark matter’s existence (Sec. 1.2) and potential DM candidates (Sec. 1.3). Next detection methods for Weakly Interacting Massive Particle (WIMP) dark matter are detailed (Sec. 1.4), and the final section covers the various categories of direct detection experiments (Sec. 1.5).

## 1.1 $\Lambda$ CDM Model

The  $\Lambda$ CDM model describes the evolution of the universe from its inception at the Big Bang to present day. It is named from its inclusion of a cosmological constant (dark energy)  $\Lambda$  and cold dark matter (CDM) (Sec. 1.3.3), and is the most successful model to date.  $\Lambda$  is understood to be an energy density that is uniform throughout the observable universe and interacts repulsively with itself to drive the universe's expansion. Cold dark matter is predicted to be a non-relativistic, non-luminous form of matter that interacts primarily through gravitation. The validity of the  $\Lambda$ CDM model is dependent on our universe being homogeneous and isotropic over large ( $\sim$ 100 Megaparsecs - Mpc) distances, Einstein's General Relativity, and a path connected universe - all of which are believed to be true. Under these assumptions Einstein's field equations can be solved for the Friedmann-Lemaître-Robertson-Walker (FLRW) metric, which in polar coordinates is

$$ds^2 = -c^2 dt^2 + a(t)^2 \left( \frac{dr^2}{1 - kr^2} + r^2 d\Omega^2 \right) \quad (1.1)$$

where  $ds$  is the distance traversed in space-time,  $c$  is the speed of light,  $t$  is time, and  $r$  and  $d\Omega = d\theta^2 + \sin^2(\theta)d\phi^2$  are spatial coordinates.  $a(t)$  is known as the scale factor with  $a = 1$  today, and  $k \in \{-1, 0, 1\}$  is the curvature of the universe. A universe with  $k = -1$  is an open universe and has negative curvature. Its geometry is hyperbolic, meaning the sum of the angles in a triangle is  $< 180^\circ$  and two lines that do not cross are never equidistant. An open universe will expand forever as long as  $\Lambda \geq 0$  (observations disqualify a universe with negative  $\Lambda$ ). A universe with  $k = 0$  is flat and has Euclidean geometry (angles in a triangle equal  $180^\circ$  and parallel lines remain equidistant). If  $\Lambda = 0$  it will expand forever at a decelerating rate, asymptotically approaching 0. For  $\Lambda > 0$  the expansion first slows due to gravity but will ultimately increase as the average density of the universe  $\rho$  decreases. A universe with  $k = 1$  is closed and has positive curvature. Its geometry is similar to a sphere: the angles in a triangle sum to  $> 180^\circ$  and all lines eventually meet. The fate of a closed universe depends on the fraction of its components. If  $\Lambda = 0$  the expansion

will come to a stop and begin to contract, returning to a singularity known as the “Big Crunch”. However, if enough dark energy is present the universe will follow an open or flat universe and expand forever. As the density of gravitationally-interacting components increases a larger  $\Lambda$  is necessary to prevent a Big Crunch.

Einstein’s field equations for the solution in Eq. 1.1 give the Friedmann Equations

$$\left(\frac{\dot{a}}{a}\right)^2 = \frac{8\pi G\rho}{3} - \frac{k}{a^2} \quad (1.2)$$

$$\frac{\ddot{a}}{a} = -\frac{4\pi G}{3}(\rho + 3p) \quad (1.3)$$

where  $\dot{a}/a$  is referred to as the Hubble constant  $H$  ( $H = H_0$  today) and  $p$  is the pressure. The density for a flat universe, known as the critical density, can be derived from Eq. 1.2 to be  $\rho_{\text{crit}} = 3H^2/8\pi G$ . A useful notation is the ratio of the density to the critical density, known as the density parameter,  $\Omega := \rho/\rho_{\text{crit}}$ . Moving forward  $\Omega$  will represent the density parameter rather than spatial coordinates as in Eq. 1.1. Substituting  $\Omega$  into Eq. 1.2 gives

$$\Omega - 1 = \frac{k}{H^2 a^2} \quad (1.4)$$

Eq. 1.4 shows that the universe will be open for  $\Omega < 1$ , flat for  $\Omega = 1$ , and closed for  $\Omega > 1$ . The density parameter can be decomposed as  $\Omega = \sum \Omega_i$  where  $\Omega_i$  is a component of the universe. Measurements estimate density parameters of  $\Omega_b \sim 0.05$  for baryonic matter,  $\Omega_{\text{dm}} \sim 0.26$  for non-baryonic (dark) matter,  $\Omega_r \sim 0$  for radiation, and  $\Omega_\Lambda \sim 0.69$  for dark energy (Sec. 1.2.3). These numbers reveal cold dark matter and dark energy are the dominant components, making up  $> 94\%$  of the total matter density.

## 1.2 Evidence for Dark Matter

### 1.2.1 Dynamical Constraints

The first evidence for Dark Matter appeared in 1933 when Swiss astronomer Fritz Zwicky was observing the Coma Cluster and noticed the velocity of the galaxies was too large to be explained by the luminous matter. He argued that if there were some additional mass that only acted gravitationally it could explain his observations, and estimated it to be approximately 400 times greater than the visible matter [1]. Today this factor is much smaller as advances in technology have shown the luminous matter is larger, but the discrepancy persists. Zwicky coined this mystery matter *dunkel Materie* or “dark matter”. Since then other galaxy clusters have been observed and support this claim.

In 1970 Vera Rubin and Kent Ford used H $\alpha$  from H II regions to measure the rotation of stars around the center of the Andromeda galaxy [2]. The virial theorem predicts  $v(r) = \sqrt{GM(r)/r}$  so that at large radii the velocity of the galaxies should decrease as  $r^{-1/2}$ . Rubin and Ford’s observations contradicted the  $M(r)$  derived from luminous mass. As with Zwicky’s measurement, the results could be explained by introducing a non-luminous feature - in this case one with  $M(r) \sim r$ . Observations of more than one hundred thousand galaxies have since shown similar results, with DM halos containing several times the luminous mass.

One example is galaxy NGC 6501. The dark halo mass density in Fig. 1.1 is estimated as  $\rho(r) = \rho_0 \left[ 1 + \left( \frac{r}{r_c} \right)^2 \right]^{-1}$  where  $\rho_0$  and  $r_c$  are the central halo mass density and radius, respectively, by fitting a least square to the velocity distribution [3]. The left panel shows the mass of luminous matter decreases after peaking at roughly 2 kiloparsecs (kpc), but the DM increases and at  $> 10$  kpc is proportional to  $r$ , causing the rotational velocity to flatten. Unfortunately, substantiated models that predict the masses of a galaxy’s disk, bulge, and halo independently do not exist, which makes dissociating the mass of baryonic matter from DM difficult. Most models expect the luminous matter to compose the galaxy’s disk and bulge while the dark matter forms the halo [4].

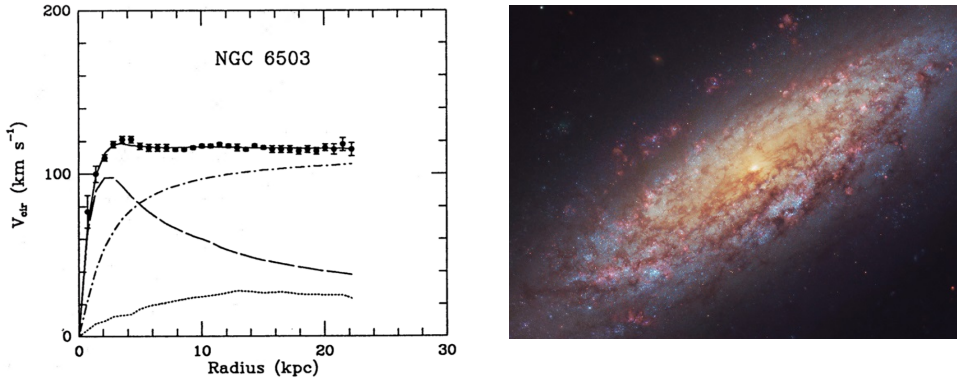


Figure 1.1: Rotational velocity vs. radius (left) and image (right) of galaxy NGC 6503. In the left panel visible components are represented by the dashed line, gas by the dotted, and dark halo by the dashed-dotted. Image credit: (left) [3], (right) [5].

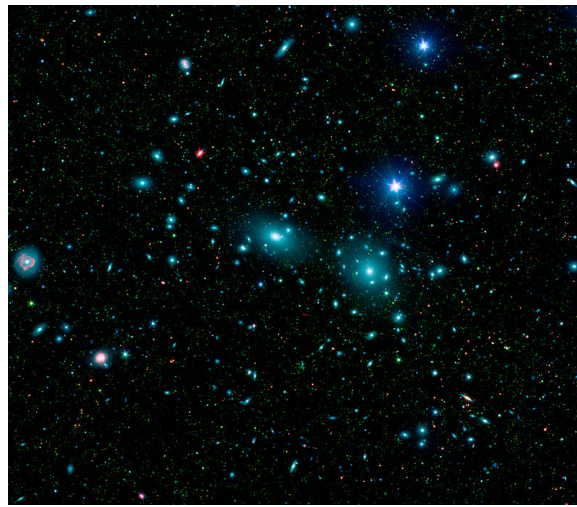


Figure 1.2: Coma Cluster as seen by Sloan Digital Sky Survey and Spitzer Space Telescope. Image credit: [6].

### 1.2.2 Gravitational Lensing

A collection of matter capable of bending electromagnetic radiation between a source and an observer is a gravitational lens. The deflection is caused by the matter's gravitational distortion of space-time, for the effects are typically most noticeable for high-density objects such as galaxies, galaxy clusters, or stars. The position of a source that is gravitationally lensed as viewed by an observer will be incorrect, as shown in the right panel of Fig. 1.3. A lens can be characterized in part by its convergence  $\kappa$ , which describes the focusing of the light rays, and shear  $\gamma$ , which characterizes the image's ellipticity. They are related to the magnification by

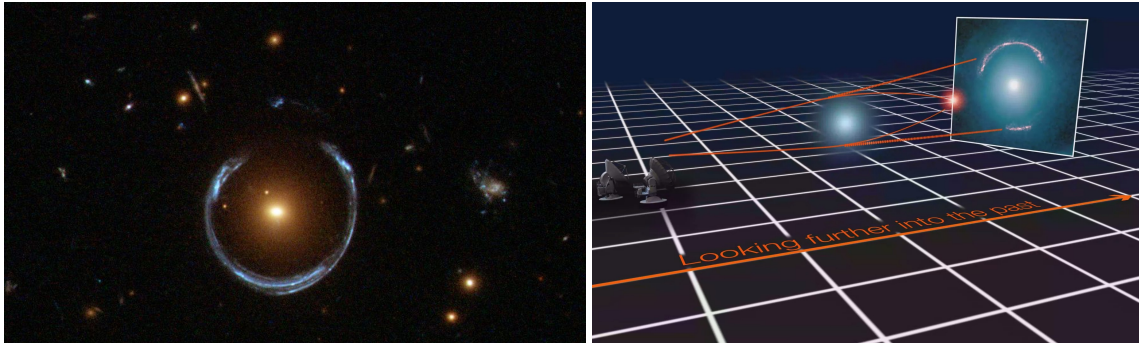


Figure 1.3: (left) A red galaxy distorts the light from a more distant blue galaxy to produce an Einstein ‘horseshoe’ ring. (right) A diagram of strong lensing. The red source is bent by the blue lens, with the solid orange lines that connect to it representing the light’s true trajectory. The observer incorrectly views the source’s position as indicated by the dashed orange lines, and the image behind them. Image credit: (left) [7], (right) [8].

$$\mu = \frac{1}{(1 - \kappa)^2 + \gamma^2} \quad (1.5)$$

This produces an increase in brightness when the source and lens are close to one another. This amplification has helped astronomers see objects that previously were thought to be too faint to observe.

In the case of strong lensing an observer will see a misshapen source as arcs. Because the magnitude of the deflection depends on the proximity to the lens, it is possible to see multiple instances of the same source. In most cases the images travel different distances so the observer will see different eras in the source’s past. In the special case when the lens is directly between the source and observer the image will appear as a circular distortion of the source around the lens, known as an Einstein ring, and no time delay will occur. Fig. 1.3 shows a photo of a strong lens and a diagram depicting the path of the light. Originally Einstein believed gravitational lensing was useless having only considered what today is known as micro lensing (deflection about a star), but Fritz Zwicky predicted galaxies could provide stronger lensing and magnification. When the arcs have a suitable size and flux the source’s luminosity can be determined.

In many astrophysical instances the light’s deflection is much more subtle. This

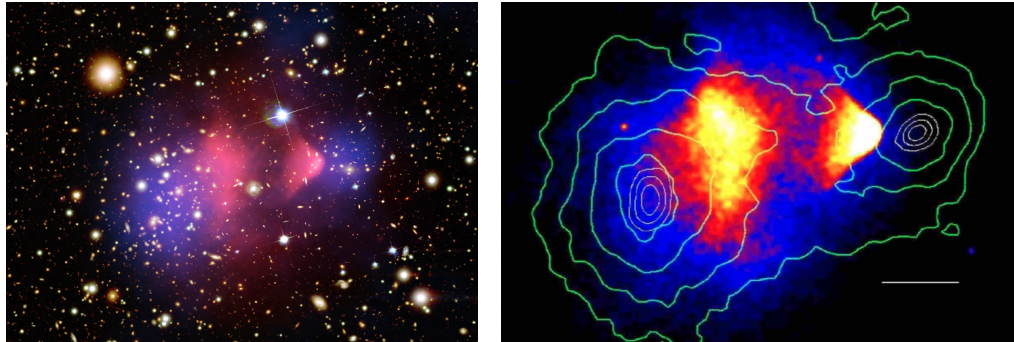


Figure 1.4: X-ray emission from hot gas (pink) and mass centroids (blue) from gravitational lensing after collision of cluster 1E 0657-558. The white bar in the right panel represents 200 kpc at cluster. The separation between the colors provides evidence for Dark Matter. Image credit: (left) [10], [11], NASA/CXC/CfA/STScI/Magellan/U.Arizona/; Lensing Map: NASA/STScI; ESO WFI; Magellan/U.Arizona/D.Clowe et al. (right) [11].

is known as weak lensing, and because the effects are fainter is more difficult to observe. Whereas strong lensing results from radiation passing around the lens, weak lensing is the passage of light through a gravitational field where tidal effects distort the shape of the image. In the latter the luminosity is often too low for a thorough analysis so astronomers may only consider the source's shear. However, because the size of the shear for weak lensing is small, systematic effects from observation (e.g. atmosphere, instrument point spread function, noise, etc.) must be small and well understood [9]. Furthermore, because galaxies are generally elliptical, decoupling the true shape from the shear can be difficult to impossible. Thus the gravitational field is calculated statistically by randomly drawing galaxies from the known galaxy ellipticity distribution. Since the number of samples must equal the number of galaxies along the line of sight, this method is most effective when the number of galaxies is large.

If the mass of the lens is well-known, the visible portion can be subtracted to yield its fraction of dark matter. This can typically be done for strong lenses as shown in Fig. 1.3 but is more difficult for weak.

A galaxy collision provides a unique setting to study dark matter. 1E0657-56, commonly known as the Bullet Cluster, is two galaxies that passed through one another  $\sim$ 150 million years ago at  $4500^{+1100}_{-800}$  km s $^{-1}$  [12]. Fig. 1.4 shows the x-ray

## 1. DARK MATTER

---

map in pink and the mass distribution from gravitational lensing measurements in blue in the left panel, and the mass contours in the right. The separation of mass from baryonic matter can be explained by dark matter. As the galaxies collide intergalactic dust interacts and heats up, creating x-rays and slowing their speed. Because dark matter does not interact electromagnetically it moves unimpeded by comparison, affected only by gravity. In addition to providing evidence of dark matter, 1E0657-56 sets a limit on the cross-section of dark matter self-interaction of  $< 1 \text{ cm}^2 \text{ g}^{-1}$  [12]. It also provides evidence against modified gravity (Sec. 1.3.4) - an alternative theory to dark matter - since the observed mass distribution lays outside of the luminous content.

### 1.2.3 Cosmic Microwave Background

The Cosmic Microwave Background (CMB) was accidentally discovered in 1965 by Arno Penzias and Robert Wilson, for which they received the Nobel Prize [13]. It is a remnant from shortly after ( $\sim 380,000 \text{ y}$ ,  $z \sim 1100$ ,  $T \sim 3000 \text{ K}$ ) the Big Bang and a near-perfect blackbody at 2.725 K today (most precise measurement is  $2.72548 \pm 0.00057 \text{ K}$  [14]). CMB photons have been traveling freely since the time of last scattering  $t_{\text{ls}}$  - when electron-atom recombination in the early universe was effectively complete, ending the period of (primarily) electron-photon scattering.

Deviations in the blackbody spectrum are small (root mean square of  $\delta T/T \sim 10^{-5}$ ) and result from a number of processes at  $t_{\text{ls}}$  that fluctuated throughout space. A dipole anisotropy is due to Earth's motion with respect to the comoving rest frame of the CMB [15]. Furthermore, energy density perturbations would cause variations in gravitational potential  $\delta\Phi$ . A photon at a larger  $\delta\Phi$  at  $t_{\text{ls}}$  would be blueshifted since as it moves its potential decreases, while one at lower  $\delta\Phi$  would be redshifted. This is known as the Sachs-Wolfe effect [16]. Details of additional effects, including intrinsic fluctuations and acoustic oscillations, can be found in [17].

The CMB provides the most precise measurements on numerous cosmological parameters including  $\Omega_b$ ,  $\Omega_{\text{dm}}$ ,  $\Omega_\Lambda$ ,  $\Omega_r$ , and  $H_0$ . It has been charted by several satellites since its discovery, most recently by Planck [19]. The CMB is shown in

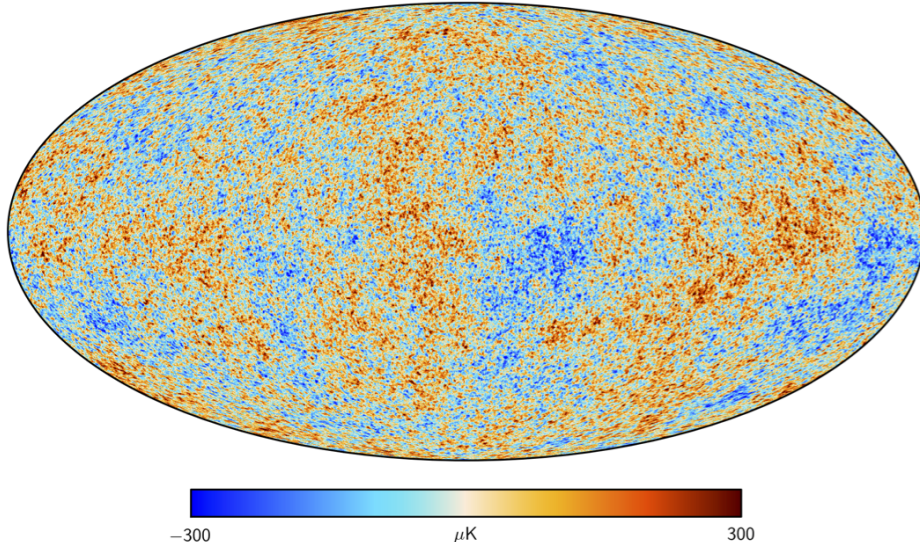


Figure 1.5: CMB as observed by Planck. Temperature deviations  $\delta T/T \sim 10^{-5}$ . Image credit: [18].

Fig. 1.5, where fluctuations are on the order of  $10^2 \mu\text{K}$ . These fluctuations were caused by the amount of each component - thus, by calculating the correlation function

$$C(\theta) = \left\langle \delta T(\hat{n}) \delta T(\hat{n}') \right\rangle \quad (1.6)$$

we can identify the cosmological makeup of the universe. To do this we use

$$\delta T = \sum_{l=0}^{\infty} \sum_{m=-l}^l a_{lm} Y_{lm}(\theta, \phi) \quad (1.7)$$

where  $\delta T = T(\theta, \phi) - \langle T \rangle$  for a given  $\theta, \phi$  on the map.  $Y_{lm}(\theta, \phi)$  are the spherical harmonics with coefficients  $a_{lm}$  such that  $\sum_{l,m} |a_{lm}|^2 = 1$ . Substituting Eq. 1.7 into Eq. 1.6 gives a correlation function of

$$C(\theta) = \frac{1}{4\pi} \sum_{l=0}^{\infty} (2l+1) C_l P_l(\cos\theta) \quad (1.8)$$

where  $P_l$  are the Legendre polynomials and  $C_l = \frac{1}{2l+1} \sum_{m=-l}^l a_{lm}$ . The only unknown is  $C_l$ , which is typically given as the angular power spectrum  $D_l^{TT} \equiv l(l+1)C_l/2\pi$  as shown in Fig. 1.6.

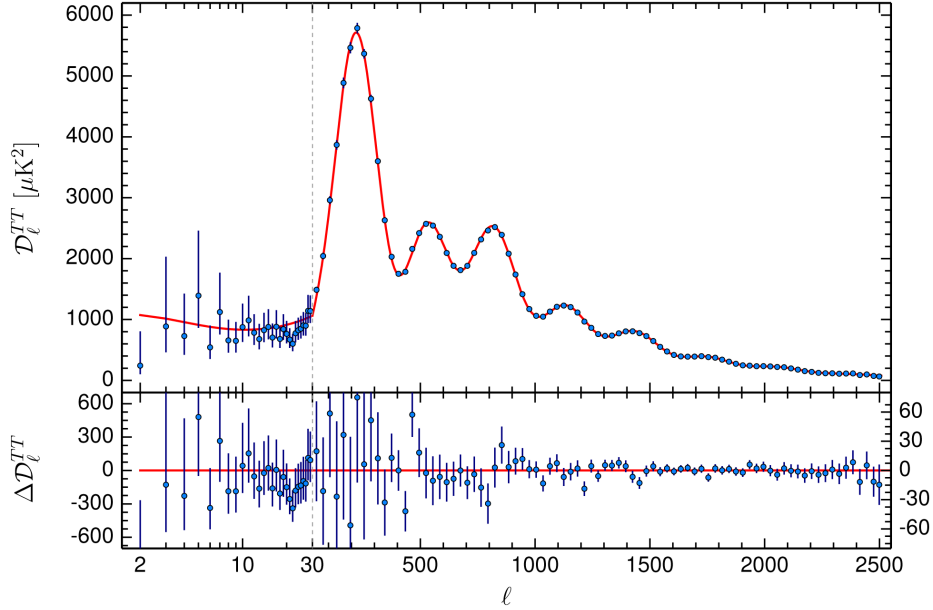


Figure 1.6: Angular power spectrum for CMB from Planck using the  $\Lambda$ CDM model. Residuals are shown in the bottom panel. The model matches the data well at  $l < 15$  and  $l > 30$ . The horizontal axis changes from linear to logarithmic at  $l = 29$  and is marked by the vertical dashed grey line. Image credit: [20].

Details about cosmological parameters including  $\Omega_i$  are contained in the angular power spectrum (e.g. information on the curvature is found in the first peak while the  $\Omega_b$  is derived from the ratio of the heights of the first two peaks). The results of the fit give  $H_0 = 67.81 \pm 0.92 \text{ km s}^{-1} \text{ Mpc}^{-1}$ ,  $\Omega_\Lambda = 0.692 \pm 0.012$ ,  $\Omega_b = 0.0484 \pm 0.0005$ ,  $\Omega_{\text{dm}} = 0.258 \pm 0.004$ , and curvature density parameter  $\Omega_k \equiv 1 - \Omega_\Lambda - \Omega_b - \Omega_{\text{dm}} = -0.005^{+0.016}_{-0.017}$ .

### 1.3 Dark Matter Candidates

Despite strong evidence for the existence of dark matter, there is little guidance for its composition. Any dark matter candidate must have a lifetime much larger than the age of the universe, be electrically neutral, and have a small matter-dark matter cross section. Of course, dark matter may constitute a class of particles so long as their sum satisfies our observations of the universe.

### 1.3.1 Axions

Charge conjugation and parity (CP) violation in strong interactions has never been observed, despite its allowance by quantum chromodynamics (QCD). This compels a theoretically unjustified fine tuning of the model, which is known as the strong CP problem. Originally hypothesized by Roberto Peccei and Helen Quinn in 1977, the axion - a new standard model particle - offered a solution [21]. Shortly after it was demonstrated that for an axion decay constant of  $f_a > 10^{12}$  axions would be overproduced in the early universe and cause the axion density  $\Omega_a > 1 > \Omega_{dm}$  [22]. However, if the decay constant were  $\sim 10^{12}$  the axion density parameter could be equivalent to  $\Omega_{dm}$ . Current mechanisms for solving the strong CP problem rely on invisible axion models Kim-Shifman-Vainshtein-Zakharov (KSVZ) [23], [24] and Dine-Fischler-Srednicki-Zhitnitsky (DFSZ) [25], [26], marked along the yellow band in Fig. 1.7.  $f_a$  is inversely proportional to the axion mass  $m_a$ .

Because axions naturally offer an explanation for dark matter there are a number of DM experiments dedicated to finding them. Several operate under the Primakoff effect [28], which states that electromagnetic fields should transform axions to photons and vice versa. Cavity searches such as the Axion Dark Matter Experiment (ADMX) [29] search the galactic dark matter halo using a resonant microwave cavity inside a superconducting magnet to convert axions at Earth into microwaves. Others, like the CERN Axion Solar Telescope (CAST) search for axions produced in the Sun's core from x-ray scattering off of protons and electrons [30]. The experiment hopes to convert solar axions back into x-rays. The Cosmic Axion Spin Precession Experiment (CASPEx) uses nuclear magnetic resonance (NMR) to detect nuclear spin precession frequencies that depend on  $m_a$  [31]. In addition axion-induced electronic recoils have been searched for in cryogenic detectors including CDMS [32], EDELWEISS [33], and XMASS [34]. The best electronic recoil coupling limits to date were set by XENON100 in 2014 [35].

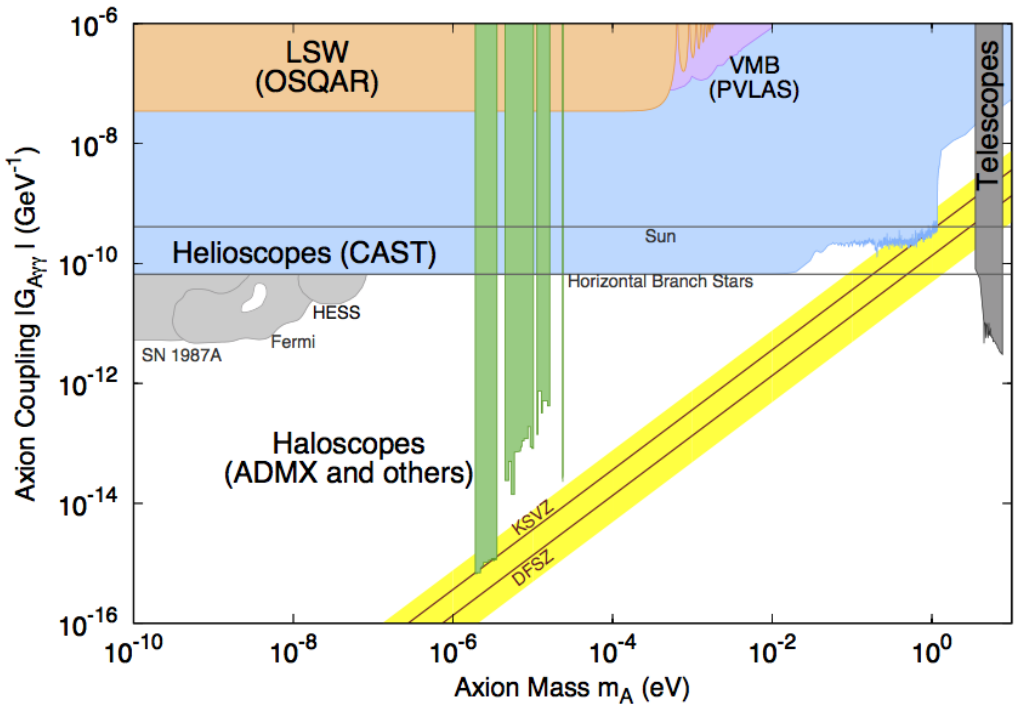


Figure 1.7: Axion-double photon coupling with respect to axion mass. The shaded regions have been excluded by different experiments. Invisible axion models KSVZ and DFSZ are drawn along the yellow band. Image credit: [27].

### 1.3.2 WIMPs

Weakly Interacting Massive Particles (WIMPs) are another favored candidate for dark matter. As their name suggests, they interact through the weak force so would be difficult to observe. They would behave similarly to neutrinos, which have a small cross-section and communicate only via the weak interaction. They must also have been produced early in the universe to account for observations of the CMB and galactic structures.

At the beginning of the universe the temperature was hot enough that particles could annihilate with their antiparticle counterpart and produce new particles, maintaining equilibrium. As the universe cooled each particle underwent its own “freeze-out”, after which they could no longer transform freely to other particles. Using the  $\Lambda$ CDM model the density of DM in the universe today is given by

$$\Omega_{\text{dm}} h^2 = \frac{3 \times 10^{-27} \text{ cm}^3 \text{ s}^{-1}}{\langle \sigma_{\text{ann}} v \rangle} \quad (1.9)$$

where  $h \equiv H_0/100$  and  $\langle \sigma_{\text{ann}} v \rangle$  is the thermally averaged self-annihilation cross section for dark matter. Assuming DM has a cross section and mass on the order of the weak scale, it would give roughly the correct relic density of DM. This is known as the “WIMP miracle”.

Another appealing argument for WIMPs is supersymmetry (SUSY), which is theorized to solve a number of problems in the standard model. Many SUSY models predict a heavy stable particle that would be weakly interacting (a favorite is the neutralino, the supersymmetric partner of the neutrino). This has historically been one of the favored arguments for WIMP dark matter.

### 1.3.3 Cold, Warm, or Hot

An important property of dark is whether it was relativistic in the early universe, typically defined using the times of decoupling from radiation and matter  $t_{\text{dec}}$  and matter-radiation equality (moment when density of matter and radiation are equivalent)  $t_{\text{rm}}$ . Hot dark matter (HDM) would have been relativistic at  $t_{\text{dec}}$  and  $t_{\text{rm}}$ . Warm dark matter (WDM) would have been relativistic at  $t_{\text{dec}}$  but not at  $t_{\text{rm}}$ . Cold dark matter (CDM) would have been non-relativistic at both. Candidates for CDM include WIMPs, axions, and primordial black holes while for WDM might be the gravitino. Neutrinos are candidates for both warm and hot dark matter, but measurements show their density is too small to account for  $\Omega_{\text{dm}}$ .

Structure formation in the universe unravels the hot/warm/cold dark matter mystery. Because the cosmological layout we observe today came from fluctuations in the earliest moments after the Big Bang (Sec. 1.2.3) it contains the imprint of dark matter.

Relativistic energies of hot dark matter would smooth out density perturbations in what is known as free streaming. In this case the first structures to form would be superclusters, followed by smaller-scale features. Observations show that this is not

the case; galaxies have been around since before the universe was 1 billion years old ( $z \sim 6$ ) and superclusters are just forming today [36].

CDM allows early density perturbations to persist, causing smaller structures to materialize first, which is consistent with galaxy surveys between  $\sim 1$  Mpc and the cosmological horizon. At scales  $< 1$  Mpc and  $M \sim 10^{11} M_{\odot}$  there are discrepancies, including under-dense cores for many galaxies that are DM-dominated and significantly fewer satellite dwarf and small galaxies than predicted [37], [38]. Possible solutions to the latter may be that dwarf galaxies have merged, been stripped by tidal forces of larger galaxies, or not accumulated enough baryonic matter to be visible [39].

WDM has received a lot of interest since the problems with CDM were discovered. Simulations have shown that WDM would result in fewer subhalos, though explaining the other CDM model-observation disagreements has been less successful [40], [41]. However, because neutrinos have mass we know there was at least some non-CDM in the early universe.

Despite problems with CDM it remains the most favorable model for dark matter. One possible outcome is there is a mix of CDM and WDM, but if that's the case CDM would make up the considerable bulk of dark matter.

### 1.3.4 Modified Gravity

A different explanation for the disparity between the mass of ordinary matter and its behavior is an incomplete understanding of gravity. This would suggest that Einstein's General Relativity works well at small distances but does not correctly explain large-scale gravitation. Since the incompatibility of current theory with observation would be resolved by proving the mysterious behavior is a consequence of ordinary matter, dark matter would not be necessary.

Major evidence against modified gravity emerged in 2004 when the collision of two galaxies 1E0657-56 (Bullet Cluster) was observed (Sec. 1.2.2). [12] reconstructed the mass distribution of the merger from gravitational lensing measurements (Fig. 1.4). Their measurements required a significant fraction of the mass distribution to be

offset from the visible matter, consistent with collisionless dark matter halos passing through one another. This presented a problem for modified gravity, which was unable to justify this.

In 2018 the ultra-diffuse galaxy NGC1052-DF2 was observed to have  $M_{\text{halo}}/M_{\text{stars}} \sim 1$ , a factor of roughly 400 lower than expected [42], [43]. This poses a challenge to modified gravity - including modified Newtonian dynamics (MOND), a popular theory that has successfully predicted a number of galactic phenomena [44] - since a large gravitational field does not appear to exist around the baryonic matter. However, several theories have claimed this may be compatible with their expectations due to its proximity to its massive host galaxy NGC1052 and large uncertainties on some of the measurements by [42], [45], [46]. Under the dark matter hypothesis, a galaxy without DM has implications outside this field - e.g. current models of structure formation cannot explain this [47], [48]. Two recent papers found conflicting results when studying the 175 SPARC galaxies [49]. The first was in agreement with MOND using gaussian priors centered around values given by SPARC by setting their uncertainty to observational errors [50]. The second included an additional 18 galaxies from THINGS [51] and with flat priors excluded MOND at  $10\sigma$  [52]. Ultimately, additional measurements and improved statistics are needed to better quantify NGC1052-DF2, but confirmation of missing dark matter would strongly constrain theories of modified gravity.

## 1.4 WIMP Detection Methods

There are three methods for detecting WIMPs. The first is using particle colliders where standard model (SM) particles would interact and create DM (Sec. 1.4.1). The second is via indirect detection, where DM would annihilate into SM particles, with the hope that they would be detectable on Earth (Sec. 1.4.2). Experiments look in high-density regions of the universe where higher concentrations of dark matter should be present. The third method is by direct detection in which DM would scatter off SM matter and produce a signal that could be observed (Sec. 1.4.3). These methods

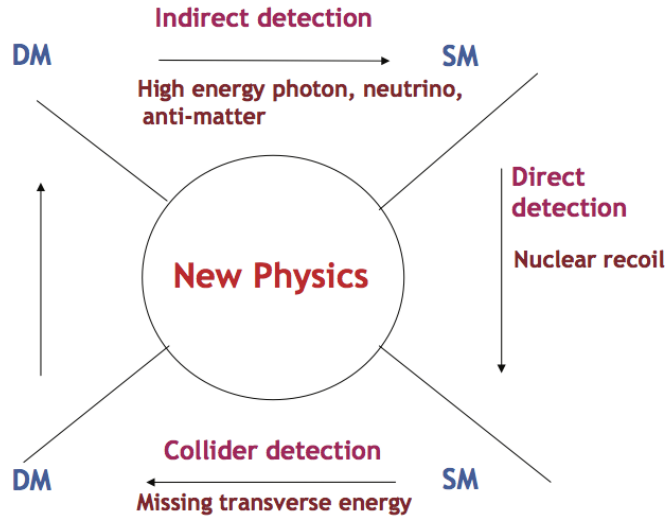


Figure 1.8: Dark matter detection methods. High energy particle collisions may create dark matter that would result in missing transverse energy (bottom). Indirect detection looks for signatures (e.g. neutrinos, photons) of possible dark matter annihilation in the universe (top). Direct detection experiments search for signs of dark matter scattering off Standard Model particles (right). Image credit: [53].

are outlined in Fig. 1.8.

### 1.4.1 Colliders

One mechanism that might lead to the discovery of WIMP dark matter is particle-antiparticle annihilation. This could be observed at particle colliders where energies can exceed several TeV, producing dark matter particle-antiparticle pairs. Though they would escape undetected, they could be measured through missing transverse energy (MET) using momentum conservation. The Large Hadron Collider (LHC) is investigating the quark sector with energies exceeding 10 TeV, while the Large Electron-Positron (LEP) Collider is doing so for leptons at  $\sim 200$  GeV. Both experiments are more competitive at lower energies than noble gas experiments (Sec. 1.5.5), particularly for spin-dependent searches [54], [55]. MET observations alone would not prove the existence of dark matter but would need indirect or direct experiments to validate their results. However, it would still be extremely useful in narrowing the search region.

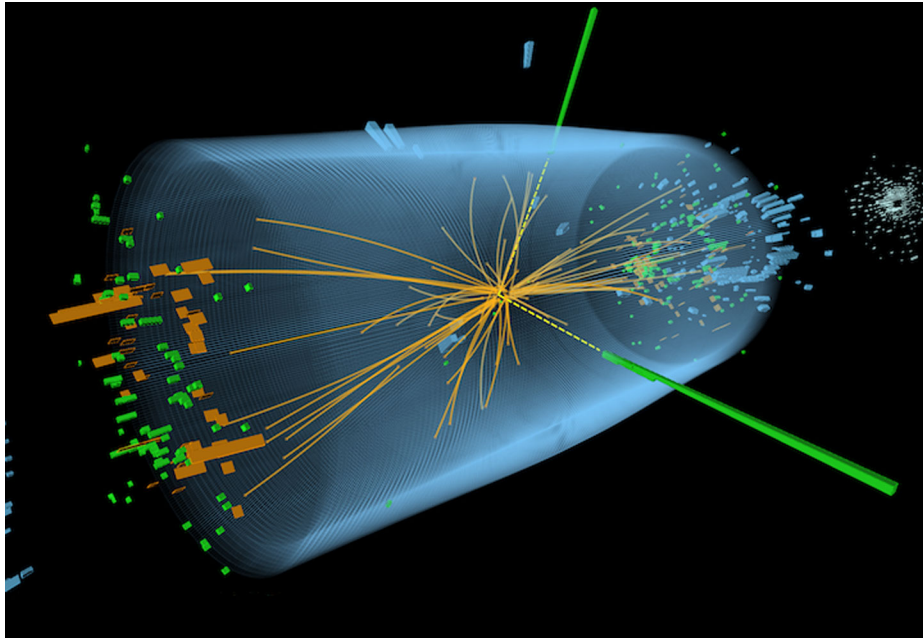


Figure 1.9: Diagram of a collision at the LHC. Image credit: [56].

### 1.4.2 Indirect Detection

Indirect detection looks for signatures of dark matter by observing standard model particles. Observables may come from dark matter annihilation, wherein two DM particles annihilate and produce standard model gamma-rays or other particle-antiparticle pairs. Alternatively, if DM is unstable (albeit with a very long half-life) it may decay into standard model particles that can be detected.

Indirect experiments look at regions where they expect a large number of interactions. The local dark matter density is estimated to be  $0.2\text{--}0.56 \text{ GeV cm}^{-3}$  [57] and experiments are observing the Sun hoping to measure a WIMP-induced high energy neutrino flux [58]. Other theories suspect DM annihilation in high-density regions of the universe such as the galactic halo would produce antiprotons, positrons, and gamma-rays that would be detectable from Earth. Because the galaxy's center has a large flux of cosmic rays it is difficult to distinguish possible dark matter from other astrophysical sources. Nearby ( $\sim 50 \text{ kpc}$ ) dwarf spherical galaxies have become an attractive target where star formation regions have low  $\gamma$ -ray backgrounds [59].

$\gamma$ -rays need to be measured in space because in the relevant energy range (GeV

to TeV) photons interact with matter via  $e^+e^-$  pair production (Fig. 2.8), and are unable to pass through Earth's atmosphere. However, ground-based detectors can look for signatures such as showers of secondary particles and their Cerenkov light as they pass through the atmosphere [60].

### 1.4.3 Direct Detection

Direct detection mainly looks for low energy ( $\sim$ 1-100 keV) nuclear recoils (some theories predict DM-lepton interactions, but they are not discussed here) [61]. The dark matter halo of a galaxy is normally assumed to be an isothermal single-component sphere with an isotropic Maxwell-Boltzmann velocity distribution function ( $f(\mathbf{v}) \propto \exp(-|\mathbf{v}|^2/v_0^2)$ ) [62], though there is not a consensus on whether this is the correct velocity parameterization [63], [64]. This is known as the Standard Halo Model (SHM). Given that the majority of dark matter must be non-relativistic (Sec. 1.3.3), the differential recoil spectrum is calculated as [65]

$$\frac{dR}{dE}(E, t) = \frac{\rho_\chi}{m_\chi m_A} \int_{v_{\min}}^{v_{\text{esc}}} v f(\mathbf{v}, t) \frac{d\sigma}{dE}(E, t) d^3\mathbf{v} \quad (1.10)$$

where  $\rho_\chi = 0.2\text{-}0.56 \text{ GeV cm}^{-3}$  is the local dark matter density (Sec. 1.4.2),  $m_\chi$  is the mass of a dark matter particle,  $m_A$  is the mass of the target element,  $v_{\text{esc}} = 533^{+54}_{-41} \text{ km s}^{-1}$  [66] is the escape velocity for WIMPs from the galaxy,  $f(\mathbf{v}, t)$  is the local velocity dispersion, and  $\frac{d\sigma}{dE}(E, t)$  is the nucleon-DM differential cross-section.  $v$  is the velocity of the dark matter in the rest frame of the detector. The minimum velocity that will produce a recoil of energy E is

$$v_{\min} = \sqrt{\frac{m_A E}{2\mu^2}} \quad (1.11)$$

where  $\mu_A = m_A m_\chi / (m_A + m_\chi)$  is the reduced WIMP-nucleus mass.

For WIMP searches most experiments look for spin-independent (SI) or spin-dependent (SD) interactions. For spin-independent all nucleons contribute equally. For spin-dependent, atoms must have an odd number of protons or neutrons since

only unpaired nucleons contribute to the search. The differential cross-section can then be written as

$$\frac{d\sigma}{dE} = \frac{m_A}{2\mu_A^2 v^2} (\sigma_{SI}^{(0)} F_{SI}^2(E) + \sigma_{SD}^{(0)} F_{SD}^2(E)) \quad (1.12)$$

where  $\sigma_{SI}^{(0)}$  and  $\sigma_{SD}^{(0)}$  are the cross sections at zero momentum for spin-independent and spin-dependent DM.  $F_{SI}^2(E)$  and  $F_{SD}^2(E)$  are the form factors, which account for the cross section's decrease with increasing energy [67]. Spin-dependence is no longer discussed but details are found in [67]. The SI form factor is the Fourier transform of the mass density ground state, and for the parameterization given in [68] is

$$F_{SI} = \frac{3j_1(qr_n)}{qr_n} e^{-(qs)^2/2} \quad (1.13)$$

where  $j_1(qr_n)$  is a Bessel function of the first kind,  $q = \sqrt{2m_A E}$  is the momentum,  $r_n = \sqrt{1.2A^{2/3} - 5s^2}$ , and  $s \sim 1$  fm is a measure of the nuclear skin [67], [69]. The cross section is given by

$$\sigma_{SI}^{(0)} = \sigma_p \frac{\mu_A^2}{\mu_p^2} \frac{[Zf_p + (A-Z)f_n]^2}{(f_p)^2} \quad (1.14)$$

where  $\sigma_p$  is the cross section of a proton,  $Z$  is the number of protons, and  $\mu_p$  is the WIMP-nucleon reduced mass.  $f_{p/n}$  is the coupling strength for protons and neutrons, which are assumed to be equivalent (see [70] for  $f_p \neq f_n$ ). Substituting Eq. 1.14 into Eq. 1.12 gives a spin-independent differential cross-section of

$$\frac{d\sigma}{dE} = \frac{m_A \sigma_p}{2\mu_p^2 v^2} A^2 |F(E)|^2 \quad (1.15)$$

This gives the differential rate as

$$\frac{dR}{dE} = \frac{\rho_\chi A^2 \sigma_p}{2m_\chi \mu_p^2} |F(E)|^2 \int_{v_{min}}^{v_{esc}} \frac{f(v)}{v} dv \quad (1.16)$$

A direct detection experiment that is sensitive between energies  $E_{min}$  and  $E_{max}$  will measure the number of signals over a time  $T$  for their target mass  $M$  as

$$N(m_\chi, \sigma) = T \times M \times \int_{E_{\min}}^{E_{\max}} \frac{dR}{dE} dE \quad (1.17)$$

Eq. 1.16 and Eq. 1.17 state that the sensitivity of an experiment improves linearly with time and target mass, but quadratically with  $A$ . This makes the atoms or molecules of the target mass an important consideration when designing a direct detection experiment.

## 1.5 Direct Detection Experiments

When a moving particle scatters off an atom or molecule that is by comparison somewhat stationary it transfers some of its energy. The energy gained by the atom will cause three effects. The first is the atom's translational energy might rise (heat) and produce phonons that propagate across the medium. The second is electrons may be excited to higher energy orbitals, and generate photons as they quickly de-excite. The third is the atom may be ionized, after which the freed electrons may recombine with their parent ion and emit photons or escape. Direct detection experiments can probe each of these effects, and many are able to measure two of the three simultaneously. The different energy channels can be seen in Fig. 1.10.

Direct detection experiments look for events outside of their expected background. This requires a comprehensive understanding of the detector background to ensure any “anomalous” events do not come from mis-modeling and a false discovery is claimed. Different approaches may be used for different methods of detection. For some experiments major efforts are going into screening the radioactivity of potential materials. Radioactivity from outside of the detector may be shielded (using e.g. water, lead). Finally, there may be backgrounds that are intrinsic to the target material.

Even with a priori screening, effective shielding, and reducing intrinsic contaminants background events are inevitable. Identifying a signal will be difficult if the signal-to-background ratio is small. This is because an experiment with a large background will report an excess with less significance than one with a low background,

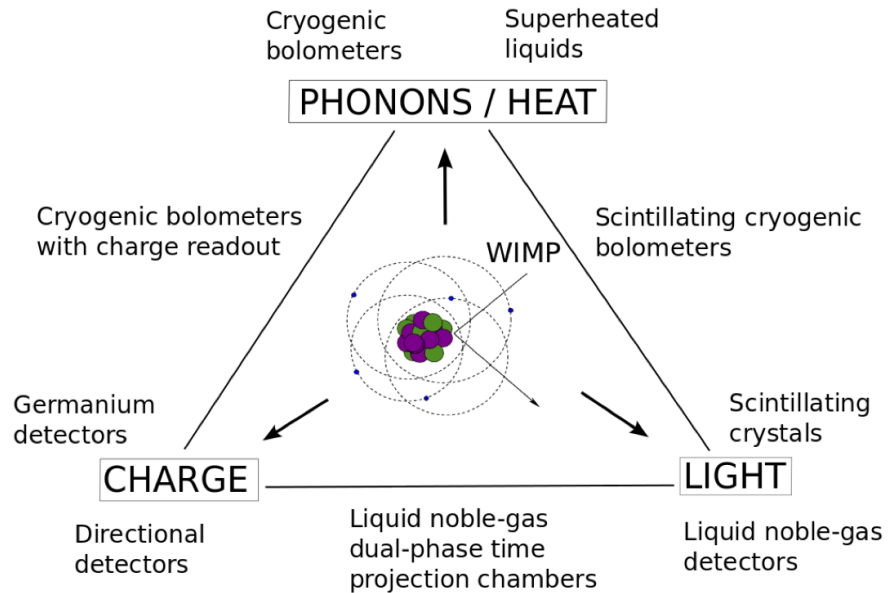


Figure 1.10: Energy channels. Image credit: [65].

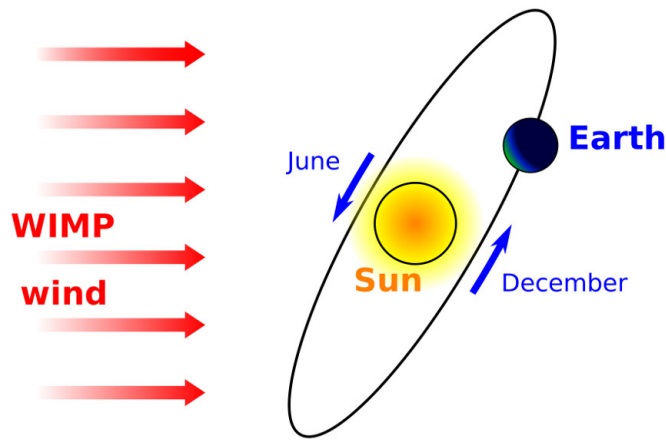


Figure 1.11: Orientation of the Earth's rotation around the Sun. The change in alignment of the Earth's and Sun's velocities causes the amount of dark matter passing through the Earth to change, appearing as a “WIMP wind” with a 1-year period. The annual modulation should be present for any DM velocity distribution as long as it does not align with that of the Sun. Image credit: [72].

i.e. a detector with a 10 event background can make a stronger claim on an excess of 5 events than one with 100. In 1986 it was proposed that due to the Earth's motion around the Sun there should be a modulation in signal [71]. Thus detectors could look for an annual variation in event rate that peaks in May, when the Earth's velocity around the Sun aligns with the Sun's velocity around the galaxy.

### 1.5.1 Superheated Liquid Detectors

Superheated liquid detectors are the most sensitive to WIMP masses in the tens of  $\text{GeV}/c^2$  range. Their limits for spin-independent WIMPs are not as stringent as dual-phase noble gas detectors (Sec. 1.5.5), but for a number of years they have consistently provided the strongest constraints in the spin-dependent WIMP-proton sector [73]. Their strong sensitivity comes from using fluorinated halocarbons, since  $^{19}\text{F}$  is the only stable isotope and its unpaired proton almost always carries 1/2 spin [74], [75].

At ambient temperatures and pressures fluorinated halocarbons are in a metastable state. A colliding particle will transfer some of its heat, which can result in nucleation that is observed acoustically or optically. By varying the temperature and pressure settings superheated detectors can reduce  $\gamma$  and  $\beta$  interactions by a factor of  $10^9$ , making them a great candidate for a spin-dependent dark matter discovery.

Superheated detector collaborations include Project In CAnada to Search for Supersymmetric Objects (PICASSO) [76], Chicagoland Observatory for Underground Particle Physics (COUPP) [77], PICO (merged from PICASSO and COUPP) [73], Superheated Instrument for Massive ParticLe Experiments (SIMPLE) [78], and Materia OSCura A Bolle (MOSCAB) [79]. Fig. 1.12 shows the exclusion plot of spin-dependent WIMP-proton cross sections.

### 1.5.2 Scintillation Crystals

Another target for DM searches is highly radiopure scintillating crystals. Typically sodium iodide ( $\text{NaI}$ ) or cesium iodide ( $\text{CsI}$ ) is chosen, with  $\text{NaI}$  being the most common. Their sensitivity to SI and SD DM, low energy threshold, room temperature operability, and ability to run over long periods of time make them an attractive option. Doping these crystals with thallium increases the yield and shifts the wavelengths of the emitted light, making the crystals more transparent and improving phototube detection efficiency [65]. However, trace amounts of radioactive elements are present in  $\text{NaI}(\text{Tl})$  crystals [88]. The 3 keV x-ray/Auger electron from the decay of  $^{40}\text{K}$  to  $^{40}\text{Ar}$  through electron capture is particularly concerning because it lays in

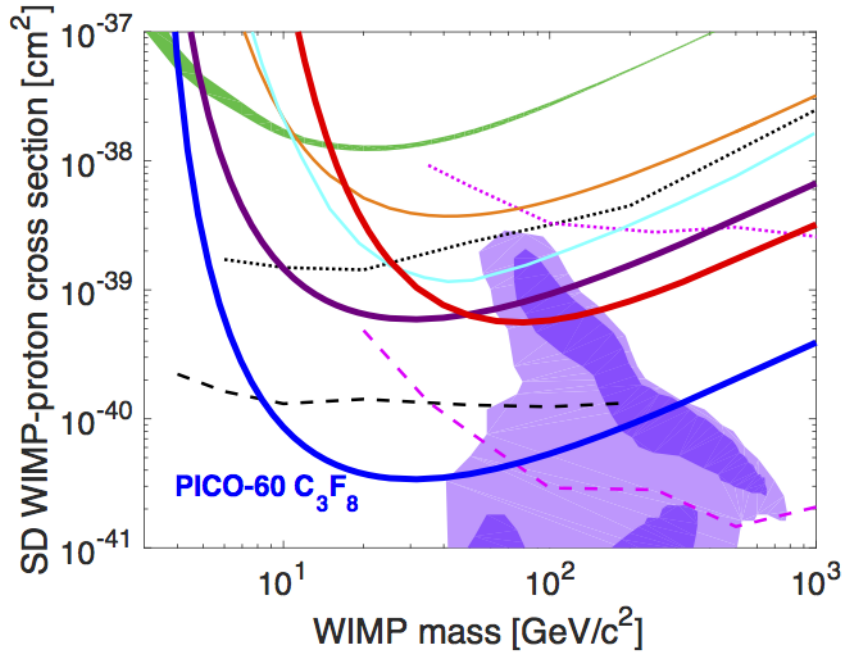


Figure 1.12: Spin-dependent WIMP-proton cross-section 90% C.L. limits for PICO-60  $\text{C}_3\text{F}_8$  (thick blue, [73]), PICO-60  $\text{CF}_3\text{I}$  (thick red, [80]), PICO-2L (thick purple, [81]), PICASSO (green, [76]), SIMPLE (orange, [82]), and PandaX-II (cyan, [83]). Indirect limits from IceCube (dashed and dotted pink, [84]) and SuperK (dashed and dotted black, [85], [86]) for  $b$  quark (dotted) and  $\tau$  lepton (dashed) annihilation are shown. The shaded purple region is constrained parameter space for the minimal supersymmetric model from [87]. Image credit: [73].

the region of interest. In addition a flat background is produced by  $^{87}\text{Rb}$  and the  $^{238}\text{U}$  and  $^{232}\text{Th}$  decay chains. Additionally, the features of the scintillation do not change for different types of interactions (e.g.  $\gamma$ -ray, neutron), so particle discrimination is not possible, with the exception of rejecting events with multiple scatters. Thus differentiating between background and signal on an event by event basis is not possible. This has made improved radiopurity an increasingly important goal [89].

The DAMA/NaI and its successor DAMA/LIBRA experiments are located underground at the Laboratori Nazionali del Gran Sasso (LNGS) in L’Aquila, Italy. They use NaI(Tl) crystals, which allows them to be sensitive to both low- (Na) and high-mass (I) WIMPs [88]. For over 14 annual cycles they have observed an annual modulation in the 2-6 keV<sub>ee</sub> (Sec. 2.6.3.3) range with  $9.3\sigma$  [91]. This corresponds to WIMP masses of 10-15 GeV/c<sup>2</sup> for sodium-scatters and 60-100 GeV/c<sup>2</sup>

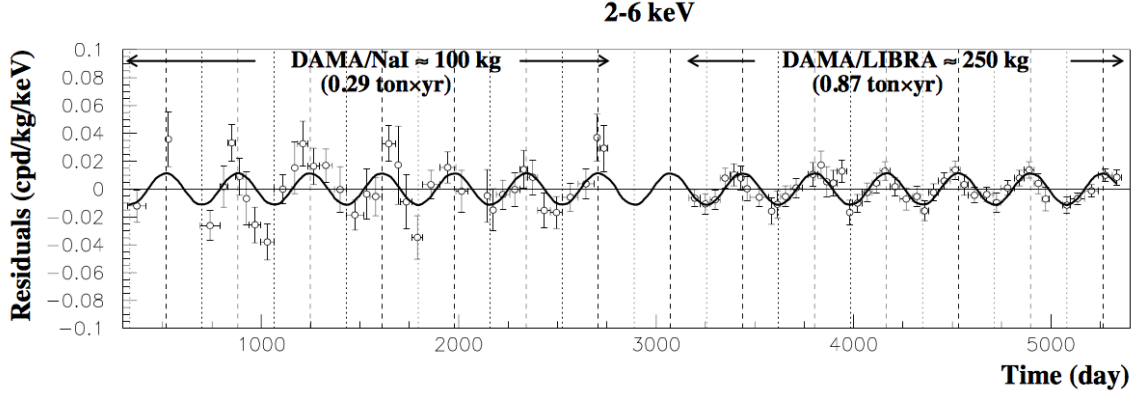


Figure 1.13: Residual event rate between 2-6 keV<sub>ee</sub> as measured by DAMA/NaI and DAMA/LIBRA. A fit of  $A \cos[\omega(t - t_0)]$  where  $t_0$  = June 2nd and  $A$  is the best-fit amplitude is overlaid, with vertical dashed lines corresponding to expected maxima. For 14 years they have observed an annual modulation with  $9.3\sigma$ . Claiming this modulation is due to dark matter is controversial, as they are unable to discriminate between different interaction types and a number of experiments have surpassed their sensitivity with no significant findings. Image credit: [90].

for iodine. Their results are shown in Fig. 1.13. Spin-independent, spin-dependent or mixed coupling [92] and inelastic scattering [93] WIMPs have been considered. Because NaI(Tl) cannot distinguish scatterings of different particles there is doubt on whether their signal is caused by WIMPs, or even dark matter. Furthermore, since they cannot specify if the interactions are with nuclei or electrons, alternative dark matter electron-coupling models [94] have been examined. Their results are controversial because other experiments have surpassed the DAMA/LIBRA sensitivity and see no signal [95]. This has prompted theories to explain the annual modulation via Standard Model particles. Hypotheses include known variation in muon flux due to changing stratosphere temperatures, which exhibits annual modulation with a phase similar to DAMA/LIBRA's findings [96], an incomplete understanding of neutron backgrounds [97], or using a combination of muon-induced neutrons and solar neutrinos [98] (this has been received pushback in [99], [100]). The Sodium iodide with Active Background REjection (SABRE) experiment is being constructed at LNGS and plans on beginning to take data by the end of 2018 [89], [101]. By using the same technology and location they will be the first experiment to directly challenge DAMA/LIBRA.

### 1.5.3 Germanium Detectors

High purity germanium (HPGe) detectors measure ionization and offer exceptional energy resolution. Like scintillation crystals, (Sec. 1.5.2) they can reach very low energies ( $\sim 0.5$  keV), making them a promising candidate for low-mass WIMP ( $\sim 10$  GeV/c $^2$ ) detection. HPGe cannot differentiate nuclear recoils from electronic, but p-type doped detectors have a dead layer on the surface and can use the pulse rise time to reject background surface events. In 2010 the Coherent Germanium Neutrino Technology (CoGeNT) experiment announced it observed an annual modulation similar to DAMA/LIBRA [102]. After continued observation they found the modulation had a best-fit WIMP mass of  $m_\chi \sim 8$  GeV/c $^2$  at  $2.2\sigma$  [103]. However, subsequent analyses with different background assumptions showed this significance fell well below  $1.7\sigma$  [104], [105]. The China Dark matter EXperiment (CDEX) uses the same setup as CoGeNT and found contradictory results [106], as did CDMS II for nuclear recoils only [107].

### 1.5.4 Cryogenic Bolometers

Cryogenic bolometers are typically cooled to 10-100 mK so they can detect phonons, allowing a low energy threshold and outstanding energy resolution. The Cryogenic Dark Matter Search (CDMS) collaboration uses silicon and germanium detectors to measure phonons and ionization. The ionization-to-phonon ratio is used for discrimination where less than 1 in  $10^6$  of all electronic recoil events fail to be rejected in the 10-100 keV range [108]. In 2013 an excess of events was reported with a best-fit WIMP mass of 8.6 GeV/c $^2$  [109]. However, subsequent measurements did not observe such an excess, nor did Expérience pour DEtecter Les WIMPS En Site Souterrain (EDELWEISS), which has an analogous setup [110].

The Cryogenic Rare Event Search with Superconducting Thermometers (CRESST-II) experiment measures phonons as well as scintillation using CaWO<sub>4</sub> crystals. They also observed excesses of events at WIMP masses of 11.6 GeV/c $^2$  at  $4.2\sigma$  and 25.3 GeV/c $^2$  at  $4.7\sigma$  [111], but after an upgrade reduced their background

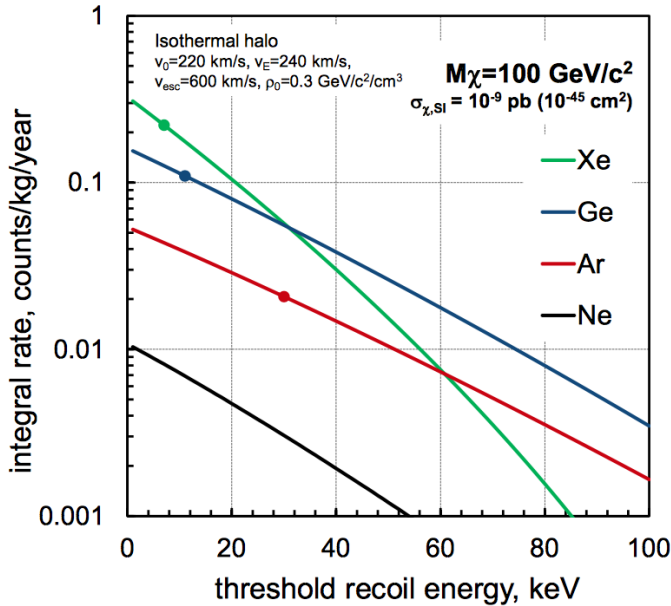


Figure 1.14: Expected integral spectra for Xe (green), Ge (blue), Ar (red), and Ne (black) for spin-independent elastic scattering of 100  $\text{GeV}/c^2$  WIMPs with cross section  $\sigma = 10^{-45} \text{ cm}^2$  per nucleon. The rates assume perfect energy resolution and are calculated using the Standard Halo Model. The dots correspond to average thresholds for each element. Image credit: [115].

they were ruled out [112].

### 1.5.5 Noble Gas Detectors

Noble gas detectors have led the field for spin-independent WIMPs at masses  $\gtrsim 20 \text{ GeV}/c^2$ , as seen in Fig. 1.15. Commissioned detectors have used either liquid argon (LAr) or liquid xenon (LXe) and the Dark matter Experiment using Argon Pulse-shape/Cryogenic Low-Energy Astrophysics with Noble liquids (DEAP/CLEAN) collaboration is constructing a detector than can house LAr and liquid neon (LNe) independently [113], [114]. Advantages of liquid noble gas detectors include scalability, particle discrimination, and self-shielding. As the target mass of these detectors passes the 1-tonne mark they are becoming sensitive to neutrinos, which introduces a new background but can also offer another branch of physics to study. Predicted integral rates for xenon, argon, and neon, as well as germanium (Sec. 1.5.3) are shown in Fig. 1.14.

Liquid noble gas detectors can be single- or dual-phase. Dual phase use an electric field to drift electrons to the liquid surface, where they are extracted across a gas gap and generate a second scintillation. Single-phase detectors measure only the scintillation and are typically spherical. Because they do not drift electrons they benefit from  $4\pi$  photo-detection (in dual phase this would interfere with the electric field). Dual phase experiments are discussed in detail in Chap. 2.

Noble gas experiments include the Argon Dark Matter (ArDM) experiment ([116], DarkSide ([117]–[119])), LUX ([120]), PandaX-II ([121]), XMASS ([122]), and XENON1T ([123]). Fig. 1.15 shows the current status of spin-independent limits.

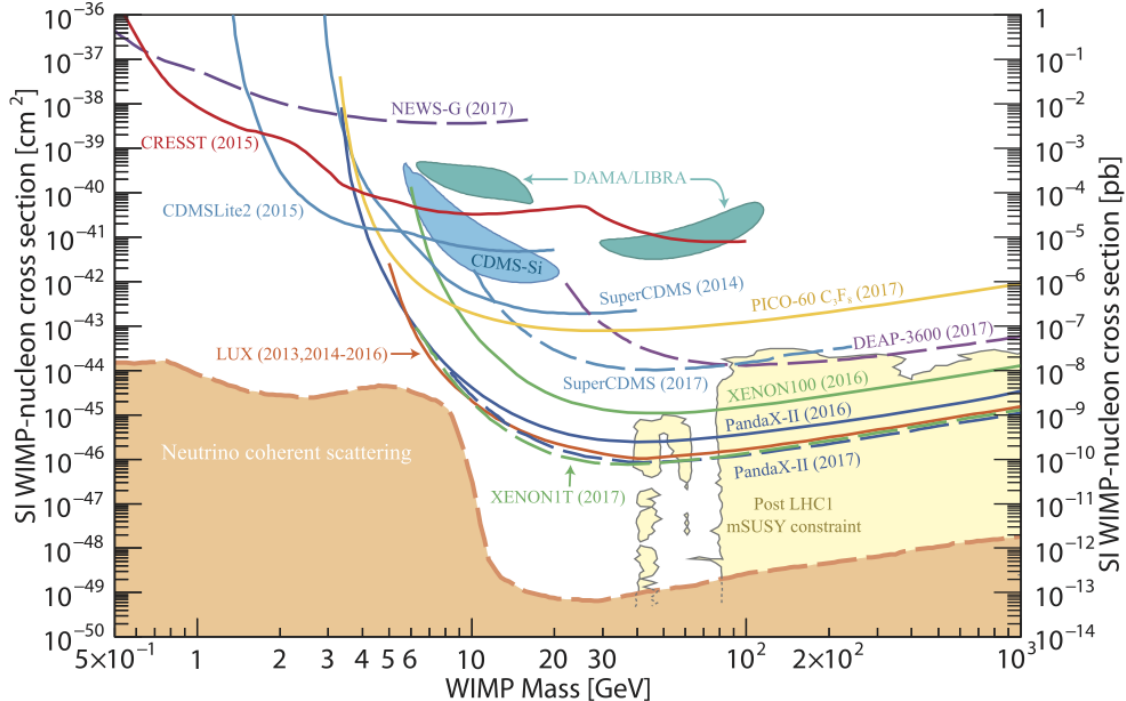


Figure 1.15: Status of spin-independent WIMP cross section from  $0.5\text{-}1000 \text{ GeV}/c^2$  before XENON1T run-combined analysis (Chap. 3). Regions of possible signals from DAMA/LIBRA (shaded green, [124]) and the silicon detector of CDMS II (shaded blue, [125]) are shown. Exclusion limits from PICO-60 (solid yellow line, [73]), DEAP-3600 (dashed purple  $> 20 \text{ GeV}/c^2$ , [126]), SuperCDMS (dashed blue, [127]), NEWS-G (dashed purple  $< 20 \text{ GeV}/c^2$ , [128]), CRESST (solid red, [129]), CDMSLite2 (solid blue, [130]), LUX (solid orange, [120]), PandaX-II (solid dark blue 2016 [83], dashed dark blue, 2017 [121]), XENON100 (solid green, [131]), and XENON1T First Results (dashed green, [132]) are plotted. Four typical super-symmetric (SUSY) models (CMSSM, NUHM1, NUHM2, and pMSSM10) with constraints from ATLAS Run 1 are shown (shaded yellow) for reference [133]. The cross section of neutrino coherent scattering is marked by the orange dashed line and shaded region. Image credit: [27].

# Chapter 2

## Liquid Xenon and Time Projection Chambers

Liquid xenon (LXe) direct detection experiments have led the field for spin-independent WIMP searches with masses  $\gtrsim 20$  for roughly a decade. More so than liquid argon (LAr), LXe results have been paved the way to new limits, surpassing on the way only those of other LXe experiments.

Commercial business, such as steelmaking and coal gasification, rely relatively pure oxygen or nitrogen. During the separation, the small amount of xenon and krypton in the air is extracted into a mixture as a by-product. A distillation process can uncouple the two, leaving highly pure xenon.

This chapter begins by discussing general properties of xenon and why it is such an effective element for a dark matter search (Sec. 2.1), followed by a summary of signal production in liquid xenon (Sec. 2.2). Next the signal properties for different types of interactions are covered (Sec. 2.3) with brief introductions on the microphysics of electronic (Sec. 2.4) and nuclear (Sec. 2.5) recoils. Finally, details of time projection chambers are discussed (Sec. 2.6).

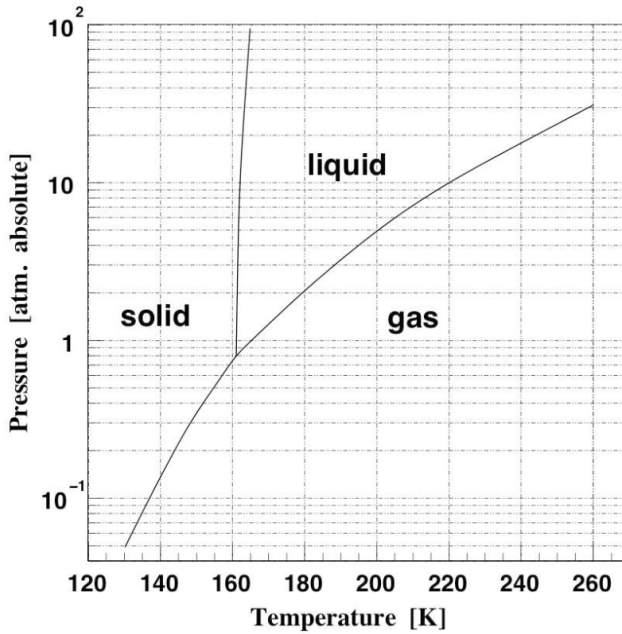


Figure 2.1: Phase diagram of xenon. Image credit: [134].

## 2.1 General Properties

Xenon is a noble gas with atomic number 54 with and a mean molar mass of 131.293 g mol<sup>-1</sup>. It is the heaviest non-radioactive noble gas and due to its full valence electron shell rarely undergoes chemical reactions. It has a concentration of 87 parts per billion (ppb) in the Earth's atmosphere at a density of 5.894 g l<sup>-1</sup>. The phase diagram for xenon is shown in Fig. 2.1 and Tab. 2.1 lists general chemical properties.

The naturally occurring xenon isotopes are listed in Tab. 2.2. <sup>136</sup>Xe, which makes up 8.8573% of natural xenon, has been measured to undergo double beta decay with a half-life of  $t_{1/2} > 2.4 \times 10^{21}$  y. <sup>124</sup>Xe, <sup>126</sup>Xe, and <sup>134</sup>Xe are also predicted to be unstable but decays have not been observed so they are not considered when building a liquid xenon detector or analyzing data [136].

Unstable isotopes with  $t_{1/2} > 1$  h are given in Tab. 2.3. The longest-lived isotope is <sup>127</sup>Xe with  $t_{1/2} = 36.4$  d. Also listed are metastable states <sup>129m</sup>Xe, <sup>131m</sup>Xe, and <sup>133m</sup>Xe with energies 163.9, 236.2, and 233.2 keV  $\gamma$ -rays, respectively. <sup>129m</sup>Xe and <sup>131m</sup>Xe are more commonly produced since <sup>129</sup>Xe and <sup>131</sup>Xe are stable and make up > 47% of natural xenon (Tab. 2.2). Following a nuclear recoil calibration they are used

Chemical Property	Value
Atomic Number	54
Molar mass	131.293 g mol <sup>-1</sup>
Melting point (1 atm)	161.4 K
Boiling point (1 atm)	165.0 K
Density as gas (298 K, 1 atm)	5.40 g l <sup>-1</sup>
Density as gas (165 K, 1 atm)	9.99 g l <sup>-1</sup>
Density as liquid (165 K, 1 atm)	2.94 g cm <sup>-3</sup>
Critical point	16.57°C, 58.4 bar, 1.11 g cm <sup>-3</sup>
Dielectric constant	1.95
Triple point	-111.85°C, 0.805 bar, 2.96 g cm <sup>-3</sup>
Volume ratio ( $\rho_{\text{gas}}/\rho_{\text{liquid}}$ )	519
Thermal conductivity	$5.65 \times 10^{-3}$ W m <sup>-1</sup> K <sup>-1</sup>
Covalent radius	140 ± 9 pm

Table 2.1: Chemical properties for xenon. Data taken from [134], [135].

to measure a number of properties about our detector including the electron lifetime (Sec. 5.2.4). Their shorter-lived 39.6 ( $^{129}\text{Xe}$ ) and 80.2 ( $^{131}\text{Xe}$ ) keV nuclear excited states, which have  $t_{1/2} = 0.97$  ns and 0.48 ns, respectively, are rarely resolvable from the signal of the particle-nucleus scatter.

Xenon has several advantages that make it a good target for dark matter detection. At \$2000/kg it is scaleable for larger detectors. Its high molar mass provides excellent self-shielding, which reduces background contamination in the region of interest due to external radiation (Sec. 3.3.3). Furthermore, nearly 50% of naturally occurring xenon is  $^{129}\text{Xe}$  or  $^{131}\text{Xe}$ , which gives it sensitivity to spin-dependent interactions. Its production of light and charge - referred to as light and charge yields (Sec. 4.3.3) - are among the highest noble gases. Finally, the expected background contribution from xenon itself comes just from  $^{136}\text{Xe}$  so is extremely small (Tab. 2.2). Therefore intrinsic radioactivity comes almost entirely from trace amounts of other radioactive noble gases, which can be reduced (Sec. 3.1.6).

Isotope	Natural Abundance [%]	Spin	Half-life	Decay mode
$^{124}\text{Xe}$	0.0952	0	$> 1.6 \times 10^{14} \text{ y}$	$2\nu\beta^+\beta^+$
$^{126}\text{Xe}$	0.089	0	$> 4.7-12 \times 10^{25} \text{ y}$	$2\nu\beta^+\beta^+$
$^{128}\text{Xe}$	1.910	0	stable	—
$^{129}\text{Xe}$	26.401	1/2	stable	—
$^{130}\text{Xe}$	4.071	0	stable	—
$^{131}\text{Xe}$	21.23	3/2	stable	—
$^{132}\text{Xe}$	26.909	0	stable	—
$^{134}\text{Xe}$	10.436	0	$> 5.8 \times 10^{22} \text{ y}$	$2\nu\beta^-\beta^-$
$^{136}\text{Xe}$	8.857	0	$> 2.4 \times 10^{21} \text{ y}$	$2\nu\beta^-\beta^-$

Table 2.2: Properties of naturally occurring xenon isotopes. Decays of  $^{124}\text{Xe}$ ,  $^{126}\text{Xe}$ , and  $^{134}\text{Xe}$  have not been observed but are predicted.  $^{124}\text{Xe}$  is predicted to also decay by  $2\nu\beta^+\text{EC}$  and  $2\nu\text{ECEC}$ . Half-life and decay information is taken from [136], [137].

Isotope	Spin	Half-life	Decay mode	Decay product
$^{122}\text{Xe}$	0	20.1 h	EC	$^{122}\text{I}$
$^{123}\text{Xe}$	1/2	2.08 h	EC	$^{123}\text{I}$
$^{125}\text{Xe}$	1/2	17.1 h	EC	$^{125}\text{I}$
$^{127}\text{Xe}$	1/2	36.4 d	EC	$^{127}\text{I}$
$^{129m}\text{Xe}$	11/2	8.88 d	$\gamma$ -ray	ground state
$^{131m}\text{Xe}$	11/2	11.93 d	$\gamma$ -ray	ground state
$^{133}\text{Xe}$	3/2	5.24 d	$\beta^-$	$^{133}\text{Cs}$
$^{133m}\text{Xe}$	11/2	2.19 d	$\gamma$ -ray	ground state
$^{135}\text{Xe}$	3/2	9.14 h	$\beta^-$	$^{135}\text{Cs}$

Table 2.3: Unstable isotopes of xenon with half-lifes of  $> 1$  hr. Spins, half-lifes, decay modes, and decay products are listed.

## 2.2 Signal Production

As radiation scatters off a xenon atom it will cause photon emission due to two effects. The first is electrons excited to higher orbitals will quickly de-excite, with the energy carried away by photons. The second possibility is ionized xenon may recombine with an electron (can but doesn't need to be its own), after which it is in an excited state equivalent to the first scenario. In the context of this and other experiments the photons are observed as primary (or prompt) scintillation. Secondary scintillation results from electrons that do not recombine and is measured only in a time-projection chamber (TPC). This chapter only considers interactions in xenon in the presence of an electric field, unless otherwise specified.

### 2.2.1 Primary Scintillation

When a particle scatters off a xenon atom it can excite or ionize its valence electrons. A freed electron can escape or recombine with a  $\text{Xe}^+$ . Excitons  $\text{Xe}^*$  can bond with another Xe atom to create dimers,  $\text{Xe}_2^*$ , commonly referred to as excimers. The processes of recombination is shown in Eq. 2.1, where  $Q$  represents heat.

If the interaction occurs in an electric field some  $e^-$  will be pulled from the site, which lowers recombination and therefore decreases primary scintillation and increases secondary scintillation (Sec. 2.2.2). The extent to which recombination changes depends on the strength of the electric field. However, even without a field there will not be 100% recombination because some of the freed  $e^-$  will escape the electromagnetic pull of their parent ions.



The  $\text{Xe}^*$  that has results from recombination is equivalent to if it had only ever been excited. At this point it de-excites via Eq. 2.2.  $\text{Xe}_2^*$  is in either a singlet ( ${}^1\Sigma$ ) or triplet ( ${}^3\Sigma$ ) state and quickly de-excites to the ground state.



The average  $\gamma$ -ray in Eq. 2.2b has a wavelength of 178 nm. Not surprisingly, the number of photons is anti-correlated with the number of electrons, since for each  $e^-$  that recombines with xenon a  $\gamma$ -ray is emitted. The lifetimes for the singlet and

Event	$^1\Sigma/{}^3\Sigma$
ER (direct excitation from $\gamma$ )	$0.17 \pm 0.05$
ER (recombination from $\gamma$ )	$0.8 \pm 0.2$
ER (from $\alpha$ )	$2.3 \pm 0.51$
NR (from neutron)	$7.8 \pm 1.5$

Table 2.4: Error-weighted average of world data for single-to-triplet ratios for various scattering cases [138].

triplet excimers are  $3.1 \pm 0.7$  ns and  $24 \pm 1$  ns, respectively [138]. The singlet-to-triplet ratios for a number of different interactions are shown in Tab. 2.4. Detecting WIMPS requires differentiating between scatters with the xenon electron shells (electronic recoils) and nucleus (nuclear recoils). Tab. 2.4 shows that nuclear recoils result in a higher fraction of singlet states. Unfortunately the  ${}^1\Sigma$  and  ${}^3\Sigma$  lifetimes are too short to resolve so they cannot be used for discrimination. This makes single-phase LXe detectors less desirable than liquid argon (LAr), which has single and triplet states of  $< 6.2$  ns and  $1.30 \pm 0.06$   $\mu\text{s}$  [139].

Fig. 2.2 shows the interaction channels of  $\beta$ - or  $\gamma$ -induced xenon recoils described in Eq. 2.1 and Eq. 2.2. It does not show photon quenching due to biexcitonic quenching or the Penning process, which are important in nuclear recoils (Sec. 2.2.4).

### 2.2.2 Secondary Scintillation

In an electric field  $E$  an  $e^-$  that is freed but does not recombine with its parent or other ions will move anti-parallel to the field at drift velocity  $v_d$ . At fields of  $\lesssim 100$  V cm $^{-1}$  the drift velocity is nearly proportional to  $E$  and is given by  $v_d = \mu E$  where  $\mu$  is the electron mobility, estimated to be  $\sim 2200$  cm $^2$  V $^{-2}$  s $^{-1}$  at these fields [141]. As  $E$  increases  $v_d \propto E^{1/2}$  until approximately 10 $^4$  V cm $^{-1}$  where it flattens at  $\sim 3$  mm  $\mu\text{s}$ . Fig. 2.3 shows  $v_d$  as a function of  $E$  and Tab. 2.2.2 gives the approximate relationship.

In liquid noble gas detectors used for dark matter searches electrons are drifted to the surface of the liquid and extracted across  $\sim 5$  mm of xenon gas. As the electrons drift across the gas they excite and ionize new xenon atoms, creating a second signal

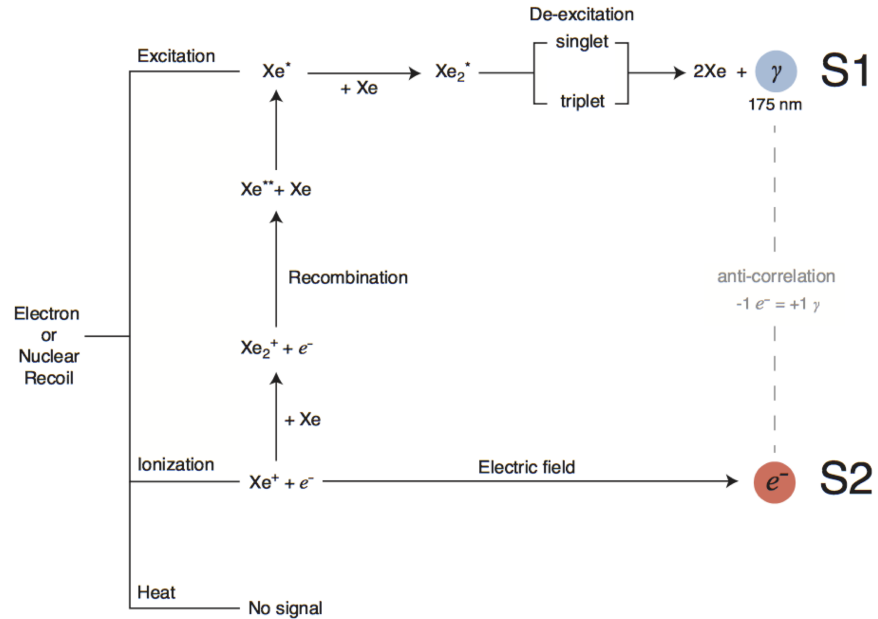


Figure 2.2: Signal generation pathways for electronic and nuclear recoils. Describe paths of electrons. Image credit: [140].

$E$ [V cm $^{-1}$ ]	$E$ dependence
$\lesssim 100$	$E$
$\sim 100\text{-}10^{3\text{-}4}$	$E^{1/2}$
$\gtrsim 10^4$	—

Table 2.5: Drift velocity  $v_d$  as a function of electric field  $E$  for LXe

referred to as secondary scintillation. Because the amount of scintillation produced per electron is independent of the number of electrons extracted this is also known as proportional scintillation. By measuring this scintillation the number of  $e^-$  extracted can be determined. Details of  $e^-$  drift and proportional scintillation is found in Sec. 2.6.1.

### 2.2.3 Stopping Power

A particle that loses energy through inelastic collisions with electrons (prompting excitation and ionization) produces an electronic recoil. The energy lost per unit

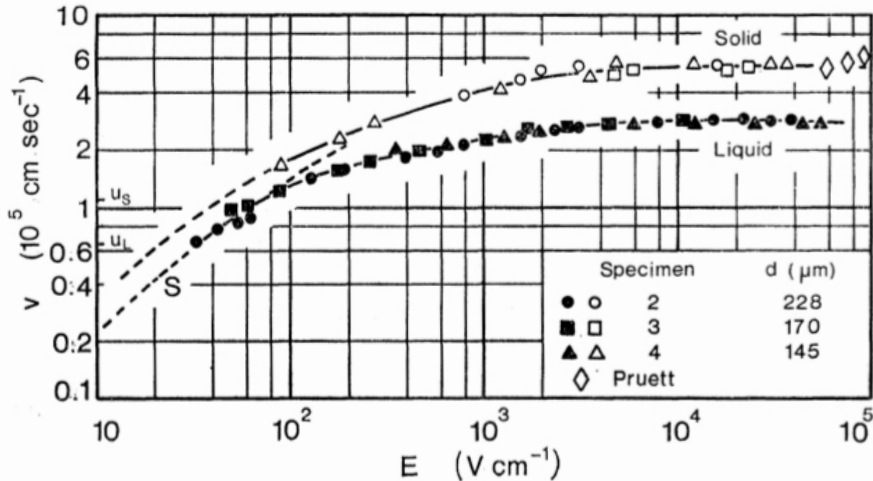


Figure 2.3: Field-dependent drift velocity for solid ( $-116^{\circ}\text{C}$ ) and liquid ( $-110^{\circ}\text{C}$ ) xenon. Image credit: [141].

length is the electronic stopping power  $S_{\text{elec}}(E) = -(dE/dx)_{\text{elec}}$  ( $S_{\text{elec}}$  is positive). It is correlated with the linear energy transfer (LET) and depends on the type and energy of the particle and properties of the medium (e.g. density and composition). A larger electronic stopping power indicates the particle will slow more quickly and transfer its energy more densely along its track. This affects recombination between  $e^-$  and ions and is discussed in Sec. 2.2.4.

The energy loss per unit length of a particle through elastic collisions with atoms is the nuclear stopping power  $S_{\text{nucl}}(E) = -(dE/dx)_{\text{nucl}}$ . In contrast to electronic stopping power,  $S_{\text{nucl}}(E)$  quantifies the slowing of the particle due to interactions with nuclei of the target and can be calculated using the repulsive potential energy between atoms.

Dividing the stopping power by the medium's density ( $S(E)/\rho$ ) gives a function of the incident particle known as the mass stopping power. Electronic (long dashed) and nuclear (short) mass stopping powers are shown for alphas, electrons, and protons in Fig. 2.4.  $S_{\text{elec}} > S_{\text{nucl}}$  over all energy except for electrons above roughly 15 MeV. The total stopping power is

$$\left(\frac{dE}{dx}\right)_{\text{tot}} = \left(\frac{dE}{dx}\right)_{\text{elec}} + \left(\frac{dE}{dx}\right)_{\text{nucl}} \quad (2.3)$$

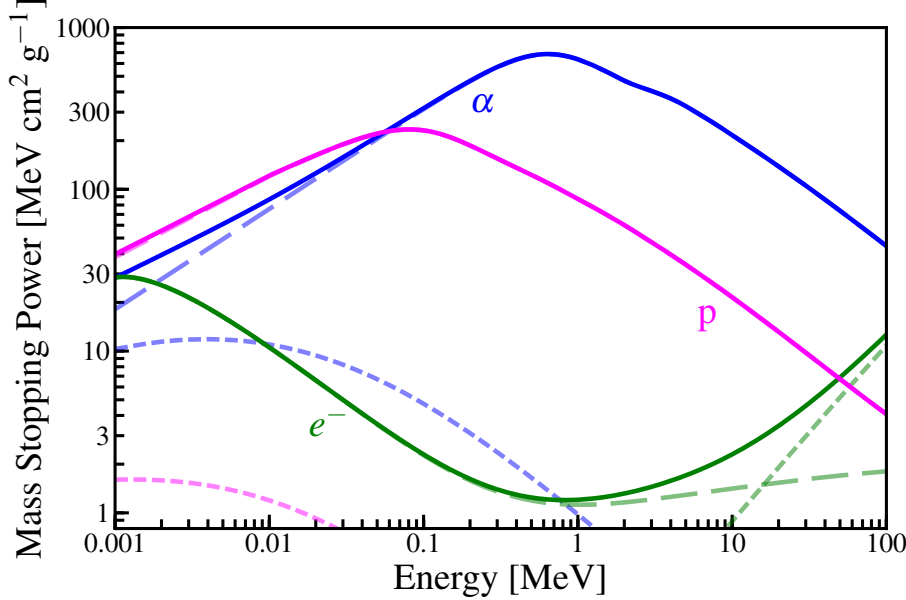


Figure 2.4: Mass stopping power for alphas (blue),  $e^-$  (green), and protons (pink). Electronic (long dashed), nuclear (short dashed), and total (solid) stopping powers for each are shown. The electronic stopping power is more significant except for  $e^-$  at  $\gtrsim 15$  MeV. Data from [142].

and is shown as the solid lines in Fig. 2.4. The mean path length of a particle with initial energy  $E_0$  can be approximated by

$$\Delta x = \int_0^{E_0} \frac{1}{S(E)} dE \quad (2.4)$$

where  $\Delta x$  is the continuous slowing down approximation (CSDA) and  $S(E) \equiv -(dE/dx)_{\text{tot}}$ . Eq. 2.4 does not account for energy-loss fluctuations. For spin-independent WIMP dark matter searches the relevant energy range for electrons is 1-20 keV. In this region  $S(E)/\rho$  decreases so electrons with more energy will travel farther by a ratio greater than their energy. Alphas do not affect our dark matter search since they are in the MeV range and are easily identified by their large primary scintillation. The  $\alpha$ -decays that are relevant in our detector sit mostly around 5-7 MeV so have a stopping power between 200-400  $\text{MeV cm}^2 \text{ g}^{-1}$ . In this region their mass stopping power also decreases with energy. The  $\alpha$  and proton curves have similar shapes because they are both described by the Bethe formula [143].

One of the biggest advantages of liquid xenon is its large stopping power (largely

due to its high atomic mass), which provides self-shielding. Because distance and stopping power are anti-correlated, particles in LXe travel relatively short distances before stopping. Self-shielding protects the interior of the detector from outside radiation, which rarely penetrates more than a few cm into the LXe, allowing a larger fiducial volume (FV) for dark matter searches. Because the stopping power is proportional to the density of the medium, LXe is more effective at self-shielding than liquid argon ( $\rho = 1.395 \text{ g cm}^{-3}$ ) and liquid neon ( $1.207 \text{ g cm}^{-3}$ ).

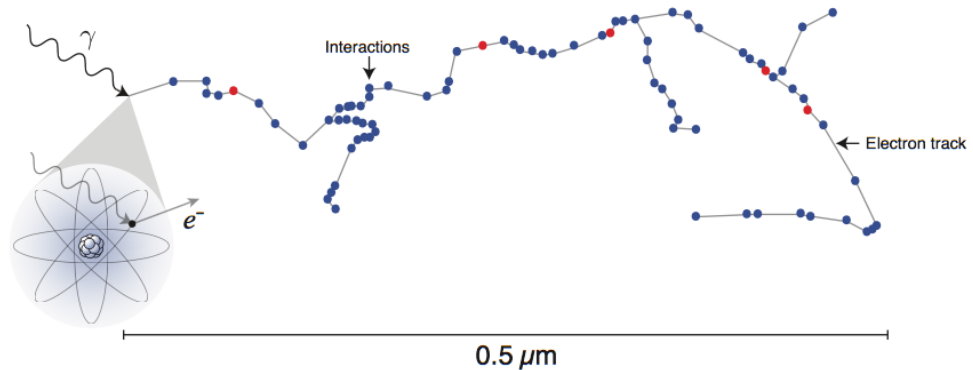
The track structure from a recoiling electron or xenon nucleus is characterized by the distribution of  $e^-$ , ions, excitons, and heat when all electrons have slowed to sub-excitation speeds [144]. Tracks are typically cylindrical with secondary branches from  $\delta$ -ray. However, aside from this basic structure they can vary considerably with particle, energy, and stopping power, and they play a major role in recombination. Fig. 2.5 shows tracks for 20 keV electronic and nuclear recoils. For the electronic recoil a  $\gamma$ -ray ionizes the atom and transfers its energy to the freed electron. As the electron moves through the xenon it excites and ionizes more atoms, creating secondary branches from  $\delta$ -rays until it comes to a rest after roughly  $0.5 \mu\text{m}$ . The number of ions is  $\sim 20$  times as high as the number of excitons. Because the  $e^-$  only interacts with the electron shells of the atom not energy is lost as heat.

For the nuclear recoil a 20 keV neutron scatters with a xenon nucleus. Unlike the electronic recoil where the energy of the  $\gamma$ -ray is passed to the electron (after small loss from ionization) for a nuclear recoil it is passed to the atom. The higher stopping power creates a denser track and a shorter average path length of approximately 10 nm. In addition to exciting and ionizing, the recoiling atom passes translational energy to other atoms that cannot be observed (Sec. 2.2.4). The exciton-to-ion ratio is roughly 1, and the higher density of ions leads to greater recombination between electrons and non-parent  $\text{Xe}^+$ .

#### 2.2.4 Recombination

A fraction of atoms that are ionized recombine with electrons. The recombination fraction depends on a number of parameters including ionization density (stopping

## Electron Recoil



## Nuclear Recoil

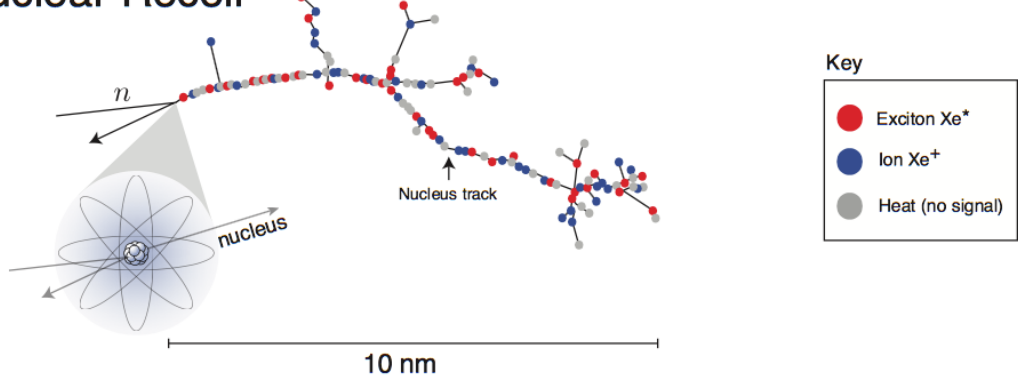


Figure 2.5: Electronic (top,  $\gamma$ ) and nuclear (bottom, neutron) recoil tracks for 20 keV scatters. Excitons (red circles), ions (blue), and heat (grey) are marked along the track. The electronic recoil produces  $\sim 20\times$  as many ions as excitons while for nuclear recoil they are roughly equal. Heat is only relevant in NRs and leads to signal quenching. The electronic recoil has a path of  $\sim 1 \mu\text{m}$  while the much denser 10 nm of the NR compels higher recombination. Image credit: [140].

## 2. LIQUID XENON AND TIME PROJECTION CHAMBERS

---

power, Sec. 2.2.3), thermal energy of ionized atoms and  $e^-$ , electron mobility, diffusion rate, electric field, and probability of recombination when an electron and ion meet.

An early theory by Onsager modeled recombination by defining what is now known as the Onsager radius as the distance between an electron-Xe<sup>+</sup> pair where the Coulomb energy equals the  $e^-$  thermal energy [145]. An electron within the Onsager radius will be unable to escape so will recombine with the ion. At the Onsager radius the probability of escape is  $e^{-1}$ . An  $e^-$  with  $E_{\text{thermal}} > E_{\text{Coulomb}}$  should not be influenced by the ion, regardless of the presence of an electric field. The thermalization range for LXe is 4000-5000 nm [146], far higher than the Onsager radius for liquid xenon of 49 nm. Without an electric field a large fraction of these electrons will recombine on timescales of  $> 1$  ms, which because of the short observation window will appear as a decrease in photons, and the electrons will be classified as having escaped (with an electric field the electrons outside the Onsager radius will drift from the interaction site and not recombine) [147].

A shortcoming of the Onsager radius is that it treats the interactions between Xe<sup>+</sup> and  $e^-$  as strictly Coulomb. However, the high coefficient of polarization of LXe produces dipole moments in the ions, causing the electric field to fall faster than  $1/r$ . In fact, the potential is steep enough that the ion travels via phonon-assisted tunneling [148], making its mobility significantly smaller (3-5 orders of magnitude [141], [149]) than that of the electrons.

As a result of these disparities another model was proposed that includes diffusion but the rate of recombination depends on the density of  $e^-$  and ions independently [150]. Its derivation comes by

$$\frac{\partial N_+}{\partial t} = -u_+ \mathbf{E}_d \cdot \nabla N_+ + d_+ \nabla^2 N_+ - \alpha N_+ N_- \quad (2.5a)$$

$$\frac{\partial N_-}{\partial t} = u_- \mathbf{E}_d \cdot \nabla N_- + d_- \nabla^2 N_- - \alpha N_+ N_- \quad (2.5b)$$

where  $N_\pm$  are the ion (+) and electron (-) charge distributions ( $N_+ = N_-$ ),  $\mu_\pm$  are

their mobilities,  $d_{\pm}$  and  $\alpha$  are the coefficients for diffusion and recombination, and  $\mathbf{E}_d$  is the electric field. The terms on the right sides of Eq. 2.5a and Eq. 2.5b correspond to the drift, diffusion, and recombination, from left to right. The diffusion in xenon is small (millimeters per drift meter [151]) and can be ignored. Likewise the ion mobility  $\mu_+$  is several orders of magnitude smaller than that of the electron and is disregarded. Thus Eq. 2.5 can be simplified to

$$\frac{\partial N_+}{\partial t} = -\alpha N_+ N_- \quad (2.6a)$$

$$\frac{\partial N_-}{\partial t} = u_- E_d \frac{\partial N_-}{\partial z} - \alpha N_+ N_- \quad (2.6b)$$

which, if each electron-ion pair is sufficiently far from all others, can be solved exactly. After some integration and algebra (detailed in [148]), the recombination fraction is

$$r = 1 - \frac{\ln(1 + N_0 \varsigma)}{N_0 \varsigma}, \quad \varsigma = \frac{\alpha}{4a^2 u_- E_d} \quad (2.7)$$

where  $N_0$  is the number of ions and electrons at  $t = 0$  that uniformly occupies over a box of dimension  $a$ . This is known as the Thomas-Imel box model [148], and is successful at explaining recombination measurements including those shown in Fig. 2.6. Zero recombination corresponds to  $\varsigma \rightarrow 0$  and complete recombination occurs when  $\varsigma \rightarrow \infty$ . In this model  $E = 0$  equates to total recombination, though as mentioned above, this likely occurs outside of the typical observation window.

The Thomas-Imel box model works well for short particle tracks but has shortcomings for longer. At long particle tracks a Birks' Law (originally developed for organic scintillators, [152], [153]) derivation for liquid noble gases yields

$$\frac{dN_{\pm}}{dt} = -\alpha N_+ N_- \quad (2.8)$$

for volume recombination - that is, for electrons to recombine with a  $\text{Xe}^+$  that is not their parent. Here  $N_{\pm}$  and  $\alpha$  have the same definitions as in the Thomas-Imel model. Eq. 2.8 is simplified by assuming  $N_+ = N_-$  and the number of each is proportional to

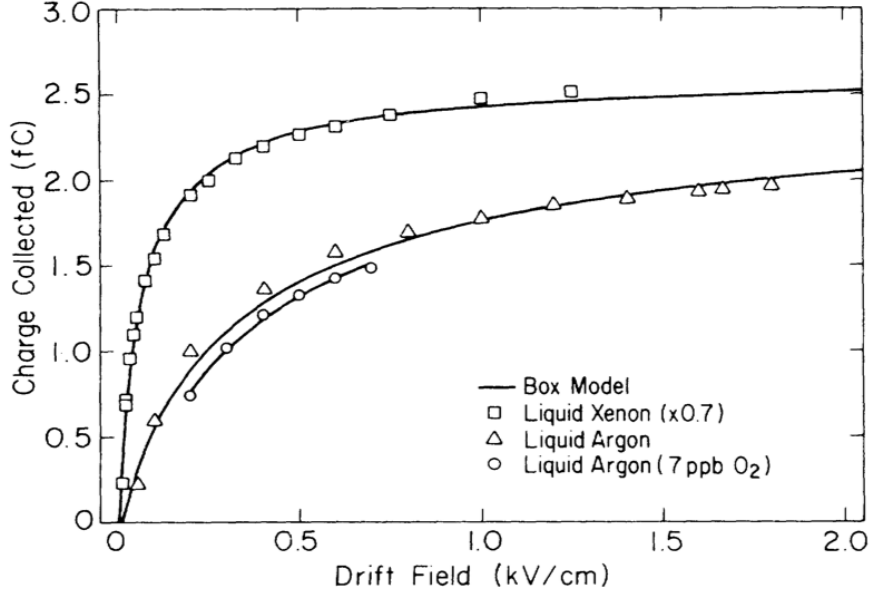


Figure 2.6: Measurements of charge collected ( $q \propto 1-r$ ) for LAr and LXe with respect to  $E_d$ . Squares correspond to LXe and were measured with  $\varsigma N_0 E = 0.15 \text{ kV cm}^{-1}$ . Triangles and circles are LAr and were measured at  $\varsigma N_0 E = 0.84 \text{ kV cm}^{-1}$ . Curves are fits to data using the Thomas-Imdel box model [148].

the stopping power  $N_{\pm} \propto dE/dx$  (Sec. 2.2.3). The latter is only valid for cylindrical, or long tracks. Short tracks, which correspond to lower LET and therefore  $dE/dx$ , are described better by a spherical excitation-ionization density [144]. This gives a recombination of

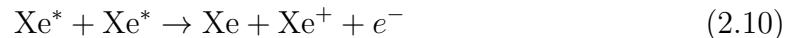
$$r = \frac{A \frac{dE}{dx}}{1 + B \frac{dE}{dx}} + C \quad (2.9)$$

where  $A$ ,  $B$ , and  $C$  are constants derived in the fit [154]. The two terms on the right side of the equation correspond to non-geminate and geminate recombination, respectively. Geminate recombination ( $C$ ) quantifies the  $e^-$  that recombine with their parent ions and is governed by Onsager's model with fixed probability for all  $dE/dx$  [155]. Non-geminate (volume) recombination is when an  $e^-$  is captured by an ion different than its parent. This has been shown to be valid at  $E \gtrsim 80 \text{ keV}$  for  $\gamma$ -rays and light ions, and  $\sim 1 \text{ MeV}$  electrons.

The considerable LET for  $\alpha$ -particles creates high-density tracks that lead to

strong and quick recombination. The density is so high only a small percent of  $e^-$  avoid recombination, even at electric fields of  $\sim 10 \text{ kV cm}^{-1}$  (for electrons this is nearly 100%) [144]. The consistency in charge collection across different fields causes difficulties in distinguishing recombination from excitation.

Birk's saturation law explains biexcitonic quenching and the Penning process, which play major roles in nuclear recoils. Biexcitonic quenching occurs as



where the  $e^-$  escapes with kinetic energy  $E = 2E_{\text{ex}} - E_g$  where  $E_{\text{ex}}$  and  $E_g$  are the energies of an exciton and band gap, respectively. The  $e^-$  will quickly lose its energy and recombine, resulting in the emission of a single photon instead of two from the initial excitons. A second quenching comes from collisions between excimers via the Penning process that results in an excited and ground molecular states [156]. For nuclear recoils these quenching factors can be parameterized by

$$f_b = \frac{1}{1 + k_B B \frac{dE}{dx}} \quad (2.11)$$

where  $k_B$  is Birks' constant [152], [153].

The decrease in scintillation yield for  $\beta$  and  $\gamma$  is only observed at low LET where the ionization density is relatively low. The lack of neighboring  $\text{Xe}^+$  reduces the probability of recombination with a non-parent ion. At higher LET the ion density is sufficient for nearly 100% recombination and results in the flat region in Fig. 2.7. However, unlike nuclear recoils this there is no true decrease in photons and electrons so this effect does not result in quenching.

## 2.3 Interactions

Because WIMPs are expected to scatter with nuclei electronic recoils are excluded in early analyses ([132], Chap. 3) as possible signals and considered only as back-

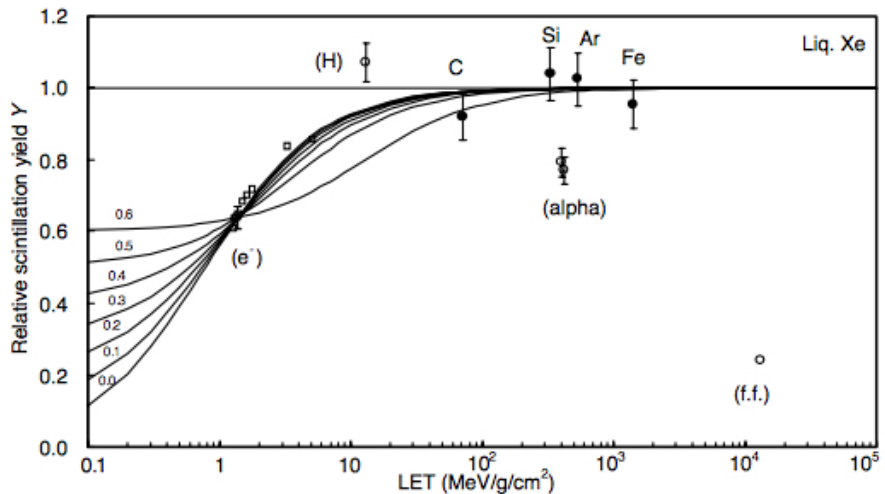


Figure 2.7: Scintillation yield as a function of LET in LXe. Open circles represent electrons, alpha particles, and fission fragments. Solid circles represent relativistic heavy particles. Open squares mark gamma-rays. Solid lines trace various fits to  $\beta$ - $\gamma$  data from [147]. Image credit: [147].

ground.<sup>1</sup> However, understanding the electronic recoil background is necessary to be able to discriminate against nuclear recoils. Detector materials have radioactive elements that decay inside the detector, and there are intrinsic backgrounds such as  $^{85}\text{Kr}$  and  $^{222}\text{Rn}$ . The latter is much more concerning since events from detectors materials cannot breach the inner volume, but intrinsic sources are uniformly distributed throughout the xenon.

To understand our detector calibrations are regularly performed (Sec. 3.2). In the tonne-scale era of liquid xenon detectors external sources, which were effective in past experiments, are less efficient because xenon's self-shielding makes it extremely difficult for radiation to penetrate the interior. Therefore radioactive sources that have short half-lives and can be mixed with the xenon such as  $^{83\text{m}}\text{Kr}$  and  $^{220}\text{Rn}$  are used. Because these sources and their progenies have short half-lifes or are stable, they do not contribute to our background after 2-3 days.

---

<sup>1</sup>Results from a WIMP-electron coupling analysis can be found in [157].

### 2.3.1 Photons

Photons produce electronic recoils as they interact with  $e^-$  via Compton scattering, pair production, or photoelectric absorption as shown in Fig. 2.8. Coherent (Rayleigh and Thomson) scattering are also shown though their net energy deposition in the xenon is zero.

In Compton scattering the photon recoils off of an  $e^-$  and transfers to it a portion of its energy. The final energy of the photon depends only on its initial energy and the scattering angle. Nuclear Compton scattering is possible but much rarer [158]. The low-energy limit of Compton Scattering (photon wavelength larger than particle Compton wavelength) is Thomson scattering. Thomson and Rayleigh scattering are elastic so they have a net energy contribution of zero, and are known as coherent scatters.

Pair production occurs when a high-energy photon produces a particle-antiparticle pair. Typically this refers to a photon passing sufficiently close to an atom's nucleus and creating an electron-positron pair. The proximity of the nucleus is required to conserve momentum so it will recoil slightly. The photon must have an energy of at least twice the electron mass  $m_e$ , or  $1.0222 \text{ MeV}/c^2$ . Pair production also occurs for a photon in the presence of an atomic electron but is less probable and requires an energy of at least  $4m_e$ . This is known as triplet production since the recoiling electron creates a track in addition to the electron-positron pair [159]. At high energies pair production becomes the dominant interaction for photons and matter.

Photoelectric absorption is when an electron absorbs the energy of the photon and is liberated from its electron shell. In this case the photon disappears entirely and the kinetic energy of the electron is equal to the photon's energy minus the electron binding energy. Photoelectric absorption was helpful for calibrating small detectors using mono-energetic  $\gamma$ -rays from elements such as  $^{137}\text{Cs}$  (661.7 keV) and  $^{60}\text{Co}$  (1.1732 and 1.3325 MeV). For large detectors self-shielding prevents even high-energy  $\gamma$ -rays from reaching the fiducial volume, so external sources cannot be used for calibration. Photoelectric absorption is the dominant interaction in the WIMP

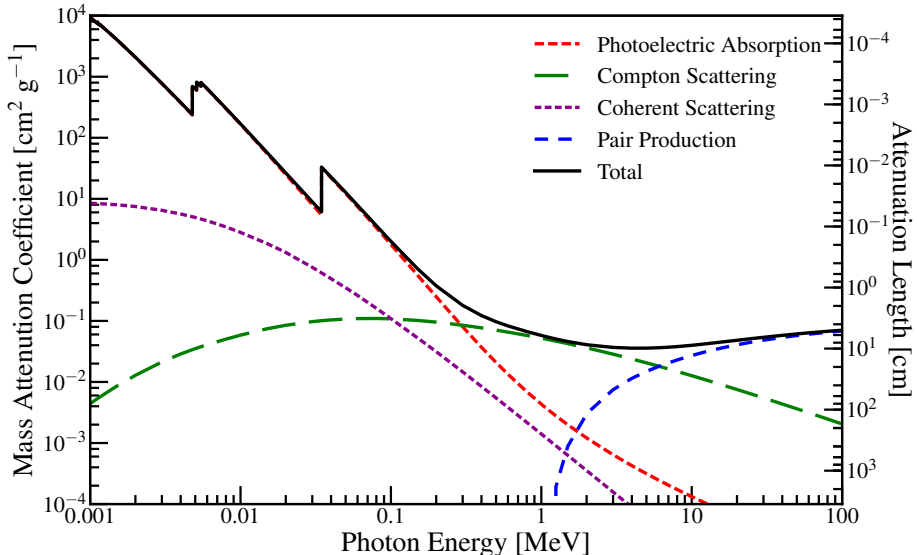


Figure 2.8: Mass attenuation coefficient and attenuation length for 1 keV to 100 MeV photons. Photoelectric absorption (red dashed), Compton scattering (green), coherent (Rayleigh and Thomson) scattering (purple), and pair production (blue) are shown in addition to the total (solid black). The discontinuity at  $\sim 5$  keV occurs just above the binding energy of the L-shell electrons and is due to an increase in photoelectric absorption. A similar process occurs for the K-shell at roughly 40 keV. Data from [160].

search energy region of interest ( $E < 20$  keV), and is shown as the red dotted line in Fig. 2.8.

### 2.3.2 $\beta$ -Decays

$\beta$ -decays are the emission of an electron-antineutrino (positron-neutrino) from a neutron (proton). As with photons, they interact with the  $e^-$  shell and produce electronic recoils. Because the neutrino carries some momentum, the energy spectrum of the  $e^-$  is not mono-energetic, so it can be difficult to identify the origin of the event. In xenon experiments low-energy  $\beta$ -decays contribute the most contamination in the search region and occur throughout the entire volume due to  $^{85}\text{Kr}$  and  $^{222}\text{Rn}$  being uniformly throughout the detector.  $^{85}\text{Kr}$  decays via



with an end-point energy of 687 keV and branching ratio of 99.53% and (remaining 0.47% is 173 keV plus 514 keV  $\gamma$ -rays). These low-energy  $\beta$ -decays contaminate the search region, and their half-life of 10.72 years ensures their presence throughout the lifetime of the experiment.

$^{222}\text{Rn}$  presents a similar problem. It is a daughter of the  $^{238}\text{U}$  decay chain emanates from the detector materials. Like  $^{85}\text{Kr}$  it is a noble gas so it mixes with the xenon. Its two most dangerous daughters are  $^{214}\text{Pb}$  and  $^{214}\text{Bi}$ , each of which undergo  $\beta$ -decay.  $^{214}\text{Bi}$  is easily identifiable because its daughter  $^{214}\text{Po}$  has a half-life of 160  $\mu\text{s}$  and undergoes  $\alpha$ -decay. Thus a cut on coincidence can remove these events.  $^{214}\text{Pb}$  is more dangerous because there is no observable hallmark of its decay. Its end-point energy when it decays to the ground state of  $^{214}\text{Bi}$



is 1019 keV. More concerning is a decay to higher energy levels, which if near the border of the fiducial volume has a risk of the subsequent  $\gamma$ -ray exiting undetected. In XENON100 recoiling daughters of the  $^{222}\text{Rn}$  decay chain were observed to drift towards the cathode - possible the result of becoming ionized from parent decays [161] - lowering the number of  $\beta$ -decays in the region of interest.

### 2.3.3 Neutrinos

Neutrinos produce both electronic and nuclear recoils at low energies. Solar neutrinos can elastically scatter off  $e^-$  and produce an electronic recoil.  $pp$  neutrinos make up 92% of these scatters, with  $^7\text{Be}$  making 7%, and all other sources contributing < 1% [162].

Coherent neutrino-nuclear scattering (CNNS) is the process by which low energy neutrinos interact coherently with protons and neutrons in nuclei. This process produces nuclear recoils with a cross section that is greatly increased due to the coherent nature of the interaction. The majority of these interactions in the energy region of interest come from Solar  $^8\text{Be}$  and  $hep$  neutrinos, as those at higher energy sources

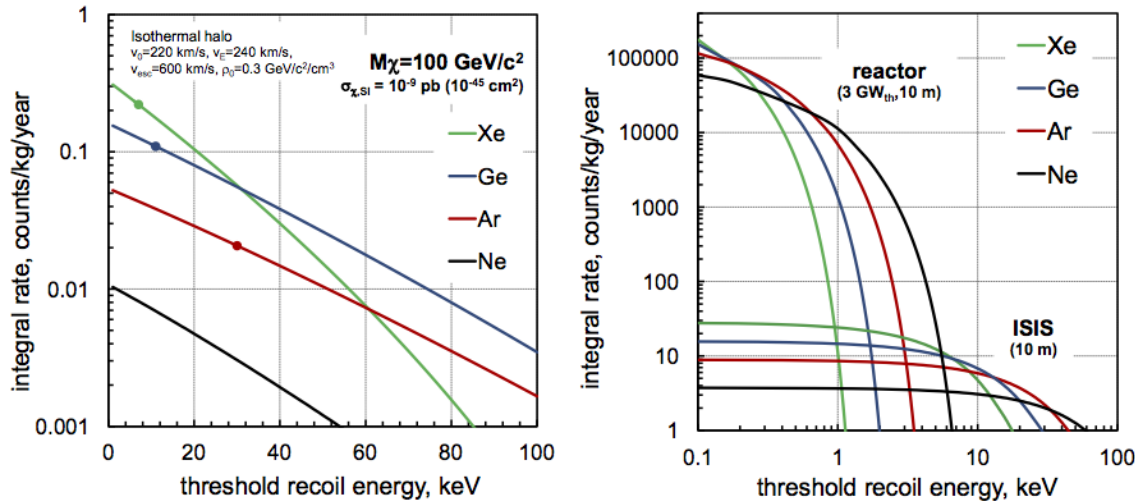


Figure 2.9: Predicted integral spectra for xenon (green), germanium (blue), argon (red), and neon (black) for WIMP elastic scattering (left) and coherent neutrino-nucleus elastic scattering (right). The expected WIMP spectra are for  $m_\chi = 100 \text{ GeV}/c^2$  with a cross section of  $10^{-45} \text{ cm}^2$  per nucleon, computed using [67] and assuming the standard halo model (Sec. 1.4.3). The circles mark characteristic thresholds. The expected CNNS integral rates are shown for 10 m from a 3 GW<sub>th</sub> nuclear reactor and the ISIS neutron spallation source [163] (fluxes of  $4 \times 10^{13}$  and  $10^7 \nu \text{ cm}^{-2} \text{ s}^{-1}$ , respectively). The majority of CNNS events occur below the thresholds of each material. Both plots assume perfect energy resolution. Image credit: [144].

such as diffuse supernovae and Earth’s atmosphere have a significantly lower rate. Integral rates for 100 GeV/c<sup>2</sup> WIMPs and two CNNS sources are shown in Fig. 2.9. The majority of CNNS events occur below the typical threshold for xenon.

Neutrinos are an irreducible background that affects our detector uniformly. Its contribution scales proportionally with mass so as detectors continue to grow its contribution will become larger. The neutrino coherent scattering cross section is shown in Fig. 1.15.

### 2.3.4 Neutrons

Neutrons in our detector come from two main sources: spontaneous fission (mainly  $\alpha$ ) of elements in primordial chains  $^{238}\text{U}$ ,  $^{235}\text{U}$ , and  $^{232}\text{Th}$  that are present in detector materials (known as radiogenic neutrons), and muons passing through the rock and

Isotope	Decay	Energy [keV]	Half-Life
$^{125}\text{Xe}$	$^{125}\text{Xe} \rightarrow ^{125}\text{I} + e^+ + \nu_e$	622.17	16.89 h
	$^{125}\text{I} + e^- \rightarrow ^{125}\text{Te} + \nu_e$	185.77	59.38 d
$^{127}\text{Xe}$	$^{127}\text{Xe} + e^- \rightarrow ^{127}\text{I} + \nu_e$	662.33	36.34 d
$^{133}\text{Xe}$	$^{133}\text{Xe} \rightarrow ^{133}\text{Cs} + e^- + \bar{\nu}_e$	427.36	5.24 d
$^{135}\text{Xe}$	$^{135}\text{Xe} \rightarrow ^{135}\text{Cs} + e^- + \bar{\nu}_e$	1164.8	9.14 h
	$^{135}\text{Cs} \rightarrow ^{135}\text{Ba} + e^- + \bar{\nu}_e$	268.66	$2.315 \times 10^6$ y

Table 2.6: Radioactive isotopes of Xe produced from neutron capture. Decays are shown to stable elements along with decay energies and half-lives

material above and around the detector (cosmogenic neutrons). Radiogenic neutrons have energies in the MeV range while cosmogenic can reach tens of GeV [162]. Neutrons have a mean free path on the order of ten cm, which makes them more difficult to shield than  $\alpha$ ,  $\beta$ , or  $\gamma$ . Furthermore, neutrons produce nuclear recoils, which can make them indistinguishable from WIMPs. It is critical then to have a thorough understanding of the neutron background so a reliable calculation of the number of background events in the signal region can be made. Failing to do so risks mistaking a neutron as a WIMP or vice versa.

Neutrons will scatter elastically, inelastically, or be radiatively absorbed by xenon nuclei. Radiative absorption is when the nucleus captures the neutron, extending its atomic mass by one. Fortunately, because the number of stable isotopes is large the increase often leads to another stable atom. Exceptions are  $^{125}\text{Xe}$ ,  $^{127}\text{Xe}$ ,  $^{133}\text{Xe}$ , and  $^{135}\text{Xe}$ , which are listed in Tab. 2.6 along with their decays and half-lives.  $^{125}\text{I}$  and  $^{135}\text{Cs}$  have sufficiently long half-lives that they will be removed by the getters from the LXe before they decay, as will with stable daughters  $^{127}\text{I}$  and  $^{133}\text{Cs}$ .

A neutron that inelastically scatters with xenon will leave the nucleus in an excited state. The neutron will still cause a nuclear recoil but the nuclear activation will de-excite with the emission of a  $\gamma$ -ray. The most relevant isotopes for our detector are  $^{129}\text{Xe}$  and  $^{131}\text{Xe}$ , which have half-lives of 0.97 and 0.48 ns and decay with energies 36.9 and 80.2 keV, respectively. These lifetimes are much shorter than the temporal resolution of the detector ( $\mathcal{O}(10)$  ns) so the recoil and de-excitation will appear as a

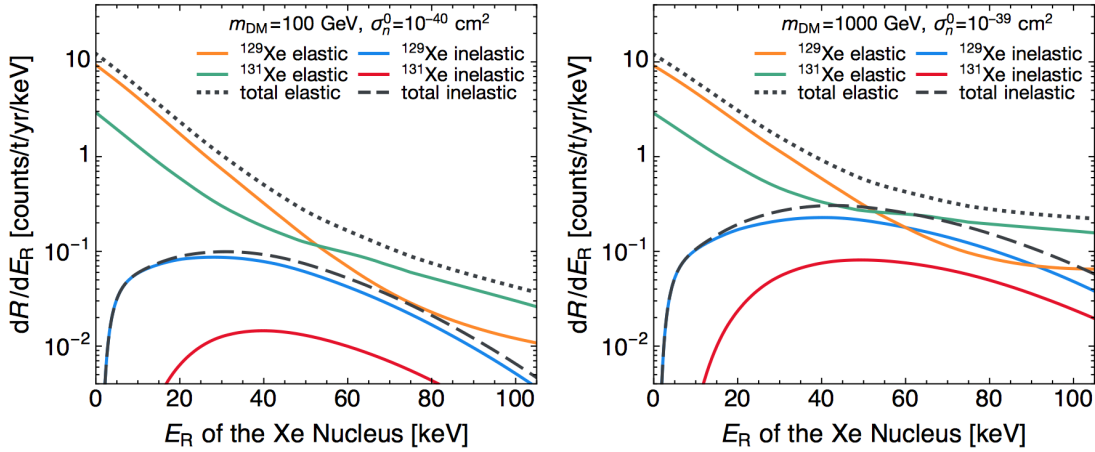


Figure 2.10: Spin-dependent recoil spectra for  $^{129}\text{Xe}$  and  $^{131}\text{Xe}$  for elastic and inelastic scatters. WIMP masses of  $100 \text{ GeV}/c^2$  with cross section  $\sigma_n^0 = 10^{-40} \text{ cm}^2$  and  $1000 \text{ GeV}/c^2$  with cross section  $\sigma_n^0 = 10^{-39} \text{ cm}^2$  are assumed. Elastic scattering is preferred across all recoil energies, though at larger  $E_R$  and  $m_\chi$  inelastic has a greater relative impact. Inelastic scattering drops to 0 at  $E_R = 0 \text{ keV}$  because conservation of momentum mandates that the nucleus cannot be excited while the atom remains at rest after an interaction. Image credit: [164].

single event. However, the mean free path for the de-excitation photon is  $\mathcal{O}(1)$  mm so they may be spatially resolvable [164]. Longer-lived activations for metastable states  $^{129\text{m}}\text{Xe}$  and  $^{131\text{m}}\text{Xe}$  decay with half-lives 8.88 and 11.93 days and energies 236.14 and 163.93 keV. The longer lifetimes allow the metastable xenon to become distributed uniformly throughout the detector and provide an internal calibration over a period of weeks, and does not affect dark matter data taking.

The final kind of interaction is elastic scattering and preserves kinetic energy. Elastic scatters probe both spin-independence and spin-dependence. Fig. 2.10 shows the expected recoil spectra for  $^{129}\text{Xe}$  and  $^{131}\text{Xe}$  elastic and inelastic scatterings for WIMPs of  $m_\chi = 100, 1000 \text{ GeV}/c^2$  with cross-sections of  $\sigma_n^0 = 10^{-40}, 10^{-39} \text{ cm}^2$ . We see that elastic scattering is dominant over inelastic, but at higher recoil energies  $E_R$  and larger WIMP masses the gap of the discrepancy decreases. This suggests a spin-dependent dark matter discovery should be first observed with elastic scatters. From here on elastic scattering will be the primary focus since it is used for the spin-independent search (a few sections will focus on  $^{129\text{m}}\text{Xe}$  and  $^{131\text{m}}\text{Xe}$ ).

## 2.4 Electronic Recoils

Xenon will undergo an electronic recoil when its electron shell interacts with a moving particle. Because no energy is lost to atomic motion the number of quanta produced is

$$n_q = \frac{E}{W} \quad (2.14)$$

where  $W = 13.7 \pm 0.2$  eV [165] is the energy required to produce a single quantum. This is made up of

$$n_q = n_{\text{ex}} + n_{\text{ion}} \quad (2.15)$$

where  $n_{\text{ex}}$  and  $n_{\text{ion}}$  is the numbers of excitons and ions, respectively. The number of electron-ion pairs has a root mean square of

$$\delta = F \times n_{\text{ion}} \quad (2.16)$$

where  $F < 1$  is known as the Fano factor [166]. Thus the fluctuations of  $n_{\text{ion}}$  are smaller than a Poisson distribution ( $F = 1$ ). Several experiments have attempted to measure  $F$  for LXe [167], [168] and estimate a value of  $F = 0.059$  for  $e^-$  and  $\gamma$ -rays. This places a limit on the fundamental energy resolution of

$$\Delta E = \sqrt{FWE} \quad (2.17)$$

where it is common to measure  $\Delta E$  is in keV,  $W$  is in eV, and the energy  $E$  is in MeV [134]. Current LXe experiments have not yet achieved a Poisson resolution, so there is a lot of progress that can be made in the future.

Rearranging Eq. 2.15 the probability that a quanta is an ion is

$$p_{\text{ion}} = \frac{1}{1 + \frac{n_{\text{ex}}}{n_{\text{ion}}}} \quad (2.18)$$

with  $p_{\text{ex}} = 1 - p_{\text{ion}}$ . The ratio  $n_{\text{ex}}/n_{\text{ion}}$  has been calculated to be 0.06 [169] but later

measurements disagree [147], [170]. Currently  $n_{\text{ex}}/n_{\text{ion}}$  is expected to be between 0.06-0.2. Following recombination the number of photons and electrons is

$$n_{\text{ph}} = n_{\text{ex}} + rn_{\text{ion}} \quad (2.19\text{a})$$

$$n_{\text{e}} = (1 - r)n_{\text{ion}} \quad (2.19\text{b})$$

where  $N_{\text{ph}}$  is the number of photons and  $N_{\text{e}}$  is the number of  $e^-$  that do not recombine.

Although noble gas detectors allow ER-NR discrimination, the two regions are near one another some events could be considered with reasonable probability to belong to either. In dark matter searches only the region of NR-space where the NR likelihood is significantly more probable is used (Sec. 3.4). A number of reduction methods are used to minimize the electronic recoil and other backgrounds. With the tonne-scale era of DM detectors underway this becomes especially critical, and significant effort has been put into material screening and distillation.

## 2.5 Nuclear Recoils

Although the vast majority of background comes from electronic recoils, nuclear recoils are more dangerous because they replicate WIMP interactions. Therefore the NR background must be well-modeled to avoid mistaking background with WIMPs.

A fraction of the energy in a nuclear recoil will increase the kinetic energy of the xenon. Liquid noble gas detectors cannot measure changes in translational motion of atoms so this portion is lost. While energetic electrons are capable of transferring very small amounts of energy to the motion of the nucleus, the reverse is not true. Atomic motion has only been observed in nuclear recoils, which implies for the same energy deposition  $n_{\text{q}}$  will differ between electronic and nuclear recoils. The fraction of energy not lost to atomic motion  $f_n$  is commonly described by the Lindhard model [171]

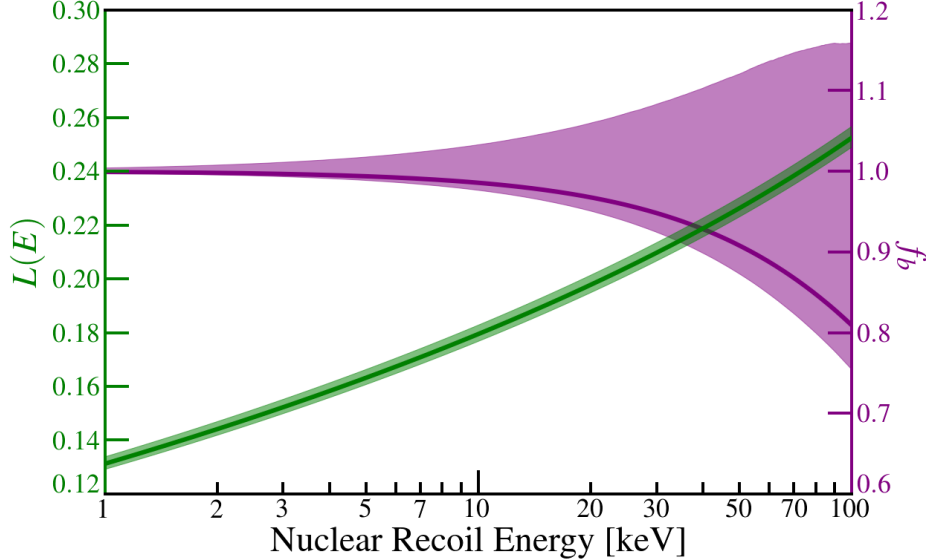


Figure 2.11: Fraction of nuclear recoil energy that produces excitons and ions  $L(E)$  in xenon using Lindhard’s theory (green) [171].

$$f_n = \frac{kg(\epsilon)}{1 + kg(\epsilon)} \quad (2.20)$$

where  $k = 0.133Z^{2/3}A^{1/2}$ ,  $g(\epsilon) = 3\epsilon^{0.15} + 0.7\epsilon^{0.6} + \epsilon$ , and  $\epsilon = 11.5(E/Z^{7/3})$  where  $Z$  is the atomic number,  $A$  is the number of nucleons, and  $E$  has units of keV.  $k$  is proportional to the ratio of electronic stopping power to particle velocity of the recoiling Xe atom [172] and  $g(\epsilon)$  is proportional to the ratio of electronic to nuclear stopping power (Sec. 2.2.3) [173]. Here  $k$  is taken from [67] but there has been some debate over its value. When parameterized by the Lindhard model the quenching factor  $f_n$  is sometimes written as  $L(E)$ . It is shown in Fig. 2.11 for the relevant energy search region.

Primary scintillation is reduced by biexcitonic quenching and the Penning process (Eq. 2.11). The total number of quanta is

$$n_q = L(E) \frac{E}{W} \quad (2.21)$$

The difference between Eq. 2.14 and Eq. 2.21 is  $L(E)$ . As with electronic recoils the probability of a quantum being an ion is

$$p_{\text{ion}} = \frac{1}{1 + \frac{n_{\text{ex}}}{n_{\text{ion}}}} \quad (2.22)$$

through the higher track density of nuclear recoils (Fig. 2.5) causes  $n_{\text{ex}}/n_{\text{ion}} \sim 1$  [172], [174]. As electrons and ions recombine biexcitonic quenching and the Penning process reduce the number of photons by  $f_b$  (Eq. 2.11).

$$n_{\text{ph}} = f_b(n_{\text{ex}} + rn_{\text{ion}}) \quad (2.23a)$$

$$n_{\text{e}} = (1 - r)n_{\text{ion}} \quad (2.23b)$$

## 2.6 Time Projection Chambers

Time projection chambers (TPCs) measure the light and charge of an interaction. They have been leading the spin-independent search for WIMP masses  $> 10 \text{ GeV}/c^2$  for  $\sim 10$  years, and as we reach the tonne-scale era are projected to continue. Fig. 2.12 shows the evolution of detectors and their spin-independent limits for roughly 30-70  $\text{GeV}/c^2$  WIMPs. This section discusses liquid noble gas TPCs used for dark matter detection. It primarily covers xenon but for most details an identical treatment can be applied to argon and neon.

### 2.6.1 Working Principle

TPCs consist of a liquid noble element with a small gas gap at the top. A minimum of three parallel metal meshes are needed: the cathode, gate, and anode. The cathode is at the bottom of the detector and applies an electric field - known as the drift field  $E_d$  - inside the active volume. The gate rests just beneath the liquid level and is grounded, so the drift field pushes electrons that do not recombine towards the surface of the liquid at drift velocity  $v_d$ . Typically an electric field cage consists of metal rings that mark the perimeter and are stacked vertically, parallel to the cathode

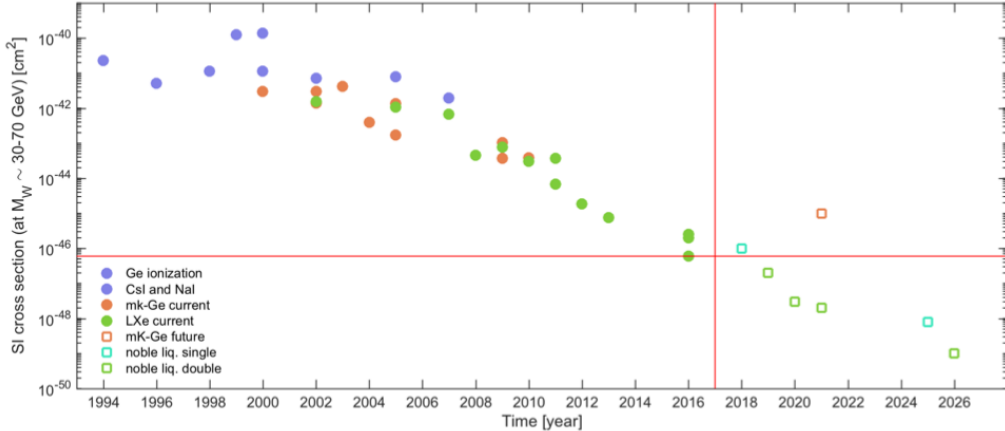


Figure 2.12: Spin-independent cross-section evolution for WIMPs with  $m_\chi \sim 30\text{-}70 \text{ GeV}/c^2$ . Solid markers represent realized values while empty squares denote projected. Purple markers refer to germanium (Sec. 1.5.3) as well as CsI and NaI detectors (Sec. 1.5.2), orange represent cryogenic bolometers (Sec. 1.5.4), turquoise denotes single-phase noble liquid chambers, and green symbolizes dual-phase. For approximately the last decade LXe detectors have led the search and are projected to continue to do so. Image credit: [135].

and gate. Identical resistors connect adjacent rings so voltage drops are equivalent and maintain drift field uniformity.

The observable that corresponds to the measurement of photons emitted from the site of the interaction is referred to as the S1, named because it is the first scintillation. The electrons, which do not contribute to the S1, drift to the surface of the liquid. Over this period the electron cloud diffuses longitudinally (in the direction of  $E_d$ ) and transversely (perpendicular). The diffusion coefficients  $D_L$  and  $D_T$  are dependent on the electric field with  $D_T/D_L \sim 10$ . The electron spread can be written as  $\sigma_{D_T} = \sqrt{D_T t_d}$  where  $t_d = d/v_d$  is the electron drift time and  $d$  is the drift distance.

Impurities that outgas from detector materials mix into the gas and liquid. Electronegative impurities in particular are a problem because they attach to drifting  $e^-$  and lower the number that reach the liquid-gas interface. The attachment process is Eq. 5.7.



where  $S$  is an impurity. The number of  $e^-$  captured depends on drift time and the

impurity attachment rate  $k_S$ , both of which vary with  $E_d$ . An advantage of larger electric fields is a greater  $v_d$  (up to a point, Fig. 2.3) to limit time in the liquid. Doping LXe with organic materials such as butane can increase  $v_d$  at large fields but are not used in DM detectors because of purification difficulties [149]. The rate at which electrons are absorbed by impurities is proportional to the number of electrons, impurities, and impurity attachment rate. Assuming the density of impurities in the liquid and  $E_d$  are uniform the charge  $q$  is described by

$$\frac{dq}{dt} = -qk_S S \quad (2.25)$$

$$q(t) = q_0 e^{-tk_S S} = q_0 e^{-t/\tau_e} \quad (2.26)$$

where  $\tau_e = (k_S S)^{-1}$  is the electron lifetime and  $q_0$  is the initial charge.  $k_S$  is the attaching rate constant and is shown in Fig. 2.13 for O<sub>2</sub>, N<sub>2</sub>O, and SF<sub>6</sub>. It increases for N<sub>2</sub>O with  $E_d$  whereas O<sub>2</sub> and SF<sub>6</sub> decrease. For LXe TPCs it is common to give the impurity concentration in O<sub>2</sub>-equivalence - the concentration of O<sub>2</sub> if it were solely responsible for  $e^-$  attachment. O<sub>2</sub> is expected to be the dominant electronegative contaminant, and its curve in Fig. 2.13 works well for modeling the electron lifetime (Chap. 5). Removing these impurities is discussed in Sec. 3.1.4 and measuring the electron lifetime is covered in Sec. 3.2.5 and 5.2.

The anode rests several millimeters above the gate. The electric field between the gate and anode  $E_g$  must be strong enough to extract the  $e^-$  that reach the liquid surface into the gas (typically  $\gtrsim 10$  kV cm<sup>-1</sup>). An extracted  $e^-$  will quickly gain enough kinetic energy to ionize atoms in the gas, whose  $e^-$  in turn follow, creating a cascade effect. Because the scintillation per electron is independent of the total number of electrons extracted this is known as proportional scintillation. It is also known as secondary scintillation or electroluminescence. The number of photons  $N_{\text{ph}}$  produced over a distance  $z$  per electron is

$$\frac{dN_{\text{ph}}}{dz} = \alpha \left( \frac{E_g}{P} - \beta \right) P \quad (2.27)$$

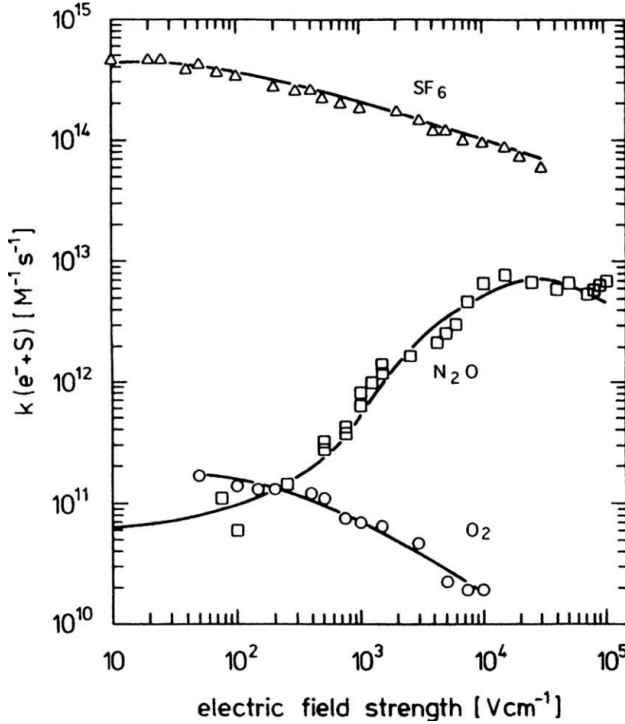


Figure 2.13: Attaching rate constant  $k_S$  for  $\text{O}_2$ ,  $\text{N}_2\text{O}$ , and  $\text{SF}_6$  with respect to electric field. At larger  $E_d$   $k_S$  increases for  $\text{N}_2\text{O}$  and decreases for  $\text{O}_2$  and  $\text{SF}_6$ . Image credit: [175].

where  $\alpha = 70$  photons  $\text{kV}^{-1}$ ,  $\beta = 1.0 \text{ kV cm}^{-1} \text{ atm}^{-1}$ , and  $P$  is the pressure in the gas [176]. The observable that corresponds to the measurement of electroluminescence is referred to as the S2, for second scintillation.

## 2.6.2 Photomultiplier Tubes

Photomultiplier tubes (PMTs) are used for light detection in TPCs. A diagram of a PMT is shown in Fig. 2.14. A photon that passes through the PMT window will most often strike the photocathode and free a photoelectron via the photoelectric effect. This process is known as single photoelectron emission (SPE). Once ejected, the photoelectron will be directed by the focusing electrode towards the first dynode. The dynodes are coupled to one another through resistors that systematically decrease their electric potential. As the photoelectron hits the first dynode it will free a second electron. The freed electrons will be drawn to the second dynode and repeat this procedure. The result is a cascade effect, amplifying the current by as much as 100

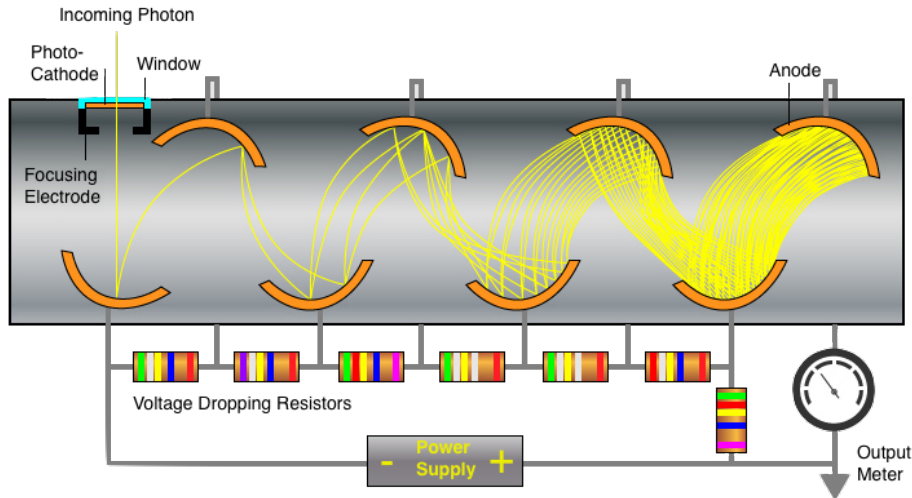


Figure 2.14: Diagram of a PMT. An incident photon hits the photocathode and ejects a photoelectron. With each dynode the more  $e^-$  are freed, creating an amplified signal. Image credit: [177].

million and ending at the anode, where the charge is output to a voltage reading device such as an oscilloscope or digitizer.

If the photon's energy is at least double the workfunction of the photocathode the number of photoelectrons ejected should follow a Poisson distribution. However, a study of several Hamamatsu vacuum ultraviolet-sensitive (VUV) PMTs showed double photoelectron emission (DPE) fractions between 18-24% depending on the PMT, higher than the expected  $\sim 15\%$  [178]. The study included PMTs used in XENON100 and XENON1T. In other cases a photon may pass through the photocathode and hit the first dynode. If it ejects an electron the PMT response will be similar to a photocathode hit with one less dynode, i.e. an under-amplified current.

The quantum efficiency (QE) is the ratio of electrons ejected from the photocathode divided by incident photons. The QE spectrum for the PMTs used in XENON1T, Hamamatsu R11410, is shown in Fig. 2.15. Its low efficiency means the majority of photons that reach our PMTs will not produce a photoelectron. Other photodetectors have been considered but lead to problems that outweigh those of PMTs. Xenon's scintillation wavelength (178 nm) is near the spectrum's maximum of approximately

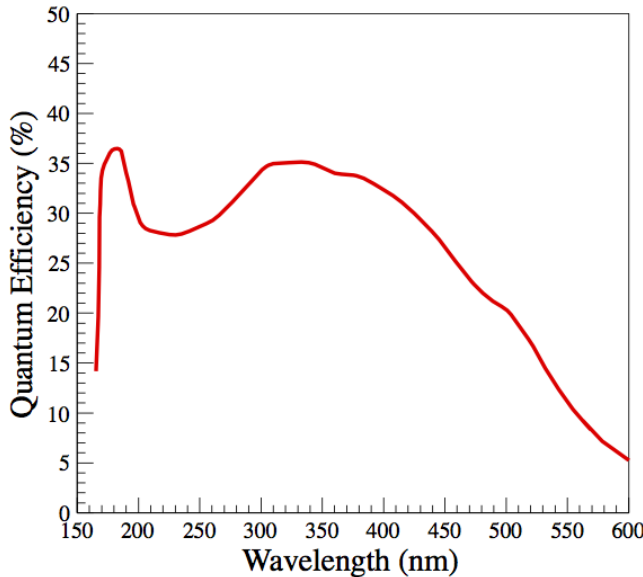


Figure 2.15: Quantum efficiency with respect to wavelength for the Hamamatsu R11410 PMT, used in XENON1T. The peak efficiency occurs near the xenon scintillation wavelength 178 nm at  $\sim 35\%$ . Image credit: [179].

35%. Liquid argon and neon have scintillation wavelengths of 128 and 78 nm, respectively. Because PMTs are not sensitive to these energies LAr experiments use wavelength shifters.

TPCs have photomultiplier tubes below the cathode and above the gate. While proportional scintillation occurs at the top of the detector and in most detector settings produces enough light to guarantee detection, prompt scintillation - especially for low energy events - can be more difficult to observe. Depending on the geometry of the detector and the location of the event the fraction of light directed towards the photodetectors can be small. PMTs cannot be fixed around the side of the TPC because their electric fields will interfere with the field cage. To increase the fraction of light that reaches the photodetectors the wall of the TPC is covered by polytetrafluoroethylene (PTFE) just inside the field cage. PTFE is reflective for liquid noble gas scintillation and is a common choice. It has been shown to have  $> 97\%$  reflectance to 178 nm light when immersed in LXe [180].

### 2.6.3 Signals

S1s (primary scintillation) and S2s (secondary) are measured in photoelectrons (PEs). An example of an event is shown in Fig. 2.17. On the left a particle scatters with the LXe, prompting photons that are almost immediately observed by the PMTs. The right side shows the  $e^-$  drifting to the LXe surface and extracted by the anode across the GXe. The colors correspond to the relative intensity of light seen by each PMT. For a typical S1 the bottom PMTs observe more light due to reflection off the LXe surface (though the amount depends on where in the TPC the interaction occurs). For S2s the top PMTs see more light since electroluminescence occurs just several centimeters underneath them. For S2s the top PMTs have an intensity profile centered around where the  $e^-$  are extracted. The profile for the bottom PMTs is more uniform since the solid angle per PMT is less.

#### 2.6.3.1 Position Reconstruction

In addition to knowing the  $z$ -coordinate of the interaction ( $z = v_d t_d$ ) TPCs can recover the  $x$  and  $y$  positions. The S2 hit pattern in the top PMT array in Fig. 2.17 shows an intensity distribution that peaks at one PMT and dissipates away from it. It is reasonable to assume the S2 was extracted beneath or nearly beneath this PMT. A number of algorithms can be applied to PMT hit patterns to estimate the  $x$ - $y$  position of the event. Typically the resolution of event reconstruction depends on the number and area of PMTs as well as the S2 size. Fig. 2.17 shows the event distribution for second XENON1T science run. The majority of events are near the wall - a consequence of radioactivity present in detector materials. The large self-shielding of LXe constrains these events to  $\sim 5$  cm of the wall. Three-dimensional position reconstruction allows us to reject events in regions where we expect a large background. Position reconstruction is discussed in greater detail in Sec. 3.2.3.

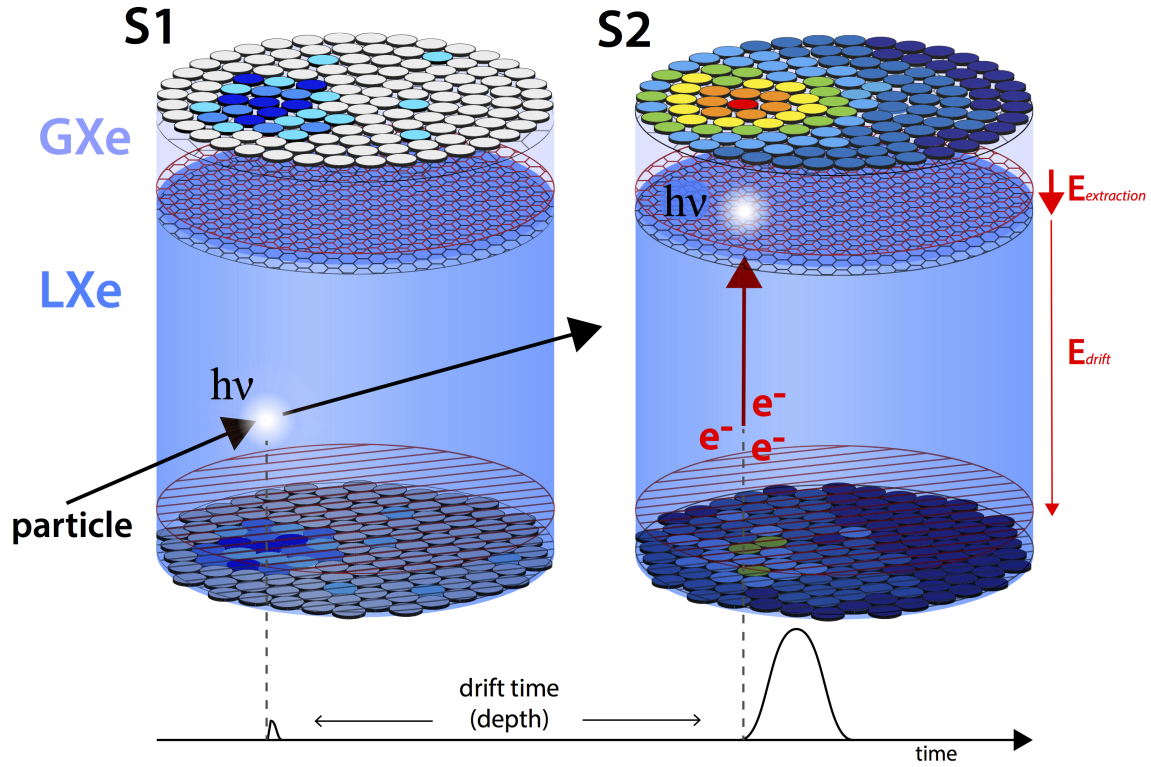


Figure 2.16: Diagram of an interaction in a LXe TPC. The S1 is immediately observed by the PMTs. The  $e^-$  drift towards the top of the detector, where they are extracted across GXe, creating the S2. A typical waveform is shown at the bottom. The S2 is significantly larger than the S1 due to the amplification of electroluminescence. The relative intensity of light in the PMTs, or PMT hit pattern, can be used to determine the  $x$ - and  $y$ -coordinates of the interaction. Image credit: Lutz Althüser.

### 2.6.3.2 Discrimination

The exciton-to-ion ratio and recombination (Sec. 2.2.4) are responsible for the fraction of quanta that produce S1s and S2s. Under identical detector conditions recombination is largely governed by the ionization density, which is determined by the stopping power (Sec. 2.2.3). Fig. 2.4 shows the mass stopping power dependence on energy and recoil type, and Fig. 2.5 shows the track structure for 20 keV electronic and nuclear recoils. Because the nuclear recoil has a greater ionization density its electron-ion pairs are more likely to recombine [140]. The disproportionate exciton-to-ion ratios and recombination fraction allow discrimination between electronic and nuclear recoils.

Fig. 2.18 shows S2 vs. S1 for electronic and nuclear recoils. The ER are from  $^{220}\text{Rn}$

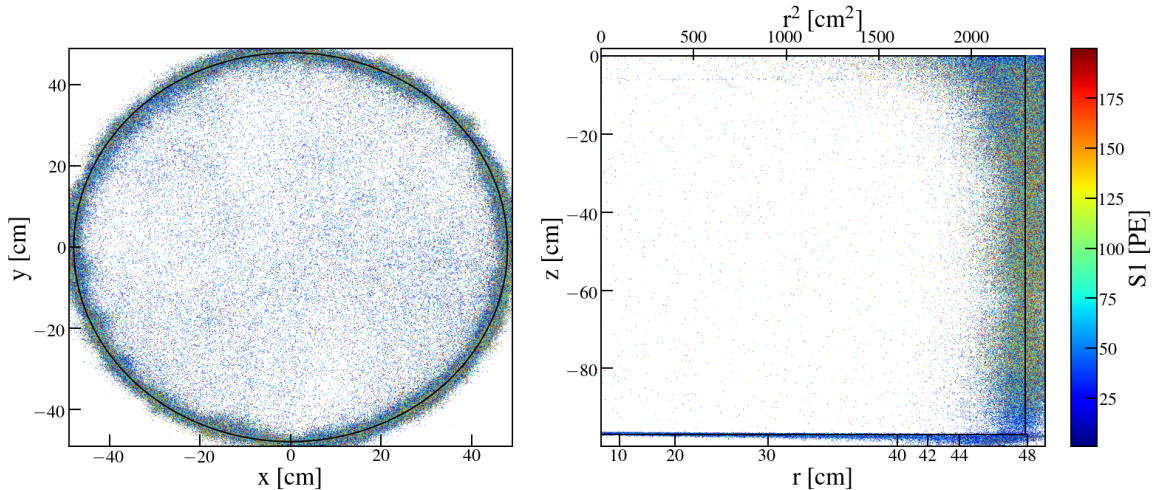


Figure 2.17: Position reconstruction for events in the second science run of XENON1T. Top PMT hit patterns are used to determine  $x$  and  $y$  while  $z = v_d t_d$ . The number of events drops dramatically at lower radii due to the self-shielding of LXe.

calibrations where its progeny  $^{212}\text{Pb}$  undergoes  $\beta$ -decay. The short lifetime of the  $^{220}\text{Rn}$  decay chain, continuous energy spectrum of  $\beta$ -decays, and uniform distribution throughout the detector make  $^{220}\text{Rn}$  an excellent choice for measuring S1 and S2 for electronic recoils.

To map the S1-S2 parameter spaces separate ER and NR calibrations are performed. Electron recoil calibrations use  $^{220}\text{Rn}$  since its progeny  $^{212}\text{Pb}$  undergoes  $\beta$ -decay. The short lifetime of the  $^{220}\text{Rn}$  decay chain ( $\sum_i t_{1/2} < 12$  h), continuous energy spectrum of  $\beta$ -decays, and uniform distribution throughout the detector make it an excellent choice for measuring S1 and S2 for electronic recoils. Events from XENON1T calibrations are shown in red in Fig. 2.18.

There are no neutron sources that can be mixed with xenon to perform internal nuclear recoil calibrations. Therefore, calibrations must be done with sources placed outside of the detector. Xenon's self-shielding ( $\sim 10$  cm mean free path for MeV neutrons [181]) causes the distribution of events to be largest near the source, and - depending on the size of the detector - can significantly reduce the fraction of events that reach the center of the detector, and force longer calibration windows. For XENON1T nuclear recoil sources include americium beryllium  $^{241}\text{AmBe}$

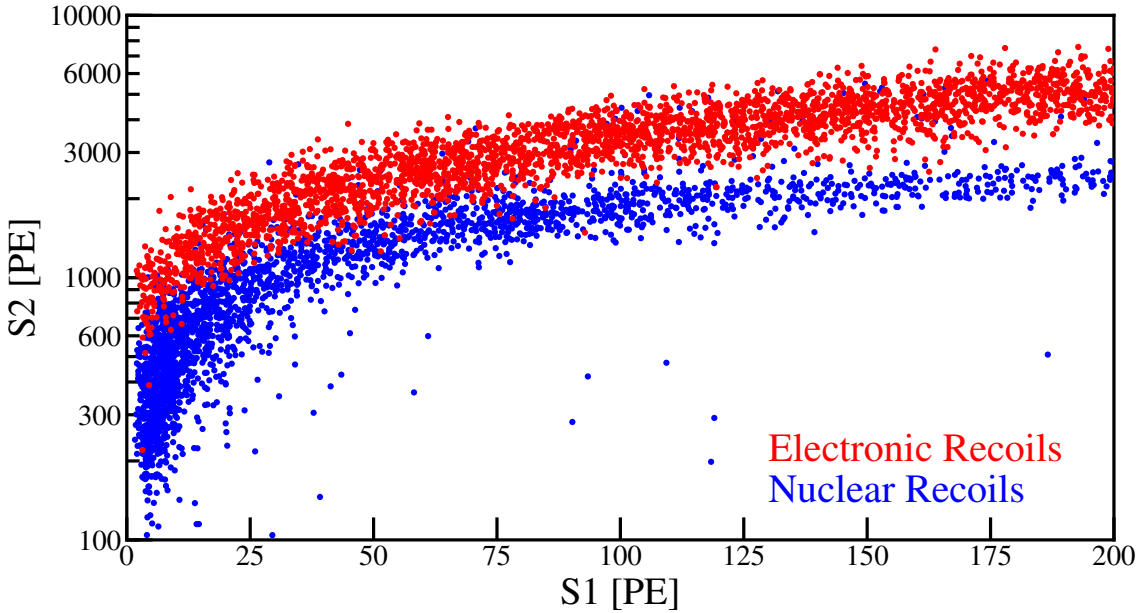


Figure 2.18: S2 (proportional) vs. S1 (prompt) for XENON1T calibration data. Electronic recoils are from the  $^{220}\text{Rn}$  decay chain as progeny  $^{212}\text{Pb}$  undergoes  $\beta$ -decay with an end-point energy of 569.9 keV (red). Nuclear recoils are from americium beryllium ( $^{241}\text{AmBe}$ ) (blue). S2/S1 is larger for electronic recoils, which enables discrimination between possible WIMPs and the ER background.

and a deuterium-deuterium (D-D) neutron generator (NG) [182]. The nuclear recoils are marked in blue in Fig. 2.18 are from the  $^{241}\text{AmBe}$  calibration during the second XENON1T science run.

As predicted above Fig. 2.18 shows nuclear recoils have a larger photon-to-electron ratio than electronic recoils due to their higher  $n_{\text{ex}}/n_{\text{ion}}$  and recombination. It shows

$$\left(\frac{\text{S2}}{\text{S1}}\right)_{\text{ER}} > \left(\frac{\text{S2}}{\text{S1}}\right)_{\text{NR}} \quad (2.28)$$

across all S1-S2 values. This data is used to characterize the ER and NR observables (S1, S2) space so that the origin of each dark matter search event can be estimated. Because a substantial fraction of energy is lost to atomic motion in a nuclear recoil the energies of the events in Fig. 2.18 differ between ER and NR. As an example, a nuclear recoil event at  $S1 = 60$  PE has an energy of  $\sim 35$  keV while for electronic recoils it is closer to 8 keV. For this reason several energy scales are used (Sec. 2.6.3.3).

The number of photons and electrons can be reconstructed from the S1 and S2.

Doing so requires knowledge of a number of detector variables including PMT quantum efficiencies (Sec. 2.6.2) and electroluminescence (Sec. 2.6.1). These are discussed in detail in Sec. 3.2 and Sec. 4.2. If the energy of an event is known the light yield and charge yield can be calculated in units of photons per energy and electrons per energy, i.e.  $n_{\text{phot}}/E$  and  $n_e/E$ . Because the light and charge yields describe detector-independent microphysics there has been an effort to measure them (Sec. 4.3.3). Measurements of photoelectrons per energy may also be referred to as light and charge yields (Sec. 3.2.9) and are useful for monitoring detector conditions (because they are detector-dependent they do not provide insight into fundamental physics). Fig. 2.19 shows the ratios of light and charge yields as a function of drift field for 122 keV electronic recoils ( $^{57}\text{Co}$   $\gamma$ -rays), 56.5 keV elastic nuclear recoils ( $^{241}\text{AmBe}$  and  $^{252}\text{Cf}$ ), and 5.3 MeV  $\alpha$ -decays ( $^{210}\text{Po}$ ). At larger  $E_d$  the light yield declines while the charge yield increases. The more significant change in ER is due to its sparser ionization density and suggests the drift field can be optimized for ER-NR discrimination.

### 2.6.3.3 Energy Reconstruction

An important component for our analysis is being able to reconstruct the energies of events. Because the light and charge yields vary according to a number of features including particle type and recoil energy, several energy scales are used. The energy scales enable comparisons between events that differ in origin and behavior on equivalent platforms. Because the microphysics changes across different energies, the energy scales may be nonlinear.

The “electronic recoil equivalent energy” is defined by the detector’s response to  $\gamma$ -rays of a known energy. Conversion to this energy scale is done using an S1 or S2 (does not require both), which is in part why light and charge yields for electronic recoils (Sec. 4.3.3) are generally listed using this metric. The units are keV<sub>ee</sub> (“keV electron-equivalent”).

The detector’s response to nuclear recoils defines the “nuclear recoil equivalent energy”. By convention it is determined by the NR S1 signal given by

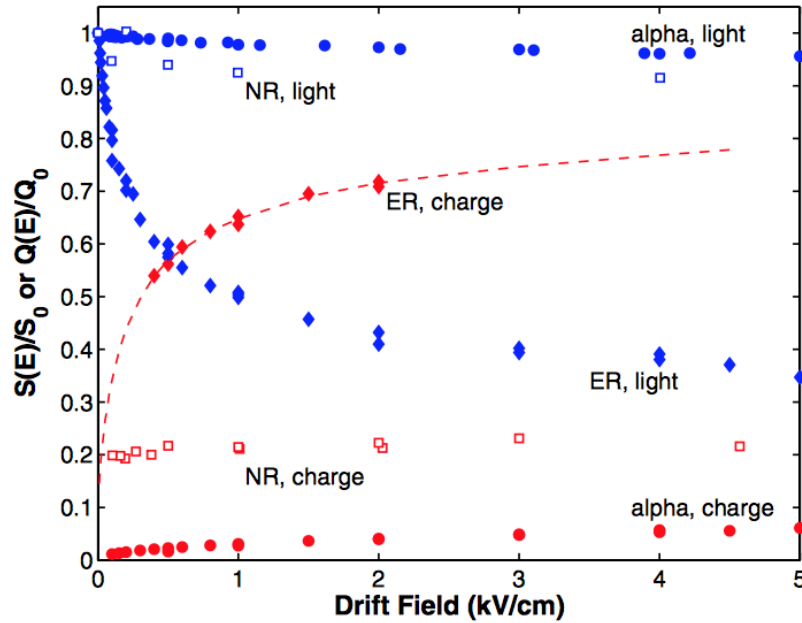


Figure 2.19: Field dependence of light ( $S(E)/S_0$ , red) and charge ( $Q(E)/Q_0$ , blue) yields.  $S_0$  is the light yield at zero field and  $Q_0$  is the charge yield at infinite field. Electronic recoils are shown as solid diamonds and are measured from  $^{57}\text{Co}$  122 keV  $\gamma$ -rays. 56.5 keV elastic neutron scatters from  $^{241}\text{AmBe}$  and  $^{252}\text{Cf}$  are marked by hollow squares. Nuclear recoils are marked by hollow squares and are from elastic 56.5 keV neutron scatters from  $^{241}\text{AmBe}$  and  $^{252}\text{Cf}$ . Solid circles represent  $^{210}\text{Po}$  5.3 MeV  $\alpha$ -decays. Sparser ionization densities precipitate stronger field-dependence for electronic scatters than for nuclear and alpha, signifying  $E_d$  can be tuned for improved ER-NR discrimination. Image credit: [183].

$$E_{\text{nr}} = \frac{S1}{L_y \mathcal{L}_{\text{eff}}} \frac{S_{\text{er}}(E)}{S_{\text{nr}}(E)} \quad (2.29)$$

where  $L_y$  is the electronic recoil light yield of a 122 keV  $\gamma$ -ray at zero electric field.  $L_y$  was chosen when detectors were small enough that the low-energy  $^{57}\text{Co}$   $\gamma$  could reach the entire volume.  $\mathcal{L}_{\text{eff}}$  is the nuclear recoil scintillation yield relative to  $L_y$ , and  $S_{\text{er}}(E)$  and  $S_{\text{nr}}(E)$  are the scintillation quenching factors for ER and NR, respectively. Units are given in  $\text{keV}_{\text{nr}}$  for “keV nuclear-equivalent”.

The “combined energy scale” is defined using

$$\frac{E}{W} = \frac{S1}{g_1} + \frac{S2}{g_2} \quad (2.30)$$

where  $W$  is the average energy to produce a single quanta,  $g_1$  is the average photon detection efficiency, and  $g_2$  is the charge amplification factor (Sec. 3.2.7).  $g_1$  and  $g_2$  have units of PE/photon and PE/electron, respectively, so Eq. 2.30 reduces to  $n_q = n_{ph} + n_e$ . For the XENON1T analysis  $g_1$  and  $g_2$  are measured using a number of mono-energetic interactions. Eq. 2.30 accounts for anti-correlation between S1 and S2 signals that arise from natural fluctuations in  $n_{ex}/n_{ion}$  and recombination, so it typically leads to better energy resolution. Because it describes electronic recoils (i.e. no quenching) the units are sometimes given in keV<sub>ee</sub> though it is generally understood that a combined energy spectrum uses ERs. Sec. 3.2.8 discusses the combined energy spectrum in XENON1T.

# Chapter 3

## The XENON1T Experiment and Dark Matter Search

XENON1T is the third generation experiment of the XENON collaboration. With a fiducial mass of more than 1000 kg, it is the first liquid xenon dark matter (DM) detector to reach the tonne-scale era of DM detection. Its large target mass and low radioactive background make it the most sensitive detector to spin-independent WIMPs with  $m_\chi > 6 \text{ GeV}/c^2$ .

This chapter presents the combined analysis of the Science Run 0 (SR0) and Science Run 1 (SR1) - the first two XENON1T dark matter runs - spin-independent WIMP search. It begins with a description of the XENON1T experiment (Sec. 3.1), followed by a discussion on detector characterization (Sec. 3.2) and backgrounds (Sec. 3.3). Finally, dark matter search results (Sec. 3.4) are presented. The original SR0-only analysis [132] is referred to as “First Results” and is cited for comparison.

### 3.1 The XENON1T Detector

#### 3.1.1 PMTs

A total of 248 Hamamatsu R11410-21 PMTs are installed in XENON1T. The 127 PMTs on the top array are positioned symmetrically in radius to optimize the res-

olution of position reconstruction in  $r$  (Sec. 3.2.3). The 121 PMTs in the bottom array are packed as densely as possible to maximize light collection. One of the most important characteristics of a PMT is its quantum efficiency (QE), i.e. the ratio of photoelectrons (electrons ejected from the photocathode) divided by number of incident photons. The R11410 window is 76.2 mm in diameter and the photocathode yields an average quantum efficiency for 178 nm of 34.5% with 2.8% standard deviation [184], [185].

PMTs with the highest QEs are placed in the bottom array while those with the lowest are stationed along the circumference of the top. The difference in arrangement is strategic. Due to liquid xenon’s relatively large dielectric constant (1.95) photons originating inside the liquid are likely to reflect off the surface and be redirected towards the bottom of the TPC. For low-energy events - the relevant range for WIMP DM searches - nuclear recoils may only emit a small number ( $\lesssim 100$ ) of photons, many of which never reach the PMTs. Positioning those with the highest quantum efficiency in the region most likely to see scintillation from an S1 captures more events and improves our sensitivity. S2s produce enough scintillation to be observed by both arrays. Therefore the QE of the top PMTs is comparatively unimportant, and could even be advantageous for large S2s that might saturate the phototubes, though these events are outside the region of interest for spin-independent WIMP dark matter. The layout of the PMTs with their respective QEs is shown in Fig. 3.1. The assembled PMT arrays are shown in Fig. 3.2.

A photoelectron (PE) is a photon ejected by an incident photon on the photocathode. It is guided by a focusing electrode disk to the first of R11410-21’s 12 dynodes. The first dynode is the largest and extends to the electrode disk to maximize the probability of capturing photoelectrons. A voltage is applied to the photocathode and dynodes, with each successive one (starting from the photocathode) lower than the previous. Upon hitting the first dynode the photoelectron will free some electrons, spurring the first stage of an electron avalanche. The electron avalanche will pass from dynode to dynode, rapidly growing with each until it reaches the anode and is directed to the data acquisition.

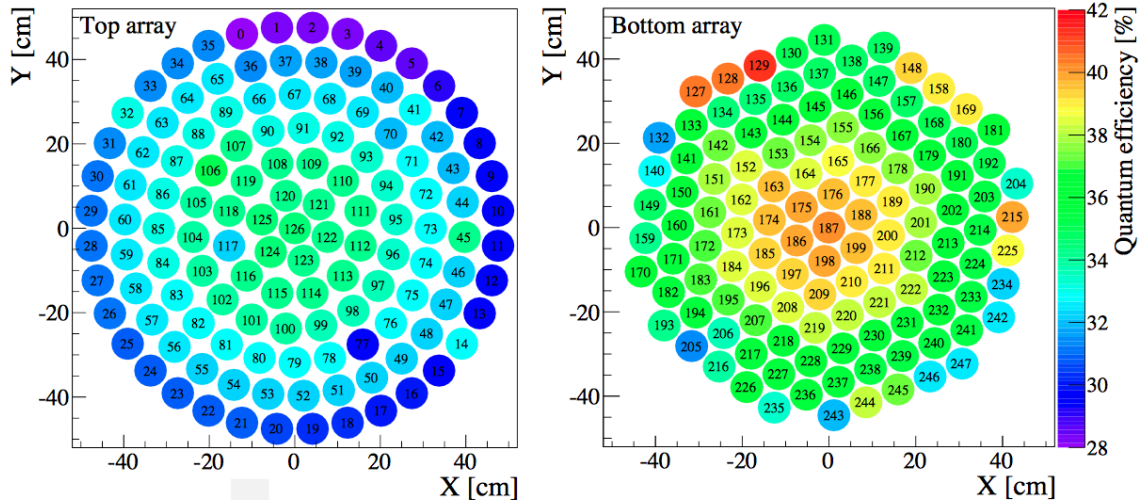


Figure 3.1: Quantum efficiency of top (left) and bottom (right) PMT arrays. PMTs with the highest QE are placed in the center of the bottom array to maximize light collection while those with the lowest are placed in the outermost region of the top array. Image credit: [184].



Figure 3.2: Top (left) and bottom (right) PMT arrays. Top PMTs are installed inside the diving bell above the anode and screening mesh in a radial distribution to minimize uncertainty in radial position reconstruction. Bottom PMTs are packed tightly below the cathode and a second screening mesh to maximize light collection. The screening meshes reduce interference between the anode (cathode) and top (bottom) PMT electric fields. Image credit: [184].

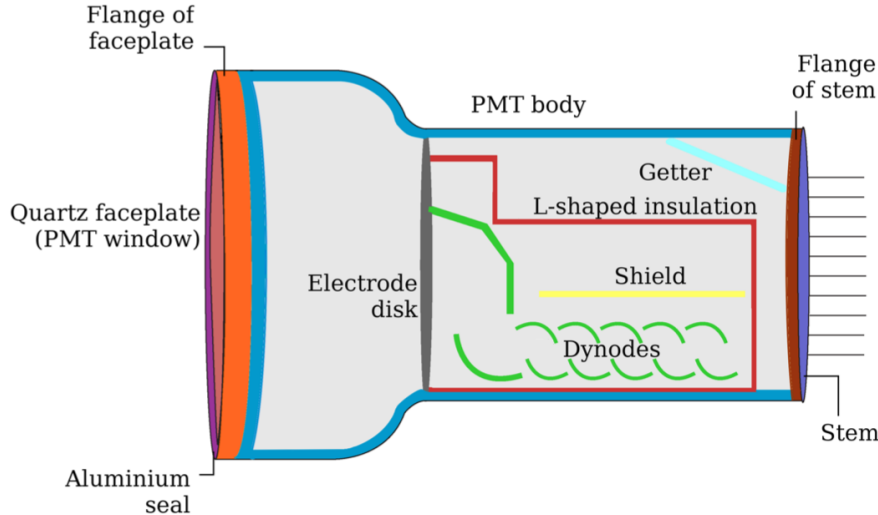


Figure 3.3: Schematic of the Hamamatsu R11410-21 PMT. Image credit: [186].

The electrode, dynodes, and shield are stainless steel and are insulated with L-shaped quartz plates [186]. Due to quartz's transparency to vacuum ultraviolet (VUV) photons the window is also made of quartz. Deposited on it is a low-temperature bialkali photocathode. The window is fixed with an aluminum seal to the faceplate flange, which along with the stem flange is constructed from Kovar. The body of the PMT is approximately 115 mm long and 35% of the total mass. It is constructed from Kovar alloy, most of which has a very low  $^{60}\text{Co}$  concentration. Finally, to insulate the connections to each dynode the stem is ceramic. A schematic can be seen in Fig. 3.3.

Because radioactivity limits the fiducial volume and increases the background, making accidental coincidence (Sec. 3.3.4) and outlier events more likely, XENON and Hamamatsu worked together to develop a highly radio-pure PMT. The original R11410 version used ceramic as a dynode insulator, standard Kovar alloy, and purity aluminum for the seal. Upgrading to quartz for the insulator, low-cobalt Kovar alloy, and high purity aluminum helped alleviate the radioactivity to an extent. For the R11410-21 nearly all the  $^{137}\text{Cs}$  and  $^{60}\text{Co}$  comes from the Kovar alloy, though the  $^{137}\text{Cs}$  content is negligible and the  $^{60}\text{Co}$  is 3-10 times lower than older models. The decay rates of the remaining screened isotopes,  $^{238}\text{U}$ ,  $^{228}\text{Th}$ ,  $^{228}\text{Ra}$ ,  $^{226}\text{Ra}$ , and  $^{40}\text{K}$ , are dominated by the ceramic stem [186]. Unfortunately a material that is more

radio-pure and can insulate the dynode connections has not been found. Sapphire was tried in one iteration but ultimately showed the reduction in background was minimal.

The number of signals per second without a light source is known as the dark count rate. At ambient temperatures the dark count rate is primarily caused by thermal electrons and scale with PMT voltage [185]. This becomes subdominant at cryogenic temperatures to electron field emission and radioactivity (internal and external) as well as cosmic rays. Higher dark count rates make accidental coincidence - when a lone-S1 and lone-S2 imitate a real event (Sec. 3.3.4) - more likely. This fake background is dangerous because it can create false events in the signal region. The value above which events are recorded, or threshold, can be tuned to increase or decrease event acceptance. Because for DM searches we would like as low of a threshold as possible, choosing PMTs with low dark count rates is essential.

Another problematic feature is photon emission from the phototube itself, where light is created inside the PMT and escapes through the window. It is known mainly to occur in one of two ways. The first is through a discharge of intense light that can last for several seconds. This “flash” is easily bright enough to be observed by itself and other PMTs facing its window. The intensity can be so strong that it can take several minutes to several hours to fully recover. Because they seem to happen spontaneously and are not well understood it is impossible to predict when a flash will occur.

The second process is an (often continuous) stream of light. Known as “micro light emission” it is considerably harder to identify. Doing so requires facing two phototubes towards one another and measuring the dark count rate of each with and without the other on. To check for micro light emission in a detector such as XENON1T requires as many trials as PMTs. The level of emission increases with temperature and bias voltage. Keeping PMTs at cryogenic temperatures reduces the frequency, and voltages can be lowered to help further. If micro light emission continues the PMT cannot be used as it risks introducing fraudulent light into otherwise good signals from events inside the TPC.

### 3. THE XENON1T EXPERIMENT AND DARK MATTER SEARCH

---

Directly following the pulse of a PMT a secondary pulse may occur. Known as afterpulses, they can occur within tens of nanoseconds to  $\lesssim 5 \mu\text{s}$ . This can make them difficult or impossible to resolve from true pulses - especially S2s - that can have widths of several microseconds. Because they are an inevitable side effect of PMTs it is important to carefully characterize and understand them.

There are three mechanisms known to cause afterpulses. The first is elastic scattering of the photoelectron with the first dynode, freeing electrons that quickly return to the dynode to produce a second, smaller electron avalanche. This creates afterpulses in the range of a few to tens of nanoseconds. A second kind is thought to come from dark noise and single electrons but is not well understood. It has a relatively uniform distribution in delay time up to several microseconds. Both of these afterpulses have areas of  $\lesssim 2 \text{ PE}$ .

The third mechanism is a photoelectron may occasionally ionize residual gas inside the PMT along its trajectory to the first dynode. The ion then drifts to the photocathode and expels additional electrons. The number of newly ejected electrons depends on the ion and position where it was ionized. The responsible ion can be determined by calculating the time between the true pulse and afterpulse. For the R11410-21 PMT this gives

$$\Delta t_{\text{ap}} = \frac{\pi}{4} \sqrt{\frac{2m}{qV_0}} L \quad (3.1)$$

where  $\Delta t_{\text{ap}}$  is the afterpulse delay time,  $m$  and  $q$  are the ion's mass and charge, and  $V_0$  and  $L$  are the potential difference and length between the photocathode and first dynode (see [185] for details). Note that  $\Delta t_{\text{ap}}$  does not depend on where the ionization occurred. Therefore, if we know the time between the true pulse and afterpulse the ion - or more specifically, the charge to mass ratio - can be determined.  $\Delta t_{\text{ap}}$  ranges from several hundred nanoseconds to several microseconds and an example is shown in Fig. 3.4. Prevalent ions are highlighted. The afterpulse delay time makes it unlikely to couple with S1s.

Because it is not possible to eliminate all residual gas every PMT suffers from some

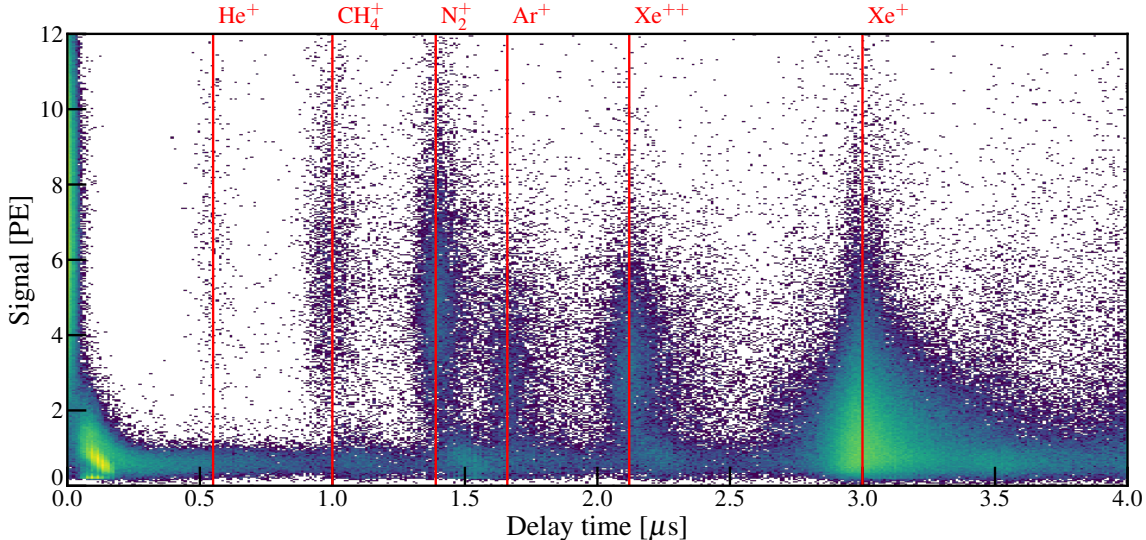


Figure 3.4: Afterpulses for a PMT from XENON1T.  $\text{He}^+$ ,  $\text{CH}_4^+$ ,  $\text{N}_2^+$ ,  $\text{Ar}^+$ , and single- and double-ionized xenon are present and marked by red lines. The large fraction of Xe suggests a leak may be present, but to confirm  $\text{Xe}^+$  and  $\text{Xe}^{++}$  should be monitored. If a leak exists afterpulsing may eventually hit a critical value at which point the PMT can no longer operate reliably. The second, less-understood afterpulsing mechanism discussed in the text is visible as the roughly uniform distribution at  $\sim 0.5$  PE.

ionization-based afterpulsing, as shown in Fig. 3.4 for one of the highest afterpulse PMTs. A better vacuum corresponds to fewer afterpulses and a “healthier” PMT. If the concentration of gas in the PMT vacuum were to increase it would escalate the afterpulse rate. Therefore if the Xe peaks grow over time the PMT likely has a leak and should be replaced if possible, as continued worsening of the vacuum will lead to deterioration and eventually inability to operate the PMT. For XENON1T there are enough PMTs that replacement is not necessary. All PMTs were tested before installation. 73 were rejected and replaced: 12 due to high dark count rates, 53 for light emission, and 8 for afterpulsing.

The transit time (TT) is the time between the photoelectron emission and the arrival of the electron avalanche at the anode. Changes in the photoelectron’s initial position, velocity, and emission angle cause variation in the TT, which is characterized by the transit time spread (TTS). Because generally many PMTs observe an event the TTS quantifies how close together the signals should be. Thus smaller TTSs lead

to a smaller integration window and can decrease accidental coincidence. The TTS for R11410-21 PMTs was measured to be  $9.1 \pm 1.3$  ns - or nearly the same as the digitizer sampling rate [185].

The probability of double photoelectron emission (DPE) in a number of PMTs including the R11410 is between 0.18-0.24 - much higher than previously thought [178]. For The R11410 the probability was measured to be  $p_{\text{dpe}} = 0.225 \pm 0.01$ . Any  $p_{\text{dpe}} > 0$  affects a number of elements in a DM search. In the past  $p_{\text{dpe}}$  was thought to be low enough to not represent a major concern. The recent measurement shows this assumption is wrong and its effects cannot be ignored. To calculate its impact it may be useful to define a quantity closely related to but not the same as the QE. Following [178] the QE is denoted as  $\eta_\mu$  and the fraction of incident photons that produce one or more photoelectrons is  $\eta_p$ . When three or more photoelectron emission is negligible they are related by

$$\eta_\mu = (1 + p_{\text{dpe}})\eta_p \quad (3.2)$$

so using the measured QE alone is incorrect. For one, it is common to require a PMT coincidence for an event to be considered good - that is,  $n$  PMTs must see a signal of a certain size within a time window (typically chosen using the TTS). Using  $\eta_\mu$  will *overestimate* the likelihood of this happening, and  $\eta_p$  should instead be used. Additionally, when the PMT response is large DPE will lead to incorrect resolution and yields unless accounted for. Details on how to appropriately account for  $p_{\text{dpe}}$  are discussed in the electronic and nuclear recoil band fitting (Sec. 4.2.3).

The two PMT arrays are supported by oxygen-free high thermal conductivity (OFHC) copper, with holes in which the PMTs are placed (Fig. 3.2). The copper is covered with polytetrafluoroethylene (PTFE) panels on the TPC-facing side. Screening meshes are situated between the bottom array and cathode as well as the anode and top array. Bias voltages can be applied to each to reduce electrical interference between the phototubes and the drift and extraction fields and extend the PMT lifetimes. While [187] showed normal operation of R11410 PMTs at  $\geq 11$  kV cm<sup>-1</sup> the

XENON1T design cathode voltage was  $10\text{--}100 \text{ kV cm}^{-1}$ .

An additional six Hamamatsu R8520 PMTs reside in LXe outside the TPC near the top electrode to study calibrations. R8520 PMTs have been used in a number of LXe TPCs including the PMT arrays in XENON100 and an electronic recoil measurement at Columbia [188], [189].

### 3.1.2 TPC

The XENON1T time projection chamber is a cylinder 96.9 cm in height and 95.8 cm in diameter and encloses a target mass of 2.0 tonnes (Fig. 3.5). The interior of the wall consists of 24 PTFE panels that were treated with diamond tools to maximize VUV reflectivity, which increases the light collection efficiency [184]. Each interlocks with adjacent panels to achieve light-tightness and the system is designed so that despite the high thermal expansion coefficient of PTFE, the radius does not contract when lowered to  $-96^\circ\text{C}$ . Outside the PTFE are 74 field shaping rings made of low-radioactivity OFHC copper, each with a cross section of  $\sim 10 \times 5 \text{ mm}^2$ . They are supported by 18 PTFE pillars stationed around the circumference. Two redundant chains connect adjoining rings via  $5 \text{ G}\Omega$  resistors and a  $25 \text{ G}\Omega$  resistor between the bottom ring and cathode [184].

There are five TPC electrodes that control the electric fields: the cathode, gate, anode, and top and bottom screening meshes. They have wired diameters of  $\mathcal{O}(100) \mu\text{m}$  and were designed to maximize light collection. The cathode is connected to a PNC150000-1 NEG high voltage supply and pre-filling tests successfully reached voltages beyond  $-100 \text{ kV}$ . 48 mm below the cathode is the bottom screening mesh (mentioned in Sec. 3.1.1). The mesh is 12 mm above the bottom PMT array and can be biased to mitigate unwanted effects from the PMT and cathode electric fields. The cathode and bottom screening mesh consist of parallel wires and are gold-plated stainless steel to increase the workfunction. The gate rests just below the liquid-gas interface and defines  $z = 0 \text{ cm}$ . The anode is situated 5 mm above the gate and is connected to a CAEN A1526P unit. The final electrode is the top screening mesh. 58 mm above the anode and 11 mm below the top PMT array, it serves the

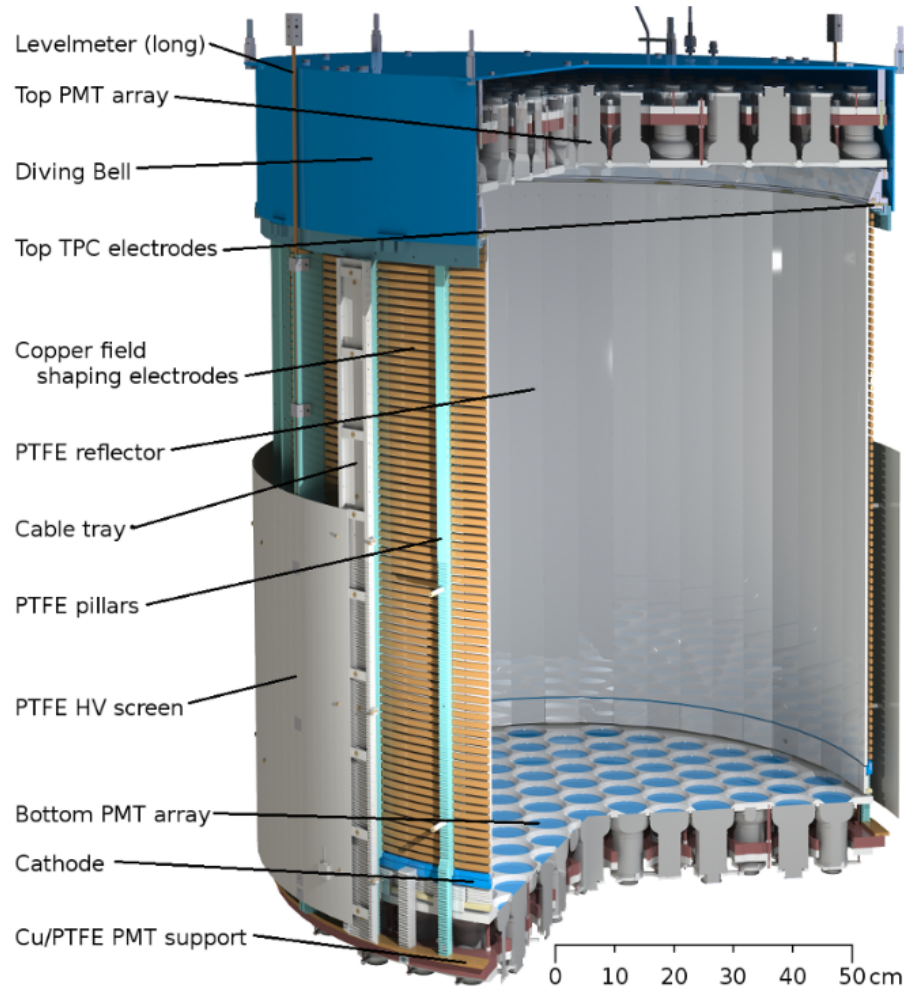


Figure 3.5: Schematic of the TPC. Image credit: [184].

same purpose is the same as the bottom screening mesh. The top three electrodes are made of stainless steel and are hex-etched. Details for each electrode is listed in Tab. 3.1. Fig. 3.6 shows the simulated electric field for the voltage settings during the first science run, Science Run 0.

Four parallel-plate capacitors measure the liquid level. They have a range of 10 mm with 30  $\mu\text{m}$  precision and can be used for measuring tilts or adjusting the height of the TPC. The liquid level's height is tunable through a gas-exhaust tube and maintained with a “diving bell” where controlled gas flow from purification pressurizes the GXe inside the TPC. Two cylindrical levelometers with a 1360 mm range extend from the bottom PMT array to above the diving bell and are used during filling and

Electrode	Type	Diamater	Material	Transparency	Position
Top screening	hex meshed	178 $\mu\text{m}$	stainless steel	96.5%	63 mm
Anode	hex meshed	178 $\mu\text{m}$	stainless steel	89.8%	5 mm
Gate	hex meshed	127 $\mu\text{m}$	stainless steel	92.7%	0 mm
Cathode	parallel wires	216 $\mu\text{m}$	gold-plated stainless steel	97.2%	-969 mm
Bottom screening	parallel wires	216 $\mu\text{m}$	gold-plated stainless steel	97.2%	-1017 mm

Table 3.1: Properties for TPC electrodes. The cathode and bottom screening mesh have high transparency to optimize S1 light collection and are gold-plated to decrease the risk of photoionization.

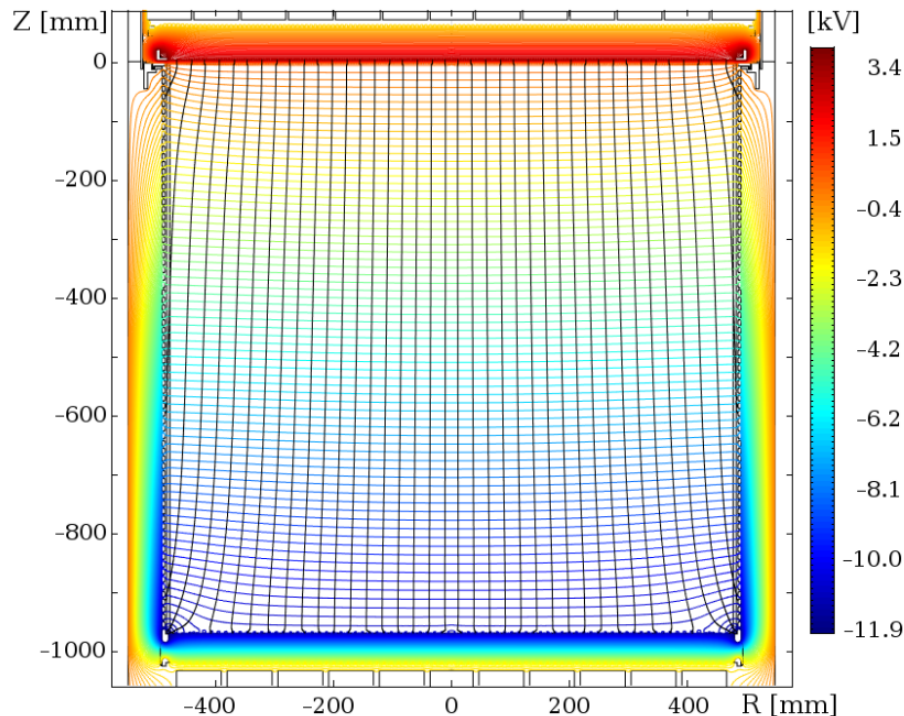


Figure 3.6: Finite element (COMSOL Multiphysics) simulation for the electric field field inside and around the TPC. Field and equipotential lines are shown. The voltages for the cathode, gate, and anode are  $-12$ ,  $0$ , and  $4$  kV, respectively, and are the settings for Science Run 0. The field is mostly uniform throughout the detector, which is important for limiting biases that come from recombination, impurity attachment, etc. Image credit: [184].

recovery. Placed around the field cage are PTFE cable trays that power and transfer signals from the PMTs and temperature sensors. The cables are held in place by pieces of PTFE that fasten to the cable trays.

### 3.1.3 Cryogenic System

The TPC is situated in the center of the water Cherenkov detector (Sec. 3.1.7) and encompassed by the inner cryostat. Because the cryostat is in direct contact with xenon it is made of stainless steel and electropolished to reduce radon emanation (Sec. 3.3.1.2). It is 1960 mm tall by 1100 mm diameter and is metal-sealed using a Helicoflex seal [184]. Surrounding it is the 2490 mm tall by 1620 mm diameter outer cryostat separated by vacuum. It is also constructed from stainless steel but because there is no contact with xenon electropolishing is unnecessary. The two are thermally isolated by Torlon polyamide-imide spacers and vacuum. Heat loss is further mitigated to  $\sim 75$  W by aluminized mylar foil wrapped around the inner vessel. Materials were screened prior to construction for radioactivity.

A 10 m high stainless steel support structure was built inside the water tank. Attached are three M20 rods that suspend the cryostat. They can be adjusted independently to customize the inclination of the LXe level with respect to the TPC. A chain secures the bottom of the outer vessel to the water tank floor to counteract buoyancy forces when the cryostat is empty. A double-walled pipe with inner and outer diameters of 254 and 406 mm, respectively, carries the PMT and auxiliary cables and encloses connections between the cryogenics system and outside components including the purification system (Sec. 3.1.4), diving bell pressurization, and emergency recovery. A separate pipe connects the cathode with the outside. A schematic of the cryostat is shown in Fig. 3.7.

A total of 3.5 tonnes of xenon is stored in the cryostat. In addition to the 2.0 t of LXe inside the TPC, 1.5 t rests between the TPC and inner vessel. The mass of the GXe is  $\sim 20\text{-}30$  kg. The nominal LXe temperature is  $T_0 = -96^\circ\text{C}$ . Gas near the top of the cryogenic system is liquified by pulse-tube refrigerators (PTRs) into a funnel and flows down to the TPC through a pipe to be deposited in the inner vessel beneath

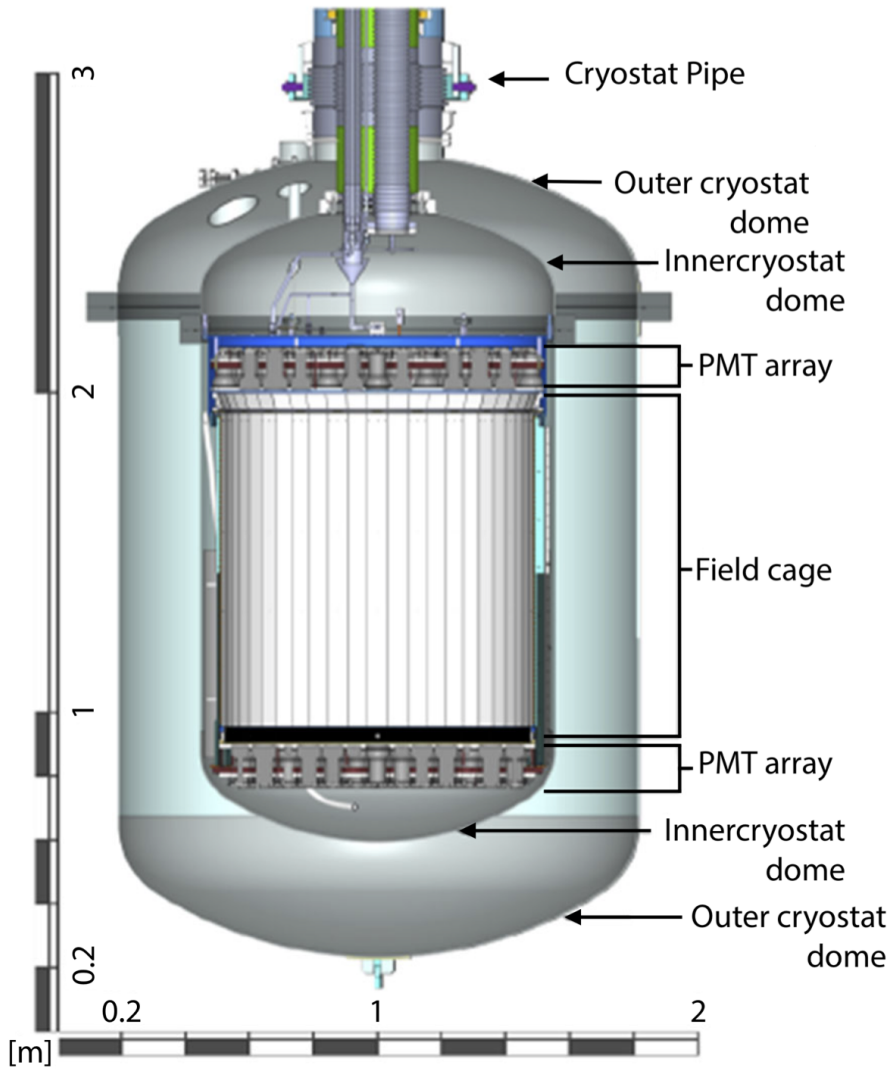


Figure 3.7: Diagram of the cryostat. Image credit: [190].

the TPC. Because the PTRs are higher than the TPC the flow is guided by gravity. Fig. 3.8 shows the layout of the cryogenic system. The cryogenic system extends from the TPC into a service building outside the water tank through a long tube known as the neck. The two PTRs occupy independent cooling towers and can each deliver 250 W of cooling power. With the xenon having a total thermal load of  $\sim 150$  W only one needs to be active at any time. The cooling towers are located in the service building. Each PTR connects to a copper coldfinger inside the inner cryostat so they can be removed without exposing the xenon to air. A proportional-integral-derivative

### 3. THE XENON1T EXPERIMENT AND DARK MATTER SEARCH

---

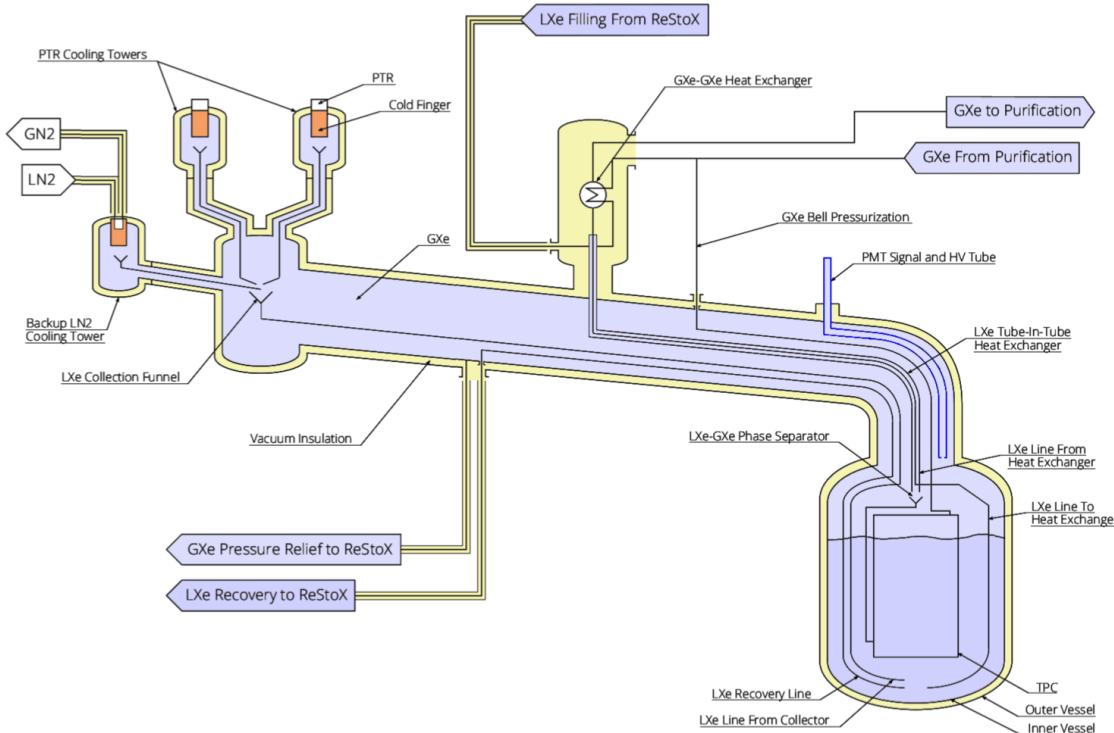


Figure 3.8: Layout of the cryogenic system. Three cooling towers - two with PTRs and one backup LN<sub>2</sub> - liquify GXe that returns to the TPC. LXe is carried from the bottom of the cryostat to the purification system (Sec. 3.1.4) through a heat exchanger system, while returning xenon flows into the bottom of the TPC with excess gas diffusing into the GXe. A portion of purified GXe is extracted before the heat exchanger and used to maintain pressure inside the diving bell. Connections with ReStoX (Sec. 3.1.5) are also shown. Image credit: [184].

(PID) controller monitors and adjusts the temperature of a resistive heater on the coldfinger to maintain stable pressure.

A third cooling tower (also in the service building) uses liquid nitrogen (LN<sub>2</sub>) and can be used in an emergency, if both PTRs are being serviced, or the heat load becomes too great from e.g. loss of power or insulation vacuum. The LN<sub>2</sub> flows from a 10m<sup>3</sup> tank that is also used by ReStoX (Sec. 3.1.5). The cooling power is regulated by adjusting the LN<sub>2</sub> evaporation rate. In the event the PTRs lose power the LN<sub>2</sub> cooling tower must react immediately to prevent rising pressure that can damage PMTs and other components. Sensors and controllers monitoring such a power loss are connected to uninterruptible power supplies (UPSs) to ensure a successful transition and operation of LN<sub>2</sub>.

Connections to the purification system and ReStoX are shown in Fig. 3.8. LXe from beneath the TPC is removed for purification. It passes through a two-phase heat exchanger system, which promotes efficient exchange of thermal energy between GXe returning to the TPC and LXe leaving. The returning xenon is cooled before it reaches the TPC, and likewise removed xenon is heated before purification. The first step of the system is the “tube-in-tube” component where two concentric tubes carrying LXe (GXe) away from (towards) the TPC. The second component is a plate heat exchanger and is closer to the purification system (i.e. returning xenon passes through before tube-in-tube). The system is extremely efficient and significantly reduces the PTR and LN<sub>2</sub> cooling power that would be necessary without it.

The heat exchange efficiency  $\epsilon$  is the fraction of heat necessary for temperature change and vaporization that stays outside of the system. A higher efficiency means better thermal energy transfer between the returning GXe and leaving LXe, and decreases the heat load on the system. This is because instead of GXe re-entering the cryostat at roughly room temperature, it does so at approximately the temperature of LXe with much of it having liquified, putting less stress on the PTRs. An essential ingredient of the heat transfer is the latent heat, which comprises  $\sim 80\%$  of the total exchange. The difference in vaporization temperature of the outgoing xenon and condensation temperature of incoming xenon is

$$\Delta T_{\text{ph}} = T_{\text{gl}}(P_i) - T_{\text{gl}}(P_o) \quad (3.3)$$

where  $T_{\text{gl}}(P)$  is the pressure-dependent temperature of the gas-liquid phase transition, and  $P_i$  and  $P_o$  are the pressures of the incoming and outgoing xenon, respectively [191]. Because the conditions of dynamical gas flow (Sec. 3.1.4) cause  $P_i > P_o$ ,  $\Delta T_{\text{ph}} > 0$ , the system can be very efficient [191]. A study with the Demonstrator - the experiment used to for research and development for XENON1T (Sec. 5.3.1) - showed a heat exchange efficiency for two heat exchangers in series of  $\geq 96\%$  [191]. Following the parallel-plate exchanger a heater provides additional thermal energy to the xenon moving towards the purification system. The different systems that handle the xenon

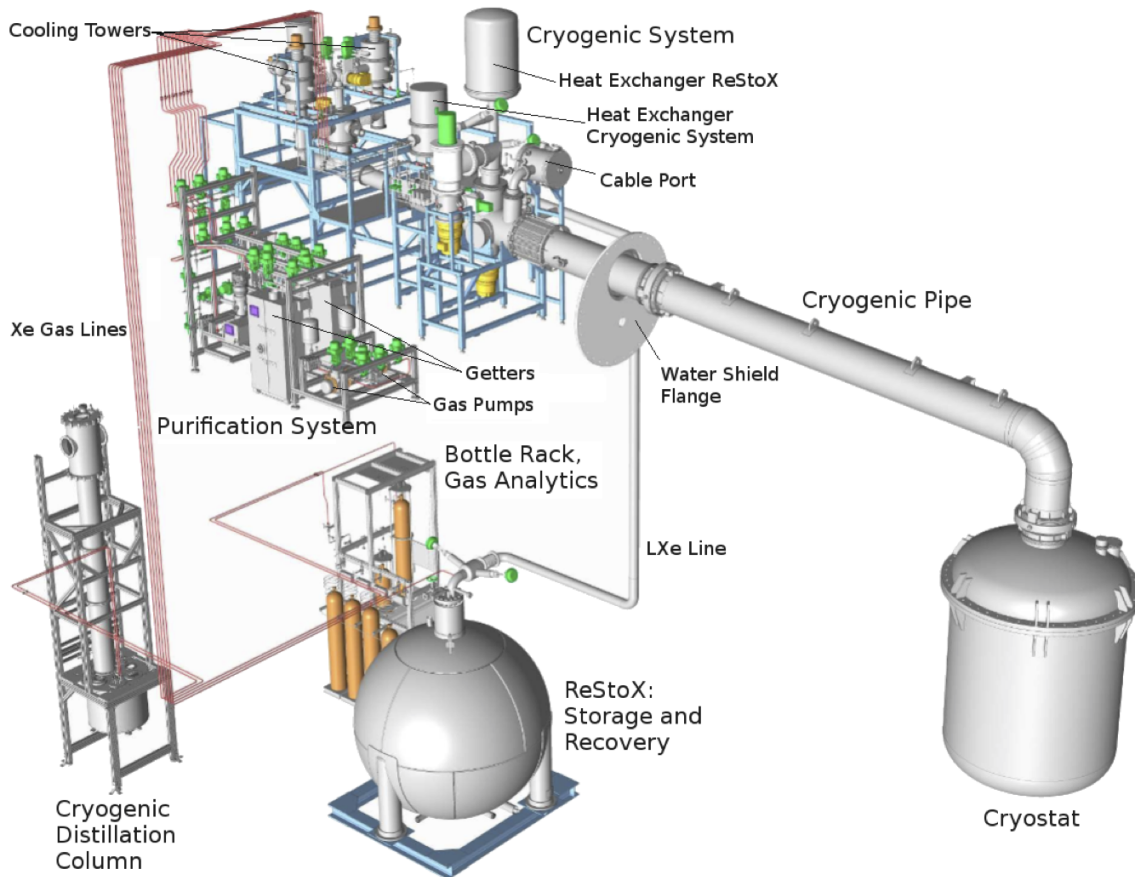


Figure 3.9: The various systems that handle xenon in the experiment: cryostat, cryogenic system, purification system, cryogenic distillation column, ReStoX, bottle racks, and gas analytics station. The water shield flange marks the boundary between the service building and the water Cherenkov detector. Image credit: [184].

can be seen in Fig. 3.9.

### 3.1.4 Purification

LXe contamination presents number of problems. As mentioned in Sec. 2.6.1 electronegative impurities (e.g. O<sub>2</sub>, H<sub>2</sub>O, N<sub>2</sub>O) will attach to drifting electrons, reducing the number that reach the liquid surface and thus the S2.

Impurities will also attenuate scintillation, which pushes our energy threshold up as fainter signals become harder to detect. This is described by

$$I(x) = I_0 e^{-x/\lambda_{\text{att}}} \quad (3.4)$$

where  $I_0$  is initial number of photons,  $I(x)$  is the number after traveling a distance  $x$ , and  $\lambda_{\text{att}}$  is the attenuation length.  $\lambda_{\text{att}}$  is dependent on the absorption and scatter lengths,  $\lambda_{\text{abs}}$  and  $\lambda_{\text{scat}}$ . The absorption length describes the true loss of photons while the scatter refers to photons that elastically scatter without energy loss. This is covered in greater detail in Sec. 5.1.1.

Electronegative impurities come primarily from outgassing of detector materials. They are measured in O<sub>2</sub>-equivalent - that is, the analogous concentration of oxygen if it were the only contaminant. For LXe experiments a concentration of 1 part per billion (ppb) or less is needed.

In addition to the xenon leaving the TPC (after passing through heat exchanger and heater as described in Sec. 3.1.3), connections are made between each of the cooling towers and the purification system. Connections are also made on the neck of the cryogenic system and to the inside of the double-walled pipe that carries the cables. The flow from the five GXe and one LXe connections can be customized. Because impurities are lighter than xenon they are anticipated to have a larger presence in the gas. While the GXe impurity concentration has no direct effect on  $e^-$  loss, impurities will migrate between the LXe and GXe. Purifying the GXe should largely reduce the impurities that pass into the liquid.

Xenon from ReStoX (Sec. 3.1.5) and bottles are also connected to the purification system. A separate heat exchanger sits between ReStoX and purification. In addition to cleaning the Xe as it is transferred from ReStoX to the cryostat, the purification system connects ReStoX to the krypton distillation column (Sec. 3.1.6). The column returns the xenon after distillation to purification. All systems that feed into the purification system do so before the getters and are available as outputs as well. A small tube between the purification and cryostat before the heat exchanger siphons GXe to pressurize the bell to maintain the liquid level, and is regulated by a flow controller. The numerous connections make the purification system a hub for transferring xenon between systems.

The purification system consists of two redundant purification loops, each of which can operate independently of the other. To circulate the xenon KNF pumps, which

### 3. THE XENON1T EXPERIMENT AND DARK MATTER SEARCH

---

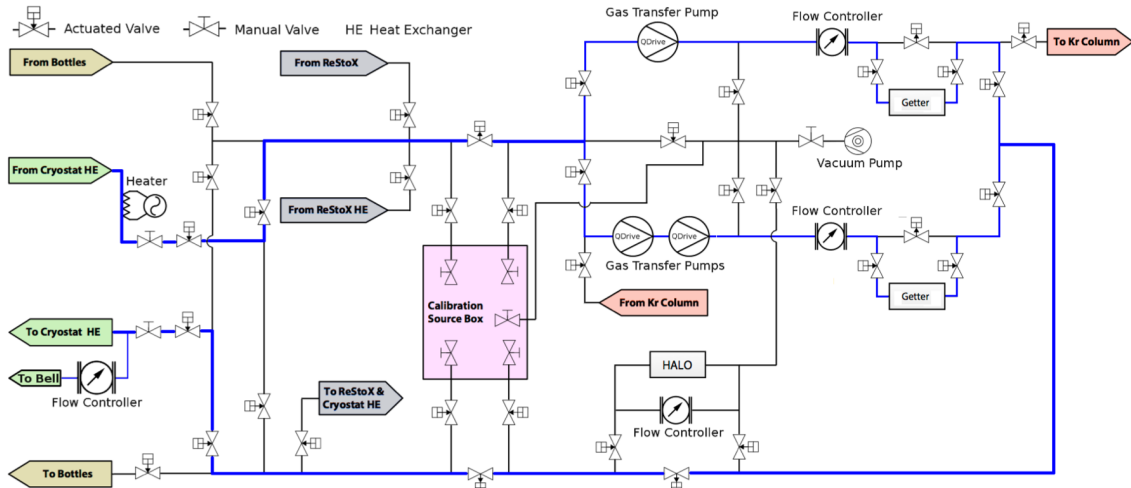


Figure 3.10: Layout of the purification system. The standard flow path during normal operations is highlighted in blue. Image credit: [184].

were used in XENON100, were originally considered. There were a number of drawbacks however that might limit the detector. KNF pumps use elastic diaphragms to move the gas through the system. The membrane is an elastomer (in XENON100 this was neoprene) and its high radon emanation increases the background. In addition, the diaphragms can vulcanize as compressions cause temperatures to reach  $\sim 150^\circ\text{C}$ , and in a worst-case scenario can rupture - as it did in XENON100 - allowing air to leak into the system. While the purity of the xenon plummets the more worrisome aspect is the increase in  $^{85}\text{Kr}$ .

CHART QDrive pumps, became a viable option during commissioning. They are hermetically sealed, have high flow capacity, and were expected to have lower radon emanation than the KNF pumps. They are magnetically-resonant and operate via a compression space with oscillating externally-driven pistons. Motors, valves, and pistons are not lubricated, making it an excellent choice for high-purity. For these reasons they were chosen. Unfortunately QDrives were realized to have high  $^{222}\text{Rn}$  emanation, and can require frequent maintenance if operated at too great a voltage. For the former Rn emanation measurements were made prior to installation with the lowest being chosen. For the latter they are operated at safe conditions and since the beginning of Science Run 0 no issues have arisen. Fig. 3.10 shows the two branches

of the purification system have one and two QDrives. A fourth QDrive could be installed but the limiting factor on circulation speed is not a result of the pumps but the pressure difference from tubes leading to the system caused by too small a radius. An upgrade was performed in April 2018 that enlarged the radii and increased the flow (Sec. 5.3.7).

The flow of the GXe is maintained by two MKA 1579A mass-flow controllers - one on either branch. The assumption before the experiment went online was these would limit the speed when necessary, but because we did not achieve our goal these have minimal impact. Still, they can be used for further restriction. The xenon then passes through SAES PS4-MT50-R high-temperature rare-gas purifiers, or getters. They use heated (400°C) zirconium to form unbreakable bonds with carbide, nitride, and oxide, lowering the impurity content to <1 ppb [184]. A bypass valve allows the xenon to pass un-purified in the event that it does not need to be cleaned.

A Tiger Optics HALO+ H<sub>2</sub>O monitor measures the water content in the purified GXe to track the purification efficiency. It can measure concentrations down to 400 ppt. Unfortunately, there is no pressure drop to push GXe through the HALO so it is bypassed during operations. The Xe is then forwarded to the cryostat, bell, ReStoX, or bottles (Kr column occurs after the purification loops before the HALO).

The components of the system are electropolished and able to be baked up to  $\sim$ 120°C for decreased outgassing (Sec. 5.3.5.1). The purification system has a number of valves that allow the versatility described in this section. The majority are pneumatic and can be operated remotely with the slow control system (Sec. 3.1.10). The remainder are manual valves situated in select locations: to and from the cryostat, inside the calibration box, and before the vacuum pump, which can be used to evacuate individual sections or the entire system. These are in place as a precaution against accidental openings of the actuated valves.

### 3.1.5 ReStoX

The Recovery and Storage system for XENON1T (ReStoX) stores xenon not in use by other systems. It is located on the ground floor of the service building. With a volume

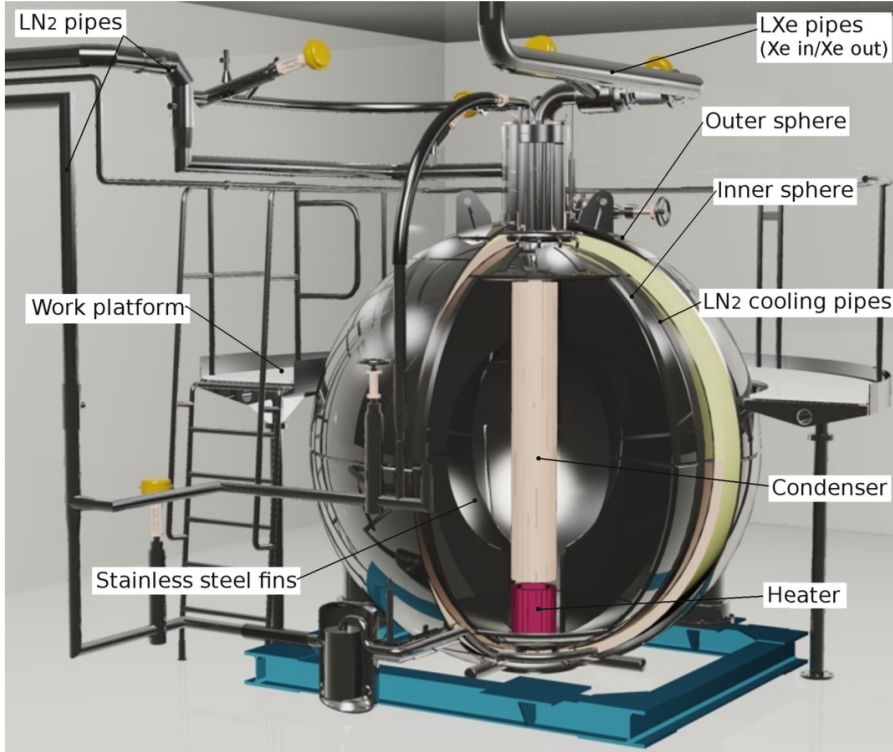


Figure 3.11: ReStoX with major components labeled. Image credit: [184].

of  $4.95 \text{ m}^3$  (diameter of  $2.1 \text{ m}$ ), wall thickness of  $28 \text{ mm}$ , and ability to withstand pressures of up to  $73 \text{ bar}$ , it can support  $7.6 \text{ tonnes}$  of xenon as a gas, liquid, or supercritical fluid. It is made from stainless steel and insulated via vacuum from an outer sphere, where thermal conductance is extremely low due to with superinsulation and limited contact to an external heat load of  $\sim 50 \text{ W}$ . To limit impurity contamination while the Xe is in ReStoX the vessel and valves are metal sealed and electropolished.

The xenon is cooled by 16 lines welded to the inner vessel's outer surface that carry  $\text{LN}_2$  that from the  $10 \text{ m}^3$  dewar adjacent to the service building. To prevent overcooling 16 stainless steel fins inside increase heat exchanging. A condenser and heater in the middle are used when the xenon is stored as a liquid, which is normally the case. The heater ensures solid xenon does not obstruct pipes so Xe can be transferred freely with other systems. The total cooling power of  $> 3 \text{ kW}$  is spread over  $4.3 \text{ m}^2$  of copper [184].

Previous LXe experiments would fill detectors by condensing the GXe from storage. Similarly, recovery was done by allowing the LXe in the cryostat to evaporate.

While this was feasible for detectors with  $\mathcal{O}(100)$  kg of xenon, doing so for XENON1T would require approximately two months, and fast recovery in the event of an emergency would not be possible. This is solved through the purification system, which as mentioned in Sec. 3.1.4 can pump xenon between systems and significantly expedite the process.

### 3.1.6 Krypton Distillation

Commercial high-purity xenon generally has krypton concentrations between 1 ppm to 10 ppb. This is not clean enough for LXe dark matter detectors so additional distillation is necessary. The reason for restricting the krypton content is  $^{85}\text{Kr}$ , which has a half-life of 10.76 years and undergoes  $\beta$ -decay with an end-point energy of 687 keV. With an expected fraction of  $^{85}\text{Kr}/{}^{\text{nat}}\text{Kr} = 2 \times 10^{-11}$ , the necessary  ${}^{\text{nat}}\text{Kr}/\text{Xe}$  concentration for the krypton background to be subdominant to that of the radon is  $< 200$  ppq [192]. Details of the  $^{85}\text{Kr}$  background can be found in Sec. 3.3.

To achieve this purity we use a krypton distillation column, seen in Fig. 3.12. The column has a total height of 5.5 m and is kept in an insulation vessel at  $10^{-5}$  mbar to minimize thermal losses [192]. GXe enters through a heat exchanger and is liquified by the input condenser, which uses a cryo-cooler (Leybold CP-50) at  $-98^\circ\text{C}$  and maximal power of 100 W. Next it moves to the package tube, built with 2.8 m of structured stainless steel package material (Sulzer EX) 45 cm in diameter that has feeding ports for both liquid and gas xenon. At the top of the tube is a second cryo-cooler (Leybold CP-140T) at  $-98^\circ\text{C}$  and capable of 200 W. Liquified xenon will fall to the bottom of the column, where it is stored and heated by a reboiler with up to 300 W. The Kr, with a smaller atomic mass and lower condensation temperature, will concentrate in the top of the column. Siphoning gas at the top removes xenon with a much higher krypton concentration than present in the inlet. The higher-purity Xe at the bottom is extracted and passes through the heat exchanged before returning to the purification system or ReStoX.

Once installed at LNGS the reduction of  ${}^{\text{nat}}\text{Kr}/\text{Xe}$  was found to be  $6.4_{-1.4}^{+1.9} \times 10^5$  [192]. Inlet flows have been shown to be stable up to 18 slpm, but running all ReStoX

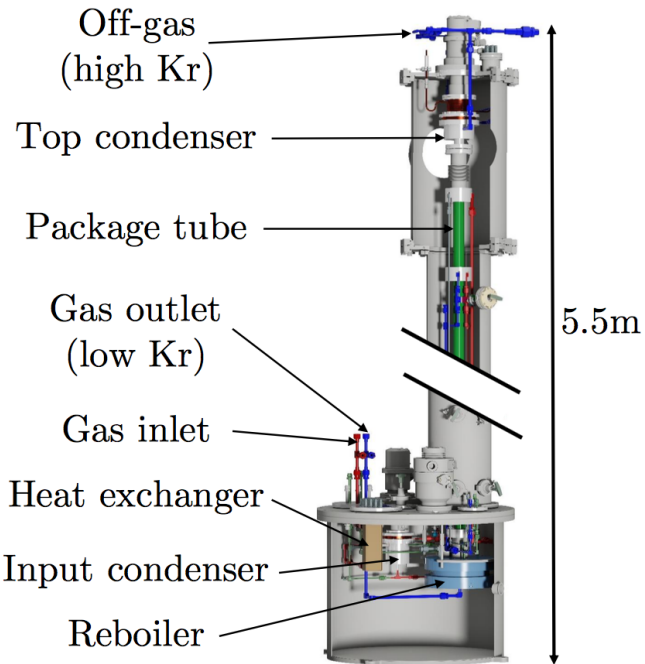


Figure 3.12: Krypton distillation column. Inlet gas is cooled by a heat exchanger and input condenser as it passes to the package tube. Xenon gas that reaches the top of the column is liquified by the cryo-cooler and falls to the bottom, where it is heated by the reboiler. Krypton cannot condense due to its lower boiling point. The off-gas removes this high-krypton xenon, and high-purity xenon at the bottom of the column is returned to the other systems via the gas outlet. Image credit: [184].

xenon through distillation on the way to the cryostat during filling would take  $\sim 3$  weeks. For this reason an online removal system was used, where the xenon was distilled during science run data taking. For over 70 days 7% of xenon passing through the purification system was diverted to the column and a total of 0.07% was removed. An initial  ${}^{\text{nat}}\text{Kr}/\text{Xe}$  concentration of 60 ppb was decreased to  $360 \pm 60$  ppq, the lowest ever achieved in a LXe dark matter experiment. Measurements of  ${}^{\text{nat}}\text{Kr}/\text{Xe}$  are done using a rare gas mass spectrometer (RGMS) that uses cryogenic gas chromatography to separate the Kr from Xe, followed by a mass spectrometer for Kr measurement [193].

The second most worrisome low-energy background comes from the  ${}^{222}\text{Rn}$  decay chain. While the distillation column was originally built and intended for Kr, it was shown to work in a single stage distillation [194] and subsequently XENON100 [195]

for radon removal. It operates using the reverse principle, i.e. radon-enriched xenon coalesces near the bottom of the column so it decays, while the more pure xenon at the top is returned to the purification system.

### 3.1.7 Water Shield

Limiting radiation from outside the experiment is essential to a dark matter search. An active water Cherenkov detector encompasses the cryostat, spanning 9.6 m in diameter and 10.2 m high. It is filled with deionized water, which can fill the Cherenkov detector at up to  $2.2 \text{ m}^3 \text{ h}^{-1}$ . The tank shields the cryostat from neutrons and  $\gamma$ -rays that originate underground (from e.g. rocks) and muon-induced neutrons, decreasing the number of events that reach the TPC by orders of magnitude.

84 Hamamatsu R5912ASSY PMTs are placed in five rings along the inner wall of the water tank, 2.5 m apart in height. The lowest ( $z = 0 \text{ m}$ ) and highest ( $z = 10 \text{ m}$ ) rings each contains 24 PMTs, while the three between them have 12 each. The quantum efficiency for each PMT is  $\sim 30\%$  between 300-600 nm. To increase the chance of photon detection the inner wall is coated with foil (3M DF2000MA) that has nearly 100% reflectivity at  $> 400 \text{ nm}$ , [196]. However,  $\sim 90\%$  of light is absorbed for  $< 370 \text{ nm}$  and  $3-7.5\%$  from  $250 \leq \lambda \leq 370 \text{ nm}$  is wavelength shifted to more favorable values for the PMTs.

The purpose of the PMTs is to identify muons and muon-induced neutrons by detecting showers initiating outside the water tank. Using the difference in arrival times to each PMT the path of the particle can be reconstructed as shown in Fig. 3.13. If an event in the TPC coincides with one in the water tank it is excluded. For this reason the system is referred to as the muon veto (MV). The flux of muons at LNGS is  $3.31 \pm 0.03 \times 10^{-8} \text{ cm}^2 \text{ s}^{-1}$  with average energy  $\sim 270 \text{ GeV}/c^2$  [184].

### 3.1.8 Calibrations

Calibrations are used for a host of purposes including understanding energy resolution, light collection efficiency, electron lifetime, electronic and nuclear recoil bands,

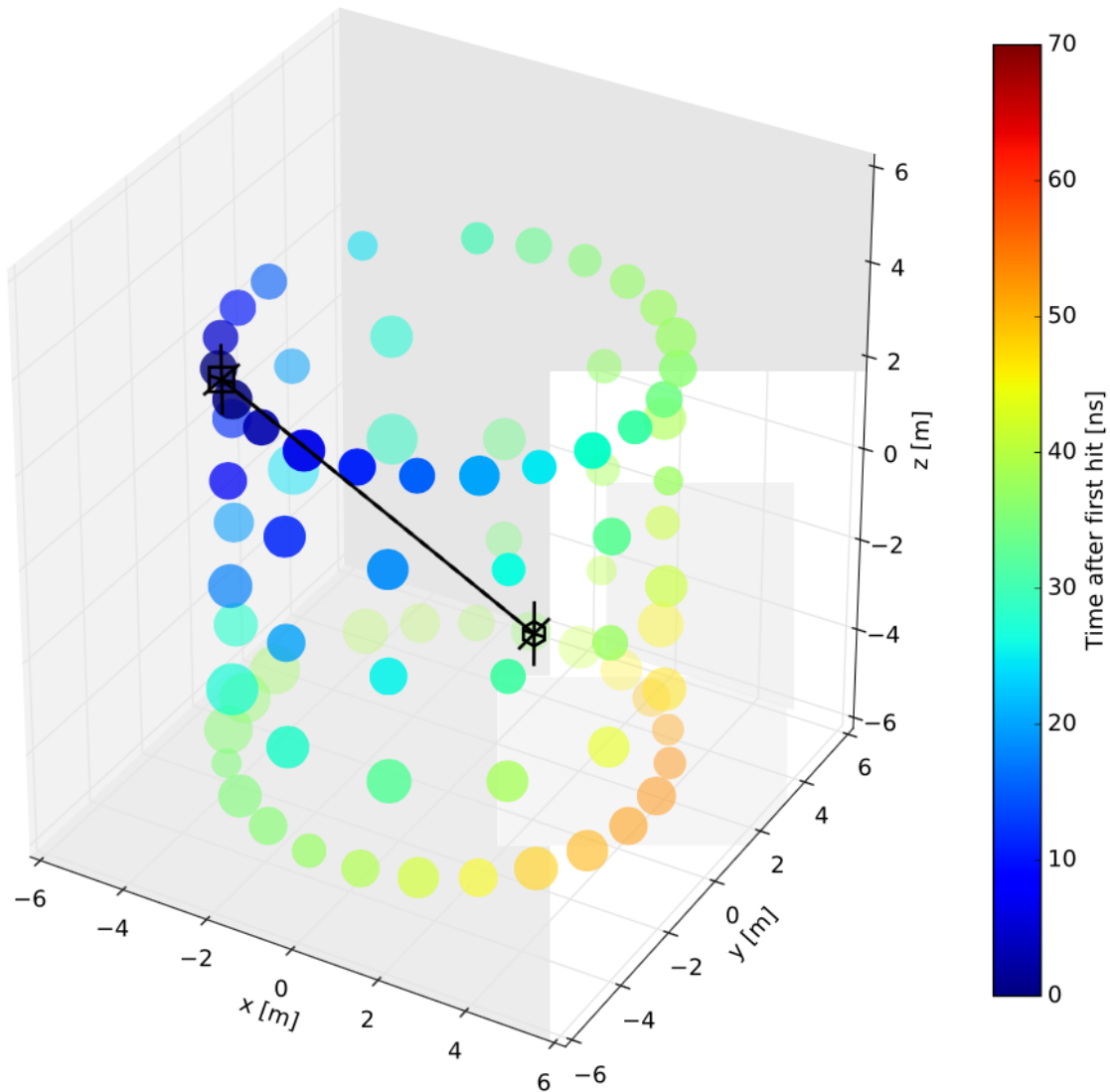


Figure 3.13: Arrival time of light to muon veto PMTs helps reconstruct the muon trajectory (black line). Image credit: [184].



Figure 3.14: Photo from inside the water tank during commissioning. The muon veto PMTs can be seen around the perimeter covered in black bags to shield them from the light. The neck of the cryogenics system extends through the hole in the back from the service building to the cryostat, with the inner vessel wrapped in mylar visible beneath.

and many more. Depending on the source they can be performed inside the TPC (internal) or outside (external). The different calibrations and the purposes they serve are discussed here; additional details and results are in Sec. 3.2.

### 3.1.8.1 Internal

Internal calibrations allow us to describe how our detector observes events throughout the entire TPC. This is preferable to external calibrations (Sec. 3.1.8.2), where events are more focused in the outer volume. The calibration source box is installed in the purification system (pink region in Fig. 3.10) and contains valves opening to the GXe both before and after the getters. This is clearer in Fig. 3.16, which shows a detailed

### 3. THE XENON1T EXPERIMENT AND DARK MATTER SEARCH

---



Figure 3.15: The XENON1T experiment with the water tank (left) and service building (right). A depiction of inside the water tank hangs on the outside. ReStoX (first floor), DAQ (second), and the cryogenic system (third) are visible in the service building.

schematic of the source box including locations of  $^{83m}\text{Kr}$ ,  $^{220}\text{Rn}$ , and  $\text{CH}_3\text{T}$ , valves and filters, and connections to the purification system and cryostat. When the valves are opened, the source will flow into the GXe stream and cryostat. Therefore only sources that do not introduce electronegative impurities are used. The source will quickly diffuse in the xenon to become uniformly distributed, allowing a number of detector characteristics and properties throughout the entire TPC to be studied.

$^{83m}\text{Kr}$  has monoenergetic decays of 32.2 ( $t_{1/2} = 1.83$  h) and 9.4 keV ( $t_{1/2} = 154.4$  ns). The short half-lives and its final decay product  $^{83}\text{Kr}$  being stable and a noble gas make it a great choice to measure the light collection efficiency (LCE), the electron lifetime, and many other important features.

$^{220}\text{Rn}$  is used to calibrate the electronic recoil (ER) band as its progeny  $^{212}\text{Pb}$  is a  $\beta$ -emitter with endpoint energy 569.91 keV. There are other  $\alpha$ - and  $\beta$ -emissions throughout the chain that can be used for additional studies, including measuring the electron lifetime with the  $^{212}\text{Bi}$   $\alpha$ -decay. The longest half-life in the chain is  $^{212}\text{Pb}$  with  $t_{1/2} = 10.6$  h (next longest is  $^{212}\text{Bi}$  with  $t_{1/2} = 1.00$  h) so dark matter data can

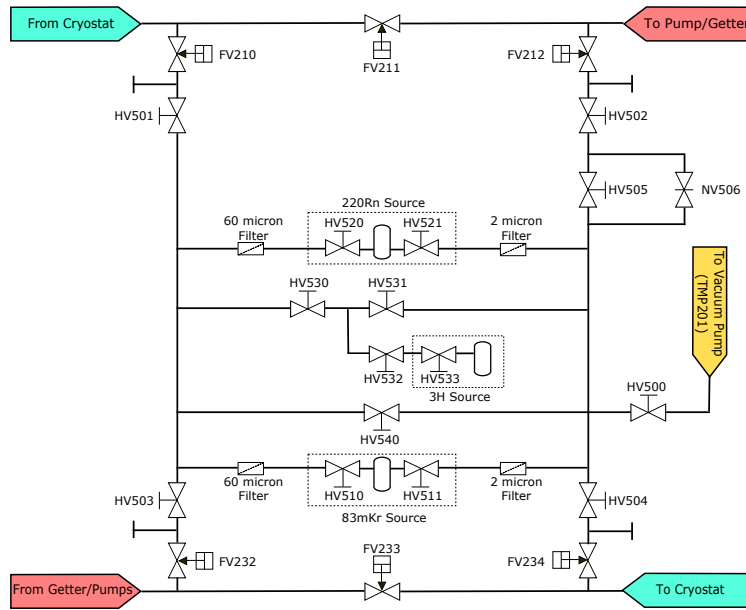


Figure 3.16: Layout of the calibration source box in the purification system. Locations of  $^{220}\text{Rn}$ ,  $^{83\text{m}}\text{Kr}$ , and  $\text{CH}_3\text{T}$  are marked by dotted rectangles. Filters are installed to catch debris. Connections to and from the cryostat (turquoise) and pumps and getters (red) are shown. The vacuum pump (yellow) is used to evacuate the chamber before use.

resume within several days.

Tritiated methane ( $\text{CH}_3\text{T}$ ) is a very attractive candidate because of its low-energy  $\beta$ -emission. With a 18.6 keV endpoint energy, it is an ideal candidate for calibrating the low-energy ( $cS1 < 60 \text{ PE}$ ) ER band and measuring the light and charge yields in an important region. This was originally done by LUX [197] and subsequently performed with XENON100 [198]. However, with a half-life of  $t_{1/2} = 12.3 \text{ y}$  it must be removed completely by the getters because introducing a new background in the dark matter region of interest would be disastrous. There is a worry that  $\text{CH}_3\text{T}$  adheres to the cryostat, prohibiting complete removal. For this reason a  $\text{CH}_3\text{T}$  calibration has not yet been conducted in XENON1T.

PMT gains are calibrated using blue LEDs at low light levels. Unlike other sources this calibration is done using fiberoptic cables that are carried from the data acquisition (Sec. 3.1.9) into the TPC. They are fixed at various heights and angles to optimize PMT calibrations and flash at periodic intervals. They are used to measure the single

photoelectron (SPE) spectrum (Fig. 3.22) and PMT afterpulsing (Fig. 3.4).

### 3.1.8.2 External

External calibrations are performed with the source outside the cryostat. In XENON100 this was done by inserting a source inside the protective lead shielding [199]; however, the size of the water tank in XENON1T requires the installation of two “I-belts” along the height of the detector and one “U-belt” that also extends underneath, as shown in Fig. 3.18. They allow the sources to be lowered from the roof of the tank and positioned at different locations along the axis of the belts.

External  $\gamma$  sources include  $^{137}\text{Cs}$  with an energy of 661.7 keV, and  $^{228}\text{Th}$  with a number of energies between 511 keV and 2.614 MeV. These are stored in W-collimators that restrict the  $\gamma$ -rays to a cone of 40°. Additionally, radioactive isotopes in the materials (e.g.  $^{60}\text{Co}$ ,  $^{214}\text{Bi}$ ) have mono-energetic  $\gamma$ -rays that can be used.

Nuclear recoil sources  $^{241}\text{AmBe}$  and a deuterium-deuterium (D-D) neutron generator (NG) are also placed in the water tank. They emit MeV neutrons (though have different spectrums) and the  $^{241}\text{AmBe}$  is housed in the W-collimator. Details are discussed in Sec. 4.2.2.

### 3.1.9 Data Acquisition

The data acquisition (DAQ) is in a temperature-controlled room on the second floor of the service building. It can record the TPC and muon veto PMTs independently or together. Signals from the TPC pass through Phillips Scientific 776 amplifiers where they undergo a 10-fold increase in amplitude. They, along with the muon veto signals, are then digitized via 100 MHz CAEN V1724 flash analogue to digital converter (ADC) boards (32 in total) that have 40 MHz bandwith, 14 bit resolution, and ranges of 2.25 V and 0.5 V, respectively. Fig. 3.19 shows a typical waveform recorded by the DAQ. A single independent clock connects to each ADC to ensure they are aligned and a 0.1 Hz synchronization signal is passed from a custom-developed GPS-synched module.

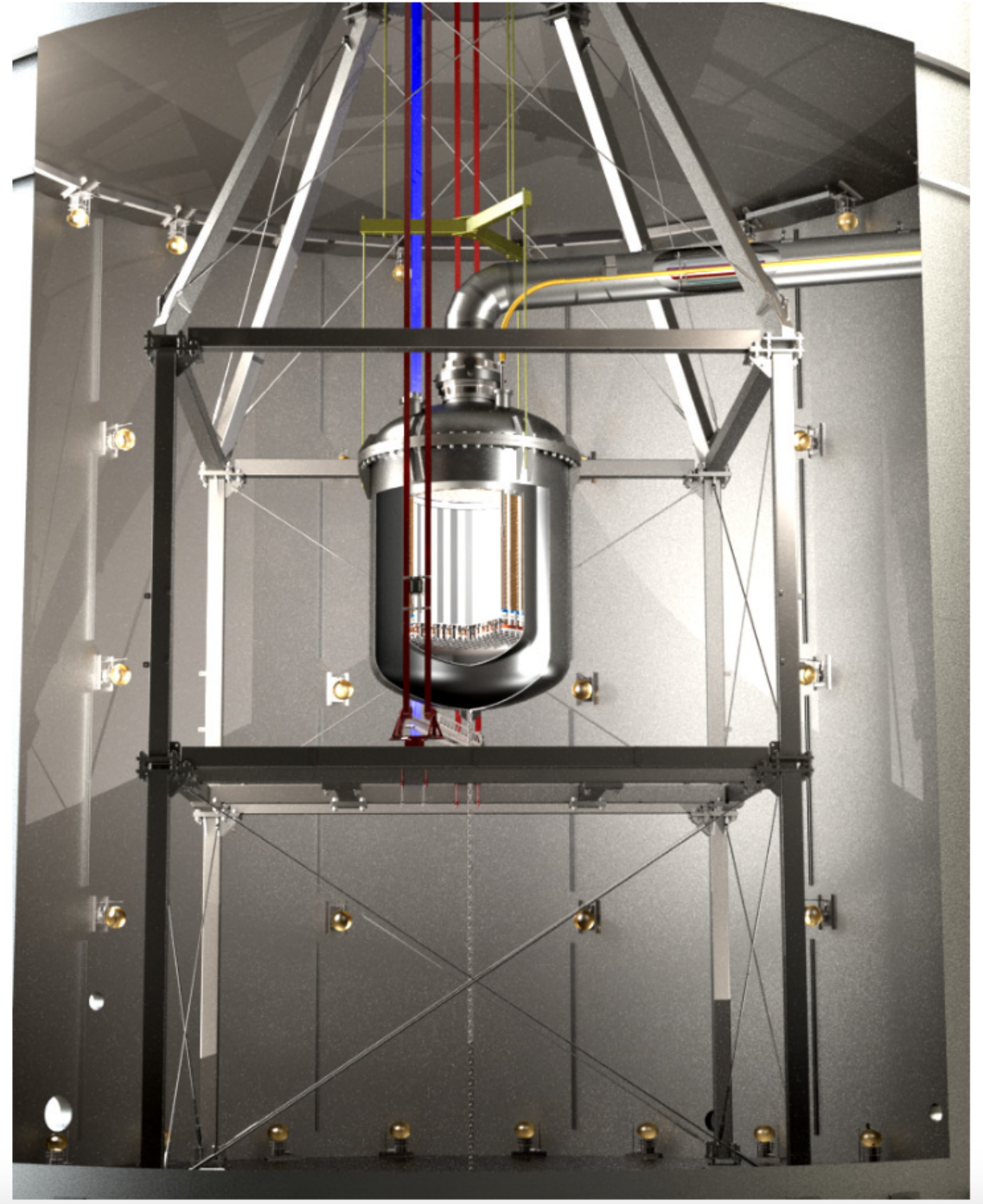


Figure 3.17: Interior of the water tank. The belts highlighted in blue, maroon, and red, and the portion of the U-belt that extends underneath the cryostat is visible. Six wires - three extending from the roof to the cross and three from the cross to the cryostat - adjust the liquid level and are marked in dark yellow. The connection from the service building to the cathode is shown in bright yellow. The chain fixes the cryostat to the floor of the water tank to counter buoyancy forces. The large metal structure is the skeleton from the below-ground clean room used while installing the TPC. PMTs for the muon veto are attached to the water tank. Image credit: [184].

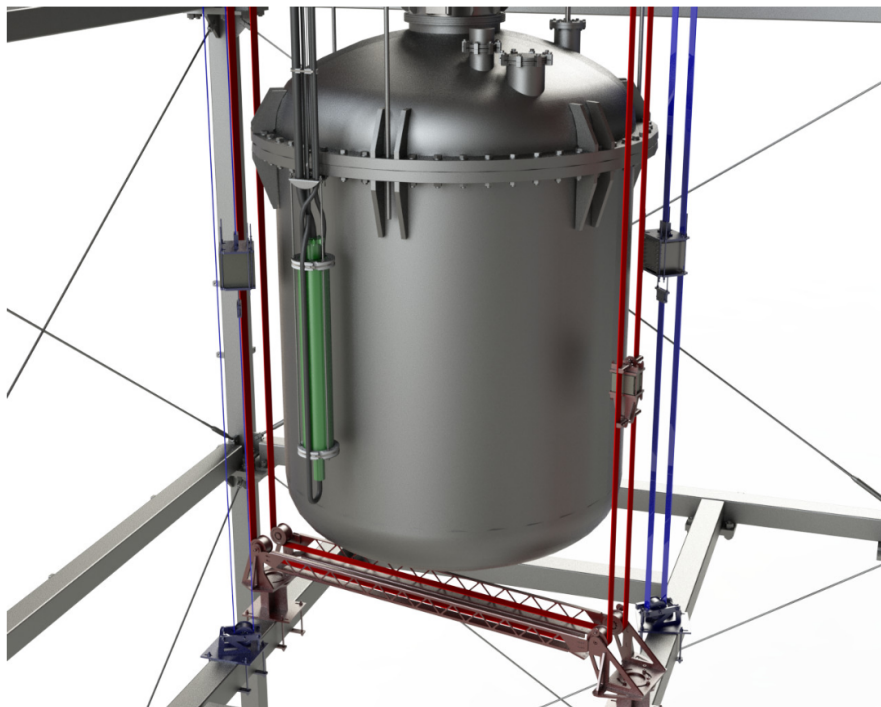


Figure 3.18: Calibration belts around the cryostat. The I-belt and U-belt are shown in blue and red and have collimators present. The green cylinder is the neutron generator. Image credit: [184].

The TPC DAQ reads every pulse  $> 0.3$  PE from each PMT independently and regardless of any signal from other channels. The read-outs of the ADC boards are passed to six computers at up to  $300 \text{ MB s}^{-1}$  ( $\sim 100 \text{ Hz}$ ) and are stored along with relevant information such as time and channel in a MongoDB database. The sum of the bottom PMTs along with veto and busy information is constantly read by a separate computer to determine the deadtime. The DAQ continuously monitors data quality parameters such as baseline, trigger, and noise.

A software eventbuilder on three server-grade machines decides in real-time if an interaction has occurred by examining the time-clustering of PMT signals, and opts whether to trigger. Metadata from the trigger decision is recorded and can be monitored online to check performance or offline for analysis. At larger than 200 PE ( $\sim 7 e^-$ ) the trigger efficiency is  $> 99\%$ . The muon veto uses a simple coincidence trigger that is directed by a CAEN V1495 VME unit.

Two 10 Gbps fibers transfer the raw data to buffer-storage at LNGS for temporary

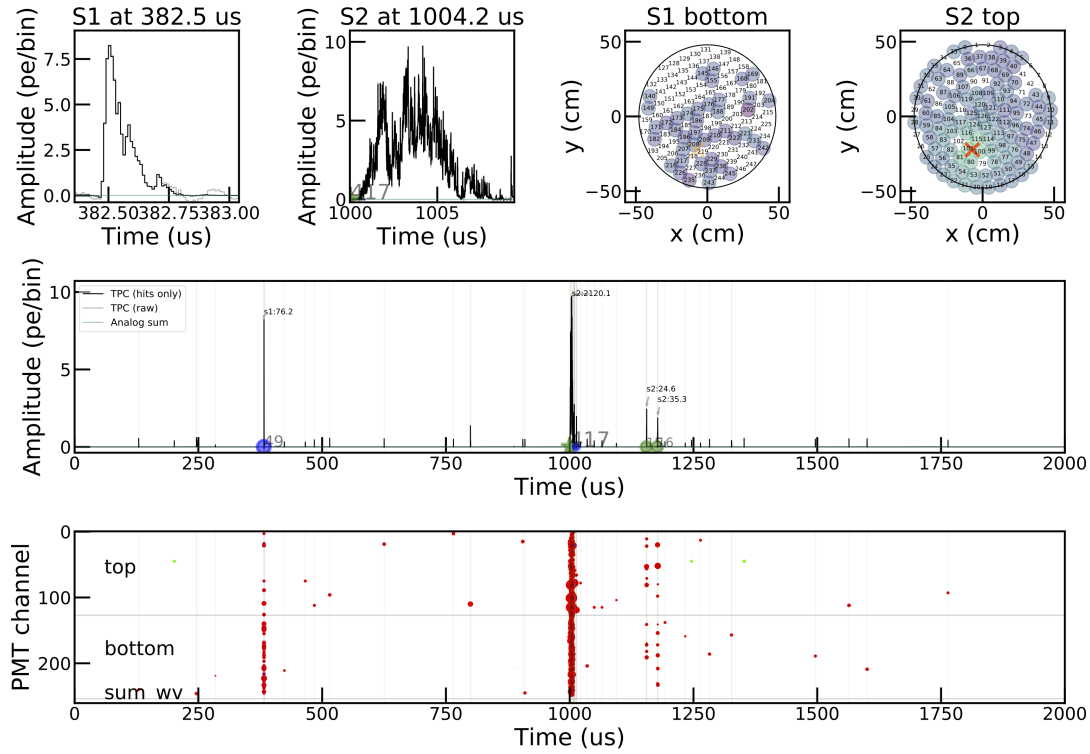


Figure 3.19: Example of a waveform from XENON1T. The bottom panel shows hits (red circles) for each PMT channel with larger areas representing greater intensity. An S1 (76.2 PE) is visible at  $\sim 380 \mu\text{s}$ , marked by the blue circle in the middle panel. The shape of the S1 (left) and the light seen by the bottom PMT array (center right) are shown in the top panel. At  $\sim 1000 \mu\text{s}$  an S2 (2120.1 PE) occurs. Its shape (center left) and light distribution in the top PMT array (right) are shown in the top panel. The red cross marks the  $x$ - $y$  coordinates from the position reconstruction algorithm (Sec. 3.2.3). PMTs near the cross that are white are turned off. S2s are marked by green circles in the middle panel. Two smaller ( $< 40$  PE) S2s follow the primary S2 by  $\sim 150 \mu\text{s}$ . Image credit: XENON1T processor.

housing. The raw data is then moved to the US Open Science Grid and European Grid Infrastructure for processing and backed up in Stockholm [184]. Fig. 3.20 shows an overview of the DAQ system.

To prevent acquisition of bad data four quality checks are performed - three of which are done in real time during data taking. The first is a *high energy veto* that goes to TRUE in the event of a very large S2. When this occurs the DDC-10 (custom module) forwards a NIM pulse to the ADC boards, which blocks data from being copied to the readers. Simultaneously a BUSY ACTIVE signal is sent from the DDC-10

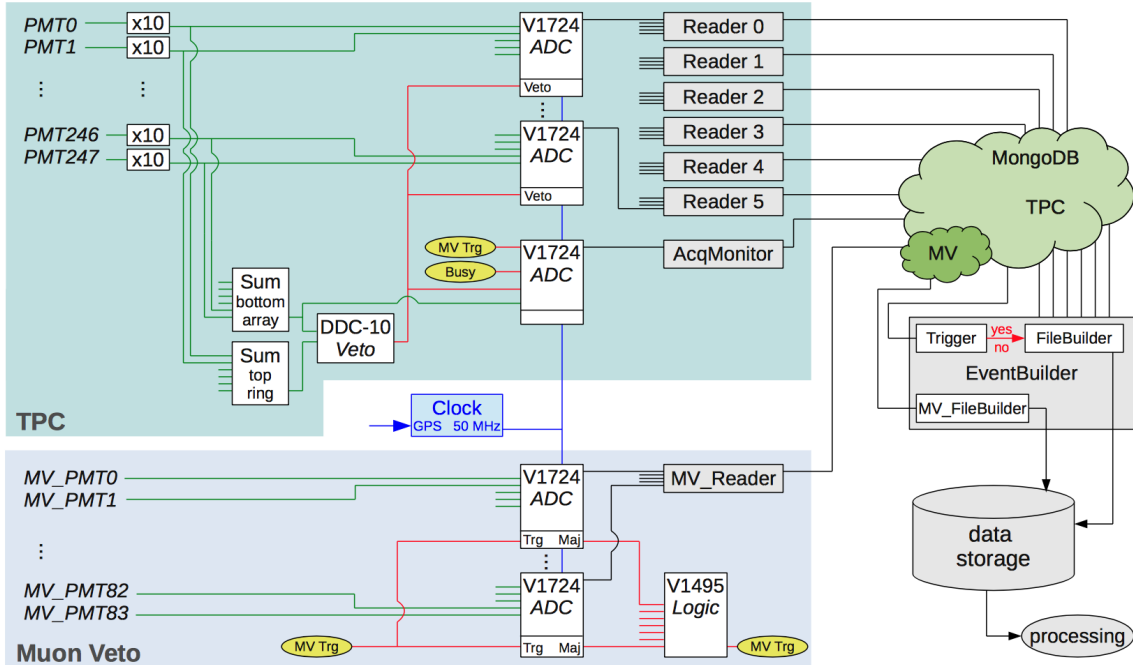


Figure 3.20: Schematic of the data acquisition. Image credit: [184].

to the acquisition monitor digitizer. After 10 ms the high energy veto returns to FALSE, ending the NIM pulse and resetting BUSY INACTIVE. This mode is only used during calibrations.

Aside from the DAQ monitor each of the 32 digitizers feeds a low-voltage differential signaling (LVDS) pulse to the V1495 logic module. Each is TRUE if the memory buffer is nearly full and FALSE otherwise. This is the *busy veto* and in a similar fashion to the high energy veto, the V1495 fans a NIM pulse to the digitizers to block copying of their data to the readers, and sends a BUSY TRUE to the DAQ monitor digitizer. The veto is lifted once all digitizers return to less than full memory or 10 ms - whichever is longer.

The final check during data acquisition is the *busy type check*. It ensures that nowhere in the event was a veto signal, i.e. the busy signal must set to BUSY FALSE. This is in part to reject events where a large S2 triggers a high energy veto that cuts off subsequent smaller S2s (or even part of the large S2) in the same waveform. It also cuts PMT flashes as they trigger a busy veto.

The final quality cut is done in processing. On a small number of occasions

events at the end of a dataset some channels would be missing. To fix this the final 21 seconds of each run are omitted from analysis. The 21 seconds comes from the internal clock of the digitizers, which count from zero to 0x3FFF in 10 ns steps, or roughly 21 seconds.

### 3.1.10 Slow Control System

The subsystems are controlled, monitored, and recorded by a slow system. The system uses General Electric (GE) Programmable Action Controllers (PACs) and Complicity Supervisory Control And Data Acquisition (SCADA) for hardware and software, respectively. Nearly 2,500 parameters are stored in a GE Proficy Historian database, which can be queried for analysis offline. Breach of alarm conditions (e.g. out of range, connection loss, failure of equipment) triggers notifications via email, pre-recorded voice messages over landline, and SMS texts to cellular phones.

Individual PACs from the GE RX3i family control sensors and actuators of the purification, cryogenic, krypton distillation, LXe storage, and water purification systems. The PACs connect to a private front-end network. PAC alarms are transmitted using the GE Alarm&Event Express tool to the alarm system. In addition to the SCADA system operations are possible via touch screens. Open Platform Communication (OPC) servers, web services, or the Modbus protocol integrate the DAQ, high-voltage supply, and calibration system motor controllers into the slow control system. For extra security the system requires certain conditions to be met before performing potentially unsafe operations.

PACs and OPC servers connect to two redundant SCADA servers on the front-end network. Two redundant fibers link the experiment to the aboveground laboratory. An aboveground building houses supervisory and data storage components including the alarm system, Historian database, slow control viewer, and primary XENON1T control room. The slow control system is connected to a backup server outside LNGS to prevent data loss during a laboratory network failure. It is powered by an extended on-battery runtime uninterruptible power supply (UPS) with generator backup.

## 3.2 Detector Characterization

Calibrations are used for detector characterization, monitoring, and measurements of fundamental physics. In XENON1T  $^{83\text{m}}\text{Kr}$ ,  $^{222}\text{Rn}$ ,  $^{137}\text{Cs}$ ,  $^{228}\text{Th}$ , americium beryllium ( $^{241}\text{AmBe}$ ), a neutron generator, and LEDs have been used for calibration.

The most frequent calibration source is  $^{83\text{m}}\text{Kr}$ . As a noble gas it can be injected directly into the xenon without loss of purity, and its short half-life and stable decay product mean rates return to normal within a day.  $^{83}\text{Rb}$ , is installed in the source box connected to the purification system (Sec. 3.1.8.1) and decays through electron capture



with a 74.8% branching ratio to the metastable state  ${}^{83\text{m}}\text{Kr}$ .  ${}^{83\text{m}}\text{Kr}$  then de-excites in two steps: emission of a 32.2 keV conversion electron with half-life  $t_{1/2} = 1.83$  h followed by a second conversion electron at 9.4 keV with  $t_{1/2} = 154.4$  ns. The short interval between the two decays makes tagging events easy and has strong discrimination power against nominal background. The events used for studies including detector characterization need to have both S1s resolved by the DAQ. To select such events the waveform must have two S1s with a time between them  $\Delta t_{\text{S1}} 500\text{-}2000$  ns. This cuts more than 96% of  ${}^{83\text{m}}\text{Kr}$  events but the high activity is still sufficient to perform high-statistic analyses. Fig. 3.21 shows S1 and cS1 for both decays, and S2<sub>b</sub> and cS2<sub>b</sub> for the 32.2 keV decay for  ${}^{83\text{m}}\text{Kr}$  events. While the  $\Delta t_{\text{S1}}$  cut rejects most  ${}^{83\text{m}}\text{Kr}$  events, it is extremely effective at removing background.

The mono-energetic decays are used for a number of detector characterizations including light collection efficiency (Sec. 3.2.2), position reconstruction (Sec. 3.2.3), S2 correction maps (Sec. 3.2.4), and electron lifetime (Sec. 3.2.5).

### 3.2.1 PMT Gain

The charge per photoelectron that reaches the PMT anode has some inherent spread and varies between phototubes. Raising the bias voltage amplifies the gain and

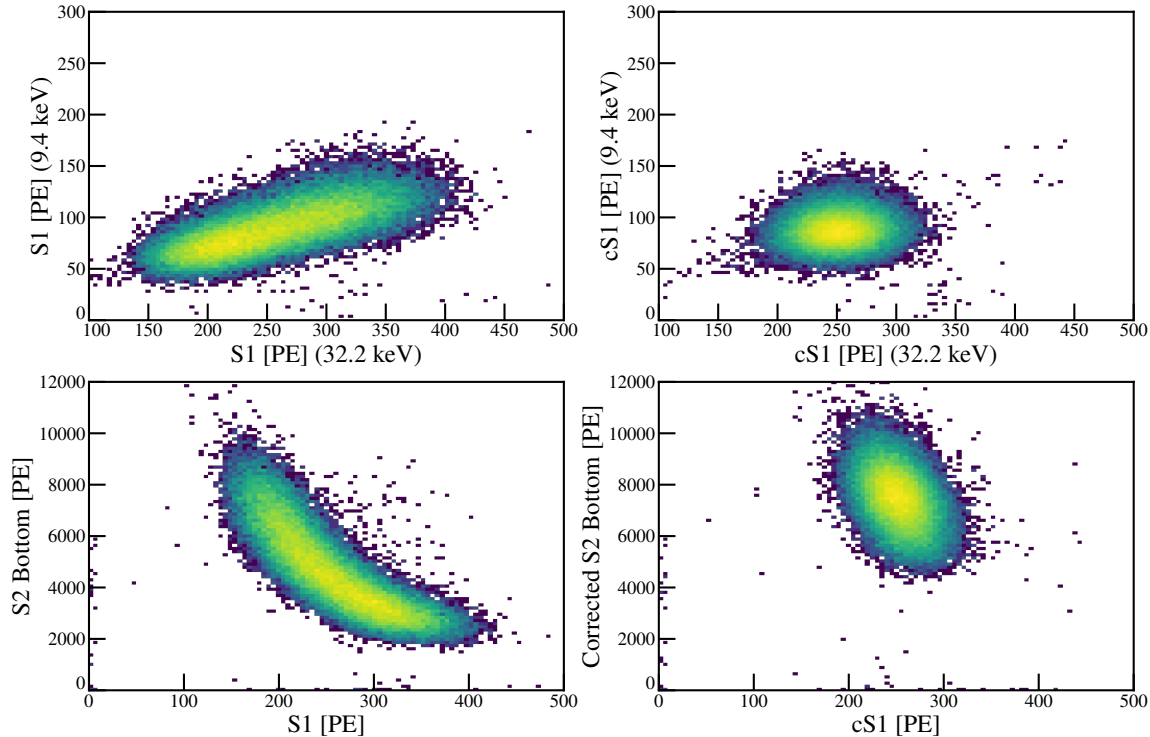


Figure 3.21:  $^{83\text{m}}\text{Kr}$  32.2 and 9.4 keV events. Uncorrected and corrected S1s for both decays are shown in the top left and top right panels. The bottom left panel shows S1 and  $S2_b$  for the 32.2 keV, and bottom right shows cS1 and cS2<sub>b</sub>.

increases sensitivity, while lowering the voltage helps prevent saturation. Gains also change from variations in temperature, overexposure to light, count rate, wear, and more. Phototubes may differ from one another for all the reasons just mentioned, as well as differences in parts, even microscopic. Monitoring the single photoelectron (SPE) response for each PMT is essential for accurately reconstructing the number of photoelectrons from an event. This is typically done with an LED inside the TPC. Blue light is used since LEDs that produce light at relevant wavelengths do not exist, which despite being far higher than 178 nm ejects a photoelectron some small fraction of the time. Each time the LED flashes the PMT signals are recorded (during normal data taking this requires a pulse larger than some threshold, Sec. 3.1.9). After a large ( $\mathcal{O}(10^5)$ ) number of trials a histogram is fit to find the SPE gain as shown in Fig. 3.22. The charge is plotted but the gain is easily found as  $g = \mu_e/e$  where  $\mu_e$  is the mean number of  $e^-$  and  $e$  is the electron charge. A large peak is centered at 0 that corresponds to the baseline noise when no photoelectrons are ejected. At higher gains

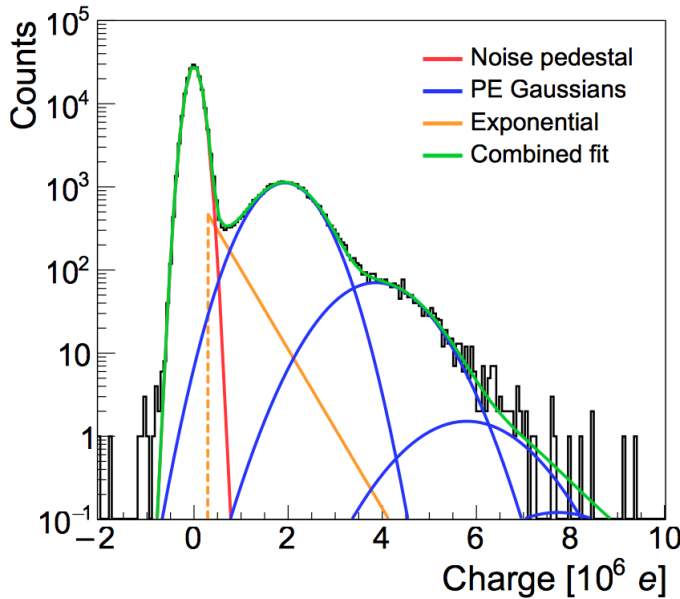


Figure 3.22: Single photoelectron spectrum of a Hamamatsu R11410 PMT. Image credit: [185].

a series of smaller, wider peaks are visible from integer numbers of photoelectrons, starting with 1 at the leftmost. There is a “shoulder” between the baseline and first peak that cannot be explained by only considering signal from integer photoelectrons. As briefly mentioned in Sec. 2.6.2 this comes from photons that pass through the photocathode and hit the first dynode, causing under-amplified electron avalanche. This is generally the most challenging aspect to model.

In Fig. 3.22 the spectrum is fit assuming the noise, baseline, and photoelectron peaks are gaussian and the under-amplification is an exponential. The PE gaussians are constrained by  $\mu_N = N\mu_e$  and  $\sigma_N = \sqrt{N}\sigma_e$  where  $\sigma_e$  is the standard deviation of the single photoelectron peak and  $\mu_N$  and  $\sigma_N$  are the mean and standard deviation for the peak with  $N$  photoelectrons. Because this simplistic model can add bias recent efforts have gone into alternative methods of characterization [200], [201]. Nonetheless, the combined fit (green) appears to agree well with the data.

The resolution of the PMT is calculated from the SPE spectrum  $R = \sigma_e/\mu_e$ . As the gain grows the resolution should sharpen until it eventually levels off. For the R11410-21 models the plateau begins around  $2-3 \times 10^6$  at a resolution of 27%. Because the stress on the PMT grows with bias voltage and larger gains create greater

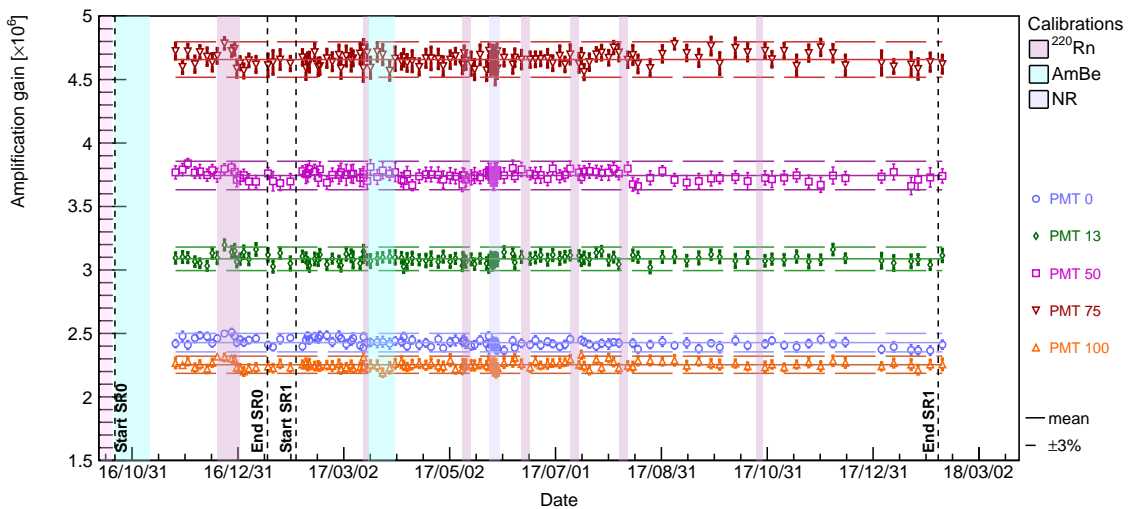


Figure 3.23: Gains for five PMTs monitored for SR0 and SR1. Means and  $\pm 3\%$  are shown. All appear to be stable.

saturation it was decided there was no benefit to exceeding this gain.

The relatively poor resolution is apparent in Fig. 3.22 as the photoelectron peaks are hard to distinguish. An important metric of the SPE spectrum is the peak-to-valley ratio, which divides the first PE peak by the valley that sits between it and the baseline noise. Like the resolution it increases for low gains and eventually levels. For gains of  $2-3 \times 10^6$  the mean peak-to-valley ratio is  $\sim 3$ . LED calibrations are regularly performed to identify changes in gain. Fig. 3.23 shows the gain for five PMTs from the beginning of Science Run 0 to the end of Science Run 1.

### 3.2.2 Light Collection Efficiency

The light observed by a PMT depends in part on the position of the event. The light collection efficiency (LCE),  $\mathcal{C}_{lce}(x, y, z)$  - seen in Fig. 3.24 - quantifies these differences. Position-dependent variations exist because the location of the interaction dictates effects due to detector features and physics. First, the solid angle encompassing the PMT arrays for an event is not uniform throughout the detector. It is greatest near the top or bottom of the TPC and at small radii. The measured intensity of the scintillation from the S1 depends on the fraction of photons that reach PMTs

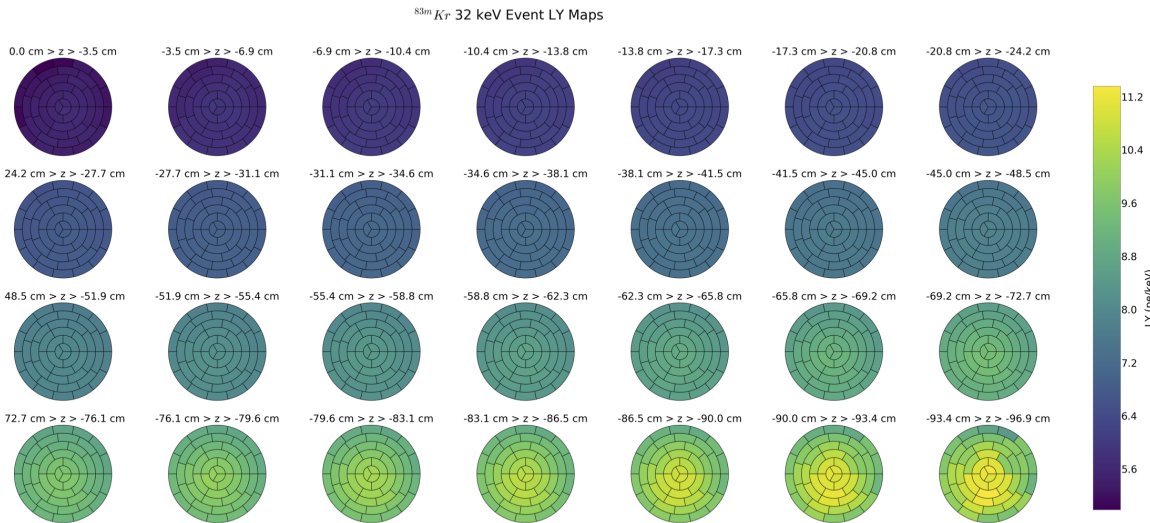


Figure 3.24: Light yield in slices of  $z$  and  $\phi$  from  $^{83\text{m}}\text{Kr}$  32.2 keV decay.

and how far the light must travel. Interactions near the wall have a lower observed intensity because of this. The quantum efficiency (QE) of the PMTs (Fig. 3.2) is also a factor, since those with larger values are more likely to produce a photoelectron. Because the PMTs with the highest QE were placed in the center of the bottom array (Sec. 3.1.1) events that happen around that region have a higher likelihood of detection, while those in the top corners have the lowest.

Because PTFE has a small but  $> 0$  absorption the intensity of the scintillation decreases with each reflection. Therefore light that is emitted in the  $\hat{r}$ -direction can be severely damped. Photon loss is amplified by the absorption of light by impurities in the LXe as well, so longer traversed distances lead to fewer photons (Sec. 5.1.1).

The index of refraction of LXe  $\sim 1.7$  gives a critical angle of  $\theta_c = 36^\circ$ . The light that reaches the top PMTs for an event at  $z = -10$  cm is restricted to a radius of just 13.6 cm at the liquid surface (the total solid angle if also at  $r = 0$  cm is  $83.9^\circ$ ). While the light will be internally reflected towards the bottom array, it will be diminished by reflections from the PTFE and extended travel distances. In comparison, light directed towards the surface from an event 10 cm above the cathode ( $r = 0$ ) has  $\theta < \theta_c$  everywhere. Some scintillation that reflects off the PTFE on the way up will rebound off the surface, but its contribution is small in comparison.

Calibrating the LCE requires a mono-energetic peak - preferably one near our DM energy range. For this we use the light from the  $^{83\text{m}}\text{Kr}$  32.2 keV conversion electron. While more than twice the DM energy range, a lower-energy option does not exist. Fig. 3.24 shows the LCE binned in  $r$ ,  $\phi$ , and  $z$ . It changes by roughly a factor of 2 between the top and bottom. Unpowered PMTs are responsible for the sudden changes in the bottom of the TPC between adjacent  $r$  and  $\phi$  bins.

Changing the electric field will cause recombination for electronic recoils of different energies to change by different amounts. The same is true for an electronic and nuclear recoil of the same energy. Therefore the LCE map in Fig. 3.24 is technically correct only for a 32.2 keV electronic recoil. However, because the TPC was designed for a uniform electric field - and simulations confirm this, especially for events more than a few cm away from the wall - differences in  $\mathcal{C}_{\text{lce}}(x, y, z)$  can be ignored.

### 3.2.3 Position Reconstruction

TPCs allow 3-dimensional position reconstruction. Since the drift velocity  $v_d$  is constant in LXe the depth is  $z = -v_d t_d$  where  $t_d$  is the drift time ( $z$  is defined to be negative with  $z = 0$  at gate). The drift fields for SR0 and SR1 were  $E_d = 118.6 \text{ V cm}^{-1}$  and  $81.3 \text{ V cm}^{-1}$ , respectively, with  $2.2 \text{ V cm}^{-1}$  RMS variations. The fields correspond to drift velocities of  $v_d = 1.440 \text{ mm } \mu\text{s}^{-1}$  and  $1.332 \text{ mm } \mu\text{s}^{-1}$  and maximum drift times of  $t_{d,\text{max}} = 672.8 \mu\text{s}$  and  $727.3 \mu\text{s}$  (TPC drift length is 96.9 cm at  $-100^\circ\text{C}$ ).

The  $x$ - $y$  coordinates are found by using the intensity of light from the S2 observed by each PMT in the top array (also known as PMT hit pattern). For XENON1T two reconstruction algorithms were mainly used to convert the PMT hit pattern to  $x$  and  $y$ . The first was a neural net (NN) using the Fast Artificial Neural Network (FANN) library with 24 and 29 nodes in the two hidden layers (sequentially). The second matches the real with expected hit patterns after weighting four separate algorithms for its seed, and is known as top pattern fit (TPF). Both algorithms were trained using Monte Carlo and optimized with  $^{83\text{m}}\text{Kr}$  data, and achieved a position resolution of  $\lesssim 2 \text{ cm}$ . For the combined-run analysis the NN was used because the TPF algorithm was more sensitive to dead PMTs and showed some artificial discontinuity in the

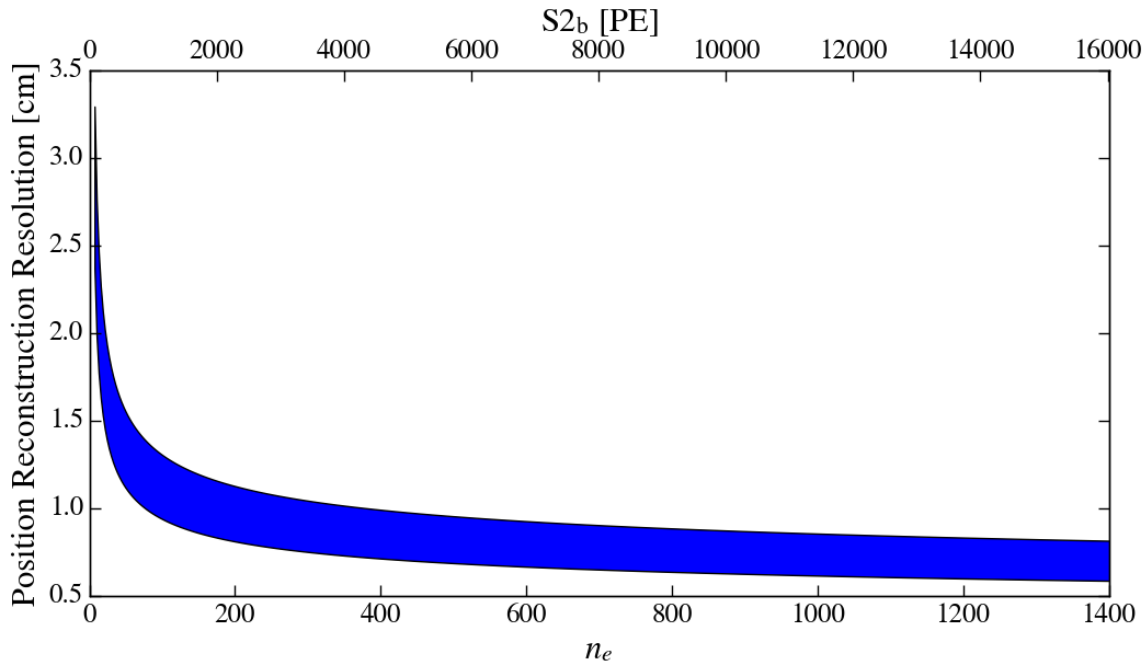


Figure 3.25:  $x$ - $y$  position reconstruction resolution  $\pm 1\sigma$  for SR1 as a function of number of electrons and  $S2_b$ . At lower  $n_e$  the resolution becomes worse due to the limited S2 scintillation. At  $n_e \lesssim 100 e^-$  ( $S2_b \lesssim 1000$  PE) the position resolution becomes extremely poor.

$\hat{r}$ -direction. The position reconstruction resolution for the NN is shown in Fig. 3.25. Fig. 3.26 shows the position distribution of events in SR1 along with the 1 tonne fiducial mass that was used in originally used in the SR0-only results [132], the 1.3 t used in the new analysis, and the active volume.

### 3.2.4 S2 $x$ - $y$ Correction

The S2 scintillation observed by PMTs depends on its  $x$ - $y$  coordinates (the  $z$ -correction is calculated using the electron lifetime in Sec. 3.2.5). Most of the light seen by the top array is focused on a small group of PMTs directly over the extraction site, while a large solid angle causes a more uniform spread on the bottom array.

The top and bottom correction maps are shown in Fig. 3.27. The relative S2 light yield is shown, which can be thought of as variations in  $g_2$  or the single electron gain  $G_e$  (Sec. 3.2.6). The local fluctuations are primarily the result of unpowered PMTs. The steeper local variations in the top array result from the light being more

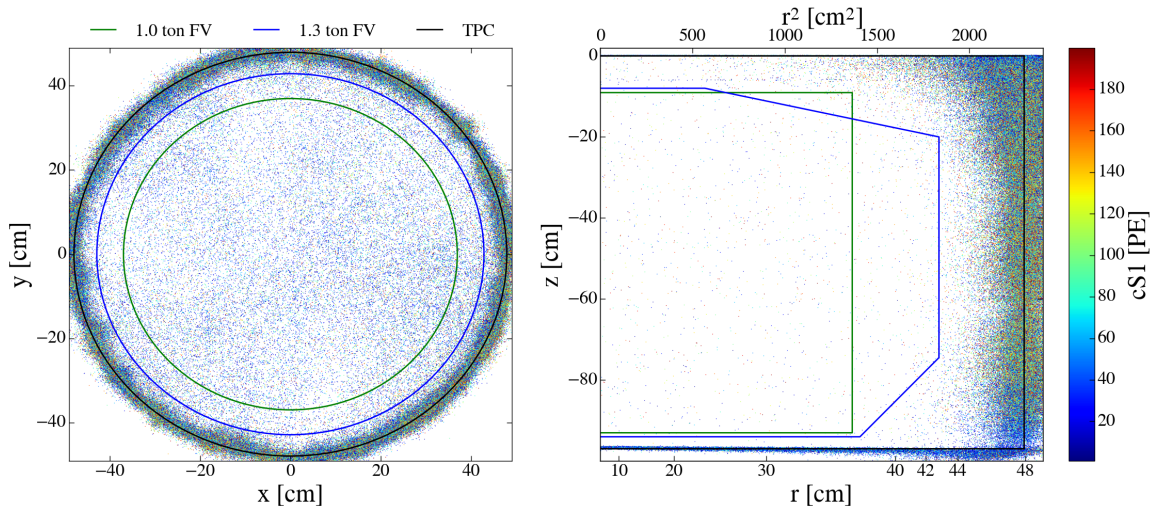


Figure 3.26: Positions of background events for SR1. The 1 tonne fiducial mass used in the SR0-only analysis is defined by  $-92.9 < z < -9$  cm,  $r < 36.94$  cm and shown in green. The 1.3 tonne fiducial mass for this analysis has a more complicated shape, having  $z_{\min} = -94$  cm,  $z_{\max} = -8$  cm, and  $r_{\max} = 42.84$  cm. It is outlined in blue ( $r_{\max}$  is shown in left panel). The active volume is marked in black. Events that appear outside the active volume are wall events that were not properly reconstructed. Those that appear below the cathode result extended drift times due to field inhomogeneities, which is why they become more exaggerated near the bottom corner of the TPC.

concentrated. At larger radii the S2s are higher due to a small sagging of the anode. The increase in the bottom array as  $r \rightarrow 0$  is mainly due to the higher QE. The large solid angle creates a roughly homogeneous azimuthal distribution.

Because the position must be reconstructed (Sec. 3.2.3) before any correction can be applied, events that have poor position resolution (mainly either below dead PMTs or low-energy) are more likely to have a greater deviation from true values.

### 3.2.5 Electron Lifetime

The electron lifetime  $\tau_e$  (see Sec. 2.6.1 for impurity attachment details) measures the charge  $q$  that is lost as electrons drift to the liquid-gas interface. It is given by

$$q(t_d) = q_0 e^{-t_d/\tau_e} \quad (3.6)$$

where  $q_0$  is the initial charge that escapes recombination. Generally when calculating

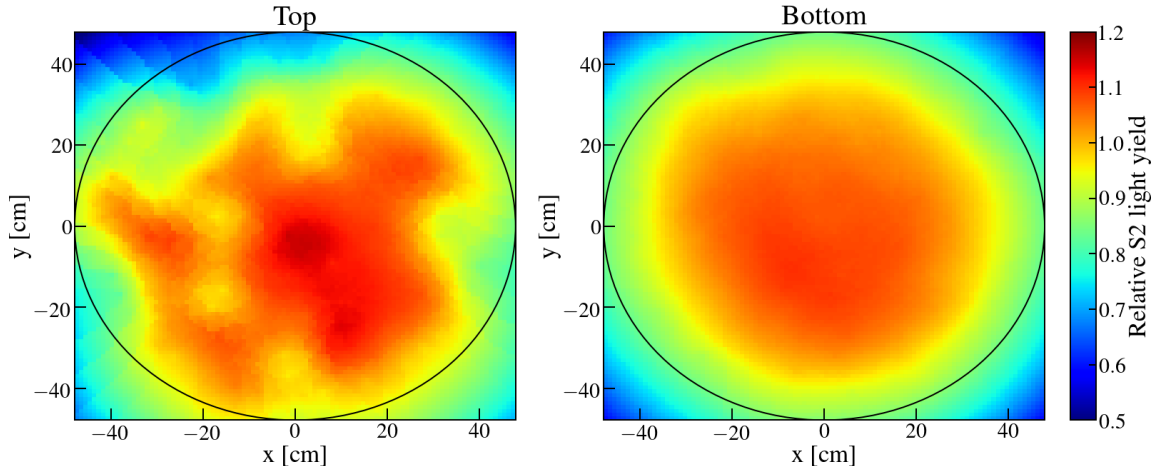


Figure 3.27: Relative S2 light yield for the top (left) and bottom (right) PMT arrays. Light from  $e^-$  extracted across the GXe is concentrated in the small number of PMTs directly above in the top array. Large fluctuations in the top array are due primarily to dead PMTs while smaller are from variation in gains. A larger solid angle results in a more uniform distribution across  $\phi$  in the bottom array.

$\tau_e$  a mono-energetic source is used so that  $q_0$  is the same throughout the detector and the collected charge is only dependent on  $t_d$ . During dark matter data taking the electron lifetime is monitored via background  $^{222}\text{Rn}$  and  $^{218}\text{Po}$   $\alpha$ -decays. Because materials with low  $^{222}\text{Rn}$  emanation were chosen, electron lifetime measurements usually require 24-48 hours of data. Alternatively, calibrations have significantly higher ( $\sim 50$  Hz) statistics, allowing measurements with much better precision.

The 41.5 keV  $^{83\text{m}}\text{Kr}$  de-excitation is an effective method to measure  $\tau_e$ . The number of events from a typical calibration of 2-3 days is in the millions, so even with  $< 4\%$  acceptance after the  $\Delta t_{S1}$  cut the number of usable events is  $\sim 10^5$  with effectively no background. Fig. 3.28 shows an example of an electron lifetime calculation using the 32.2 keV de-excitation of  $^{83\text{m}}\text{Kr}$ .

Another high-statistic measurement is possible during  $^{220}\text{Rn}$  calibrations. Primarily used for the 569.9 keV  $\beta$ -emission of its decay chain progeny  $^{212}\text{Pb}$  (Sec. 4.2.1), a number of elements along the chain undergo  $\alpha$ -decays and can be used to measure  $\tau_e$ . Tab. 3.2 lists the main  $\alpha$ -emitters in both the  $^{222}\text{Rn}$  and  $^{220}\text{Rn}$  chains. Because  $^{220}\text{Rn}$  calibration data is only used after the source valve is closed,  $^{220}\text{Rn}$  and  $^{216}\text{Po}$  won't be present due to their short half-lives of 55.6 s and 145 ms. However  $^{212}\text{Bi}$  emits a

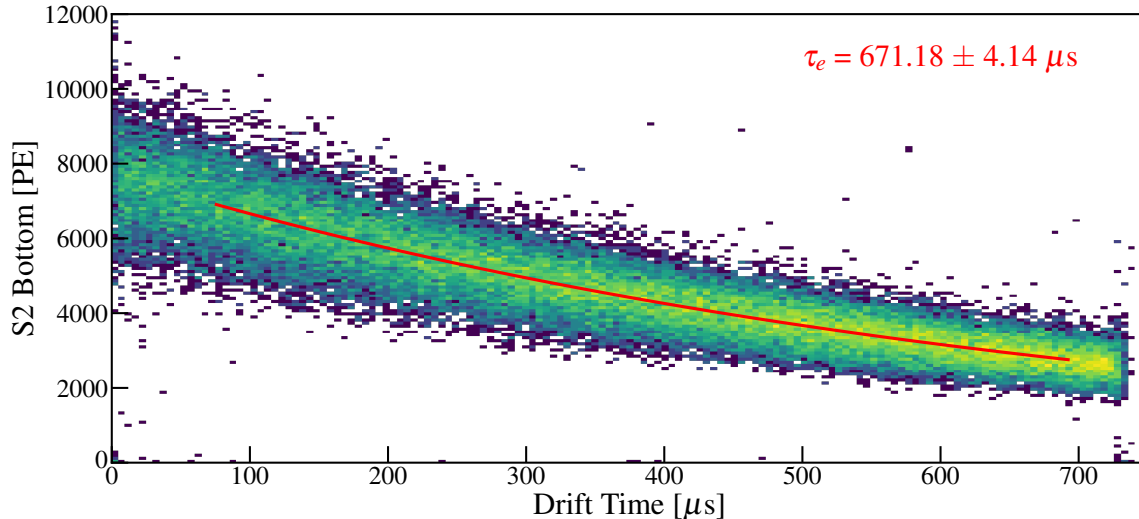


Figure 3.28: Electron lifetime measurement using  $^{83m}\text{Kr}$ . The red line represents the best-fit value of  $671.18 \pm 4.14 \mu\text{s}$  and extends over the region the fit was computed. Details on the method of the fit are in Sec. 5.2.3.

6.207 MeV  $\alpha$  as it decays to  $^{208}\text{Tl}$  with a branching ratio of 36.9%.

In past experiments external  $\gamma$ -ray sources were an effective tool for measuring  $\tau_e$ . The ease of placing a source near the detector for calibration and removing when finished meant background data could resume immediately. One of the most common sources has been  $^{137}\text{Cs}$ , whose decay



leaves barium in metastable state. As  $^{137m}\text{Ba}$  de-excites it emits a 661.7 keV  $\gamma$ -ray, whose mean free path of  $\sim 5$  cm was generally large enough to reach the fiducial volumes. For XENON1T and other tonne-scale detectors to come it is less effective, as an attempt shortly after the detector came online showed. Using  $^{137}\text{Cs}$  a Compton spectrum and total absorption peak were visible but only in the region closest to the source and after many hours of data. The 163.9 and 236.2 keV de-excitations of  $^{131m}\text{Xe}$  and  $^{129m}\text{Xe}$  following a nuclear recoil calibration are useful because they uniformly distribute throughout the xenon. However, in SR0 and SR1 their activities at their highest were only roughly the same as  $^{222}\text{Rn}$ , and their half-lives (11.8 and 8.9 days, respectively) limited their use to just several weeks.

Isotope	Daughter	Energy	$t_{1/2}$	Chain
$^{222}\text{Rn}$	$^{218}\text{Po}$	5.590 MeV	3.82 d	$^{222}\text{Rn}$
$^{218}\text{Po}$	$^{214}\text{Pb}$	6.115 MeV	3.10 m	$^{222}\text{Rn}$
$^{214}\text{Po}$	$^{210}\text{Pb}$	7.833 MeV	$164.3\ \mu\text{s}$	$^{222}\text{Rn}$
$^{210}\text{Po}$	$^{206}\text{Pb}$	5.407 MeV	138.4 d	$^{222}\text{Rn}$
$^{220}\text{Rn}$	$^{216}\text{Po}$	6.405 MeV	55.6 s	$^{220}\text{Rn}$
$^{216}\text{Po}$	$^{212}\text{Pb}$	6.906 MeV	145 ms	$^{220}\text{Rn}$
$^{212}\text{Bi}$	$^{208}\text{Tl}$	6.207 MeV	1.01 d	$^{220}\text{Rn}$
$^{212}\text{Po}$	$^{208}\text{Pb}$	8.954 MeV	299 ns	$^{220}\text{Rn}$

Table 3.2:  $\alpha$ -decays with high branching ratios for  $^{222}\text{Rn}$  and  $^{220}\text{Rn}$  decay chains.  $^{222}\text{Rn}$  emanates from detector materials and makes up part of our background so it and  $^{218}\text{Po}$  are used to continually monitor  $\tau_e$ .  $^{220}\text{Rn}$  is used for electronic recoil calibrations, so a high-statistic measurement with  $^{212}\text{Bi}$  is possible. Those with  $< 0.1\%$  branching ratio ( $^{218}\text{At}$ ,  $^{218}\text{Rn}$ ,  $^{214}\text{Bi}$ ,  $^{210}\text{Pb}$ ,  $^{210}\text{Bi}$ ,  $^{209}\text{Bi}$  for  $^{222}\text{Rn}$  chain,  $^{220}\text{Ra}$  and  $^{216}\text{Rn}$  for  $^{220}\text{Rn}$  chain) are not listed.

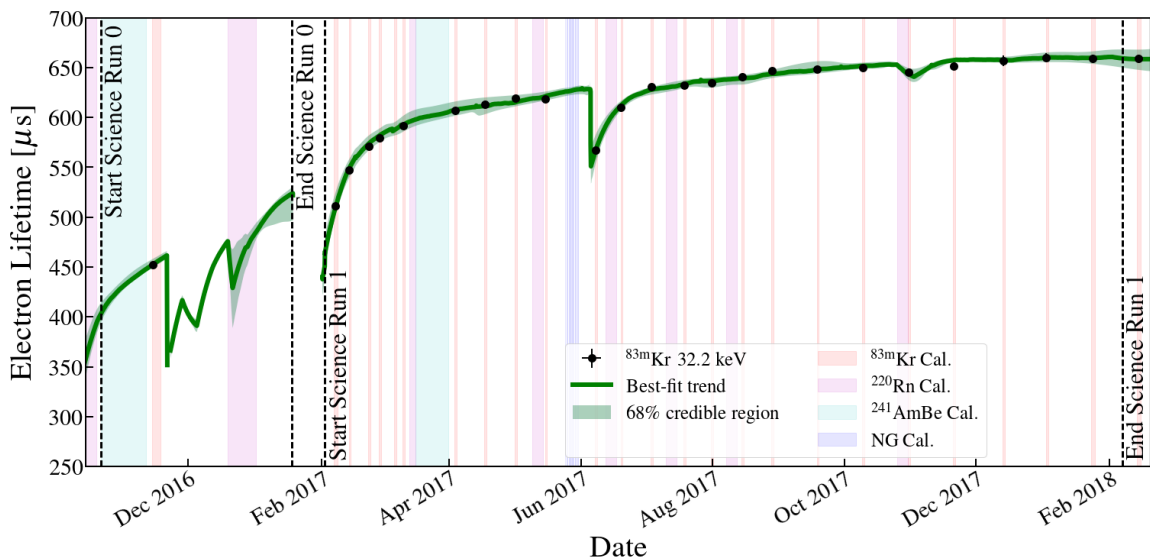


Figure 3.29: Electron lifetime over SR0 and SR1. Markers represent measurements using the 32.2 keV decay of  $^{83\text{m}}\text{Kr}$ . The green line and shaded region represent the median and credible region using the posterior of the fit. A hotspot in June forced a gate washing, where the gate was briefly lifted out of the LXe. It is suspected the LXe came in contact with parts of the TPC previously only in gas, injecting impurities into the liquid. The model is derived using  $\alpha$ -decays from  $^{222}\text{Rn}$ ,  $^{220}\text{Rn}$ , and  $^{218}\text{Po}$  and is discussed in Sec. 5.3.

The electron lifetimes from  $\alpha$ -decays was observed to be smaller than  $\beta$ s or  $\gamma$ s. While energies of  $\alpha$ -decays are significantly higher the charge yield is extremely low (Fig. 2.19). Because the dark matter region of interest is low-energy and unaffected by  $\alpha$  interactions the electron lifetime derived from  $^{83m}\text{Kr}$  was used for this analysis. The electron lifetime used for Science Runs 0 and 1 is shown in Fig. 3.29. The flattening in  $\tau_e$  around November 2017 may be indicative of a leak as mentioned in Sec. 3.3.1.1. Details on the electron lifetime model are discussed in Sec. 5.3.

### 3.2.6 Secondary Scintillation Gain

While S2s are measured in photoelectrons, an important parameter of interest is the number of  $e^-$  that were extracted across the GXe. To convert between the two we need to measure the number of detected photons per  $e^-$ , also known as the *secondary scintillation gain*, or *single electron gain*  $G_e$ . To do so we look at the smallest features in the waveforms of events that have the width of an S2, and therefore may be a low integer of  $e^-$ . These can result from photoionization of detector metals such as the gate or cathode, photoionization of impurities in the LXe, and delayed extraction of  $e^-$  from the surface.

The number of photons emitted depends on - among other things - the electric field between the anode and gate  $E_g$ . Details of the relation can be found in Sec. 2.6.1 and Eq. 2.27. The sagging - although small - of the anode changes  $E_g$  slightly along  $r$  as mentioned in Sec. 3.2.4 and shown in Fig. 3.27 (top). Additionally the dielectric constant of LXe and GXe are different, so a change in liquid level causes an inhomogeneous shift in field, so levelmeters continually monitor it.

Poisson processes give a good approximation to both  $G_e$  and the number of photons detected by the PMTs. Effects like variation in  $E_g$  and PMT detection efficiencies produce smearing. The single electron spectrum can be modeled as

$$\frac{1}{1 + e^{-(x-A)/B}} \sum_{k=1} h_k \exp\left(-\frac{(x-k\mu_1)^2}{2k\sigma_1^2}\right) \quad (3.8)$$

where here  $x = \text{S2}$ . Each term in the sum refers to a peak composed of  $k$  electrons

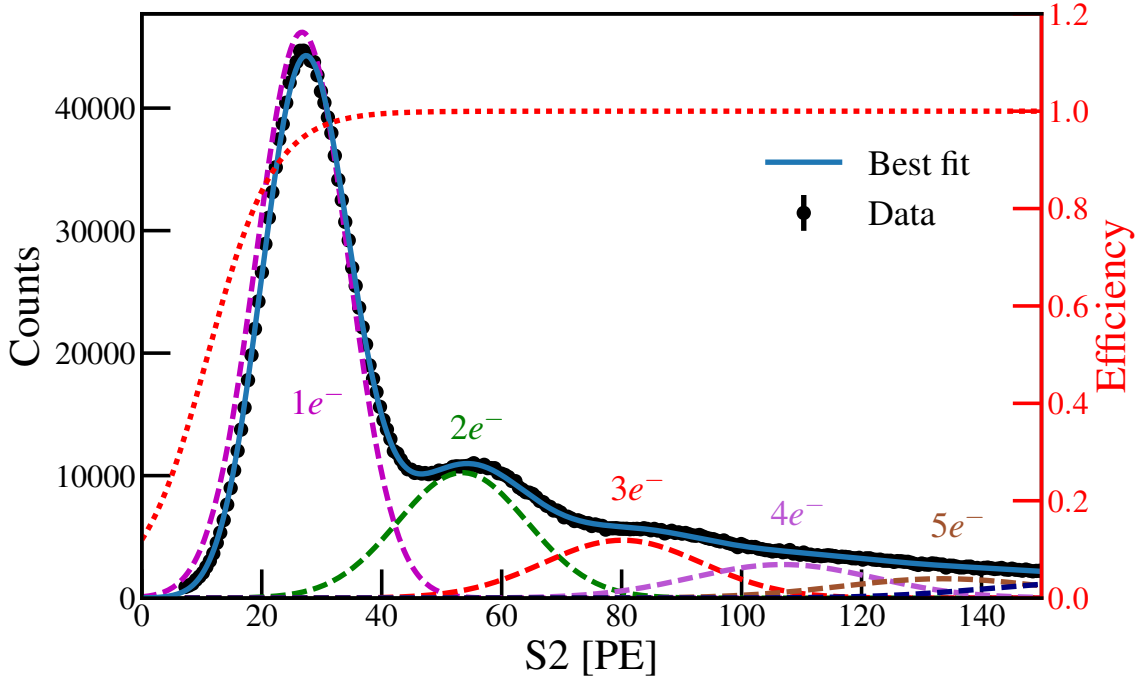


Figure 3.30: Single electron spectrum. Peaks correspond to integer numbers of  $e^-$  and are visible and the spectrum is fit with Eq. 3.8 (blue). Individual peaks for  $1e^-$  (magenta),  $2e^-$  (green),  $3e^-$  (red),  $4e^-$  (light purple),  $5e^-$  (brown), and  $6e^-$  (dark blue), along with the processor efficiency (red) are drawn. Best-fit values are listed in Tab. 3.3.

with amplitude  $h_k$ . The peaks are assumed gaussian with constraints  $\mu_k = k\mu_1$  and  $\sigma_k^2 = k\sigma_1^2$ . A Fermi-Dirac is used to model the efficiency of the S2 peak finder algorithm.

Single electrons can be easily found by looking after the primary S2, where photoionization may liberate some small number of  $e^-$ . An example of a single electron spectrum is shown in Fig. 3.30 where S2s that occurred between 60-727.3  $\mu$ s after the primary S2. The lower bound of 60  $\mu$ s is chosen to ensure the single electrons are from photoionization, while the upper bound is set to the maximum drift time since the longest between the primary and single electron S2s should be from photoionization of the cathode. The best-fit values from Eq. 3.8 are given in Tab. 3.3.

Variable	Best-fit value	Units	$f$
$A$	$11.02 \pm .27$	PE	—
$B$	$5.52 \pm 0.20$	PE	—
$\mu_1$	$26.71 \pm 0.05$	PE	—
$\sigma_1$	$7.64 \pm 0.02$	PE	—
$h_1$	$(4.62 \pm 0.04) \times 10^4$	—	0.691
$h_2$	$(1.024 \pm 0.005) \times 10^4$	—	0.153
$h_3$	$4726 \pm 29$	—	0.071
$h_4$	$2242 \pm 27$	—	0.041
$h_5$	$1583 \pm 36$	—	0.024
$h_6$	$1330 \pm 55$	—	0.020

Table 3.3: Best-fit values of Fig. 3.30 using Eq. 3.8 with  $1-6e^-$ . The fraction of total events  $f$  for the  $k^{\text{th}}$  peak is defined as  $h_k / \sum_{k=1}^6 h_k$  using the best-fit parameters.

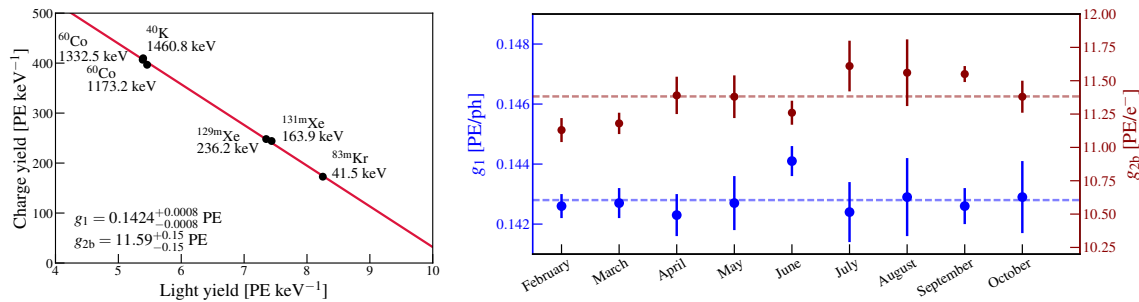


Figure 3.31: (left) Example of fitting cS1 and cS2<sub>b</sub> from mono-energetic signals to find  $g_1$  and  $g_{2b}$ . (right) Evolution of  $g_1$  and  $g_{2b}$  over the first eight months of SR1. They are stable to within 0.4% and 1.4% ( $\pm 1\sigma$  credible intervals) respectively.

### 3.2.7 Average Photon Detection and Charge Extraction Efficiencies

Applying the above corrections converts S1  $\rightarrow$  cS1 and S2  $\rightarrow$  cS2 where cS1 and cS2 are the corrected S1 and S2. An event of the same energy and type at the same electric field will result in cS1s and cS2s that only differ due to physical fluctuations. For XENON1T the top PMT array for S2s is ignored. To differentiate from the total S2, S2<sub>b</sub> and cS2<sub>b</sub> are used to represent the portion of the S2 and cS2 observed by the bottom array. Everything that follows in this chapter uses S2<sub>b</sub> and cS2<sub>b</sub>.

The processes for light and charge production were described in Sec. 2.2. For electronic recoils atomic motion is not a factor so all of the energy produces a number of quanta  $n_q = E_{er}/W$  where  $E_{er}$  is the ER energy and  $W = 13.7 \pm 0.2$  eV is the

average energy to create an exciton or electron-ion pair [165]. The number of quanta can be broken down as

$$n_q = n_\gamma + n_e \quad (3.9)$$

where  $n_\gamma$  and  $n_e$  are the number of photons and  $e^-$  produced, respectively. This can be rewritten in terms of observables as

$$\frac{E_{er}}{W} = \frac{cS1}{g_1} + \frac{cS2_b}{\eta G_e} \quad (3.10)$$

where  $n_\gamma = cS1/g_1$  and  $n_e = cS2_b/\eta G_e$  (here we now take  $G_e$  to be the single electron gain as measured by the bottom PMT array) where  $g_1$  is the average light collection efficiency and  $\eta$  is the *extraction efficiency* - that is, the probability of extracting an  $e^-$  from the liquid into the gas. The average gain for an  $e^-$  then that escapes recombination is  $g_{2b} = \eta G_e$ . Eq. 3.10 has two unknowns:  $g_1$  and  $\eta$  (or  $g_{2b}$ ). Rearranging gives

$$\frac{cS2_b}{E_{er}} = \frac{g_{2b}}{g_1} \frac{cS1}{E_{er}} - \frac{g_{2b}}{W} \quad (3.11)$$

and shows  $g_1$  and  $g_{2b}$  can be found by using a linear fit if more than one energy is used. Fig. 3.31 (left) presents this for several lines during SR1, giving  $g_1 = 0.1426 \pm 0.0001_{\text{stat}} \pm 0.0017_{\text{sys}}$  PE/ph and  $g_{2b} = 11.55 \pm 0.01_{\text{stat}} \pm 0.24_{\text{sys}}$  PE/ $e^-$  ( $\eta = 0.933$ ). Because  $g_1$  depends on the PMTs,  $\eta$  on the anode-gate electric field, and  $G_e$  on  $E_g$ , pressure, and distance between the gate and anode they are independent of the drift field.  $g_1$  and  $g_{2b}$  were monitored over the course of SR0 + SR1. Fig. 3.31 (right) shows both were stable to  $< 1.5\%$ .

### 3.2.8 Combined Energy Spectrum

After solving for  $g_1/\eta/g_{2b}$  in Eq. 3.10  $E$  can be reconstructed for electronic recoil events. The XENON1T background combined energy spectrum is shown in Fig. 3.32 for the 1 t fiducial volume during SR1. Peaks are labeled with their respective

Energy [keV]	Isotope	Half-life	Comments
41.5	$^{83m}\text{Kr}$	1.83 h	Compound decay: 32.2 + 9.4 keV
163.9	$^{131m}\text{Xe}$	11.8 d	
236.2	$^{129m}\text{Xe}$	8.9 d	Compound decay: 196.6 + 39.6 keV
351.9	$^{214}\text{Pb}$	26.8 m	$^{238}\text{U}$ chain
510.8	$^{208}\text{Tl}$	3.05 m	$^{232}\text{Th}$ chain
609.3	$^{214}\text{Bi}$	19.9 m	$^{238}\text{U}$ chain
1120.3	$^{214}\text{Bi}$	19.9 m	$^{238}\text{U}$ chain
1173.2	$^{60}\text{Co}$	5.271 y	
1332.5	$^{60}\text{Co}$	5.271 y	
1460.8	$^{40}\text{K}$	$1.277 \times 10^9$ y	
1764.5	$^{214}\text{Bi}$	19.9 m	$^{238}\text{U}$ chain
2204.1	$^{214}\text{Bi}$	19.9 m	$^{238}\text{U}$ chain
2614.5	$^{208}\text{Tl}$	3.05 m	$^{232}\text{Th}$ chain

Table 3.4: Details of monoenergetic peaks in the XENON1T background spectrum. Spectrum is shown in Fig. 3.33.

energy and responsible isotope. Fig. 3.32 shows during DM data taking some  $^{83m}\text{Kr}$  is present, most likely from  $^{83}\text{Rb}$  that was absorbed in the getters and later decayed ( $t_{1/2} = 86.2$  days).  $^{129m}\text{Xe}$  and  $^{131m}\text{Xe}$  are also visible though the majority of their de-excitations occur in the weeks following the  $^{241}\text{AmBe}$  and the NG calibrations. Other visible lines are listed in Tab. 3.4.

High energy  $\gamma$ -rays can Compton scatter a number of times before photoelectric absorption (Fig. 2.8) or leaving the detector. This, along with the  $2\nu\beta\beta$ -decay of  $^{136}\text{Xe}$  and  $\beta$ -decays of isotopes such as  $^{214}\text{Pb}$  create the underlying irregular background.

Better energy resolution allows differentiation of nearby energy features, allowing improved discrimination between signal and background. It is calculated by fitting a mono-energetic  $\gamma$ -ray line with a gaussian and dividing the width by the mean. This is done for a number of background lines as shown in Fig. 3.33. Our energy resolution is  $\sigma_E/E = (27.30 \pm 0.37)/\sqrt{E} + (0.65 \pm 0.03)$  using all energy lines and  $\sigma_E/E = (30.98 \pm 0.43)/\sqrt{E} + (0.37 \pm 0.03)$  excluding those with  $E > 1.5$  MeV. The second term refers to the fundamental limit of the resolution. We can see our energy resolution is better than XENON100 [189], PandaX [203], and in some places LUX [204].

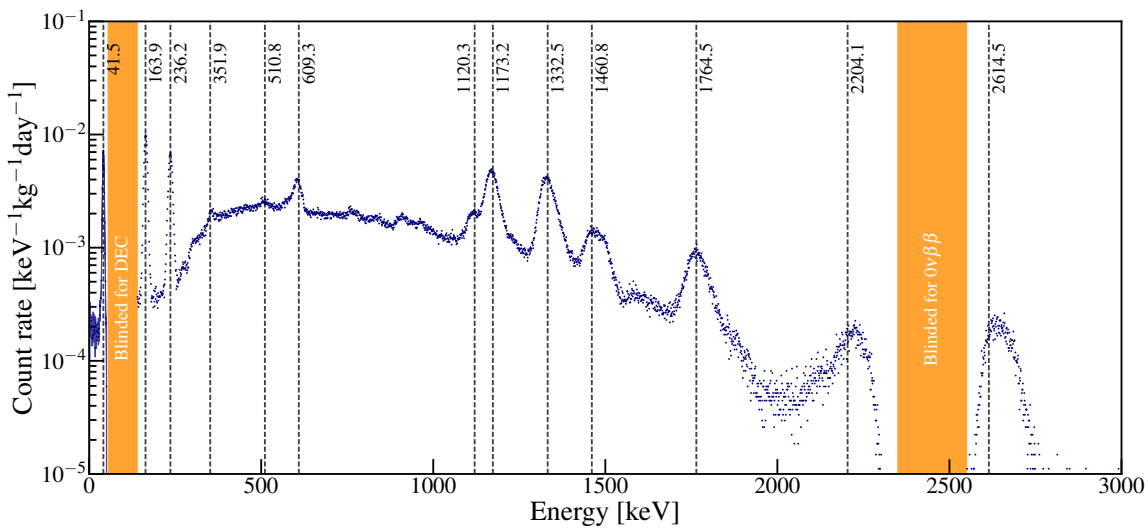


Figure 3.32: Combined energy spectrum for XENON1T. Regions between  $55 < E < 140$  and  $2350 < E < 2550$  keV are blinded for  $^{124}\text{Xe}$  double-electron capture and the theorized  $^{136}\text{Xe}$  neutrinoless double  $\beta$ -decay.

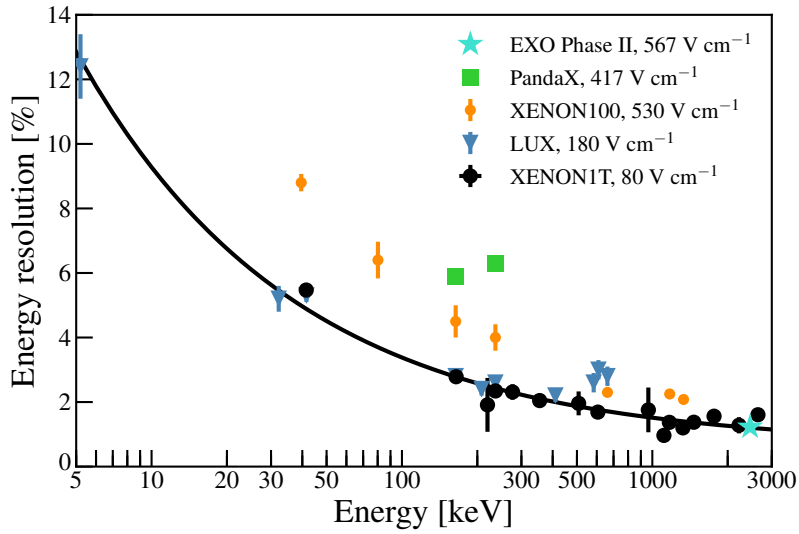


Figure 3.33: Energy resolution  $\sigma_E/E$  using for the monoenergetic interactions in Fig. 3.33. Data is from EXO Phase II (turquoise stars, [202]), PandaX (green squares, [203]), XENON100 (orange circles, [189]), and LUX (blue triangles, [204]).

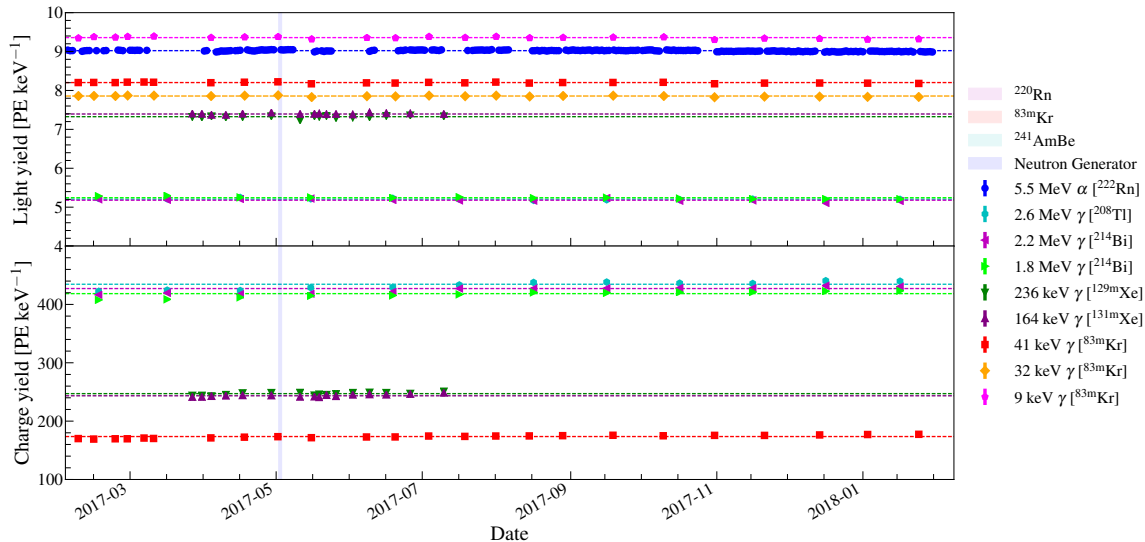


Figure 3.34: Light and charge yield from mono-energetic signals. Note that unlike the light and charge yield discussed in Sec. 4.3.3 the units are  $\text{PE keV}^{-1}$  (instead of  $\text{ph keV}^{-1}$  and  $e^- \text{ keV}^{-1}$ , respectively) and are calculated by dividing the cS1 (cS2<sub>b</sub>) by the energy of the interaction. Dashed lines correspond to the median yields. We can see the charge yield increasing slightly, which is possibly due to the growing rate of single  $e^-$  from the gate climbing. Charge yield is not shown for  $^{222}\text{Rn}$  because it is significantly lower than its electronic recoil counterparts at  $6.47 \pm 0.10 \text{ PE keV}^{-1}$  due to the fact it decays via  $\alpha$ -emission.

### 3.2.9 Light and Charge Yield

Light and charge yields are the number of photons and electrons produced from a recoil. They are a fundamental process independent of detector conditions or features that vary with energy, field, and recoil type. The results from this analysis are presented in Sec. 4.3.3. In this section light and charge yield referred to are measured in  $\text{PE keV}^{-1}$  by dividing the cS1 and cS2<sub>b</sub> by the energy. Because in stable conditions the photoelectrons observed per energy should remain constant measuring the light and charge yields is a good way to look for changes.

Fig. 3.34 shows the light and charge yields for a number of mono-energetic  $\gamma$ -rays and  $^{222}\text{Rn}$  over SR1. Aside from the 9.4 keV  $^{83\text{m}}\text{Kr}$  line the  $^{222}\text{Rn}$   $\alpha$ -decay has the largest light yield, though its charge yield is more than an order of magnitude below the  $\gamma$  values. The light yields for all energies appear stable over SR1, but the charge yields are increasing. This is suspected to result from a higher rate of single electron

extraction, what contaminates S2s and makes them seem larger than they truly are.

### 3.2.10 Bias and Smearing

Effects such as noise from the PMTs and data acquisition will cause the digitized signal to be distorted. For large pulses the effect is not significant but it can impact low-energy events. The mean shift in signal is known as the bias and the standard deviation is referred to as smearing. Unfortunately they cannot be measured using data since there is no way to know the true signal. Instead, a waveform generator is used. It takes either an S1 or S2 plus a truth number of photoelectrons as input, and generates a waveform using parameters based on our understanding of the detector. The simulated waveforms are processed with the standard framework. The fractional bias is calculated with

$$f_{\Delta S1} = \frac{S1_{\text{rec}} - S1_{\text{truth}}}{S1_{\text{truth}}} \quad (3.12a)$$

$$f_{\Delta S2} = \frac{S2_{\text{rec}} - S2_{\text{truth}}}{S2_{\text{truth}}} \quad (3.12b)$$

where  $S1_{\text{rec}}/S2_{\text{rec}}$  are the reconstructed signals and  $S1_{\text{truth}}/S2_{\text{truth}}$  are the waveform generator input. Slices in S1 and S2 are fit with gaussians, with the fractional bias and smearing taken as the means and standard deviations. This is shown for SR1 in Fig. 3.35. S1s are on average reconstructed to smaller values, particularly at low energies. S2s are reconstructed as larger, with a linear-like discrepancy between S2 and  $f_{\Delta S2}$ . In both cases the smearing extends further from the bias at low S1 and S2 since less signal leads to greater relative fluctuations. The spin-independent WIMP dark matter search discussed in this chapter uses  $3 < cS1 < 70$ .

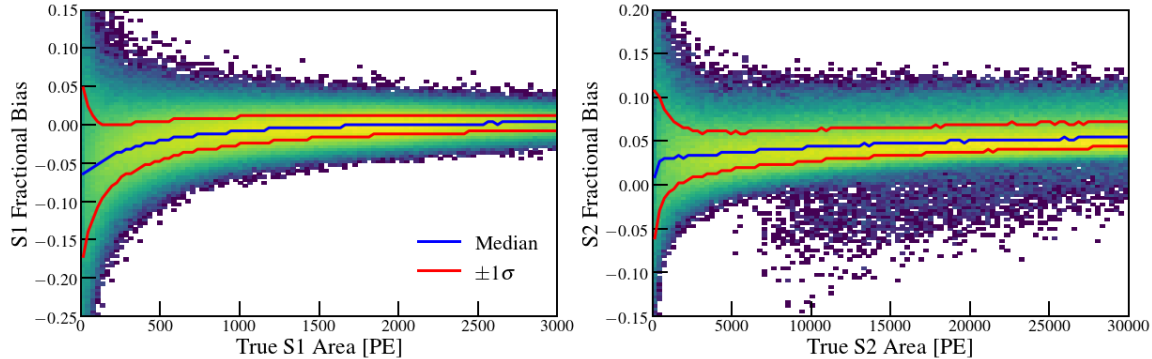


Figure 3.35: S1 (left) and S2 (right) fractional bias and smearing. The S1 fractional bias (blue) at low values is negative but moves towards 0. The S2 fractional bias converges to roughly 0.05 at large values. The S1 and S2 fractional smearing (red) have a range of  $\sim 0.2$  at low values and tighten to within a few percent at large S1 and S2.

## 3.3 Backgrounds

To reach the desired sensitivity it is crucial to lower our backgrounds as much as possible - and just as importantly, understand them. Backgrounds mainly come from detector materials, radioactive isotopes distributed inside the xenon, and outer space.

### 3.3.1 Electronic Recoils

While the majority of background events come from detector materials (Sec. 3.3.3) and are stopped within the first few cm of LXe, there is a smaller population distributed roughly uniformly throughout the xenon. They are either trace amounts of noble gases left from commercial distillation - and therefore cannot be removed by the purification system - or neutrinos passing through the Earth. Because they exist everywhere in the LXe it is not possible to remove them with a FV cut.

#### 3.3.1.1 $^{85}\text{Kr}$

With a half-life of 10.76 y and 3.1% of its  $\beta^-$ -decays (end-point energy of 687 keV) below 15 keV,  $^{85}\text{Kr}$  is a concern for LXe dark matter experiments. It decays to  $^{85}\text{Rb}$ , which itself is stable. Mainly produced by  $^{235}\text{U}$  and  $^{239}\text{Pu}$  in nuclear fission and then released by nuclear weapons tests and fuel reprocessing plants, measure-

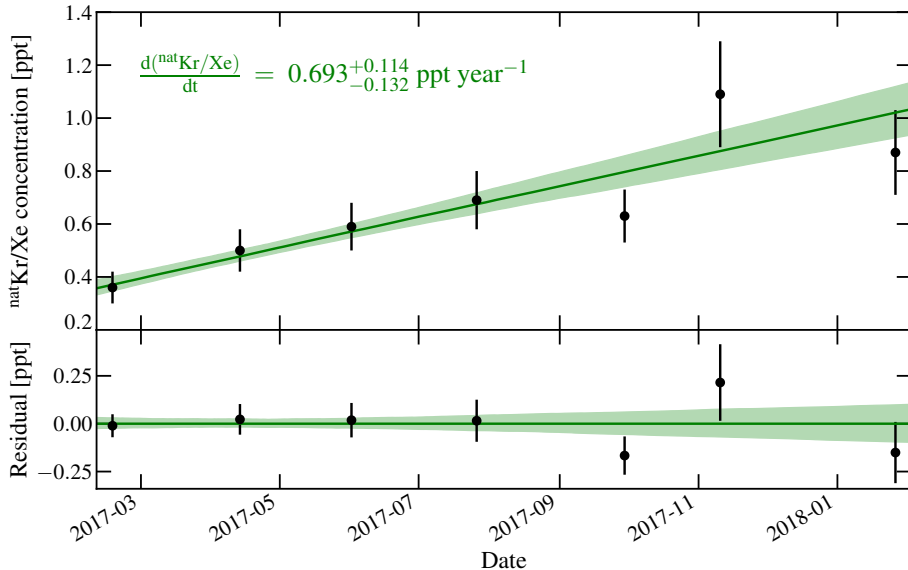


Figure 3.36:  ${}^{\text{nat}}\text{Kr}/\text{Xe}$  concentration during Science Run 1. An average value of  $0.66 \pm 0.11$  is found over the combined run analysis. SR0 is not shown as online krypton distillation (Sec. 3.1.6) decreased the concentration by more than a factor of 100. An increase of  $0.693_{-0.132}^{+0.114}$  ppt  $\text{y}^{-1}$  is observed for SR1.

ments show that  ${}^{85}\text{Kr}/{}^{\text{nat}}\text{Kr} = 2 \times 10^{-11}$  [205]. Its long half-life and low-energy contamination threaten WIMP DM searches, especially if  ${}^{\text{nat}}\text{Kr}/\text{Xe}$  at the ppm to ppb level. As discussed in Sec. 3.1.6 a krypton distillation column was installed in the service building and connected to the cryostat through the purification system. In the first science run a level of  $0.36 \pm 0.06$  ppt was reached, corresponding to a rate of around 50 low-energy electronic recoils per year in a 1 tonne fiducial mass. In Science Run 1  ${}^{\text{nat}}\text{Kr}/\text{Xe}$  increased at a rate  $0.693_{-0.132}^{+0.114}$  ppt  $\text{y}^{-1}$ , as shown in Fig. 3.36. The February-July measurements show a steady increase, though those beginning in September display a less coherent trend. The filament at RGMS was replaced between the September and November measurements. The average concentration over SR0 + SR1 was  ${}^{\text{nat}}\text{Kr}/\text{Xe} = 0.66 \pm 0.11$  ppt.

### 3.3.1.2 ${}^{222}\text{Rn}$

The largest background in the 1 and 1.3 t fiducial masses comes from  ${}^{222}\text{Rn}$ , which is part of the  ${}^{238}\text{U}$  chain (Fig. 3.42). It originates primarily from components of the detector (e.g. QDrives) that have large  ${}^{222}\text{Rn}$  emanation, though the 3.8 d half-life

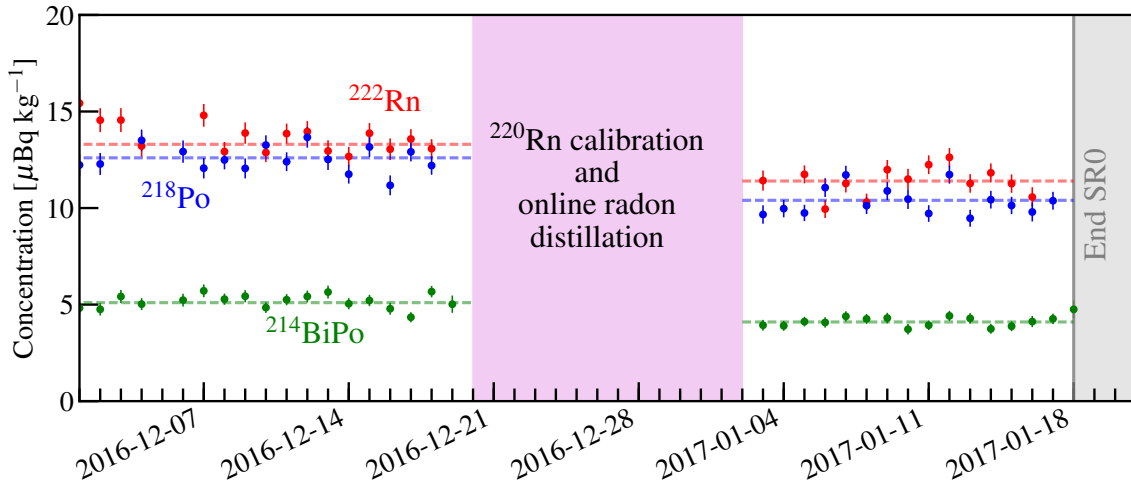


Figure 3.37:  $^{222}\text{Rn}$  (red),  $^{218}\text{Po}$  (blue), and  $^{214}\text{BiPo}$  (green) event rates before and after radon distillation. A decrease of  $\sim 20\%$  is observed.  $^{222}\text{Rn}$  has a higher rate because its progenies may be left in a charged state and pulled outside the FV.

may be long enough for a small amount of diffusion through valves and seals exposed to air.

$^{222}\text{Rn}$  decays via 5.59 MeV  $\alpha$ -emission and therefore is not a danger for WIMP searches. However, two of its progenies undergo  $\beta$ -decay:  $^{214}\text{Pb}$  and  $^{214}\text{Bi}$  ( $^{210}\text{Tl}$  is also a  $\beta^-$ -emitter but has a branching ratio of just 0.021%). The  $\beta$ -emission of  $^{214}\text{Bi}$  is not concerning because its daughter,  $^{214}\text{Po}$ , has a half-life of 164.3  $\mu\text{s}$  so a coincidence cut can remove these events (known as  $^{214}\text{BiPo}$  events).

The more dangerous is the decay of  $^{214}\text{Pb}$ , with an end-point energy of 1019 keV and 100% branching ratio. A fraction of its decays ( $E \lesssim 10$  keV) will be in our region of interest. With a half-life of just  $t_{1/2} = 26.8$  m its prevalence is directly related to the amount of  $^{222}\text{Rn}$  entering the detector and is the largest background component.

The  $^{218}\text{Po}$  and  $^{214}\text{BiPo}$  decay rates are used to estimate the  $^{214}\text{Pb}$  background. Fig. 3.37 shows the  $^{222}\text{Rn}$ ,  $^{218}\text{Po}$ , and  $^{214}\text{BiPo}$  decay rates, which decrease according to where in the decay chain they fall. As an example,  $^{218}\text{Po}$  may be charged following the  $^{222}\text{Rn}$   $\alpha$ -decay and dragged from the fiducial volume.  $^{214}\text{Pb}$  occurs between  $^{218}\text{Po}$  and  $^{214}\text{BiPo}$  so its decay rate should lay somewhere between them. For this analysis it is then between  $12.6 \pm 0.8$  and  $5.1 \pm 0.5$   $\mu\text{Bq kg}^{-1}$ .

During the  $^{220}\text{Rn}$  calibration in SR0 the krypton column (Sec. 3.1.6) was used

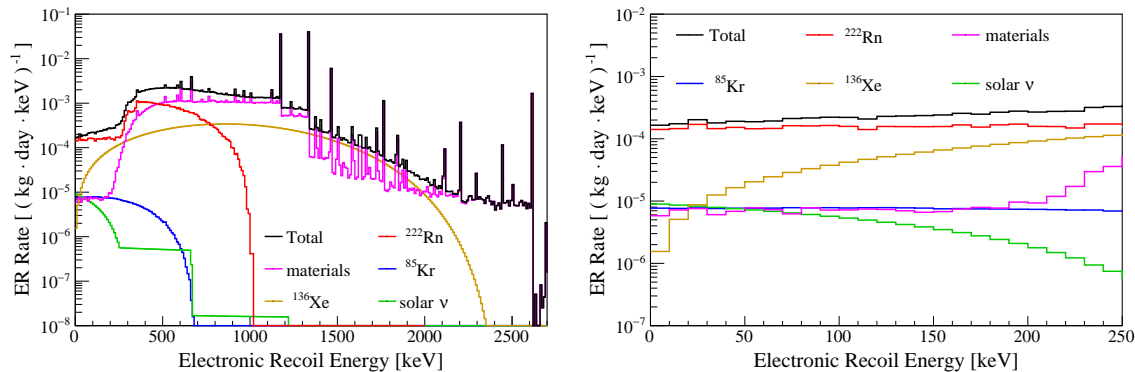


Figure 3.38: Predicted electronic recoil energy background spectrum in a 1 t fiducial volume from Monte Carlo. The left panel gives the ER expectation from 0 to  $>2614.5$  keV ( $^{208}\text{Tl}$ ). The right panel examines the 0–250 keV range. Predictions can be compared to combined energy spectrum in Fig. 3.32. Image credit: [162].

to reduce the  $^{222}\text{Rn}$  concentration. The column essentially operated in reverse: the more buoyant xenon should have a lower (higher) radon concentration at the top (bottom) of the column. The gas at the top was funneled back to the purification system while the bottom was siphoned to bottles. The event rates of  $^{220}\text{Rn}$ ,  $^{218}\text{Po}$ , and  $^{214}\text{BiPo}$  before and after the distillation are shown in Fig. 3.37. The rates dropped from  $13.3 \pm 0.8 \rightarrow 11.4 \pm 0.7$ ,  $12.6 \pm 0.8 \rightarrow 10.4 \pm 0.7$ , and  $5.1 \pm 0.5 \rightarrow 4.1 \pm 0.3 \mu\text{Bq kg}^{-1}$ , respectively. Although the decrease of  $\sim 20\%$  is relatively small with respect to krypton removal,  $^{214}\text{Pb}$  is expected to be the largest background contributor so such a reduction is still significant.

### 3.3.1.3 $^{136}\text{Xe}$

$^{136}\text{Xe}$  is the only unstable isotope of naturally occurring xenon. It undergoes  $2\nu\beta\beta$  decay with  $t_{1/2} = 2.17 \times 10^{21}$  years [206] and a Q-value of 2458 keV. Because of its abundance in natural xenon ( $^{136}\text{Xe}/\text{Xe} = 8.9\%$ ) its presence is unavoidable. At the scale of XENON1T it is subdominant – only responsible for  $\sim 2\%$  of the total ER background, as seen in Fig. 3.38 (right). However, as detectors continue to grow it will become more consequential.

### 3.3.1.4 Solar Neutrinos

Solar neutrinos can elastically scatter off electrons, causing low-energy electronic recoils. The recoil spectrum is the green line in Fig. 3.38. As with the  $^{136}\text{Xe}$   $2\nu\beta\beta$  decay its contribution is small, but as an irreducible background it will become more problematic as detectors grow.

## 3.3.2 Nuclear Recoils

The nuclear recoil background comes from neutrons and neutrinos. Whereas  $\gamma$ -rays are stopped within several cm of LXe, MeV neutrons have mean free paths of  $\sim 10$  cm, allowing them to move through the LXe volume more easily and giving them a higher probability of scattering inside the FV. Neutrinos move freely and cannot be shielded. The nuclear recoil background is composed of radiogenic and muon-induced neutrons as well as astrophysical neutrinos.

### 3.3.2.1 Radiogenic Neutrons

Radiogenic neutrons are produced by primordial decay chains  $^{238}\text{U}$ ,  $^{235}\text{U}$  and  $^{232}\text{Th}$  in detector materials (see Sec. 3.3.3 for discussion on electronic and  $\alpha$  recoils). They are released in  $(\alpha, n)$  reactions that result from  $\alpha$ -emissions along the decay chains, as well as spontaneous fission (SF). For heavier nuclei radiogenic neutrons are generated almost exclusively by SF as the  $(\alpha, n)$  reaction is suppressed by the large Coulomb barrier [162].

Fig. 3.39 shows the neutron yield as a function of energy for PTFE and copper from Monte Carlo predictions. The  $^{238}\text{U}$  and  $^{232}\text{Th}$  chains are separated at  $^{226}\text{Ra}$  and  $^{228}\text{Th}$  to account for the disequilibrium in decay rate that is observed. The PTFE has on average a lighter  $Z$  than the copper, giving it a larger  $(\alpha, n)$  contribution. Fig. 3.41 shows that for  $E \gtrsim 3$  keV radiogenic neutrons are the dominating contribution for the NR backgrounds. The expected rate for a 1 tonne fiducial mass is  $0.6 \pm 0.1 \text{ y}^{-1}$  [162].

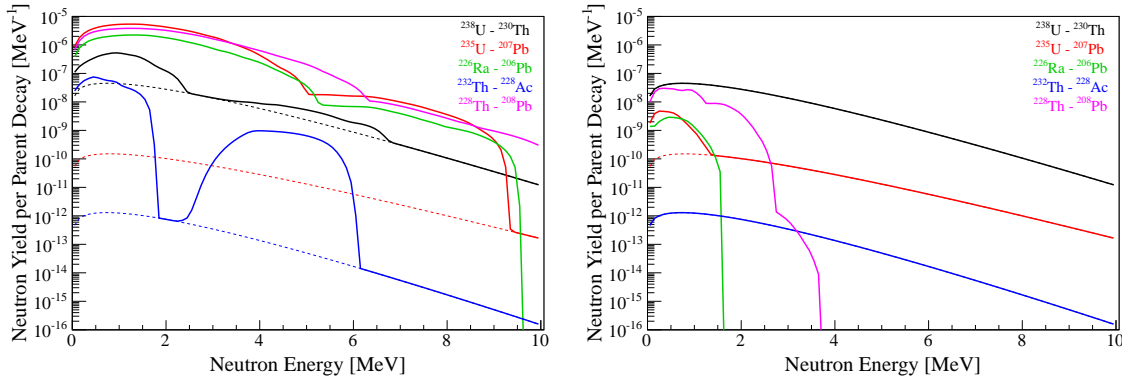


Figure 3.39: PTFE (left) and copper (right) differential yields for radiogenic neutrons per decay of parent nucleus. Dashed lines show the contributions of spontaneous fission only while solid show SF and ( $\alpha$ , n) reactions. Decays are shown for  $^{238}\text{U} \rightarrow ^{230}\text{Th}$  (black),  $^{235}\text{U} \rightarrow ^{207}\text{Pb}$  (red),  $^{226}\text{Ra} \rightarrow ^{206}\text{Pb}$  (green),  $^{232}\text{Th} \rightarrow ^{228}\text{Ac}$  (blue), and  $^{228}\text{Th} \rightarrow ^{208}\text{Pb}$  (pink). Image credit: [162].

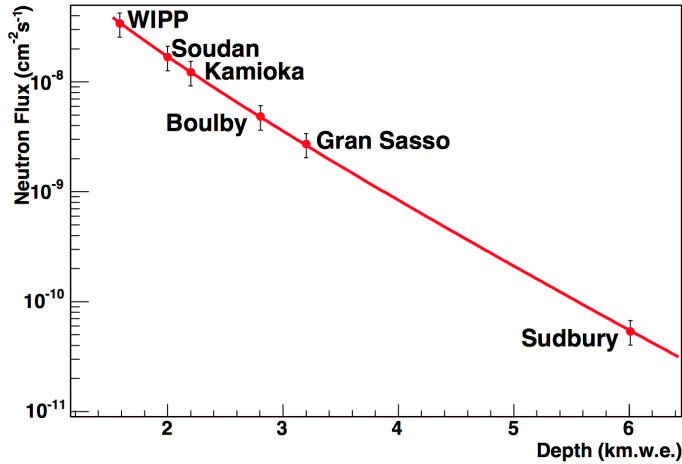


Figure 3.40: Neutron flux for WIPP, Soudan, Kamioka, Boulby, Gran Sasso, and Sudbury labs. Image credit: [207].

### 3.3.2.2 Muon Induced Neutrons

Cosmic muons that interact with the rock above the detector can produce up to GeV neutrons. Such high-energy neutrons have a large mean free path and it is possible they pass through the water shield (Sec. 3.1.7). However, simulations show that if the associated showers from the muon interaction also enter the tank the tagging efficiency is  $> 70\%$ . The predicted rate is  $< 0.01 \text{ y}^{-1}$  for 1 t and is represented by the blue line in Fig. 3.41.

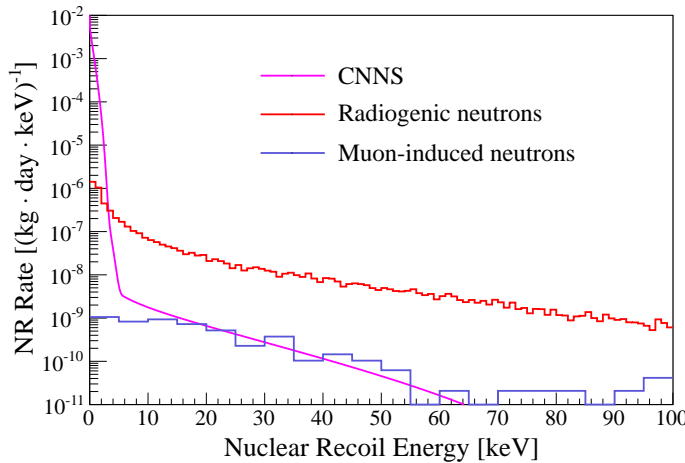


Figure 3.41: Energy spectrum of the nuclear recoil background in the 1 t FV broken down by component. Image credit: [162].

### 3.3.2.3 Neutrinos

The final contribution to the NR background comes from neutrinos that participate in coherent neutrino-nucleus scattering. The primary contributor to the integrated NR rate is solar  ${}^8\text{B}$  neutrinos, which is orders of magnitude larger than other sources. Solar *hep*, atmosphere, and diffuse supernova neutrinos also contribute. We can see in Fig. 3.41 that neutrinos are the principal concern for recoils at  $< 3$  keV. The number of detected events at  $> 1$  keV was predicted to be  $\sim 90 \text{ t}^{-1} \text{ y}^{-1}$ . While this is below our threshold, Poissonian variations may put a small fraction into our detection region. By looking at the expected number of events closer to our threshold ( $\sim 4$  keV) this drops to  $1.8 \times 10^{-2} \text{ t}^{-1} \text{ y}^{-1}$ . As mentioned in Sec. 3.3.1.4 neutrinos will compose a greater fraction of our background in larger detectors due to the inability to shield them.

### 3.3.3 Surface Background

Detector materials were screened for radioactivity before purchasing (Sec. 3.1.1 and 3.1.3) to minimize our background from surface events, i.e. events near the boundaries of the active volume. The high self-shielding of LXe prevents the radiation from penetrating deep into the detector, restricting the majority of surface events

to the outermost several cm of the TPC. It is important to understand our surface background, in large part to optimize our sensitivity. Knowledge of the position-dependent event rate enables us to calculate where the sensitivity gain from increasing the fiducial volume is outweighed by the rise in background. This is crucial because an inaccurate estimate of the number of surface events that will “leak” into the FV, known as “leakage events”, can compromise our sensitivity (upward or downward). In addition to sensitivity optimization, surface events can be used to characterize the detector in ways unique from the methods discussed in Sec. 3.2.

The primary isotopes from materials that play a role in our background are  $^{40}\text{K}$ ,  $^{60}\text{Co}$ , and the decay chains of  $^{238}\text{U}$ ,  $^{235}\text{U}$ ,  $^{232}\text{Th}$ ,  $^{228}\text{Th}$ , and  $^{226}\text{Ra}$ . In fact, although  $^{226}\text{Ra}$  and  $^{228}\text{Th}$  are part of the  $^{238}\text{U}$  and  $^{232}\text{Th}$  chains, the disequilibrium between their decay rates motivates separation to  $^{238}\text{U} \rightarrow ^{230}\text{Th}$  and  $^{226}\text{Ra} \rightarrow ^{206}\text{Pb}$  for  $^{238}\text{U}$ , and  $^{232}\text{Th} \rightarrow ^{228}\text{Ac}$  and  $^{228}\text{Th} \rightarrow ^{208}\text{Pb}$  for  $^{232}\text{Th}$ . The full  $^{238}\text{U}$  and  $^{232}\text{Th}$  chains can be seen in Fig. 3.42.

Evidence suggests that as  $e^-$  from surface events near the wall drift to the surface, a fraction will attach to the PTFE. The decrease in S2 causes three main effects: 1) an increase in position reconstruction uncertainty, 2) leakage into the NR band, and 3) small changes to the electric field (from continued charge accumulation on the PTFE).

A major constraint on the radius of our fiducial volume is the radioactivity from the PTFE panels - both the rate and reconstructed positions, the latter of which has significant uncertainty at  $S2_b \lesssim 1000$  PE as seen in Fig. 3.25. This makes  $^{210}\text{Pb}$  on the PTFE panels concerning since its  $\beta$ -decay has a Q-value of just 63.5 keV and electron loss could result in a seemingly normal NR event inside the FV. Moreover, despite a chemical cleaning process during commissioning [184], a large amount of  $^{210}\text{Pb}$  is known to be present from  $\alpha$ -decays of its progeny  $^{210}\text{Po}$ . With a half-life of  $t_{1/2} = 22.1$  y and the continual addition of  $^{222}\text{Rn}$  (Sec. 3.3.1.2), which decays to  $^{210}\text{Pb}$  within days, its background rate will likely increase (albeit slowly) over the lifetime of the detector.

To address the first two points we model our expected contamination with events

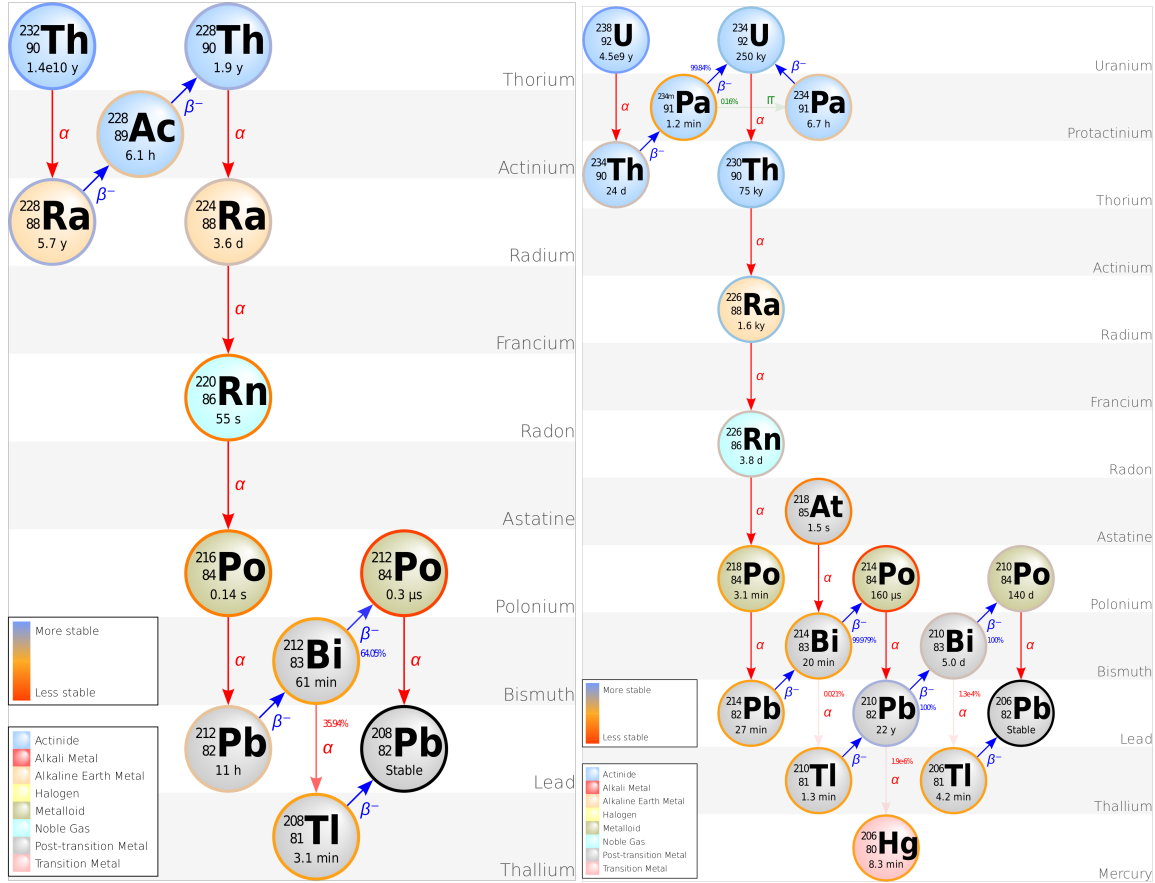


Figure 3.42: Decay chains for  $^{232}\text{Th}$  (left) and  $^{238}\text{U}$  (right). Image credit: [208], [209].

whose positions are reconstructed outside the TPC ( $r > 47.9$  cm). The S2, cS1, cS2<sub>b</sub>, and  $z$  distributions were found to be symmetric inside and outside the TPC, which was expected since the S2 was detected at the boundary and inward and outward reconstruction are equally likely. The  $r > 47.9$  cm data was unblinded and the energy distribution was obtained via a fixed kernel density estimator (KDE) using superpositions of gaussians for each point in S2, cS1, cS2<sub>b</sub>, and  $z$  space.

The accumulation of charge on the PTFE panels was discovered by the author by tracking the  $^{222}\text{Rn}$  and  $^{218}\text{Po}$  decay rates. While the rate of events throughout the entire volume of the TPC was consistent, a radius cut-dependent rate was found. This is shown in Fig. 3.45, where events reconstructed inside different radii (29, 32, 36.94, and 39 cm) are plotted from February to September in SR1. For  $r < 29$  cm limited statistics prevent precise measurements.

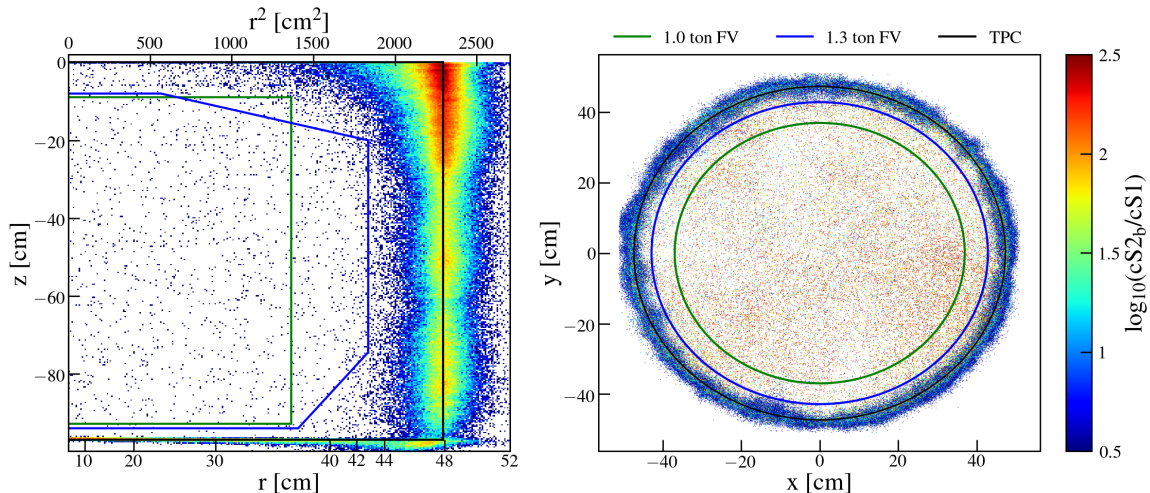


Figure 3.43: Science Run 1 background events. Events are plotted in  $r$ - $z$  ( $r^2$ - $z$ ) in the left panel. By selecting events inside the 1.3 t fiducial volume (blue) the background rate decreases by more than a factor of 200. Wall events are reconstructed symmetrically about the TPC boundary due to imperfect position reconstruction resolution (Sec. 3.2.3), with the exception of  $z \gtrsim 10$  cm where events from PMTs and other materials occur at smaller  $r$ .  $x$ - $y$  position are shown on the right with the colors corresponding to  $\log_{10}(cS2_b/cS1)$ . Events in the center are the electronic recoil background. Events along the walls lose charge as they drift, resulting in an undercorrected S2<sub>b</sub> and can leak into the nuclear recoil band ( $\log_{10}(cS2_b/cS1) \approx 1.25\text{--}2$ ). The 1 t (green) and TPC boundary (black) are marked. The color bar is for the right panel only.

The decay rates  $R$  grow over time, with larger  $r$  corresponding to greater increases. One explanation might be a leak, but the short half-lives of  $^{222}\text{Rn}$  and  $^{218}\text{Po}$  demand the leak be growing, which is in disagreement. Additionally, a growing leak should increase the decay rate across the entire detector, which is not observed. This does not disqualify a constant leak since the decay rates would be elevated and unchanging but does not explain Fig. 3.45.

A second explanation is charge buildup on the PTFE. Drifting  $e^-$  from events near the wall that attach to the PTFE may slowly alter the electric field, primarily along  $\hat{r}$ . The cumulative decay rate would not be impacted but events will move inward as this effect becomes stronger. Furthermore, the rate of increase should grow with radius as the field distortion becomes more significant until it reaches a point where more events are lost than gained. 39 cm is likely too far from the wall to see a decrease in events, so Fig. 3.45 supports the charge buildup hypothesis as the

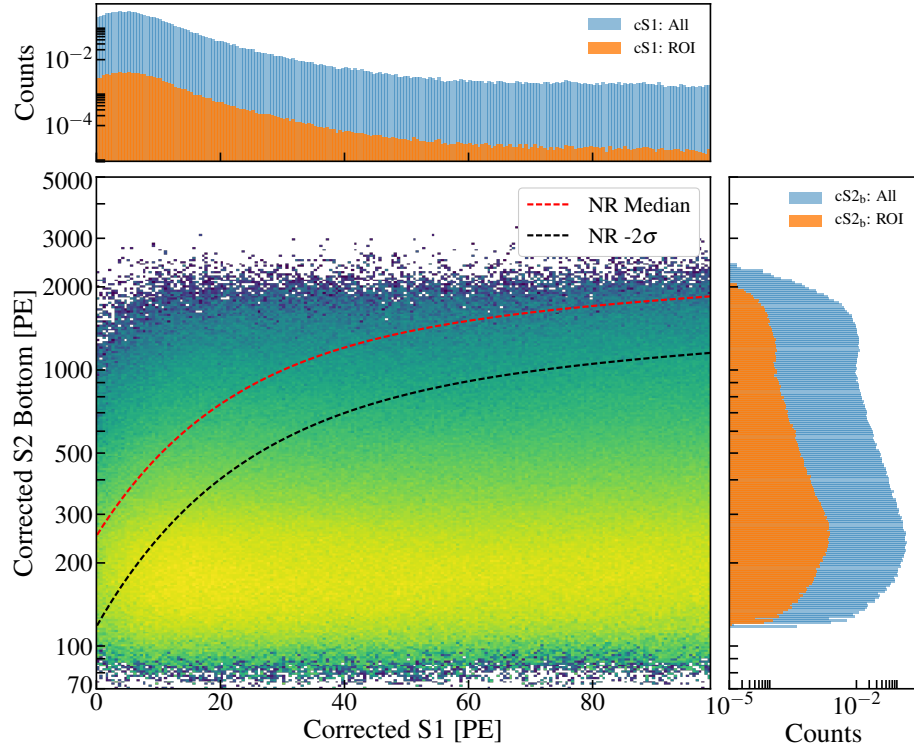


Figure 3.44: Expected surface background distribution in cS1-cS2<sub>b</sub>. Electrons from wall events attach to the PTFE as they drift, decreasing the S2 and potentially moving it into the NR band. Projections are shown for cS1 (top) and cS2<sub>b</sub> (right) for all events in blue, and between the NR median (red dashed line) and  $-2\sigma$  (solid black) in orange. The surface background's largest contribution in our ROI is predicted to be at  $cS2_b \lesssim 400$  PE,  $cS1 \lesssim 20$  PE.

slope for each fit grows with  $r$ . The decay rates differ because <sup>218</sup>Po may be left in a charged state following the decay of <sup>222</sup>Rn and pulled out of the FV, which is evident when comparing the  $z$ -distributions. Further research into the mechanism by which electrons attach to the PTFE is required before we can conclusively state this theory is correct.

Fig. 3.46 shows the expected rate increase dependence on  $r^2$  using the best-fit values from Fig. 3.45. Both figures raise the concern that the FV will grow over time as more events are pushed inwards. To account for this a time-dependent field distortion correction (Sec. 3.2.3) model is developed.

Surface events dominate the detector background at  $E \gtrsim 500$  keV, with the exception of  $\sim 1400$ -2100 keV where <sup>136</sup>Xe is slightly larger. In the energy region for

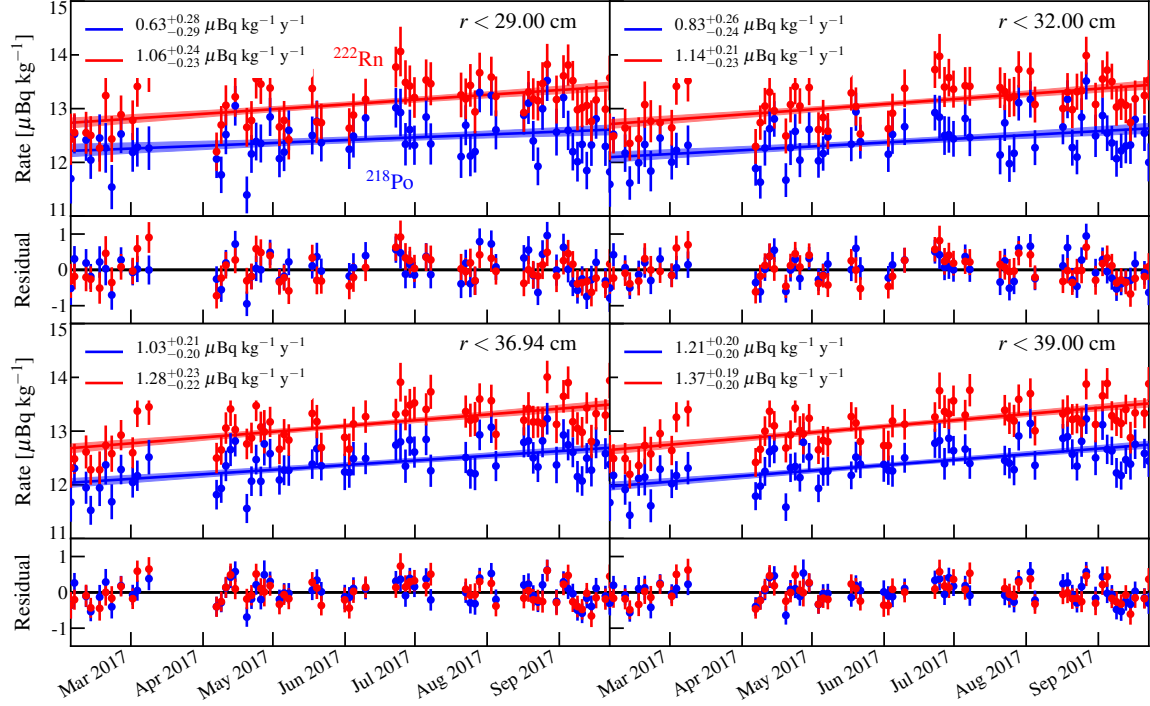


Figure 3.45:  $^{222}\text{Rn}$  and  $^{218}\text{Po}$  decay rates ( $R_{^{222}\text{Rn}}$ ,  $R_{^{218}\text{Po}}$ ) from February-September 2017 for radial cuts of 29, 32, 36.94, and 39 cm. For all cuts  $R_{^{222}\text{Rn}} > R_{^{218}\text{Po}}$  and  $dR_{^{222}\text{Rn}}/dt > dR_{^{218}\text{Po}}/dt$ , though the latter converge at larger radii. The increase is caused by  $e^-$  buildup on the teflon that pushes events in the  $-\hat{r}$  direction. Residuals (in same units) show no bias from fits.

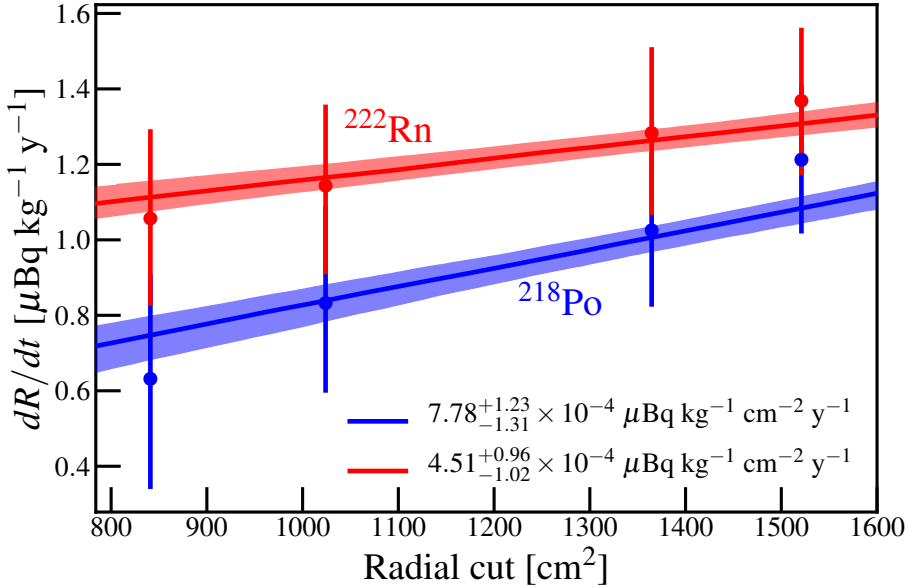


Figure 3.46: Decay rate increase (Fig. 3.45) dependence on  $r^2$ . Larger radii produce a greater rate increase due to their proximity to the wall. This helps estimate the scale of  $dR/dt$  when selecting the FV.

spin-independent WIMP dark matter  $^{136}\text{Xe}$  is outpaced by approximately two orders of magnitude by  $^{214}\text{Pb}$  inside the 1 t fiducial mass. Fig. 3.38 shows the predicted ER backgrounds using Monte Carlo.

### 3.3.4 Accidental Coincidence

In certain cases we may not be able to observe both the S1 and S2. Interactions with only an S1, or lone-S1 events, are suspected to result almost entirely from PMT dark rate pile-up at low energies, below-cathode scatters at higher energies, and mis-identified single electrons. Those with just an S2, or lone-S2 events, come from interactions near the cathode and gate where the large electric field can significantly quench the S1. The lone-S2s could at least in part be explained by  $^{210}\text{Pb}$ , which given its presence on the PTFE panels, suggest it may also exist on the electrodes.

Generally lone-S1 and lone-S2 events do impact our data, but occasionally they may occur close enough to one another to mimic a real event, known as accidental coincidence (AC). Because we cannot know which events are AC, those that pass our cuts (Sec. 4.2.4) - including a shape cut for S1s to eliminate single electrons - end up in our final dataset. It is therefore important to calculate the number of expected events and their distribution. The rate of AC events is given by

$$R_{\text{AC}} = R_{\text{LS1}} \times R_{\text{LS2}} \times t_{d,\text{max}} \quad (3.13)$$

where  $R_{\text{LS1}}$  and  $R_{\text{LS2}}$  are the lone-S1 and -S2 rates and  $t_{d,\text{max}}$  is the maximum TPC drift time. S1s, especially at low energy, are too small to trigger the DAQ. Therefore, to calculate  $R_{\text{LS1}}$  we select higher energy good events that contain an S1 and S2, and search the region before the primary S1. This method makes two assumptions. The first is that lone-S1s should be uncorrelated in time, and thus distributed uniformly over large timescales. The second is that the S1s we find do not have a complementary S2. The former seems reasonable since we do not expect PMT dark rates and below-cathode scatters to follow any pattern. The latter is valid because the probability of having two interactions in the same time window is negligible.

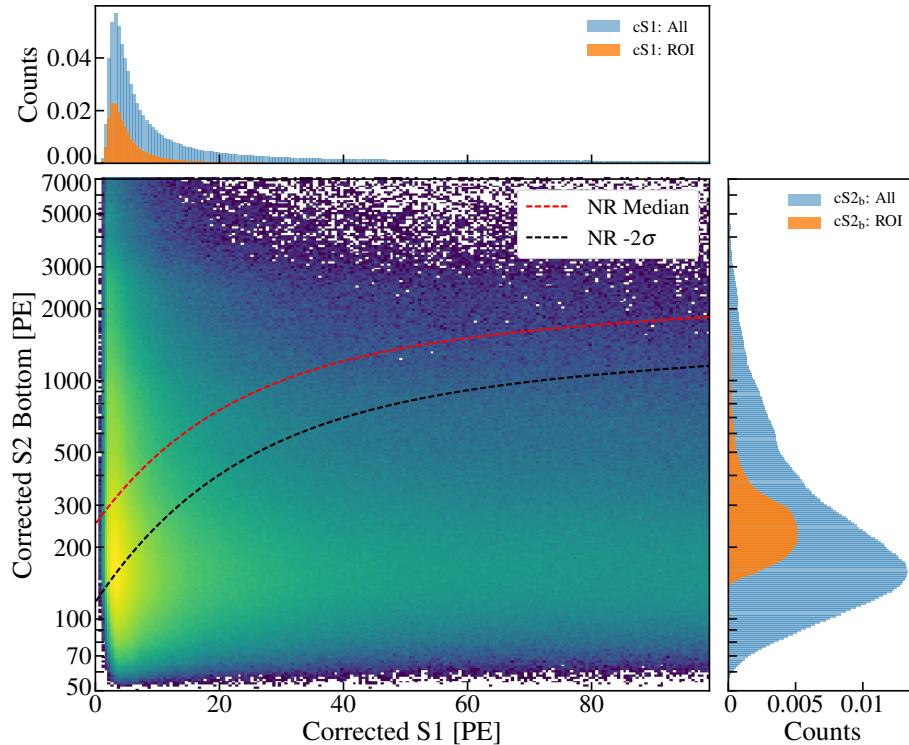


Figure 3.47: Expected accidental coincidence distribution in cS1-cS2<sub>b</sub> space for the 1.3 t FV. Isolated S1s and S2s are randomly coupled to imitate real events in the TPC. S1 and S2 corrections are applied and events that pass the cuts are plotted. Projections are shown for cS1 (top) and cS2<sub>b</sub> (right) for all events in blue, and between the NR median (red dashed line) and  $-2\sigma$  (solid black) in orange. The majority of events in the reference region are in  $cS1 \lesssim 10$  PE,  $cS2_b \lesssim 500$  PE.

Accidental coincidences do not benefit from fiducialization like much of our other background. In fact, Eq. 3.13 shows  $R_{ac}$  increases with detector size. Still, its total contribution is comparatively small to the whole background. AC is source or background-dependent, so for this analysis distributions for  $^{220}\text{Rn}$ ,  $^{241}\text{AmBe}$ , and NG data were each included in the electronic and nuclear recoil band fitting (Chap. 4). Fig. 3.47 shows the expected AC distribution for the 1.3 t FV in cS1-cS2<sub>b</sub> for dark matter data, space with the region of interest marked by the dotted red (median) and solid black ( $-2\sigma$ ).

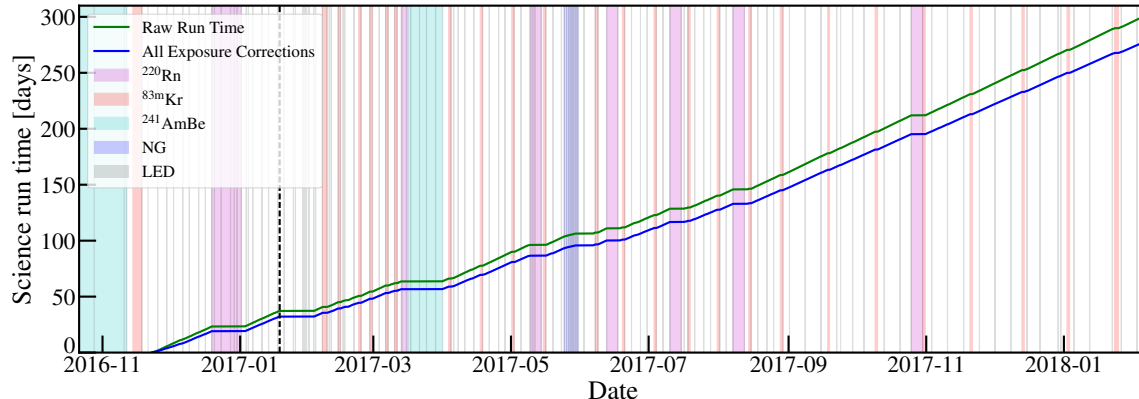


Figure 3.48: Dark matter detection livetime. The green line displays the total run time for all dark matter data before livetime losses to DAQ insensitivity to events (7.8% SR0, 1.2% SR1), times when the muon veto was either deactivated or triggered coincidentally with the TPC (1.2%), and photo-ionization and delayed electron extraction due to high energy events in the TPC (4.4%). The blue line is the final exposure used in this analysis totaling 278.8 days. Shaded regions represent  $^{220}\text{Rn}$  (pink),  $^{83\text{m}}\text{Kr}$  (red),  $^{241}\text{AmBe}$  (aqua), NG (blue), and LED (grey) calibrations. The dashed black line marks the earthquake on January 18, 2017.

## 3.4 Dark Matter Results

Science Run 0 spanned from November 22, 2016 to January 18, 2017, when an earthquake at LNGS caused the run to stop prematurely. Science Run 1 began February 2, 2017 and ended February 8, 2018. They yielded 32.1 (SR0) and 246.7 (SR1) for a total of 278.8 days of dark matter data. Fig. 3.48 shows the exposure over this period with  $^{220}\text{Rn}$ ,  $^{83\text{m}}\text{Kr}$ ,  $^{241}\text{AmBe}$ , NG, and LED calibrations highlighted. The green line depicts the total DM run time before DAQ insensitivity to events (7.8% SR0, 1.2% SR1), times when the muon veto was either deactivated or triggered coincidentally with the TPC (1.2%), and photo-ionization and delayed electron extraction due to high energy events in the TPC (4.4%). The final exposure after corrections is shown in blue.

### 3.4.1 Electronic and Nuclear Recoil Calibrations

To differentiate our signal region from ER and AC background, electronic and nuclear recoil calibrations were performed. Electronic recoils were calibrated using  $^{220}\text{Rn}$

seven times (one in SR0 and six in SR1).  $^{241}\text{AmBe}$  and a deuterium-deuterium (D-D) neutron generator (NG) were used for nuclear recoils, positioned in the water tank outside the cryostat.  $^{241}\text{AmBe}$  calibrations were done once in each science run and a NG calibration was performed in SR1 only.

Having dependable probabilities for each of the different possible origins of an event is essential for a rare event search. Fitting the electronic and nuclear recoil bands (Chap. 4) creates probability density functions (PDFs) for our ER background and signal regions. Mass-dependent WIMP PDFs are generated using the signal model.<sup>1</sup> In addition, PDFs from surface events (Sec. 3.3.3) and accidental coincidence (Sec. 3.3.4) are included. The data is compared to the total PDF for each WIMP mass and cross section to calculate its agreement with the signal model (Sec. 3.4.3). A limit is set where cross sections below some value match the data, and a discovery is claimed if the data prefers a signal with background model above some threshold  $\sigma$ .

### 3.4.2 Acceptances

Events during dark matter data-taking that are below the  $-2\sigma$  quantile of the ER cS1-cS2<sub>b</sub> band are removed before analysis in what is known as “blinding”. This prevents bias that might occur from adjusting analyses to explain or reject these events as dark matter. Data selection includes a valid (e.g.  $0 < t_d < t_{d,\max}$ ) S1 and S2 with  $\geq 3$  PMTs observing the S1 in  $< 100$  ns. A position reconstruction cut requires the difference between the neural network and likelihood-fit algorithms to be less than 2 (larger S2s) to 5 (smaller) cm. A cS1 threshold  $3 \leq \text{cS1} \leq 70$  PE, corresponding to roughly [1.4, 10.6] keV<sub>ee</sub> and [4.9, 40.9] keV<sub>nr</sub>, marks the energy region of interest.

Fig. 3.49 shows the SR0 and SR1 acceptances calculated using 400 randomly-drawn samples from the electronic and nuclear recoil band fit posterior (Chap. 4). Efficiencies are shown for the 1) S1 peak finding efficiency (“Detection”), 2) S1 peak

---

<sup>1</sup>For this analysis the signal is a spin-independent WIMP but other analyses investigate alternative signal models [35], [95], [157], [210]–[212].

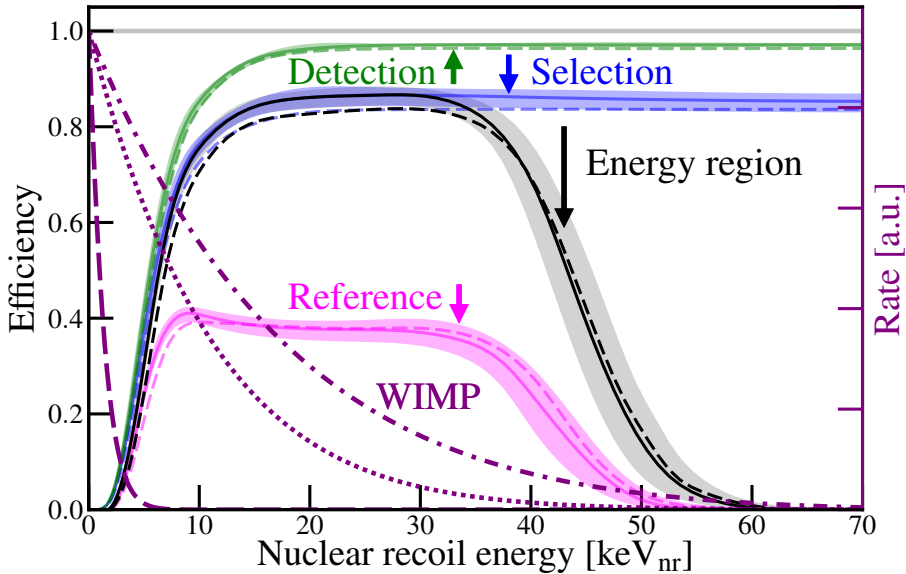


Figure 3.49: Nuclear recoil acceptances for WIMPs from this analysis. Processor efficiency is shown in green, processor efficiency with S1 and S2 cuts in blue, total acceptance across all cS2<sub>b</sub> in black, and total acceptance inside the reference region in pink. Dashed and solid acceptance lines correspond to SR0 and SR1 acceptances, respectively. The shaded regions are the 68% credible interval for SR1. Spectra are shown for 10 (dashed), 50 (dotted), and 200 (dash-dotted) GeV/c<sup>2</sup> WIMPs. The 10 GeV/c<sup>2</sup> WIMP has significantly less overlap with the acceptance (true also with proper rates) than the 50 and 200 GeV/c<sup>2</sup> WIMPs, which will lead to a worse limit.

finding efficiency with S1 and S2 cuts (“Selection”), 3) total, ignoring the reference region (“Energy region”), and 4) total, including the reference region (“Reference”). The energy region efficiency is the product of the efficiencies shown in Fig. 4.25: S1 peak finding efficiency, S2 threshold, cS1 threshold, and cut efficiencies. Events inside the fiducial volume that are reconstructed outside - or vice versa - are expected to have a negligible effect so are not included. The efficiencies in Fig. 3.49 are calculated using the 1 t mass from the band fitting, but are not predicted to have any appreciable deviation from the 1.3 t FV.

### 3.4.3 Findings

The magenta line in Fig. 3.51 encloses the 1.3 t fiducial mass used for this analysis. Its highest point is 8 cm below the gate to avoid capturing poorly reconstructed GXe

events and 2.9 cm above the cathode to exclude interactions in a larger and less uniform electric field. A 42.8 cm maximum radius was selected to limit the number of surface events to  $\lesssim 100$ . The corners are cut to maintain a background rate of  $< 10\%$  across  $z$  in slices of  $r$ , ensuring the contribution from detector materials to the ER background is less than the uniformly distributed  $^{214}\text{Pb}$ . The total exposure for the combined run analysis is  $278.8 \text{ d} \times 1.30 \text{ t} = 1.0 \text{ t y}$ .

Mass (cS1, cS2 <sub>b</sub> )	1.3 t Full	1.3 t Reference	1 t Reference	0.9 Reference
ER	$627 \pm 18$	$1.62 \pm 0.30$	$1.12 \pm 0.21$	$0.60 \pm 0.13$
neutron	$1.43 \pm 0.66$	$0.77 \pm 0.35$	$0.41 \pm 0.19$	$0.14 \pm 0.07$
CE $\nu$ NS	$0.05 \pm 0.01$	$0.03 \pm 0.01$	$0.02$	$0.01$
AC	$0.47^{+0.27}_{-0.00}$	$0.10^{+0.06}_{-0.00}$	$0.06^{+0.03}_{-0.00}$	$0.04^{+0.02}_{-0.00}$
Surface	$106 \pm 8$	$4.84 \pm 0.40$	$0.02$	$0.01$
Total BG	$735 \pm 20$	$7.36 \pm 0.61$	$1.62 \pm 0.28$	$0.80 \pm 0.14$
WIMP <sub>best-fit</sub>	3.56	1.70	1.16	0.83
Data	739	14	2	2

Table 3.5: Best-fit background and WIMP total events from combined run analysis for 1.3 t fiducial mass in ROI and 1.3, 0.9, and 0.65 t in signal reference region. Expected rates are listed by type as well as total. The best-fit WIMP rate is assuming a 200 GeV/c<sup>2</sup> WIMP with  $\sigma_{SI} = 4.7 \times 10^{-47} \text{ cm}^2$ . The number of events observed in data is listed for comparison. Table from XENON1T run-combined results paper [123].

The electronic recoil background rate during the combined run analysis was measured to be  $82^{+5}_{-3}(\text{sys}) \pm 3(\text{stat})$  events  $\text{t}^{-1} \text{ yr}^{-1} \text{ keV}_{\text{ee}}^{-1}$  - the lowest ever achieved by a dark matter experiment. From RGMS measurements (Sec. 3.1.6) we expect  $7.7 \pm 1.3$  events  $\text{t}^{-1} \text{ yr}^{-1} \text{ keV}_{\text{ee}}^{-1}$  from  $^{85}\text{Kr}$  (Sec. 3.3.1.1).  $\beta$ -decays originating from  $^{214}\text{Pb}$  make up as much as  $69 \pm 4$  to as little as  $29 \pm 4$  events  $\text{t}^{-1} \text{ yr}^{-1} \text{ keV}_{\text{ee}}^{-1}$  following measurements using  $^{218}\text{Po}$   $\alpha$ -decays and  $^{214}\text{BiPo}$  time-coincidence, respectively (Sec. 3.3.1.2).

An unbinned extended likelihood with profiling over nuisance parameters is used to interpret the data in the 1.3 t fiducial mass [213], [214]. The expansion from the 1 t volume is allowed by including an  $r$  dimension to model the surface background and boosts the sensitivity by 10%, and events are classified according to whether they

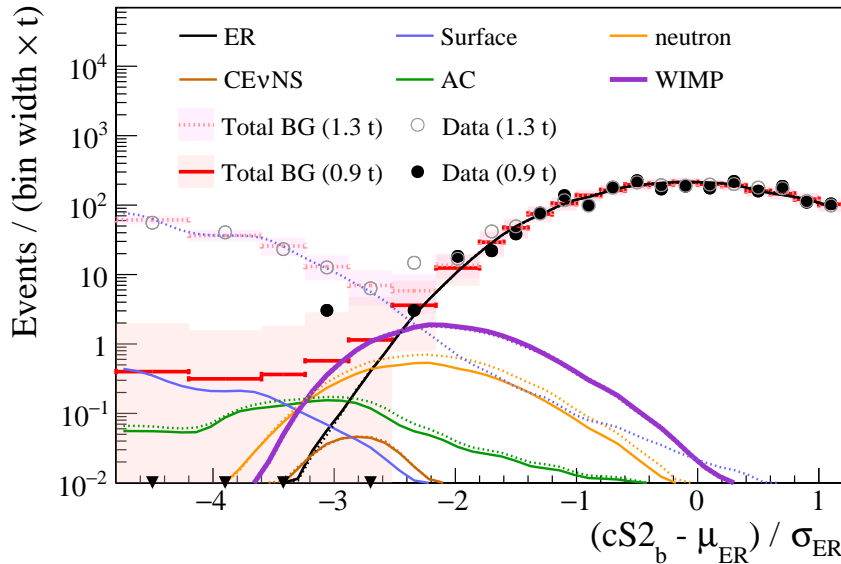


Figure 3.50: Best-fit background and 200 GeV/c<sup>2</sup> WIMP predictions for combined run analysis assuming  $\sigma_{\text{SI}} = 4.7 \times 10^{-47}$  cm<sup>2</sup>. Dashed (solid) lines and hollow (filled) markers represent 1.3 t and 0.9 t volumes, respectively. The horizontal axis is the projection along  $cS2_b$  normalized by subtracting the electronic recoil mean  $\mu_{\text{ER}}$  and dividing by the  $1\sigma_{\text{ER}}$  quantile. Most backgrounds do not change significantly between the two volumes, with the exception of the surface. The best-fit WIMP signal is shown in purple. Shaded regions represent the 68% Poisson probability region for the expectation of total background. Image credit: [123].

occur inside the 0.65 t mass. Model uncertainties are included as nuisance parameters and a mis-modeling “safeguard” is included in the ER model [215]. The safeguard is a WIMP-like component and added to account for potential shortcomings in the ER model. It is constrained by data from <sup>220</sup>Rn calibrations.

SR0 and SR1 are fit simultaneously with the only correlated parameters being neutron rate, ER recombination, WIMP mass, and  $\sigma_{\text{SI}}$ . “Profile construction” using MC simulations was used to calculate confidence intervals for  $\sigma_{\text{SI}}$  and coverage was tested for by varying values of nuisance parameters [27], [216].

A decision was made before unblinding to “salt” the data - that is, to include an unknown number of events to prevent post-unblinding model and selection fine-tuning. These were eventually revealed to be two <sup>241</sup>AmBe events, and had not prompted any post-unblinding investigation.

### 3. THE XENON1T EXPERIMENT AND DARK MATTER SEARCH

---

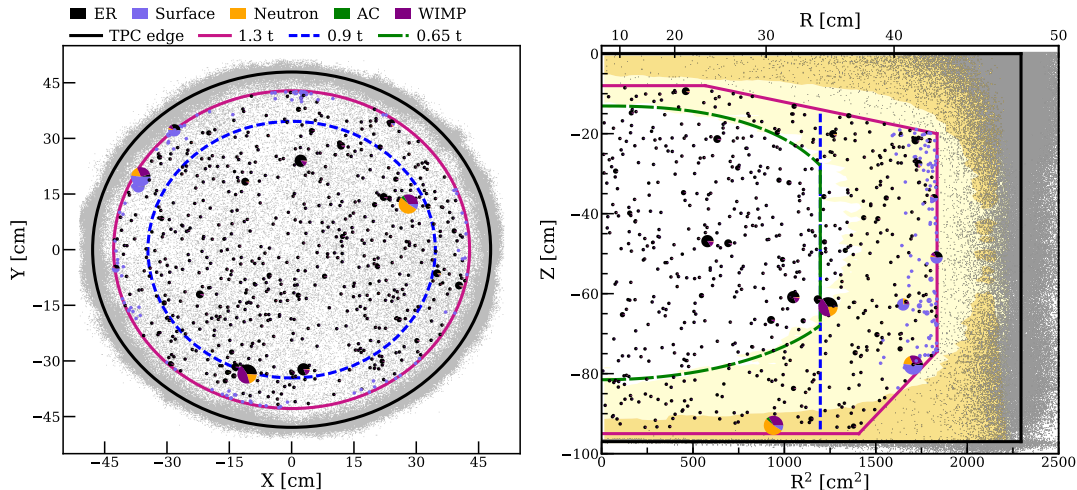


Figure 3.51: Dark matter search data spatial distributions. 1.3, 0.9, and 0.65 t masses are marked by solid pink, short-dashed blue, and long-dashed green, respectively, with the solid black line tracing the TPC boundary. Events inside the 1.3 fiducial mass are drawn as pie charts representing the relative probabilities of background and signal components using the best-fit  $\sigma_{SI} = 4.7 \times 10^{-47} \text{ cm}^2$  for a 200 GeV/c<sup>2</sup> WIMP. Grey dots represent events outside of the FV. Dark and light yellow regions illustrate the 1 $\sigma$  and 2 $\sigma$  radiogenic neutron background for SR1. Image credit: [123].

Of the  $627 \pm 18$  ER events  $1.62 \pm 0.30$  are estimated to be in our signal reference region for 1.3 t - a rejection of 99.7%. The contribution from the surface background is higher, decreasing from  $106 \pm 8$  to  $4.84 \pm 0.40$  (Sec. 3.3.3). The best-fit event rates for each background as well as a 200 GeV/c<sup>2</sup> WIMP are listed in Tab. 3.5 and are plotted in Fig. 3.50.

Fig. 3.51 shows the position distribution for events in the dark matter search data. 0.65, 0.9, and 1.3 t masses are marked and events that fall inside the 1.3 t mass are displayed as pie charts with probabilities of background and signal origin. Fig. 3.52 shows the events in cS1-cS2<sub>b</sub> and  $r_{\text{rec}}^2$ -cS2<sub>b</sub> parameter spaces.

Of the 739 dark matter search events three stand out. The most promising candidate is on the 25 keV<sub>nr</sub> line ( $cS2_b \sim 1000$  PE) in Fig. 3.52 (left) and is located in our signal reference region. Its proximity to both the ER band and 1 $\sigma$  however keep the WIMP relative probability at < 50%.

The second candidate is at  $\sim 16$  keV<sub>nr</sub> ( $cS2_b \sim 700$  PE). Like the first event it rests nicely in our energy ROI, but we can see it lies near the fiducial edge, making

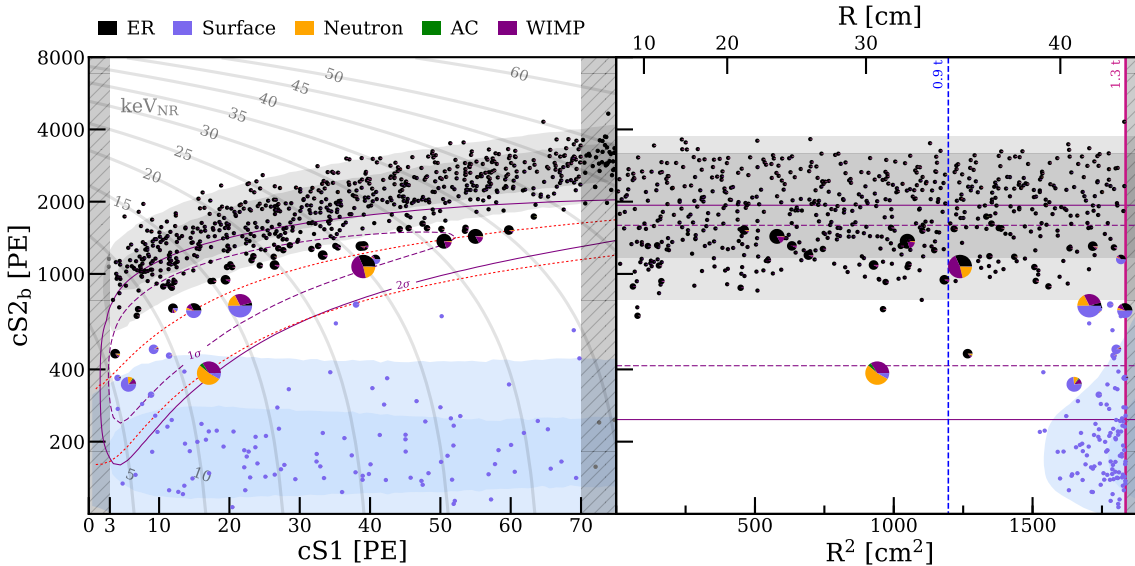


Figure 3.52: Dark matter search data in  $cS1-cS2_b$  (left) and  $r_{rec}^2-cS2_b$  (right) parameter space for 1.3 t fiducial mass. Events are drawn as pie charts following Fig. 3.51. Dark (light) shaded regions correspond to  $1\sigma$  ( $2\sigma$ ) percentiles of ER (grey) and surface (blue) backgrounds. Purple dashed and solid lines correspond to  $1\sigma$  and  $2\sigma$  regions for a 200 GeV/c $^2$  WIMP. The red dotted lines (left) represent the signal region and the vertical lines (right) mark the 0.9 t (dashed blue) and 1.3 t (solid magenta) fiducial masses. The vertical shaded regions are outside the region of interest. The grey lines (left) display iso-energy contours in keV<sub>nr</sub>. Image credit: [123].

it likely to be surface or neutron background.

The third at  $\sim 12$  keV<sub>nr</sub> ( $cS2_b \sim 400$  PE) is situated just below the NR  $-2\sigma$  line. This candidate motivated a post-unblinding decision to reconsider the model for neutron-X contamination, i.e. neutrons that scatter below the cathode and once in the TPC. The near-simultaneity of the scatters leads the DAQ to resolve only a single S1, shifting its position in Fig. 3.52. It also prompted a fiducial mass segmentation to more accurately reflect our understanding of the neutron  $z$  distribution, which was the inception of the 0.65 t mass. These revisions moved the probability of neutron origin from 35% to 75%, while a 50 GeV/c $^2$  WIMP decreased from 49% to just 7%.

No significant excesses in the 1.3 t mass were indicated by the profile likelihood analysis for any WIMP mass, with p-values for a background-only hypothesis for 6, 50, and 200 GeV/c $^2$  of 0.28, 0.41, and 0.22. Fig. 3.53 shows the results from this analysis for the 90% confidence level upper limit for  $\sigma_{SI}$  along with  $1\sigma$  and  $2\sigma$

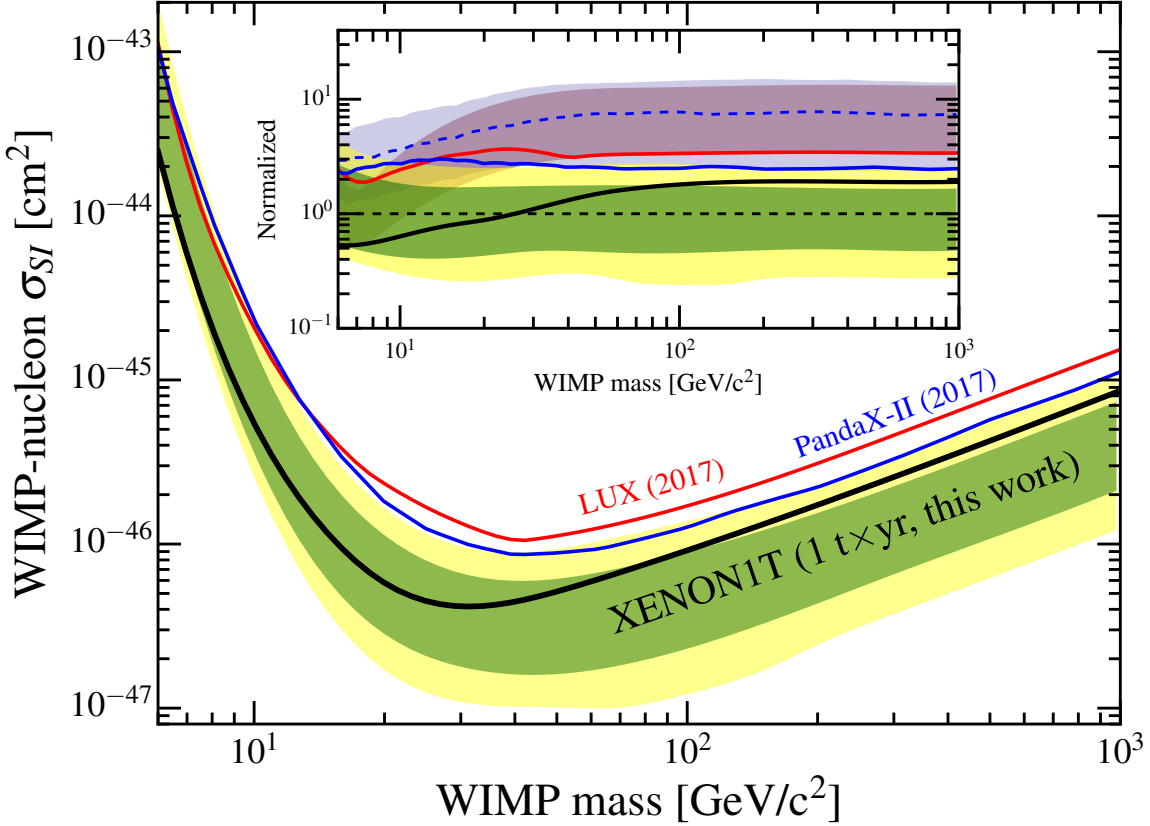


Figure 3.53: 90% confidence level upper limit on spin-independent WIMP cross section from this analysis (black line) with  $1\sigma$  (green) and  $2\sigma$  (yellow) sensitivity bands. Previous LUX [120] and PandaX-II [121] results are plotted in red and blue for comparison. The inset shows these limits and  $\pm 1\sigma$  bands normalized to the median sensitivity of this analysis as well as the normalized median of the PandaX-II sensitivity band (dotted blue line). Image credit: [123].

sensitivity bands. The steep increase at  $m_\chi < 20$  GeV/c $^2$  results from our loss in acceptance at low mass (Fig. 3.49). A minimum cross section of  $4.1 \times 10^{-47}$  cm $^2$  is found at 30 GeV/c $^2$ . The rise at  $m_\chi > 30$  GeV/c $^2$  is mainly the result of fewer WIMPs  $n_\chi = \rho_\chi/m_\chi$  (Eq. 1.16).

# Chapter 4

## Electronic and Nuclear Recoil Calibrations

A band is a region in cS1-cS2<sub>b</sub> (or some variation thereof) space where events of a certain recoil type occur. To differentiate the nuclear from electronic recoil bands, calibrations for each are performed and fit. These are critical as they provide information on the reference region and discrimination power between potential WIMP signals and background. <sup>220</sup>Rn calibrations are used for the ER band and are performed regularly. For NR, <sup>241</sup>AmBe and a deuterium-deuterium neutron generator (NG) are used, both of which are positioned in the water tank outside the cryostat. <sup>241</sup>AmBe calibrations are done in both science runs and a NG calibration is performed in SR1 only.

For this analysis all five sets of calibration data from both science runs were fit simultaneously. This was significant because it forced values that are common to some or all of the calibrations (e.g.  $W$ ,  $p_{\text{dpe}}$  are shared between all five, while  $g_1$ ,  $g_{2b}$  are shared within science runs) to be described by a single value.<sup>1</sup>

This chapter presents the electronic and nuclear recoil band fitting used in the run-combined analysis (Chap. 3). It begins with a summary of the importance of the calibrations (Sec. 4.1) followed by a description of how the parameters in the fit are

---

<sup>1</sup>For First Results the <sup>220</sup>Rn and <sup>241</sup>AmBe were independently fit.

determined (Sec. 4.2). Lastly, the results of the fit are presented (Sec. 4.3).

## 4.1 Purpose of Calibrations

For any event we would like to be able to calculate the probabilities of its possible origins. Fitting the electronic and nuclear recoil bands creates probability density functions (PDFs) for the ER background and WIMP signals, respectively. Since they overlap (the ER  $-2\sigma$  is at roughly the NR median) it is important to carefully characterize their PDFs so events can be classified as accurately as possible. This approach improves sensitivity over data-driven approaches. The method in this section requires a complete understanding of the TPC backgrounds, which in addition to electronic recoils includes wall leakage (Sec. 3.3.3) and accidental coincidence (Sec. 3.3.4). It also demands that the physical processes that occur - from the decay of the source to the data acquisition - are correctly modeled and can be simulated on a reasonable time scale.

Following the fit, a signal PDF is generated using the nuclear recoil result. For this analysis the signal is a spin-independent WIMP but this approach will work for other signal models. The shape of the signal PDF depends on the WIMP mass, as shown in Fig. 4.1. The ER band is the bright yellow region and the horizontal band around  $cS2_b = 150$  PE is accidental coincidence. The overlap between signal and background emphasizes the importance of the electronic and nuclear recoil band fit. An incorrect fit might shift the positions of the bands, changing our understanding of the origins of the events. The data is compared to the sum of the background and WIMP PDFs for each WIMP mass and cross section, and a discovery can be claimed if the data prefers a signal plus background over exclusively background model. If an excess is not observed a limit is set where cross sections below some value match the data.

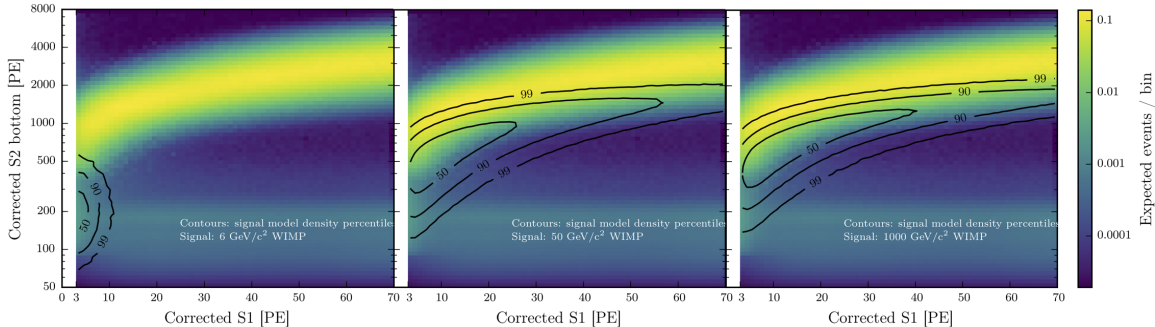


Figure 4.1: Total background model from First Results with 50, 90, and 99% contours for 6 (left), 50 (center), and 1000 (right)  $\text{GeV}/c^2$  WIMPs. The bright yellow region is the electronic recoil band, which was fit using a similar method to this section. Accidental coincidence is visible as the horizontal strip around  $cS2_b = 150$  PE. The expected signal region changes with WIMP mass.

## 4.2 Liquid Xenon TPC Modeling

This approach compares the distributions of Monte Carlo events and data to infer physics model parameters. Because of the nearly flat distribution of events in the energy region of interest and homogeneous position distribution, Monte Carlo variables  $E_{\text{true}}$ ,  $x_{\text{true}}$ ,  $y_{\text{true}}$ , and  $z_{\text{true}}$  for  $^{220}\text{Rn}$  are each randomly drawn from uniform distributions for each event.  $^{241}\text{AmBe}$  and neutron generator Monte Carlo are simulated using GEANT4 [217], and include the number of scatters for each neutron. The small volume of energy deposition for  $\beta^-$  ( $\mathcal{O}(\sim 1)$   $\mu\text{m}$ ) in our energy region of interest means it is not necessary to track the number of scatters for  $^{220}\text{Rn}$ .<sup>2</sup> These values represent the “truth” information - that is, these are the true interaction values, and are inputs to the full simulation. Reconstructed  $x$ - $y$  values will be referred to as  $x_{\text{rec}}$  and  $y_{\text{rec}}$ . Effects such as electric field non-uniformity and drift time measurement resolution cause  $\|z_{\text{rec}} - z_{\text{true}}\| > 0$ . However, these effects are small enough that they can be ignored, so moving forward true and reconstructed depths will be assumed equivalent and denoted by  $z$ . Likewise,  $E_{\text{rec}} \neq E_{\text{true}}$  since S1 and S2 are used for energy reconstruction (Sec. 2.6.3.3). Because the energy reconstruction method is usually specified,  $E \equiv E_{\text{true}}$  for the remainder of this chapter.

Fig. 4.2 shows the flow chart for the band fit. Each Monte Carlo event is simulated

<sup>2</sup>1-10 keV  $\beta^-$  have stopping powers of  $\sim 28.4$ - $85.2$  keV  $\mu\text{m}^{-1}$  (Sec. 2.2.3).

through a series of physical models that mimic our best understanding of the expected processes in the detector as closely as possible. The parameters in the fit come from a variety of sources including microphysics reported from literature and detector characterization measurements (Sec. 3.2). The simulation takes the true energy from a Monte Carlo event and outputs observables  $cS1$  and  $cS2_b$ . These in turn are binned in  $cS1$ - $\log_{10}(cS2_b/cS1)$  space, and the likelihood for equivalent bins between data and MC is calculated (Sec. 4.2.6). Our energy region of interest is defined as  $0 \leq cS1 \leq 100$  and  $0.5 \leq \log_{10}(cS2_b/cS1) \leq 3.5$ . As the parameters vary, the likelihood will increase or decrease and the minimizer will find the best-fit values.

The process of converting the truth MC to  $cS1$  and  $cS2_b$  is referred to as a “fast MC” (random numbers are drawn from probability distributions to generate sets of parameters). “Truth MC” refers to the simulated events before the fast MC ( $E_{\text{true}}$ ,  $x_{\text{true}}$ ,  $y_{\text{true}}$ ,  $z_{\text{true}}$ , and number of scatters). “MC” will denote the sum of all the fast MC results, usually in the form of a PDF or histogram, for comparison with data. Finally, a Markov Chain Monte Carlo (MCMC) is used to sample the likelihood defined by the data and MC and the best-fit values are derived from the resulting posterior. Sec. 4.2.1 (ER) and Sec. 4.2.2 (NR) discusses the physical steps that occur beginning with energy deposition and ending with  $cS1$  and  $cS2_b$ , which are modeled in the fast MC.

The number of fast MC events simulated for each likelihood iteration is  $\mathcal{O}(10^6)$ . A fast MC event randomly selects one of the truth input events. Such large statistics are necessary to reliably model the bands; however, nominal running time is far higher than any sensible time-scale. This was solved by using graphical processing units (GPUs), which can run the events in parallel, providing a boost in speed by a factor of  $10^{2-3}$  and reducing the required time to a reasonable level.

The calibrations were fit in the First Results FV ( $-92.9 < z < -9$  cm,  $r_{\text{rec}} < 36.94$  cm Fig. 3.26) despite the 1.3 t fiducial mass used for the dark matter analysis. This was done to minimize surface events and other contamination from materials at the top and bottom of the TPC.

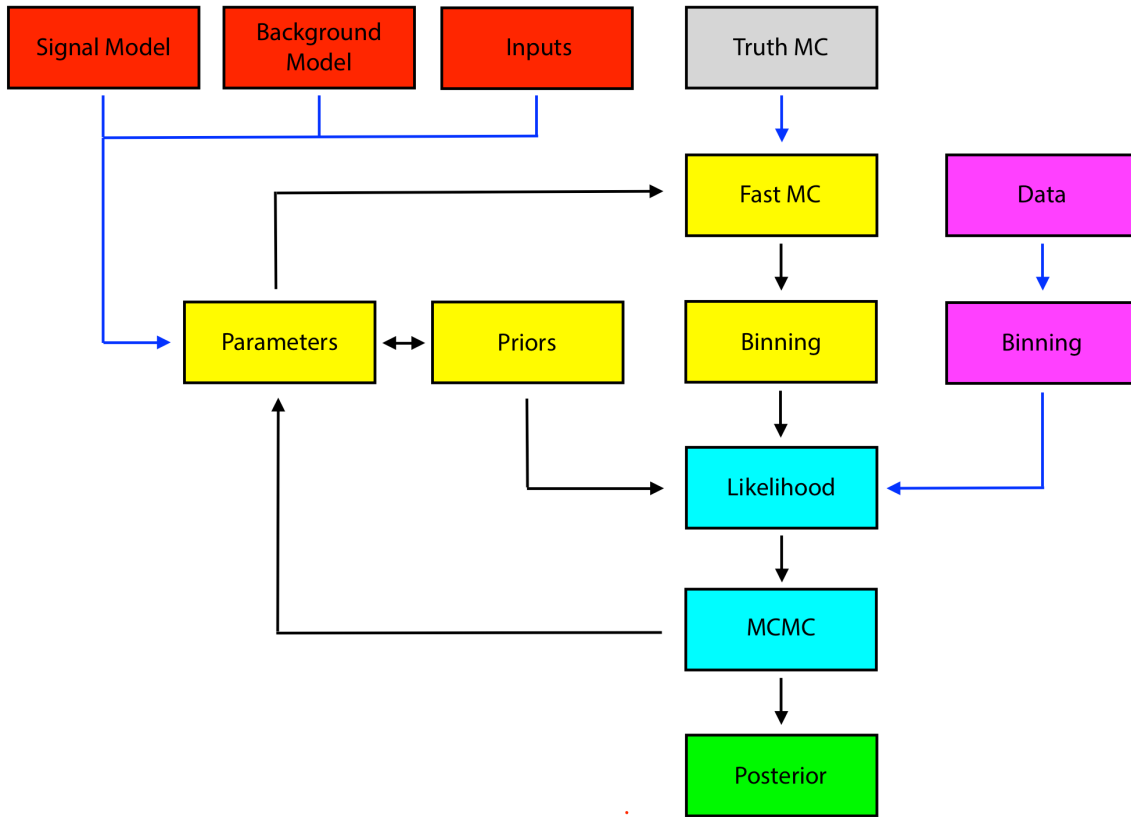


Figure 4.2: Steps for fitting electronic and nuclear recoil bands. The signal (NR) model, background (ER) model, and additional inputs (e.g. detector model, S2 threshold, AC) (red) make up the parameters (yellow) in the fit. Each parameter is constrained by its prior distribution (yellow). Parameters convert truth MC (grey) to cS1 and cS2<sub>b</sub> in the fast MC (yellow), which is then binned. Data (pink) from calibrations is binned and the likelihood (aqua) is computed using the histograms and prior distributions. A Markov Chain Monte Carlo (MCMC) (aqua) calculates the values of the parameters for the next iteration. The posterior is shown in green. Blue arrows represent steps that are only done once.

### 4.2.1 Electronic Recoils

The electronic recoil calibration is performed using  $^{220}\text{Rn}$  (decay chain shown in the left panel of Fig. 3.42). It is used because of the  $^{212}\text{Pb}$   $\beta$ -decay (Q-value of 569.9 keV), can be performed as an internal calibration.<sup>3</sup> A total of six calibrations were performed during SR0 and SR1.

<sup>3</sup>In the future we hope to use tritiated methane CH<sub>3</sub>T, which undergoes  $\beta$ -decay with a maximum energy of 18.6 keV. This would provide significantly more statistics in our region of interest in a shorter amount of time. However, as mentioned in Sec. 3.1.8.1 CH<sub>3</sub>T has a half-life of 12.3 y and there is concern it may attach to the cryostat.

When energy is deposited in LXe a number of quanta  $n_q$  will be produced. For electronic recoils this follows the normal distribution

$$n_q \sim \text{Norm}\left(\mu = \frac{E}{W}, \sigma^2 = \frac{EF}{W}\right) \quad (4.1)$$

where  $F$  is the Fano Factor [166] discussed in Sec. 2.4. Its derivation and subsequent measurements demonstrates that fluctuations in  $n_q$  are smaller than a Poisson distribution, and is estimated to be  $F = 0.059$  [167]. For the fast MC,  $F$  is fixed. Although a later measurement found different best-fit values, their result was compatible with [167] when including uncertainty [168]. The average energy to produce a single quanta,  $W$ , is constrained by a Gaussian with  $\mu = 13.7$ ,  $\sigma = 0.2$  eV following the measurement of [165].

For electronic recoils, quenching is negligible so is not considered. The quanta will be divided into excitons and electron-ion pairs  $n_q = n_{\text{ex}} + n_{\text{ion}}$  according to a binomial distribution

$$n_{\text{ion}} \sim \text{Binom}\left(n = n_q, p = \frac{1}{1 + \frac{n_{\text{ex}}}{n_{\text{ion}}}}\right) \quad (4.2)$$

where  $n_{\text{ex}}/n_{\text{ion}}$  is constrained to 0.06-0.2 and expected to be energy independent [155]. Some  $e^-$  will recombine with  $\text{Xe}^+$  to form excitons and emit photons as they decay to the ground state. The recombination fraction  $r$  depends on the field in the LXe and the interaction energy, and has intrinsic fluctuations  $\Delta r$  [197], [198]. A truncated Gaussian is assumed

$$r \sim \text{Norm}\left(\mu = \langle r \rangle, \sigma^2 = (\Delta r)^2\right) \quad (4.3)$$

where  $0 \leq r, \Delta r \leq 1$  and is parameterized using a modified Thomas-Imel box model [148]

$$\langle r \rangle = \frac{1}{1 + e^{-(E-E_0)/E_1}} \left[ 1 - \frac{\ln(1 + n_{\text{ion}}\varsigma/4)}{n_{\text{ion}}\varsigma/4} \right], \quad \varsigma = \gamma_{\text{er}} e^{-E/\omega_{\text{er}}} E_d^{-\delta_{\text{er}}} \quad (4.4)$$

for the fit. Here  $\varsigma$  has been adapted from Eq. 2.7 to include a power law field-dependence to allow simultaneous fitting of SR0 and SR1, and an exponential energy term to extend compatibility to high energy ( $\sim 20$  keV<sub>ee</sub>). An energy-dependent

Fermi-Dirac suppresses recombination at  $\lesssim 2 \text{ keV}_{\text{ee}}$  to allow more freedom to fit the data and literature. The parameters do not have well-defined priors and are constrained to  $0 \leq \gamma_{\text{er}} \leq 0.5$ ,  $0 \leq E_0, E_1 < \infty$ , and  $-\infty < \omega_{\text{er}}, \delta_{\text{er}} < \infty$ .

Recombination fluctuations are modeled as

$$\Delta r = A(1 - e^{-E/B}) \quad (4.5)$$

where parameters  $A, B > 0$  are allowed to vary freely. The number of electron-ion pairs that recombine is

$$n_{\text{rec}} \sim \text{Binom}(n = n_{\text{ion}}, p = r) \quad (4.6)$$

yielding final numbers of photons and electrons

$$n_{\text{ph}} = n_{\text{ex}} + r n_{\text{ion}} \quad (4.7a)$$

$$n_{\text{e}} = (1 - r)n_{\text{ion}} \quad (4.7b)$$

### 4.2.2 Nuclear Recoils

Two nuclear recoil sources were used for calibrations: americium beryllium ( $^{241}\text{AmBe}$ ) and a neutron generator (NG).  $^{241}\text{Am}$  decays to  $^{237}\text{Np}$  by  $\alpha$ -emission and the large  $^9\text{Be}$   $\alpha$  cross-section prompts a second decay



emitting a  $< 11 \text{ MeV}$  neutron. The neutron generator (NSD Gradel Fusion NSD-35-DD-C-W-S) uses deuterium-deuterium (D-D) fusion



where the  $^3\text{He}$  and  $\text{n}$  are emitted at 0.82 and 2.45 MeV, respectively. The energy spectrum can be seen in Fig. 4.3. It shows two peaks - one at 2.2 MeV and the other at 2.7 MeV. These are the energies seen in the lab frame (2.45 MeV is in the rest frame of the deuteron) and correspond to neutrons emitted at  $180^\circ$  and  $0^\circ$ , respectively. The NG can operate at rates as low as  $10 \text{ n s}^{-1}$  and as high as  $10^7 \text{ n s}^{-1}$ , which allows

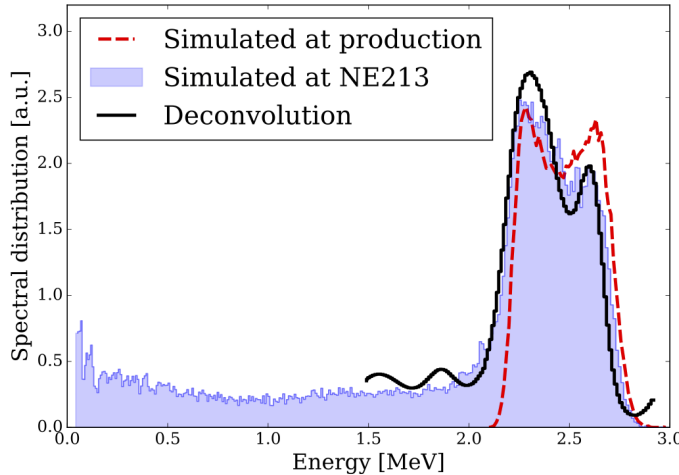


Figure 4.3: Simulated neutron energy spectra in fusion region of the NG (red dashed line) and at the pulse shape discriminator during calibration before installation at LNGS (blue shaded region). Deconvolution of data from calibration (black solid line) is also shown. Spectra are normalized by the 2.2-2.7 MeV range. Image credit: [182].

flexibility for our objectives. A higher-energy neutron population is produced by tritium via



where the neutron is expelled at 14.1 MeV. The contribution of deuterium-tritium fusion was measured to be  $3.5 \pm 0.2\%$  before installation at LNGS [182]. Because the tritium is created in deuterium-deuterium fusion and has  $t_{1/2} = 12.3$  y, its fraction will increase with continued use. For details on the characterization of the NG please refer to [182].

The positions for  $^{241}\text{AmBe}$  and NG events are shown in Fig. 4.4 and Fig. 4.5. Their  $\sim 10$  cm mean free path causes clustering closest to the calibration source. Because we expect our detector does not vary over  $r$  and  $\phi$  inside the 1 t FV the results of the asymmetric position distribution are applied to the entire active volume. Events in the region furthest from the source are mostly background. Fewer background events are present in the NG data because of the shorter calibration time. SR0  $^{241}\text{AmBe}$  is not shown but its distribution of NR events is similar to Fig. 4.4 because the location of the source was the same. Many more ER events, however, were present since it

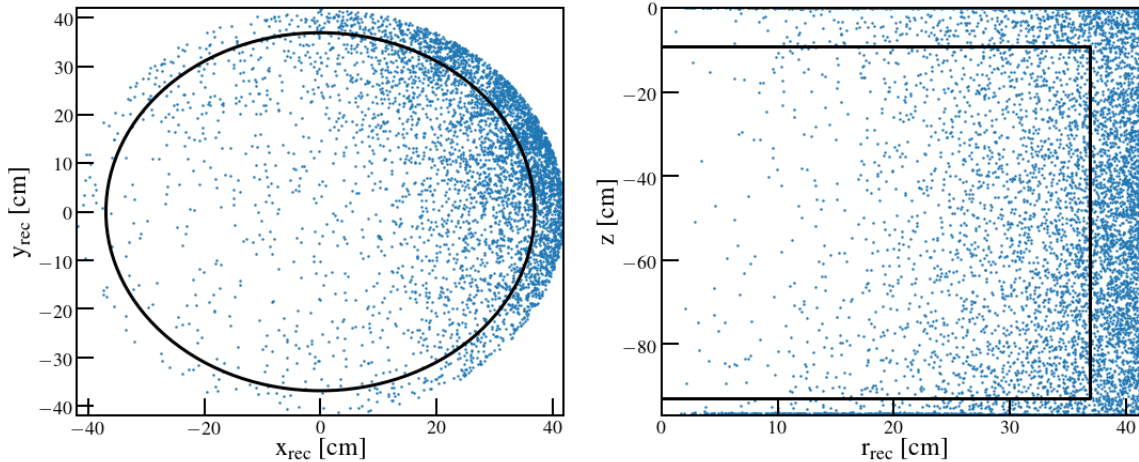


Figure 4.4: Positions of events from SR1  $^{241}\text{AmBe}$  calibration. Events are clustered in the region of the detector closest to the  $^{241}\text{AmBe}$  source. The black line marks the 1 t fiducial volume. Aside from the higher ER background, the SR0 distribution looks similar since the source was placed in the same location inside the water tank.

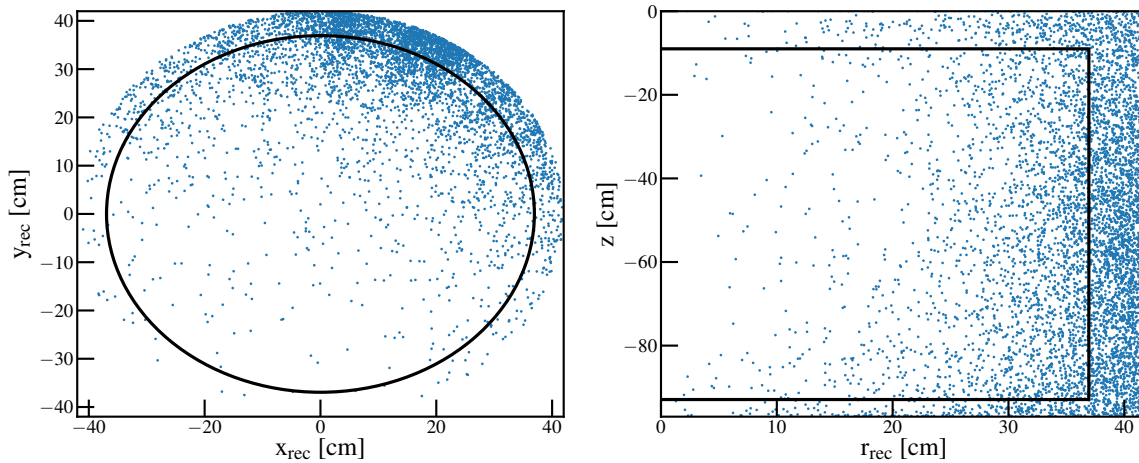


Figure 4.5: Positions of events from SR1 neutron generator calibration. Events are densely distributed in the region of the TPC closest to the NG source. The black line shows the 1 t fiducial volume.

preceded the online distillation (Sec. 3.1.6).

The microphysical processes that follow a nuclear recoil differ from ER (Sec. 4.2.1). As discussed in Sec. 2.5 a sizable portion of the energy is lost to atomic motion. To

model this we use the Lindhard theory in Eq. 4.11:

$$\epsilon = 11.5 \left( \frac{E}{\text{keV}} \right) Z^{-7/3} \quad (4.11\text{a})$$

$$g(\epsilon) = 3\epsilon^{0.15} + 0.7\epsilon^{0.6} + \epsilon \quad (4.11\text{b})$$

$$L(\epsilon) = \frac{kg(\epsilon)}{1 + kg(\epsilon)} \quad (4.11\text{c})$$

where  $k$  is the proportionality constant between the electronic stopping power and recoiling nucleus velocity. The Lindhard factor  $L(\epsilon)$  is the fraction of energy converted to excitons or electron-ion pairs, or total quanta

$$n_q \sim P \left( \mu = \frac{EL}{W} \right) \quad (4.12)$$

that follows a Poisson distribution as an approximation. In reality the track structure of nuclear recoils makes the true distribution more complicated. The number of ions is found in the same way as electronic recoils

$$n_{\text{ion}} \sim \text{Binom} \left( n = n_q, p = \frac{1}{1 + \frac{n_{\text{ex}}}{n_{\text{ion}}}} \right) \quad (4.13)$$

and  $n_{\text{ex}} = n_q - n_{\text{ion}}$ . Recombination is given by

$$n_{\text{rec}} \sim \text{Binom} (n = n_{\text{ion}}, p = r) \quad (4.14)$$

where  $r$  described by the Thomas-Imel model

$$r = 1 - \frac{\ln(1 + n_{\text{ion}}\varsigma)}{n_{\text{ion}}\varsigma} \quad (4.15)$$

with  $\varsigma$  field-dependent. Unlike ER, no recombination fluctuations have been observed for nuclear recoils so  $\Delta r$  is not included. Biexcitonic quenching and Penning processes, both of which decrease  $n_{\text{ph}}$ , must also be considered. Biexcitonic quenching arises when two  $\text{Xe}^*$  interact to free an  $e^-$ , which quickly loses its kinetic energy and recombines with a  $\text{Xe}^+$ . Thus, what would have been two photons instead results in one. The Penning process describes when two excimers interact and result in an excited and ground state [156]. Both of these depend on the exciton density,

which is proportional to the ionization density and therefore stopping power  $dE/dx$  (Sec. 2.2.3). They result in quenching and can be described by Birks' saturation law, Eq. 4.16 [152], [153]:

$$f_b = \frac{1}{1 + k_B B \frac{dE}{dx}} = \frac{1}{1 + \eta \epsilon^\lambda} \quad (4.16)$$

where  $k_B$  is Birks' constant (calculated in [156] to be  $2.015 \times 10^{-3}$  g MeV $^{-1}$  cm $^{-2}$ ),  $B$  is the coefficient for the stopping power, and  $\eta$  is defined to be their product. The total quenching from biexcitonic quenching and the Penning process is

$$n_{\text{quench}} = \text{Binom}(n = n_{\text{ex}}, p = f_b) \quad (4.17)$$

where  $n_{\text{quench}}$  is the number of excitons that do not emit a photon. Thus the number of excitons moving forward is  $n_{\text{ex}} \leftarrow n_{\text{ex}} - n_{\text{quench}}$ .

The parameters in the nuclear recoil model were constrained by previous measurements of light and charge yield. This decision was made to prevent detector effects from compensating for changes in the liquid xenon response model. We used the results from [173], which used nuclear recoil light and charge yield measurements between 1-300 keV and electric fields of 0-4060 V cm $^{-1}$  to fit the model detailed in this section. Although none of the measurements were made for light and charge yields simultaneously, [173] performed a single fit of all data.

The model is parameterized by setting

$$\frac{n_{\text{ex}}}{n_{\text{ion}}} = \alpha E_d^{-\zeta} (1 - e^{-\beta \epsilon}) \quad (4.18)$$

$$\zeta = \gamma E_d^{-\delta} \quad (4.19)$$

where,  $E_d$  is the drift field. From Eq. 4.18,  $n_{\text{ex}}/n_{\text{ion}}$  has a power dependence on  $E_d$ , which is suspected to be caused by geminate recombination: when electrons and parent ions recombine much more quickly than Thomas-Imel recombination. In addition,  $n_{\text{ex}}/n_{\text{ion}}$  depends exponentially on energy such that at higher energy a larger fraction of excitons is favored.

We see in Eq. 4.19 that  $\zeta$  is proportional to a power of  $E_d$ . The Thomas-Imel

Parameter	Best Fit	Equation
$\alpha$	$1.240^{+0.079}_{-0.073}$	Eq. 4.18
$\zeta$	$0.0472^{+0.0088}_{-0.0073}$	Eq. 4.18
$\beta$	$239^{+28}_{-8.8}$	Eq. 4.18
$\gamma$	$0.01385^{+0.00058}_{-0.00073}$	Eq. 4.19
$\delta$	$0.0620^{+0.0056}_{-0.0064}$	Eq. 4.19
$k$	$0.1394^{+0.0032}_{-0.0026}$	Eq. 4.11
$\eta$	$3.3^{+5.3}_{-0.7}$	Eq. 4.16
$\lambda$	$1.14^{+0.45}_{-0.09}$	Eq. 4.16

Table 4.1: Best-fit values along with 68% credible intervals for nuclear recoil micro-physics parameters from [173]. These are used as gaussian priors for  $^{241}\text{AmBe}$  and NG band fitting.

theory predicts

$$\varsigma = \frac{\alpha'}{4a^2 u_- E_d} \quad (4.20)$$

where  $\alpha'$  is a recombination coefficient,  $a$  is the dimension of the box, and  $u_-$  is the electron mobility. While here  $\delta$  is strictly 1, Dahl's model predicts  $\delta \sim 0.1$  [165].

The marginalized posteriors from [173] of  $k$  (Eq. 4.11),  $\eta$  and  $\lambda$  (Eq. 4.16),  $\alpha$ ,  $\zeta$  and  $\beta$  (Eq. 4.18), and  $\gamma$  and  $\delta$  (Eq. 4.19) are listed in Tab. 4.1. They are used as gaussian priors for this analysis.

Using this model the expected number of photons and electrons is

$$n_{\text{ph}} = L(E) f_b \frac{E}{W} \left[ 1 - \frac{1}{1 + n_{\text{ex}}/n_{\text{ion}}} (1 - r) \right] \quad (4.21\text{a})$$

$$n_{\text{e}} = L(E) \frac{E}{W} \frac{1}{1 + n_{\text{ex}}/n_{\text{ion}}} (1 - r) \quad (4.21\text{b})$$

### 4.2.3 Detector Effects

After the microphysics emission processes, the properties of our detector become relevant as they convert  $n_{\text{ph}} \rightarrow \text{S1}$  and  $n_{\text{e}} \rightarrow \text{S2}$ . This is in part why the characterizations detailed in Sec. 3.2 are essential. Although the  $^{220}\text{Rn}$ ,  $^{241}\text{AmBe}$ , and NG calibrations were performed at different times they were fit simultaneously. Changes in detector

conditions are accounted for by having different central values of the relevant detector parameters. Parameters that are expected to be correlated between calibrations are characterized with a single prior (e.g. though SR0 and SR1 have different S1 cut efficiencies, the relative change from central values is shared).

The first process following the microphysics model to consider is position reconstruction (Sec. 3.2.3). The reason is that any position-dependent correction is applied to the position we measure since we cannot know the truth. The  $x$ - $y$  position reconstruction resolution  $((x_{\text{rec}} - x_{\text{true}})^2 + (y_{\text{rec}} - y_{\text{true}})^2)^{1/2}$  is shown in Fig. 3.25. The poor resolution at  $n_e \lesssim 100 \text{ e}^-$  ( $S_{2b} \lesssim 1000 \text{ PE}$ ) indicates that in our lowest dark matter energy region events inside (outside) the FV will have a reasonable chance of being reconstructed outside (inside) - especially near the boundary. After simulating the position reconstruction  $x_{\text{truth}} \rightarrow x_{\text{rec}}$  and  $y_{\text{truth}} \rightarrow y_{\text{rec}}$ , the truth values are no longer considered in the analysis of the fast MC.

The number of photons from the interaction site that produce one or more photoelectrons is dependent on two effects. The first is the position-dependent light collection efficiency (LCE)  $\mathcal{C}_{\text{lce}}(x_{\text{rec}}, y_{\text{rec}}, z)$ , which accounts for detector effects such as <100% PTFE reflectivity and absorption of light by impurities that reduce the amount of light that reaches the PMTs (Sec. 3.2.2). The second is the probability of double photoelectron emission (DPE)  $p_{\text{dpe}}$ , which was found to be much higher than originally thought, ranging from 0.18-0.24 for the various PMTs tested by [178] and  $0.225 \pm 0.01$  for the Hamamatsu R11410 model (Sec. 3.1.1). The parameter of interest therefore is not the quantum efficiency  $\eta_\mu$ , but rather the fraction of incident photons that generate at least one PE  $\eta_p$ . As shown in Eq. 3.2  $\eta_\mu/\eta_p = 1 + p_{\text{dpe}}$ . Accounting for both of these effects the number of photons that generate  $\geq 1$  PE is shown in Eq. 4.22.

$$n_p = \text{Binom}\left(n = n_{\text{ph}}, p = \frac{g_1 \mathcal{C}_{\text{lce}}(x_{\text{rec}}, y_{\text{rec}}, z)}{1 + p_{\text{dpe}}}\right) \quad (4.22)$$

To calculate the total number of photons that produce DPE

$$n_{\text{dpe}} = \text{Binom}(n = n_p, p = p_{\text{dpe}}) \quad (4.23\text{a})$$

$$n_{\text{pe,S1}} = n_p + n_{\text{dpe}} \quad (4.23\text{b})$$

where  $n_{\text{pe,S1}}$  is the total number of photoelectrons.

As the signals from the PMTs are fed into and recorded by the DAQ (Sec. 3.1.9) and later processed, three effects are introduced: S1 peak finding (processor) efficiency, bias, and smearing - all of which are the most influential at low photon counts. The S1 peak finding efficiency is the probability that the S1 is recognized by the reconstruction and classification algorithm amongst PMT dark count, DAQ, and other electronic noise, as well as low-energy S2s that are known to occasionally follow large S2s (known as S2 “tails”). Additionally, if less than three PMTs observe the S1 it is discarded. The processor efficiency cannot be modeled using data since it is not possible to know when a signal was not found. Instead simulated waveforms are processed with the reconstruction and classification algorithm. The waveforms are generated with DAQ conditions that have been measured in order to replicate real waveforms as well as possible. Separate efficiencies are used for the SR0  $^{241}\text{AmBe}$  calibration (performed before installation of filter boxes), SR0, and SR1. It is expected to be reasonably accurate and is shown as the red shaded regions in Fig. 4.6. For the fit the relative deviation from the median is expected to be a systematic effect so is correlated between the three inputs.

Bias and smearing (Sec. 3.2.10) characterize the difference between true and reconstructed areas of the scintillation. They originate from noise, S2 tails, and the clustering and separation ability of the reconstruction and classification algorithm. As with the efficiency, it is impossible to measure directly from data since the true area is not known beforehand. By using waveform simulations however, input “truth” values are compared with the reconstructed values. Slices in  $(S1_{\text{rec}} - S1_{\text{truth}})/S1_{\text{truth}}$ , where  $S1_{\text{rec}}$  and  $S1_{\text{truth}}$  are the reconstructed and truth S1s, are fit with gaussians. The mean is known as the fractional bias  $\mu_{b,\text{S1}}$  and standard deviation as fractional

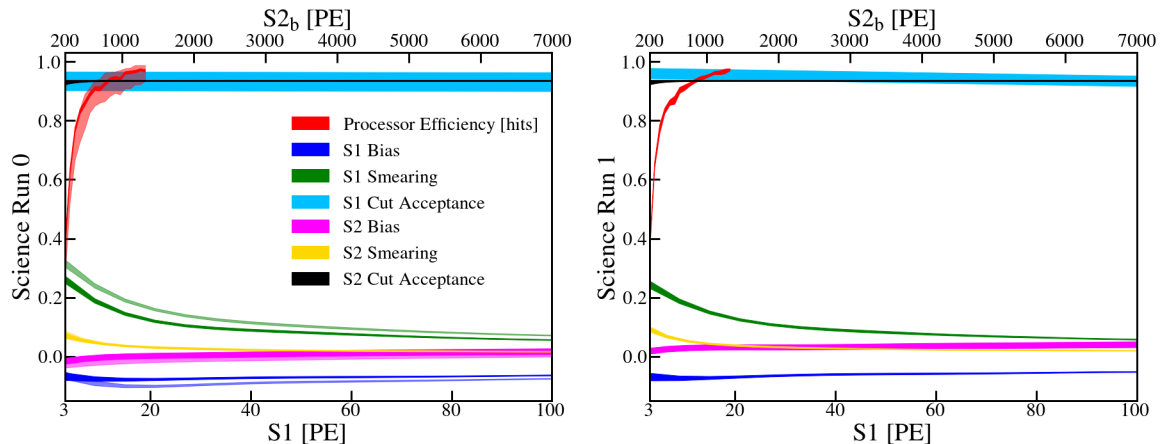


Figure 4.6: S1- and S2<sub>b</sub>-dependent detector parameter 68% credible intervals for SR0 (left) and SR1 (right). Processor efficiency (red) is plotted with respect to the S1 axis but in units of hits. Filter boxes were installed on the DAQ between the SR0 <sup>241</sup>AmBe calibration and dark matter data taking so separate processor efficiencies and S1 and S2 biases and smearings are used (shown as transparent in same color). The filter boxes led to improvement, particularly for the processor efficiency and S1 bias and smearing. The uncertainty on the processor efficiency also decreased.

smearing  $\sigma_{b,S1}$  for each bin. They are shown as the blue and green shaded regions in Fig. 4.6. As with the processor efficiency, the bias and smearing changed after the filter boxes were installed, and the three inputs share an uncertainty that accounts for systematic effects (bias and smearing have independent parameters). For the fit, they are constrained to the shaded regions and applied in the fast MC via Eq. 4.24.

$$S1 = n_{pe,S1} \left[ 1 + \text{Norm}(\mu = \mu_{b,S1}, \sigma^2 = \sigma_{b,S1}^2) \right] \quad (4.24)$$

Because multiple scatters happen so close in time the S1s are typically not resolvable. Thus in the fast MC all S1s are summed, though this only affects <sup>241</sup>AmBe and NG data ( $\beta$ -decay of <sup>212</sup>Pb should not multiple-scatter). The LCE map is applied

$$cS1 = \frac{S1}{\mathcal{C}_{lce}(x_{rec}, y_{rec}, z)} \quad (4.25)$$

to obtain the corrected S1. In the case of multiple scatters the S1 will be corrected by a single  $\mathcal{C}_{lce}(x_{rec}, y_{rec}, z)$  with  $x_{rec}, y_{rec}, z$  calculated from the S2 (Sec. 3.2.3), though in reality the various interactions have likely occurred in different regions of the detector. The cS1 then is not fully representative of the total light yield. However, a single

scatter cut is applied that requires the energy of additional depositions to be below a threshold (Sec. 4.2.4). In addition, to be consistent we apply an identical correction in the fast MC, so (assuming our GEANT4 MC multiple-scatter model is sufficiently valid) this does not impact our results.

The  $e^-$  move from the interaction site towards the liquid-gas interface. As they drift, electronegative impurities will bind to them, reducing the total number that reach the surface and are extracted across the GXe. The attachment rate is field-dependent, and for O<sub>2</sub> - expected to be the largest contributor - decreases with larger  $E_d$  (Sec. 2.6.1).

Inhomogeneities in  $E_d$  influence the charge yield in two ways. First, the impurity attachment rate will change depending on the position in the TPC. This causes the number of  $e^-$  that reach the surface from events in different regions to be biased. The second is the light and charge yield vary with electric field (shown in Fig. 2.19). Therefore events at the same energy may have different yields depending on where in the TPC they occur. Neither of these effects are considered in the fast MC, introducing a small systematic error. However, because  $E_d$  is extremely uniform inside the FV, as shown in Fig. 3.6, the error should be small.

The electron lifetime used is randomly selected from the collection of lifetimes measured for each calibration. Any global systematic error in measured lifetimes Eq. 3.6 is accounted for with a normal distribution

$$\tau_{e,\text{true}} = \tau_{e,\text{rec}} \left[ 1 + \text{Norm}(\mu = 0, \sigma^2 = \sigma_e^2) \right] \quad (4.26)$$

where  $\tau_{e,\text{rec}}$  and  $\tau_{e,\text{true}}$  refer to the reconstructed (measured) and true electron lifetimes, and  $\sigma_e$  is the systematic uncertainty on  $\tau_{e,\text{rec}}$ . It is set to  $\sigma_{e,\text{SR0}} = 0.04$  and  $\sigma_{e,\text{SR1}} = 0.5\sigma_{e,\text{SR0}}$ . The difference is because we are more confident in the electron lifetimes for SR1 (Fig. 3.29). The true and reconstructed electron survival probabilities are given in Eq. 4.27.

$$p_{\text{rec}}(t_d) = e^{-t_d/\tau_{e,\text{rec}}} \quad (4.27\text{a})$$

$$p_{\text{true}}(t_d) = e^{-t_d/\tau_{e,\text{true}}} \quad (4.27\text{b})$$

The number of  $e^-$  that survive to the surface  $n_{\text{surv}}$  is calculated using

$$n_{\text{surv}} = \text{Binom}\left(n = n_e, p = p_{\text{surv}}\right), \quad p_{\text{surv}} = p_{\text{true}} \times (1 - p_{\text{wall}}) \quad (4.28)$$

where  $p_{\text{wall}}$  refers to the probability an  $e^-$  attaches to the wall; however, because this is only relevant in the 1-2 cm next to the PTFE we can ignore its effects and set  $p_{\text{wall}} = 0$ . The number of electrons extracted from the liquid  $n_{\text{extr}}$  depends only on  $n_{\text{surv}}$  and the probability of extraction  $\eta_{EE}$

$$n_{\text{extr}} = \text{Binom}\left(n = n_{\text{surv}}, p = \eta_{EE}\right) \quad (4.29)$$

where  $\eta_{EE} = 0.936$  and  $0.933$  for SR0 and SR1, respectively, and is fixed in the fast MC (the change in notation from Sec. 3.2.7 is to avoid confusion with  $\eta$  in the nuclear recoil model, Eq. 4.16). The single electron gain is given by

$$G(x, y) = \frac{g_{2b}\mathcal{C}_{S2b}(x_{\text{rec}}, y_{\text{rec}})}{\eta_{EE}} = G_e\mathcal{C}_{S2b}(x_{\text{rec}}, y_{\text{rec}}) \quad (4.30)$$

where  $G_e$  is the nominal position-averaged gas gain (Sec. 3.2.6) and  $\mathcal{C}_{S2b}(x, y)$  is the S2b  $x$ - $y$  correction map (Sec. 3.2.4). Approximating the amplification as a gaussian the number of photoelectrons is

$$n_{\text{pe},S2b} = \text{Norm}\left(\mu = n_{\text{extr}}G, \sigma^2 = n_{\text{extr}}\sigma_G^2G^2\right) \quad (4.31)$$

where  $G = G(x, y)$  to simplify notation and  $\sigma_G$  is the gas gain resolution and is 0.24 and 0.25 for SR0 and SR1. Similar to the S1, there will be bias and smearing. Using the same assumptions we find

$$\text{S2}_b = n_{\text{pe},S2b} \left[ 1 + \text{Norm}(\mu = \mu_{b,S2b}, \sigma^2 = \sigma_{b,S2b}^2) \right] \quad (4.32)$$

where  $\mu_{b,S2b}$  and  $\sigma_{b,S2b}$  are the S2b fractional bias and smearing, respectively. They

are shown as the pink and yellow bands in Fig. 4.6, and deviations in the fit are parameterized by a single variable. In practice Eq. 4.30 to 4.32 are applied for the total S2 - however, in the fast MC the treatment is slightly different. After Eq. 4.31 we calculate  $S2 = S2_b/(1 - f_{aft})$  where  $f_{aft} = 0.627$  (fixed) is the mean fraction of light from an S2 that is observed by the top PMT array. Bias and smearing are then applied. While in reality the total bias and smearing can differ from that of the bottom array, to save memory we use  $\mu_{b,S2_b}$  and  $\sigma_{b,S2_b}$ . Any difference is too small to affect the results so can be disregarded.  $\mu_{b,S2_b}$  and  $\sigma_{b,S2_b}$  are shown in the right panel of Fig. 4.6 and as with the S1, are constrained to the shaded regions for the fit.

Lastly the electron lifetime and S2 position corrections are applied to calculate the corrected S2.

$$cS2_b = \frac{S2_b}{C_{S2_b} p_{\text{rec}}} \quad (4.33)$$

#### 4.2.4 Selection Criteria

Each event in the data must pass a series of selection criteria. Because the criteria were developed to select good events - that is, events that are clearly the result of an interaction in the LXe - most are not necessary for the fast-MC since “bad” events are not simulated. An example is the requirement on the fraction of the S1 observed by the top PMT array must fall within a range determined by analysis, in part to reject events in the GXe. This is irrelevant to the fast-MC since only events in the LXe are included as input.

There are a couple of criteria that, assuming the data quality is good, select which events to keep. The first is a requirement that  $S2 > 200$  PE, referred to as the S2 threshold. The second criteria is introduced to remove events that have more than one scatter by rejecting those where the second-largest  $S2_b$  falls above some  $S2_b$ -dependent threshold. However, it can be difficult to determine if multiple scatters occurred - particularly at low energy, and for nuclear recoils, which have a long mean free path and low light and charge yields. Thus some multi-scatter events are inevitably included, with the restriction that the ratio of the first to second scatters

is large. This is not a concern for  $^{220}\text{Rn}$ .

For the remainder of the selection criteria S1 and S2 efficiencies are computed using the data to understand what fraction of good events are lost as a result of each selection. The product of all efficiencies is included in the fast MC for consistency and are used to accept events with a fraction equivalent to the data. They are shown as the light blue (S1) and black (S2) bands in Fig. 4.6.

### 4.2.5 Backgrounds

While the majority of events recorded during a calibration are from the source a subset comes from background. These are included in the analysis to avoid fitting events that are not described by the recoil model of the source.

Electronic recoils (Sec. 3.3.1) are by far the largest background. For  $^{220}\text{Rn}$  they do not present a problem but need to be included in the NR fits. The ER model, constrained by the  $^{220}\text{Rn}$  data, is also used in the likelihood for NR calibration data.

The higher event rate causes increased accidental coincidence (Sec. 3.3.4). This is more dramatic for  $^{241}\text{AmBe}$  and NG data where neutrons with small scattering angles may produce a very small S1 or S2. AC distributions are included in all five calibrations. SR0 and SR1  $^{220}\text{Rn}$  AC constrain one other through  $R_{\text{AC}}^{(\text{SR1})} = 3.75R_{\text{AC}}^{(\text{SR0})} - 0.0625$ . SR0 and SR1  $^{241}\text{AmBe}$  have the same AC expectation since the location and activity of the source and duration were the same. However, they do not share parameters so are independently fit. AC is not simulated in the fast MC, and only the amplitude of the distributions are allowed to vary by gaussian-constrained parameters.

Surface events were not included because they are far from the fiducial volume.

### 4.2.6 Statistical Inference

The fit is performed with a binned likelihood approach using Bayesian inference. Fast MC events (typically  $\mathcal{O}(10^6)$ ) and data are each binned in cS1 vs.  $\log_{10}(\text{cS2}_b/\text{cS1})$ .

The log-likelihood for the  $i^{\text{th}}$  bin is computed as

$$\mathcal{L}_i = \frac{\hat{b}_i^{b_i} e^{-\hat{b}_i}}{b_i!} \quad (4.34\text{a})$$

$$\ln \mathcal{L}_i = b_i \ln(\hat{b}_i) - \hat{b}_i - \ln(b_i!) \quad (4.34\text{b})$$

where  $\hat{b}_i$  and  $b_i$  are the expected (MC) and true (data) number of events in the bin, respectively. The log-likelihood is

$$\mathcal{L} = \prod_i \mathcal{L}_i \quad (4.35\text{a})$$

$$\ln \mathcal{L} = \sum_i \ln \mathcal{L}_i = \sum_i b_i \ln(\hat{b}_i) - \hat{b}_i - \ln(b_i!) \quad (4.35\text{b})$$

over all bins. The parameters responsible for the fast Monte Carlo ( $\hat{b}_i$ ) were detailed in Sec. 4.2.1–4.2.4. As discussed, each parameter is constrained by our understanding before the fit using a prior distribution. For the cases where we expect the error to be either negligible or contained in a dependent parameter the value is fixed. Components where we have good knowledge on the uncertainty (e.g.  $W$ ,  $g_1$ ,  $g_{2b}$  etc.) are constrained with a gaussian. The S1 and S2 selection efficiencies as well as the S1 peak finding efficiency are modeled by a gaussian distribution with mean  $\mu = 0$  corresponding to the median value and  $\sigma = \pm 1$  to the lower and upper bounds in the credible interval. Parameters that have a range of preferred values (e.g.  $n_{\text{ex}}/n_{\text{ion}}$ ,  $p_{\text{dpe}}$ , bias and smearing, etc.) are restricted to within these bounds. Finally, in cases where there is little knowledge, the priors are left free - though this is only applied to parameters in the electronic recoil recombination model (Sec. 4.2.1). Applying more stringent constraints on well-understood parameters reduces degeneracies and provides more information on those that are less known.

In Bayesian inference a posterior probability is defined based on Bayes' formula

$$p(\boldsymbol{\theta}|\mathbf{x}, \boldsymbol{\alpha}) = \frac{p(\mathbf{x}|\boldsymbol{\theta})p(\boldsymbol{\theta}|\boldsymbol{\alpha})}{p(\mathbf{x}|\boldsymbol{\alpha})} = \frac{\mathcal{L}(\boldsymbol{\theta}|\mathbf{x})p(\boldsymbol{\theta}|\boldsymbol{\alpha})}{p(\mathbf{x}|\boldsymbol{\alpha})} \quad (4.36)$$

where  $p(\boldsymbol{\theta}|\boldsymbol{\alpha})$  captures the prior understanding of the model and is known as the *prior probability*. Constraints on model parameters (parameters of interest and nui-

sance parameters)  $\boldsymbol{\theta}$  - generally from physical restrictions or previous measurements or knowledge - are stored in hyperparameters  $\boldsymbol{\alpha}$ .  $p(\boldsymbol{\theta}|\mathbf{x}, \boldsymbol{\alpha})$  is the probability of parameters  $\boldsymbol{\theta}$  of dimension  $n$  given the data  $\mathbf{x}$  and is known as the *posterior probability density*, or *target density*.  $p(\mathbf{x}|\boldsymbol{\theta})$  is the probability of the data  $\mathbf{x}$  given the parameters  $\boldsymbol{\theta}$  and is commonly referred to as the *likelihood*  $\mathcal{L}(\boldsymbol{\theta}|\mathbf{x})$ .  $p(\mathbf{x}|\boldsymbol{\alpha})$  is known as the *marginal likelihood* and can be computed using Eq. 4.37. Because it does not depend on  $\boldsymbol{\theta}$  it is model-independent so does not contribute to the relative likelihoods between different  $\boldsymbol{\theta}$ .

$$p(\mathbf{x}|\boldsymbol{\alpha}) = \int_{\Theta} p(\mathbf{x}|\boldsymbol{\theta})p(\boldsymbol{\theta}|\boldsymbol{\alpha}) d^n\boldsymbol{\theta} \quad (4.37)$$

Unfortunately for nearly all models - including those of interest to this analysis -  $p(\mathbf{x}|\boldsymbol{\alpha})$  is not calculable. Sec. 4.2.7 discusses a solution that allows us to estimate the posterior without needing to solve Eq. 4.37.

#### 4.2.7 Markov Chain Monte Carlo

To estimate the values  $\boldsymbol{\theta}$  that best fit the data by  $\mathbf{x}$  a Markov Chain Monte Carlo (MCMC) is used. MCMCs are a class of algorithms that sample a probability distribution, and are in part desirable because they give complete knowledge of the full posterior probability distribution. An MCMC consists of  $k \geq 1$  “walkers” with each walker representing an independent set of parameters  $\boldsymbol{\theta}_i$ . A large subpopulation of MCMC algorithms - including the method used in this analysis - use random walk Monte Carlo algorithms, meaning the walkers randomly sample the parameter space.

A MCMC runs for  $T$  iterations or “steps” so the total number of samples is  $k \times T$ . An array of  $k$  walkers of  $\boldsymbol{\theta}$  over  $T$  iterations forms a “chain” that contains the history of the walkers. Each sample contributes to the total integral. In looking for its next move a walker may make a number of trial steps around its perimeter looking for a point with a high integrand. A step is dependent solely on the current positions of all  $\boldsymbol{\theta}$ . Sometimes referred to as “memorylessness” this means that with respect to knowing only the walker’s current state, knowledge of its entire history would not improve predictions of its future state, i.e. a walker’s past and future states are

independent.

The next state in a Markov Chain is computed by

$$f^{(t+1)}(\theta) = \int f^{(t)}(\theta') p(\theta|\theta') d\theta' \quad (4.38)$$

where  $f^{(t)}, f^{(t+1)}$  are the marginal distributions at steps  $t$  and  $t + 1$  (to simplify notation  $\theta$  is used in place of multi-dimensional  $\boldsymbol{\theta}$ ). Therefore, beginning from step  $t$ , any state at  $m$  steps into the future can be computed. In the case when initial distribution  $f^{(0)}$  is given every state in the Markov Chain can be calculated.

A Markov Chain is *reversible* if there exists a probability density  $\pi(\theta')$  such that

$$\pi(\theta') p(\theta'|\theta) = \pi(\theta) p(\theta|\theta') \quad (4.39)$$

for some transition kernel probability density  $p(\theta'|\theta)$  that defines the probability of moving to state  $\theta'$  from  $\theta$  in one step. In other words, Eq. 4.39 states that being in state  $\theta$  and transitioning to  $\theta'$  must have the same probability as being in state  $\theta'$  and transitioning to  $\theta$ . When this is true for all pairs of  $\theta, \theta'$  (all states can communicate with one another) the Markov Chain is said to be *irreducible*. A chain that does not cycle to any state  $\theta$  in a predictable way is *aperiodic*. Eq. 4.39 is known as the *detailed balance condition* and cannot be solved for all Markov Chains. For those that can, a simple integration gives

$$\begin{aligned} \int \pi(\theta') p(\theta|\theta') d\theta' &= \int \pi(\theta) p(\theta'|\theta) d\theta' \\ &= \pi(\theta) \int p(\theta|\theta') d\theta' \\ &= \pi(\theta) \end{aligned} \quad (4.40)$$

which reveals  $\pi(\cdot)$  is a *stationary distribution*. Eq. 4.40 is a special case of Eq. 4.38 in that  $\pi(\cdot)$  is invariant across all iterations (for this reason it is also referred to as an *invariant distribution*). When  $p(\theta'|\theta)$  is irreducible and aperiodic it will have a single stationary distribution and is *ergodic*, or guaranteed to converge as  $t \rightarrow \infty$  regardless of initial distribution.

$$\lim_{t \rightarrow \infty} f^{(t)}(\theta) \rightarrow \pi(\theta) \quad \forall f^{(0)} \quad (4.41)$$

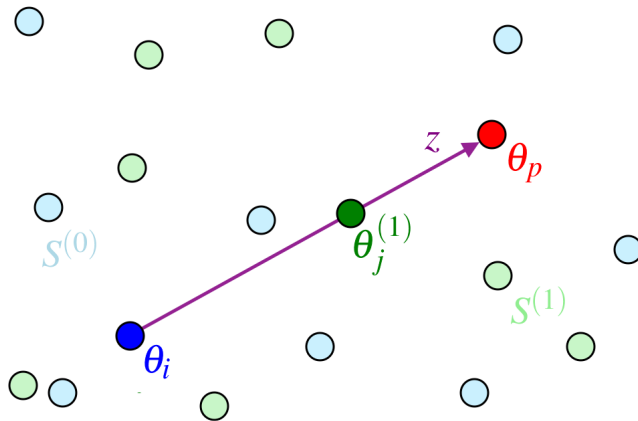


Figure 4.7: Proposed stretch move update step for walker  $\theta_i$  (blue) with the Affine-Invariant Ensemble Sampler MCMC in two dimensions. The proposed state  $\theta_p$  (red) uses the difference between  $\theta_i$  and a randomly selected walker  $\theta_j^{(1)}$  (green) from  $S^{(1)}$  and a scale factor  $z$ . Additional walkers from  $S^{(0)}$  (light blue) and  $S^{(1)}$  (light green) are shown.

A frequent objective in developing MCMC algorithms is to create Markov Chains that are reversible, ergodic, homogeneous (no variation in  $p(\boldsymbol{\theta}'|\boldsymbol{\theta})$  in  $t$ ), and has its target distribution as its stationary distribution.

$\boldsymbol{\theta}$  may contain parameters that are necessary for the model but of little interest, known as *nuisance parameters*,  $\boldsymbol{\theta}^{(N)}$  ( $\boldsymbol{\theta} = [\boldsymbol{\theta}^{(I)}, \boldsymbol{\theta}^{(N)}]$  with  $\boldsymbol{\theta}^{(I)}$  representing parameters of interest). It can often be the case that we wish to *marginalize*, or integrate over  $\boldsymbol{\theta}^{(N)}$

$$p(\boldsymbol{\theta}^{(I)}|\mathbf{x}, \boldsymbol{\alpha}) = \int_{\Theta^{(N)}} p(\boldsymbol{\theta}^{(I)}, \boldsymbol{\theta}^{(N)}|\mathbf{x}, \boldsymbol{\alpha}) d^{n^{(N)}} \boldsymbol{\theta}^{(N)} \quad (4.42)$$

though this in general may be difficult to compute. However, sampling from the MCMC posterior joint distribution  $p(\boldsymbol{\theta}^{(I)}, \boldsymbol{\theta}^{(N)}|\mathbf{x}, \boldsymbol{\alpha})$  naturally provides values for  $\boldsymbol{\theta}^{(I)}$  from the marginalized posterior  $p(\boldsymbol{\theta}^{(I)}|\mathbf{x}, \boldsymbol{\alpha})$ . This technique can be done in general for any number of parameters in  $\boldsymbol{\theta}$ . Often it is interesting to know the posterior of a single parameter, in which case all others would be marginalized over. This is an advantage over many other techniques.

MCMCs have become increasingly popular in recent years as advances in methods and computer processing speeds have made them a powerful tool that can be run in reasonable timescales. For this analysis an implementation by [218] of the Affine-

Invariant Ensemble Sampler proposed by [219] modified to allow stretch move update step parallelization is used as outlined below. A Differential Evolution Markov Chain (DEMC) is used in Sec. 5.4.2 for the electron lifetime analysis.

1. Initialize  $k$  walkers of  $n$ -dimensional parameter space to some state  $\boldsymbol{\theta}(t = 0)$  (for this analysis samples are randomly drawn from  $p(\boldsymbol{\theta}|\boldsymbol{\alpha})$ ).
2. Divide the ensemble into subsets  $S^{(0)} = \{\boldsymbol{\theta}_i, \forall i = 1, \dots, k/2\}$ , and  $S^{(1)} = \{\boldsymbol{\theta}_i, \forall i = k/2 + 1, \dots, k\}$ .
3. For each walker in  $S^{(0)}$  randomly select a walker  $\boldsymbol{\theta}_j^{(1)}$  from  $S^{(1)}$  and propose a new state

$$\boldsymbol{\theta}_p = \boldsymbol{\theta}_j^{(1)} + z[\boldsymbol{\theta}_i(t) - \boldsymbol{\theta}_j^{(1)}] \quad (4.43)$$

where  $z$  is randomly drawn from distribution  $g(z)$ . This affine-invariant stretch move is shown in Fig. 4.7. Choosing  $g(z^{-1}) = zg(z)$  keeps Eq. 4.43 symmetric - that is, the proposal distributions for  $\boldsymbol{\theta}_i \rightarrow \boldsymbol{\theta}_p$  and  $\boldsymbol{\theta}_p \rightarrow \boldsymbol{\theta}_i$  are equivalent. Choosing the acceptance probability of the proposed stretch move update step as

$$q = \min\left(1, z^{n-1} \frac{\mathcal{L}(\boldsymbol{\theta}_p)p(\boldsymbol{\theta}_p|\boldsymbol{\alpha}_p)}{\mathcal{L}(\boldsymbol{\theta}_i)p(\boldsymbol{\theta}_i|\boldsymbol{\alpha}_i)}\right) \quad (4.44)$$

ensuring the chain will satisfy detailed balance. [218] uses

$$g(z) \propto \begin{cases} \frac{1}{\sqrt{z}} & \text{if } z \in \left[\frac{1}{a}, a\right], \\ 0 & \text{otherwise} \end{cases} \quad (4.45)$$

with  $a$  as a scalable parameter as recommended by [219].

4. Generate a random number from a uniform distribution  $r \in [0, 1]$ . If  $r \leq q$  then accept proposed state  $\boldsymbol{\theta}_i(t+1/2) = \boldsymbol{\theta}_p$ , otherwise keep present state  $\boldsymbol{\theta}_i(t+1/2) = \boldsymbol{\theta}_i(t)$ .
5. Set  $t = t + 1/2$ .
6. Repeat steps 3–5 for  $S^{(1)}$  using the updated  $S^{(0)}$ .
7. Repeat 3–6 for  $T$  iterations.

The advantage of the above implementation is the computationally expensive stretch move update steps (3–5) are run for each walker in parallel, saving enormous amounts of time with sufficient computing power. Running all  $k$  walkers in parallel would break detailed balance, but splitting into two groups satisfies it.

Because the Affine-Invariant Ensemble Sampler satisfies Eq. 4.41 it is guaranteed to converge as  $t \rightarrow \infty$ . However, having a finite number of samples allows us to test for convergence, though it can never be proved. An important metric for evaluating the results is the acceptance fraction  $\mathcal{F}$ . This is the fraction of proposed stretch move update steps that are accepted by a walker (step item 4). There is no consensus on an optimal value.  $\mathcal{F} \sim 0$  would mean nearly all steps are rejected so there would be few independent samples and the target density would be poorly explored.  $\mathcal{F} \sim 1$  means nearly every proposal is accepted in which case the chain is in a random walk with little regard for the posterior. A reasonable range is considered to be 0.2–0.5.

Thus  $\mathcal{F}$  is the fraction of proposals that are accepted over the course of the fit. Even if the posterior of  $\theta_p$  is less than that of  $\theta_i$  the proposal may be accepted. We do not need to know the marginal likelihood (Eq. 4.37) to perform an Affine-Invariant Ensemble Sampler MCMC fit.

A metric to assess convergence is the autocorrelation time, which measures the number of evaluations to produce independent samples of the target density and is recommended by [218]. The Affine-Invariant Ensemble Sampler has been shown to have a smaller autocorrelation time than the popular Metropolis-Hastings algorithm [219]. The autocorrelation time is affine-invariant, which makes it a reasonable measurement to quantify the convergence of samplers with varying levels of density anisotropy.

A second metric and the main one used in this analysis is the Gelman-Rubin statistic  $\hat{R}$  [220]. It compares the average variance of the individual chains with the variance between chains, with the idea being the two should be nearly equivalent when the fit has converged.

For this analysis the electronic and nuclear recoil bands are fit with  $n = 44$  parameters and an Affine-Invariant Ensemble Sampler with  $k = 200$  walkers over

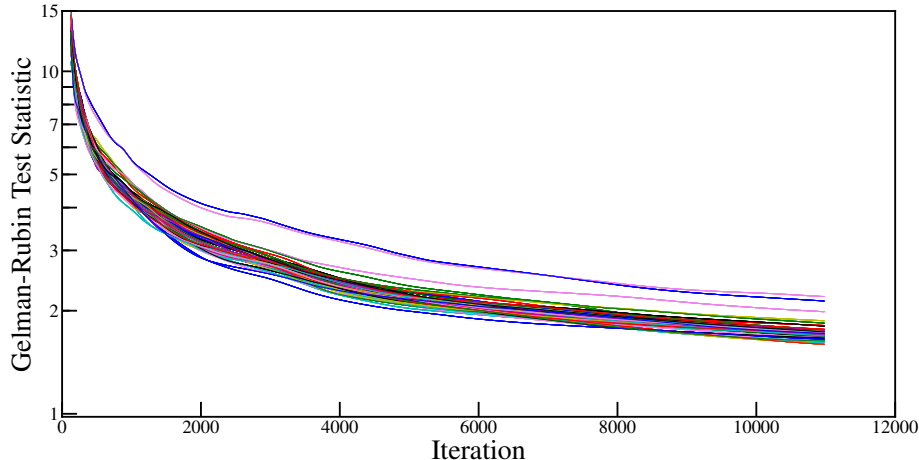


Figure 4.8: Gelman-Rubin test statistic for the electronic and nuclear recoil band fitting.

11,000 steps.

## 4.3 Results

With the model and statistical inference outlined in Sec. 4.2 the results are now presented. A “burn-in” period exists in the beginning of the MCMC as walkers move from their initialized values to fill the parameter space that should be ignored in the posterior. For this analysis the burn-in lasted  $\sim 1000$  iterations. The posterior of the MCMC fit is defined as the final 1000 iterations for the 200 walkers. Marginalized posteriors in Tab. 4.2–4.4 are calculated using these 200,000 samples. Medians and credible regions shown in figures are computed using 400 samples randomly drawn from the posterior. The Gelman-Rubin statistic in this region is shown in Fig. 4.8 and is  $\sim 2$ . Ideally it would be closer to 1 but time restrictions did not allow continued fitting. Regardless,  $\hat{R} \sim 2$  indicates the fit is likely close to the best-fit PDF, though as mentioned above convergence can never be proven for a finite number of steps.

### 4.3.1 Detector Physics Model and Backgrounds

Once the microphysics of the interaction has occurred (results in Sec. 4.3.3), the photons and  $e^-$  are influenced by detector effects (Sec. 4.2.3). In addition, an S2

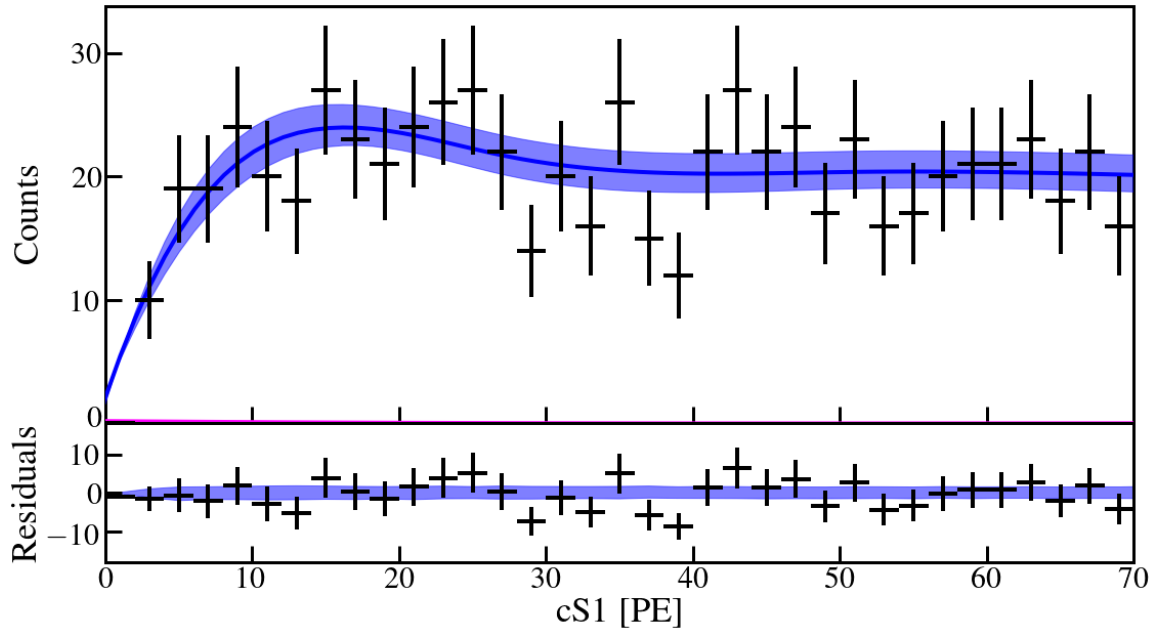


Figure 4.9: cS1 for SR0  $^{220}\text{Rn}$  calibration. The median and 68% credible region from the posterior are shown as the solid lines and shaded regions, respectively, and matches the data well. Aside from  $^{220}\text{Rn}$ , the only contributor to data is accidental coincidence, which has a small contribution and is visible in pink at the bottom. The sum of AC and  $^{220}\text{Rn}$  is shown in blue.

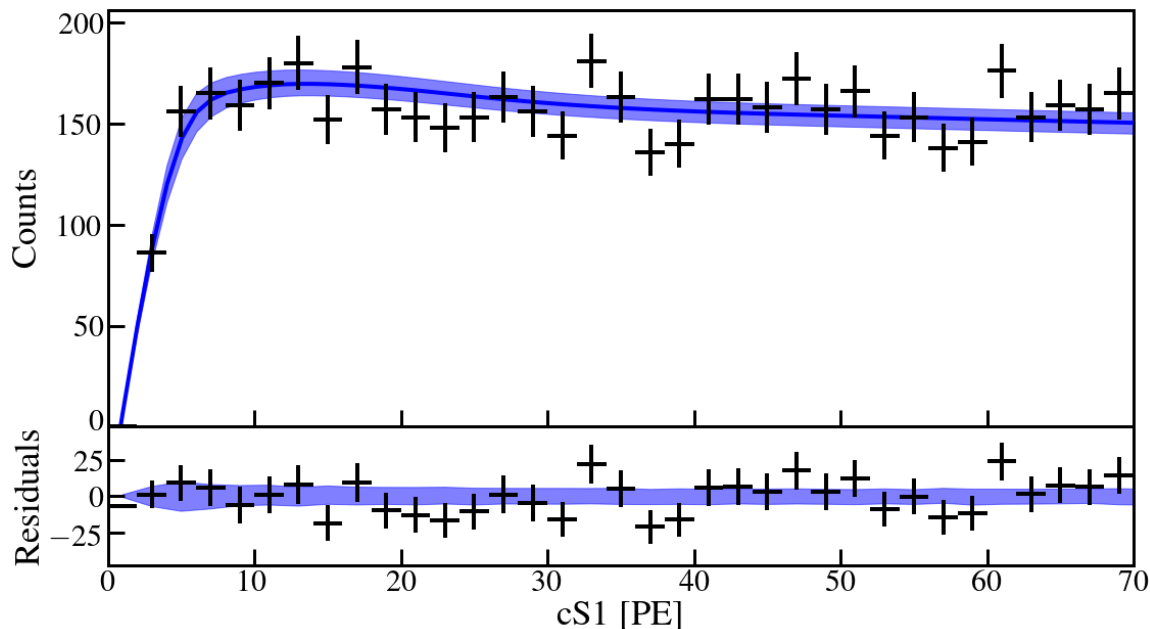


Figure 4.10: cS1 for SR1  $^{220}\text{Rn}$  calibration. The median and 68% credible region match the data well. AC is shown in pink at the bottom of the plot. The sum of  $^{220}\text{Rn}$  and AC are shown in blue.

#### 4. ELECTRONIC AND NUCLEAR RECOIL CALIBRATIONS

---

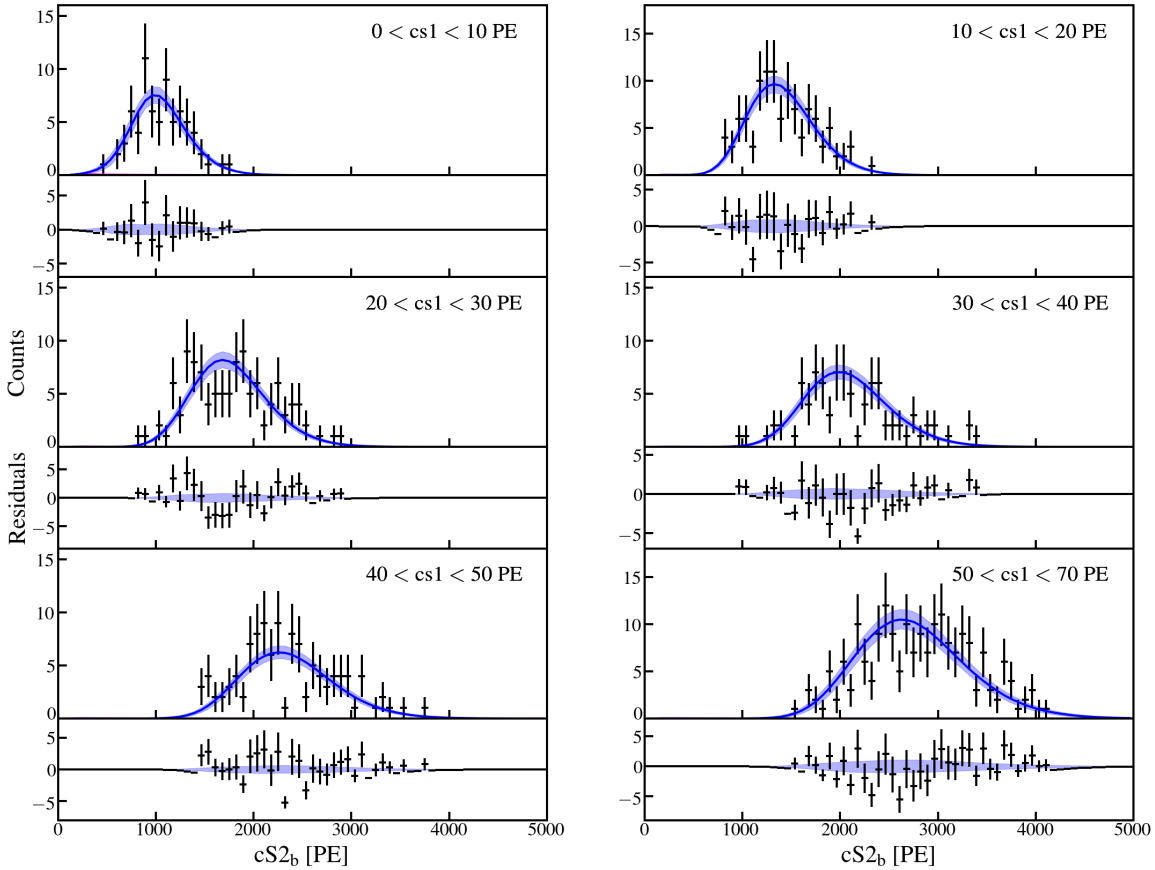


Figure 4.11:  $cS2_b$  for SR0  $^{220}\text{Rn}$  data with median and 68% credible interval in slices of  $cS1$ . The model matches the data well, with the possible exception of the  $50 < cS1 < 70$  PE slice where the model may predict slightly lower  $cS2_b$ , but limited statistics make it difficult to tell.

threshold requirement, S1 peak finding efficiency, and S1 and S2 selection efficiencies remove some events (results in Sec. 4.3.2). Parameters are shared within and across science runs and listed in Tab. 4.2.

Accidental coincidence and electronic recoil backgrounds during calibrations (surface events are absent or negligible at  $r_{\text{rec}} < 36.94$  cm) are considered. AC distributions and expectations are computed separately for each source and tightly constrained by the method in Sec. 4.2.5. SR0 and SR1  $^{220}\text{Rn}$  calibrations are constrained by a single parameter since they are expected to be correlated as  $R_{\text{AC}}^{(\text{SR1})} = 3.75R_{\text{AC}}^{(\text{SR0})} - 0.0625$ . ER backgrounds - only relevant for  $^{241}\text{AmBe}$  and NG (for  $^{220}\text{Rn}$  it simply contributes to the ER band) - is required to be  $\geq 0$  but otherwise is unconstrained. The initial values, ranges, and posteriors are given in

Parameter	Value	Units	Prior Distribution	Posterior	Comment
$\eta_{EE,SR0}$	0.936	—	Fixed	—	SR0 extraction efficiency
$\eta_{EE,SR1}$	0.933	—	Fixed	—	SR1 extraction efficiency
$\sigma_{G,SR0}$	0.240	—	Fixed	—	SR0 gas gain resolution
$\sigma_{G,SR1}$	0.250	—	Fixed	—	SR1 gas gain resolution
$v_{d,SR0}$	0.144	$\text{mm } \mu\text{s}^{-1}$	Fixed	—	SR0 drift velocity
$v_{d,SR1}$	0.134	$\text{mm } \mu\text{s}^{-1}$	Fixed	—	SR1 drift velocity
$f_{\text{aft}}$	0.627	—	Fixed	—	S2 fraction by top PMTs
$E_{d,SR0}$	120	$\text{kV cm}^{-1}$	Fixed	—	SR0 drift field
$E_{d,SR1}$	82	$\text{kV cm}^{-1}$	Fixed	—	SR1 drift field
$g_1$	$0.1424 \pm 0.0062$	PE/ph	Normal	$0.142^{+0.005}_{-0.005}$	Eq. 4.22
$g_{2b}$	$11.44 \pm 0.20$	PE/e <sup>-</sup>	Normal	$11.38^{+0.18}_{-0.18}$	Eq. 4.30
$p_{\text{dpe}}$	0.18-0.24	—	Uniform	$0.219^{+0.015}_{-0.024}$	Eq. 4.22, Eq. 4.23, [178]
$\sigma_{e,SR1}$	$0 \pm 0.02$	—	Normal	$0.006^{+0.012}_{-0.011}$	$\sigma_{e,SR0} = 2\sigma_{e,SR1}$ , Eq. 4.26
Multiscatter Cut	0-1	—	Uniform	$0.52^{+0.34}_{-0.38}$	
$\mu_{b,S1}$	0-1	—	Uniform	$0.63^{+0.25}_{-0.40}$	Eq. 4.24
$\sigma_{b,S1}$	0-1	—	Uniform	$0.32^{+0.39}_{-0.25}$	Eq. 4.24
$\mu_{b,S2}$	0-1	—	Uniform	$0.45^{+0.37}_{-0.29}$	Eq. 4.32
$\sigma_{b,S2}$	0-1	—	Uniform	$0.52^{+0.35}_{-0.34}$	Eq. 4.32
S2 Threshold	200	PE	Fixed	—	Cut
S1 Peak-Finder Efficiency	$0 \pm 1$	—	Normal	$-0.25^{+0.93}_{-0.98}$	
S1 Cut Efficiency	$0 \pm 1$	—	Normal	$0.08^{+0.92}_{-1.17}$	
S2 Cut Efficiency	$0 \pm 1$	—	Normal	$-0.1^{+1.1}_{-1.0}$	

Table 4.2: Median and 68% credible intervals for detector, processor, and analysis effects from the posterior of the fit. Biases and smearings are constrained between their lower (0) and upper (1) limits. S1 peak finding efficiency and selection efficiencies are constrained by a normal distribution centered at the 50th percentile, with standard deviation ( $\pm 1$ ) representing the 16th and 84th percentiles. Biases, smearings, selection efficiencies, and S1 peak finding efficiencies are expected to be equally impacted by systematic effects so the relative deviation is correlated between the three inputs ( ${}^{241}\text{AmBe}$  SR0, SR0, and SR1) for each parameter.

Tab. 4.3. Fig. 4.15–4.23 show the AC and ER spectra.

Some portion of events in the  ${}^{241}\text{AmBe}$  and NG data are from neutrons that scatter more than once in the TPC. As mentioned in Sec. 4.2.4, a single scatter selection is applied to remove multiple-scatter events. However, it can be difficult in some cases to determine if in fact additional scatters occurred - particularly at low energy. The fast MC framework applies the same selection used on the data to replicate this effect as closely as possible. Extracting the spectra of single and multiple scatters separately provides a powerful tool to examine this. The  ${}^{241}\text{AmBe}$  (Fig. 4.15–4.20) and NG (Fig. 4.21–4.23) figures show the single- and multiple-scatter contributions in cS1, cS2<sub>b</sub>, and cS1- $\log_{10}(cS2_b/cS1)$ .

#### 4. ELECTRONIC AND NUCLEAR RECOIL CALIBRATIONS

---

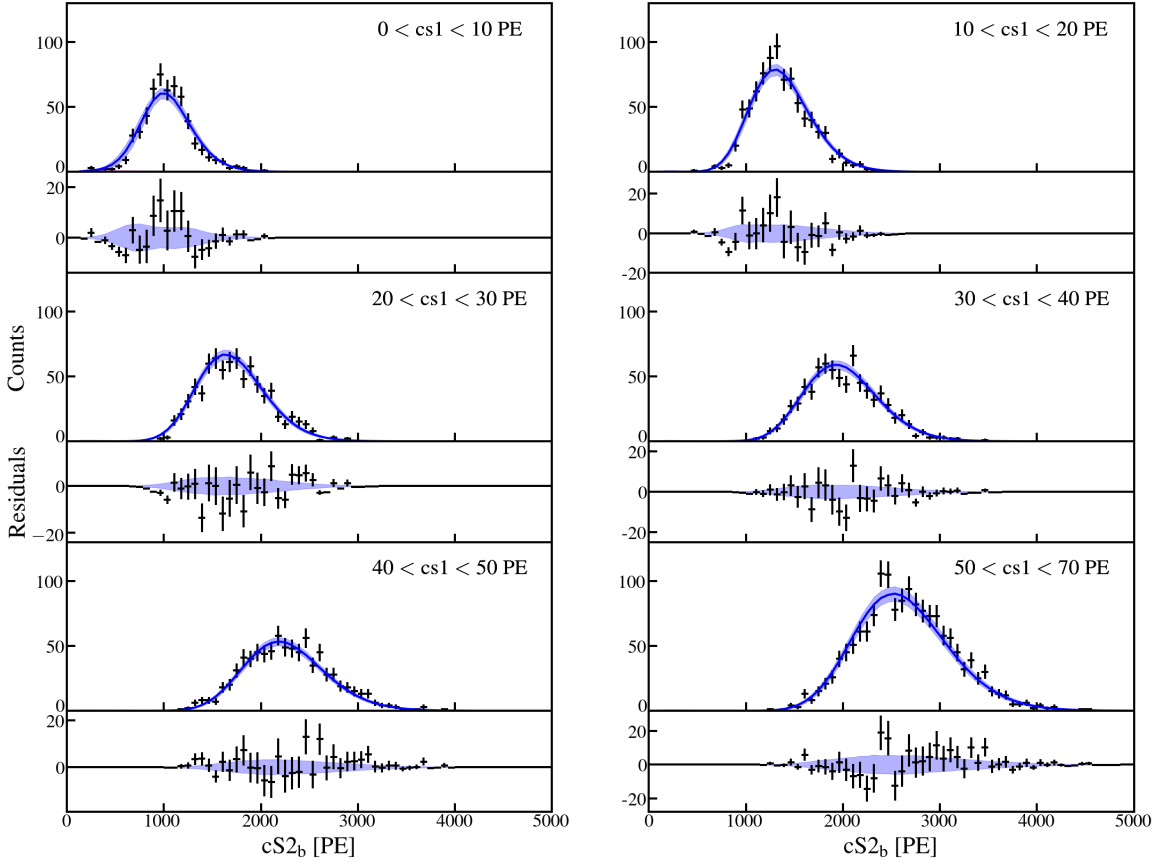


Figure 4.12:  $cS2_b$  for SR1  $^{220}\text{Rn}$  calibration in slices of  $cS1$ . The results from the band fitting match the data well, though in the  $0 < cS1 < 10 \text{ PE}$  slice the data may follow a slightly narrower distribution, and the  $50 < cS1 < 70 \text{ PE}$  slice, which similar to the SR0 results (Fig. 4.11) suggests the model predicts lower  $cS2_b$ .

The fraction of  $^{241}\text{AmBe}$  data that comes from single scatters is  $f_{^{241}\text{AmBe},\text{ss}} = 0.6742_{-0.0081}^{+0.0096}$  (fraction of multiple scatters is  $f_{^{241}\text{AmBe},\text{ms}} = 0.3258_{-0.0096}^{+0.0081}$ ). For NG data it is  $f_{\text{NG},\text{ss}} = 0.6483_{-0.0079}^{+0.0092}$  ( $f_{\text{NG},\text{ms}} = 0.3517_{-0.0092}^{+0.0079}$ ). Despite the single scatter selection roughly one third of events in the final data come from multiple scatters. This is because the vast majority of events occur at low energy, which is where the selection is least effective. Because multiple-scatter neutrons are considered in the fast MC this should not have a large bias on our final result.

The fraction of nuclear recoil events that scatter more than once and pass the multiple scatter (and other) selection for the SR1  $^{241}\text{AmBe}$  calibration is shown in Fig. 4.24. Because S1s cannot be resolved, events with multiple scatters will have an inflated S1. The resulting decrease in  $\log_{10}(cS2_b/cS1)$  will become more dramatic

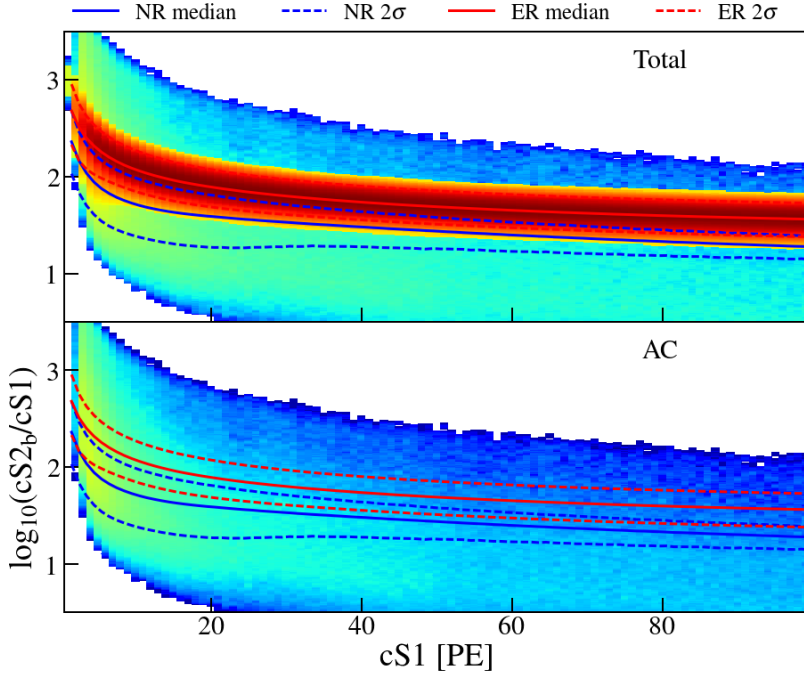


Figure 4.13:  $cS1 \cdot \log_{10}(cS2_b/cS1)$  distribution for the SR0  $^{220}\text{Rn}$  calibration. Electronic (red) and nuclear (blue) recoil (calculated using SR0  $^{241}\text{AmBe}$  fit) medians and  $\pm 2\sigma$  are marked in solid and dashed lines. Accidental coincidence is shown in the bottom panel.

Parameter	Prior Value	Prior Distribution	Posterior	Comment
Science Run 0 $^{220}\text{Rn}$	$\geq 0$	Free	$996^{+89}_{-70}$	Shared with SR1
	$1.59 \pm 0.32$	Normal	$1.62^{+0.31}_{-0.33}$	
Science Run 0 $^{241}\text{AmBe}$	$\geq 0$	Free	$1980^{+114}_{-118}$	
	$1.6 \pm 0.32$	Normal	$1.701^{+0.270}_{-0.325}$	
	$\geq 0$	Free	$0.248^{+0.047}_{-0.033}$	
Science Run 1 $^{220}\text{Rn}$	$\geq 0$	Free	$7528^{+211}_{-278}$	Shared with SR0
	$5.9 \pm 1.2$	Normal	$6.32^{+1.01}_{-1.22}$	
Science Run 1 $^{241}\text{AmBe}$	$\geq 0$	Free	$2020^{+131}_{-131}$	
	$1.6 \pm 0.32$	Normal	$1.69^{+0.36}_{-0.32}$	
	$\geq 0$	Free	$0.031^{+0.014}_{-0.011}$	
Science Run 1 NG	$\geq 0$	Free	$2058^{+137}_{-125}$	
	$7.94 \pm 1.588$	Normal	$8.6^{+1.5}_{-1.7}$	
	$\geq 0$	Free	$0.0127^{+0.010}_{-0.007}$	

Table 4.3: Accidental coincidence and electronic recoil background distributions for  $^{220}\text{Rn}$ ,  $^{241}\text{AmBe}$ , and NG calibrations calculated using the posterior of the band fits. AC is tightly constrained via the method outlined in Sec. 4.2.5. ER background in  $^{241}\text{AmBe}$  and NG data is left free.

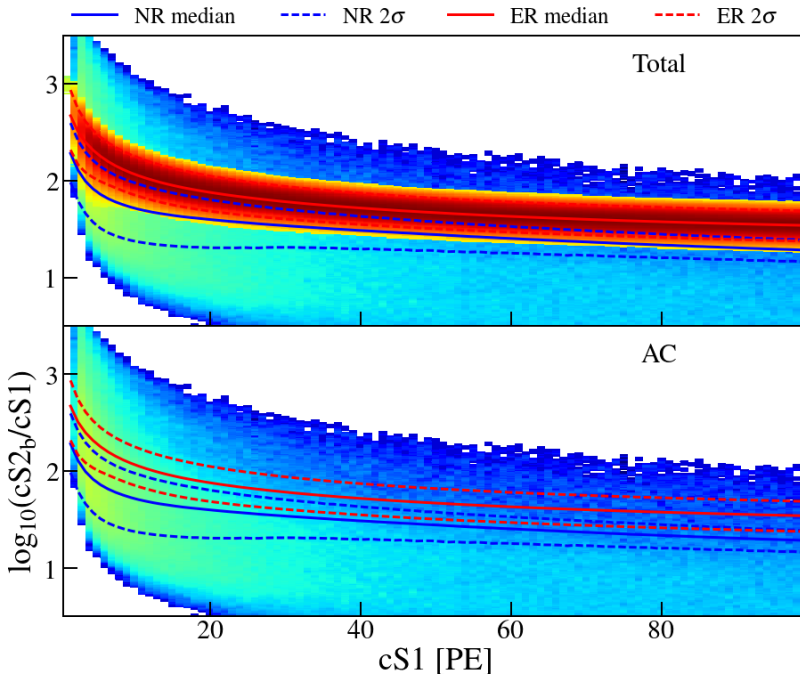


Figure 4.14:  $cS1 \cdot \log_{10}(cS2_b/cS1)$  distribution for the SR1  $^{220}\text{Rn}$  calibration. Electronic recoil median and  $\pm 2\sigma$  are shown as red solid and dashed lines. Nuclear recoil are computed using the SR1  $^{241}\text{AmBe}$  calibration fit and shown in blue.

for events with a larger number of scatters. In addition, the LCE map correction (Eq. 4.25) uses the position of the highest-energy event. This increases the spread in the  $cS1$  distribution since additional scatters in lower or higher LCE region will be under- or over-corrected, respectively. As the highest-energy event increases, the relative effect becomes smaller since the multiple scatter cut prevents large secondary  $S2_b$  and therefore large  $S1$ s.

### 4.3.2 Acceptances

The acceptances are calculated using 400 randomly-drawn samples from the posterior and an expected WIMP spectrum. While the 1.3 t fiducial mass is used for the dark matter analysis, the acceptances are calculated using the 1 t mass from the band fit, though they are not expected to differ significantly. The posterior for the  $S1$  peak-finding efficiency and  $S1$  and  $S2$  cut efficiencies are listed in Tab. 4.2. They, along with the  $S2$  and  $cS1$  thresholds, are shown in Fig. 4.25 for SR0 and SR1. The  $S1$

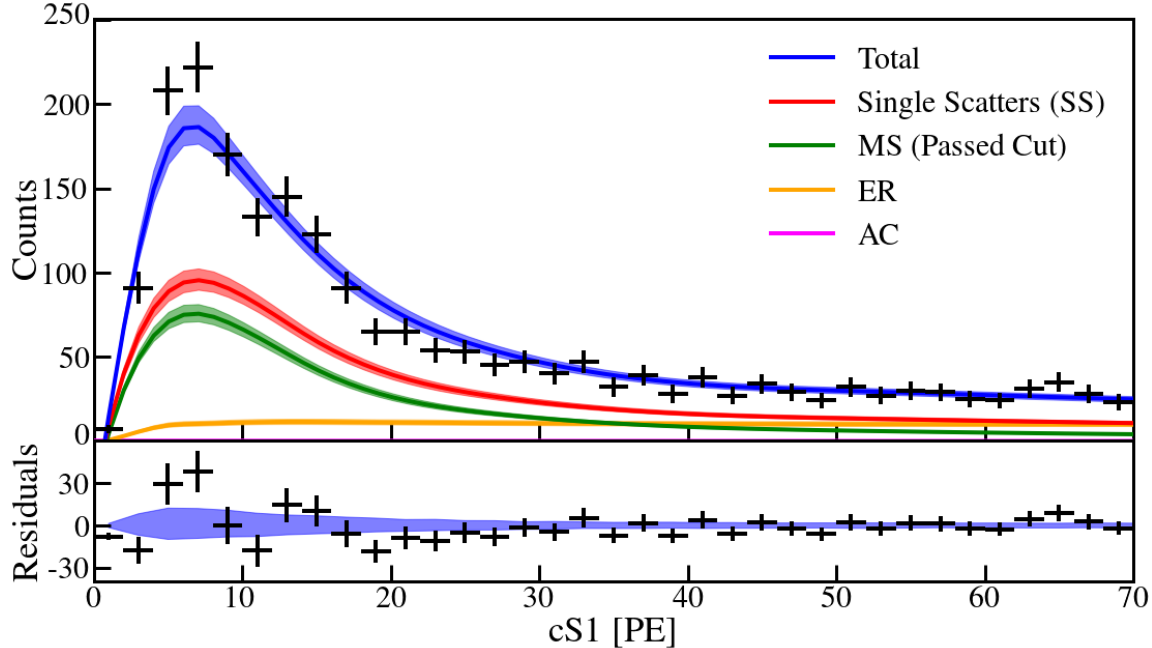


Figure 4.15: cS1 for SR0  $^{241}\text{AmBe}$  calibration. The total number of events (blue) agrees reasonably well with the data. Single- (red) and multiple-scatter (green) neutrons are shown. Multiple-scatters make up a larger fraction of events at low cS1. Electronic recoils (gold) make up a decent fraction of the total events, especially at  $\text{cS1} \gtrsim 50$  PE where they are >30%. Accidental coincidence is barely visible along the bottom and is expected to be responsible for  $\sim 2$  events.

and S2 cut efficiencies (Sec. 4.2.4) are shown in pink and light blue, and show little variation across energy. The S2 threshold is only relevant at low energies ( $\lesssim 5 \text{ keV}_{\text{nr}}$ ) and is highlighted in green. The processor efficiency is marked in red.

The cS1 threshold  $3 \leq \text{cS1} \leq 70$  PE (blue in Fig. 4.25) marks the energy region of interest, corresponding to roughly  $[1.4, 10.6]$   $\text{keV}_{\text{ee}}$  and  $[4.9, 40.9]$   $\text{keV}_{\text{nr}}$ . The total acceptance is the product of the acceptances shown in Fig. 4.25. Effects from events that are gained or lost at the edge of the fiducial volume are expected to be small so are not considered.

Fig. 4.26 (redrawn from Sec. 4.3.2) shows the efficiencies for 1) S1 peak finding (“Detection”), 2) S1 peak finding and S1 and S2 selections (“Selection”), 3) total, excluding the reference region (“Energy region”), and 4) total, including the reference region (“Reference”).

The acceptances are used in the likelihood calculation in Sec. 3.4.3.

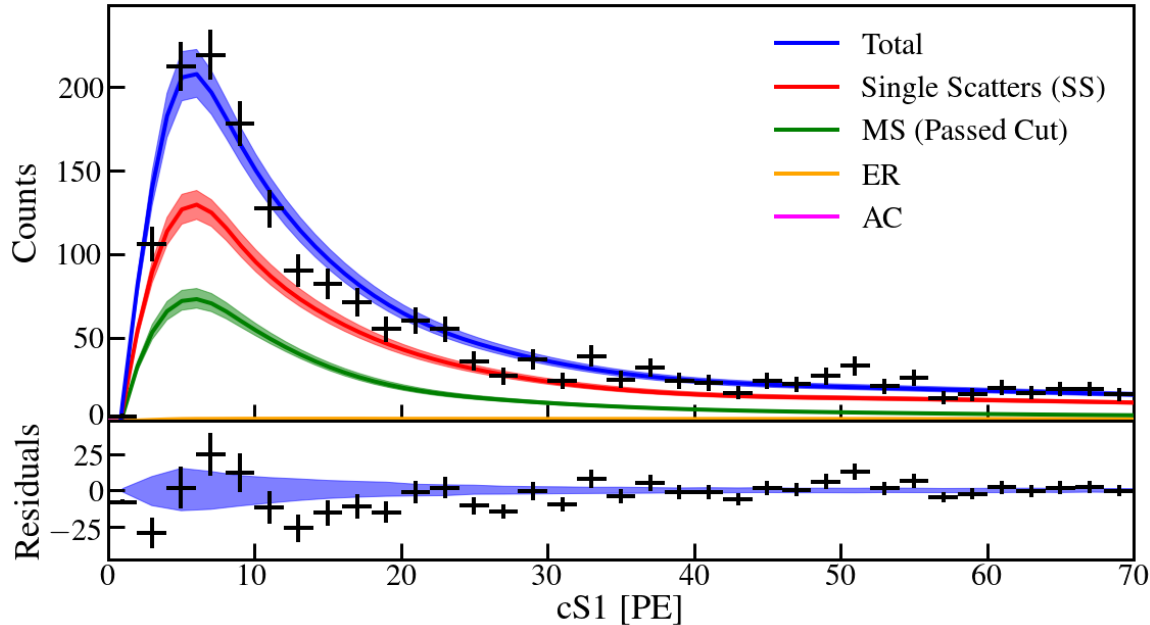


Figure 4.16:  $cS1$  for SR1  $^{241}\text{AmBe}$  calibration. The total number of events from the band fitting (blue) is compared with data. Single- (red) and multiple-scatter (green) nuclear recoils are shown. The fraction of multiple-scatter events increases at low  $cS1$ . The low-ER background (gold) and AC (pink) contribute  $\sim 60$  and  $\lesssim 2$  events, respectively.

### 4.3.3 Light and Charge Yields

In Sec. 4.2.1 and 4.2.2 the number of photons and electrons produced were calculated for electronic and nuclear recoils using models that describe the microphysics of xenon interactions. Because dark matter searches rely on energy reconstruction, having dependable models is crucial. Values are quoted as light (or photon) yield,  $L_y$ , and charge (or electron) yield  $Q_y$  and are defined as  $n_{\text{ph}}/E$  and  $n_e/E$ , respectively.

The microphysics model for electronic recoils depends on the mean energy per quanta  $W$ , Fano Factor  $F$ , and exciton-to-ion ratio  $n_{\text{ex}}/n_{\text{ion}}$ . Recombination is computed using a modified Thomas-Imel box model (Eq. 4.4) and recombination fluctuations (Eq. 4.5). The priors and marginalized posteriors are shown in Tab. 4.4.

Fig. 4.27 shows the light and charge yields for electronic recoils for this result along with values from previous experiments. Because the ER model parameters were not constrained (aside from physical restrictions) our result is an independent measurement of  $L_y$  and  $Q_y$ . Our  $82 \text{ V cm}^{-1}$  seems to be higher (lower) in  $L_y$  ( $Q_y$ )

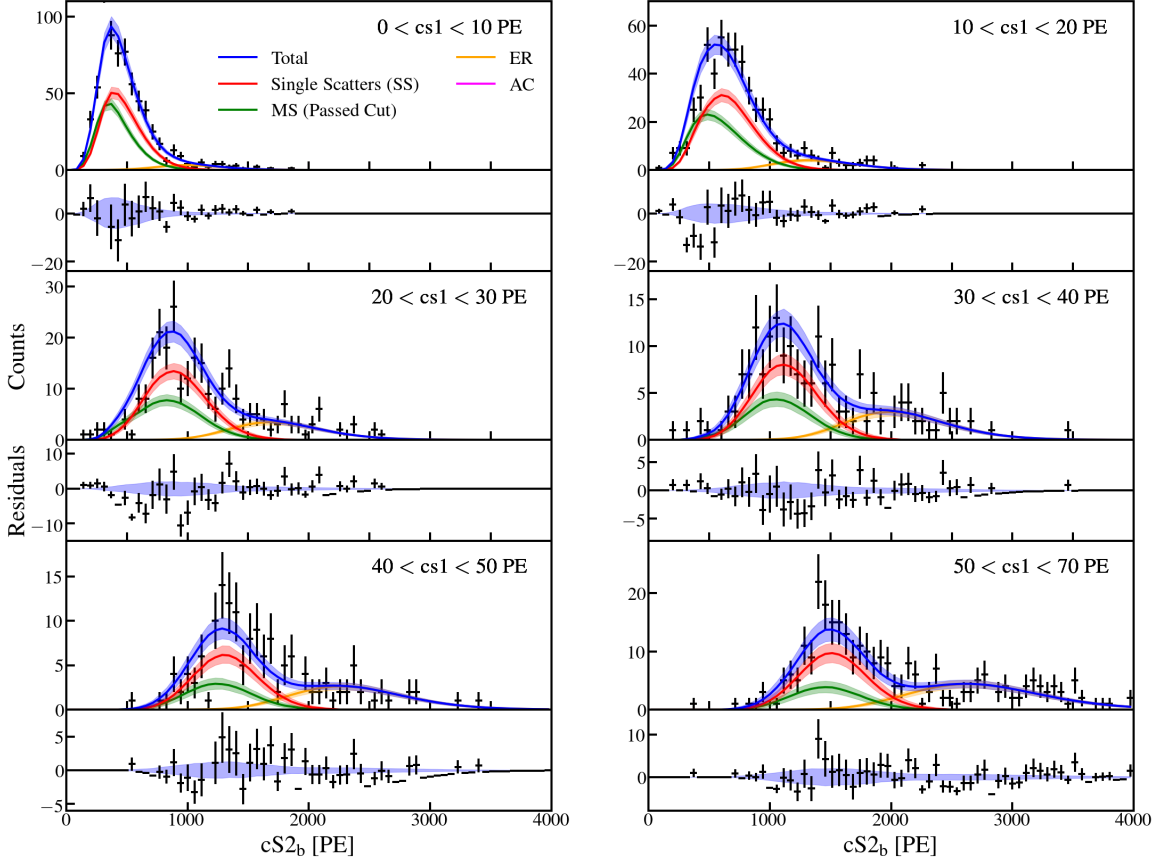


Figure 4.17:  $cS2_b$  in slices of  $cS1$  for SR0  $^{241}\text{AmBe}$  data. The band fitting results (blue) match the data nicely. The ratio of multi- (green) to single-scatter (red) neutrons is higher at low  $cS2_b$ . The electronic recoil band (gold) is easily visible. AC (pink) is too low to observe.

at  $E \gtrsim 2$  keV than other measurements, while the  $200 \text{ V cm}^{-1}$  agrees well with all but the PIXeY  $^{37}\text{Ar}$ . However, we should be careful when comparing measurements since different electric fields change the  $L_y/Q_y$  ratio.

The microphysics for nuclear recoils is described by  $\alpha, \zeta, \beta, \gamma, \delta, k, \eta$ , and  $\lambda$ . It shares only one parameter,  $W$ , with the electronic recoil model. The exciton-to-ion ratio is parameterized differently than for electronic recoils. To date, recombination fluctuations (RFs) have not been observed for nuclear recoils so they are omitted from the model. The priors and marginalized posteriors are shown in Tab. 4.4. Because asymmetric gaussian distributions are not used, the uncertainties differ slightly from the NEST results (Tab. 4.1), with generally the larger of the two selected [173].

Historically nuclear recoil light yield measurements have been quoted as  $\mathcal{L}_{eff}$ , the

#### 4. ELECTRONIC AND NUCLEAR RECOIL CALIBRATIONS

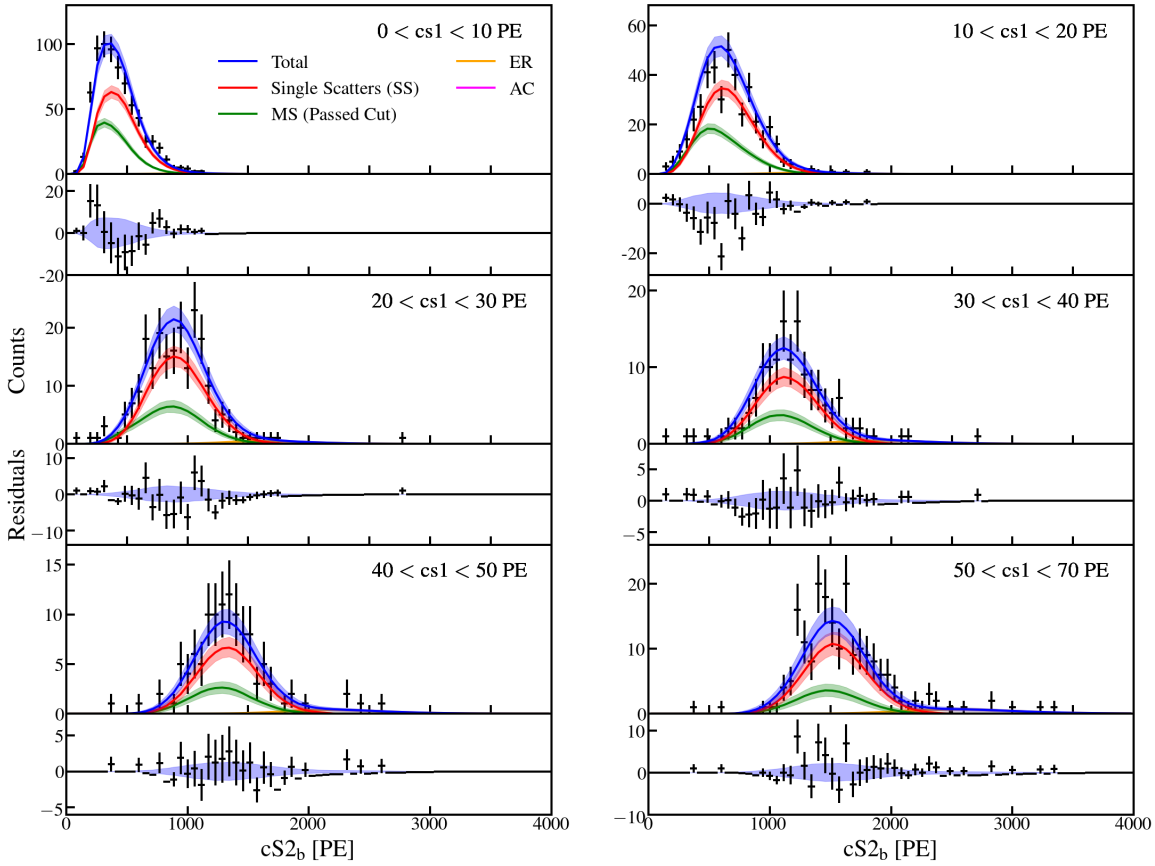


Figure 4.18:  $cS2_b$  for SR1  $^{241}\text{AmBe}$  calibration data in slices of  $cS1$ . The median and 68% credible interval of the fit (blue) is compared to the data. Single-scatter (red) and multiple-scatter (green) nuclear recoils, ER (gold), and AC (pink) are shown. The ER background contributes only  $\sim 3\%$  of all events. AC is too small to be visible.

ratio of scintillation yields of nuclear recoils to that of the  $^{57}\text{Co}$  122 keV  $\gamma$ -ray at zero electric field. This was done in part to account for detector effects so long as a second measurement with  $^{57}\text{Co}$  was performed. 122 keV photons have an attenuation length of just 3 mm so can probe only the very outermost region of tonne-scale TPCs. Therefore the absolute light yield  $L_y = \mathcal{L}_{eff} \times 63 \text{ ph keV}^{-1}$  has become the standard notation. Fig. 4.28 shows the light and charge yields for nuclear recoils. Unlike the electronic recoil result, this is not an independent measurement of  $L_y$  and  $Q_y$  since the emission model parameters are constrained by [173]. The  $L_y$  agrees well at  $\gtrsim 3$  keV but there is larger disagreement in  $Q_y$ . Strangely, it diverges significantly at  $E > 40$  keV where our acceptance is high ( $\sim 80\%$ ). As with Fig. 4.27 we should exercise caution when comparing yields at different fields, though the effect for nuclear

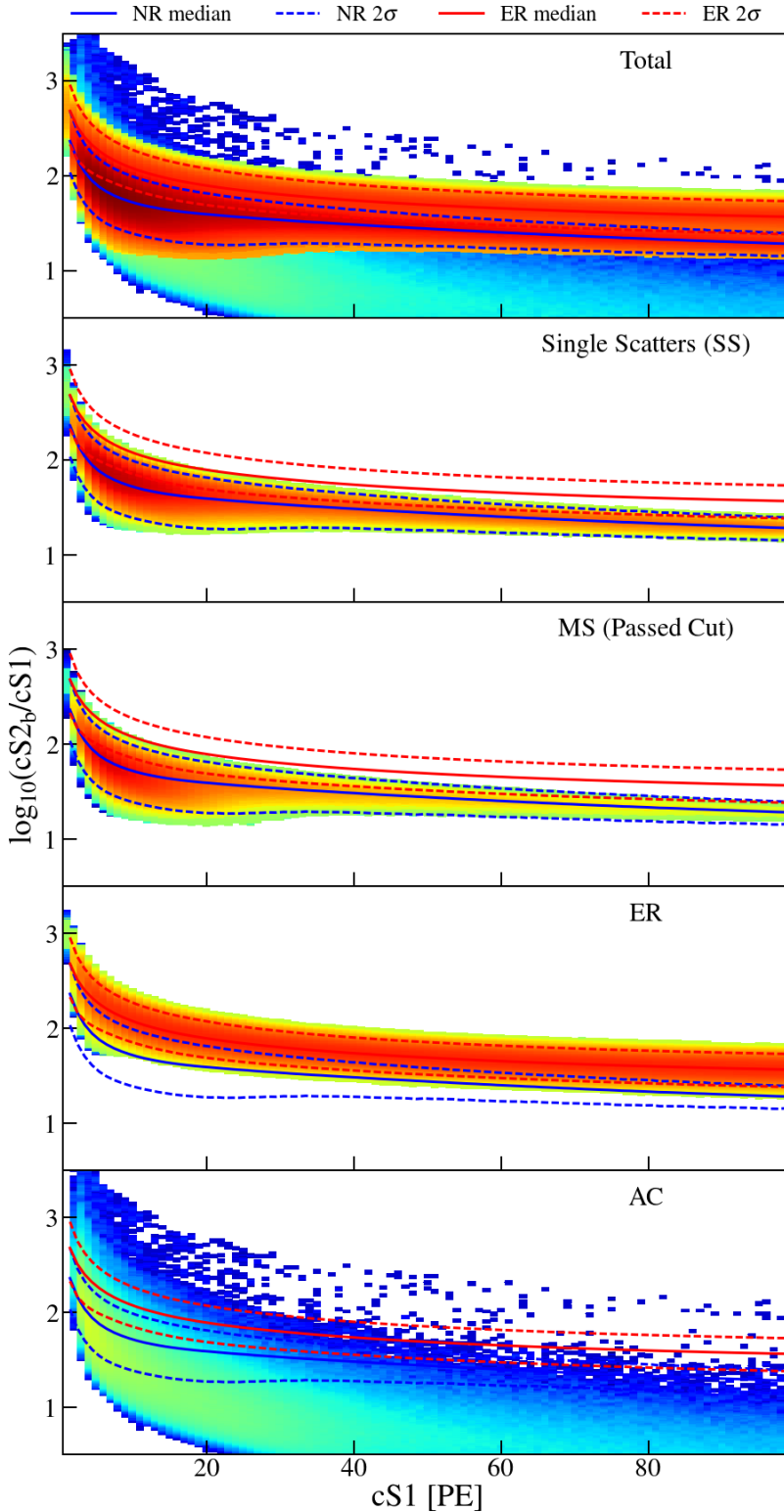


Figure 4.19:  $cS1 \cdot \log_{10}(cS2_b/cS1)$  distribution for the SR0  $^{241}\text{AmBe}$  calibration. The top panel shows the total while the rest show the contributions from different components normalized with respect to the total. Medians and  $\pm 2\sigma$  from electronic (red) and nuclear (blue) recoil bands are shown as solid and dashed lines. The ER lines are taken from SR0 ER band fit.

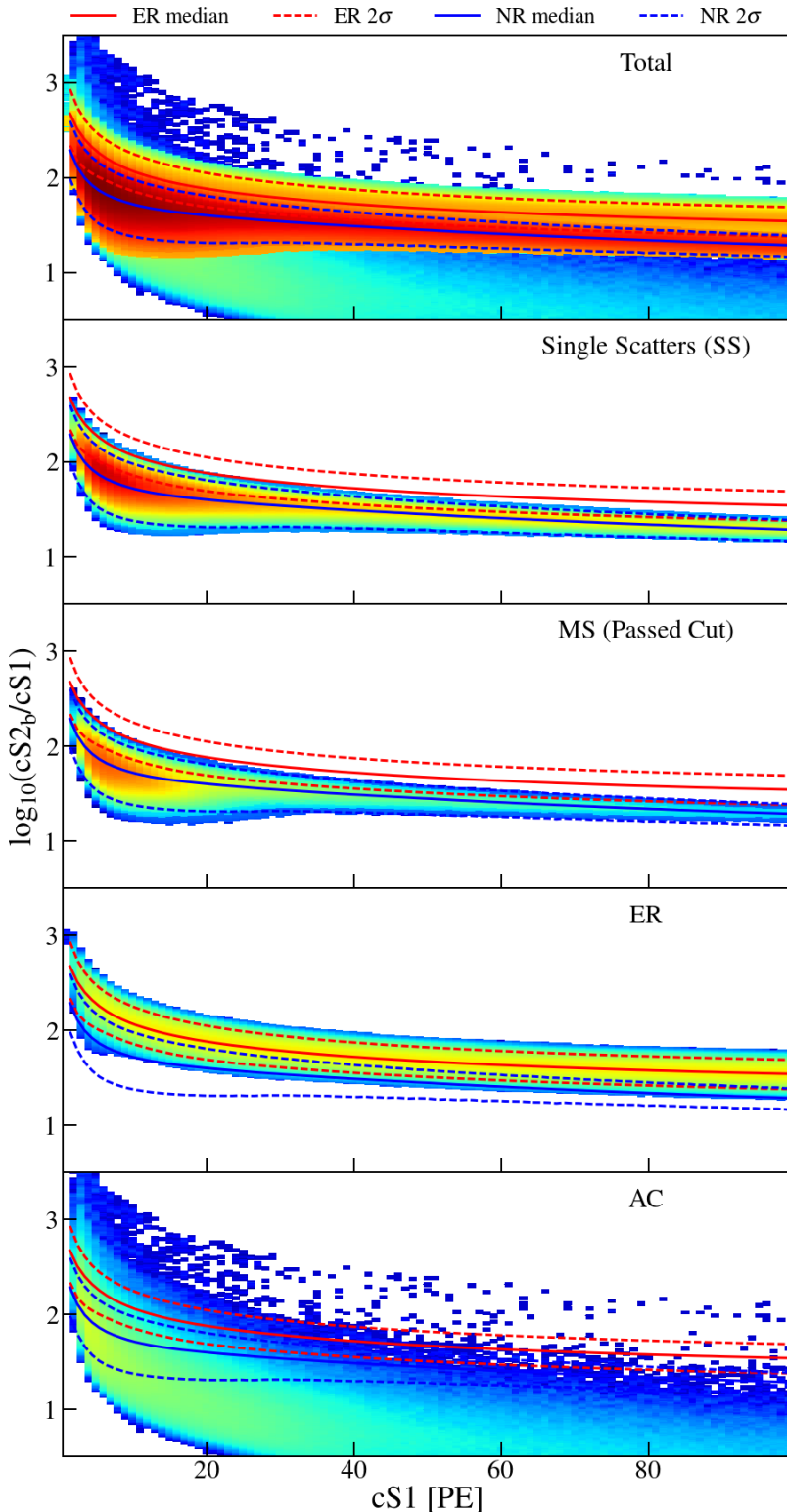


Figure 4.20:  $cS1-\log_{10}(cS2_b/cS1)$  distribution for the SR1  $^{241}\text{AmBe}$  calibration. The total is shown in the top panel with the separate contributors displayed below. The electronic recoil band median and  $\pm 2\sigma$  are derived from the SR1 ER band from the fit. Nuclear recoil lines are blue.

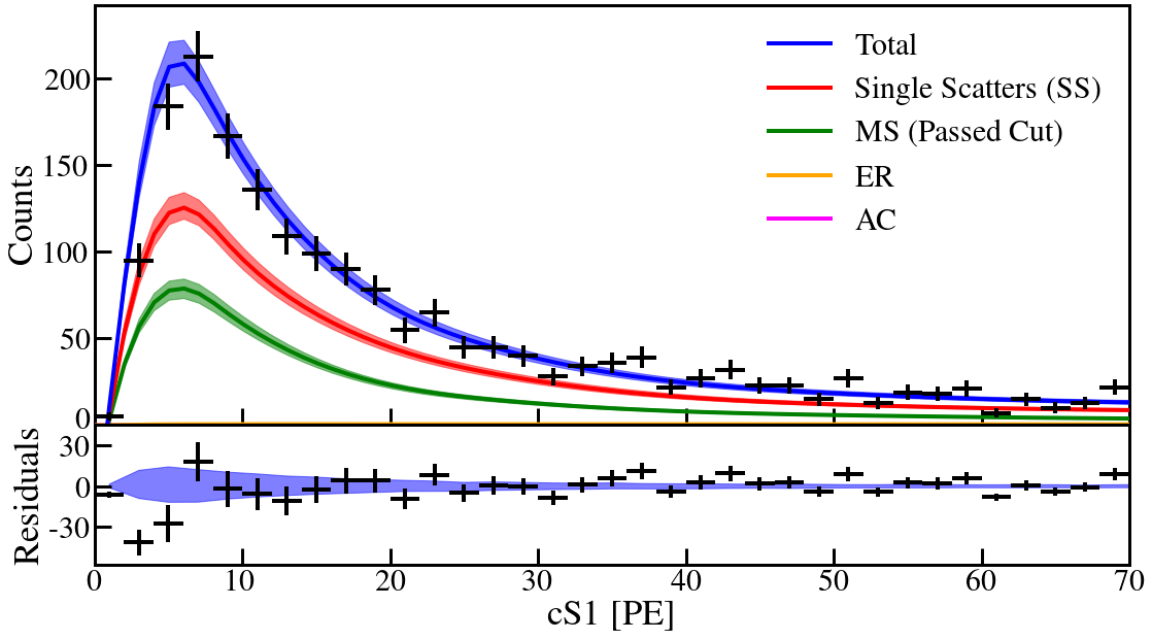


Figure 4.21:  $cS1$  for NG calibration. The fit agrees with the data. Single-scatter (red) and multiple-scatter (green) neutrons are shown. ER background (gold) is responsible for  $\lesssim 25$  events. Accidental coincidence (pink) is too small to be observed but makes up 7-10 events.

Parameter	Prior	Prior Distribution	Posterior	Source	Comment
$W$	$13.7 \pm 0.2$ eV	Normal	$13.78^{+0.21}_{-0.21}$	${}^{220}\text{Rn}, {}^{241}\text{AmBe}$ , NG	Eq. 4.1 and 4.12, [165]
Electronic Recoils					
$F$	0.059	Fixed	—	${}^{220}\text{Rn}$	[167], Eq. 4.1
$n_{\text{ex}}/n_{\text{ion}}$	0.06-0.2	Uniform	$0.150^{+0.034}_{-0.053}$	${}^{220}\text{Rn}$	Eq. 4.2, see Sec. 4.2.2 for NR
$E_0$	$\geq 0$	Free	$1.133^{+0.231}_{-0.332}$	${}^{220}\text{Rn}$	Recombination, Eq. 4.4
$E_1$	$\geq 0$	Free	$0.473^{+0.171}_{-0.141}$	${}^{220}\text{Rn}$	Recombination, Eq. 4.4
$\gamma_{\text{er}}$	0-0.5	Free	$0.125^{+0.029}_{-0.028}$	${}^{220}\text{Rn}$	Recombination, Eq. 4.4
$\omega_{\text{er}}$		Free	$30.5^{+4.1}_{-3.3}$	${}^{220}\text{Rn}$	Recombination, Eq. 4.4
$\delta_{\text{er}}$		Free	$-0.243^{+0.056}_{-0.055}$	${}^{220}\text{Rn}$	Recombination, Eq. 4.4
$A$	$\geq 0$	Free	$0.0408^{+0.0058}_{-0.0056}$	${}^{220}\text{Rn}$	RF, Eq. 4.5
$B$	$\geq 0$	Free	$1.735^{+1.320}_{-1.148}$	${}^{220}\text{Rn}$	RF, Eq. 4.5
Nuclear Recoils					
$\alpha$	$1.240 \pm 0.079$	Normal	$1.283^{+0.070}_{-0.063}$	${}^{241}\text{AmBe}$ , NG	Eq. 4.18
$\zeta$	$0.0472 \pm 0.0088$	Normal	$0.0451^{+0.0085}_{-0.0083}$	${}^{241}\text{AmBe}$ , NG	Eq. 4.18
$\beta$	$239 \pm 28$	Normal	$271^{+22}_{-18}$	${}^{241}\text{AmBe}$ , NG	Eq. 4.18
$\gamma$	$0.01385 \pm 0.00073$	Normal	$0.01415^{+0.00059}_{-0.00060}$	${}^{241}\text{AmBe}$ , NG	Eq. 4.19
$\delta$	$0.0620 \pm 0.0064$	Normal	$0.0615^{+0.0054}_{-0.0064}$	${}^{241}\text{AmBe}$ , NG	Eq. 4.19
$k$	$0.1394 \pm 0.0032$	Normal	$0.138^{+0.003}_{-0.003}$	${}^{241}\text{AmBe}$ , NG	Eq. 4.11
$\eta$	$3.3 \pm 0.7$	Normal	$3.283^{+0.675}_{-0.525}$	${}^{241}\text{AmBe}$ , NG	Eq. 4.16
$\lambda$	$1.14 \pm 0.45$	Normal	$1.139^{+0.354}_{-0.246}$	${}^{241}\text{AmBe}$ , NG	Eq. 4.16

Table 4.4: Median and 68% credible intervals for electronic and nuclear recoil micro-physics models using the final 1000 steps of the fit. The NR model is adopted from [173] and described in Sec. 4.2.2.

#### 4. ELECTRONIC AND NUCLEAR RECOIL CALIBRATIONS

---

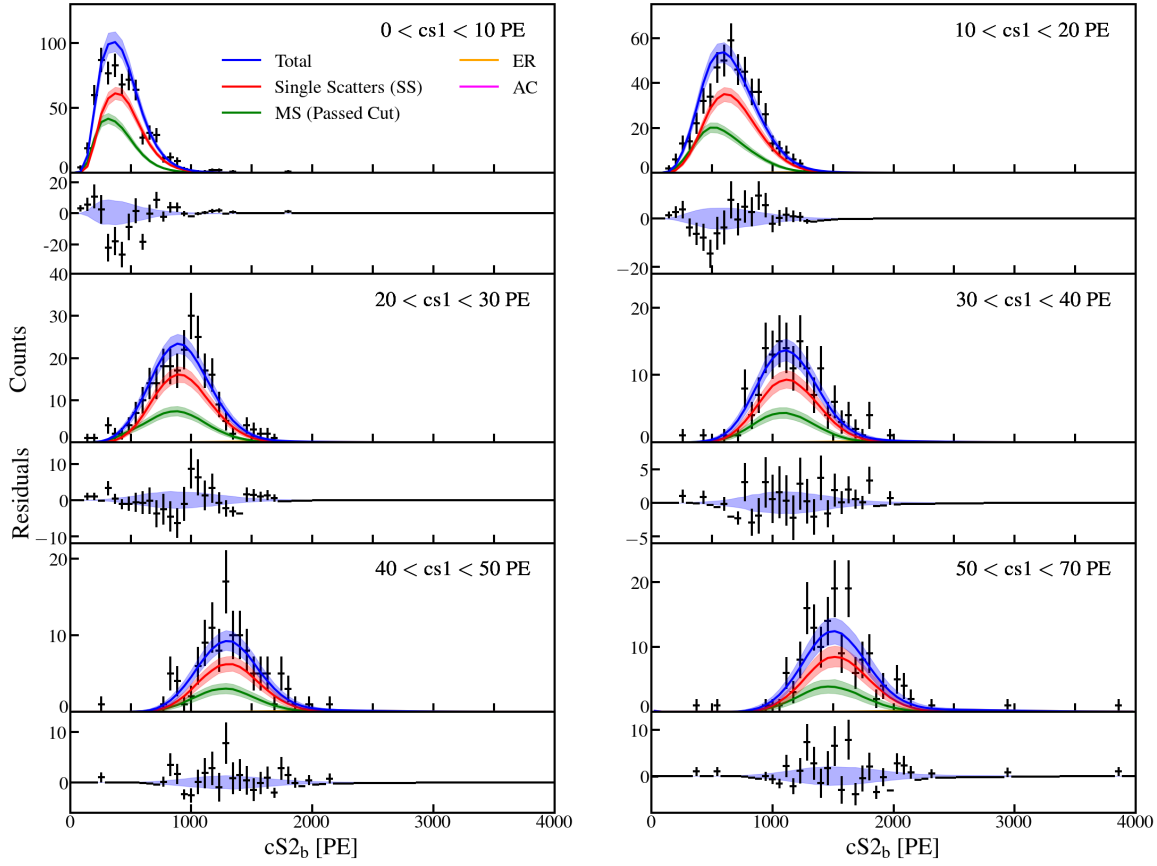


Figure 4.22:  $cS2_b$  for SR1 NG calibration in slices of  $cS1$ . The fit (blue) matches the data nicely, though in the  $10 < cS1 < 20$  PE slice the model predicts a lower  $cS2_b$ . Similar to  $^{241}\text{AmBe}$  the ratio of multi- (green) to single-scatter neutrons (red) is larger at low  $cS2_b$ . ER background (gold) and AC (pink) have too few events to be visible.

recoils is known to be less stark.

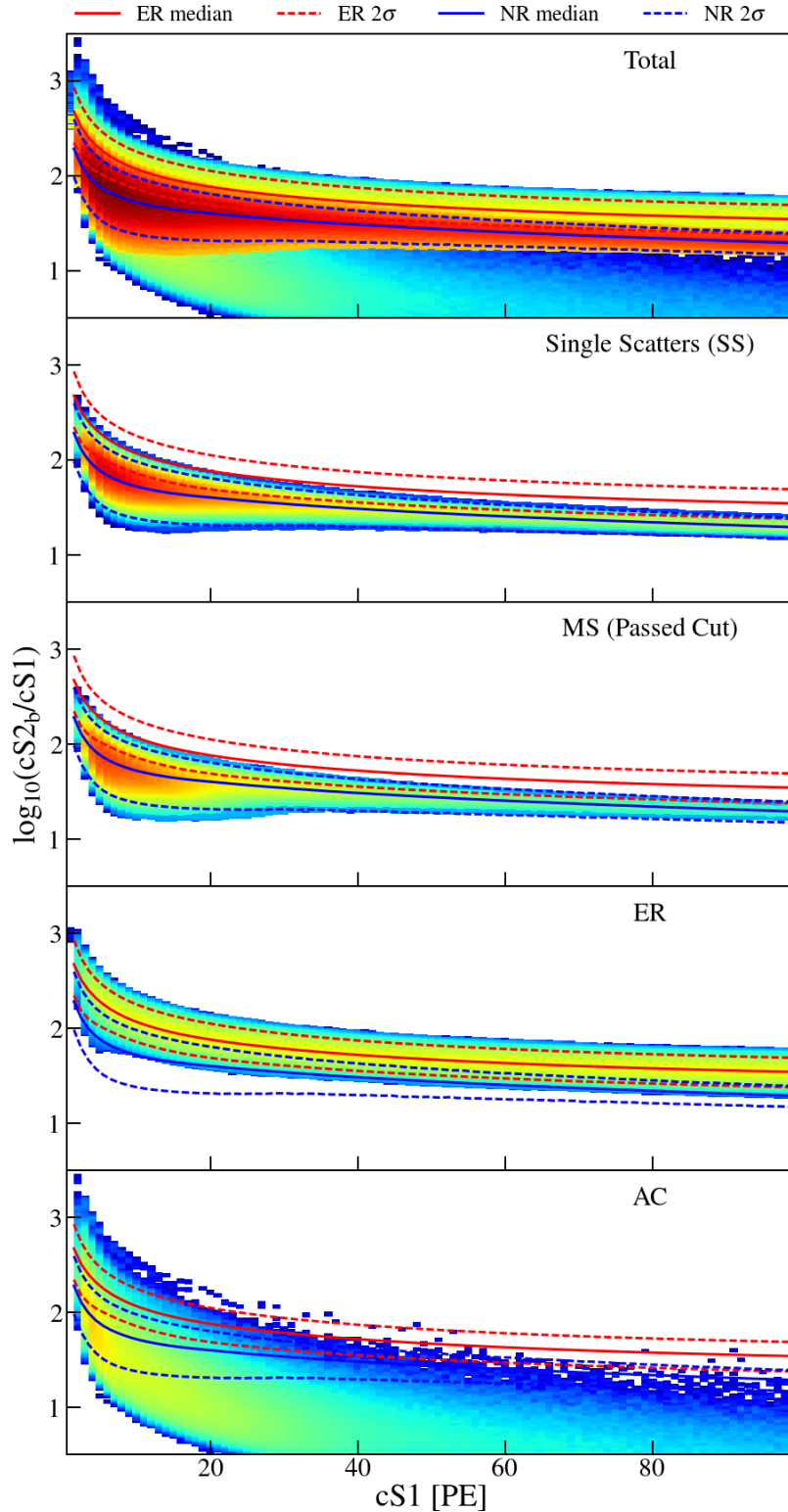


Figure 4.23:  $cS1 \cdot \log_{10}(cS2_b/cS1)$  distribution for the SR1 neutron generator calibration band fitting. Medians and  $\pm 2\sigma$  for the electronic (red) and nuclear (blue) recoil bands are shown as solid and dashed lines, respectively. Electronic recoil lines are taken from the SR1 ER model from the fit.

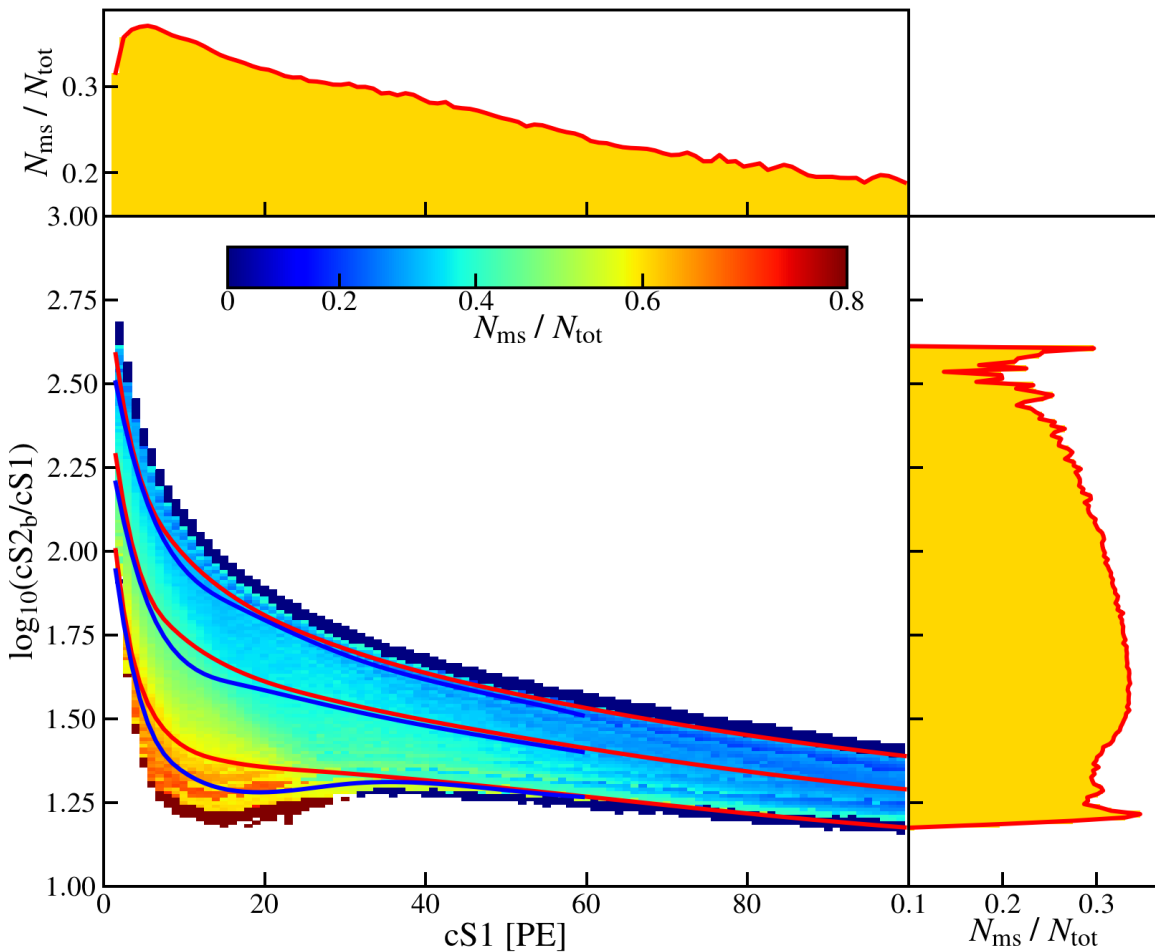


Figure 4.24: Fraction of nuclear recoil events in SR1  $^{241}\text{AmBe}$  calibration that result from multiple scatters. In the main panel red and blue lines mark the median and  $\pm 2\sigma$  for single and multiple scatters, respectively (at  $cS1 > 60$  PE the number of multiple scatter events is too low for calculation). Multiple scatters will be pushed to smaller  $\log_{10}(cS2_b/cS1)$ . The effect becomes more dramatic at lower  $\log_{10}(cS2_b/cS1)$  due to a couple effects. The first is a larger number of scatters will lead to a smaller  $cS2_b/cS1$ . Additionally the S1s are corrected by the LCE map according the position of the largest scatter, so S1s in a higher-LCE region would be over-corrected. This also leads to the magnitude of the dip between SS and MS percentiles extending to higher  $cS1$  at lower  $\log_{10}(cS2_b/cS1)$ . At sufficiently high  $cS1$  ( $\gtrsim 40$  PE) the  $cS2_b$  must be large enough that S1s from other scatters do not have much effect, since a secondary scatter with a large S1 should also contain a large  $S2_b$  and fail the multiple scatter cut. The top and right panels are integrated over the main panel and show the multiple scatter fraction with respect to  $cS1$  (top) and  $\log_{10}(cS2_b/cS1)$  (right).

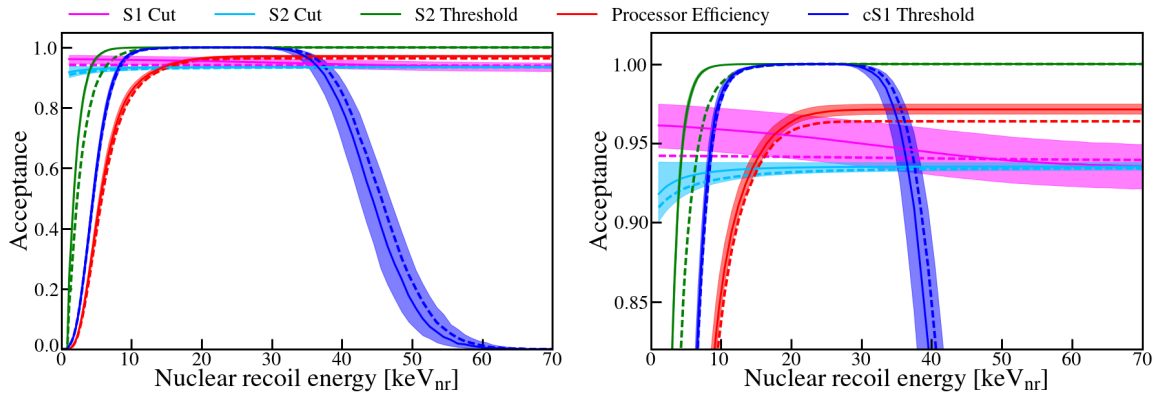


Figure 4.25: Nuclear recoil energy-dependent efficiencies calculated using 400 samples randomly drawn from the posterior of the band fit. Best-fit values are shown for S1 (pink) and S2 (light blue) selection, S2 threshold (green), processor (red), and cS1 threshold (dark blue) efficiencies. Dashed lines represent medians from SR0 while solid lines and shaded regions show SR1 medians and 68% credible regions.

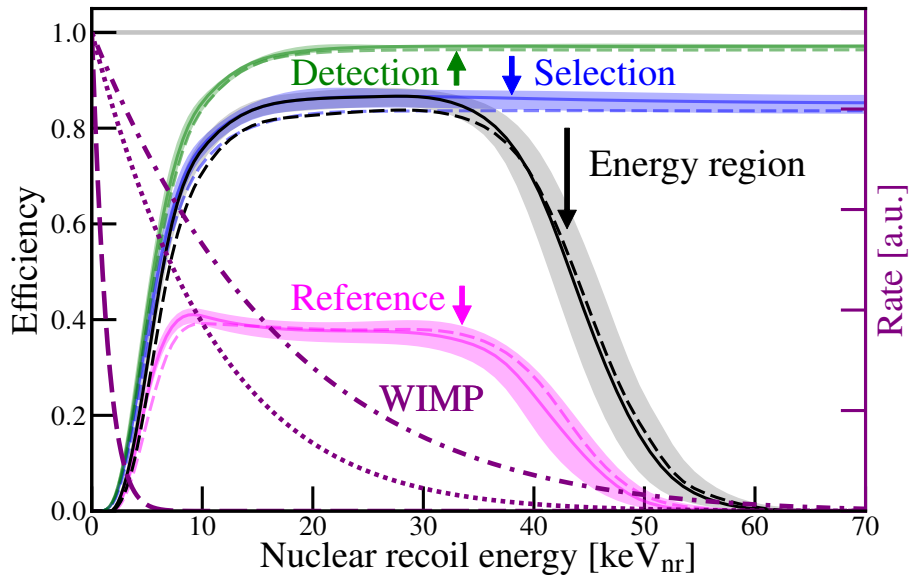


Figure 4.26: Nuclear recoil energy-dependent efficiencies for WIMPs from this analysis. Processor (green), processor with S1 and S2 selection (blue), total ignoring the reference region (black), and total in the reference region (pink) efficiencies are shown. Dashed and solid acceptance lines correspond to SR0 and SR1 acceptances, respectively. The shaded regions are the 68% credible interval for SR1. Spectra are shown for 10 (dashed), 50 (dotted), and 200 (dash-dotted)  $\text{GeV}/c^2$  WIMPs in purple.

## 4. ELECTRONIC AND NUCLEAR RECOIL CALIBRATIONS

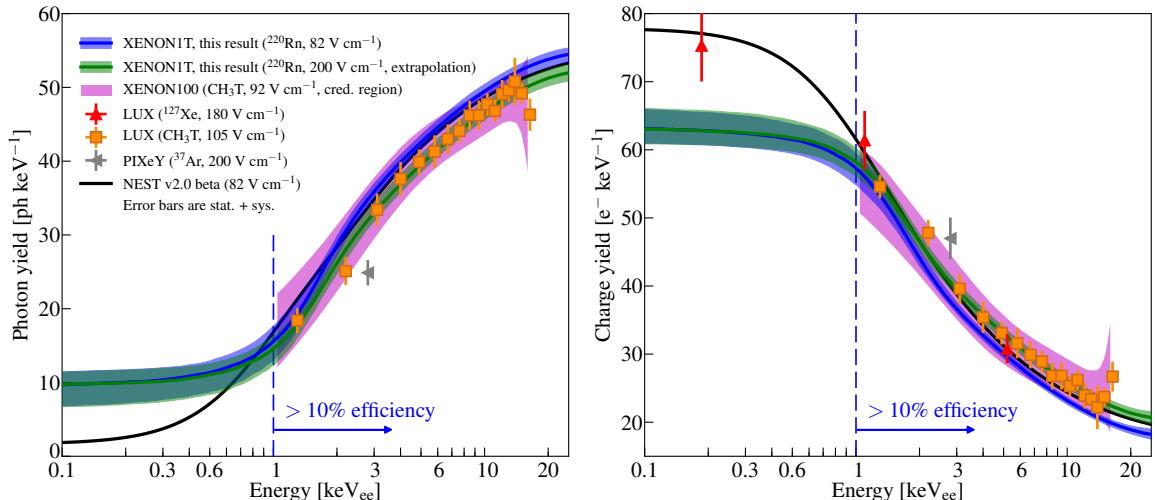


Figure 4.27: Photon and charge yields for electronic recoils. This result is shown in blue at  $82 \text{ V cm}^{-1}$  (SR1) and its extrapolation to  $200 \text{ V cm}^{-1}$  is shown in green. The purple band represents XENON100 tritium calibration [198], red triangles and orange squares represent LUX  $^{127}\text{Xe}$  [221] and tritium [197], respectively, and grey triangles represent PIXeY  $^{37}\text{Ar}$  [222]. The black line shows the NEST v2.0 beta at  $82 \text{ V cm}^{-1}$  prediction. This analysis has  $> 10\%$  acceptance for events with energies higher than the dashed blue line (Sec. 4.3.2).

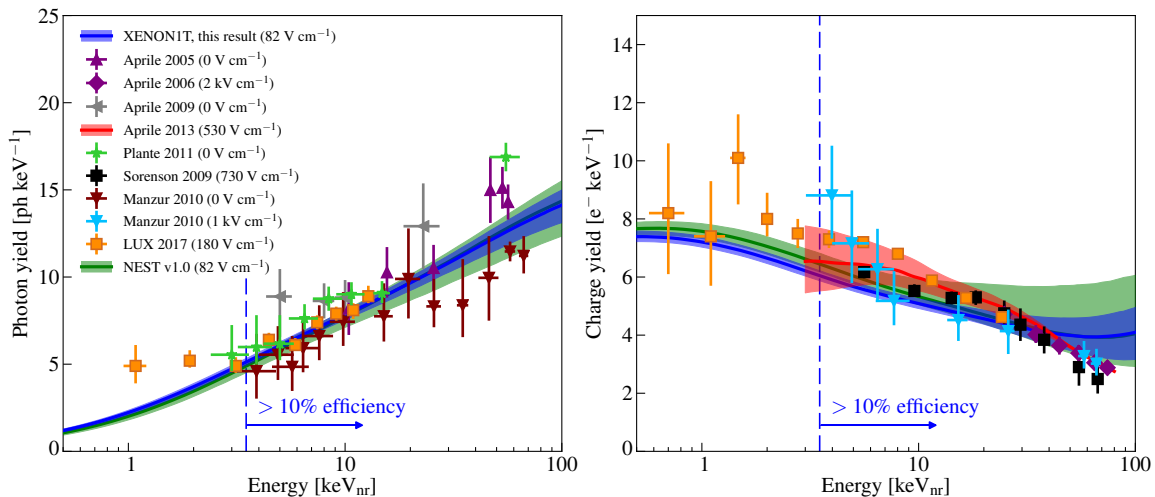


Figure 4.28: Photon and charge yields for nuclear recoils. This result at  $82 \text{ V cm}^{-1}$  is shown in blue. It is not an independent measurement since the model is constrained by previous work.  $L_y$  measurements are represented by purple triangles [223], grey triangles [224], light green triangles [225], and magenta triangles [226].  $Q_y$  are represented by purple diamonds [183], red band [227], black squares [228] and light blue triangles [226].  $L_y$  and  $Q_y$  from the same measurement are shown by orange squares [229]. The NEST v1.0 model was used to constrain our fit and is shown as the green band [173]. This analysis has  $> 10\%$  acceptance for events with energies higher than indicated by the dashed blue line (Sec. 4.3.2).

# Chapter 5

## Purity and the Electron Lifetime

In a noble element dark matter detection experiment the purity of the target mass is an essential consideration and must be consistently measured. The effects of electronegative impurities - which attenuate light and charge - are easily measured through the electron lifetime. However, a reliable model for the evolution of the impurities does not exist to explain and predict the behavior.

This chapter focuses on the effects of impurities (Sec. 5.1), electron lifetime measurements (Sec. 5.2), the derivation of the electron lifetime model (Sec. 5.3), and the results (Sec. 5.4).

### 5.1 Effects of Electronegative Impurities

Electronegative impurities mainly come from outgassing from detector materials.

Purity usually refers to two distinct but correlated group, though the degree of the correlation can depend on the experiment. The first is background contamination from radioactive elements of other noble elements inside the TPC. For xenon the primary challenges are  $^{85}\text{Kr}$  (Sec. 3.3.1.1) and  $^{222}\text{Rn}$  (Sec. 3.3.1.2) as they have low-energy decays that can reach our region of interest.

The second type is the density of electronegative impurities such as  $\text{O}_2$  or  $\text{N}_2$ , which attach to drifting electrons, lowering or even eliminating the S2. This can have the largest impact at low energies since the number of  $e^-$  is much fewer. To

correct for the expected initial number of electrons we can use the electron lifetime  $\tau_e$ . Of course, if the entire cloud of electrons is removed by these impurities we cannot apply a correction since we have no knowledge of where in the detector it occurred or the energy deposition. Even if some electrons make it to the surface a low electron lifetime creates more uncertainty when correcting the S2. This chapter is focused electronegative impurities, though its examination necessitates consideration of the radioactive background concentration.

### 5.1.1 Photon Attenuation

Xe scintillation (178 nm with  $\sim$ 14 nm spectral FWHM) is absorbed by a number of electronegative impurities [230], [231]. At concentrations of ppm or higher the fraction of VUV photons that reach the PMTs can be considerably decreased - especially for large detectors where longer travel distances are required. The intensity drop due to photon attenuation is given by

$$I(x) = I_0 e^{-x/\lambda_{\text{att}}} \quad (5.1)$$

where  $I_0$  is initial intensity,  $x$  is distance, and  $\lambda_{\text{att}}$  is the attenuation length, and  $1/\lambda_{\text{att}} = 1/\lambda_{\text{abs}} + 1/\lambda_{\text{scatt}}$  where  $\lambda_{\text{abs}}$  and  $\lambda_{\text{scatt}}$  are the absorption and scattering lengths, respectively. The absorption length describes loss of photons due to absorption by an element or molecule while the scattering length describes the elastic scattering of photons. For perfectly pure xenon  $\lambda_{\text{abs}} \sim \infty$  ([232] found  $\lambda_{\text{abs}} > 100$  cm at 90% confidence level).

High levels of impurities, however, can shorten the absorption length. Fig. 5.1 shows the absorption coefficients ( $\lambda_{\text{abs}}^{-1}$ ) for 1 ppm H<sub>2</sub>O and O<sub>2</sub> from 130-200 nm. They overlap with shorter wavelengths of the xenon spectrum (included for comparison), meaning light detected by PMTs will have an asymmetric distribution. With a nearly 1-meter tall detector a 1 ppm concentration of H<sub>2</sub>O would have at 10% effect or more at  $\lesssim 180$  nm.

The relative intensities for different H<sub>2</sub>O/Xe and O<sub>2</sub>/Xe concentrations from 0-60 cm are shown in Fig. 5.2. At the level of  $\mathcal{O}(100)$  ppb of oxygen  $I/I_0 > 0.8$

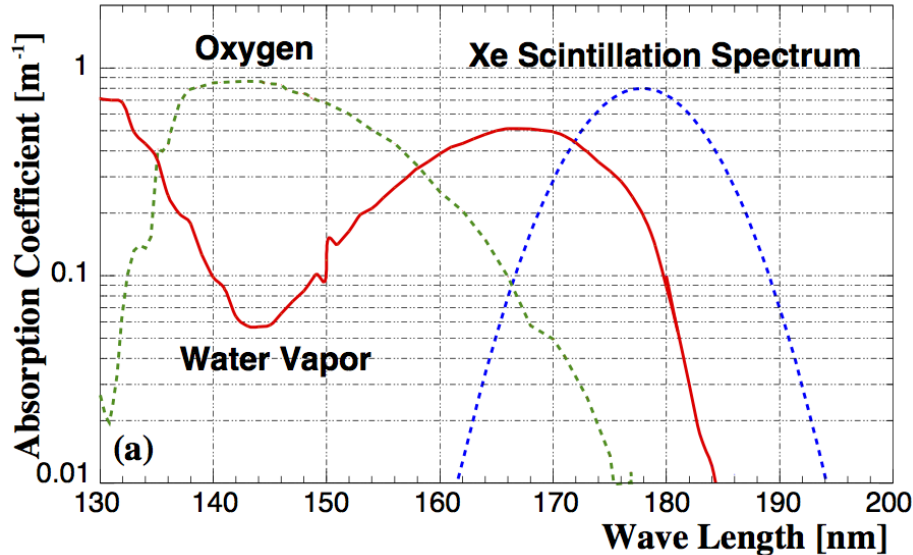


Figure 5.1: Absorption coefficient for photons at 1 ppm H<sub>2</sub>O vapor (solid red) and O<sub>2</sub> (dashed green). The Xe scintillation spectrum is overlaid for comparison (dashed blue). H<sub>2</sub>O impacts Xe scintillation considerably more than O<sub>2</sub> when at the same concentration. Image credit: [233], H<sub>2</sub>O data from [234].

at 60 cm. The effect of water is substantially worse with  $I/I_0 < 0.3$ , highlighting the need for significant reduction LXe experiments. Even with a LXe purity that is appreciably better than Fig. 5.2  $\lambda_{\text{att}} \approx \lambda_{\text{abs}}$  since the effects of scattering are subdominant with respect to absorption.

Photon attenuation ultimately increases our energy threshold as we are less sensitive to lower energies as few photons are measured.

### 5.1.2 Charge Depletion

As the electron cloud following a recoil drifts it diffuses longitudinally (in the direction of  $E_d$ ) and transversely (perpendicular to  $E_d$ ). The diffusion coefficients  $D_L$  and  $D_T$  depend on the electric field with  $D_T/D_L \sim 10$ . The electron spread is  $\sigma_{D_T} = \sqrt{D_T t_d}$  where  $t_d = d/v_d$  is the drift time and  $d$  is the drift distance.

The behavior of electrons can be classified according to their mobility in the limit of  $E \rightarrow 0$ ,  $\mu_0$ . When LXe is polarized by electrons its high polarizability ( $4.0 \times 10^{-24} \text{ cm}^3$ , highest for among noble gases) make it attract  $e^-$  and interact with

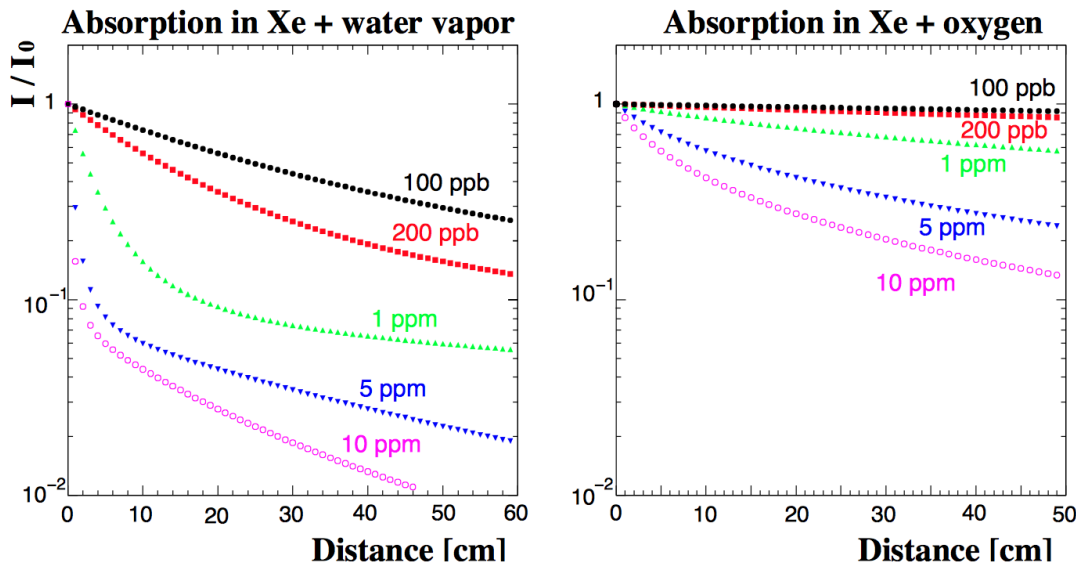


Figure 5.2: Fraction of initial intensity of xenon scintillation with distance for various concentrations of  $\text{H}_2\text{O}$  (left) and  $\text{O}_2$  (right). Image credit: [233].

nearby Xe atoms through dipole-dipole interactions. The equilibrium of these two effects determines the potential energy of the ground state of electrons  $V_0$ , which is anti-correlated with  $\mu_0$ . For LXe these have been measured to be  $V_0 = -0.61 \pm 0.05$  K [235] and  $\mu_0 = 2200 \pm 200$   $\text{cm}^2 \text{V}^{-1} \text{s}^{-1}$  [149] at 165 K (in addition  $\mu_0$  was found to be 1900 and 2200  $\text{cm}^2 \text{V}^{-1} \text{s}^{-1}$  at 163 K by [149] and [141], respectively). The large electron mobilities indicate the electrons are *quasifree*, and have drift velocities that can exceed even those of GXe, as shown in Fig. 5.3.

Ions exhibit significantly lower mobility than electrons. Their mobilities are parameterized as  $\mu \approx \eta^{-\alpha}$  where  $\eta$  is the liquid viscosity and  $\alpha = 1\text{-}2$ . The diffusion coefficients can be calculated with the Nernst-Einstein equation

$$\frac{eD(E)}{\mu(E)} = \mathcal{F}\langle E \rangle \quad (5.2)$$

where  $\mathcal{F} = 0.5\text{-}1$  depends on the electron distribution function (e.g.  $\mathcal{F} = 2/3$  for a Maxwellian distribution).

The mobilities for holes,  $\text{TMSi}^+$ ,  $\text{O}_2^-$ ,  $^{226}\text{Th}$ ,  $^{208}\text{Tl}$ , and  $\text{Xe}_2^+$  in LXe are listed in Tab. 5.1. They are  $\sim 10^6$  times smaller than the electron mobility.

Hole mobility can be described by the hopping model of charge carrier transport.

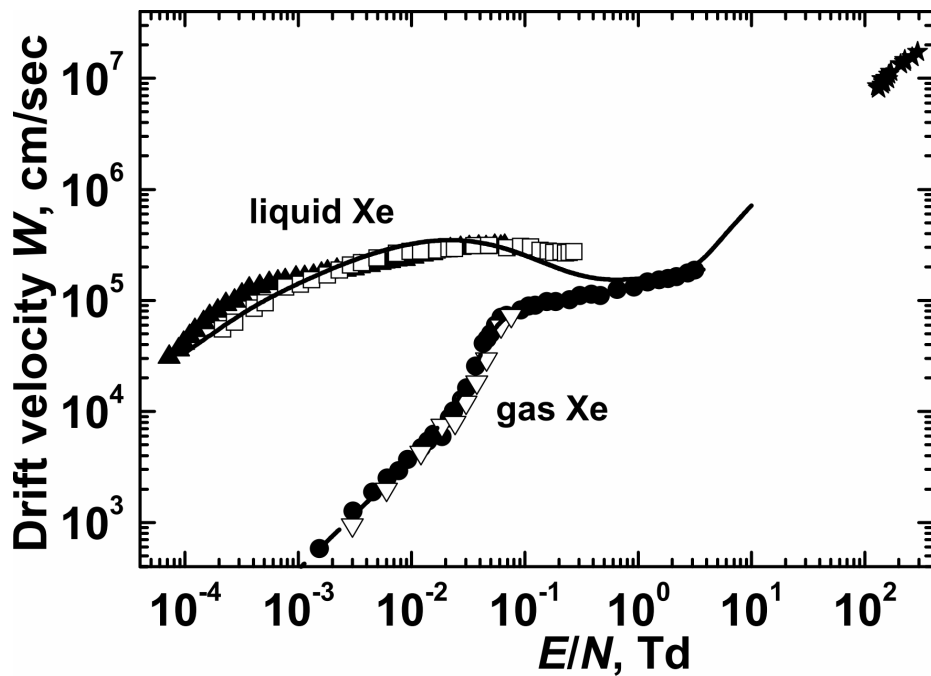


Figure 5.3: Drift velocity (here defined as  $W$ ) dependence on reduced electric field  $E_d/N$  where  $N$  is the number of molecules per volume. Points are from experimental data [236]–[239] and curves are from calculations. 1 Td =  $10^{-17}$  V cm $^2$ . LXe has a higher drift velocity than GXe at  $E_d/N \lesssim 1$  Td (1 Td =  $10^{-17}$  V cm $^2$ ). Image credit: [240].

Ion	T [K]	$\mu$ [ $10^{-4}$ cm $^2$ V $^{-1}$ s $^{-1}$ ]	Ref.
holes	161	35	[241]
holes	230	46	[241]
TMSi $^+$	162	2	[242]
TMSi $^+$	192	3	[242]
O $_2^-$	162	6	[242]
O $_2^-$	192	10	[242]
$^{226}\text{Th}^+$	162	2.4	[243]
$^{208}\text{Tl}^+$	163	1.33	[244]
Xe $_2^+$	184.2	2.85	[245]
Xe $_2^+$	192.1	3.17	[245]

Table 5.1: Ion mobilities in LXe. All ions listed are positive with the exception of O $_2^-$ . Positive holes have mobilities that are  $\sim 10$  times larger than ions. Summarized data is given in [246].

## 5. PURITY AND THE ELECTRON LIFETIME

---

In this temperature-dependent model charge is propagated through jumps between traps yielding

$$\mu = \frac{eb^2}{k_B T} \omega \quad (5.3)$$

where  $b$  is the average jump distance and  $\omega$  is the jumping frequency, parameterized as

$$\omega = P\left(\frac{\omega_0}{2\pi}\right) e^{-E_a/k_B T} \quad (5.4)$$

where  $\omega_0$  is the phonon frequency and  $P(\omega_0/2\pi)$  is the tunneling probability between adjacent holes with activation energy  $E_a$ . Fig. 5.4 shows hole mobility in LXe. The solid curve represents a model that parameterizes Eq. 5.3 as

$$b^3(T) = \sqrt{2M/\rho(T)} \quad (5.5)$$

where  $M$  is the atomic mass of xenon and  $\rho(T)$  is the temperature-dependent density [241]. It additionally assumes the hole is self-trapped between two rare atoms in a potential well, forming a polaron. It gives a hole mobility of

$$\mu(T) = \frac{eb^2(T)}{k_B} \frac{2\pi}{h} \sqrt{\frac{\pi}{4E_a k_B T}} J_0^2 e^{-2\alpha b(T)} e^{-E_a/k_B T} \quad (5.6)$$

where  $h$  is Planck's constant and  $J(T) = J_0 e^{-\alpha b(t)}$  is the transfer integral.

As the electron cloud drifts electronegative impurities bond to  $e^-$



where  $S$  refers to the impurity (e.g.  $e^- + O_2 \rightarrow O_2^-$ ).

1. Radiative attachment is given by



where  $XY$  is some atom or molecule.

2. Dissociative electron attachment (DEA) is when a low-energy electron bonds to a molecule causing it to fracture. The process is given by

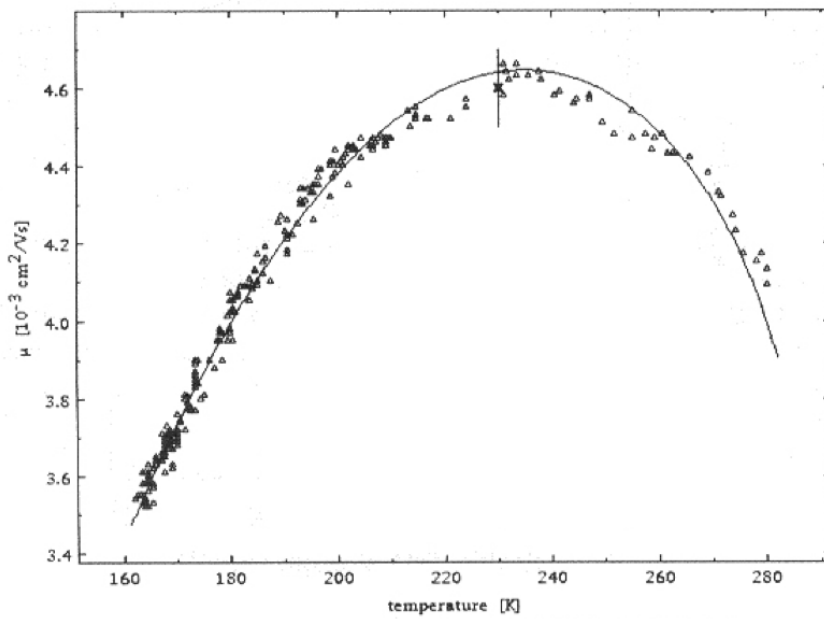
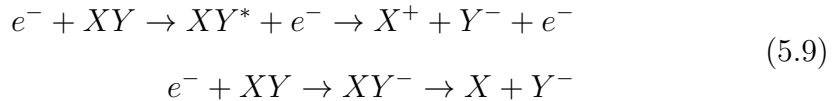
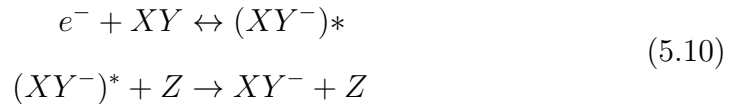


Figure 5.4: Temperature-dependent drift mobility for holes in LXe. Data is shown as empty triangles. A fit using Eq. 5.6 is shown as the solid line. Image credit: [246] (redrawn from [241]).



where molecule  $XY$  is separated into components  $X$  and  $Y$ .  $O_2$  has 5.116 eV dissociation energy (the energy needed to separate the oxygen) and  $O^-$  has electron affinity (energy released in forming ion) of 1.461 eV.

3. Three-body attachment proceeds via the two-stage Bloch-Bradbury reaction [247], [248]



where  $Z$  is an atom or molecule from the majority gas population. It carries out the bonding energy between the  $e^-$  and electronegative  $XY$ . Oxygen was studied [249]–[251].

## 5.2 Measuring the Electron Lifetime

Mono-energetic radioactive decays are used to measure the electron lifetime. For XENON1T electron lifetimes were calculated using elements distributed in the xenon, since external  $\gamma$ -ray sources such as  $^{137}\text{Cs}$  and wall events could not reach the FV. This was done primarily with  $^{83\text{m}}\text{Kr}$ ,  $^{129\text{m}}\text{Xe}$ ,  $^{131\text{m}}\text{Xe}$ ,  $^{212}\text{Bi}$ ,  $^{218}\text{Po}$ , and  $^{222}\text{Rn}$  (other lines such as the 39.6 keV of  $^{129}\text{Xe}$  and 80.2 keV of  $^{131}\text{Xe}$  during nuclear recoil calibrations were used but the short half-lives made measurements difficult). Information for each element is listed in Tab. 5.2. An additional method of minimizing the  $S_{2\text{b}}$  width of the  $^{212}\text{Pb}$  electronic recoil band to address a discrepancy between  $^{83\text{m}}\text{Kr}$  and  $\alpha$ -decays (Sec. 5.2.5) was tried but the uncertainty was too large to draw any conclusions.

### 5.2.1 S2/S1

In the period immediately following XENON1T coming online the electron lifetime was  $\sim 0$  since purification began at roughly the same time. The first in-situ calibration was not performed until almost three months later and mono-energetic background decays had not yet been investigated, though  $^{222}\text{Rn}$  and  $^{218}\text{Po}$  would have had too few events in the top of the detector to be reliable anyways. However, S2/S1 - though not energy-independent - was enough so to give reasonable estimates. It was too early to have official cuts but the ones used were sufficient and based on a history of knowledge of TPC detectors.

S1 (S2) single scatter cuts required that the second largest S1 (S2) be  $< 0.2$  that of the first. The purpose of these cuts was to prevent S1-S2 mismatching: the S1 cut would remove the possibility that we do not observe the S2 of a scatter deep in the TPC, while the S2 eliminated any ambiguity in matching a single S1 with two potential S2s.

To reject noise at least three PMTs were required to observe the S1. This is the same cut that was used in the dark matter analysis. Finally, the fraction of light seen on the top PMT array must fall between 0.2-0.6 for S1s and 0.5-0.9 for S2s.

On a few occasions a  $^{137}\text{Cs}$  was placed outside the detector. While the water and

Isotope	Decay	Energy	$t_{1/2}$	Section	Notes
$^{83m}\text{Kr}$	IC	32.2 keV	1.83 h	Sec. 5.2.3	Calibration
$^{129m}\text{Xe}$	$\gamma$	236.2 keV	8.88 d	Sec. 5.2.4	Background following NR cal.
$^{131m}\text{Xe}$	$\gamma$	163.9 keV	11.93 d	Sec. 5.2.4	Background following NR cal.
$^{212}\text{Bi}$	$\alpha$	6.207 MeV	60.55 m	Sec. 5.2.2	$^{220}\text{Rn}$ calibration
$^{218}\text{Po}$	$\alpha$	6.115 MeV	3.10 m	Sec. 5.2.2	Background
$^{222}\text{Rn}$	$\alpha$	5.590 MeV	3.82 d	Sec. 5.2.2	Background

Table 5.2: Isotopes used for electron lifetime analysis. Background  $^{222}\text{Rn}$  and  $^{218}\text{Po}$   $\alpha$ -decays allow continual monitoring but have relatively low statistics.  $^{83m}\text{Kr}$  and  $^{212}\text{Bi}$  have high statistics but are only available during calibrations. Excited nuclear states  $^{131m}\text{Xe}$  and  $^{129m}\text{Xe}$  are present in background after nuclear recoil calibrations but their half-lives limit their viability after several weeks.

LXe self-shielding limited the fraction of radiation that made it inside the TPC, there were enough events for measurements. This method was used until early August 2016.

### 5.2.2 $\alpha$ -decays

The high energy and substantial stopping power (Fig. 2.4) of  $\alpha$  interactions causes a large fraction of electrons to recombine with their parent or nearby  $\text{Xe}^+$  atoms. Their S1s are significantly higher than electronic or nuclear recoils so are easily distinguishable. Because they are so recognizable and do not scatter many of the cuts developed for the science run analysis are not necessary (some may not be reliable since they were developed using low-energy electronic recoils). Therefore, just a small number of cuts are used.

Events must have  $r_{\text{rec}} < 36.94$  cm. This is in part for consistency with the First Results FV [132], but also because the greatest inhomogeneities in the electric field are expected to be largest at the top, bottom, and sides of the TPC as seen in Fig. 3.6. Changes in field will produce different light and charge yields (Sec. 3.2.9), so the number of photons and electrons would vary according to position. In addition, the impurity attachment rate dependence on field will cause the rate of electron removal to change inside the TPC (Sec. 5.3.9). Finally, the radial cut removes  $\alpha$ -decays near the wall that would lose drifting  $e^-$  to the PTFE.

The fraction of light seen by the top PMTs from electroluminescence is tightly

constrained by stable detector conditions (Eq. 2.27). The percentage of events that fail this cut is small but it is important to remove any “fake” or gas events (a cut on the S1 fraction seen by the top PMTs will also remove GXe events).

In addition data acquisition quality cuts are used in data selection. The first is the high energy veto, which is triggered by a very large S2. The second is produced by one or more digitizers nearly filling its memory buffer, and is called a busy veto. The third is a busy type check, which removes events that have a busy signal anywhere in the waveform. The final is an end of run check, which disqualifies the last 21 seconds per run (each run is 1 hour). Details for each are given in Sec. 3.1.9.

Fig. 5.5 shows cS1 dependence on  $z$  for the  $\alpha$ -decays of  $^{222}\text{Rn}$  ( $\sim 5.1 \times 10^4$  PE) and  $^{218}\text{Po}$  ( $\sim 5.6 \times 10^4$  PE) after these cuts. The large S1s from events deep in the detector saturate PMTs in the bottom array, which leads to under-corrected cS1s as shown in the left panel. To correct for this the data are split into slices in  $z$  and fit in cS1 with gaussians. Fits in the region  $-40 \lesssim z \lesssim -10$  cm, where saturation is not present, are used to define the correct cS1 distribution, which is extrapolated across the entire length of the TPC. Differences in fit parameters are used to relocate events deeper in the detector into the proper cS1 band. The  $\alpha$ -corrected cS1 distribution is shown in the right panel of Fig. 5.5.

Even with the  $\alpha$ -corrected cS1s there is saturation near the very bottom of the TPC. The saturation is so great here that events from  $^{222}\text{Rn}$  and  $^{218}\text{Po}$  cannot be distinguished from one another. This is generally not a problem since it lays outside the fiducial volume. There is also some distortion at  $z \gtrsim -5$  cm from events near the LXe surface, whose light is tightly concentrated in the top PMT array.

Selected  $^{222}\text{Rn}$  and  $^{218}\text{Po}$  events are indicated by red and blue boxes, respectively. Events with  $-89 < z < -9$  cm and  $4.9 \times 10^4 < \alpha\text{-corrected cS1} < 5.3 \times 10^4$  PE ( $^{222}\text{Rn}$ ) and  $5.35 \times 10^4 < \alpha\text{-corrected cS1} < 5.8 \times 10^4$  PE ( $^{218}\text{Po}$ ) are used. The electron lifetimes are calculated independently, which provides a nice cross-check. Because the decay of  $^{222}\text{Rn}$  can leave  $^{218}\text{Po}$  in a charged state it has slightly fewer (5-10%) events. Electron lifetimes are calculated using 48 hours of data in order to get sufficient statistics.

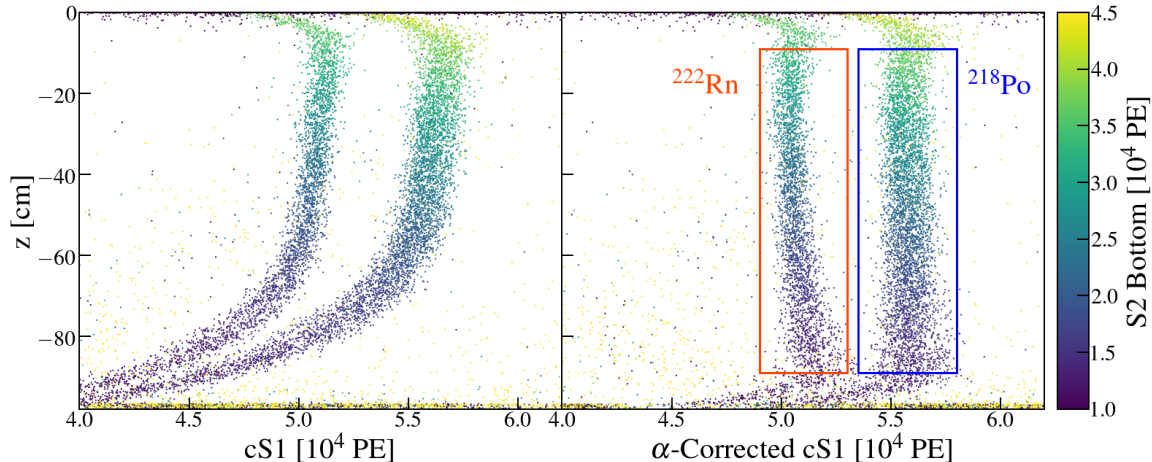


Figure 5.5: cS1 (left) and  $\alpha$ -corrected cS1 (right) dependence on  $z$ . The large  $\alpha$ -decay S1s deep in the TPC sature the bottom PMTs, causing an under-corrected cS1, which results in the distortion seen in the left panel. Near the top ( $z \gtrsim -5$  cm) a similar effect is observed from top PMT saturation. The distortion is corrected in the right panel where the effect is much less significant. The red and blue boxes highlight the events selected to calculate  $\tau_e$ . The colors of data markers correspond to  $S2_b$ .

The data is binned in drift time slices  $\Delta t_d$  and an initial fit is performed on the 50th percentiles of the  $S2_b$  distributions from each slice. The purpose of this preliminary electron lifetime  $\tau_e^{(p)}$  is to remove events that are far from the distribution. The data in each  $\Delta t_d$  slice is binned in cS1 and fit with a gaussian. The means and standard deviations are then fit with an exponential to give the final electron lifetime  $\tau_e$ . An example can be seen in Fig. 5.6. The pink dashed lines define the boundaries above and below which events were cut using the preliminary fit.  $^{222}\text{Rn}$  (left) and  $^{218}\text{Po}$  (right) have good agreement.

In Fig. 5.6 the results of both fits are plotted in each panel for comparison. It is clear that without the  $\alpha$ -corrected cS1 cut the overlap in  $S2_b$  would make it impossible to decouple the  $^{222}\text{Rn}$  from  $^{218}\text{Po}$  events. Originally a cS1  $\alpha$ -correction map did not exist so  $^{222}\text{Rn}$  and  $^{218}\text{Po}$  were fit together. This turned out to give slightly lower electron lifetimes than independent fits. Once the  $\alpha$ -correction was developed  $\tau_{e\text{fit}}$  was re-computed; however, this was not possible for some of the pre-SR0 data that had been deleted.

This method can in principle be used for any  $\alpha$ -emitting element distributed

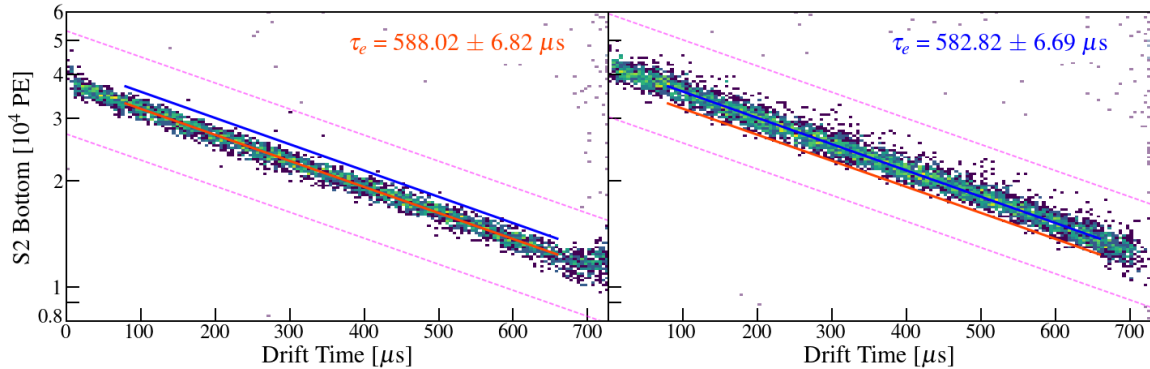


Figure 5.6: Electron lifetime measurements using  $^{222}\text{Rn}$  (left) and  $^{218}\text{Po}$  (right) from October 29-31, 2017. The red and blue lines correspond to  $^{222}\text{Rn}$  and  $^{218}\text{Po}$ , respectively, and are drawn in the drift time region that was used for the fit (see text for event selection). They are each drawn in both panels to show the  $\text{S2}_b$  overlap, highlighting the need for the  $\alpha$ -corrected cS1 cut. The pink dashed lines mark the boundaries derived from the preliminary fit outside of which events were not considered for the final fit. The electron lifetime measurements agree within uncertainty.

throughout the FV of the detector and is done so for  $^{212}\text{Bi}$  during  $^{220}\text{Rn}$  calibrations. Despite  $^{220}\text{Rn}$  and  $^{216}\text{Po}$  also being  $\alpha$ -emitters their short half-lives (55.6 s and 145 ms, respectively) exclude them from consideration.  $^{220}\text{Rn}$  and  $^{216}\text{Po}$  are also  $\alpha$ -emitters and are visible when the source valve is open. However, between the requirement that the source valve be closed and the time it takes to see the rate stabilize and switch to good data taking their short half-lives (55.6 s and 145 ms, respectively) exclude them from observation. Even if this were not the case the  $\alpha$ -corrected cS1s of  $^{220}\text{Rn}$  (6.405 MeV) and  $^{212}\text{Bi}$  (6.207 MeV) overlap, so a joint measurement is likely to lead to a biased  $\tau_e$ . Due to the enormous number of events there is also some small overlap between  $^{220}\text{Rn}$  and  $^{216}\text{Po}$  (6.906 MeV).

### 5.2.3 $^{83\text{m}}\text{Kr}$

$^{83}\text{Rb}$  electron capture produces  $^{83\text{m}}\text{Kr}$  with a 74.8% branching ratio. The delayed coincidence between the 32.2 and 9.4 keV conversion electrons differentiate  $^{83\text{m}}\text{Kr}$  from background. With  $t_{1/2} = 154.4$  ns for the 9.4 keV a large fraction of the S1s will overlap. To select events that should always have distinguishable S1s a cut requires the time between S1s  $\Delta t_{\text{S1}}$  to be between 500 and 2000 ns ( $< 3 \times 10^{-4}\%$  of events

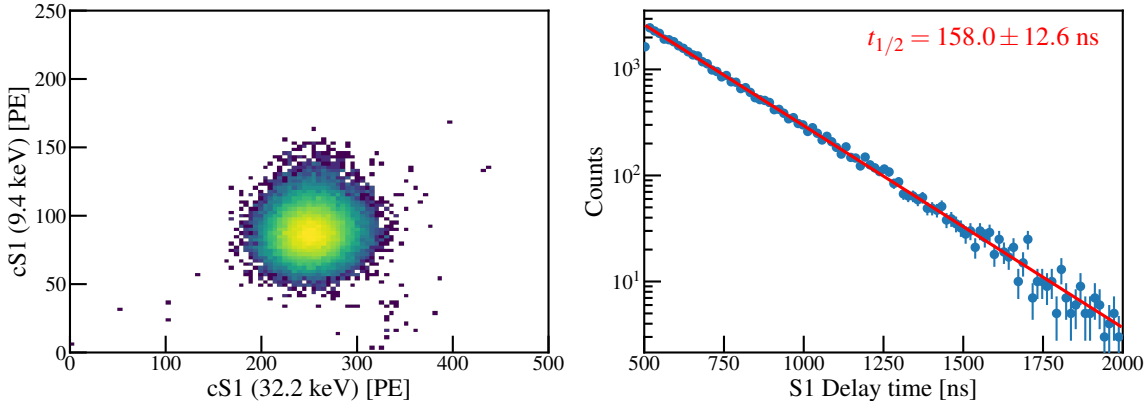


Figure 5.7: cS1s for  $^{83\text{m}}\text{Kr}$  during final Science Run 1 calibration (left). The S1 delay time cut is remarkably efficient at selecting  $^{83\text{m}}\text{Kr}$  and rejecting background. S1 delay time dependence of events from 500-2000 ns (right). A fit with an exponential gives a half-life of  $158 \pm 12.6$  ns, which is in agreement with the accepted value of 154.4 ns.

have  $\Delta t_{\text{S}1} > 2000$  ns). This cut eliminates more than 96% of  $^{83\text{m}}\text{Kr}$  events, but the remaining events are high enough that  $\tau_e$  measurements (and other studies, Sec. 3.2) can be done. To avoid PMT noise coincidence that might mimic the 9.4 keV S1 the number of PMTs that see the low-energy peak must be  $\geq 3$ . However, to ensure the coincidence is from  $^{83\text{m}}\text{Kr}$  events it is also required to be  $\leq 30$ .

The S1 and S2 from each decay are matched by size of signal. With such a short half-life  $z$  cannot change much between decays so  $\tau_e$  does not have an important role at this stage. Once the position coordinates are calculated from the S2 the S1s are corrected. The left panel of Fig. 5.7 shows the cS1s for both peaks inside the 1 t FV. From the almost entirely empty background it is clear how effective the  $\Delta t_{\text{S}1}$  cut is. The number of events vs.  $\Delta t_{\text{S}1}$  is shown in the right panel. A fit to an exponential gives  $t_{1/2} = 158 \pm 12.6$  ns, which agrees with the accepted value.

The electron lifetime is calculated using the 32.2 keV decay with a procedure similar to that of  $\alpha$ -decays Sec. 5.2.2. An preliminary fit is performed using the median  $S2_b$  in each drift time slice. However, the high statistics and near-total background removal by the  $\Delta t_{\text{S}1}$  cut removes the need to exclude events far from the true  $^{83\text{m}}\text{Kr}$  (events farther than pink dashed lines in Fig. 5.6). Each slice in drift time is fit with a gaussian, and an exponential is fit to the results.

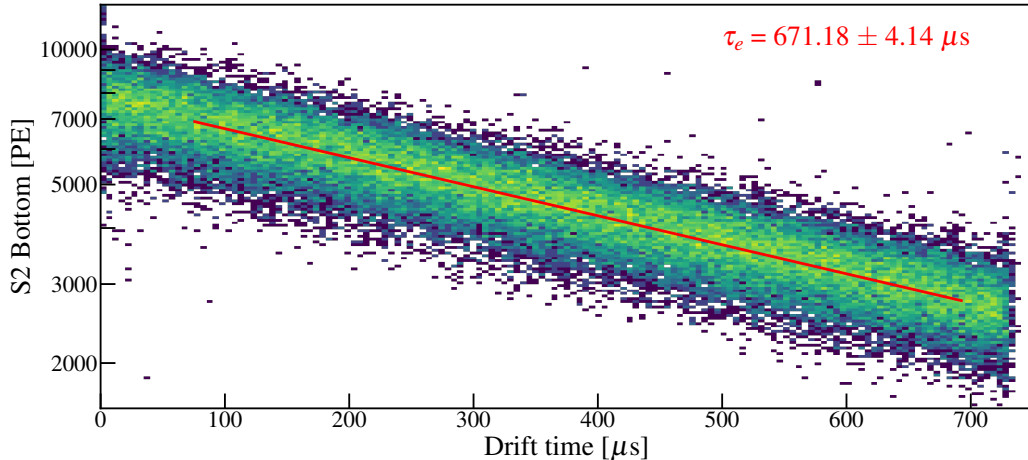


Figure 5.8: Electron lifetime measurement using  $^{83m}\text{Kr}$  from January 23-25, 2018.

The large statistics provide  $\tau_e$  measurements with precision that is only rivaled by  $^{212}\text{Bi}$ . Unfortunately, unlike  $\alpha$ -decays there are no other electronic recoil  $\tau_e$  measurements performed regularly to corroborate these results, aside from  $^{129m}\text{Xe}$  and  $^{131m}\text{Xe}$  following  $^{241}\text{AmBe}$  and NG calibrations. Sec. 5.2.5 discusses the reason for the discrepancy between  $\alpha$ -decays and  $^{83m}\text{Kr}$  and which to use when correcting data.

#### 5.2.4 $\gamma$ -rays

The full absorption peak of  $\gamma$ -rays make them great candidates for electron lifetime measurements. Unfortunately nearly all  $\gamma$ -rays in the TPC come from elements in detector materials or external sources placed inside the water tank (e.g.  $^{137}\text{Cs}$ ). However, nuclear recoils can excite  $^{129}\text{Xe}$  and  $^{131}\text{Xe}$  nuclei to metastable states with half-lives of 8.88 and 11.93 days, respectively. These metastable states serve as an in-situ calibration that are used to measure a number of detector parameters including light and charge yield (Sec. 3.2.9),  $g_1/g_{2b}$  (Sec. 3.2.7), and electron lifetime. While these evaluations can validate electronic recoil measurements from  $^{83m}\text{Kr}$ , their short half-lives limit them to the few weeks following an  $^{241}\text{AmBe}$  or NG calibration.

Selecting  $^{129m}\text{Xe}$  and  $^{131m}\text{Xe}$  events is trickier than  $\alpha$  or  $^{83}\text{Kr}$ . This is in part because they sit on top of an ER background (see Fig. 3.33 for background energy spectrum), have a relatively low event rate, and do not have properties that allow

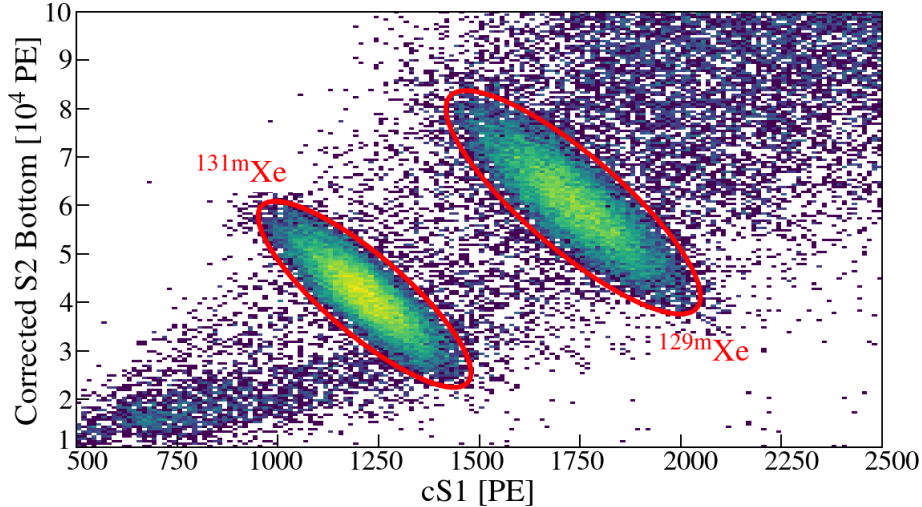


Figure 5.9: cS1 vs. cS2<sub>b</sub> for  $r_{\text{rec}} < 36.94$  cm,  $-6 < z < -85$  cm for dark matter search data from April 1-7, 2017 following the SR1  $^{241}\text{AmBe}$  calibration.  $^{129\text{m}}\text{Xe}$  and  $^{131\text{m}}\text{Xe}$  photopeaks are fit with a 2-dimensional gaussian to reject other background. The red contours mark the  $4\sigma$  lines.

a high-percentage cut efficiency (e.g.  $^{83}\text{Kr}$  delayed coincidence or high  $\alpha$ -decay S1). Instead a number of cuts are required to remove unwanted data before the fit.

To select the 163.9 and 236.2 keV peaks an S2 single scatter cut (same as in nuclear recoil band fitting, Sec. 4.2.4) is used to remove much of the underlying background. Additional data quality cuts include ensuring the fraction of the S2 seen by the top PMTs and the width of the S2 fall within expected distributions. For the FV the usual  $r_{\text{rec}} < 36.94$  cm is applied but we require  $-85 < z < -10$  cm to remove  $\gamma$ -rays of the same energy from materials that penetrate deeper into the detector.

Because cS1 is known (from position reconstruction) fitting the  $\gamma$  peaks is reasonably simple, especially if the electron lifetime can be roughly estimated. In Fig. 5.9 the peaks are surrounded by contours from two-dimension gaussian fits. The y-axis is labeled as cS2<sub>b</sub> because for this data  $\tau_e$  is known within a small uncertainty - however, in general this may not be the case. The final cut removes data outside some number of  $\sigma$ .

To verify the data we've selected is mostly  $^{129\text{m}}\text{Xe}$  and  $^{131\text{m}}\text{Xe}$  the event rate is fit. Fig. 5.10 shows the number of decays in the two months following the SR0  $^{241}\text{AmBe}$  calibration. The fits give half-lifes that agree with the accepted values. A constant

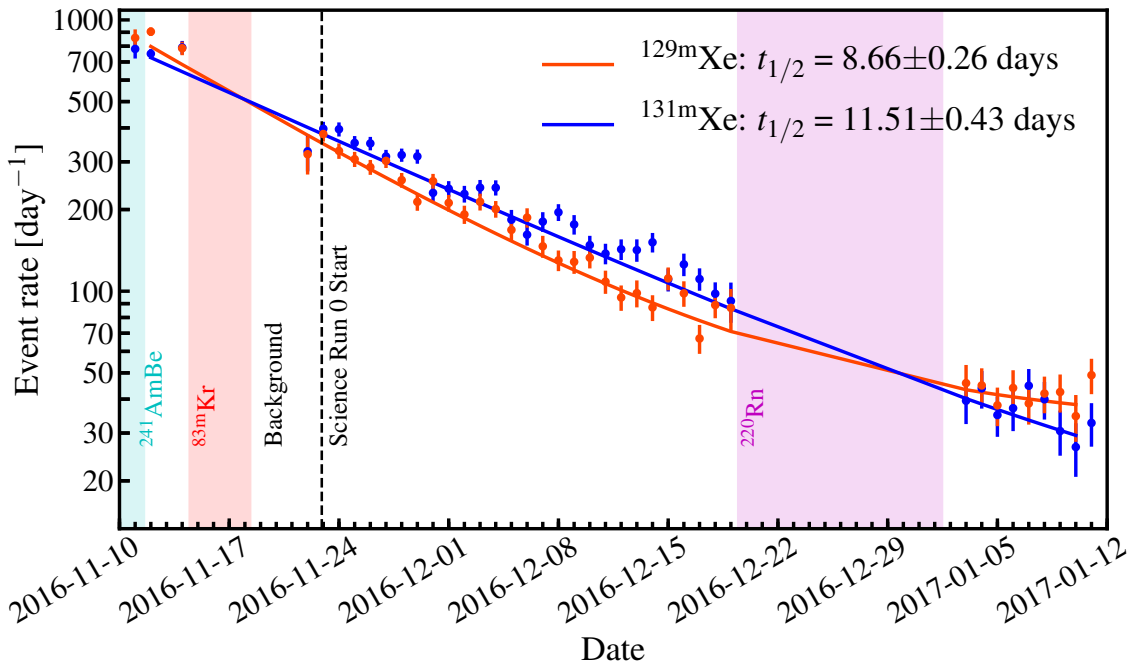


Figure 5.10:  $^{129m}\text{Xe}$  and  $^{131m}\text{Xe}$  events following the SR0  $^{241}\text{AmBe}$  calibration. Data is omitted during  $^{83m}\text{Kr}$  and  $^{220}\text{Rn}$  calibrations. Fits using  $R(t) = R_0 \exp(-t/t_{1/2}) + C$  give half-lives of  $8.66 \pm 0.26$  and  $11.51 \pm 0.43$  days, respectively, which match the known values of 8.88 and 11.93 days.

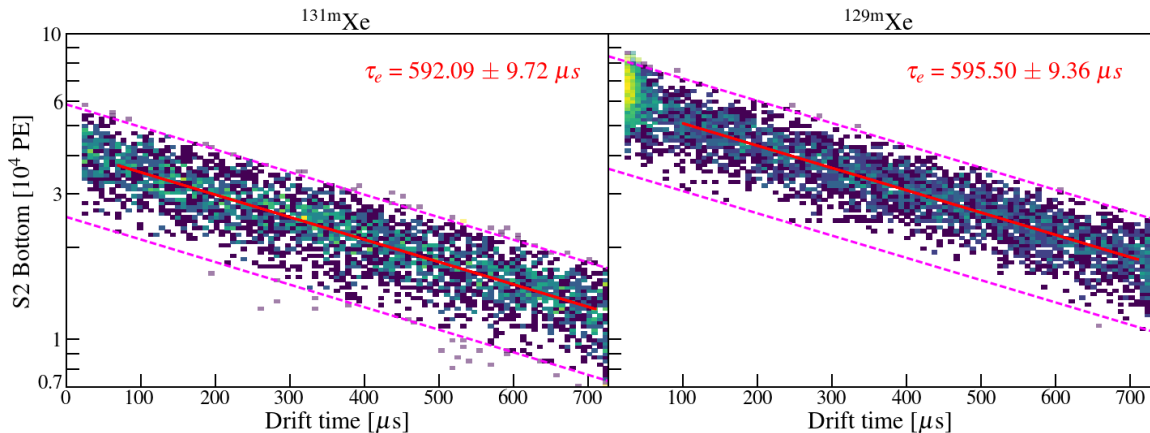


Figure 5.11: Electron lifetimes for  $^{131m}\text{Xe}$  (left) and  $^{129m}\text{Xe}$  (right) for April 1-7, 2017 (same as in Fig. 5.9). The red lines mark the region of the fit -  $70 < t_d < 710 \mu\text{s}$  and  $100 < t_d < 710 \mu\text{s}$  for  $^{131m}\text{Xe}$  and  $^{129m}\text{Xe}$ , respectively. The change in fit boundary is to remove higher energy events from detector materials that reach deeper inside the LXe, visible at  $t_d \lesssim 50 \mu\text{s}$  in the right panel. The electron lifetimes agree with one another.

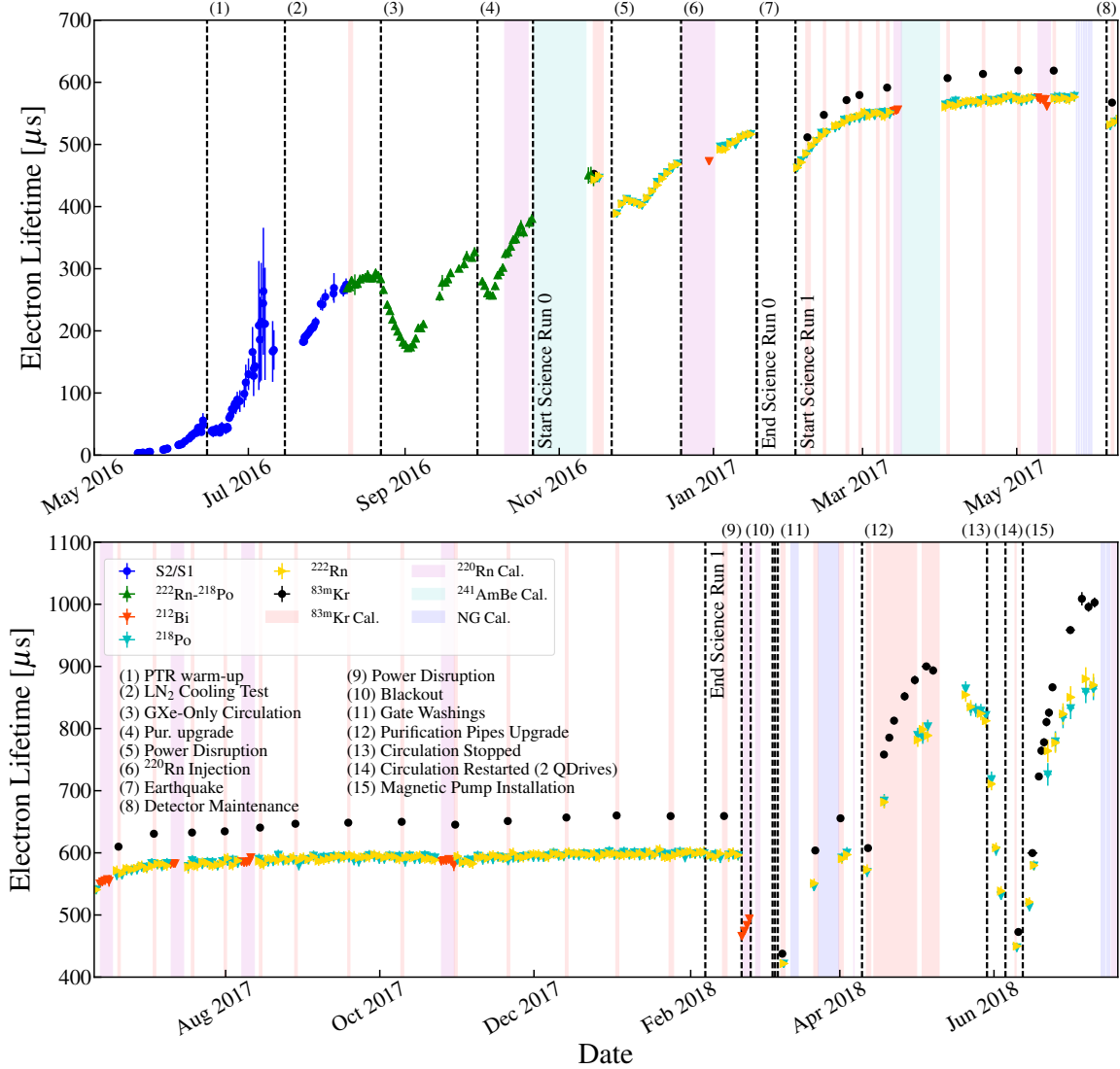


Figure 5.12: Electron lifetime measurements from S2/S1 (blue circles), combined  $^{222}\text{Rn}$ - $^{218}\text{Po}$  (green triangles),  $^{222}\text{Rn}$  (yellow triangles),  $^{220}\text{Rn}$  (red triangles),  $^{218}\text{Po}$  (turquoise triangles), and  $^{83\text{m}}\text{Kr}$  (black circles).  $^{83\text{m}}\text{Kr}$  (orange shaded),  $^{220}\text{Rn}$  (red),  $^{241}\text{AmBe}$  (green), and NG (blue) calibrations are shown as highlighted regions. Events that disrupt the electron lifetime evolution are marked by numbers at the top of each panel.

is included to account for underlying background.

The procedure to calculate  $\tau_e$  is the same as in Sec. 5.2.2. The result for the 7 days following the SR1  $^{241}\text{AmBe}$  data in Fig. 5.10 (April 1-7, 2017) is shown in Fig. 5.11.

### 5.2.5 $^{222}\text{Rn}$ vs. $^{83\text{m}}\text{Kr}$

Fig. 5.12 shows a clear disagreement in electron lifetimes between  $\alpha$ -emitters and  $^{83\text{m}}\text{Kr}$  at  $\tau_e \gtrsim 400 \mu\text{s}$ . This presents a challenge in knowing how to properly correct S2<sub>b</sub> for signals in the TPC.

The discrepancy is the result of field non-uniformity in the TPC (Fig. 3.6). Because the change in recombination of  $\alpha$ -decays with respect to field differs from that of electronic recoils (Fig. 2.19) the ratio of the charge yields vary inhomogeneously across the detector. Thus two issues are apparent. The first is bias will be present between any two events of equal energy and type (ER, NR,  $\alpha$ ) that occur at different fields in the detector. Therefore we cannot expect electron lifetime measurements to accurately report the xenon purity unless field distortion is accounted for. The second is two events whose  $e^-$  yield changes with respect to electric field  $dE/de^-$  are dissimilar require independent lifetime corrections. LUX also observed a disparity between  $^{83\text{m}}\text{Kr}$  and  $^{222}\text{Rn}$  lifetimes as well as field inhomogeneity, though the effects were not as stark [252], [253].

In Fig. 5.13 the electron yields for  $^{129\text{m}}\text{Xe}$  and  $^{222}\text{Rn}$  are shown throughout the TPC according to NEST assuming azimuthal symmetry [254]. The yields are normalized to the region  $[-90 \leq z \leq -85 \text{ cm}, r < 36.94 \text{ cm}]$ . The 1 t fiducial volume is marked by the black line. Both have decreasing yields in the  $-z$  direction, with the deviation for  $^{222}\text{Rn}$  being more than twice as large as  $^{129\text{m}}\text{Xe}$ . This means while  $\tau_e$  is biased towards smaller values for both elements, the effect is more significant for  $^{222}\text{Rn}$  and other  $\alpha$ -emitters.

S1 below 10 keV has minimal field dependence because recombination is minimal. Over 10 keV recombination increases.

The  $z$ -dependence of electron yields for  $^{129\text{m}}\text{Xe}$ ,  $^{131\text{m}}\text{Xe}$ ,  $^{60}\text{Co}$ ,  $^{208}\text{Tl}$ , and  $^{222}\text{Rn}$  is plotted in Fig. 5.14 (averaged over  $r < 36.94 \text{ cm}$ ). The NEST results are normalized to the same region as Fig. 5.13.  $^{60}\text{Co}$  and  $^{208}\text{Tl}$  (1173.2 and 2614.5 keV, respectively) are shown for comparison with  $^{131\text{m}}\text{Xe}$ . The difference in relative yields is small - though because in reality the distribution of these detector material-driven events

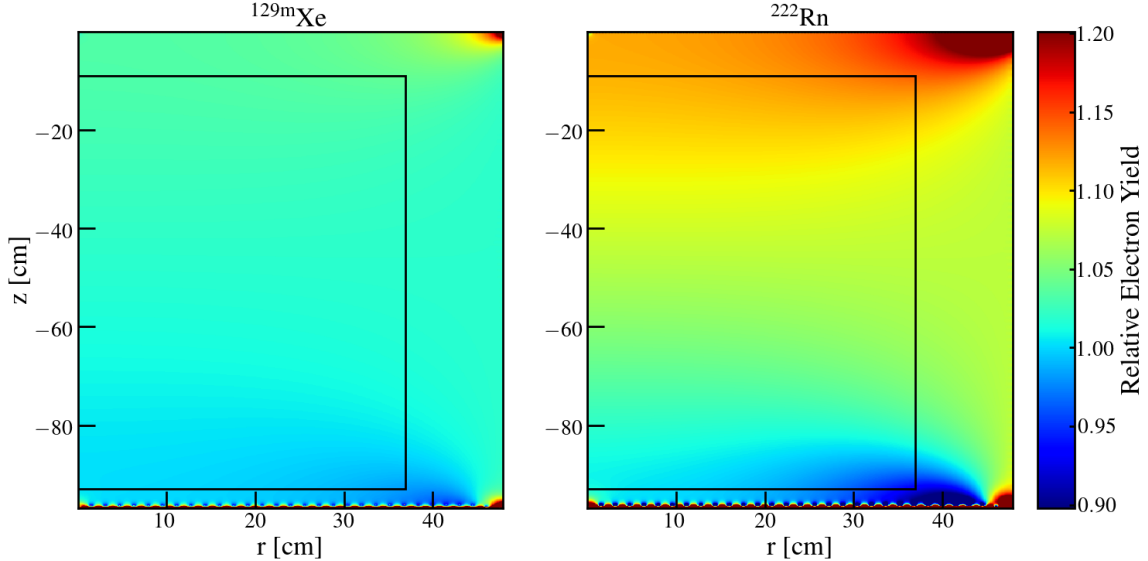


Figure 5.13: Relative electron yield with respect to  $[-90 \leq z \leq -85 \text{ cm}, r < 36.94 \text{ cm}]$  for  $^{129\text{m}}\text{Xe}$  (left) and  $^{222}\text{Rn}$  (right) for  $V_c = 8 \text{ kV}$  ( $\sim 80 \text{ V cm}^{-1}$ ) inside the 1T FV (black line). A decline in yield in the  $-z$  direction leads to the incorrect observation that the electron lifetime is lower than its true value. The imbalance between the top and bottom of the TPC is  $\gtrsim 2\times$  larger for  $^{222}\text{Rn}$ , causing its  $\tau_e$  to appear lower than its  $\gamma$  counterparts.

is more condensed at larger  $r$  where there is moderately more  $z$ -dependent variation they may be higher. Nonetheless, in either case this would explain the inconsistencies at higher energies in the combined energy spectrum (Fig. 3.33). The effect of  $^{222}\text{Rn}$  is more substantial and demonstrates that calculations of  $\tau_e$  - which depend on slices in  $z$  - suffer from greater bias as a result of change in recombination with respect to field. The higher sensitivity of  $\alpha$ -decays in part explains the lower measured lifetime. A separate field-dependent effect is discussed in Sec. 5.3.9.

We expect nuclear recoils to have a different bias than electronic or  $\alpha$ -decays. In the dark matter analysis all science run and calibration data were corrected using the  $^{83\text{m}}\text{Kr}$  electron lifetime. Nuclear recoil cS2<sub>b</sub> were then incorrect and had some bias with respect to ER. However, the disparity between NR and ER should be much smaller than  $\alpha$  so we can expect this effect to be small if not negligible.

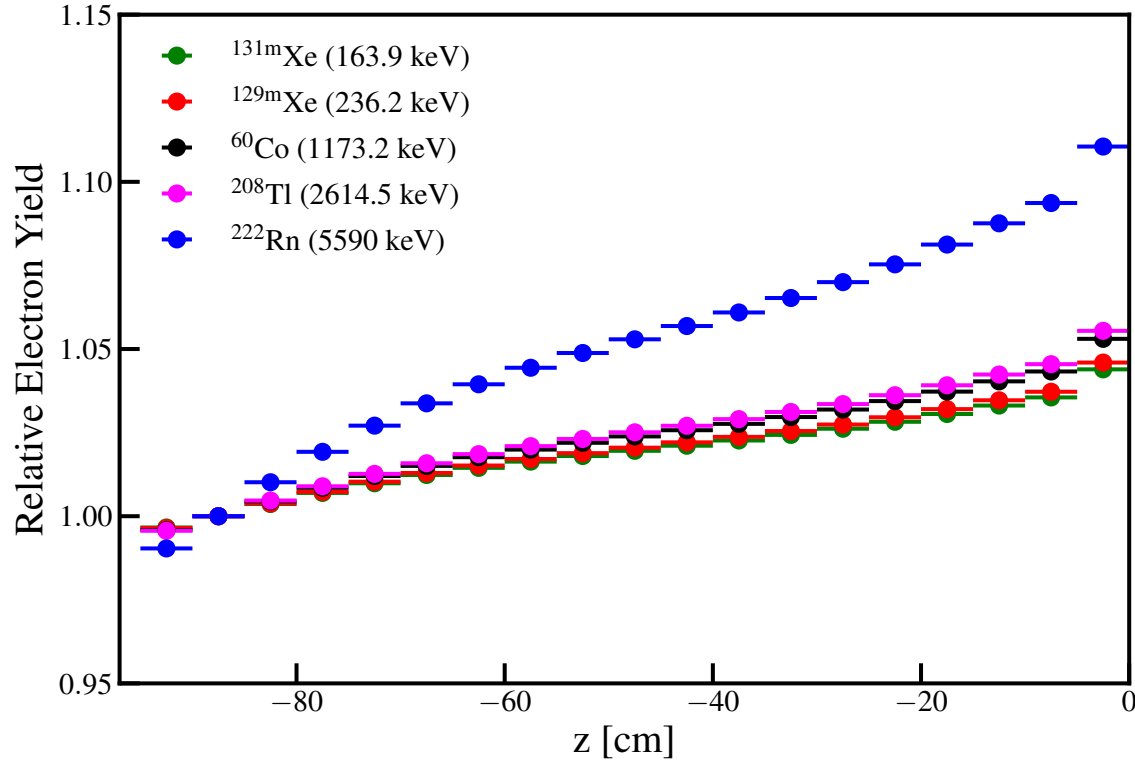


Figure 5.14: Relative electron yield dependence on  $z$  with respect to the region  $-90 \leq z \leq -85$  cm and  $r < 36.94$  cm at  $V_c = 8$  kV ( $\sim 80$  V cm $^{-1}$ ) using NEST [254]. Internal  $\gamma$  sources  $^{131\text{m}}\text{Xe}$  (green) and  $^{129\text{m}}\text{Xe}$  (red) are shown, with higher energies  $^{60}\text{Co}$  (black) and  $^{208}\text{Tl}$  (pink) plotted for comparison. Their relative light yields vary by  $\sim 5\%$ , with the higher-energy lines having only  $\sim 1\%$  greater difference than  $^{131\text{m}}\text{Xe}$  and  $^{129\text{m}}\text{Xe}$ .  $^{222}\text{Rn}$  (blue) changes by  $> 10\%$ . The disproportionate growth demonstrates the ratio between  $\alpha$  and  $\gamma$  electron yields is largest at the top of the detector, causing the fewer  $e^-$  from deep  $\alpha$ -decays to mimic a smaller  $\tau_e$ .  $^{83\text{m}}\text{Kr}$  cannot be compared as the NEST version is only for high-energy.

### 5.3 Electron Lifetime Model

To construct the electron lifetime model a number of factors were considered. The model was fit to the  $^{222}\text{Rn}$   $\alpha$ -emissions because they could continually monitor the electron lifetime. The best-fit trend was then scaled to match the  $^{83\text{m}}\text{Kr}$  data using a “scaling function” and applied to science data to account for the discrepancy between  $\alpha$ -decays and  $^{83\text{m}}\text{Kr}$  (Sec. 5.2.5).

The model tracks the impurity concentration in LXe ( $I_L$ ) and GXe ( $I_G$ ) - the latter of which is necessary because of the exchange of atoms and molecules through

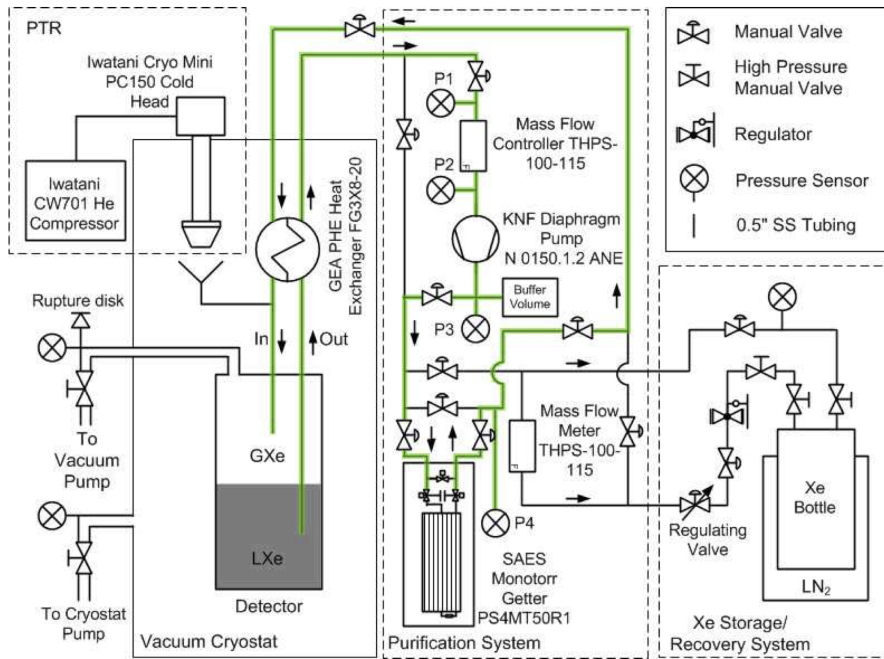


Figure 5.15: Schematic of the Columbia Demonstrator in its initial state. The connection from the GXe to the getter was not yet installed at the time of publication (Sec. 5.3.4). The path of xenon to and from the getter is marked in green. Image credit: [191].

vaporization and condensation (Sec. 5.3.3).

### 5.3.1 Columbia Demonstrator

To address new challenges in upgrading to a ton-scale detector a prototype was constructed at Columbia. While much smaller in total volume ( $\sim 26$  kg total,  $\sim 4$  kg active volume) one of the goals was to assess the feasibility of a 1 meter drift length, which required a significant improvement in xenon purification compared to the  $\sim 5$  slpm of XENON100 [189].

Fig. 5.15 shows a schematic of the Demonstrator. LXe passes through the heat exchanger on its way to the getter and again upon its return as GXe. The getter is a SAES PS4-MT50-R-1, the same model that was chosen for XENON1T. A KNF diaphragm pump, common among LXe experiments, was initially set up and planned for XENON1T but was eventually replaced by a QDrive (Sec. 3.1.4). Pipes for GXe circulation were not installed until later so they are not shown.

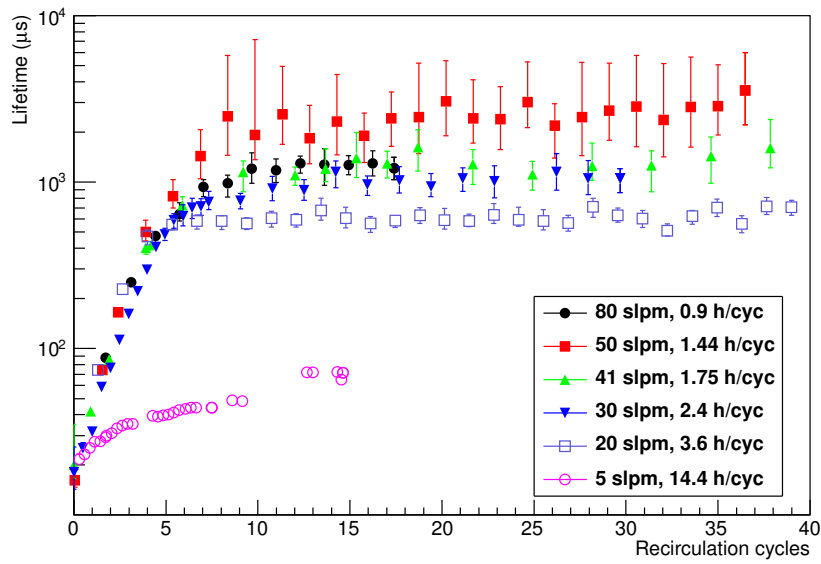


Figure 5.16: Electron lifetime dependence on flow rate through getter for the Columbia Demonstrator. Measurements are done for 5 (pink circles), 20 (blue squares), 30 (blue triangles), 41 (green triangles), 50 (red squares), and 80 (black circles) slpm. With exception of 5 slpm, the lifetimes increase at roughly the same rate per cycle for the first  $\lesssim 7$  cycles. From 0 to 50 slpm an increase in flow produces a higher final electron lifetime. At 80 slpm  $\tau_e$  drops below that at 50 slpm. An explanation may be that at high speeds impurities cannot be removed as efficiently due to the short time spent in the getter. Image credit: [255].

### 5.3.2 Impurity Removal

Impurities are removed in the purification system (Sec. 3.1.4) by two SAES PS4-MT50-R getters. They operate between 5-100 slpm and uses heated zirconium ( $400^\circ\text{C}$  nominal operating temperature) to form irreversible chemical bonds with  $\text{O}_2$ ,  $\text{CO}$ ,  $\text{CO}_2$ ,  $\text{H}_2\text{O}$ ,  $\text{H}_2$ ,  $\text{N}_2$ , and  $\text{CH}_4$ , and is capable of achieving levels of  $< 1$  ppb.

Fig. 5.16 shows electron lifetimes using flow speeds of 5-80 slpm in the Demonstrator. For flows larger of 20 slpm and greater the rate of increase per cycle is approximately the same in the beginning (the rate with respect to time depends on the circulation speed). This indicates the influx of new impurities per time is small compared to the rate of removal by the getter, except for in the 5 slpm case. For 20-50 slpm the final value for  $\tau_e$  increases with flow speed - however, it drops at 80 slpm. This is thought to result from gas passing through the getter too quickly to

remove the impurities completely.

For XENON1T the two getters cleaned a combined flow of  $\lesssim 50$  slpm until after SR1. This was only half of the design value and was largely the result of the 1/2" outer diameter pipes connecting the cryogenic system to the purification system producing higher than expected resistance. A series of upgrades were performed in April-June 2018 that increased flows to  $\sim 80$  slpm (Sec. 5.3.8). Because in both cases the flow through each getter never exceeded 50 slpm the electron lifetime model assumes 100% of contaminants are absorbed by the zirconium, though we cannot know if this is truly the case. However, including a variable in the model to reflect a portion of impurities returned to the detector would be equally problematic because Fig. 5.16 suggests any inefficiency is flow-dependent. A more systematic study is needed to characterize the relationship before it can be reliably included. The HALO monitor (Sec. 3.1.4) might be able to provide some insight if it were usable during normal operating conditions, since it measures the H<sub>2</sub>O concentration of purified xenon. The low circulation over the course of the experiment makes 100% getter efficiency a reasonable estimate.

The rates of impurity removal by the purification system are

$$M_G \frac{dI_G}{dt}^{(\text{pur})} = -\rho_{\text{GXe}} F_G I_G \quad (5.11\text{a})$$

$$M_L \frac{dI_L}{dt}^{(\text{pur})} = -\rho_{\text{GXe}} F_L I_L \quad (5.11\text{b})$$

where  $\rho_{\text{GXe}} = 5.984 \text{ g l}^{-1}$  is the density of GXe.  $F_G$  and  $f_L$  are the flows of the gas and liquid, and are included by using their values stored in the slow control system (Sec. 3.1.10). Using the slow control system to automatically integrate these time-varying nuisance parameters into the model is incredibly advantageous over manually assigning the flow.

The schematic of the purification slow control system is shown in Fig. 5.17. While a large number of parameters are monitored only a small fraction need to be included. The three flow control valves (FCVs) that independently regulate GXe flow from the cryogenics system to purification (Sec. 5.3.4) are not shown but precede the “From Cryostat GXe” marker. LXe from the cryostat that passes through the heat exchanger

## 5. PURITY AND THE ELECTRON LIFETIME

---

Parameter	Function	Color	Comments
CRY_FCV101	GXe flow control (cables)	—	Precedes “From Cryostat GXe”
CRY_FCV102	GXe flow control (mid-cryostat)	—	Precedes “From Cryostat GXe”
CRY_FCV103	GXe flow control (cooling towers)	—	Precedes “From Cryostat GXe”
PUR_FC201	Flow control (bottom loop)	purple	
PUR_FC202	Flow control (top loop)	purple	
PUR_FV217	Valve (bottom loop)	pink	Bypass Getter 201
PUR_FV224	Valve (top loop)	pink	Bypass Getter 202

Table 5.3: Parameters queried from the slow control system to calculate  $F_G$  and  $F_L$ . Those in Fig. 5.17 are highlighted in the color listed.

(HE) and heater is labeled “From Cryostat HE”. Returning GXe is sent to the TPC Bell (“GXe to TPC Bell”) through flow control valve FCV104 to maintain cryostat pressure or is liquified in the HE (“To Cryostat HE”) before entering the bottom of the TPC (xenon that does not condense returns to the GXe in the cryogenic system). FCV104 is not necessary to monitor since returning xenon is modeled as 100% pure. The flux through the system is measured with flow controllers FC201 and FC202 that precede the getters. Valves FV217 and FV224 must be monitored because if they are open the xenon will bypass the getters. The top and bottom paths in Fig. 5.17 have one and two QDrives, respectively, so the flow through the bottom is larger. Installing a second QDrive on the top loop would not increase the flow because it was restricted by the pipes (as mentioned above this was eventually fixed) and would increase  $^{222}\text{Rn}$  emanation.

Because the mass of xenon has been mostly stable since the detector came online valves leading to and from ReStoX (Sec. 3.1.5) and bottles do not need to be tracked. The total mass of xenon removed by the krypton column (Sec. 3.1.6) is negligible (0.07% through SR1) and can be ignored. The slow control parameters are summarized in Tab. 5.3.

The GXe flow into the purification system is calculated as

$$F_G^{(\text{in})} = \sum_i F_i \quad (5.12)$$

where  $F_i$  is the flow for  $i = \text{FCV101}, \text{FCV102}, \text{FCV103}$ . The inlet LXe flow is calculated

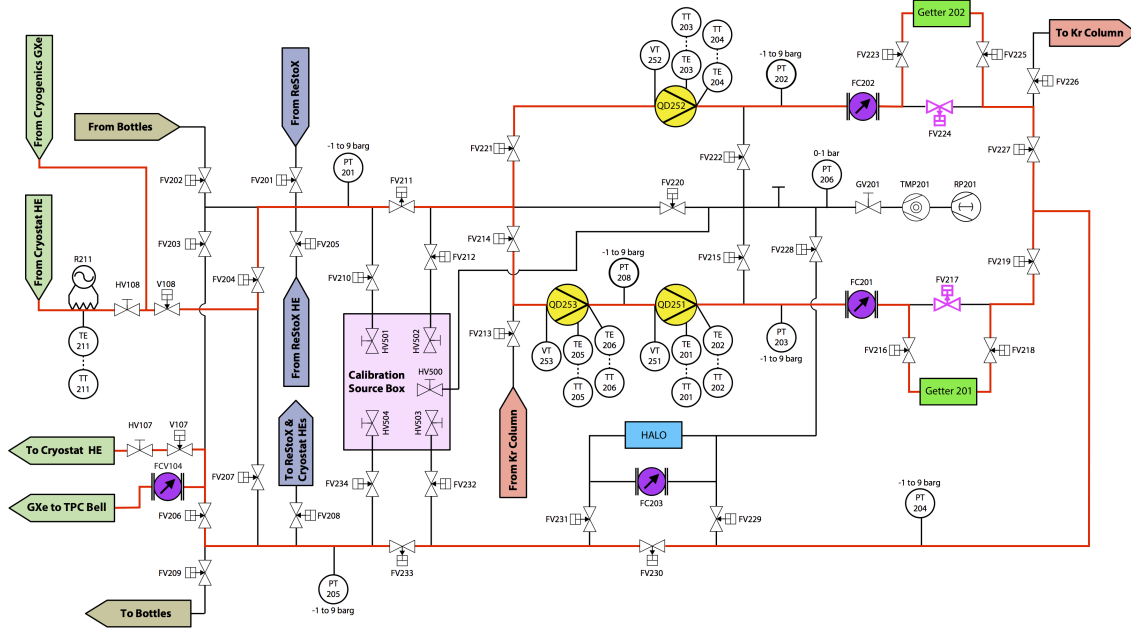


Figure 5.17: Schematic for purification system from slow control. LXe and GXe enter the purification system and pass through the top or bottom branch. They reunite before returning through the heat exchanger or as pressurized gas to the TPC Bell. QDrives (yellow), flow controls FC201 and FC202 (purple), getters (green), bypass valves (pink) and the HALO monitor (red) are highlighted. The path of xenon during ordinary operations is shown in red.

$$F_L^{(\text{in})} = \sum_j F_j - F_G^{(\text{in})} \quad (5.13)$$

for  $j = \text{FC201}, \text{FC202}$ . The flow that is purified is

$$F_G = F_G^{(\text{in})} \left[ (1 - \text{Status}(\text{FV217})) \frac{F_{\text{FC201}}}{F^{(\text{in})}} + (1 - \text{Status}(\text{FV224})) \frac{F_{\text{FC202}}}{F^{(\text{in})}} \right] \quad (5.14a)$$

$$F_L = F_L^{(\text{in})} \left[ (1 - \text{Status}(\text{FV217})) \frac{F_{\text{FC201}}}{F^{(\text{in})}} + (1 - \text{Status}(\text{FV224})) \frac{F_{\text{FC202}}}{F^{(\text{in})}} \right] \quad (5.14b)$$

where  $\text{Status}()$  is 0 if closed and 1 if open.  $F^{(\text{in})}$  is  $F_G^{(\text{in})} + F_L^{(\text{in})} = F_{\text{FC201}} + F_{\text{FC202}}$ .

### 5.3.3 Vaporization and Condensation

Impurity migration between the liquid and gas requires consideration of both volumes rather than strictly the liquid. Electronegative particles (e.g. O<sub>2</sub>, CO, etc.) are expected to be more densely distributed in the GXe due to their lighter atomic mass. To parameterize the migration rates for an impurity from the liquid to the gas or vice versa, the condensation and vaporization rates need to be included.

The pulse-tube refrigerators (PTRs) and LN<sub>2</sub> supply the cooling power to the system (Sec. 3.1.3) and are balanced by heat from the GXe and resistive heaters (one on each coldfinger) that keep detector conditions stable. The resistive heaters are run by proportional-integral-derivative (PID) controllers and adjust in real-time to maintain a stable coldfinger temperature. Because there is no flow of heat into or out of the coldfinger the three balance

$$\dot{Q}_{\text{CF}} + \dot{Q}_{\text{GXe}} + \dot{Q}_{\text{H}} = 0 \quad (5.15)$$

where  $\dot{Q}$  is the heat transfer rate with  $\dot{Q}_{\text{CF}} < 0$  and  $\dot{Q}_{\text{GXe}}, \dot{Q}_{\text{H}} > 0$ . Because the slow control system only monitors the resistive heaters the other two are disentangled via a measurement of  $\dot{Q}_{\text{H}}$  when the inner vessel was under vacuum before filling ( $\dot{Q}_{\text{GXe}} = 0$ ). It was found to be  $\dot{Q}_{\text{CF}} = -\dot{Q}_{\text{H}} = -260$  W. Eq. 5.15 can be rewritten as

$$\dot{Q}_{\text{GXe}} + \dot{Q}_{\text{H}} = 260 \text{ W} \quad (5.16)$$

so as the heat load from the xenon increases the current in the resistive heater decreases.

Purification has the greatest variability among heat sources during stable conditions as a result of changes in circulation speed. For roughly two days shortly after XENON1T came online purification was halted entirely, as shown in Fig. 5.18. Once the system stabilized  $\dot{Q}_0 \equiv \dot{Q}_{\text{GXe}}$  was calculated via Eq. 5.16 to be 140 W. Because the system was stable the vaporization and condensation rates must be equivalent. The total xenon mass has remained unchanged by >99% so it is reasonable to assume the  $\dot{Q}_{\text{H}}$  and vaporization and condensation rates under these conditions hold true today.

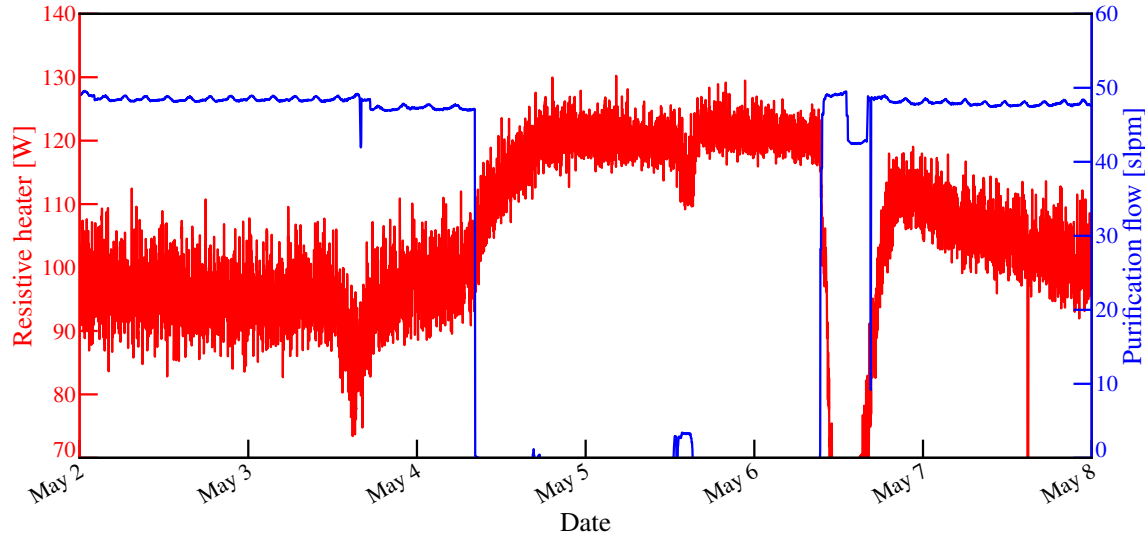


Figure 5.18: Heater power  $\dot{Q}_H$  (red) and purification flow (blue) from May 2–8, 2016. On May 4th circulation is stopped, decreasing the heat load in the GXe.  $\dot{Q}_H$  rises to  $\sim 120$  W, so to satisfy Eq. 5.16  $\dot{Q}_{\text{GXe}} \sim 140$  W. When purification resumes on May 6th there is a sharp drop in  $\dot{Q}_H$  while the heat exchanger and other materials equilibrate before returning to a stable value.

While xenon returning from purification will add heat to the system, with a total mass of more than 3 t and narrow temperature range ( $< 1^\circ\text{C}$  between bottommost and topmost sensors) the thermal load of the liquid xenon does not appreciably change. Therefore the vaporization rate is constant regardless of flow and can be modeled using the zero-flow period

$$M_G \frac{dI_G}{dt}^{(\text{vap})} = -M_L \frac{dI_L}{dt}^{(\text{vap})} = \frac{\epsilon_{\text{vap}} \dot{Q}_0 I_L}{L} \quad (5.17)$$

where  $\epsilon_{\text{vap}}$  is the vaporization probability for impurities in the liquid and  $L = 9.6 \times 10^4 \text{ J kg}^{-1}$  is the latent heat of vaporization.

The excess heat will increase the thermal load of the gas so its contribution to the coldfinger will grow. The specific heat for xenon gas at constant pressure is  $c_p = 158 \text{ J kg}^{-1} \text{ K}^{-1}$ . The condensation rate for xenon is

$$\begin{aligned}\dot{Q}_{\text{GXe}}^{\Delta T} + \dot{Q}_{\text{GXe}}^{(\text{cond})} &= \dot{Q}_{\text{GXe}} \\ \dot{m}c_p\Delta T + \dot{m}L &= \dot{Q}_{\text{GXe}} \\ \dot{m} &= \frac{\dot{Q}_{\text{GXe}}}{c_p\Delta T + L}\end{aligned}\tag{5.18}$$

where  $\Delta T$  is the difference between the initial and vaporization temperatures. The condensation term in the model is

$$-M_{\text{G}} \frac{dI_{\text{G}}}{dt}^{(\text{cond})} = M_{\text{L}} \frac{dI_{\text{L}}}{dt}^{(\text{cond})} = \frac{\epsilon_{\text{cond}} \dot{Q}_{\text{GXe}} I_{\text{G}}}{c_p(T - T_0) + L}\tag{5.19}$$

where  $\epsilon_{\text{cond}}$  is the probability of condensation for impurities in the gas and  $T$  is the temperature of the GXe inside the unpowered PTR cooling tower. Selecting a temperature sensor is somewhat arbitrary since the gas inside the inner vessel - despite a temperature range of  $> 100^{\circ}\text{C}$  - should exhibit similar behavior. To account for this  $T_0$  is left as a free parameter but constrained so that  $T - T_0$  is within the vaporization and maximum detector temperatures.

A complication in calculating  $\dot{Q}_{\text{GXe}}$  is  $\dot{Q}_{\text{CF}}$  is known to decrease in time. This can be indirectly observed by the long-term behavior in  $\dot{Q}_{\text{H}}$  as shown in Fig. 5.19. As a result Eq. 5.16 leads to increasing overestimation of the condensation over time if not corrected, though this can be difficult since  $\dot{Q}_{\text{H}}$  also corrects for real temperature changes of the GXe. In addition, the rate of decrease is not consistent so piecewise corrections are applied. Fig. 5.19 shows the raw (from slow control) and corrected  $\dot{Q}_{\text{H}}$  over the course of the experiment.

### 5.3.4 GXe Purification

Because only the electrons drifting in the LXe lead to an S2 purifying the GXe was in the past not considered necessary. However, the light masses of electronegative impurities and higher temperatures that produce greater outgassing suggest that their concentration may be greater in the gas. Because impurities are exchanged between the liquid and gas (Sec. 5.3.3) their potential to compromise the electron lifetime is significant.

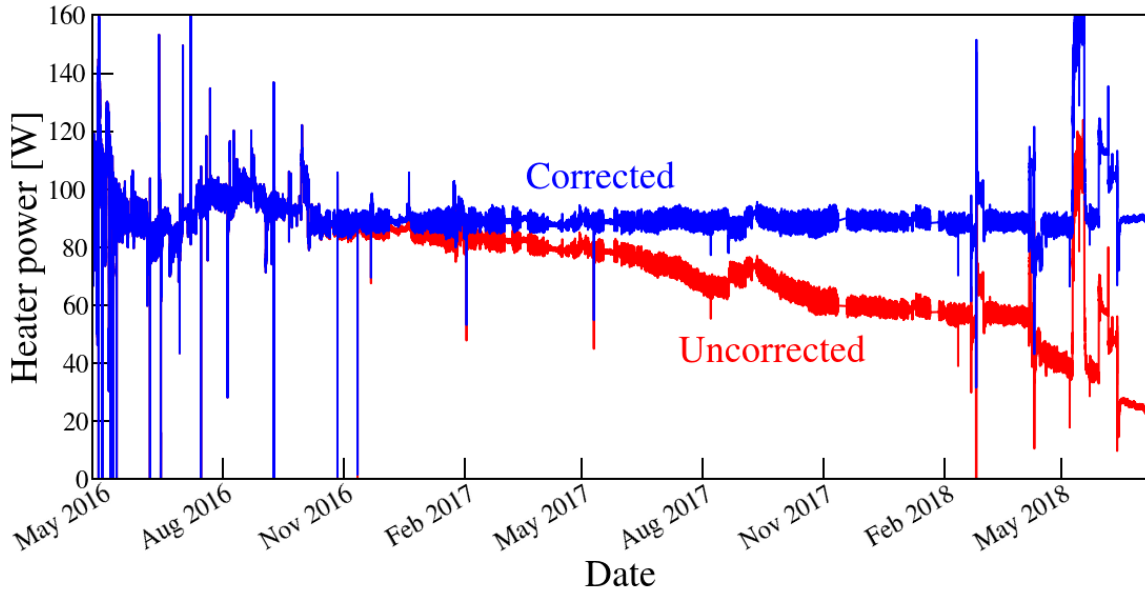


Figure 5.19:  $\dot{Q}_H$  over the lifetime of XENON1T. Sudden spikes and sporadic behavior result from compensating for rapid increases or decreases in heat from the GXe. Long-term downward trend is caused by the PTR cooling power decreasing over time. The corrected trend used in the fit is shown.

As part of the work leading up to XENON1T the Demonstrator installed piping connecting GXe outside the TPC to the purification system to investigate this effect. Fig. 5.20 shows the electron lifetimes over the course of the measurement using the 661.7 keV  $^{137}\text{Cs}$   $\gamma$ -ray. Two periods with GXe and LXe circulation were observed and are highlighted in blue. Each shows an increase in  $\tau_e$ , though the second run only lasted a few days. The first measurement improves the lifetime from  $\sim 200 \mu\text{s}$  to  $\sim 450 \mu\text{s}$  and does not show signs of leveling off when the LXe-only circulation is restored. This confirmed the intuition that electronegative impurities in the GXe play an important role in the electron lifetime, and our dark matter search would benefit from assembling XENON1T for GXe purification.

Five lines connect the GXe volume of the XENON1T inner vessel to the purification system (Sec. 3.1.4). Three lines are attached to the cooling towers (one to each) since as the highest points they should contain the greatest impurity concentration. In addition they are warmest regions so their outgassing is expected to be the most substantial (Fig. 3.8 and 3.9). The three lines are joined before a flow control valve

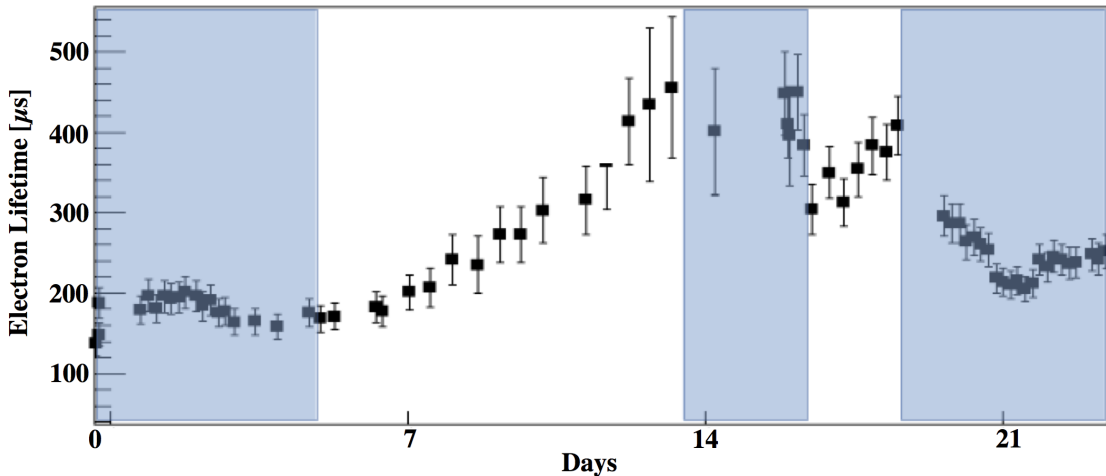


Figure 5.20: Electron lifetime using LXe with (white region) and without (blue) GXe circulation for the Demonstrator. The electron lifetime more than doubles in the first iteration over a roughly 10-day span. A period follows with only LXe purification, but is too short to observe much decrease. Upon re-initiating GXe flow the lifetime drops a bit - possibly due to trapped impurities in the GXe tubing - but then begins to climb again. The final block reveals the electron lifetime does decrease with LXe-only circulation. Longer periods with and without GXe purification are needed for better assessment. Image credit: [255].

that regulates their flux. A fourth conduit is linked to the tube that carries the PMT signal and high voltage cables between the TPC and data acquisition. This region was selected because the cables were suspected of having high radon emanation, and the larger surface area means greater outgassing. Connecting directly to the purification system allows cleaning of higher impurity concentration gas and distillation of the radon. The flow is strong enough that the odds of an impurity or radon atom making it into the bell against the current is negligible. The final line is stationed approximately halfway between the TPC and cooling towers to purify GXe from the neck of the cryogenic system. This location was chosen to address two challenges: elevated radon emanation levels from cryogenics materials, and a predicted  $\sim 20\times$  higher oxygen level in the gas than liquid. The line is connected to the inner vessel in the service building at the point immediately outside the water tank to lessen the contaminants that reach the LXe through condensation either at the liquid-gas surface or from the PTR (Sec. 5.3.3). Both this line as well as the one connected to the cable tube have flow control valves that are independent from each other and the

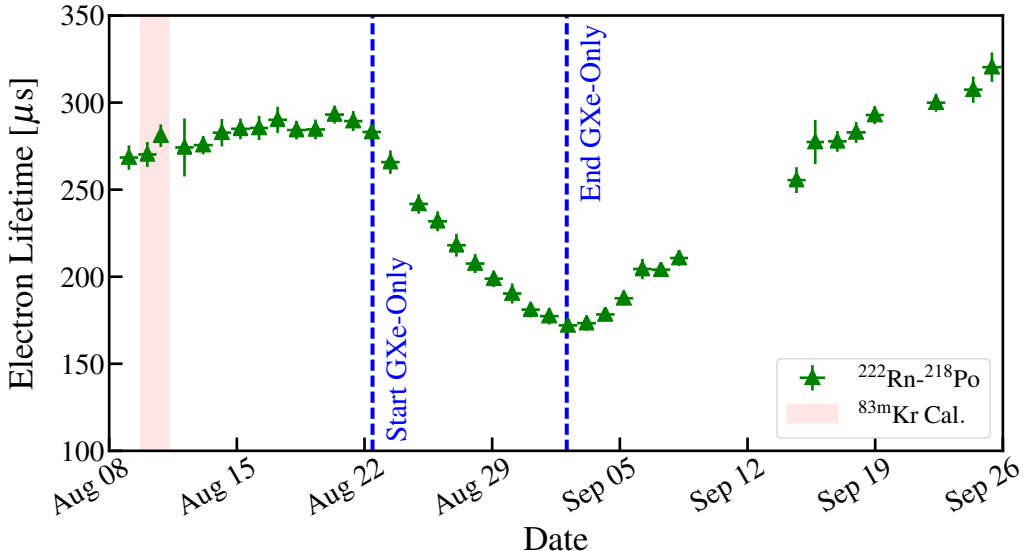


Figure 5.21: Purification of only xenon gas from August 22 - September 2, 2016, marked by green dashed lines. Electron lifetime measurements are from  $^{222}\text{Rn}$ - $^{218}\text{Po}$  combined data. The purpose of the operation was to study the exchange of impurities between the gas and liquid, which depends on vaporization/condensation and outgassing.

cooling tower pipes, allowing custom ratios of flow between the three.

During standard operations GXe is passed through the getters at  $F_{\text{G}} \sim 3.75$  slpm, or roughly 7-8% of the total flow during SR0 and SR1.

From August 22 to September 2, 2016 LXe purification was halted to study the effect that GXe purification has by decoupling it from the liquid. The electron lifetime decreased more rapidly than anticipated, indicating that while the impurities in the GXe were influential, they were not to the extent predicted by the Demonstrator. The physics of the GXe-only circulations in the Demonstrator and XENON1T is not yet fully understood, but future detectors may continue to provide insight into the interplay of GXe-LXe impurity exchange in a TPC. Modeling the GXe period of the evolution constrains the outgassing, vaporization, and condensation rates.

### 5.3.5 Outgassing and Leak

Xenon is continuously contaminated with impurities that outgas from detector materials. Therefore the outgassing model plays a critical role in the outcome of the

electron lifetime model. Historically electron lifetimes have followed a Fermi-Dirac during periods of rapid increase that result from a higher rate of impurity removal than influx. Once this phase has finished  $\tau_e$  follows a linear-like upward trend, presumed to be tracking the decrease in outgassing. In the event of a purity degradation a Fermi-Dirac will ensue and the electron lifetime will return to the same line as before.

In the beginning of SR1 the  $\alpha$  electron lifetime rapidly rose to  $\sim 580 \mu\text{s}$  ( $630 \mu\text{s}$  for  $^{83\text{m}}\text{Kr}$ ) and began the expected linear-growth stage. However, instead of continuing this trend it plateaued around  $\sim 600 \mu\text{s}$  ( $650 \mu\text{s}$   $^{83\text{m}}\text{Kr}$ ). A time-independent outgassing model is known to be incorrect and gave a poor fit to the full evolution. A more likely scenario is the presence of a leak. While we cannot say definitively that a leak is the cause as it was never searched for, the presence of a time-independent impurity source is referred to in this chapter as a leak, and in the event it is not truly a leak the results do not change. Therefore the influx of impurities is modeled with outgassing and leak rates.

### 5.3.5.1 Outgassing Sources

There are three time-dependent outgassing sources: vaporization, diffusion, and desorption. These are well-understood for vacuum systems and while the pressure in the cryogenic system is  $> 1 \text{ atm}$ , much of the physics remains relevant for our detector.

**Vaporization** is the release of particles by producing a phase transition from a solid or liquid via heat. When the rate of particles evaporating is equivalent to the rate arriving the system is in dynamic equilibrium. If the vapor and solid/liquid host are at the same temperature in dynamic equilibrium the pressure of the vapor over the surface is equivalent to the vapor pressure of the solid/liquid. The flux of impurities leaving the surface is

$$n \left( \frac{k_B T}{2\pi m} \right)^{1/2} = nv/4 \quad (5.20)$$

where  $v = (8k_B T/\pi m)^{1/2}$  is the mean speed for an ideal gas. Because the cryogenic system is designed to be thermally stable vaporization from new heat sources is mostly

irrelevant, with the exception of detector component replacement (Sec. 5.3.8). Instead vaporization primarily applies to atoms and molecules that have diffused to the inner surface from inside the material bulk.

**Diffusion** is the movement of one material through another. Particles inside our detector materials are naturally drawn to the surfaces by their own gas pressure. For a uniform initial concentration  $C_0$  of dissolved gas inside a solid the outgassing rate is obtained by the diffusion equation to be

$$q = C_0 \left( \frac{D}{\pi t} \right)^{1/2} \left[ 1 + 2 \sum_{n=1}^{\infty} (-1)^n e^{-n^2 d^2 / Dt} \right] \quad (5.21)$$

where  $D$  is the diffusion constant and  $2d$  is the thickness of the solid [256]. At small and large  $t$  the outgassing rate becomes

$$q(t) \approx \begin{cases} C_0 \left( \frac{D}{\pi t} \right)^{1/2} & t \ll \frac{d^2}{D}, \\ \frac{2DC_0}{d} e^{-\pi^2 Dt / 4d^2} & t \gg \frac{d^2}{D} \end{cases} \quad (5.22a)$$

$$(5.22b)$$

where Eq. 5.22 is derived by redefining the initial conditions in Eq. 5.21. For the lifetime of XENON1T the diffusion can be approximated by Eq. 5.22. This process is typically much slower than desorption so after desorption of initial surface contaminants diffusion dictates the outgassing rate.

The diffusion constant for a gas in a solid decreases as

$$D = D_0 e^{-E_D / RT} \quad (5.23)$$

where  $E_D$  is a measure of the attraction between a molecule and the surface to which it's adsorbed known as the *thermal activation energy*. Tab. 5.4 lists  $E_D$  and the relative fraction adsorbed for the most prevalent gases in normal air.  $D_0$  is typically between 0.01-10 cm<sup>2</sup> s<sup>-1</sup> for solids [257]. Eq. 5.23 explains why heating materials is such an effective method to reduce outgassing: even a small change in temperature can substantially expedite the time to reach lower outgassing. This is demonstrated in Fig. 5.22 where a sampler is heated from  $T_1$  to  $T_2$  for some duration before returning

Molecule	$E_D$ [cal g <sup>-1</sup> mole <sup>-1</sup> ]	$P_i$ [torr]	$P_i/P_{\text{tot}}$	$f_{\text{abs}}$
N <sub>2</sub>	1630	592	0.78	$7 \times 10^{-7}$
O <sub>2</sub>	1335	152	0.2	$1 \times 10^{-7}$
H <sub>2</sub> O	9720	11	0.014	1
Ar	1558	5	0.007	$6 \times 10^{-9}$
CO <sub>2</sub>	6030	0.23	$3 \times 10^{-4}$	$5 \times 10^{-7}$
H <sub>2</sub>	216	$3.8 \times 10^{-4}$	$4 \times 10^{-7}$	$4 \times 10^{-10}$

Table 5.4: Activation energies  $E_D$  for normal air at 300°K. Data taken from [257].

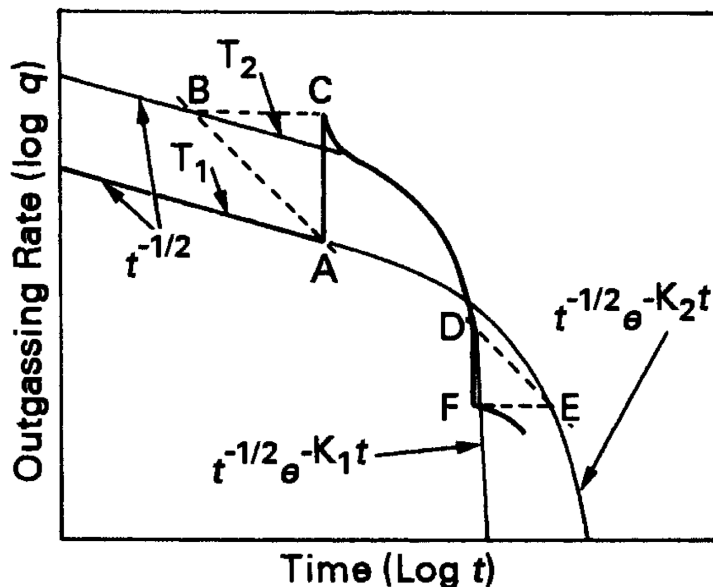


Figure 5.22: Outgassing rate  $q$  as a function of time for outdiffusion. A sample at temperature  $T_1$  is heated to  $T_2$  at point A. Because the gas concentration in the sample remains unchanged during this process (assume quickly heated) the outgassing at C is equivalent to B (diagonal dashed lines represent constant concentration). From C  $q$  quickly joins the  $T_2$  curve, which begins its exponential descent (Eq. 5.22) earlier. At D the sample is restored to  $T_1$  where it returns to its original curve at E but at an earlier time F. Image credit: [256].

to  $T_1$ . The difference in pressure can be calculated using the reparameterization of Eq. 5.21 used in Eq. 5.22 to give

$$P_F = \frac{D_1}{D_2} P_D \quad (5.24)$$

where  $D_1$  and  $D_2$  correspond to the diffusion rates at lower and higher temperatures and  $P_F$ ,  $P_D$  are the pressures at F and D [258].

Sample	Treatment	Outgassing rates [ $10^{-13}$ Torr l s $^{-1}$ cm $^{-2}$ ]			
		H <sub>2</sub> O	CO <sub>2</sub>	H <sub>2</sub>	CO
A	Vacuum for 75 h	430	10	670	65
	150°C bakeout for 50 h	13	0.03	290	4.5
B	300°C bakeout for 40 h	0.5	0.01	62	1.7
C	400°C degassing for 20 h in vacuum	0.2	0.08	14	0.33
D	800°C degassing for 2 h in vacuum	-	0.04	2.7	0.05
5-month exposure to atmosphere then vacuum for 24 h		55	10	-	50
150°C bakeout for 20 h		-	0.03	2.5	0.06

Table 5.5: Outgassing rates of H<sub>2</sub>O, CO<sub>2</sub>, H<sub>2</sub>, and CO from 316L stainless steel after various treatments. Significant reductions from bakeouts can be seen. Before treatment each sample was subjected to a two-hour degreasing with perchlorethylene vapor at 125°C, followed by a one-hour ultrasonic washing at 55°C, and finally were rinsed with clean water and dried. Data is taken from [259].

Fig. 5.22 shows how heating a material accelerates its transition from Eq. 5.22 to Eq. 5.22. Thus baking materials shortens the time until the exponential decrease of gas in the solid and reduce the outgassing in the detector.

**Desorption** is the release of gases that were previously adsorbed on the wall of the system. The gases on the surface may be from diffusion, permeation (Sec. 5.3.5.3), or exposure to a previous or current environment.

In thermal desorption particles that are bound to a surface via weak van der Waals forces of  $< 40$  MJ kg $^{-1}$  mole $^{-1}$  are labeled as *physisorbed* and are desorbed quickly under vacuum, while those at larger energy are *chemisorbed* and do so slowly unless external heat is applied. When more than one layer of particles exist on the surface they will desorb at a constant rate. However, once the coverage becomes less than one layer it will slow and become proportional to the surface concentration. Some molecules dissociate upon adsorption and recombine before desorption. This process depends on the square of the surface concentration so it can be much slower than normal desorption. This is especially relevant for diatomic molecules on metals.

In modeling desorption, re-adsorption of freed gases may need to be included. When baking it is necessary to heat all surfaces as any excluded regions will dominate outgassing once conditions are returned to equilibrium. The elevated pressure during a bake will cause larger than normal re-adsorption in these regions. If baking is done correctly the reduction in outgassing will be similar to diffusion - a slow initial process

but as the solid depletes its gases the decrease becomes exponential.

Outgassing rates for 316L stainless steel after various treatments are listed in Tab. 5.5 [259]. An unbaked sample has much higher outgassing than one that is baked at just 150°C for 50 hours. For these results the bakeouts were *in situ*, meaning the outer walls were exposed to atmosphere while the inner were in vacuum. This is a popular method because if kept at vacuum the detector is not re-exposed to large amounts of atoms and molecules. Sample B underwent a 300°C 40-hour bakeout and achieved <4% the H<sub>2</sub>O outgassing rate of Sample A (150°C), highlighting the importance of temperature. Samples C and D were subjected to high-temperature degassing in an ultravacuum furnace. At 400°C for 20 hours C performs better than B in all elements except CO<sub>2</sub>. D is degassed for just 2 hours at 800°C and performs better than C. It is then exposed to atmosphere for five months, followed by 24 hours in vacuum. It performs better than Sample A at vacuum exposure for 75 hours with no heat. After just a 150°C 20-hour bakeout its outgassing returns to the values of five months earlier. This suggests a high-temperature bake can cause a permanent (or at least long-term) decrease in the outgassing rate.

More details on desorption - including stimulated desorption (incident particles on solid surfaces releasing adsorbed gases) can be found in [256].

### 5.3.5.2 Outgassing Model

The outgassing models in the gas ( $\Lambda_G$ ) and liquid ( $\Lambda_L$ ) xenon characterize the rate of impurities outgassed from detector materials that freely roam throughout the GXe and LXe. This is different than modeling the total number of outgassed impurities because we only care about those that impact  $\tau_e$ . Specifically  $\Lambda_G$  and  $\Lambda_L$  describe time-varying contamination. While the outgassing in Sec. 5.3.5.1 is based on research of vacuum systems the physical processes should be comparable to our detector. However, in a detector with so many components, temperatures ranging from roughly −100°C to 20°C, and time-dependent effects (e.g. purification flow, temperatures outside regions that are not vacuum insulated) building a truly accurate model is not feasible, and including too many terms will lead to overfitting. Everything must

instead be integrated into a single model that can describe the data.

To begin structuring the model we know outgassing decreases over time and is temperature-dependent. If temperatures are stable they can be ignored - or if only a handful of changes exist these periods can be supplemented with additional parameters. This is preferred because selecting specific temperature sensors will make the model partial to those regions, e.g. if the temperature rises in a cooling tower the entire GXe outgassing model should not be scaled accordingly - though in general the gas or liquid xenon should experience a similar reaction. Furthermore because the locations of the sensors were strategically selected to monitor the health of XENON1T, there are sections where knowledge about the temperatures are limited.

Temperature variations for three strategic regions are shown in Fig. 5.23. The narrow temperature range and good thermal isolation of the LXe keeps its temperature stable to well under 1%, with the exception of May and June 2016 when a number of operations were performed to understand and optimize detector conditions. The temperature sensor used for the LXe curve is situated just below the liquid surface and was chosen since warmer regions are of more interest. For the same reason the GXe sensor plotted is from the unpowered cooling tower. It fluctuates by roughly 2% through September 2016 but has not exceeded 1% since. The LN<sub>2</sub> coldfinger is more turbulent. It has been kept at 90°C since June 2016 by flushing GN<sub>2</sub> from the nitrogen storage tank. The larger variations may be because the temperature is a balancing act of the different heat transfer rates (Eq. 5.15) so it is more susceptible to sudden drops and rises than the GXe and LXe that have large thermal reservoirs. In addition the cooling power may experience fluctuations from small imperfections in the nitrogen flow or temperature. It appears to be increasing slightly but the total change is within 1%. From Fig. 5.17 it seems reasonable to ignore temperature dependence in the outgassing model.

Components within the gas and liquid do not have their own outgassing model since this would increase the number of parameters and lead to overfitting. However, the upgrades to the purification system in April-June 2018 likely disrupts this model as parts were removed and added. Thus while the same outgassing model is used

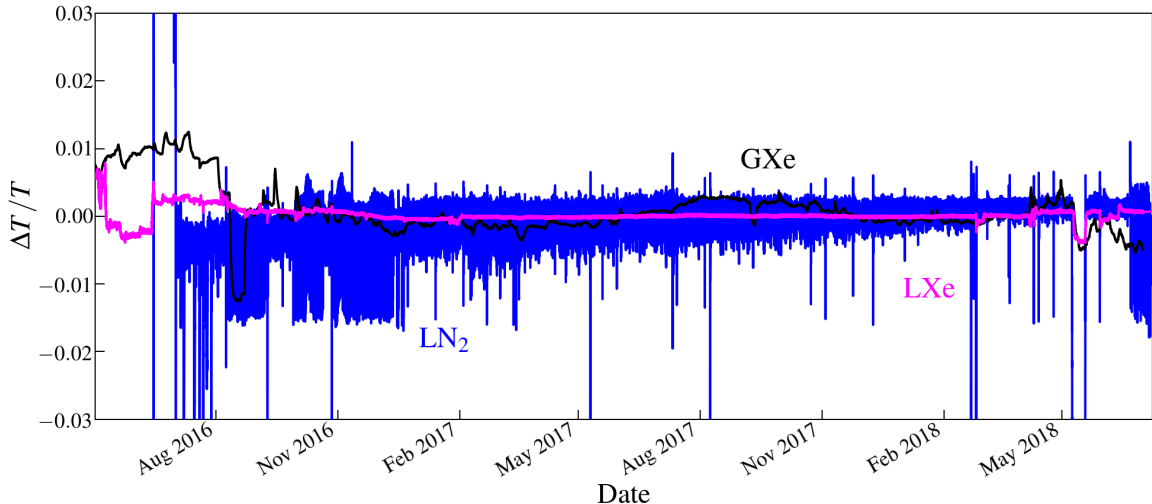


Figure 5.23: Relative temperature variations for sensors on the  $\text{LN}_2$  coldfinger (blue), in the unpowered cooling tower (black), and just below the  $\text{LXe}$  surface (pink). The variation is defined as the  $(T - T_{\text{med}})/T_{\text{med}}$  where  $T_{\text{med}}$  is the median temperature across all data. The  $\text{LN}_2$  coldfinger shows the most volatility. The GXe changes by  $\sim 2\%$  in the first several months of operation but is since stable within 1%. The LXe decreases by roughly 1% in the first couple months as adjustments to the detector were made. Since then its variation is  $\ll 1\%$ .

throughout the entire XENON1T lifetime, some outgassing parameters are limited to particular times.

The outgassing of the system should rapidly decrease in the beginning of the experiment and continue to do so more slowly as time goes on. A logical parameterization is an exponential. However, this cannot be expected to describe the entire outgassing for a complex system. The outgassing model that best describes the electron lifetime evolution is

$$\Lambda_G(t) = A_G(e^{-\beta_1 t} - \beta_2 t) \quad (5.25a)$$

$$\Lambda_L(t) = A_L(e^{-\beta_3 t} - \beta_4 t) \quad (5.25b)$$

where  $A$  and  $\beta_i, \forall i \in \{1, 2, 3, 4\}$  are free parameters in the fit.

### 5.3.5.3 Time-Invariant Impurity Sources

Once  $\tau_e$  flattens any time-invariant inflow of impurities should be the dominating contributor to the electronegative impurity concentration. There are two that are

relevant for XENON1T: permeation and leaks.

**Permeation** is the migration of particles from outside to inside the detector. A particle will adsorb onto the outer surface of the solid, diffuse through the material, and be desorbed on the interior. The rate of permeation will increase slowly until it ultimately reaches a steady-state influx of impurities.

Diatom molecules typically dissociate upon adsorption so they pass through the bulk as individual atoms. For steady-state permeation the molecule will dissociate upon the surface with equilibrium constant  $k_1$ . Atoms on the surface then are admitted into the solid with equilibrium constant  $k_2$ . Taking hydrogen as an example, the interior concentration is  $n_H = k_2(k_1 n_{H_2})$  where  $n_H$  is the concentration of hydrogen atoms inside the solid and  $n_{H_2}$  is the hydrogen molecules on the exterior surface. The permeation flux is

$$Q_k = \frac{K_p(P_2^{1/2} - P_1^{1/2})A}{2d} \quad (5.26)$$

where  $K_p$  is the permeation constant,  $P_1$  and  $P_2$  are the interior and exterior pressures of the element,  $A$  is the surface area, and  $d$  is half the thickness of the material [256]. While Eq. 5.26 describes steady-state permeation

Permeation has a much weaker contribution than the outgassing sources discussed in Sec. 5.3.5.1. It is not expected to be seen in the lifetime of the experiment, so does not need to be included in this analysis.

**Leaks** present a more concerning problem as they are possible at any point during the experiment. There are two types of leaks: internal, where gas trapped inside the detector in or between materials streams out, and real, where gas originating outside of the system drifts through an opening.

The presence of a leak is supported by the flattening of  $\tau_e$  around  $600\ \mu s$  for  $\alpha$ -decays and  $650\ \mu s$  for  $^{83m}\text{Kr}$  during Science Run 1. The residual gas analyzer (RGA) measurements of the vacuum between the inner and outer vessels did not reveal an increase in xenon, which should accompany the inflow of impurities if the leak existed between the vessels. Therefore the leak would either need to be internal, or from a component exposed to air. There are a number of possible candidates for the latter

including the pipes leading to and from the purification system, ReStoX, and the signal and HV feedthrough. The leak was never looked for because it would have required emptying the vessel.

#### 5.3.5.4 Leak Model

Fits that supposed the leak was in the liquid matched the data better than those presuming the gas. This eliminates the cable feedthrough and lines to ReStoX since they are only in contact with GXe (during filling ReStoX can pump liquid). Supposing the leak is not internal the most likely candidate is the purification system, of which the majority of returning xenon goes to the liquid phase of the TPC.

Because  $\tau_e$  is unchanging the LXe impurity concentration must be constant. Reducing the impurity influx into the LXe to that of the leak gives a rough estimate of the rate (while subdominant, nominal outgassing is still present). The calculation also assumes vaporization and condensation rates are in equilibrium - whether or not they actually does not matter for the fit. It then must be equivalent to impurity removal by the getters (Sec. 5.3.2)

$$R_I \equiv \frac{dI_L}{dt}^{(\text{leak})} = -\frac{dI_L}{dt}^{(\text{pur})} = \rho_{\text{GXe}} F_L I_L \quad (5.27)$$

where  $R_I$  is the leak rate and the right side is taken from Eq. 5.11b. The liquid impurity concentration is equivalent to

$$I_L = (\tau_e k)^{-1} \quad (5.28)$$

where  $k = k(e^- + O_2)$  is the field-dependent  $e^-$  attachment coefficient described in Sec. 5.3.9. The purification flow during SR1 is  $\sim 48$  slpm so

$$\begin{aligned}
R_I &= F_L \rho_{\text{GXe}} (\tau_e k)^{-1} \\
&= (48 \text{ slpm}) (5.984 \text{ g l}^{-1}) (600 \mu\text{s})^{-1} (0.004 \text{ s } \mu\text{s}^{-1} \text{ ppb}^{-1})^{-1} \\
&= (48 \text{ slpm}) (5.984 \text{ g l}^{-1}) (2.5 \text{ ppb}^{-1})^{-1} \\
&= 165 \text{ ppb kg day}^{-1}
\end{aligned} \tag{5.29}$$

where the  $\alpha$ -decay electron lifetime is used (for  ${}^{83\text{m}}\text{Kr}$   $R_I = 150 \text{ ppb kg day}^{\text{k}-1}$ ). Eq. 5.29 estimates the O<sub>2</sub>-equivalent impurity concentration is in the low ppb realm, though still less than the designed value by more than a factor of 2. Being field-limited by the single electron hotspot prevents decreasing the attachment rate and thus increasing  $\tau_e$  as shown in Fig. 5.28. Because outgassing should still make up a fraction of the impurity rate, electron lifetime measurements have uncertainty, vaporization and condensation rates may not be equivalent (though they be close), and  $F_L$  fluctuates slightly  $165 \text{ ppb kg day}^{-1}$  should serve only as an approximation.

### 5.3.6 Getter Defficiencies

One of the stranger effects observed in the beginning of SR0 was a slow decrease in lifetime when it seemed detection conditions were not changing over a number of ( $\lesssim 10$ ) days. Two more have appeared since then showing the same behavior. They are referred to as “getter defficiencies” because the evolution during these times follows  $< 100\%$  removal of contaminants by the getters, and there is evidence to support this was the case for at least two of the three periods.

The first getter defficiency began on November 26, 2016 shortly after the  ${}^{241}\text{AmBe}$  and  ${}^{83\text{m}}\text{Kr}$  calibrations and ended on December 5. A power glitch occurred several days before that released a small number of impurities into the chamber (Sec. 5.3.7) but the lifetime was recovering when this decline began. This is the one getter defficiency that lacks an explanation. There were a number of ongoing operations at the time including  ${}^{85}\text{Kr}$  distillation and pipette filling for RGMS - both of which use the purification system - but they don’t align perfectly with the dates. The electron lifetime over this period decreases by  $\sim 10 \mu\text{s}$  and is shown in the left panel of Fig. 5.24.

## 5. PURITY AND THE ELECTRON LIFETIME

---

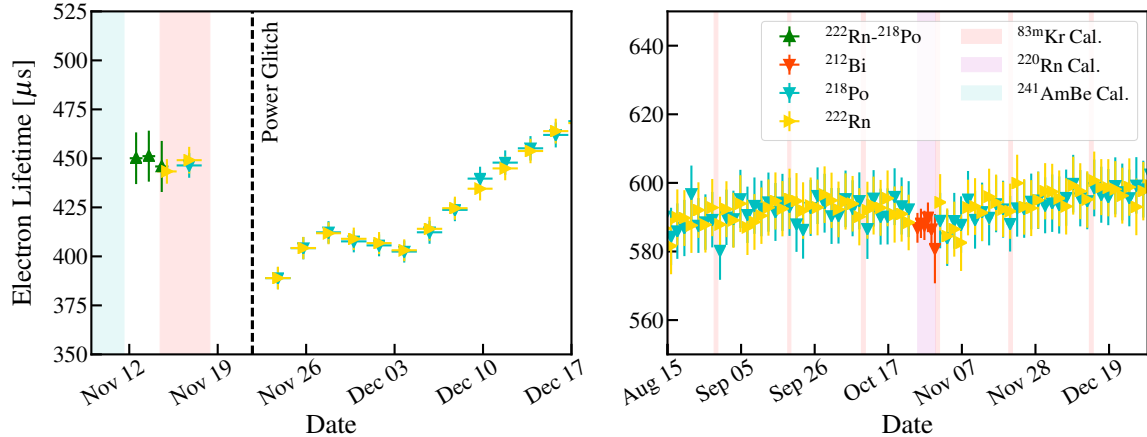


Figure 5.24: Periods of getter defficiencies for November 26 - December 5, 2016 (left) and October 25-30, 2017 (right).  $^{222}\text{Rn}$ - $^{218}\text{Po}$  combined (green),  $^{222}\text{Rn}$ , (yellow triangles),  $^{218}\text{Po}$  (turquoise), and  $^{212}\text{Bi}$  (red) electron lifetimes are shown.  $^{83\text{m}}\text{Kr}$  (shaded orange),  $^{220}\text{Rn}$  (purple), and  $^{241}\text{AmBe}$  (green) calibrations are highlighted. The cause of the first deficiency in 2016 is not understood, as detector parameters are stable during this period. The getter deficiency in October 2017 is likely caused by an excess of impurities that were released from the  $^{220}\text{Rn}$  calibration. Each resulted in a total drop of  $\lesssim 10 \mu\text{s}$ . The power glitch on November 21, 2016 causes a sudden purity decrease (Sec. 5.3.7).

The second instance was during the Science Run 0  $^{220}\text{Rn}$  calibration. Despite the calibration lasting for 13 days (December 19, 2016 to January 1, 2017) the first  $\sim 10$  days or so were not useable as the valve in the calibration box Fig. 3.10 and 3.16 was left open.  $^{220}\text{Rn}$  and  $^{216}\text{Po}$  made it impossible to select  $^{212}\text{Bi}$   $\alpha$ -decays, and the mixing of the three gives a rough value of  $\tau_e$  but cannot be expected to be entirely accurate as learned from  $^{222}\text{Rn}$ - $^{218}\text{Po}$  simultaneous fitting (Sec. 5.2.2). Although the values from these measurements should not be included in the fit, they still track the behavior of the evolution during this period. They show a steep decrease at the beginning of the calibration before returning to the expected evolution model.

The dip can be explained by considering impurity buildup inside the calibration source box.  $^{220}\text{Rn}$  had been injected into the TPC roughly two months earlier but because it was for commissioning and not a true calibration the event rate was kept small ( $\lesssim 50,000$  events  $\text{hr}^{-1}$ ). Impurities from the calibration source box would have also been low and more likely to be removed by the getters. In the following months impurities from outgassing and handling would have likely accumulated, and

for the SR0 calibration the rate reached  $> 200,000$  events  $\text{hr}^{-1}$  within 7 hours and  $> 300,000$  events  $\text{hr}^{-1}$  within 17 hours. The higher influx from the source box would have carried with it larger concentrations of impurities, which would explain the dip and - once the high concentration of impurities from inside the source box became sufficiently low - the return to the previous trend.

The third period was the final  $^{220}\text{Rn}$  calibration of Science Run 1 (October 25-30, 2017). Instead of the 3-4 week spacing between calibrations - as with the previous three - more than 10 weeks passed. As with SR0, impurity buildup may have become large enough to lower the getter efficiency. The total drop in purity is  $\lesssim 10 \mu\text{s}$ , and is shown in the right panel of Fig. 5.24.

To model the getter defficiencies Eq. 5.11a and 5.11b become

$$\frac{dI_G}{dt}^{\text{(gd)}} = \alpha_i \frac{dI_G}{dt}^{\text{(pur)}} = -\alpha_i \rho_{\text{GXe}} F_G I_G \quad (5.30\text{a})$$

$$\frac{dI_L}{dt}^{\text{(gd)}} = \alpha_i \frac{dI_L}{dt}^{\text{(pur)}} = -\alpha_i \rho_{\text{GXe}} F_L I_L \quad (5.30\text{b})$$

with  $\alpha_i \in [0, 1]$  where  $\alpha_i$  is the  $i^{\text{th}}$  getter defficiency.

### 5.3.7 Impurity Spikes

April 14 18:27 LXe level too high, adjusted by Ops Manager. April 16 17:05 normal power turned off. April 19 9:03 and 9:09 normal power turned off. PTR with LN2 test May 9-18.

On a number of occasions sudden drops in purity occurred. Unlike the getter defficiencies (Sec. 5.3.6), these drops were immediate and had no measurable duration. In all cases they were traceable to changes in the state of the detector. In total there were two impurity spikes before science run data, two during Science Run 0, one during Science Run 1, and three following SR1 (Sec. 5.3.8). They all align with changes in parameters monitored by the slow control system (in most cases due to part of detector being unpowered). In some instances it is difficult to distinguish the responsible parties because several abnormalities occurred. Each case is listed in

## 5. PURITY AND THE ELECTRON LIFETIME

---

Date	Origin	Region	Possible cause	$\sim\tau_e$ [μs]	$\sim\Delta\tau_e$ [μs]
June 14, 2016	Power glitch	GXe	PTR power → 0	65	-30
July 15, 2016	LN <sub>2</sub> test	GXe	PTR power → 0	225*	-100
Nov. 21, 2016	Power disruption	LXe	Temperature increase	450	-75
Jan. 18-Feb. 1, 2017	Earthquake	GXe + LXe	Liquid level change	520*	-120
June 5, 2017	Gate washing	LXe	Liquid level change	575	-50
Feb. 21, 2018	Power glitch	GXe	PTR power drop of ~50%	600	-150
Feb. 24, 2018	Blackout	GXe + LXe	PTR power → 0, $F_G = F_L = 0$	500*	-150
Mar. 5-7, 2018	Gate washings	LXe	Liquid level change	450	-70

Table 5.6: Purity drops over the lifetime of XENON1T. Dates and expected causes are listed, along with the detector region (GXe or LXe) in which the impurity release is thought to occur. Possible causes,  $\tau_e$ , and change in  $\tau_e$  from  $\alpha$  lifetime measurements are given. Cases where data is not available for several days or weeks following a drop are marked with \*.

Tab. 5.12 along with relevant information.

**June 14, 2016** The first impurity spike happened when a power glitch shut off the operating PTR. The coldfinger, which is kept at -98°C warmed, releasing impurities that had condensed on and around its surface into the GXe. Power was quickly restored and the detector remained stable, but the impurities condensed and diffused into the liquid, causing a dip of  $\Delta\tau_e \sim -30$  μs.

**July 15, 2016** The second purity drop occurred during a LN<sub>2</sub> test. In the event both PTRs lose power and the uninterruptible power supply (UPS) does not work properly, LN<sub>2</sub> from the dewar outside the service building is transferred to the third cooling tower to maintain safe detector conditions (it is nominally kept at -90°C to quicken the transition). A test was performed to ensure it worked properly. Like the first spike, the warming of the PTR allowed contaminants to diffuse into the GXe. The electron lifetime dropped by approximately 100 μs.

**November 21, 2016** In the beginning of SR0 (following the <sup>241</sup>AmBe and <sup>83m</sup>Kr calibrations but before dark matter data taking) the experiment experienced a power disruption. The PTR was stable but temperature sensors show a small increase in the liquid, leading to drop of roughly 75 μs. It is visible in the left panel of Fig. 5.24.

**January 18-February 1, 2017** Science Run 0 ended because of an earthquake in the Gran Sasso area. Following the earthquake electron emission, or a *hotspot*, was observed while running at the SR0 cathode voltage  $V_c = 12$  kV. Over the next two

weeks the hotspot did not disappear except at lower voltages so it was decided to use  $V_c = 8$  kV for SR1. During this window the liquid level increased for a period before returning to the SR0 height. A number of operations were done so it is possible one or more are responsible. Since the conditions were unstable this data was not used in the combined analysis, so  $\tau_e$  did not need to be measured. A rough estimate of the change in  $\tau_e$  is  $-120\ \mu\text{s}$ , but this value is dependent on when the drop (or drops) occurred.

**June 5, 2017** At the end of May 2017 a hotspot appeared on the gate. Lowering the anode voltage from 4 to 3.6 kV eliminated the electron emission but also decreased the extraction efficiency (Sec. 3.2.7). To fix this a “gate washing” - lifting the TPC slightly so the gate rises out of the LXe and submerging it again - was done. The hope that whatever was causing the hotspot (e.g. a particle) would be “washed” away. Upon returning the anode voltage to 4 kV the hotspot had disappeared and normal dark matter data taking resumed. The dip in  $\tau_e$  ( $-50\ \mu\text{s}$ ) is suspected to come from impurities nested in the PTFE just above the liquid level that were dispersed throughout the LXe once submerged.

**February 21, 2018** Roughly two weeks after the end of SR1 the PTR power dropped by  $\sim 50\%$  because of a power glitch. The change in  $\tau_e$  was approximately  $-150\ \mu\text{s}$ . The decrease in  $\tau_e$  was larger than that from June 5th, indicating the concentration of impurities on the coldfinger may be larger compared to those on the PTFE near the LXe surface, though this is likely dependent on other factors such as temperature and time between drops.

**February 24, 2018** Three days after the power glitch there was a blackout that turned off the PTR and a number of other components. In addition, purification was stopped for  $\sim 12$  hours so impurities inside the tube that connects the LXe to the purification system would have been able to diffuse into the liquid.<sup>1</sup> The cathode remained off for nearly two weeks. The decrease in electron lifetime is estimated at  $-150\ \mu\text{s}$ .

---

<sup>1</sup>During normal operations it is extremely rare that an impurity will reach the LXe against the flow.

## 5. PURITY AND THE ELECTRON LIFETIME

---

**March 5-7, 2018** Upon ramping  $V_c$  back to 8 kV after the blackout a hotspot on the gate emerged. Three gate washings spaced roughly 24 hours apart were able to remove the hotspot. As with the June 5, 2017 gate washing it is likely impurities near the liquid surface would have been submerged. This resulted in a decrease of 70  $\mu\text{s}$ .

The purity drops are modeled as

$$\text{GXe purity drop} = M_G \Delta I_G^{(i)} \int \delta(t - t_G^{(i)}) dt \quad (5.31\text{a})$$

$$\text{LXe purity drop} = M_L \Delta I_L^{(i)} \int \delta(t - t_L^{(i)}) dt \quad (5.31\text{b})$$

where  $\Delta I_L^{(i)}$  and  $\Delta I_G^{(i)}$  are free parameters representing the magnitude of the drops and  $\delta(t - t^{(i)})$  is the delta function for the  $i^{\text{th}}$  instance.

Once the detector returns to nominal operating conditions the impurities are removed by the getters and within a period of days to weeks - depending on  $\tau_e$  and  $\Delta I_{G/L}^{(i)}$  - the electron lifetime returns to its original trend. However, for a stretch of time during or following the spike the governing physics of the electron lifetime evolution may deviate from predicted behavior.

When the coldfinger is warmed the concentration of attached impurities decreases as they get enough thermal energy to leave. Following a return to normal conditions the concentration of contaminants passed to the liquid via condensation (Sec. 5.3.3) is lower. Additionally the rate of evaporation of contaminants from the coldfinger should also decrease, though at  $-98^\circ\text{C}$  this should have a small effect.

Aside from the itself modeling these changes can be difficult because the physics of these processes is not well understood. Studies of to what extent impurities coalesced on the coldfinger have on  $\epsilon_{\text{cond}}$ , or how impurities bond to materials in and out of LXe need to be investigated. These effects are not modeled in the electron lifetime evolution, though because they are brief and the net effect is an immediate purity drop it is not necessary.

### 5.3.8 Hardware Upgrades

The most difficult parts of the electron lifetime model to characterize are online detector operations. The reason is they disrupt the system and in many cases the change is permanent and its effect on the model can be difficult to diagnose.

The first major operation was the installation of the third QDrive to the purification system from September 29 - October 5, 2016. The circulation was at  $\sim$ 45 slpm - just 45% of the designed flow - and required running the QDrives at high voltages. The suspension of flow through one of the two purification branches led to a decrease in  $\tau_e$  as shown in Fig. 5.25. Once the upgrade was completed the flow increased to  $\sim$ 55 slpm with the QDrives running at safe voltages. In addition to the QDrive, buffer volumes were installed to relieve pressure between the pumps. These additions likely added more outgassing (additionally the QDrive increased  $^{222}\text{Rn}$ , though this is irrelevant to the electronegative purity). However, since xenon passes through the getter after the QDrives it is not expected to change the outgassing model or purity because the model assumes that 100% of all contaminants are absorbed by the zirconium. However, there are plausible scenarios when this would not be the case, such as large initial impurity residue on the materials from exposure to air during installation, an sizable initial outgassing that overwhelms the getters, or the rise in flow speed (Sec. 5.3.2).

During Science Runs 0 and 1 no hardware was exchanged so detector conditions were stable. In April 2018 pipes in the purification system were upgraded from 1/2" outer diameter to 1" to increase conductance. When purification resumed the circulation speed reached 70 slpm.

The final hardware upgrade was in the middle of June when a magnetic pump was installed in parallel to the QDrives. With the QDrives off it reached  $\sim$ 80 slpm.

The QDrives were chosen in part because they did not risk exposure to air if something were to break, unlike KNF pumps used in the past. However, they could be unreliable - especially at higher flows - and are one of the highest contributors to the  $^{222}\text{Rn}$  background with an estimated contribution of 30% from screening during

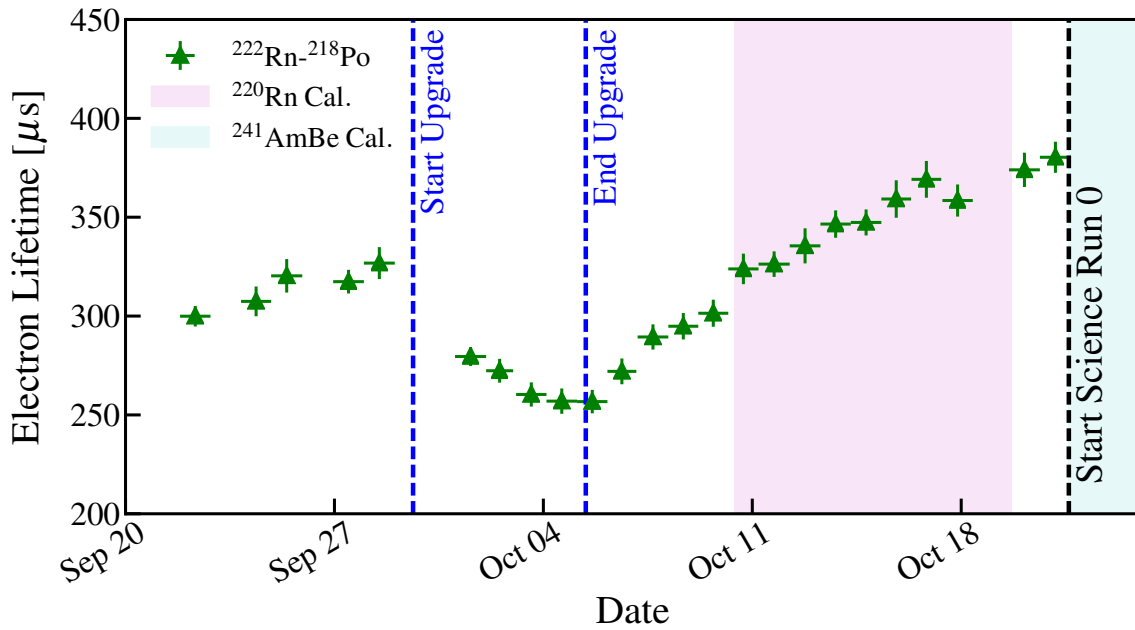


Figure 5.25: Installation of the third QDrive in the purification system from September 29 - October 5, 2016. Lifetimes are measured with  $^{222}\text{Rn}$ - $^{218}\text{Po}$  combined data (green).  $^{220}\text{Rn}$  and  $^{241}\text{AmBe}$  calibrations are shaded purple and turquoise, respectively.

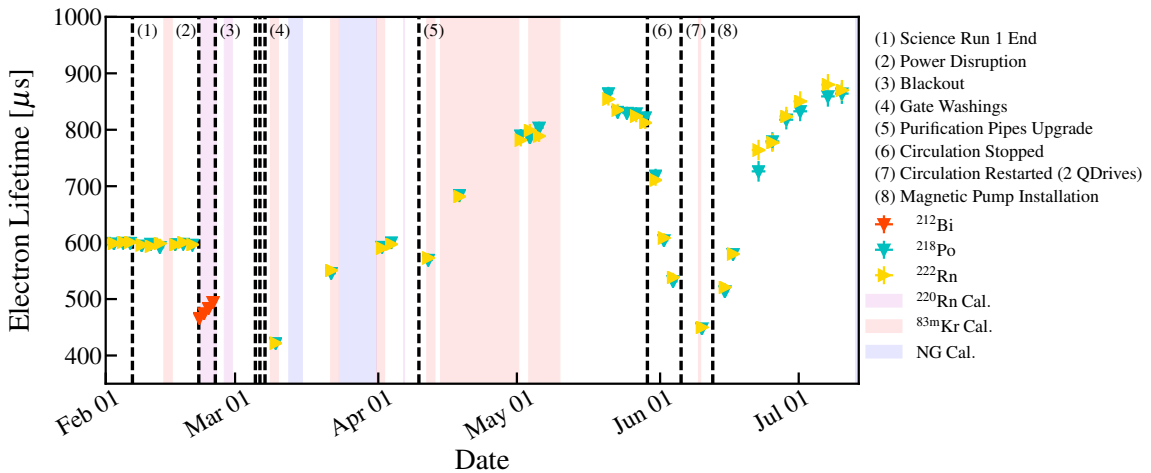
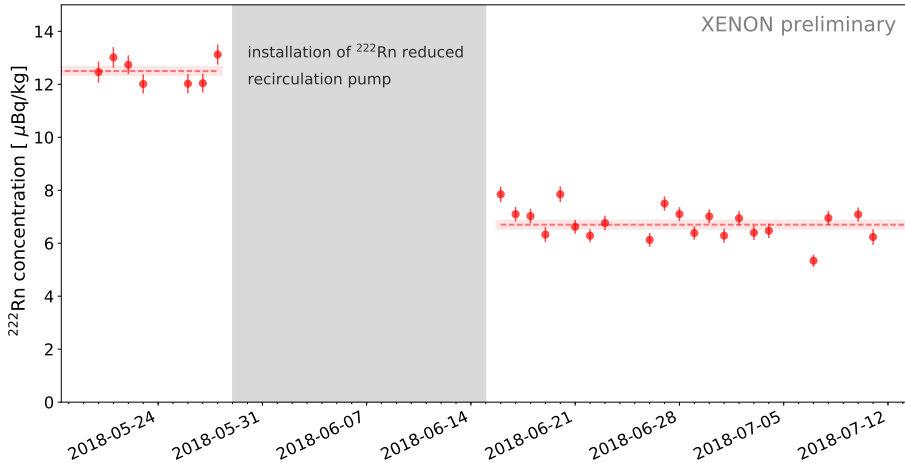


Figure 5.26: Electron lifetime measurements following the end of SR1. Initial drops in purity are due to a power disruption, blackout, and gate washings. Subsequent changes are caused by upgrades to the purification system.



commissioning. Once the QDrives were removed from circulation the  $^{222}\text{Rn}$  event rate dropped from  $12.5 \pm 0.2$  to  $6.8 \pm 0.2 \mu\text{Bq kg}^{-1}$ , or  $\sim 45\%$ , as shown in Fig. 5.27. The larger than expected decrease may be due to only two of the three QDrives in service having been screened (QD251 and QD253) to estimate the contribution. Higher radon emanation from the third would inflate the QDrive fraction of the radon budget. A second possibility is the screening tests were performed at room temperature, but higher temperature while running might escalate emanation.

The success of the magnetic pump is encouraging for XENONnT where the electron lifetime needs significant improvement and the background needs to be smaller. It has only been in use for  $< 3$  months so other beneficial or adverse effects may appear, but so far the upgrade appears promising.

The number of hardware updates for the purification system reflects the shortcomings in meeting design specifications: 100 slpm and  $\tau_e > 1$  ms. This was the first attempt at ton-scale purification and what has been learned will be applied to the XENONnT upgrade.

### 5.3.9 Field Dependence

In addition to inhomogeneous variations in charge yields (Sec. 5.2.5) the electric field affects the attachment rate constant  $k$  for the reaction

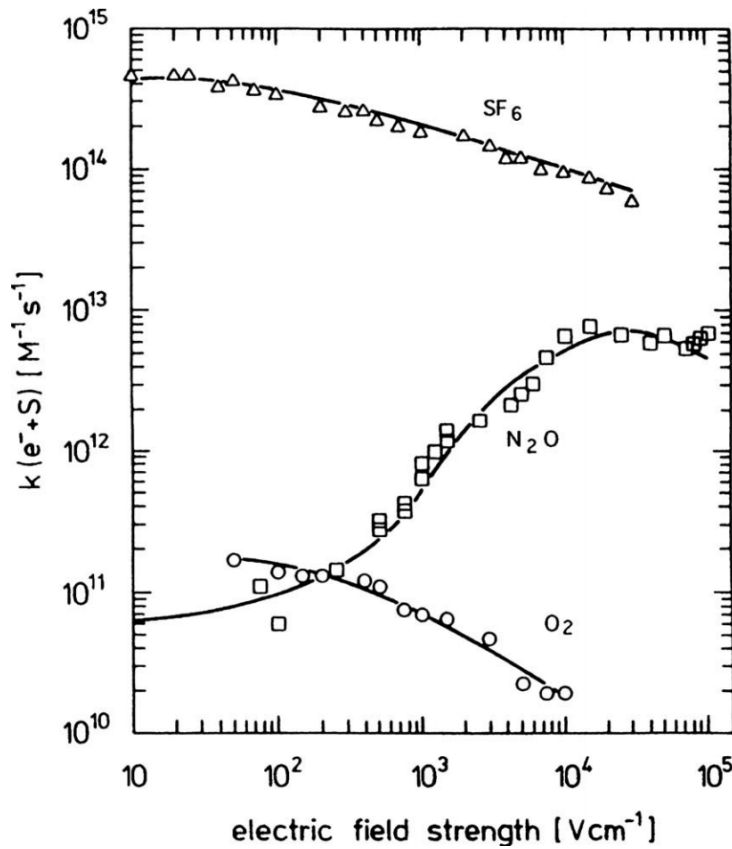


Figure 5.28: Field-dependent attachment rates for  $\text{O}_2$ ,  $\text{N}_2\text{O}$ , and  $\text{SF}_6$ . Because analysis uses  $\text{O}_2$  to model all impurities the attachment rate will decrease with electric field. Image credit: [175].



for some impurity S. The attachment rate describes the attraction between electrons and some element or molecule. Because oxygen is expected to have the highest concentration the model uses the  $\text{O}_2$  attachment rate (thus impurities fit are modeled in  $\text{O}_2$ -equivalence). Unfortunately very little research has been done on this topic so the model uses a measurement from 1976 [175], shown in Fig. 5.28. It measured the oxygen attachment rate constant  $k(\text{O}_2 + e^-)$  decreases at higher  $E_d$ .  $\text{SF}_6$  follows this trend though is larger, while  $\text{N}_2\text{O}$  increases at larger field.

Oxygen is expected to be by far the most prevalent and dangerous contaminant. But small quantities of other molecules exist whose electron attachment rate constants are unknown are not considered. The magnitude of the effect is likely small but

should not be overlooked. Because the results in Fig. 5.28 are the sole measurement additional measurements are needed.

The electron lifetime is calculated as

$$\tau_e = \frac{1}{I_L k} \quad (5.33)$$

which is used to compute the log-likelihood in the fit (Sec. 5.4.1).

## 5.4 Electron Lifetime Fit

Putting the elements from Sec. 5.3 together gives the impurity evolution model

$$M_G \frac{dI_G}{dt} = -\alpha F_G \rho_{GXe} I_G + \frac{\epsilon_{vap} \dot{Q}_0 I_L}{L} - \frac{\epsilon_{cond} \dot{Q}_{GXe} I_G}{c_p \Delta T + L} + \Lambda_G + \sum_i M_G \Delta I_G^{(i)} \int \delta(t - t_G^{(i)}) dt \quad (5.34a)$$

$$M_L \frac{dI_L}{dt} = -\alpha F_L \rho_{GXe} I_L - \frac{\epsilon_{vap} \dot{Q}_0 I_L}{L} + \frac{\epsilon_{cond} \dot{Q}_{GXe} I_G}{c_p \Delta T + L} + \Lambda_L + R_I + \sum_i M_L \Delta I_L^{(i)} \int \delta(t - t_L^{(i)}) dt \quad (5.34b)$$

with  $\alpha = 1$  for all times except periods of getter defficiencies (Sec. 5.3.6).

### 5.4.1 Statistical Inference

The majority of the model is fit to electron lifetime measurements from  $^{222}\text{Rn}$  (Sec. 5.2.2) because its emanation from detector materials meant it could be continually used to measure  $\tau_e$ . However, in beginning of the experiment electron lifetime measurements were done using S2/S1 (Sec. 5.2.1), and once the  $\alpha$  background could be used the lifetimes were computed using  $\alpha$ -decays from  $^{222}\text{Rn}$ - $^{218}\text{Po}$  together. Late it was realized that this combined fit slightly underestimated the lifetime so  $\tau_e$  was recalculated with separate fits for  $^{222}\text{Rn}$  and  $^{218}\text{Po}$ . However, the electron lifetimes preceding SR0 could not be recalculated because the data had been deleted. A com-

parison between the two was used to adjust the  $^{222}\text{Rn}$ - $^{218}\text{Po}$  fits to align with expected values.

For this analysis the likelihood is calculated as

$$\mathcal{L}_i = \exp \left[ -\frac{(\tau_{e,i} - \hat{\tau}_{e,i})^2}{2\sigma_{e,i}^2} \right] \quad (5.35\text{a})$$

$$\mathcal{L} = \prod_i \mathcal{L}_i \quad (5.35\text{b})$$

$$\ln \mathcal{L} = - \sum_i \frac{(\tau_{e,i} - \hat{\tau}_{e,i})^2}{2\sigma_{e,i}^2} \quad (5.35\text{c})$$

where  $\tau_{e,i}$  and  $\hat{\tau}_{e,i}$  are the measured (Sec. 5.2) and predicted electron lifetimes, respectively. Because previous measurements do not exist the only constraints on  $p(\boldsymbol{\theta}|\boldsymbol{\alpha})$  come from physical limitations. A Markov Chain Monte Carlo is used to fit  $\ln \mathcal{L}$  (Sec. 5.4.2).

### 5.4.2 Markov Chain Monte Carlo

Similar to the electronic and nuclear recoil banding fitting for the dark matter search analysis (Sec. 4.2.7) this analysis uses a Markov Chain Monte Carlo (MCMC). MCMCs use  $k$  walkers to explore the target distribution over  $T$  iterations. Each walker  $i \in \{1, \dots, k\}$  has parameters  $\boldsymbol{\theta}_i$  with proposed steps based on the current positions of the walkers, making MCMCs memoryless - that is, there is no advantage to having knowledge of previous steps.

This analysis uses a Differential Evolution Markov Chain (DEMC) rather than the Affine-Invariant Ensemble Sampler used in the dark matter search. The two are similar in that they are both random walk Monte Carlos and companion walkers are used to draw proposals. Both are homogeneous, satisfy detailed balance, and have their posteriors as their stationary distributions (see Sec. 4.2.7 for details concerning MCMCs).

The DEMC method used in this fit follows from [260] with improvements suggested in [261] and a snooker updater outlined in [262].

1. Initialize  $k$  walkers of  $n$ -dimensional parameter space to some state  $\boldsymbol{\theta}(t = 0)$  (for this analysis random samples are drawn from within a specified range).
2. Set  $\gamma_0 = 2.38/(2n)^{1/2} = 2.38/(2\dot{5}1)^{1/2} = 0.236$  and  $\sigma_\gamma = 10^{-4}$ .
3. Update each  $\{\boldsymbol{\theta}_i, \forall i = 1, \dots, k\}$ .
  - a) With 80% probability use the standard DEMC from [260], [261]. Randomly select two of the  $k - 1$  walkers,  $\boldsymbol{\theta}_{r_1}, \boldsymbol{\theta}_{r_2}$  and propose step

$$\boldsymbol{\theta}_p = \boldsymbol{\theta}_i + \boldsymbol{\Theta}_{r_1, r_2} \boldsymbol{\gamma} \quad (5.36)$$

where  $\boldsymbol{\Theta}_{r_1, r_2}$  is a matrix with  $\boldsymbol{\theta}_{r_1} - \boldsymbol{\theta}_{r_2}$  diagonal elements

$$\Theta_{ij} = (\theta_{i, r_1} - \theta_{i, r_2})\delta_{ij} \quad (5.37)$$

where  $\delta_{ij}$  is the Kronecker delta and  $\boldsymbol{\gamma} = \gamma_0(\mathbf{1} + \mathbf{z})$  where  $\mathbf{z} \sim \text{Norm}(0, \sigma_\gamma)^n$ .  $\mathbf{z}$  is necessarily symmetric to guarantee the jump from  $\boldsymbol{\theta}_i$  to  $\boldsymbol{\theta}_p$  is as likely as the reverse, and must be included to ensure any state can be reached with probability  $> 0$ . The acceptance probability of the new step is chosen as

$$q = \min\left(1, \frac{\mathcal{L}(\boldsymbol{\theta}_p)p(\boldsymbol{\theta}_p|\boldsymbol{\alpha})}{\mathcal{L}(\boldsymbol{\theta}_i)p(\boldsymbol{\theta}_i|\boldsymbol{\alpha})}\right) \quad (5.38)$$

which is just the Metropolis ratio. An illustration of this method is shown in the left panel of Fig. 5.29.

- b) The remaining 20% of proposals will be drawn using a snooker updater [262]. This method begins by randomly selecting three of the  $k - 1$  chains such that  $\boldsymbol{\theta}_i, \boldsymbol{\theta}_{r_1}, \boldsymbol{\theta}_{r_2}, \boldsymbol{\theta}_{r_3}$  are each distinct. Projections of the first two are calculated

$$\boldsymbol{\theta}_{p_1} = \left[ (\boldsymbol{\theta}_{r_1} - \boldsymbol{\theta}_i) \cdot (\boldsymbol{\theta}_{r_3} - \boldsymbol{\theta}_i) \right] \frac{\boldsymbol{\theta}_{r_3} - \boldsymbol{\theta}_i}{\|\boldsymbol{\theta}_{r_3} - \boldsymbol{\theta}_i\|^2} \quad (5.39a)$$

$$\boldsymbol{\theta}_{p_2} = \left[ (\boldsymbol{\theta}_{r_2} - \boldsymbol{\theta}_i) \cdot (\boldsymbol{\theta}_{r_3} - \boldsymbol{\theta}_i) \right] \frac{\boldsymbol{\theta}_{r_3} - \boldsymbol{\theta}_i}{\|\boldsymbol{\theta}_{r_3} - \boldsymbol{\theta}_i\|^2} \quad (5.39b)$$

as shown in the right panel of Fig. 5.29. A step is proposed

$$\boldsymbol{\theta}_p = \boldsymbol{\theta}_i + \gamma_0(\boldsymbol{\theta}_{p_1} - \boldsymbol{\theta}_{p_2}) \quad (5.40)$$

using the projections from Eq. 5.39. Finally, the acceptance probability is

$$q = \min\left(1, \frac{\mathcal{L}(\boldsymbol{\theta}_p)p(\boldsymbol{\theta}_p|\boldsymbol{\alpha})}{\mathcal{L}(\boldsymbol{\theta}_i)p(\boldsymbol{\theta}_i|\boldsymbol{\alpha})} \frac{||\boldsymbol{\theta}_p - \boldsymbol{\theta}_{r_3}||^{n-1}}{||\boldsymbol{\theta}_i - \boldsymbol{\theta}_{r_3}||^{n-1}}\right) \quad (5.41)$$

and we can see that  $q$  becomes small for  $\boldsymbol{\theta}_p \approx \boldsymbol{\theta}_{r_3}$ .

4. Generate a random number from a uniform distribution  $r \in [0, 1]$ . If  $r < q$  then accept  $\boldsymbol{\theta}_p$ , otherwise reject and remain in current state.
5. Define the acceptance of proposed states across all chains as  $f = k_{\text{acc}}/k$  where  $k_{\text{acc}}$  is the number of accepted proposals in current iteration.
6. Adjust  $\gamma_0$  to maintain an acceptance fraction of  $\sim 0.25$ . If it dips too low  $\boldsymbol{\theta}_p$  may on average be over-extending to regions of low likelihood, while if too high it may be a sign that there are more farther regions that should be explored. It is reset to 1 every 100 iterations to account for multi-modal distributions.
  - (i) If  $100 | t$  then  $\gamma_0 = 1$ .
  - (ii) If  $f < 0.2$  then  $\gamma_0 = 0.9\gamma_0$ .
  - (iii) If  $f > 0.31$  then  $\gamma_0 = 1.1\gamma_0$ .
  - (iv) Otherwise  $\gamma_0 = \gamma_0(2f^{1/2})$ .
7. Set  $t = t + 1$ .
8. Repeat steps 3–7 for  $T$  iterations.

The acceptance probability in Eq. 5.38 can be rewritten

$$\frac{\mathcal{L}(\boldsymbol{\theta}_p)p(\boldsymbol{\theta}_p|\boldsymbol{\alpha}_p)}{\mathcal{L}(\boldsymbol{\theta}_i)p(\boldsymbol{\theta}_i|\boldsymbol{\alpha}_i)} = \frac{\frac{\mathcal{L}(\boldsymbol{\theta}_p)p(\boldsymbol{\theta}_p|\boldsymbol{\alpha}_p)}{p(\mathbf{x}|\boldsymbol{\alpha}_p)}}{\frac{\mathcal{L}(\boldsymbol{\theta}_i)p(\boldsymbol{\theta}_i|\boldsymbol{\alpha}_i)}{p(\mathbf{x}|\boldsymbol{\alpha}_i)}} = \frac{p(\boldsymbol{\theta}_p|\mathbf{x}, \boldsymbol{\alpha}_p)}{p(\boldsymbol{\theta}_i|\mathbf{x}, \boldsymbol{\alpha}_i)} \quad (5.42)$$

so the probability a proposal is accepted is just the ratio of the posteriors of  $\boldsymbol{\theta}_p$  and  $\boldsymbol{\theta}_i$ . In fact, Eq. 4.44 and Eq. 5.41 are just the ratio of the posteriors scaled by  $z^{n-1}$  and  $(||\boldsymbol{\theta}_p - \boldsymbol{\theta}_{r_3}||/||\boldsymbol{\theta}_i - \boldsymbol{\theta}_{r_3}||)^{n-1}$ , respectively - both of which reduce to Eq. 5.42 when  $n = 1$ .

The electron lifetime evolution MCMC uses 400 walkers for  $n = 51$  parameters over 8000 iterations.

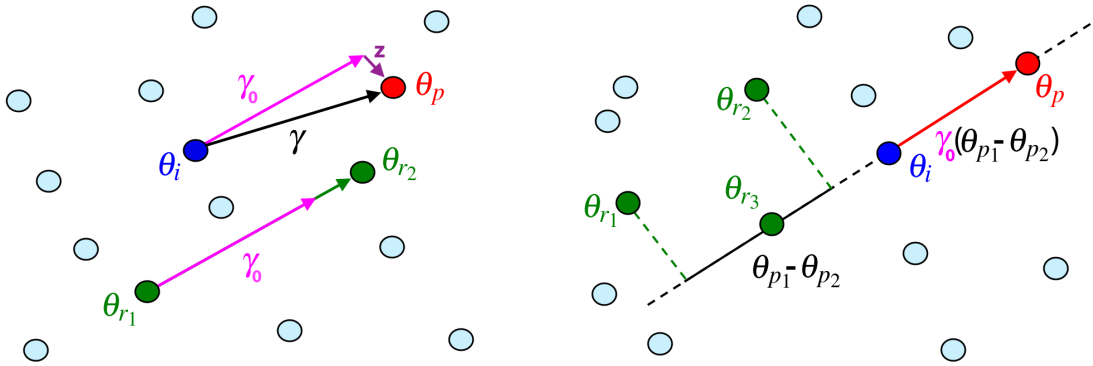


Figure 5.29: Examples of  $\theta_p$  using DEMC (left) and DEMC snooker update (right) in two dimensions. Example of normal DEMC proposal (item 3a). The difference between two randomly selected walkers  $\theta_{r_1}, \theta_{r_2}$  is used to propose an update to the  $i^{\text{th}}$  walker using Eq. 5.36 in two dimensions.  $\theta_p$  and  $\theta_{r_1} - \theta_{r_2}$  are at a slight tilt with respect one another due to  $\mathbf{z}$ . Example of DEMC snooker update proposal (item 3b). An update is proposed using difference of projections of  $\theta_{r_1}, \theta_{r_2}$  along  $\theta_{r_3} - \theta_i$  where  $\theta_{r_3}$  is a third randomly drawn walker using Eq. 5.40.

### 5.4.3 Results

With the electron lifetime evolution model described in Sec. 5.3 and the fit method in Sec. 5.4, the results are presented. The final 1000 iterations of the MCMC are used for the posterior.

Parameters in the model (Eq. 5.34) that are assumed to be constant over the lifetime of the experiment are shown in Tab. 5.7. These values are not queried from the slow control system and are fixed in the fit. Some in fact may change slightly (e.g.  $M_G$  and  $M_L$  during distillation) but are expected to have negligible effects. The cooling power when the circulation through the various XENON1T systems (Fig. 3.9) is zero  $\dot{Q}_0$  was only measured in the beginning of the experiment (Sec. 5.3.3). Recalibrating would require halting the flow through the purification system, which would cause a drop in electron lifetime that would take weeks to recover. Therefore,  $\dot{Q}_0$  has the lowest degree of certainty among the fixed values.

There are four free parameters that are time-invariant, i.e. their value is unchanging over the lifetime of the experiment. They are the initial (May 1, 2016) gas and liquid xenon impurity concentrations ( $I_G^0$  and  $I_L^0$ , respectively), probability of an impurity in the LXe to vaporize ( $\epsilon_{\text{vap}}$ ), and probability of an impurity in the

## 5. PURITY AND THE ELECTRON LIFETIME

---

Parameter	Value	Units	Comment
$M_G$	23	kg	GXe mass
$M_L$	3157	kg	LXe mass
$\rho_{\text{GXe}}$	5.894	$\text{g l}^{-1}$	GXe density
$c_p$	158	$\text{J kg}^{-1} \text{ K}^{-1}$	Constant pressure specific heat of GXe, Sec. 5.3.3
$L$	$9.5587 \times 10^4$	$\text{J kg}^{-1}$	Latent heat of GXe, Sec. 5.3.3
$\dot{Q}_0$	140	W	GXe cooling power when $F_G = F_L = 0$ , Sec. 5.3.3

Table 5.7: Parameters in the electron lifetime evolution model that are fixed.

Parameter	Prior distribution	Units	Posterior	Comment
$I_G^0$	$\geq 0$	ppb	$9951^{+8538}_{-6224}$	Initial GXe impurity concentration
$I_L^0$	$\geq 0$	ppb	$75.3^{+80.9}_{-58.2}$	Initial LXe impurity concentration
$\epsilon_{\text{vap}}$	0-1	—	$0.288^{+0.310}_{-0.214}$	Probability of LXe impurity vaporization, Sec. 5.3.3
$\epsilon_{\text{cond}}$	0-1	—	$0.994^{+0.005}_{-0.015}$	Probability of GXe impurity condensation, Sec. 5.3.3

Table 5.8: Time-independent parameters in the fit.

GXE to condense ( $\epsilon_{\text{cond}}$ ).  $I_G$  and  $I_L$  are anti-correlated, since a larger initial impurity concentration in one implies a smaller concentration in the other.

The results for the outgassing model are shown in Tab. 5.9. The outgassing is split into four periods. The first is from commissioning until the start of Science Run 1. The second begins with SR1 and continues until April 2018 when the pipes in the purification system were enlarged. The reason this period is separate is because the new materials may add new outgassing to the system. The pipes that were exchanged lay before the getters but there is evidence of  $< 100\%$  getter efficiency (Sec. 5.3.2), particularly at high speeds. Because the upgrade increased the circulation speed it becomes more likely that any imperfections in impurity removal become more dramatic.

The fourth period begins on June 12, 2018 with the installation of the magnetic pump. The reason for the isolation of parameters is similar to the previous period. New materials were added to the system and the purification flow increased again.

The leak rate in all four periods falls close to one another, at roughly 160-170 ppb kg day $^{-1}$ . This agrees nicely with the expected value from Eq. 5.29 of 165 ppb kg day $^{-1}$ .

In some cases the behavior of the outgassing may temporarily change due to

Parameter	Prior distribution	Units	Start	Posterior	Comment
$A_G$	$\geq 0$	$\text{ppb kg day}^{-1}$	May 1, 2016	$321^{+77}_{-76}$	Sec. 5.3.5.2
			February 1, 2017	$2.2^{+2.4}_{-1.6}$	
			April 10, 2018	$7.1^{+8.2}_{-4.5}$	
			June 12, 2018	$15.1^{+12.6}_{-9.7}$	
$\beta_1$	$\geq 0$	$\text{day}^{-1}$	May 1, 2016	$0.0027^{+0.0020}_{-0.0014}$	Sec. 5.3.5.2
			February 1, 2017	$0.0048^{+0.0053}_{-0.0035}$	
			April 10, 2018	$0.0086^{+0.0070}_{-0.0058}$	
			June 12, 2018	$0.0060^{+0.0067}_{-0.0038}$	
$\beta_2$		$\text{day}^{-1}$	May 1, 2016	$5.37^{+10.2}_{-9.71} \times 10^{-4}$	Sec. 5.3.5.2
			February 1, 2017	$0.0043^{+0.1382}_{-0.0750}$	
			April 10, 2018	$0.09^{+0.14}_{-0.10}$	
			June 12, 2018	$0.10^{+0.11}_{-0.10}$	
$A_L$	$\geq 0$	$\text{ppb kg day}^{-1}$	May 1, 2016	$49.3^{+28.5}_{-25.2}$	Sec. 5.3.5.2
			February 1, 2017	$11.7^{+1.8}_{-1.8}$	
			April 10, 2018	$3.4^{+2.6}_{-2.3}$	
			June 12, 2018	$7.5^{+4.7}_{-4.3}$	
$\beta_3$	$\geq 0$	$\text{day}^{-1}$	May 1, 2016	$0.0069^{+0.0053}_{-0.0051}$	Sec. 5.3.5.2
			February 1, 2017	$0.0107^{+0.0017}_{-0.0016}$	
			April 10, 2018	$0.0031^{+0.0040}_{-0.0021}$	
			June 12, 2018	$0.0042^{+0.0053}_{-0.0028}$	
$\beta_4$		$\text{day}^{-1}$	May 1, 2016	$0.0017^{+0.0046}_{-0.0052}$	Sec. 5.3.5.2
			February 1, 2017	$0.00221^{+0.00076}_{-0.00053}$	
			April 10, 2018	$0.031^{+0.034}_{-0.027}$	
			June 12, 2018	$0.037^{+0.054}_{-0.040}$	
$R_I$	$\geq 0$	$\text{ppb kg day}^{-1}$	May 1, 2016	$170^{+64}_{-58}$	Sec. 5.3.5.4
			February 1, 2017	$159.5^{+3.3}_{-2.3}$	
			April 10, 2018	$172.5^{+3.7}_{-3.5}$	
			June 12, 2018	$176.9^{+6.53}_{-6.7}$	

Table 5.9: Outgassing and leak medians and 68% credible intervals. The outgassing is separated into four periods due to changes in the experiment that are expected to permanently change the behavior. The leak values agree nicely with the predicted value of  $165 \text{ ppb kg day}^{-1}$ .

## 5. PURITY AND THE ELECTRON LIFETIME

---

Date	Prior distribution	Region	Posterior	Comment
Aug. 22-Sep. 2, 2016	0-1	GXE	$0.628^{+0.236}_{-0.333}$	GXE-only purification
Aug. 22-Sep. 2, 2016	0-1	LXE	$0.632^{+0.081}_{-0.118}$	GXE-only purification
May 8-18, 2018	0-1	GXE	$0.436^{+0.388}_{-0.328}$	$\text{LN}_2$ cooling
May 8-18, 2018	0-1	LXE	$0.889^{+0.033}_{-0.031}$	$\text{LN}_2$ cooling
May 29-June 5, 2018	$\geq 0$	GXE	$1.48^{+1.11}_{-1.04}$	Circulation stopped
May 29-June 5, 2018	0-1	LXE	$0.306^{+0.077}_{-0.064}$	Circulation stopped
June 5-12, 2018	$\geq 0$	LXE	$1.34^{+0.83}_{-0.79}$	Magnetic pump installation

Table 5.10: Fraction of outgassing during periods where system conditions changed. Medians and 68% credible intervals are listed, along with change in conditions.

detector operations. Situations where this becomes relevant are listed in Tab. 5.10 and include the GXe-only purification,  $\text{LN}_2$  cooling, and halting of purification. For the GXe-only purification none of the GXe returning to the cryostat will condense, so the balance of clean xenon entering the liquid is upset. While this is not a change in outgassing, parameterizing it as such allows the effect to be corrected for still. Because outgassing is temperature-dependent, changing the  $\text{LN}_2$  coldfinger temperature will change the rate. Complete stoppage is expected to change the outgassing behavior temporarily because contaminants that outgas from pipes that circulate the xenon towards the purification system would normally be removed by the getter. Without the flow the impurities are more likely to penetrate the bulk GXe or LXe. The same effect should exist during the magnetic pump installation.

Getter deficiencies model periods when the electron lifetime begins to decrease without an explanation. There are three that are modeled in the fit, the latter two of which are expected to result from excess impurities inside the calibration box, released during  ${}^{220}\text{Rn}$  calibrations.

Impurity spikes are modeled as instant increases in impurities. Tab. 5.12 lists them along with relevant information and the median and 68% credible interval using the posterior.

The electron lifetime model is shown in Fig. 5.30. The model is shown in red with its 68% credible interval highlighted in blue. Sudden changes where there is not an event (marked by numbers with dashed black lines) are from the cathode voltage

Parameter	Date	Prior distribution	Posterior	Comment
$\alpha_1$	Nov. 26-Dec. 5, 2016	0-1	$0.822^{+0.019}_{-0.018}$	
$\alpha_2$	Dec. 19-21, 2016	0-1	$0.687^{+0.208}_{-0.272}$	$^{220}\text{Rn}$ calibration
$\alpha_3$	Oct. 25-30, 2017	0-1	$0.979^{+0.014}_{-0.017}$	$^{220}\text{Rn}$ calibration

Table 5.11: Getter defficiencies medians and 68% credible intervals. The first getter defficiency is not understood, but the latter two are thought to result from high levels of impurities inside the calibration source box, since they occur simultaneously with the start of  $^{220}\text{Rn}$  calibrations.

Date	Origin	Region	Possible cause	$\sim\tau_e$ [μs]	$\sim\Delta\tau_e$ [μs]	$\Delta I$ [ppb]
June 14, 2016	Power glitch	GXe	PTR power $\rightarrow$ 0	65	-30	$73.9^{+25.4}_{-29.5}$
July 15, 2016	LN <sub>2</sub> test	GXe	PTR power $\rightarrow$ 0	225*	-100	$32.2^{+2.3}_{-2.6}$
Nov. 21, 2016	Power disruption	LXe	Temperature increase	450	-75	$2.96^{+0.29}_{-0.26}$
Jan. 18-Feb. 1, 2017	Earthquake	GXe + LXe	Liquid level change	520*	-120	$2.57^{+0.21}_{-0.23}$
June 5, 2017	Gate washing	LXe	Liquid level change	575	-50	$1.03^{+0.14}_{-0.14}$
Feb. 21, 2018	Power glitch	GXe	PTR power drop of $\sim$ 50%	600	-150	$3.79^{+0.11}_{-0.09}$
Feb. 24, 2018	Blackout	GXe + LXe	PTR power $\rightarrow$ 0, $F_G = F_L = 0$	500*	-150	$3.31^{+1.84}_{-1.76}$
Mar. 5-7, 2018	Gate washings	LXe	Liquid level change	450	-70	$2.02^{+0.76}_{-0.78}$

Table 5.12: Impurity spikes in XENON1T. Relevant information along with the medians and 68% credible intervals are listed. Values with a \* have a period of days to weeks following where no electron lifetime measurements exist so have a larger uncertainty.

changing.

#### 5.4.4 $^{83\text{m}}\text{Kr}$ Evolution

An separate electron lifetime trend is needed to describe the  $^{83\text{m}}\text{Kr}$  measurements. Because the evolution of the trend is independent of the isotope used for the measurement the alpha model will describe the  $^{83\text{m}}\text{Kr}$  model if it can be adjusted upwards. The ratio between the two becomes larger at higher  $\tau_e$  so scaling by a constant will not work.

To determine which electron lifetime model should be used to correct background data the combined energy spectrum (Sec. 3.2.8) is examined. Fig. 5.31 shows the combined energy spectrum as a function of depth using both trends. The spectrum corrected with lifetimes from  $\alpha$ -decays shows a shift to higher energy at larger  $z$ , meaning it is over-corrected. The spectrum using  $^{83\text{m}}\text{Kr}$  is consistent across the depth

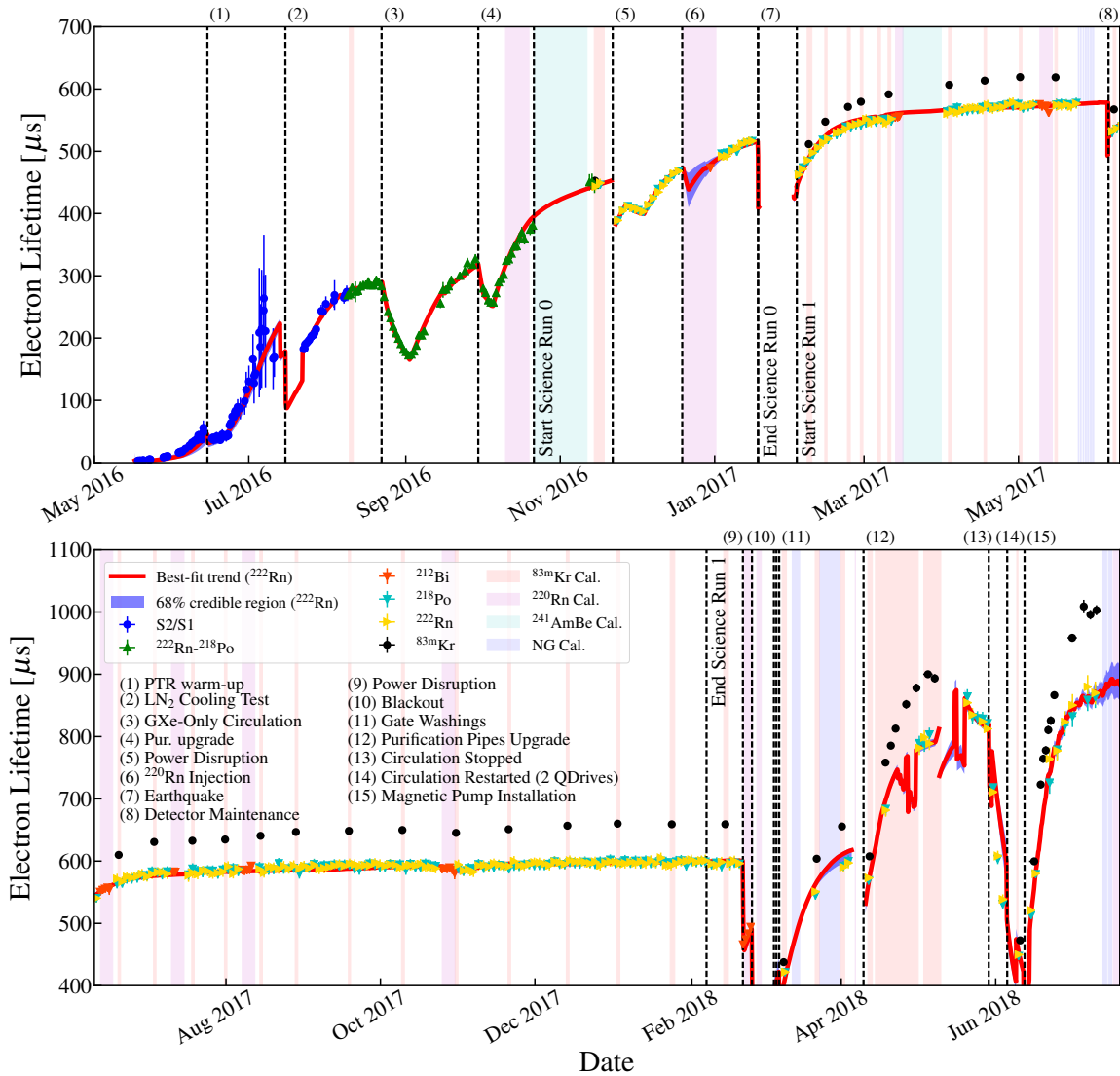


Figure 5.30: Electron lifetime model and data over the lifetime of XENON1T. Electron lifetimes calculated via the S2/S1 method (blue circle),  $^{222}\text{Rn-}^{218}\text{Po}$  (green triangle),  $^{212}\text{Bi}$  (red triangle),  $^{218}\text{Po}$  (turquoise triangle),  $^{222}\text{Rn}$  (yellow triangle), and  $^{83m}\text{Kr}$  (black circle) are shown. The best-fit trend (red line) and 68% credible region (shaded blue) are overlaid for comparison. Dashed lines correspond to events that affected the evolution of the electron lifetime.

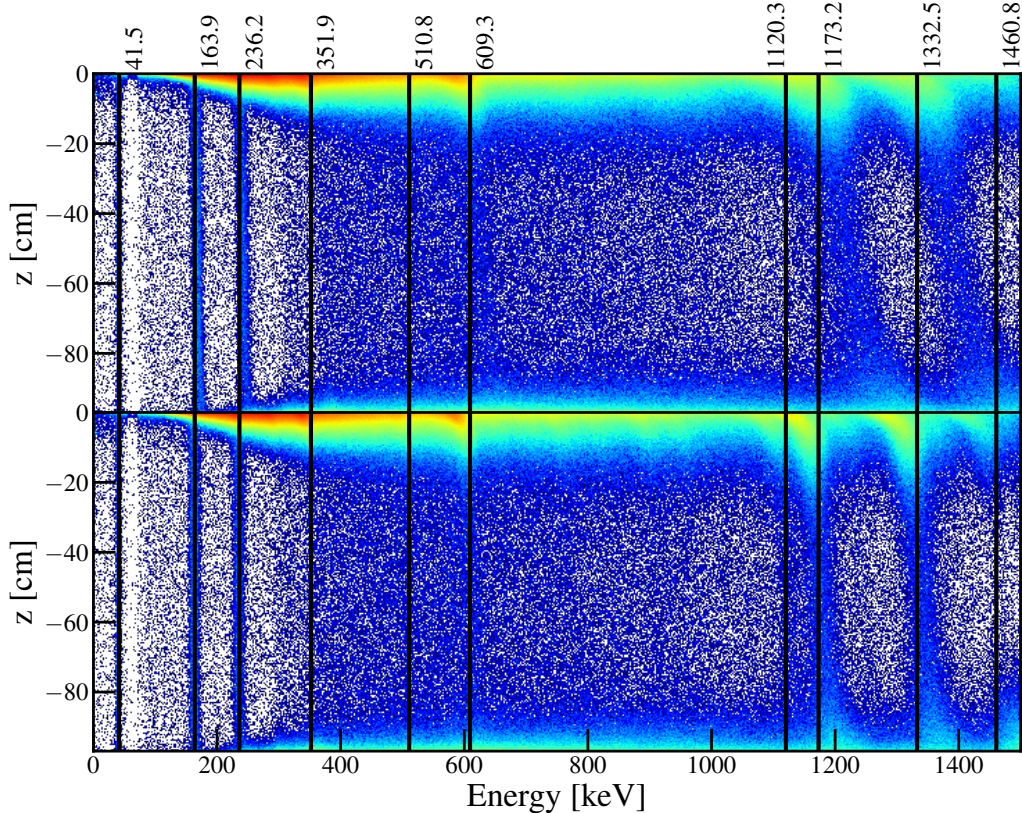


Figure 5.31: Combined energy spectrum over  $z$  for 0-1500 keV using the  $\alpha$ -decay (top) and  $^{83\text{m}}\text{Kr}$  (bottom)  $S2_b$  corrections. For the  $\alpha$ -corrected spectrum the mono-energetic peaks curve towards higher  $E$  deeper in the detector, indicating they are overcorrected. This occurs to an extent with the  $^{83\text{m}}\text{Kr}$ -corrected spectrum at higher energy, but can be explained by the effects of an inhomogeneous electric field. Events near the top of the detector may saturate PMTs in the top array.

of the detector. This is expected since the background is almost entirely electronic recoils.

At higher energies in Fig. 5.31 some of the mono-energetic lines begin to appear under-corrected. This is explained by Fig. 5.14 where the  $^{60}\text{Co}$  (1173.2 keV) and  $^{208}\text{Tl}$  (2614.5 keV) have higher charge yields than  $^{129\text{m}}\text{Xe}$  and  $^{131\text{m}}\text{Xe}$  so  $\tau_e$  measurements would be lower. Correcting their  $S2_s$ s with the  $^{83\text{m}}\text{Kr}$  values falls short. The effect is much smaller than using the  $\alpha$ -decay trend, but for analyses using these high-energy lines the distortion would need to be fixed. Aside from using the electron lifetime, the peaks can be corrected by minimizing their width if the underlying background is well understood and there are enough statistics. This would also result in a measurement

## 5. PURITY AND THE ELECTRON LIFETIME

---

of the electron lifetime.

From this analysis it is found that S2s from  $\alpha$ -decays and electronic recoils require different electron lifetime corrections. Because the LXe purity has the same effect on both, the behavior of the electron lifetime evolution for the two are the same. Therefore, the  $^{83m}\text{Kr}$  trend is used for the dark matter search since the background in our region of interest comes primarily from electronic recoils. Furthermore, nuclear recoils are expected to have a lifetime correction that is similar to that of ERs.

# Bibliography

- [1] F. Zwicky, “Die Rotverschiebung von extragalaktischen Nebeln,” *Helvetica Physica Acta*, vol. 6, pp. 110–127, 1933.
- [2] V. C. Rubin and W. K. Ford Jr., “Rotation of the Andromeda Nebula from a Spectroscopic Survey of Emission Regions,” *The Astrophysical Journal*, vol. 159, p. 379, Feb. 1970. DOI: [10.1086/150317](https://doi.org/10.1086/150317).
- [3] K. G. Begeman, A. H. Broeils, and R. H. Sanders, “Extended rotation curves of spiral galaxies - Dark haloes and modified dynamics,” *MNRAS*, vol. 249, pp. 523–537, Apr. 1991. DOI: [10.1093/mnras/249.3.523](https://doi.org/10.1093/mnras/249.3.523).
- [4] Y. Sofue and V. Rubin, “Rotation Curves of Spiral Galaxies,” *Annual Review of Astronomy and Astrophysics*, vol. 39, pp. 137–174, 2001. DOI: [10.1146/annurev.astro.39.1.137](https://doi.org/10.1146/annurev.astro.39.1.137).
- [5] R. Gendler and the Subaru Telescope (NAOJ) and the Hubble Legacy Archive. (2013). NGC 6503, Spiral Galaxy in Draco, [Online]. Available: <http://www.robgendlerastropics.com/NGC6503-HST-Subaru.html> (visited on 08/10/2018).
- [6] NASA/JPL-Caltech/GSFC/SDSS. (May 2007). Dwarfs in Coma Cluster, [Online]. Available: <https://www.jpl.nasa.gov/spaceimages/details.php?id=PIA09561> (visited on 08/10/2018).
- [7] ESA/Hubble & NASA. (Dec. 2011). A Horseshoe Einstein Ring from Hubble, [Online]. Available: <https://apod.nasa.gov/apod/ap111221.html> (visited on 08/10/2018).
- [8] ALMA (NRAO/ESO/NAOJ)/Luis Calçada (ESO). (Jun. 2015). Gravitational lensing of distant star-forming galaxies (schematic), [Online]. Available: [https://en.wikipedia.org/wiki/File:Gravitational\\_lensing\\_of\\_distant\\_star-forming\\_galaxies\\_schematic.png](https://en.wikipedia.org/wiki/File:Gravitational_lensing_of_distant_star-forming_galaxies_schematic.png) (visited on 08/10/2018).

## BIBLIOGRAPHY

---

- [9] F. De Paolis, M. Giordano, G. Ingrosso, L. Manni, A. Nucita, and F. Strafella, “The Scales of Gravitational Lensing,” *Universe*, vol. 2, p. 6, Mar. 2016. DOI: [10.3390/universe2010006](https://doi.org/10.3390/universe2010006). arXiv: [1604.06601](https://arxiv.org/abs/1604.06601).
- [10] M. Markevitch, “Chandra Observation of the Most Interesting Cluster in the Universe,” in *The X-ray Universe 2005*, A. Wilson, Ed., ser. ESA Special Publication, vol. 604, Jan. 2006, p. 723. eprint: [astro-ph/0511345](https://arxiv.org/abs/astro-ph/0511345).
- [11] D. Clowe, M. Bradač, A. H. Gonzalez, M. Markevitch, S. W. Randall, C. Jones, and D. Zaritsky, “A Direct Empirical Proof of the Existence of Dark Matter,” *The Astrophysical Journal Letters*, vol. 648, pp. L109–L113, Sep. 2006. DOI: [10.1086/508162](https://doi.org/10.1086/508162).
- [12] M. Markevitch, A. H. Gonzalez, D. Clowe, A. Vikhlinin, W. Forman, C. Jones, S. Murray, and W. Tucker, “Direct Constraints on the Dark Matter Self-Interaction Cross Section from the Merging Galaxy Cluster 1E 0657-56,” *The Astrophysical Journal*, vol. 606, pp. 819–824, May 2004. DOI: [10.1086/383178](https://doi.org/10.1086/383178).
- [13] A. A. Penzias and R. W. Wilson, “A Measurement of Excess Antenna Temperature at 4080 Mc/s.,” *The Astrophysical Journal*, vol. 142, pp. 419–421, Jul. 1965. DOI: [10.1086/148307](https://doi.org/10.1086/148307).
- [14] D. J. Fixsen, “The Temperature of the Cosmic Microwave Background,” *The Astrophysical Journal*, vol. 707, pp. 916–920, Dec. 2009. DOI: [10.1088/0004-637X/707/2/916](https://doi.org/10.1088/0004-637X/707/2/916). arXiv: [0911.1955](https://arxiv.org/abs/0911.1955).
- [15] G. F. Smoot *et al.*, “First results of the COBE satellite measurement of the anisotropy of the cosmic microwave background radiation,” *Advances in Space Research*, vol. 11, pp. 193–205, 1991. DOI: [10.1016/0273-1177\(91\)90490-B](https://doi.org/10.1016/0273-1177(91)90490-B).
- [16] R. K. Sachs and A. M. Wolfe, “Perturbations of a Cosmological Model and Angular Variations of the Microwave Background,” *The Astrophysical Journal*, vol. 147, p. 73, Jan. 1967. DOI: [10.1086/148982](https://doi.org/10.1086/148982).
- [17] S. Dodelson, *Modern Cosmology*. Elsevier, 2003, vol. A volume in International Series of Monographs in Electronics and Instrumentation, ISBN: 978-0-12-219141-1.
- [18] Planck Collaboration. (2015). Map of CMB temperature from SMICA, [Online]. Available: <https://www.cosmos.esa.int/web/planck/picture-gallery> (visited on 01/18/2018).

- 
- [19] P. A. R. Ade *et al.*, “Planck early results. I. The Planck mission,” *Astronomy & Astrophysics*, vol. 536, A1, A1, Dec. 2011. DOI: [10.1051/0004-6361/201116464](https://doi.org/10.1051/0004-6361/201116464). arXiv: [1101.2022 \[astro-ph.IM\]](https://arxiv.org/abs/1101.2022).
  - [20] ——, “Planck 2015 results. XIII. Cosmological parameters,” *Astronomy & Astrophysics*, vol. 594, A13, A13, Sep. 2016. DOI: [10.1051/0004-6361/201525830](https://doi.org/10.1051/0004-6361/201525830). arXiv: [1502.01589](https://arxiv.org/abs/1502.01589).
  - [21] R. D. Peccei and H. R. Quinn, “CP conservation in the presence of pseudoparticles,” *Physical Review Letters*, vol. 38, pp. 1440–1443, Jun. 1977. DOI: [10.1103/PhysRevLett.38.1440](https://doi.org/10.1103/PhysRevLett.38.1440).
  - [22] J. Preskill, M. B. Wise, and F. Wilczek, “Cosmology of the invisible axion,” *Physical Letters B*, vol. 120, pp. 127–132, Jan. 1983. DOI: [10.1016/0370-2693\(83\)90637-8](https://doi.org/10.1016/0370-2693(83)90637-8).
  - [23] J. E. Kim, “Weak-Interaction Singlet and Strong CP Invariance,” *Physical Review Letters*, vol. 43, pp. 103–107, 2 1979. DOI: [10.1103/PhysRevLett.43.103](https://doi.org/10.1103/PhysRevLett.43.103).
  - [24] M. A. Shifman, A. I. Vainshtein, and V. I. Zakharov, “Can confinement ensure natural CP invariance of strong interactions?” *Nuclear Physics B*, vol. 166, no. 3, pp. 493–506, Apr. 1980, ISSN: 0550-3213. DOI: [10.1016/0550-3213\(80\)90209-6](https://doi.org/10.1016/0550-3213(80)90209-6).
  - [25] A. R. Zhitnitsky, “On Possible Suppression of the Axion Hadron Interactions,” *Soviet Journal of Nuclear Physics*, vol. 31, pp. 260–263, 1980. [Online]. Available: <http://inspirehep.net/record/157263?ln=en>.
  - [26] M. Dine, W. Fischler, and M. Srednicki, “A simple solution to the strong CP problem with a harmless axion,” *Physical Letters B*, vol. 104, no. 3, pp. 199 –202, 1981, ISSN: 0370-2693. DOI: [10.1016/0370-2693\(81\)90590-6](https://doi.org/10.1016/0370-2693(81)90590-6).
  - [27] C. Patrignani and P. D. Group, “Review of Particle Physics,” *Chinese Physics C*, vol. 40, no. 10, p. 100001, 2016. [Online]. Available: <http://stacks.iop.org/1674-1137/40/i=10/a=100001>.
  - [28] H. Primakoff, “Photo-Production of Neutral Mesons in Nuclear Electric Fields and the Mean Life of the Neutral Meson,” *Physical Review*, vol. 81, pp. 899–899, 5 1951. DOI: [10.1103/PhysRev.81.899](https://doi.org/10.1103/PhysRev.81.899).
  - [29] N. Du *et al.*, “Search for invisible axion dark matter with the axion dark matter experiment,” *Physical Review Letters*, vol. 120, p. 151301, 15 2018. DOI: [10.1103/PhysRevLett.120.151301](https://doi.org/10.1103/PhysRevLett.120.151301).

- [30] V. Anastassopoulos *et al.*, “New CAST limit on the axion-photon interaction,” *Nature Physics*, vol. 13, pp. 584–590, Jun. 2017. DOI: [10.1038/nphys4109](https://doi.org/10.1038/nphys4109).
- [31] A. Garcon *et al.*, “The cosmic axion spin precession experiment (CASPER): a dark-matter search with nuclear magnetic resonance,” *Quantum Science and Technology*, vol. 3, no. 1, p. 014008, Jan. 2018. DOI: [10.1088/2058-9565/aa9861](https://doi.org/10.1088/2058-9565/aa9861). arXiv: [1707.05312 \[physics.ins-det\]](https://arxiv.org/abs/1707.05312).
- [32] Z. Ahmed *et al.*, “Search for Axions with the CDMS Experiment,” *Physical Review Letters*, vol. 103, no. 14, 141802, p. 141802, Oct. 2009. DOI: [10.1103/PhysRevLett.103.141802](https://doi.org/10.1103/PhysRevLett.103.141802). arXiv: [0902.4693 \[hep-ex\]](https://arxiv.org/abs/0902.4693).
- [33] E. Armengaud *et al.*, “Axion searches with the EDELWEISS-II experiment,” *JCAP*, vol. 11, 067, p. 067, Nov. 2013. DOI: [10.1088/1475-7516/2013/11/067](https://doi.org/10.1088/1475-7516/2013/11/067). arXiv: [1307.1488](https://arxiv.org/abs/1307.1488).
- [34] K. Abe *et al.*, “Search for solar axions in XMASS, a large liquid-xenon detector,” *Physical Letters B*, vol. 724, pp. 46–50, Jul. 2013. DOI: [10.1016/j.physletb.2013.05.060](https://doi.org/10.1016/j.physletb.2013.05.060). arXiv: [1212.6153 \[astro-ph.CO\]](https://arxiv.org/abs/1212.6153).
- [35] E. Aprile *et al.*, “First axion results from the XENON100 experiment,” *Physical Review D*, vol. 90, no. 6, 062009, p. 062009, Sep. 2014. DOI: [10.1103/PhysRevD.90.062009](https://doi.org/10.1103/PhysRevD.90.062009). arXiv: [1404.1455](https://arxiv.org/abs/1404.1455).
- [36] B. Ryden, *Introduction to Cosmology*. Addison Wesley, 2003.
- [37] B. Moore, S. Ghigna, F. Governato, G. Lake, T. Quinn, J. Stadel, and P. Tozzi, “Dark Matter Substructure within Galactic Halos,” *The Astrophysical Journal Letters*, vol. 524, pp. L19–L22, Oct. 1999. DOI: [10.1086/312287](https://doi.org/10.1086/312287).
- [38] A. Klypin, A. V. Kravtsov, O. Valenzuela, and F. Prada, “Where Are the Missing Galactic Satellites?” *The Astrophysical Journal*, vol. 522, pp. 82–92, Sep. 1999. DOI: [10.1086/307643](https://doi.org/10.1086/307643).
- [39] J. D. Simon and M. Geha, “The Kinematics of the Ultra-faint Milky Way Satellites: Solving the Missing Satellite Problem,” *The Astrophysical Journal*, vol. 670, pp. 313–331, Nov. 2007. DOI: [10.1086/521816](https://doi.org/10.1086/521816). arXiv: [0706.0516](https://arxiv.org/abs/0706.0516).
- [40] J. S. Bullock and M. Boylan-Kolchin, “Small-Scale Challenges to the  $\Lambda$ CDM Paradigm,” *Annual Review of Astronomy and Astrophysics*, vol. 55, pp. 343–387, Aug. 2017. DOI: [10.1146/annurev-astro-091916-055313](https://doi.org/10.1146/annurev-astro-091916-055313). arXiv: [1707.04256](https://arxiv.org/abs/1707.04256).

- 
- [41] G. Ogiya and O. Hahn, “What sets the central structure of dark matter haloes?” *MNRAS*, vol. 473, pp. 4339–4359, Feb. 2018. DOI: [10.1093/mnras/stx2639](https://doi.org/10.1093/mnras/stx2639). arXiv: [1707.07693](https://arxiv.org/abs/1707.07693).
  - [42] P. van Dokkum *et al.*, “A galaxy lacking dark matter,” *Nature*, vol. 555, pp. 629–632, Mar. 2018. DOI: [10.1038/nature25767](https://doi.org/10.1038/nature25767). arXiv: [1803.10237](https://arxiv.org/abs/1803.10237).
  - [43] ——, “An Enigmatic Population of Luminous Globular Clusters in a Galaxy Lacking Dark Matter,” *The Astrophysical Journal Letters*, vol. 856, L30, p. L30, Apr. 2018. DOI: [10.3847/2041-8213/aab60b](https://doi.org/10.3847/2041-8213/aab60b). arXiv: [1803.10240](https://arxiv.org/abs/1803.10240).
  - [44] M. Milgrom, “A modification of the Newtonian dynamics as a possible alternative to the hidden mass hypothesis,” *The Astrophysical Journal*, vol. 270, pp. 365–370, Jul. 1983. DOI: [10.1086/161130](https://doi.org/10.1086/161130).
  - [45] B. Famaey, S. McGaugh, and M. Milgrom, “MOND and the dynamics of NGC1052-DF2,” *arXiv e-prints*, Apr. 2018. arXiv: [1804.04167](https://arxiv.org/abs/1804.04167).
  - [46] J. W. Moffat and V. T. Toth, “NGC 1052-DF2 And Modified Gravity (MOG) Without Dark Matter,” *arXiv e-prints*, May 2018. arXiv: [1805.01117 \[gr-qc\]](https://arxiv.org/abs/1805.01117).
  - [47] R. Abraham *et al.*, “The Maybe Stream: A Possible Cold Stellar Stream in the Ultra-diffuse Galaxy NGC1052-DF2,” *Research Notes of the American Astronomical Society*, vol. 2, 16, p. 16, May 2018. DOI: [10.3847/2515-5172/aac087](https://doi.org/10.3847/2515-5172/aac087).
  - [48] G. Ogiya, “Tidal stripping as a possible origin of the ultra diffuse galaxy lacking dark matter,” *arXiv e-prints*, Apr. 2018. arXiv: [1804.06421](https://arxiv.org/abs/1804.06421).
  - [49] F. Lelli, S. S. McGaugh, and J. M. Schombert, “SPARC: Mass Models for 175 Disk Galaxies with Spitzer Photometry and Accurate Rotation Curves,” *The Astronomical Journal*, vol. 152, 157, p. 157, Dec. 2016. DOI: [10.3847/0004-6256/152/6/157](https://doi.org/10.3847/0004-6256/152/6/157). arXiv: [1606.09251](https://arxiv.org/abs/1606.09251).
  - [50] P. Li, F. Lelli, S. McGaugh, and J. Schombert, “Fitting the Radial Acceleration Relation to Individual SPARC Galaxies,” *arXiv e-prints*, Feb. 2018. arXiv: [1803.00022](https://arxiv.org/abs/1803.00022).
  - [51] W. J. G. de Blok, F. Walter, E. Brinks, C. Trachternach, S.-H. Oh, and R. C. Kennicutt Jr., “High-Resolution Rotation Curves and Galaxy Mass Models from THINGS,” *The Astronomical Journal*, vol. 136, pp. 2648–2719, Dec. 2008. DOI: [10.1088/0004-6256/136/6/2648](https://doi.org/10.1088/0004-6256/136/6/2648). arXiv: [0810.2100](https://arxiv.org/abs/0810.2100).

- [52] D. C. Rodrigues, V. Marra, A. del Popolo, and Z. Davari, “Absence of a fundamental acceleration scale in galaxies,” *Nature Astronomy*, Jun. 2018. DOI: [10.1038/s41550-018-0498-9](https://doi.org/10.1038/s41550-018-0498-9). arXiv: [1806.06803](https://arxiv.org/abs/1806.06803).
- [53] X.-J. Bi, P.-F. Yin, and Q. Yuan, “Status of dark matter detection,” *Frontiers of Physics*, vol. 8, pp. 794–827, Dec. 2013. DOI: [10.1007/s11467-013-0330-z](https://doi.org/10.1007/s11467-013-0330-z). arXiv: [1409.4590 \[hep-ph\]](https://arxiv.org/abs/1409.4590).
- [54] P. J. Fox, R. Harnik, J. Kopp, and Y. Tsai, “LEP shines light on dark matter,” *Physical Review D*, vol. 84, no. 1, 014028, p. 014 028, Jul. 2011. DOI: [10.1103/PhysRevD.84.014028](https://doi.org/10.1103/PhysRevD.84.014028). arXiv: [1103.0240 \[hep-ph\]](https://arxiv.org/abs/1103.0240).
- [55] C. Alpigiani, “Searches for Dark Matter in ATLAS,” *arXiv e-prints*, Aug. 2017. arXiv: [1708.09674 \[hep-ex\]](https://arxiv.org/abs/1708.09674).
- [56] CERN. (2015). LHC experiments join forces to zoom in on the Higgs boson, [Online]. Available: <https://home.cern/about/updates/2015/03/lhc-experiments-join-forces-zoom-higgs> (visited on 08/09/2018).
- [57] J. I. Read, “The local dark matter density,” *Journal of Physics G*, vol. 41, no. 6, 063101, p. 063 101, Jun. 2014. DOI: [10.1088/0954-3899/41/6/063101](https://doi.org/10.1088/0954-3899/41/6/063101). arXiv: [1404.1938](https://arxiv.org/abs/1404.1938).
- [58] J. Ellis, R. A. Flores, K. Freese, S. Ritz, D. Seckel, and J. Silk, “Cosmic ray constraints on the annihilations of relic particles in the galactic halo,” *Physical Letters B*, vol. 214, pp. 403–412, Nov. 1988. DOI: [10.1016/0370-2693\(88\)91385-8](https://doi.org/10.1016/0370-2693(88)91385-8).
- [59] B. Zitzer *et al.*, “A Search for Dark Matter from Dwarf Galaxies using VERITAS,” in *Proceedings of the 38th International Conference on High Energy Physics (ICHEP2016). 3-10 August 2016. Chicago, USA.*, 2016, p. 446. arXiv: [1509.01105 \[astro-ph.HE\]](https://arxiv.org/abs/1509.01105).
- [60] G. Bertone, D. Hooper, and J. Silk, “Particle dark matter: evidence, candidates and constraints,” *Physical Reports*, vol. 405, pp. 279–390, Jan. 2005. DOI: [10.1016/j.physrep.2004.08.031](https://doi.org/10.1016/j.physrep.2004.08.031).
- [61] J. Kopp, V. Niro, T. Schwetz, and J. Zupan, “DAMA/LIBRA data and leptonically interacting dark matter,” *Physical Review D*, vol. 80, no. 8, 083502, p. 083 502, Oct. 2009. DOI: [10.1103/PhysRevD.80.083502](https://doi.org/10.1103/PhysRevD.80.083502). arXiv: [0907.3159 \[hep-ph\]](https://arxiv.org/abs/0907.3159).
- [62] P. Bhattacharjee, S. Chaudhury, S. Kundu, and S. Majumdar, “Deriving the velocity distribution of Galactic dark matter particles from the rotation curve

- data,” *Physical Review D*, vol. 87, no. 8, 083525, p. 083 525, Apr. 2013. DOI: [10.1103/PhysRevD.87.083525](https://doi.org/10.1103/PhysRevD.87.083525). arXiv: [1210.2328 \[astro-ph.GA\]](https://arxiv.org/abs/1210.2328).
- [63] J. Diemand, B. Moore, and J. Stadel, “Velocity and spatial biases in cold dark matter subhalo distributions,” *MNRAS*, vol. 352, pp. 535–546, Aug. 2004. DOI: [10.1111/j.1365-2966.2004.07940.x](https://doi.org/10.1111/j.1365-2966.2004.07940.x).
- [64] M. Kuhlen *et al.*, “Dark matter direct detection with non-Maxwellian velocity structure,” *JCAP*, vol. 2, 030, p. 030, Feb. 2010. DOI: [10.1088/1475-7516/2010/02/030](https://doi.org/10.1088/1475-7516/2010/02/030). arXiv: [0912.2358](https://arxiv.org/abs/0912.2358).
- [65] T. Marrodán Undagoitia and L. Rauch, “Dark matter direct-detection experiments,” *Journal of Physics G*, vol. 43, no. 1, 013001, p. 013 001, Jan. 2016. DOI: [10.1088/0954-3899/43/1/013001](https://doi.org/10.1088/0954-3899/43/1/013001). arXiv: [1509.08767 \[physics.ins-det\]](https://arxiv.org/abs/1509.08767).
- [66] T. Piffl *et al.*, “The RAVE survey: the Galactic escape speed and the mass of the Milky Way,” *Astronomy & Astrophysics*, vol. 562, A91, A91, Feb. 2014. DOI: [10.1051/0004-6361/201322531](https://doi.org/10.1051/0004-6361/201322531). arXiv: [1309.4293 \[astro-ph.GA\]](https://arxiv.org/abs/1309.4293).
- [67] J. D. Lewin and P. F. Smith, “Review of mathematics, numerical factors, and corrections for dark matter experiments based on elastic nuclear recoil,” *Astroparticle Physics*, vol. 6, pp. 87–112, Dec. 1996. DOI: [10.1016/S0927-6505\(96\)00047-3](https://doi.org/10.1016/S0927-6505(96)00047-3).
- [68] R. H. Helm, “Inelastic and elastic scattering of 187-mev electrons from selected even-even nuclei,” *Physical Review*, vol. 104, pp. 1466–1475, 5 1956. DOI: [10.1103/PhysRev.104.1466](https://doi.org/10.1103/PhysRev.104.1466).
- [69] J. Engel, “Nuclear form factors for the scattering of weakly interacting massive particles,” *Physical Letters B*, vol. 264, no. 1, pp. 114 –119, 1991, ISSN: 0370-2693. DOI: [10.1016/0370-2693\(91\)90712-Y](https://doi.org/10.1016/0370-2693(91)90712-Y).
- [70] C. E. Yaguna, “Isospin-violating dark matter in the light of recent data,” *Physical Review D*, vol. 95, no. 5, 055015, p. 055 015, Mar. 2017. DOI: [10.1103/PhysRevD.95.055015](https://doi.org/10.1103/PhysRevD.95.055015). arXiv: [1610.08683 \[hep-ph\]](https://arxiv.org/abs/1610.08683).
- [71] A. K. Drukier, K. Freese, and D. N. Spergel, “Detecting cold dark-matter candidates,” *Physical Review D*, vol. 33, pp. 3495–3508, Jun. 1986. DOI: [10.1103/PhysRevD.33.3495](https://doi.org/10.1103/PhysRevD.33.3495).
- [72] K. Freese, M. Lisanti, and C. Savage, “Colloquium: Annual modulation of dark matter,” *Review of Modern Physics*, vol. 85, pp. 1561–1581, Oct. 2013. DOI: [10.1103/RevModPhys.85.1561](https://doi.org/10.1103/RevModPhys.85.1561). arXiv: [1209.3339](https://arxiv.org/abs/1209.3339).

- [73] C. Amole *et al.*, “Dark Matter Search Results from the PICO-60  $\text{C}_3\text{F}_8$  Bubble Chamber,” *Physical Review Letters*, vol. 118, no. 25, 251301, p. 251 301, Jun. 2017. DOI: [10.1103/PhysRevLett.118.251301](https://doi.org/10.1103/PhysRevLett.118.251301). arXiv: [1702.07666](https://arxiv.org/abs/1702.07666).
- [74] J. Ellis and R. A. Flores, “Elastic supersymmetric relic-nucleus scattering revisited,” *Physical Letters B*, vol. 263, pp. 259–266, Jul. 1991. DOI: [10.1016/0370-2693\(91\)90597-J](https://doi.org/10.1016/0370-2693(91)90597-J).
- [75] S. Archambault *et al.*, “Constraints on low-mass WIMP interactions on  $^{19}\text{F}$  from PICASSO,” *Physical Letters B*, vol. 711, pp. 153–161, May 2012. DOI: [10.1016/j.physletb.2012.03.078](https://doi.org/10.1016/j.physletb.2012.03.078). arXiv: [1202.1240 \[hep-ex\]](https://arxiv.org/abs/1202.1240).
- [76] E. Behnke *et al.*, “Final results of the PICASSO dark matter search experiment,” *Astroparticle Physics*, vol. 90, pp. 85–92, Apr. 2017. DOI: [10.1016/j.astropartphys.2017.02.005](https://doi.org/10.1016/j.astropartphys.2017.02.005). arXiv: [1611.01499 \[hep-ex\]](https://arxiv.org/abs/1611.01499).
- [77] ——, “First dark matter search results from a 4-kg  $\text{CF}_3\text{I}$  bubble chamber operated in a deep underground site,” *Physical Review D*, vol. 86, no. 5, 052001, p. 052 001, Sep. 2012. DOI: [10.1103/PhysRevD.86.052001](https://doi.org/10.1103/PhysRevD.86.052001). arXiv: [1204.3094 \[astro-ph.CO\]](https://arxiv.org/abs/1204.3094).
- [78] M. Felizardo *et al.*, “Final Analysis and Results of the Phase II SIMPLE Dark Matter Search,” *Physical Review Letters*, vol. 108, no. 20, 201302, p. 201 302, May 2012. DOI: [10.1103/PhysRevLett.108.201302](https://doi.org/10.1103/PhysRevLett.108.201302). arXiv: [1106.3014](https://arxiv.org/abs/1106.3014).
- [79] A. Antonicci *et al.*, “MOSCAB: A geyser-concept bubble chamber to be used in a dark matter search,” *arXiv e-prints*, Jul. 2017. arXiv: [1708.00101 \[physics.ins-det\]](https://arxiv.org/abs/1708.00101).
- [80] C. Amole *et al.*, “Dark matter search results from the PICO-60  $\text{CF}_3\text{I}$  bubble chamber,” *Physical Review D*, vol. 93, no. 5, 052014, p. 052 014, Mar. 2016. DOI: [10.1103/PhysRevD.93.052014](https://doi.org/10.1103/PhysRevD.93.052014). arXiv: [1510.07754 \[hep-ex\]](https://arxiv.org/abs/1510.07754).
- [81] ——, “Improved dark matter search results from PICO-2L Run 2,” *Physical Review D*, vol. 93, no. 6, 061101, p. 061 101, Mar. 2016. DOI: [10.1103/PhysRevD.93.061101](https://doi.org/10.1103/PhysRevD.93.061101). arXiv: [1601.03729](https://arxiv.org/abs/1601.03729).
- [82] M. Felizardo *et al.*, “The SIMPLE Phase II dark matter search,” *Physical Review D*, vol. 89, no. 7, 072013, p. 072 013, Apr. 2014. DOI: [10.1103/PhysRevD.89.072013](https://doi.org/10.1103/PhysRevD.89.072013). arXiv: [1404.4309 \[hep-ph\]](https://arxiv.org/abs/1404.4309).
- [83] C. Fu *et al.*, “Spin-Dependent Weakly-Interacting-Massive-Particle-Nucleon Cross Section Limits from First Data of PandaX-II Experiment,” *Physical Review Letters*, vol. 118, no. 7, 071301, p. 071 301, Feb. 2017. DOI: [10.1103/PhysRevLett.118.071301](https://doi.org/10.1103/PhysRevLett.118.071301). arXiv: [1611.06553 \[hep-ex\]](https://arxiv.org/abs/1611.06553).

- 
- [84] M. G. Aartsen *et al.*, “Search for annihilating dark matter in the Sun with 3 years of IceCube data,” *The European Physical Journal C*, vol. 77, 146, p. 146, Mar. 2017. DOI: [10.1140/epjc/s10052-017-4689-9](https://doi.org/10.1140/epjc/s10052-017-4689-9). arXiv: [1612.05949 \[astro-ph.HE\]](https://arxiv.org/abs/1612.05949).
  - [85] T. Tanaka *et al.*, “An Indirect Search for Weakly Interacting Massive Particles in the Sun Using 3109.6 Days of Upward-going Muons in Super-Kamiokande,” *The Astrophysical Journal*, vol. 742, 78, p. 78, Dec. 2011. DOI: [10.1088/0004-637X/742/2/78](https://doi.org/10.1088/0004-637X/742/2/78). arXiv: [1108.3384 \[astro-ph.HE\]](https://arxiv.org/abs/1108.3384).
  - [86] K. Choi *et al.*, “Search for Neutrinos from Annihilation of Captured Low-Mass Dark Matter Particles in the Sun by Super-Kamiokande,” *Physical Review Letters*, vol. 114, no. 14, 141301, p. 141301, Apr. 2015. DOI: [10.1103/PhysRevLett.114.141301](https://doi.org/10.1103/PhysRevLett.114.141301).
  - [87] L. Roszkowski, R. Ruiz de Austri, and R. Trotta, “Implications for the Constrained MSSM from a new prediction for  $b \rightarrow s\gamma$ ,” *Journal of High Energy Physics*, vol. 7, 075, p. 075, Jul. 2007. DOI: [10.1088/1126-6708/2007/07/075](https://doi.org/10.1088/1126-6708/2007/07/075). arXiv: [0705.2012 \[hep-ph\]](https://arxiv.org/abs/0705.2012).
  - [88] R. Bernabei *et al.*, “The DAMA/LIBRA apparatus,” *Nuclear Instruments and Methods in Physics Research A*, vol. 592, pp. 297–315, Jul. 2008. DOI: [10.1016/j.nima.2008.04.082](https://doi.org/10.1016/j.nima.2008.04.082). arXiv: [0804.2738](https://arxiv.org/abs/0804.2738).
  - [89] E. Shields, J. Xu, and F. Calaprice, “SABRE: A New NaI(Tl) Dark Matter Direct Detection Experiment,” *Physics Procedia*, vol. 61, pp. 169–178, 2015. DOI: [10.1016/j.phpro.2014.12.028](https://doi.org/10.1016/j.phpro.2014.12.028).
  - [90] R. Bernabei *et al.*, “DAMA/LIBRA results and perspectives,” *arXiv e-prints*, Jan. 2013. arXiv: [1301.6243 \[astro-ph.GA\]](https://arxiv.org/abs/1301.6243).
  - [91] ——, “Final model independent result of DAMA/LIBRA-phase1,” *The European Physical Journal C*, vol. 73, 2648, p. 2648, Dec. 2013. DOI: [10.1140/epjc/s10052-013-2648-7](https://doi.org/10.1140/epjc/s10052-013-2648-7). arXiv: [1308.5109](https://arxiv.org/abs/1308.5109).
  - [92] R. Bernabei *et al.*, “Investigating the DAMA annual modulation data in a mixed coupling framework,” *Physical Letters B*, vol. 509, no. 3, pp. 197–203, 2001, ISSN: 0370-2693. DOI: [10.1016/S0370-2693\(01\)00493-2](https://doi.org/10.1016/S0370-2693(01)00493-2).
  - [93] R. Bernabei *et al.*, “Investigating the DAMA annual modulation data in the framework of inelastic dark matter,” *The European Physical Journal C*, vol. 23, pp. 61–64, Mar. 2002. DOI: [10.1007/s100520100854](https://doi.org/10.1007/s100520100854).

- [94] ——, “Investigating Pseudoscalar and Scalar Dark Matter,” *International Journal of Modern Physics A*, vol. 21, pp. 1445–1469, 2006. DOI: [10.1142/S0217751X06030874](https://doi.org/10.1142/S0217751X06030874).
- [95] E. Aprile *et al.*, “Search for Electronic Recoil Event Rate Modulation with 4 Years of XENON100 Data,” *Physical Review Letters*, vol. 118, p. 101 101, 10 2017. DOI: [10.1103/PhysRevLett.118.101101](https://doi.org/10.1103/PhysRevLett.118.101101).
- [96] K. Blum, “DAMA vs. the annually modulated muon background,” *ArXiv e-prints*, Oct. 2011. arXiv: [1110.0857 \[astro-ph.HE\]](https://arxiv.org/abs/1110.0857).
- [97] J. P. Ralston, “One Model Explains DAMA/LIBRA, CoGENT, CDMS, and XENON,” *ArXiv e-prints*, Jun. 2010. arXiv: [1006.5255 \[hep-ph\]](https://arxiv.org/abs/1006.5255).
- [98] J. H. Davis, “Fitting the Annual Modulation in DAMA with Neutrons from Muons and Neutrinos,” *Physical Review Letters*, vol. 113, no. 8, 081302, p. 081302, Aug. 2014. DOI: [10.1103/PhysRevLett.113.081302](https://doi.org/10.1103/PhysRevLett.113.081302). arXiv: [1407.1052 \[hep-ph\]](https://arxiv.org/abs/1407.1052).
- [99] P. S. Barbeau, J. I. Collar, Y. Efremenko, and K. Scholberg, “Comment on “Fitting the Annual Modulation in DAMA with Neutrons from Muons and Neutrinos”,” *Physical Review Letters*, vol. 113, no. 22, 229001, p. 229 001, Nov. 2014. DOI: [10.1103/PhysRevLett.113.229001](https://doi.org/10.1103/PhysRevLett.113.229001). arXiv: [1409.3185 \[hep-ph\]](https://arxiv.org/abs/1409.3185).
- [100] J. Klinger and V. A. Kudryavtsev, “Muon-Induced Neutrons Do Not Explain the DAMA Data,” *Physical Review Letters*, vol. 114, no. 15, 151301, p. 151 301, Apr. 2015. DOI: [10.1103/PhysRevLett.114.151301](https://doi.org/10.1103/PhysRevLett.114.151301). arXiv: [1503.07225 \[hep-ph\]](https://arxiv.org/abs/1503.07225).
- [101] G. D’Imperio *et al.*, “Dark matter search with the SABRE experiment,” *arXiv e-prints*, Jul. 2018. arXiv: [1807.00584 \[physics.ins-det\]](https://arxiv.org/abs/1807.00584).
- [102] D. Hooper, J. I. Collar, J. Hall, D. McKinsey, and C. M. Kelso, “Consistent dark matter interpretation for CoGeNT and DAMA/LIBRA,” *Physical Review D*, vol. 82, no. 12, 123509, p. 123 509, Dec. 2010. DOI: [10.1103/PhysRevD.82.123509](https://doi.org/10.1103/PhysRevD.82.123509). arXiv: [1007.1005 \[hep-ph\]](https://arxiv.org/abs/1007.1005).
- [103] C. E. Aalseth *et al.*, “Search for An Annual Modulation in Three Years of CoGeNT Dark Matter Detector Data,” *ArXiv e-prints*, Jan. 2014. arXiv: [1401.3295 \[astro-ph.CO\]](https://arxiv.org/abs/1401.3295).
- [104] ——, “Maximum Likelihood Signal Extraction Method Applied to 3.4 years of CoGeNT Data,” *arXiv e-prints*, Jan. 2014. arXiv: [1401.6234](https://arxiv.org/abs/1401.6234).

- [105] J. H. Davis, C. McCabe, and C. Boehm, “Quantifying the evidence for dark matter in CoGeNT data,” *JCAP*, vol. 8, 014, p. 014, Aug. 2014. DOI: [10.1088/1475-7516/2014/08/014](https://doi.org/10.1088/1475-7516/2014/08/014). arXiv: [1405.0495 \[hep-ph\]](https://arxiv.org/abs/1405.0495).
- [106] Q. Yue *et al.*, “Limits on light weakly interacting massive particles from the CDEX-1 experiment with a p-type point-contact germanium detector at the China Jinping Underground Laboratory,” *Physical Review D*, vol. 90, no. 9, 091701, p. 091701, Nov. 2014. DOI: [10.1103/PhysRevD.90.091701](https://doi.org/10.1103/PhysRevD.90.091701). arXiv: [1404.4946 \[hep-ex\]](https://arxiv.org/abs/1404.4946).
- [107] Z. Ahmed *et al.*, “Search for annual modulation in low-energy CDMS-II data,” *ArXiv e-prints*, Mar. 2012. arXiv: [1203.1309 \[astro-ph.CO\]](https://arxiv.org/abs/1203.1309).
- [108] R. Agnese *et al.*, “Improved WIMP-search reach of the CDMS II germanium data,” *Physical Review D*, vol. 92, no. 7, 072003, p. 072003, Oct. 2015. DOI: [10.1103/PhysRevD.92.072003](https://doi.org/10.1103/PhysRevD.92.072003). arXiv: [1504.05871 \[hep-ex\]](https://arxiv.org/abs/1504.05871).
- [109] R. Agnese *et al.*, “Silicon detector dark matter results from the final exposure of cdms ii,” *Physical Review Letters*, vol. 111, p. 251301, 25 2013. DOI: [10.1103/PhysRevLett.111.251301](https://doi.org/10.1103/PhysRevLett.111.251301).
- [110] E. Armengaud *et al.*, “Constraints on low-mass WIMPs from the EDELWEISS-III dark matter search,” *JCAP*, vol. 5, 019, p. 019, May 2016. DOI: [10.1088/1475-7516/2016/05/019](https://doi.org/10.1088/1475-7516/2016/05/019). arXiv: [1603.05120](https://arxiv.org/abs/1603.05120).
- [111] G. Angloher *et al.*, “Results from 730 kg days of the CRESST-II Dark Matter search,” *The European Physical Journal C*, vol. 72, 1971, p. 1971, Apr. 2012. DOI: [10.1140/epjc/s10052-012-1971-8](https://doi.org/10.1140/epjc/s10052-012-1971-8). arXiv: [1109.0702](https://arxiv.org/abs/1109.0702).
- [112] R. Strauss *et al.*, “A detector module with highly efficient surface-alpha event rejection operated in CRESST-II Phase 2,” *The European Physical Journal C*, vol. 75, 352, p. 352, Aug. 2015. DOI: [10.1140/epjc/s10052-015-3572-9](https://doi.org/10.1140/epjc/s10052-015-3572-9). arXiv: [1410.1753 \[physics.ins-det\]](https://arxiv.org/abs/1410.1753).
- [113] W. H. Lippincott, K. J. Coakley, D. Gastler, E. Kearns, D. N. McKinsey, and J. A. Nikkel, “Scintillation yield and time dependence from electronic and nuclear recoils in liquid neon,” *Physical Review C*, vol. 86, no. 1, 015807, p. 015807, Jul. 2012. DOI: [10.1103/PhysRevC.86.015807](https://doi.org/10.1103/PhysRevC.86.015807). arXiv: [1111.3260 \[nucl-ex\]](https://arxiv.org/abs/1111.3260).
- [114] K. a. Rielage, “Update on the MiniCLEAN Dark Matter Experiment,” *Physics Procedia*, vol. 61, pp. 144–152, 2015. DOI: [10.1016/j.phpro.2014.12.024](https://doi.org/10.1016/j.phpro.2014.12.024). arXiv: [1403.4842 \[physics.ins-det\]](https://arxiv.org/abs/1403.4842).

## BIBLIOGRAPHY

---

- [115] P. Cushman *et al.*, “Snowmass CF1 Summary: WIMP Dark Matter Direct Detection,” *arXiv e-prints*, Oct. 2013. arXiv: [1310.8327 \[hep-ex\]](#).
- [116] A. Badertscher *et al.*, “ArDM: first results from underground commissioning,” *Journal of Instrumentation*, vol. 8, C09005, p. C09005, Sep. 2013. DOI: [10.1088/1748-0221/8/09/C09005](#). arXiv: [1309.3992 \[physics.ins-det\]](#).
- [117] P. Agnes *et al.*, “DarkSide-50 532-day Dark Matter Search with Low-Radioactivity Argon,” *arXiv e-prints*, Feb. 2018. arXiv: [1802.07198](#).
- [118] ——, “Low-mass Dark Matter Search with the DarkSide-50 Experiment,” *arXiv e-prints*, Feb. 2018. arXiv: [1802.06994 \[astro-ph.HE\]](#).
- [119] C. E. Aalseth *et al.*, “DarkSide-20k: A 20 tonne two-phase LAr TPC for direct dark matter detection at LNGS,” *The European Physical Journal Plus*, vol. 133, 131, p. 131, Mar. 2018. DOI: [10.1140/epjp/i2018-11973-4](#). arXiv: [1707.08145 \[physics.ins-det\]](#).
- [120] D. S. Akerib *et al.*, “Results from a search for dark matter in the complete lux exposure,” *Physical Review Letters*, vol. 118, p. 021303, 2 2017. DOI: [10.1103/PhysRevLett.118.021303](#).
- [121] X. Cui *et al.*, “Dark Matter Results From 54-Ton-Day Exposure of PandaX-II Experiment,” *Physical Review Letters*, vol. 119, p. 181302, 18 Oct. 2017. DOI: [10.1103/PhysRevLett.119.181302](#). arXiv: [1708.06917](#).
- [122] XMASS Collaboration, “A direct dark matter search in XMASS-I,” *arXiv e-prints*, Apr. 2018. arXiv: [1804.02180](#).
- [123] E. Aprile *et al.*, “Dark Matter Search Results from a One Tonne×Year Exposure of XENON1T,” *arXiv e-prints*, May 2018. arXiv: [1805.12562](#).
- [124] C. Savage, G. Gelmini, P. Gondolo, and K. Freese, “Compatibility of DAMA/LIBRA dark matter detection with other searches,” *JCAP*, vol. 4, 010, p. 010, Apr. 2009. DOI: [10.1088/1475-7516/2009/04/010](#). arXiv: [0808.3607](#).
- [125] R. Agnese *et al.*, “Silicon Detector Dark Matter Results from the Final Exposure of CDMS II,” *Physical Review Letters*, vol. 111, no. 25, 251301, p. 251 301, Dec. 2013. DOI: [10.1103/PhysRevLett.111.251301](#).
- [126] P.-A. Amaudruz *et al.*, “First Results from the DEAP-3600 Dark Matter Search with Argon at SNOLAB,” *Physical Review Letters*, vol. 121, no. 7, 071801, p. 071 801, Aug. 2018. DOI: [10.1103/PhysRevLett.121.071801](#).

- [127] R. Agnese *et al.*, “Results from the Super Cryogenic Dark Matter Search Experiment at Soudan,” *Physical Review Letters*, vol. 120, no. 6, 061802, p. 061802, Feb. 2018. DOI: [10.1103/PhysRevLett.120.061802](https://doi.org/10.1103/PhysRevLett.120.061802).
- [128] Q. Arnaud *et al.*, “First results from the NEWS-G direct dark matter search experiment at the LSM,” *Astroparticle Physics*, vol. 97, pp. 54–62, Jan. 2018. DOI: [10.1016/j.astropartphys.2017.10.009](https://doi.org/10.1016/j.astropartphys.2017.10.009). arXiv: [1706.04934 \[astro-ph.IM\]](https://arxiv.org/abs/1706.04934).
- [129] G. Angloher *et al.*, “Results on light dark matter particles with a low-threshold CRESST-II detector,” *The European Physical Journal C*, vol. 76, 25, p. 25, Jan. 2016. DOI: [10.1140/epjc/s10052-016-3877-3](https://doi.org/10.1140/epjc/s10052-016-3877-3). arXiv: [1509.01515](https://arxiv.org/abs/1509.01515).
- [130] R. Agnese *et al.*, “New Results from the Search for Low-Mass Weakly Interacting Massive Particles with the CDMS Low Ionization Threshold Experiment,” *Physical Review Letters*, vol. 116, no. 7, 071301, p. 071301, Feb. 2016. DOI: [10.1103/PhysRevLett.116.071301](https://doi.org/10.1103/PhysRevLett.116.071301).
- [131] E. Aprile *et al.*, “Dark Matter Results from 225 Live Days of XENON100 Data,” *Physical Review Letters*, vol. 109, no. 18, 181301, p. 181301, Nov. 2012. DOI: [10.1103/PhysRevLett.109.181301](https://doi.org/10.1103/PhysRevLett.109.181301). arXiv: [1207.5988 \[astro-ph.CO\]](https://arxiv.org/abs/1207.5988).
- [132] ——, “First Dark Matter Search Results from the XENON1T Experiment,” *Physical Review Letters*, vol. 119, no. 18, 181301, p. 181301, Nov. 2017. DOI: [10.1103/PhysRevLett.119.181301](https://doi.org/10.1103/PhysRevLett.119.181301). arXiv: [1705.06655](https://arxiv.org/abs/1705.06655).
- [133] E. A. Bagnaschi *et al.*, “Supersymmetric dark matter after LHC run 1,” *The European Physical Journal C*, vol. 75, 500, p. 500, Oct. 2015. DOI: [10.1140/epjc/s10052-015-3718-9](https://doi.org/10.1140/epjc/s10052-015-3718-9). arXiv: [1508.01173 \[hep-ph\]](https://arxiv.org/abs/1508.01173).
- [134] E. Aprile and T. Doke, “Liquid xenon detectors for particle physics and astrophysics,” *Review of Modern Physics*, vol. 82, pp. 2053–2097, Jul. 2010. DOI: [10.1103/RevModPhys.82.2053](https://doi.org/10.1103/RevModPhys.82.2053). arXiv: [0910.4956 \[physics.ins-det\]](https://arxiv.org/abs/0910.4956).
- [135] L. Baudis, “WIMP dark matter direct-detection searches in noble gases,” *Physics of the Dark Universe*, vol. 4, pp. 50–59, Sep. 2014. DOI: [10.1016/j.dark.2014.07.001](https://doi.org/10.1016/j.dark.2014.07.001). arXiv: [1408.4371 \[astro-ph.IM\]](https://arxiv.org/abs/1408.4371).
- [136] N. Barros, J. Thurn, and K. Zuber, “Double beta decay searches of  $^{134}\text{Xe}$ ,  $^{126}\text{Xe}$  and  $^{124}\text{Xe}$  with large scale Xe detectors,” *Journal of Physics G*, vol. 41, no. 11, 115105, p. 115105, Nov. 2014. DOI: [10.1088/0954-3899/41/11/115105](https://doi.org/10.1088/0954-3899/41/11/115105). arXiv: [1409.8308 \[nucl-ex\]](https://arxiv.org/abs/1409.8308).
- [137] S. Singh, R. Chandra, P. K. Rath, P. K. Raina, and J. G. Hirsch, “Nuclear deformation and the two-neutrino double- $\beta$  decay in  $^{124,126}\text{Xe}$ ,

## BIBLIOGRAPHY

---

- $^{128,130}\text{Te}$ ,  $^{130,132}\text{Ba}$  and  $^{150}\text{Nd}$  isotopes,” *The European Physical Journal A*, vol. 33, pp. 375–388, Sep. 2007. DOI: [10.1140/epja/i2007-10481-7](https://doi.org/10.1140/epja/i2007-10481-7). arXiv: [0706.4357 \[nucl-th\]](https://arxiv.org/abs/0706.4357).
- [138] J. Mock *et al.*, “Modeling pulse characteristics in Xenon with NEST,” *Journal of Instrumentation*, vol. 9, T04002, T04002, Apr. 2014. DOI: [10.1088/1748-0221/9/04/T04002](https://doi.org/10.1088/1748-0221/9/04/T04002). arXiv: [1310.1117 \[physics.ins-det\]](https://arxiv.org/abs/1310.1117).
- [139] T. Heindl *et al.*, “Table-top setup for investigating the scintillation properties of liquid argon,” *Journal of Instrumentation*, vol. 6, p. 2011, Feb. 2011. DOI: [10.1088/1748-0221/6/02/P02011](https://doi.org/10.1088/1748-0221/6/02/P02011). arXiv: [1511.07720 \[physics.ins-det\]](https://arxiv.org/abs/1511.07720).
- [140] C. H. Faham, “Prototype, Surface Commissioning and Photomultiplier Tube Characterization for the Large Underground Xenon (LUX) Direct Dark Matter Search Experiment,” PhD thesis, Brown University, May 2014.
- [141] L. S. Miller, S. Howe, and W. E. Spear, “Charge Transport in Solid and Liquid Ar, Kr, and Xe,” *Physical Review*, vol. 166, pp. 871–878, Feb. 1968. DOI: [10.1103/PhysRev.166.871](https://doi.org/10.1103/PhysRev.166.871).
- [142] M. J. Berger, J. S. Coursey, M. A. Zucker, and J. Chang. (2017). ESTAR, PSTAR, and ASTAR: Computer Programs for Calculating Stopping-Power and Range Tables for Electrons, Protons, and Helium Ions (version 1.2.3), [Online]. Available: <https://physics.nist.gov/Star> (visited on 01/16/2018).
- [143] H. A. Bethe, “Nuclear Physics B. Nuclear Dynamics, Theoretical,” *Review of Modern Physics*, vol. 9, pp. 69–244, Apr. 1937. DOI: [10.1103/RevModPhys.9.69](https://doi.org/10.1103/RevModPhys.9.69).
- [144] V. Chepel and H. Araújo, “Liquid noble gas detectors for low energy particle physics,” *Journal of Instrumentation*, vol. 8, R04001, R04001, Apr. 2013. DOI: [10.1088/1748-0221/8/04/R04001](https://doi.org/10.1088/1748-0221/8/04/R04001). arXiv: [1207.2292 \[physics.ins-det\]](https://arxiv.org/abs/1207.2292).
- [145] L. Onsager, “Initial Recombination of Ions,” *Physical Review*, vol. 54, pp. 554–557, 8 1938. DOI: [10.1103/PhysRev.54.554](https://doi.org/10.1103/PhysRev.54.554).
- [146] A. Mozumder, “Free-ion yield and electron-ion recombination rate in liquid xenon,” *Chemical Physics Letters*, vol. 245, pp. 359–363, Nov. 1995. DOI: [10.1016/0009-2614\(95\)01024-4](https://doi.org/10.1016/0009-2614(95)01024-4).
- [147] T. Doke, A. Hitachi, J. Kikuchi, K. Masuda, H. Okada, and E. Shibamura, “Absolute Scintillation Yields in Liquid Argon and Xenon for Various Particles,” *Japanese Journal of Applied Physics*, vol. 41, p. 1538, Mar. 2002. DOI: [10.1143/JJAP.41.1538](https://doi.org/10.1143/JJAP.41.1538).

- [148] J. Thomas and D. A. Imel, “Recombination of electron-ion pairs in liquid argon and liquid xenon,” *Physical Review A*, vol. 36, pp. 614–616, Jul. 1987. DOI: [10.1103/PhysRevA.36.614](https://doi.org/10.1103/PhysRevA.36.614).
- [149] K. Yoshino, U. Sowada, and W. F. Schmidt, “Effect of molecular solutes on the electron drift velocity in liquid Ar, Kr, and Xe,” *Physical Review A*, vol. 14, pp. 438–444, 1 1976. DOI: [10.1103/PhysRevA.14.438](https://doi.org/10.1103/PhysRevA.14.438).
- [150] G. Jaffé, “Zur Theorie der Ionisation in Kolonnen,” *Annalen der Physik*, vol. 347, no. 12, pp. 303–344, 1913, ISSN: 1521-3889. DOI: [10.1002/andp.19133471205](https://doi.org/10.1002/andp.19133471205). [Online]. Available: <http://dx.doi.org/10.1002/andp.19133471205>.
- [151] K. Deiters *et al.*, “Test of a liquid argon multistrip ionization chamber with  $8.5 \mu$  RMS resolution,” *Nuclear Instruments and Methods*, vol. 180, pp. 45–52, Feb. 1981. DOI: [10.1016/0029-554X\(81\)90008-2](https://doi.org/10.1016/0029-554X(81)90008-2).
- [152] J. B. Birks and F. A. Black, “Letters to the Editor: Deterioration of Anthracene under  $\alpha$ -Particle Irradiation,” *Proceedings of the Physical Society A*, vol. 64, pp. 511–512, May 1951. DOI: [10.1088/0370-1298/64/5/112](https://doi.org/10.1088/0370-1298/64/5/112).
- [153] J. Birks, D. Fry, L. Costrell, and K. Kandiah, *The Theory and Practice of Scintillation Counting*. Elsevier, 1964, vol. A volume in International Series of Monographs in Electronics and Instrumentation, ISBN: 978-0-08-010472-0.
- [154] T. Doke *et al.*, “Let dependence of scintillation yields in liquid argon,” *Nuclear Instruments and Methods in Physics Research A*, vol. 269, pp. 291–296, Jun. 1988. DOI: [10.1016/0168-9002\(88\)90892-3](https://doi.org/10.1016/0168-9002(88)90892-3).
- [155] M. Szydagis *et al.*, “NEST: A Comprehensive Model for Scintillation Yield in Liquid Xenon,” *ArXiv e-prints*, Jun. 2011. arXiv: [1106.1613 \[physics.ins-det\]](https://arxiv.org/abs/1106.1613).
- [156] D.-M. Mei, Z.-B. Yin, L. C. Stonehill, and A. Hime, “A model of nuclear recoil scintillation efficiency in noble liquids,” *Astroparticle Physics*, vol. 30, pp. 12–17, Aug. 2008. DOI: [10.1016/j.astropartphys.2008.06.001](https://doi.org/10.1016/j.astropartphys.2008.06.001). arXiv: [0712.2470 \[nucl-ex\]](https://arxiv.org/abs/0712.2470).
- [157] E. Aprile *et al.*, “Exclusion of leptophilic dark matter models using XENON100 electronic recoil data,” *Science*, vol. 349, pp. 851–854, Aug. 2015. DOI: [10.1126/science.aab2069](https://doi.org/10.1126/science.aab2069).
- [158] P. Christillin, “Nuclear Compton scattering,” *Journal of Physics G*, vol. 12, pp. 837–851, Sep. 1986. DOI: [10.1088/0305-4616/12/9/008](https://doi.org/10.1088/0305-4616/12/9/008).

## BIBLIOGRAPHY

---

- [159] J. H. Hubbell, “Electron positron pair production by photons: A historical overview,” *Radiation Physics and Chemistry*, vol. 75, pp. 614–623, Jun. 2006. DOI: [10.1016/j.radphyschem.2005.10.008](https://doi.org/10.1016/j.radphyschem.2005.10.008).
- [160] M. J. Berger *et al.* (2010). XCOM: Photon Cross Sections Database, [Online]. Available: <https://www.nist.gov/pml/xcom-photon-cross-sections-database> (visited on 01/16/2018).
- [161] M. Weber, “Gentle Neutron Signals and Noble Background in the XENON100 Dark Matter Search Experiment,” PhD thesis, 2013.
- [162] E. Aprile *et al.*, “Physics reach of the XENON1T dark matter experiment.,” *JCAP*, vol. 4, 027, p. 027, Apr. 2016. DOI: [10.1088/1475-7516/2016/04/027](https://doi.org/10.1088/1475-7516/2016/04/027). arXiv: [1512.07501 \[physics.ins-det\]](https://arxiv.org/abs/1512.07501).
- [163] R. L. Burman, A. C. Dodd, and P. Plischke, “Neutrino flux calculations for the ISIS spallation neutron facility,” *Nuclear Instruments and Methods in Physics Research A*, vol. 368, pp. 416–424, Jan. 1996. DOI: [10.1016/0168-9002\(95\)00627-3](https://doi.org/10.1016/0168-9002(95)00627-3).
- [164] C. McCabe, “Prospects for dark matter detection with inelastic transitions of xenon,” *JCAP*, vol. 5, 033, p. 033, May 2016. DOI: [10.1088/1475-7516/2016/05/033](https://doi.org/10.1088/1475-7516/2016/05/033). arXiv: [1512.00460 \[hep-ph\]](https://arxiv.org/abs/1512.00460).
- [165] C. E. Dahl, “The physics of background discrimination in liquid xenon, and first results from Xenon10 in the hunt for WIMP dark matter,” English, PhD thesis, 2009, p. 182, ISBN: 9781109255294. [Online]. Available: <http://inspirehep.net/record/1374815/files/E.Dahlthesis.pdf>.
- [166] U. Fano, “Ionization Yield of Radiations. II. The Fluctuations of the Number of Ions,” *Physical Review*, vol. 72, pp. 26–29, Jul. 1947. DOI: [10.1103/PhysRev.72.26](https://doi.org/10.1103/PhysRev.72.26).
- [167] T. Doke, A. Hitachi, S. Kubota, A. Nakamoto, and T. Takahashi, “Estimation of Fano factors in liquid argon, krypton, xenon and xenon-doped liquid argon,” *Nuclear Instruments and Methods*, vol. 134, pp. 353–357, Apr. 1976. DOI: [10.1016/0029-554X\(76\)90292-5](https://doi.org/10.1016/0029-554X(76)90292-5).
- [168] J. Seguinot, J. Tischhauser, and T. Ypsilantis, “Liquid xenon scintillation: photon yield and Fano factor measurements,” *Nuclear Instruments and Methods in Physics Research A*, vol. 354, pp. 280–287, Feb. 1995. DOI: [10.1016/0168-9002\(94\)01236-9](https://doi.org/10.1016/0168-9002(94)01236-9).

- [169] T. Takahashi *et al.*, “Average energy expended per ion pair in liquid xenon,” *Physical Review A*, vol. 12, pp. 1771–1775, Nov. 1975. DOI: [10.1103/PhysRevA.12.1771](https://doi.org/10.1103/PhysRevA.12.1771).
- [170] E. Aprile, K. L. Giboni, P. Majewski, K. Ni, and M. Yamashita, “Observation of anticorrelation between scintillation and ionization for MeV gamma rays in liquid xenon,” *Physical Review B*, vol. 76, p. 014115, 1 2007. DOI: [10.1103/PhysRevB.76.014115](https://doi.org/10.1103/PhysRevB.76.014115).
- [171] J. Lindhard, V. Nielsen, M. Scharff, and P. Thomsen, “Integral equations governing radiation effects (notes on atomic collisions, iii),” *Mat. Fys. Medd. Dan. Vid. Selsk*, vol. Vol: 33: No. 10, 1963.
- [172] P. Sorensen and C. E. Dahl, “Nuclear recoil energy scale in liquid xenon with application to the direct detection of dark matter,” *Physical Review D*, vol. 83, no. 6, 063501, p. 063501, Mar. 2011. DOI: [10.1103/PhysRevD.83.063501](https://doi.org/10.1103/PhysRevD.83.063501). arXiv: [1101.6080 \[astro-ph.IM\]](https://arxiv.org/abs/1101.6080).
- [173] B. Lenardo, K. Kazkaz, A. Manalaysay, J. Mock, M. Szydagis, and M. Tripathi, “A Global Analysis of Light and Charge Yields in Liquid Xenon,” *IEEE Transactions on Nuclear Science*, vol. 62, pp. 3387–3396, Dec. 2015. DOI: [10.1109/TNS.2015.2481322](https://doi.org/10.1109/TNS.2015.2481322). arXiv: [1412.4417 \[astro-ph.IM\]](https://arxiv.org/abs/1412.4417).
- [174] J. Angle *et al.*, “Search for Light Dark Matter in XENON10 Data,” *Physical Review Letters*, vol. 107, no. 5, 051301, p. 051301, Jul. 2011. DOI: [10.1103/PhysRevLett.107.051301](https://doi.org/10.1103/PhysRevLett.107.051301). arXiv: [1104.3088 \[astro-ph.CO\]](https://arxiv.org/abs/1104.3088).
- [175] G. Bakale, U. Sowada, and W. F. Schmidt, “Effect of an electric field on electron attachment to sulfur hexafluoride, nitrous oxide, and molecular oxygen in liquid argon and xenon,” *Journal of Physical Chemistry*, vol. 80, no. 23, pp. 2556–2559, 1976. DOI: [10.1021/j100564a006](https://doi.org/10.1021/j100564a006).
- [176] S. Belogurov *et al.*, “High pressure gas scintillation drift chamber with photomultipliers inside of working medium,” IEEE Nuclear Science Symposium and Medical Imaging Conference Record, 1995.
- [177] CHROMacademy. (), [Online]. Available: <http://www.chromacademy.com/lms/sco736/images> (visited on 01/29/2018).
- [178] C. H. Faham, V. M. Gehman, A. Currie, A. Dobi, P. Sorensen, and R. J. Gaitskell, “Measurements of wavelength-dependent double photoelectron emission from single photons in VUV-sensitive photomultiplier tubes,” *Journal of Instrumentation*, vol. 10, P09010, P09010, Sep. 2015. DOI: [10.1088/1748-0221/2015/9/P09010](https://doi.org/10.1088/1748-0221/2015/9/P09010). arXiv: [1506.08748 \[physics.ins-det\]](https://arxiv.org/abs/1506.08748).

## BIBLIOGRAPHY

---

- [179] K. Lung *et al.*, “Characterization of the Hamamatsu R11410-10 3-in. photomultiplier tube for liquid xenon dark matter direct detection experiments,” *Nuclear Instruments and Methods in Physics Research A*, vol. 696, pp. 32–39, Dec. 2012. DOI: [10.1016/j.nima.2012.08.052](https://doi.org/10.1016/j.nima.2012.08.052). arXiv: [1202.2628 \[physics.ins-det\]](https://arxiv.org/abs/1202.2628).
- [180] F. Neves *et al.*, “Measurement of the absolute reflectance of polytetrafluoroethylene (PTFE) immersed in liquid xenon,” *Journal of Instrumentation*, vol. 12, P01017, Jan. 2017. DOI: [10.1088/1748-0221/12/01/P01017](https://doi.org/10.1088/1748-0221/12/01/P01017). arXiv: [1612.07965 \[physics.ins-det\]](https://arxiv.org/abs/1612.07965).
- [181] I. Israelashvili *et al.*, “A comprehensive simulation study of a Liquid-Xe detector for contraband detection,” *Journal of Instrumentation*, vol. 10, P03030, P03030, Mar. 2015. DOI: [10.1088/1748-0221/10/03/P03030](https://doi.org/10.1088/1748-0221/10/03/P03030). arXiv: [1501.00150 \[physics.ins-det\]](https://arxiv.org/abs/1501.00150).
- [182] R. F. Lang *et al.*, “Characterization of a deuterium-deuterium plasma fusion neutron generator,” *Nuclear Instruments and Methods in Physics Research A*, vol. 879, pp. 31–38, Jan. 2018. DOI: [10.1016/j.nima.2017.10.001](https://doi.org/10.1016/j.nima.2017.10.001). arXiv: [1705.04741 \[physics.ins-det\]](https://arxiv.org/abs/1705.04741).
- [183] E. Aprile *et al.*, “Simultaneous Measurement of Ionization and Scintillation from Nuclear Recoils in Liquid Xenon for a Dark Matter Experiment,” *Physical Review Letters*, vol. 97, no. 8, 081302, p. 081302, Aug. 2006. DOI: [10.1103/PhysRevLett.97.081302](https://doi.org/10.1103/PhysRevLett.97.081302).
- [184] ——, “The XENON1T dark matter experiment,” *The European Physical Journal C*, vol. 77, 881, p. 881, Dec. 2017. DOI: [10.1140/epjc/s10052-017-5326-3](https://doi.org/10.1140/epjc/s10052-017-5326-3). arXiv: [1708.07051 \[astro-ph.IM\]](https://arxiv.org/abs/1708.07051).
- [185] P. Barrow *et al.*, “Qualification tests of the R11410-21 photomultiplier tubes for the XENON1T detector,” *Journal of Instrumentation*, vol. 12, P01024, Jan. 2017. DOI: [10.1088/1748-0221/12/01/P01024](https://doi.org/10.1088/1748-0221/12/01/P01024). arXiv: [1609.01654 \[astro-ph.IM\]](https://arxiv.org/abs/1609.01654).
- [186] E. Aprile *et al.*, “Lowering the radioactivity of the photomultiplier tubes for the XENON1T dark matter experiment,” *The European Physical Journal C*, vol. 75, 546, p. 546, Nov. 2015. DOI: [10.1140/epjc/s10052-015-3657-5](https://doi.org/10.1140/epjc/s10052-015-3657-5). arXiv: [1503.07698 \[astro-ph.IM\]](https://arxiv.org/abs/1503.07698).
- [187] L. Baudis *et al.*, “Performance of the Hamamatsu R11410 photomultiplier tube in cryogenic xenon environments,” *Journal of Instrumentation*, vol. 8, P04026, P04026, Apr. 2013. DOI: [10.1088/1748-0221/8/04/P04026](https://doi.org/10.1088/1748-0221/8/04/P04026). arXiv: [1303.0226 \[astro-ph.IM\]](https://arxiv.org/abs/1303.0226).

- [188] L. W. Goetzke, E. Aprile, M. Anthony, G. Plante, and M. Weber, “Measurement of light and charge yield of low-energy electronic recoils in liquid xenon,” *Physical Review D*, vol. 96, no. 10, 103007, p. 103007, Nov. 2017. DOI: [10.1103/PhysRevD.96.103007](https://doi.org/10.1103/PhysRevD.96.103007). arXiv: [1611.10322 \[astro-ph.IM\]](https://arxiv.org/abs/1611.10322).
- [189] E. Aprile *et al.*, “The XENON100 dark matter experiment,” *Astroparticle Physics*, vol. 35, pp. 573–590, Apr. 2012. DOI: [10.1016/j.astropartphys.2012.01.003](https://doi.org/10.1016/j.astropartphys.2012.01.003). arXiv: [1107.2155 \[astro-ph.IM\]](https://arxiv.org/abs/1107.2155).
- [190] ——, “Material radioassay and selection for the XENON1T dark matter experiment,” *The European Physical Journal C*, vol. 77, 890, p. 890, Dec. 2017. DOI: [10.1140/epjc/s10052-017-5329-0](https://doi.org/10.1140/epjc/s10052-017-5329-0). arXiv: [1705.01828 \[physics.ins-det\]](https://arxiv.org/abs/1705.01828).
- [191] ——, “Performance of a cryogenic system prototype for the XENON1T detector,” *Journal of Instrumentation*, vol. 7, p. 10001, Oct. 2012. DOI: [10.1088/1748-0221/7/10/P10001](https://doi.org/10.1088/1748-0221/7/10/P10001). arXiv: [1208.2001 \[physics.ins-det\]](https://arxiv.org/abs/1208.2001).
- [192] ——, “Removing krypton from xenon by cryogenic distillation to the ppq level,” *The European Physical Journal C*, vol. 77, 275, p. 275, May 2017. DOI: [10.1140/epjc/s10052-017-4757-1](https://doi.org/10.1140/epjc/s10052-017-4757-1).
- [193] S. Lindemann and H. Simgen, “Krypton assay in xenon at the ppq level using a gas chromatographic system and mass spectrometer,” *The European Physical Journal C*, vol. 74, 2746, p. 2746, Feb. 2014. DOI: [10.1140/epjc/s10052-014-2746-1](https://doi.org/10.1140/epjc/s10052-014-2746-1). arXiv: [1308.4806 \[physics.ins-det\]](https://arxiv.org/abs/1308.4806).
- [194] S. Bruenner, D. Cichon, S. Lindemann, T. M. Undagoitia, and H. Simgen, “Radon depletion in xenon boil-off gas,” *The European Physical Journal C*, vol. 77, 143, p. 143, Mar. 2017. DOI: [10.1140/epjc/s10052-017-4676-1](https://doi.org/10.1140/epjc/s10052-017-4676-1). arXiv: [1611.03737 \[physics.ins-det\]](https://arxiv.org/abs/1611.03737).
- [195] E. Aprile *et al.*, “Online  $^{222}\text{Rn}$  removal by cryogenic distillation in the XENON100 experiment,” *The European Physical Journal C*, vol. 77, 358, p. 358, Jun. 2017. DOI: [10.1140/epjc/s10052-017-4902-x](https://doi.org/10.1140/epjc/s10052-017-4902-x).
- [196] C. Geis, C. Grignon, U. Oberlack, D. Ramírez García, and Q. Weitzel, “Optical response of highly reflective film used in the water Cherenkov muon veto of the XENON1T dark matter experiment,” *Journal of Instrumentation*, vol. 12, P06017, Jun. 2017. DOI: [10.1088/1748-0221/12/06/P06017](https://doi.org/10.1088/1748-0221/12/06/P06017). arXiv: [1706.03687 \[physics.ins-det\]](https://arxiv.org/abs/1706.03687).

- [197] D. S. Akerib *et al.*, “Tritium calibration of the LUX dark matter experiment,” *Physical Review D*, vol. 93, no. 7, 072009, p. 072 009, Apr. 2016. DOI: [10.1103/PhysRevD.93.072009](https://doi.org/10.1103/PhysRevD.93.072009).
- [198] E. Aprile *et al.*, “Signal yields of keV electronic recoils and their discrimination from nuclear recoils in liquid xenon,” *Physical Review D*, vol. 97, no. 9, 092007, p. 092 007, May 2018. DOI: [10.1103/PhysRevD.97.092007](https://doi.org/10.1103/PhysRevD.97.092007). arXiv: [1709.10149 \[astro-ph.IM\]](https://arxiv.org/abs/1709.10149).
- [199] ——, “First Dark Matter Results from the XENON100 Experiment,” *Physical Review Letters*, vol. 105, no. 13, 131302, p. 131 302, Sep. 2010. DOI: [10.1103/PhysRevLett.105.131302](https://doi.org/10.1103/PhysRevLett.105.131302). arXiv: [1005.0380 \[astro-ph.CO\]](https://arxiv.org/abs/1005.0380).
- [200] R. Saldanha, L. Grandi, Y. Guardincerri, and T. Wester, “Model independent approach to the single photoelectron calibration of photomultiplier tubes,” *Nuclear Instruments and Methods in Physics Research A*, vol. 863, pp. 35–46, Aug. 2017. DOI: [10.1016/j.nima.2017.02.086](https://doi.org/10.1016/j.nima.2017.02.086). arXiv: [1602.03150 \[physics.ins-det\]](https://arxiv.org/abs/1602.03150).
- [201] M. Anthony, E. Aprile, L. Grandi, Q. Lin, and R. Saldanha, “Characterization of photomultiplier tubes with a realistic model through GPU-boosted simulation,” *Journal of Instrumentation*, vol. 13, T02011, Feb. 2018. DOI: [10.1088/1748-0221/13/02/T02011](https://doi.org/10.1088/1748-0221/13/02/T02011). arXiv: [1710.00219 \[astro-ph.IM\]](https://arxiv.org/abs/1710.00219).
- [202] J. B. Albert *et al.*, “Search for Neutrinoless Double-Beta Decay with the Upgraded EXO-200 Detector,” *Physical Review Letters*, vol. 120, no. 7, 072701, p. 072 701, Feb. 2018. DOI: [10.1103/PhysRevLett.120.072701](https://doi.org/10.1103/PhysRevLett.120.072701). arXiv: [1707.08707 \[hep-ex\]](https://arxiv.org/abs/1707.08707).
- [203] X. Ji, “Status of the PandaX Experiment at China Jinping Underground Lab,” UCLA Dark Matter 2016, 2016, [Online]. Available: <https://conferences.pa.ucla.edu/dm16/talks/xiangdongji.pdf>.
- [204] D. S. Akerib *et al.*, “Signal yields, energy resolution, and recombination fluctuations in liquid xenon,” *Physical Review D*, vol. 95, no. 1, 012008, p. 012 008, Jan. 2017. DOI: [10.1103/PhysRevD.95.012008](https://doi.org/10.1103/PhysRevD.95.012008). arXiv: [1610.02076 \[physics.ins-det\]](https://arxiv.org/abs/1610.02076).
- [205] X. Du, K. Bailey, Z.-T. Lu, P. Mueller, T. P. O’Connor, and L. Young, “An atom trap system for practical  $^{81}\text{Kr}$  dating,” *Review of Scientific Instruments*, vol. 75, pp. 3224–3232, Oct. 2004. DOI: [10.1063/1.1790562](https://doi.org/10.1063/1.1790562).
- [206] J. B. Albert *et al.*, “Improved measurement of the  $2\nu\beta\beta$  half-life of  $^{136}\text{Xe}$  with the EXO-200 detector,” *Physical Review C*, vol. 89, no. 1,

- 015502, p. 015 502, Jan. 2014. DOI: [10.1103/PhysRevC.89.015502](https://doi.org/10.1103/PhysRevC.89.015502). arXiv: [1306.6106 \[nucl-ex\]](https://arxiv.org/abs/1306.6106).
- [207] D.-M. Mei and A. Hime, “Muon-induced background study for underground laboratories,” *Physical Review D*, vol. 73, no. 5, 053004, p. 053 004, Mar. 2006. DOI: [10.1103/PhysRevD.73.053004](https://doi.org/10.1103/PhysRevD.73.053004).
- [208] Wikimedia Commons. (2017). Decay Chain of Thorium-232, [Online]. Available: [https://commons.wikimedia.org/wiki/File:Decay\\_Chain\\_of\\_Thorium-232.svg](https://commons.wikimedia.org/wiki/File:Decay_Chain_of_Thorium-232.svg) (visited on 02/26/2018).
- [209] ——, (2017). Decay Chain of Uranium-238, [Online]. Available: [https://commons.wikimedia.org/wiki/File:Decay\\_Chain\\_of\\_Uranium-238.svg](https://commons.wikimedia.org/wiki/File:Decay_Chain_of_Uranium-238.svg) (visited on 02/26/2018).
- [210] E. Aprile *et al.*, “Limits on Spin-Dependent WIMP-Nucleon Cross Sections from 225 Live Days of XENON100 Data,” *Physical Review Letters*, vol. 111, no. 2, 021301, p. 021 301, Jul. 2013. DOI: [10.1103/PhysRevLett.111.021301](https://doi.org/10.1103/PhysRevLett.111.021301). arXiv: [1301.6620 \[astro-ph.CO\]](https://arxiv.org/abs/1301.6620).
- [211] ——, “Search for bosonic super-WIMP interactions with the XENON100 experiment,” *Physical Review D*, vol. 96, no. 12, 122002, p. 122 002, Dec. 2017. DOI: [10.1103/PhysRevD.96.122002](https://doi.org/10.1103/PhysRevD.96.122002). arXiv: [1709.02222](https://arxiv.org/abs/1709.02222).
- [212] ——, “Search for WIMP inelastic scattering off xenon nuclei with XENON100,” *Physical Review D*, vol. 96, no. 2, 022008, p. 022 008, Jul. 2017. DOI: [10.1103/PhysRevD.96.022008](https://doi.org/10.1103/PhysRevD.96.022008). arXiv: [1705.05830 \[hep-ex\]](https://arxiv.org/abs/1705.05830).
- [213] F. James, “Interpretation of the shape of the likelihood function around its minimum,” *Computer Physics Communications*, vol. 20, no. 1, pp. 29–35, 1980, ISSN: 0010-4655. DOI: [10.1016/0010-4655\(80\)90103-4](https://doi.org/10.1016/0010-4655(80)90103-4).
- [214] M. S. Bartlett, “Approximate Confidence Intervals: More Than One Unknown Parameter,” *Biometrika*, vol. 40, no. 3-4, pp. 306–317, 1953. DOI: [10.1093/biomet/40.3-4.306](https://doi.org/10.1093/biomet/40.3-4.306).
- [215] N. Priel, L. Rauch, H. Landsman, A. Manfredini, and R. Budnik, “A model independent safeguard against background mismodeling for statistical inference,” *JCAP*, vol. 5, 013, p. 013, May 2017. DOI: [10.1088/1475-7516/2017/05/013](https://doi.org/10.1088/1475-7516/2017/05/013). arXiv: [1610.02643 \[physics.data-an\]](https://arxiv.org/abs/1610.02643).
- [216] G. J. Feldman and R. D. Cousins, “Unified approach to the classical statistical analysis of small signals,” *Phys. Rev. D*, vol. 57, pp. 3873–3889, 7 Apr. 1998. DOI: [10.1103/PhysRevD.57.3873](https://doi.org/10.1103/PhysRevD.57.3873). [Online]. Available: <https://link.aps.org/doi/10.1103/PhysRevD.57.3873>.

- [217] S. Agostinelli *et al.*, “GEANT4 - a simulation toolkit,” *Nuclear Instruments and Methods in Physics Research A*, vol. 506, pp. 250–303, Jul. 2003. doi: [10.1016/S0168-9002\(03\)01368-8](https://doi.org/10.1016/S0168-9002(03)01368-8).
- [218] D. Foreman-Mackey, D. W. Hogg, D. Lang, and J. Goodman, “emcee: The MCMC Hammer,” *Publication of the Astronomical Society of the Pacific*, vol. 125, p. 306, Mar. 2013. doi: [10.1086/670067](https://doi.org/10.1086/670067). arXiv: [1202.3665 \[astro-ph.IM\]](https://arxiv.org/abs/1202.3665).
- [219] J. Goodman and J. Weare, “Ensemble samplers with affine invariance,” *Communications in Applied Mathematics and Computational Science*, vol. 5, no. 1, 025808, pp. 65–80, Jan. 2010. doi: [10.2140/camcos.2010.5.65](https://doi.org/10.2140/camcos.2010.5.65).
- [220] A. Gelman and D. B. Rubin, “Inference from Iterative Simulation Using Multiple Sequences,” *Statistical Science*, vol. 7, no. 4, pp. 457–472, Nov. 1992.
- [221] D. S. Akerib *et al.*, “Ultra-Low Energy Calibration of LUX Detector using  $^{127}\text{Xe}$  Electron Capture,” *arXiv e-prints*, Sep. 2017. arXiv: [1709.00800 \[physics.ins-det\]](https://arxiv.org/abs/1709.00800).
- [222] E. M. Boulton *et al.*, “Calibration of a two-phase xenon time projection chamber with a  $^{37}\text{Ar}$  source,” *Journal of Instrumentation*, vol. 12, P08004, Aug. 2017. doi: [10.1088/1748-0221/12/08/P08004](https://doi.org/10.1088/1748-0221/12/08/P08004). arXiv: [1705.08958 \[physics.ins-det\]](https://arxiv.org/abs/1705.08958).
- [223] E. Aprile *et al.*, “Scintillation response of liquid xenon to low energy nuclear recoils,” *Physical Review D*, vol. 72, no. 7, 072006, p. 072 006, Oct. 2005. doi: [10.1103/PhysRevD.72.072006](https://doi.org/10.1103/PhysRevD.72.072006).
- [224] ——, “New measurement of the relative scintillation efficiency of xenon nuclear recoils below 10 keV,” *Physical Review C*, vol. 79, no. 4, 045807, p. 045 807, Apr. 2009. doi: [10.1103/PhysRevC.79.045807](https://doi.org/10.1103/PhysRevC.79.045807). arXiv: [0810.0274](https://arxiv.org/abs/0810.0274).
- [225] G. Plante *et al.*, “New measurement of the scintillation efficiency of low-energy nuclear recoils in liquid xenon,” *Physical Review C*, vol. 84, no. 4, 045805, p. 045 805, Oct. 2011. doi: [10.1103/PhysRevC.84.045805](https://doi.org/10.1103/PhysRevC.84.045805). arXiv: [1104.2587 \[nucl-ex\]](https://arxiv.org/abs/1104.2587).
- [226] A. Manzur, A. Curioni, L. Kastens, D. N. McKinsey, K. Ni, and T. Wongjirad, “Scintillation efficiency and ionization yield of liquid xenon for monoenergetic nuclear recoils down to 4 keV,” *Physical Review C*, vol. 81, no. 2, 025808, p. 025 808, Feb. 2010. doi: [10.1103/PhysRevC.81.025808](https://doi.org/10.1103/PhysRevC.81.025808). arXiv: [0909.1063 \[physics.ins-det\]](https://arxiv.org/abs/0909.1063).

- [227] E. Aprile *et al.*, “Response of the XENON100 dark matter detector to nuclear recoils,” *Physical Review D*, vol. 88, no. 1, 012006, p. 012 006, Jul. 2013. DOI: [10.1103/PhysRevD.88.012006](https://doi.org/10.1103/PhysRevD.88.012006). arXiv: [1304.1427 \[astro-ph.IM\]](https://arxiv.org/abs/1304.1427).
- [228] P. Sorensen *et al.*, “The scintillation and ionization yield of liquid xenon for nuclear recoils,” *Nuclear Instruments and Methods in Physics Research A*, vol. 601, pp. 339–346, Apr. 2009. DOI: [10.1016/j.nima.2008.12.197](https://doi.org/10.1016/j.nima.2008.12.197). arXiv: [0807.0459](https://arxiv.org/abs/0807.0459).
- [229] D. S. Akerib *et al.*, “Low-energy (0.7–74 keV) nuclear recoil calibration of the LUX dark matter experiment using D-D neutron scattering kinematics,” *arXiv e-prints*, Aug. 2016. arXiv: [1608.05381 \[physics.ins-det\]](https://arxiv.org/abs/1608.05381).
- [230] K. Watanabe, E. C. Y. Inn, and M. Zelikoff, “Absorption Coefficients of Oxygen in the Vacuum Ultraviolet,” *Journal of Chemical Physics*, vol. 21, no. 6, pp. 1026–1030, 1953. DOI: [10.1063/1.1699104](https://doi.org/10.1063/1.1699104).
- [231] K. Watanabe and M. Zelikoff, “Absorption coefficients of water vapor in the vacuum ultraviolet,” *Journal of the Optical Society of America*, vol. 43, no. 9, pp. 753–755, 1953. DOI: [10.1364/JOSA.43.000753](https://doi.org/10.1364/JOSA.43.000753).
- [232] A. Baldini *et al.*, “Absorption of scintillation light in a 100 l liquid xenon  $\gamma$ -ray detector and expected detector performance,” *Nuclear Instruments and Methods in Physics Research A*, vol. 545, pp. 753–764, Jun. 2005. DOI: [10.1016/j.nima.2005.02.029](https://doi.org/10.1016/j.nima.2005.02.029).
- [233] K. Ozone, “Liquid Xenon Scintillation Detector for the New  $\mu \rightarrow e\gamma$  Search Experiment,” English, PhD thesis, Mar. 2005. [Online]. Available: <http://meg.icepp.s.u-tokyo.ac.jp/docs/theses/ozoned.pdf>.
- [234] K. Yoshino, J. R. Esmond, W. H. Parkinson, K. Ito, and T. Matsui, “Absorption cross section measurements of water vapor in the wavelength region 120 to 188 nm,” *Chemical Physics*, vol. 211, pp. 387–391, Nov. 1996. DOI: [10.1016/0301-0104\(96\)00210-8](https://doi.org/10.1016/0301-0104(96)00210-8).
- [235] W. Tauchert, H. Jungblut, and W. F. Schmidt, “Photoelectric determination of  $V_0$  values and electron ranges in some cryogenic liquids,” *Canadian Journal of Chemistry*, vol. 55, no. 11, pp. 1860–1866, 1977. DOI: [10.1139/v77-260](https://doi.org/10.1139/v77-260).
- [236] E. M. Gushchin, K. A., and O. I. M., “Electron dynamics in condensed argon and xenon,” *JETP*, vol. 82, pp. 1114–1125, Apr. 1982.
- [237] S. S.-S. Huang and G. R. Freeman, “Electron mobilities in gaseous, critical, and liquid xenon: Density, electric field, and temperature effects: Quasilocal-

- ization,” *Journal of Chemical Physics*, vol. 68, pp. 1355–1362, Feb. 1978. DOI: [10.1063/1.435954](https://doi.org/10.1063/1.435954).
- [238] E. B. Wagner, F. J. Davis, and G. S. Hurst, “Time-of-Flight Investigations of Electron Transport in Some Atomic and Molecular Gases,” *Journal of Chemical Physics*, vol. 47, pp. 3138–3147, Nov. 1967. DOI: [10.1063/1.1712365](https://doi.org/10.1063/1.1712365).
- [239] J. L. Pack, R. E. Voshall, A. V. Phelps, and L. E. Kline, “Longitudinal electron diffusion coefficients in gases: Noble gases,” *Journal of Applied Physics*, vol. 71, pp. 5363–5371, Jun. 1992. DOI: [10.1063/1.350555](https://doi.org/10.1063/1.350555).
- [240] V. M. Atrazhev, A. V. Berezhnov, D. O. Dunikov, I. V. Chernysheva, V. V. Dmitrenko, and G. Kapralova, “Electron transport coefficients in liquid xenon,” in *IEEE International Conference on Dielectric Liquids, 2005. ICDL 2005.*, Jun. 2005, pp. 329–332. DOI: [10.1109/ICDL.2005.1490092](https://doi.org/10.1109/ICDL.2005.1490092).
- [241] O. Hilt and W. F. Schmidt, “Positive-hole mobility in liquid xenon as a function of temperature,” *Journal of Physics: Condensed Matter*, vol. 6, pp. L735–L738, Nov. 1994. DOI: [10.1088/0953-8984/6/47/003](https://doi.org/10.1088/0953-8984/6/47/003).
- [242] O. Hilt, W. F. Schmidt, and A. G Khrapak, “Ionic mobilities in liquid xenon,” *IEEE Transactions Dielectrics Electrical Insulation*, vol. 1, pp. 648–656, Aug. 1994. DOI: [10.1109/94.311708](https://doi.org/10.1109/94.311708).
- [243] K. Wamba *et al.*, “Mobility of thorium ions in liquid xenon,” *Nuclear Instruments and Methods in Physics Research A*, vol. 555, pp. 205–210, Dec. 2005. DOI: [10.1016/j.nima.2005.09.023](https://doi.org/10.1016/j.nima.2005.09.023).
- [244] A. J. Walters and L. W. Mitchell, “Mobility and lifetime of  $^{208}\text{Tl}$  ions in liquid xenon,” *Journal of Physics D*, vol. 36, pp. 1323–1331, Jun. 2003. DOI: [10.1088/0022-3727/36/11/313](https://doi.org/10.1088/0022-3727/36/11/313).
- [245] H. T. Davis, S. A. Rice, and L. Meyer, “On the Kinetic Theory of Dense Fluids. XIII. The Mobility of Negative Ions in Liquid Ar, Kr, Xe,” *Journal of Chemical Physics*, vol. 37, pp. 2470–2472, Nov. 1962. DOI: [10.1063/1.1733029](https://doi.org/10.1063/1.1733029).
- [246] E. Aprile, A. E. Bolotnikov, A. I. Bolozdynya, and T. Doke, *Noble Gas Detectors*. WILEY-VCH Verlag GmbH & Co. KGaA, 2006, ISBN: 978-3-527-40597-8.
- [247] F. Bloch and N. E. Bradbury, “On the Mechanism of Unimolecular Electron Capture,” *Physical Review*, vol. 48, pp. 689–695, Oct. 1935. DOI: [10.1103/PhysRev.48.689](https://doi.org/10.1103/PhysRev.48.689).

- [248] A. Herzenberg, “Attachment of Slow Electrons to Oxygen Molecules,” *Journal of Chemical Physics*, vol. 51, pp. 4942–4950, Dec. 1969. DOI: [10.1063/1.1671887](https://doi.org/10.1063/1.1671887).
- [249] N. L. Aleksandrov, “Three-body electron attachment to O<sub>2</sub>(a<sup>1</sup>Δ<sub>g</sub>)”, *Chemical Physics Letters*, vol. 212, pp. 409–412, Sep. 1993. DOI: [10.1016/0009-2614\(93\)89346-J](https://doi.org/10.1016/0009-2614(93)89346-J).
- [250] ——, “Breakup of O<sub>2</sub>-/- ions in collisions with molecules,” *High Temperature Science*, vol. 18, pp. 911–917, Mar. 1981.
- [251] N. L. Aleksandrov and E. M. Anokhin, “Low-energy electron attachment and detachment in vibrationally excited oxygen,” *Journal of Physics D*, vol. 42, no. 22, 225210, p. 225 210, Nov. 2009. DOI: [10.1088/0022-3727/42/22/225210](https://doi.org/10.1088/0022-3727/42/22/225210).
- [252] D. S. Akerib *et al.*, “<sup>83m</sup>Kr calibration of the 2013 LUX dark matter search,” *Physical Review D*, vol. 96, no. 11, 112009, p. 112 009, Dec. 2017. DOI: [10.1103/PhysRevD.96.112009](https://doi.org/10.1103/PhysRevD.96.112009).
- [253] R. Knoche, “Signal Corrections and Calibrations in the LUX Dark Matter Detector,” PhD thesis, 2016.
- [254] M. Szydagis, A. Fyhrie, D. Thorngren, and M. Tripathi, “Enhancement of NEST capabilities for simulating low-energy recoils in liquid xenon,” *Journal of Instrumentation*, vol. 8, C10003, p. C10003, Oct. 2013. DOI: [10.1088/1748-0221/8/10/C10003](https://doi.org/10.1088/1748-0221/8/10/C10003). arXiv: [1307.6601 \[physics.ins-det\]](https://arxiv.org/abs/1307.6601).
- [255] E. Aprile *et al.*, “High speed purification of Xenon and implication for ton scale detectors,” in prep.
- [256] J. F. O’Hanlon, *A User’s Guide to Vacuum Technology*, 3rd. Wiley, 2003.
- [257] D. H. Holkeboer, D. W. Jones, F. Pagano, and D. J. Santeler, “Vacuum technology and space simulation,” Aero. Vac. Corp., Troy, NY, Tech. Rep. 19660026839, Jan. 1966, p. 315. [Online]. Available: <https://ntrs.nasa.gov/search.jsp?R=19660026839>.
- [258] D. G. Bills, “Ultimate Pressure Limitations,” *Journal of Vacuum Science and Technology*, vol. 6, p. 166, Jan. 1969. DOI: [10.1116/1.1492650](https://doi.org/10.1116/1.1492650).
- [259] R. Nuvolone, “Technology of low-pressure systems-establishment of optimum conditions to obtain low degassing rates on 316 L stainless steel by heat treatments,” *Journal of Vacuum Science and Technology*, vol. 14, p. 1210, Sep. 1977. DOI: [10.1116/1.569388](https://doi.org/10.1116/1.569388).

## BIBLIOGRAPHY

---

- [260] C. J. F. Ter Braak, “A Markov Chain Monte Carlo version of the genetic algorithm Differential Evolution: easy Bayesian computing for real parameter spaces,” *Statistics and Computing*, vol. 16, no. 3, pp. 239–249, Sep. 2006, ISSN: 1573-1375. DOI: [10.1007/s11222-006-8769-1](https://doi.org/10.1007/s11222-006-8769-1).
- [261] B. Nelson, E. B. Ford, and M. J. Payne, “RUN DMC: An Efficient, Parallel Code for Analyzing Radial Velocity Observations Using N-body Integrations and Differential Evolution Markov Chain Monte Carlo,” *The Astrophysical Journal Supplemental Series*, vol. 210, 11, p. 11, Jan. 2014. DOI: [10.1088/0067-0049/210/1/11](https://doi.org/10.1088/0067-0049/210/1/11). arXiv: [1311.5229 \[astro-ph.EP\]](https://arxiv.org/abs/1311.5229).
- [262] C. J. F. ter Braak and J. A. Vrugt, “Differential Evolution Markov Chain with snooker updater and fewer chains,” *Statistics and Computing*, vol. 18, no. 4, pp. 435–446, Dec. 2008, ISSN: 1573-1375. DOI: [10.1007/s11222-008-9104-9](https://doi.org/10.1007/s11222-008-9104-9).